

FEBRUARY 2022

AJNR

VOLUME 43 • PP 159-318

AJNR

AMERICAN JOURNAL OF NEURORADIOLOGY

FEBRUARY 2022
VOLUME 43
NUMBER 2
WWW.AJNR.ORG

THE JOURNAL OF DIAGNOSTIC AND
INTERVENTIONAL NEURORADIOLOGY

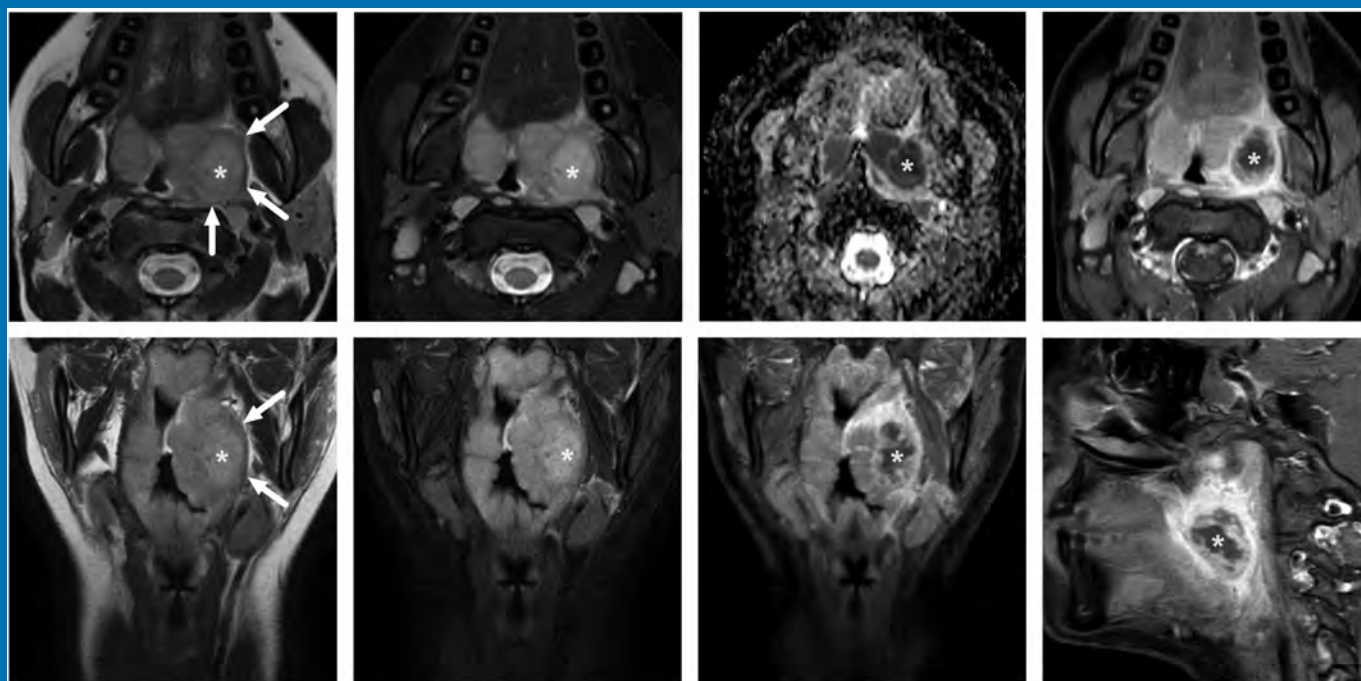
Sodium MRI at 7T for intracranial tumors

MRI of tonsillar infections

Arterial collapse during thrombectomy for stroke

Predictive value of imaging for NPH

Official Journal ASNR • ASFNR • ASHNR • ASPNR • ASSR





WEB™ Embolization: Clinically Proven

12,000 +
Patients Treated

100 +
Publications

10  **Years**
of Continuous
Innovation

 **MicroVention™**
TERUMO

microvention.com

WEB™ 17

Aneurysm Embolization System

LOWER PROFILE



NEW SIZES



MORE ACCESS OPTIONS



INDICATIONS FOR USE:

The WEB Aneurysm Embolization System is intended for the endovascular embolization of ruptured and unruptured intracranial aneurysms and other neurovascular abnormalities such as arteriovenous fistulae (AVF). The WEB Aneurysm Embolization System is also intended for vascular occlusion of blood vessels within the neurovascular system to permanently obstruct blood flow to an aneurysm or other vascular malformation.

POTENTIAL COMPLICATIONS:

Potential complications include but are not limited to the following: hematoma at the site of entry, aneurysm rupture, emboli, vessel perforation, parent artery occlusion, hemorrhage, ischemia, vasospasm, clot formation, device migration or misplacement, premature or difficult device detachment, non-detachment, incomplete aneurysm filling, revascularization, post-embolization syndrome, and neurological deficits including stroke and death. For complete indications, potential complications, warnings, precautions, and instructions, see instructions for use (IFU provided with the device).

VIA 21, 27, 33 - The VIA Microcatheter is intended for the introduction of interventional devices (such as the WEB device/stents/flow diverters) and infusion of diagnostic agents (such as contrast media) into the neuro, peripheral, and coronary vasculature.

VIA 17, 17 Preshaped - The VIA Microcatheter is intended for the introduction of interventional devices (such as the WEB device/stents/flow diverters) and infusion of diagnostic agents (such as contrast media) into the neuro, peripheral, and coronary vasculature.

The VIA Microcatheter is contraindicated for use with liquid embolic materials, such as n-butyl 2-cyanoacrylate or ethylene vinyl alcohol & DMSO (dimethyl sulfoxide).

The device should only be used by physicians who have undergone training in all aspects of the WEB Aneurysm Embolization System procedure as prescribed by the manufacturer.

RX Only: Federal law restricts this device to sale by or on the order of a physician.

For healthcare professional intended use only.



MicroVention Worldwide
Innovation Center

PH +1.714.247.8000

35 Enterprise
Aliso Viejo, CA 92656 USA
MicroVention UK Limited
MicroVention Europe, S.A.R.L.
MicroVention Deutschland GmbH
Website

PH +44 (0) 191 258 6777
PH +33 (1) 39 21 77 46
PH +49 211 210 798-0
microvention.com



WEB™ and VIA™ are registered trademarks
of Sequent Medical, Inc. in the United States.

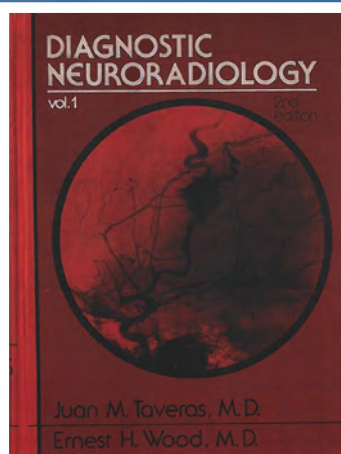
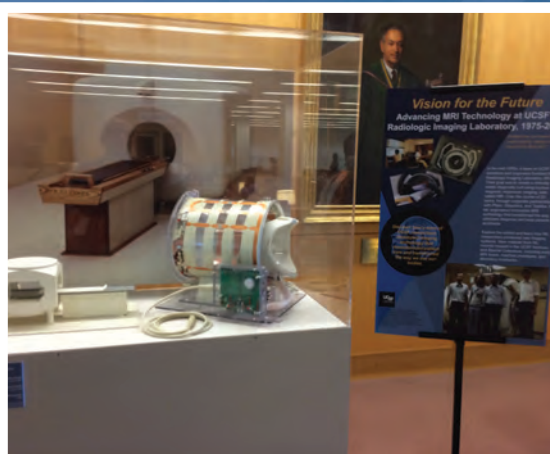
©2021 MicroVention, Inc. MM1184 WW 11/2021

Celebrating 60 Years

1962-2022

The American Society of Neuroradiology was formed on April 18, 1962, in New York City. The following purposes of the organization were unanimously adopted by the fourteen founding members:

1. To develop and support standards for the training in the practice of Neuroradiology.
2. To foster independent research in Neuroradiology.
3. To promote a closer fellowship and exchange of ideas among Neuroradiologists.



Visit www.asnr.org for more photos, videos and historical facts and be sure to follow **#ASNR60th** on social media so you don't miss a single thing. We have lots planned for 2022!

CALL FOR AJNR EDITORIAL FELLOWSHIP CANDIDATES

2022 Candidate Information and Requirements

ASNR and AJNR are pleased once again to join efforts with other imaging-related journals that have training programs on editorial aspects of publishing for trainees or junior staff (<5 years on staff), including Radiology (Olmsted fellowship), AJR (Figley and Rogers fellowships), JACR (Bruce J. Hillman fellowship), and Radiologia.

GOALS

- Increase interest in editorial and publication-related activities in younger individuals.
- Increase understanding and participation in the AJNR review process.
- Incorporate into AJNR's Editorial Board younger individuals who have previous experience in the review and publication process.
- Fill a specific need in neuroradiology not offered by other similar fellowships.
- Increase the relationship between "new" generation of neuroradiologists and more established individuals.
- Increase visibility of AJNR among younger neuroradiologists.

ACTIVITIES OF THE FELLOWSHIP

- Serve as Editorial Fellow for one year. This individual will be listed on the masthead as such.
- Review at least one manuscript per month for 12 months. Evaluate all review articles submitted to AJNR.
- Learn how electronic manuscript review systems work.
- Be involved in the final decision of selected manuscripts together with the Editor-in-Chief.
- Participate in all monthly Senior Editor telephone conference calls.
- Participate in all meetings of the Editors during the annual meetings of ASNR and RSNA and the Radiology Editors Forum as per candidate's availability. The Foundation of the ASNR will provide \$2000 funding for this activity.
- Evaluate progress and adjust program to specific needs in annual meeting or telephone conference with the Editor-in-Chief.
- Embark on an editorial scientific or bibliometric project that will lead to the submission of an article to AJNR or another appropriate journal as determined by the Editor-in-Chief. This project will be presented by the Editorial Fellow at the ASNR annual meeting.
- Recruit trainees as reviewers as determined by the Editor-in-Chief.
- Organize and host a Fellows' Journal Club podcast.
- Serve as Guest Editor for an issue of AJNR's News Digest with a timely topic.

QUALIFICATIONS

- Be a fellow in neuroradiology from North America, including Canada (this may be extended to include other countries).
- Be a junior faculty neuroradiology member (< 5 years) in either an academic or private environment.
- Be an "in-training" or member of ASNR in any other category.

APPLICATION

- Include a short letter of intent with statement of goals and desired research project. CV must be included.
- Include a letter of recommendation from the Division Chief or fellowship program director. A statement of protected time to perform the functions outlined is desirable.
- Applications will be evaluated by AJNR's Senior Editors prior to the ASNR annual meeting. The name of the selected individual will be announced at the meeting.
- Applications should be received by March 1, 2022 and sent to Ms. Karen Halm, AJNR Managing Editor, electronically at khalm@asnir.org.

AJNR *go green*

***AJNR* urges American Society of Neuroradiology members to reduce their environmental footprint by voluntarily suspending their print subscription.**

The savings in paper, printing, transportation, and postage directly fund new electronic enhancements and expanded content.

The digital edition of *AJNR* presents the print version in its entirety, along with extra features including:

- Publication Preview
- Case Collection
- Podcasts
- The *AJNR* News Digest
- The *AJNR* Blog

It also reaches subscribers much faster than print. An electronic table of contents will be sent directly to your mailbox to notify you as soon as it publishes.

Readers can search, reference, and bookmark current and archived content 24 hours a day on www.ajnr.org.

ASNR members who wish to opt out of print can do so by using the *AJNR* Go Green link on the *AJNR* Website (<http://www.ajnr.org/content/subscriber-help-and-services>). Just type your name in the email form to stop print and spare our ecosystem.

I am a trained neuroradiologist.
I am a teacher.
I am compassionate.
I am a researcher.
I am a leader.
I am part of a talented community.
I am curious.
I am a collaborative team player.
I am a volunteer.
I am ASNR.

Don't miss out on the tools, resources and relationships you've come to rely on. Log in and renew your ASNR membership today! www.asnr.org

CALL FOR AJNR EDITOR-IN-CHIEF CANDIDATES

Over the last 41 years, the editorial team of the *American Journal of Neuroradiology (AJNR)* has played a pivotal role in shaping our specialty of neuroradiology. In June 2023, Jeffrey S. Ross, MD, will complete an 8-year term as the sixth Editor-in-Chief (EIC) of the *AJNR*. He was preceded by a number of distinguished editors including our first *AJNR* EIC, Juan M. Taveras, MD (1980-1989), followed by Michael S. Huckman, MD (1990-1997), Robert M. Quencer, MD (1997-2005), Robert I. Grossman, MD (2006-2007), and Mauricio Castillo, MD (2007-2015).

We especially wish to thank Dr. Jeffrey Ross for his extraordinary dedication and exceptional contributions to the *AJNR*. Under his strong leadership, the *AJNR* remains the premier clinical neuroimaging journal with high-quality, peer-reviewed articles that serve as a beacon for achieving excellence in patient care, research, and teaching. There are an impressive 6867 subscribers across the globe: 1389 are in print and 5472 are digital.

Dr. Ross has assembled a talented international editorial board during his tenure. The *AJNR* issues 12 journals each year (± 200 pages per issue)—all with peer-reviewed articles from highly respected researchers in the field. With 1700+ papers, the number of submissions to the journal was record-breaking in 2020. Over 80 COVID-19 papers have received expedited publication to date, and more than 1300 original submissions are projected for 2021. The *AJNR* website had an incredible 11.7 million visits in 2021. There is also a strong presence on social media and subscribers may now avail themselves of an enhanced website platform. There are 3 monthly podcasts including “Issue Highlights,” “Fellows’ Journal Club,” and “Annotated Bibliography,” which offers continuing medical education. In addition, during Dr. Ross’ tenure, the Impact Factor and h-index for the journal have steadily increased and contribute to the *AJNR*’s international recognition as the leading journal for all aspects of neuroimaging research, education, and best practice.

A search for a new Editor-in-Chief will begin in early 2022.

The new Editor-in-Chief will be announced in December 2022 and will transition into the position beginning in January 2023. The actual term will begin July 1, 2023. The EIC will provide leadership and strategic vision for the journal as well as report on all editorial matters to the ASNR Board of Directors (BOD). Other responsibilities include maintaining the journal’s standard of excellence building on its reputation nationally and internationally. The EIC will be responsible for conducting, directing, and/or supervising the solicitation, evaluation, revision, and selection of all scientific and other materials to be published in the *American Journal of Neuroradiology*. The incumbent will work efficiently with the journal’s online manuscript processing system to conduct initial screening of manuscripts; make timely decisions about reviewed and revised submissions; provide constructive comments for authors as appropriate; write editorials; and meet with *AJNR* staff.

In addition, the EIC shall decide upon and approve of the content and design of tables of contents, letters to the editor, book reviews, advertisements, and other pages published in the *AJNR* as well as oversight of social media related to the journal. The EIC will also work collaboratively with the journal’s editorial board to determine the organizational structure, titles, functions, appointments, and terms of all editorial positions including reviewers, editorial advisory boards, and senior editors. The EIC may appoint senior editors who must be senior members of the ASNR. The number of senior editors shall be budgeted and approved by the ASNR BOD. Senior editors will serve at the pleasure of the EIC who shall establish the terms of service, including supervising and evaluating performance, and will exercise the right to retain or replace any senior editor as the workflow or operational demands require. The appointments of senior editors will be for a term of 1 year initially and may be extended at the discretion of the EIC.

The EIC in performing duties will observe the general Policies and Procedures established by the ASNR BOD, and will operate within the budget approved by the Board of Directors. The EIC will be consulted about, and will participate in *AJNR* operations including advertising, publication channels, expense management, and new or renewed contracts. The EIC will report regularly to the ASNR BOD and will attend Board of Director Meetings and other meetings as requested by the Executive Director. Each year the Editor will develop a budget along with the Managing Editor for approval by the ASNR Financial Management Committee and Board of Directors. This will be done in a manner consistent with the fiscal policies established by the Society.

QUALIFICATIONS OF THE SUCCESSFUL CANDIDATE INCLUDE:

- MD degree; Senior Member of ASNR in North America, neuroradiology subspecialty certification
- Familiarity with *AJNR* and its mission
- Familiarity with ASNR and its mission

- Presently or recently engaged in a leadership role in neuroradiology with broad neuroradiology knowledge
- Excellent leadership and supervisory skills to motivate and inspire professional staff as well as interpersonal skills—impartiality, diplomacy, high ethical standards and integrity including a clear understanding of the ethical guidelines established for scholarly publishing
- Leadership needed to develop and articulate a vision and the ability to inspire people with that vision
- Demonstrated track record of academic excellence including extensive experience in both publishing in and reviewing for peer-reviewed journals
- Excellent communication and writing skills and experience in critically appraising scientific articles
- Creativity and passion about finding new ways to expand the journal content
- The ability to formulate a budget and assist leadership in oversight of journal business decisions such as selecting major vendors (e.g., printing, composition, redaction, copyediting, and other technical aspects affecting journal operations), as well as expense and revenue related decisions
- Ability to appoint a strong, diverse, and representative team of editors
- High level of organizational skills
- Editorial board or prior editorial experience preferred

The term is for 5 years renewable for an additional 3 years for a total of 8 years and subject to annual review by the ASNR Board of Directors. It is expected the EIC will devote 16-20 hours per week to these duties and a stipend will be provided.

A diverse, experienced, and knowledgeable search committee has been tasked with identifying leading candidates. The search committee consists of Tina Young Poussaint, MD, FACR, Chair, Mauricio Castillo, MD, FACR, Pina Sanelli, MD, MPH, FACR, Carolyn Meltzer, MD, FACR, Erin Simon Schwartz, MD, FACR, Joshua Nickerson, MD, Courtney Tomlinson, MD, and senior editors including Harry Cloft, MD, PhD, Christopher Filippi, MD, Thierry Huisman, MD, Peter D. Chang, MD, Lubdha Shah, MD, Gregory Zaharchuk MD, PhD, C. Douglas Phillips, MD, Yvonne Lui, MD, and Bryan Comstock. The search process will include recruiting and nominating candidates, interviewing candidates, and reviewing vision statements submitted by finalists. The appointment of the new *AJNR* Editor-in-Chief will be announced in December 2022.

All interested physicians are invited to provide their curriculum vitae and a vision statement to Dr. Tina Young Poussaint, tina.poussaint@childrens.harvard.edu and Karen Halm, khalm@asn.org. To ensure a broad and diverse pool of candidates, the committee welcomes nominations from the ASNR membership. The deadline for receipt of submissions is August 1, 2022.

Tina Young Poussaint, MD, FACR
Chair, Editor-in-Chief Search Committee
President, American Society of Neuroradiology

Medtronic

Pipeline™ Flex
Embolization Device
with Shield Technology™

Take no chances

Shield Technology™
reduces material
thrombogenicity^{1,2*}

Learn more



* Data is derived from referenced pre-clinical studies and bench testing and may not be representative of clinical performance.

1. Girdhar G, Andersen A, Pangerl E, Jahanbekam R, Ubl S, Nguyen K, Wainwright J, Wolf MF. Thrombogenicity assessment of Pipeline Flex, Pipeline Shield, and FRED flow diverters in an in vitro human blood physiological flow loop model. J Biomed Mater Res A. 2018 Dec;106(12):3195-3202.doi:10.1002/jbm.a.36514. Epub 2018 Sep 22.PMID:30242950 PMCID: PMC6282594.

2. Girdhar G Li J, Kostousov L, Wainwright J, Chandler WL. In-vitro thrombogenicity assessment of flow diversion and aneurysm bridging devices. J Thromb Thrombolysis. 2015 Nov;40(4):437-43.doi:10.1007/s11239-015-1228-0. PMID:25975924.

CAUTION: Federal (USA) law restricts this device to sale, distribution and use by or on the order of a physician. Indications, contraindications, warnings and instructions for use for the Pipeline™ Flex Embolization Device with Shield Technology™ can be viewed at www.medtronic.com/manuals.

Risk may include thromboembolic complications and intracranial hemorrhage.

For more risk information, visit
www.medtronic.com/pipeline-ifu.

UC202209053 EN © 2021 Medtronic. Medtronic, Medtronic logo, and Engineering the extraordinary are trademarks of Medtronic. All other brands are trademarks of a Medtronic company. 9775 Toledo Way, Irvine, CA 92618

AJNR

AMERICAN JOURNAL OF NEURORADIOLOGY

FEBRUARY 2022
VOLUME 43
NUMBER 2
WWW.AJNR.ORG

Publication Preview at www.ajnr.org features articles released in advance of print.
Visit www.ajnrblog.org to comment on AJNR content and chat with colleagues
and AJNR's News Digest at <http://ajnrdigest.org> to read the stories behind the
latest research in neuroimaging.

159 **PERSPECTIVES** *J.P. Nickerson*

REVIEW ARTICLES

  160 **Endovascular Management of Intracranial Dural AVFs: Principles**
K.D. Bhatia, et al.

INTERVENTIONAL

  167 **Arachnoid Membranes: Crawling Back into Radiologic
Consciousness** *S. Lu, et al.*

ADULT BRAIN

PRACTICE PERSPECTIVES

176 **Optimizing Small, Low-Risk, Unruptured Intracranial Aneurysm
Treatment Using Game Theory** *A.T. Boltyenkov, et al.*

GENERAL CONTENTS

   181 **Sodium MRI at 7T for Early Response Evaluation of Intracranial Tumors
following Stereotactic Radiotherapy Using the CyberKnife**
L. Huang, et al.


**ADULT BRAIN
FUNCTIONAL**

 188 **Automated Color-Coding of Lesion Changes in Contrast-Enhanced 3D
T1-Weighted Sequences for MRI Follow-up of Brain Metastases**
D. Zopfs, et al.

ADULT BRAIN

 195 **Clinical Feasibility of Ultrafast Contrast-Enhanced T1-Weighted 3D-EPI
for Evaluating Intracranial Enhancing Lesions in Oncology Patients:
Comparison with Standard 3D MPRAGE Sequence** *K.H. Ryu, et al.*

ADULT BRAIN

 202 **Pretreatment ADC Histogram Analysis as a Prognostic Imaging
Biomarker for Patients with Recurrent Glioblastoma Treated with
Bevacizumab: A Systematic Review and Meta-analysis** *R. Kurokawa, et al.*


**ADULT BRAIN
FUNCTIONAL**

  207 **Large Culprit Plaque and More Intracranial Plaques Are Associated with
Recurrent Stroke: A Case-Control Study Using Vessel Wall Imaging**
G. Wu, et al.

ADULT BRAIN

  216 **Stroke Mimics in the Acute Setting: Role of Multimodal CT Protocol**
E. Prodi, et al.

ADULT BRAIN

 223 **Can Shunt Response in Patients with Idiopathic Normal Pressure
Hydrocephalus Be Predicted from Preoperative Brain Imaging?
A Retrospective Study of the Diagnostic Use of the Normal
Pressure Hydrocephalus Radscale in 119 Patients** *J.F. Carlsen, et al.*

ADULT BRAIN

AJNR (Am J Neuroradiol ISSN 0195–6108) is a journal published monthly, owned and published by the American Society of Neuroradiology (ASNR), 820 Jorie Boulevard, Oak Brook, IL 60523. Annual dues for the ASNR include approximately 21% for a journal subscription. The journal is printed by Intellicor Communications, 330 Eden Road, Lancaster, PA 17601; Periodicals postage paid at Oak Brook, IL and additional mailing offices. Printed in the U.S.A. POSTMASTER: Please send address changes to American Journal of Neuroradiology, P.O. Box 3000, Denville, NJ 07834, U.S.A. Subscription rates: nonmember \$430 (\$505 foreign) print and online, \$320 online only; institutions \$495 (\$565 foreign) print and basic online, \$980 (\$1050 foreign) print and extended online, \$380 online only (basic), \$825 online only (extended); single copies are \$35 each (\$40 foreign). Indexed by PubMed/MEDLINE, BIOSIS Previews, Current Contents (Clinical Medicine and Life Sciences), EMBASE, Google Scholar, HighWire Press, Q-Sensei, RefSeek, Science Citation Index, SCI Expanded, ReadCube, and Semantic Scholar. Copyright © American Society of Neuroradiology.

- 230 **Decreased Craniocervical CSF Flow in Patients with Normal Pressure Hydrocephalus: A Pilot Study** *S.M. Stöcklein, et al.* **ADULT BRAIN**
- 238 **Lesion Volume in Relapsing Multiple Sclerosis is Associated with Perivascular Space Enlargement at the Level of the Basal Ganglia** *S.C. Kolbe, et al.* **ADULT BRAIN**
- 245 **A Comparison of Global Brain Volumetrics Obtained from CT versus MRI Using 2 Publicly Available Software Packages** *S.W. Fielden, et al.* **ADULT BRAIN**
- 251 **Arterial Collapse during Thrombectomy for Stroke: Clinical Evidence and Experimental Findings in Human Brains and In Vivo Models** *Y. Liu, et al.* **INTERVENTIONAL**
- 258 **Postprocedural Thrombosis following Endovascular Treatment of Intracranial Aneurysm with Flow Diverters or Coiling: A Histologic Study** *J.A. Larco, et al.* **INTERVENTIONAL**
- 265 **Proximal Region of Carotid Atherosclerotic Plaque Shows More Intraplaque Hemorrhage: The Plaque at Risk Study** *G.A.J.C. Crombag, et al.* **EXTRACRANIAL VASCULAR**
- 272 **Impact Analysis of Different CT Configurations of Carotid Artery Plaque Calcifications on Cerebrovascular Events** *L. Saba, et al.* **EXTRACRANIAL VASCULAR**
- 280 **Thin-Slice Pituitary MRI with Deep Learning–Based Reconstruction for Preoperative Prediction of Cavernous Sinus Invasion by Pituitary Adenoma: A Prospective Study** *M. Kim, et al.* **HEAD & NECK FUNCTIONAL**
- 286 **MRI Findings in Acute Tonsillar Infections** *J. Heikkinen, et al.* **HEAD & NECK**
- 292 **Morphologic Variants of the Hand Motor Cortex in Developing Brains from Neonates through Childhood Assessed by MR Imaging** *F. Wu, et al.* **PEDIATRICS**
- 299 **Pretreatment Normal WM Magnetization Transfer Ratio Predicts Risk of Radiation Necrosis in Patients with Medulloblastoma** *J.H. Harrel, et al.* **PEDIATRICS FUNCTIONAL**
- 304 **Features of Visually AcceSABle Rembrandt Images: Interrater Reliability in Pediatric Brain Tumors** *A. Biswas, et al.* **PEDIATRICS**
- 309 **Re-Examining the Cochlea in Branchio-Oto-Renal Syndrome: Genotype-Phenotype Correlation** *J. Pao, et al.* **PEDIATRICS**
- 315 **Rates of Epidural Blood Patch following Lumbar Puncture Comparing Atraumatic versus Bevel-Tip Needles Stratified for Body Mass Index** *J.T. Philip, et al.* **SPINE**

ONLINE FEATURES

LETTERS

- E1 **MRI Shrimp Sign in Sarcoidosis-Associated Cerebellar Progressive Multifocal Leukoencephalopathy** *P. Anand, et al.*

BOOK REVIEWS *R.M. Quencer, Section Editor*

Please visit www.ajnrblog.org to read and comment on Book Reviews.



Images of an uncomplicated peritonsillar abscess from Heikkinen, et al, in this issue.



Indicates Editor's Choices selection



Indicates Fellows' Journal Club selection



Indicates open access to non-subscribers at www.ajnr.org



Indicates article with supplemental online data



Indicates article with supplemental online video



Evidence-Based Medicine Level 1



Evidence-Based Medicine Level 2

EDITOR-IN-CHIEF

Jeffrey S. Ross, MD

Professor of Radiology, Department of Radiology,
Mayo Clinic College of Medicine, Phoenix, AZ

SENIOR EDITORS

Harry J. Cloft, MD, PhD

Professor of Radiology and Neurosurgery,
Department of Radiology, Mayo Clinic College of
Medicine, Rochester, MN

Christopher G. Filippi, MD

Professor and Alice Ettinger-Jack R. Dreyfuss
Chair of Radiology,
Tufts University School of Medicine,
Radiologist-in-Chief
Tufts University Medical Center, Boston, MA

Thierry A.G.M. Huisman, MD

Radiologist-in-Chief, Texas Children's Hospital,
Houston, TX

Yvonne W. Lui, MD

Associate Professor of Radiology,
Chief of Neuroradiology,
New York University School of Medicine,
New York, NY

C.D. Phillips, MD, FACR

Professor of Radiology, Weill Cornell Medical
College, Director of Head and Neck Imaging,
New York-Presbyterian Hospital, New York, NY

Lubdhra M. Shah, MD, MS

Professor of Radiology and Director of Spine
Imaging, University of Utah Department of
Radiology and Imaging Sciences, Salt Lake City, UT

STATISTICAL SENIOR EDITOR

Bryan A. Comstock, MS

Senior Biostatistician,
Department of Biostatistics,
University of Washington, Seattle, WA

ARTIFICIAL INTELLIGENCE DEPUTY EDITOR

Peter D. Chang, MD

Assistant Professor-in-Residence,
Departments of Radiological Sciences,
Computer Sciences, and Pathology,
Director, Center for Artificial Intelligence in
Diagnostic Medicine (CAIDM),
University of California, Irvine, Irvine, CA

EDITORIAL BOARD

Ashley H. Aiken, Atlanta, GA

Lea M. Alhilali, Phoenix, AZ

Mohammed A. Almekhlafi, Calgary, Alberta,
Canada

Joachim Berkefeld, Frankfurt, Germany

Aashim Bhatia, Pittsburgh, PA

Waleed Brinjikji, Rochester, MN

Judah Burns, New York, NY

Danielle Byrne, Dublin, Ireland

Federico Cagnazzo, Montpellier, France

J. Levi Chazen, New York, NY

James Y. Chen, San Diego, CA

Gloria C. Chiang, New York, NY

Daniel Chow, Irvine, CA

Kars C.J. Compagne, Rotterdam, The Netherlands

Arturo Consoli, Suresnes, France

Seena Dehkharghani, New York, NY

Nilesh K. Desai, Houston, TX

Yonghong Ding, Rochester, MN

Birgit Ertl-Wagner, Toronto, Ontario, Canada

Clifford J. Eskey, Hanover, NH

Massimo Filippi, Milan, Italy

Nils D. Forkert, Calgary, Alberta, Canada

Ana M. Franceschi, New York, NY

Frank Gaillard, Melbourne, Australia

Joseph J. Gemmete, Ann Arbor, Michigan

Wende N. Gibbs, Phoenix, AZ

Philipp Gölitz, Erlangen, Germany

Brent Griffith, Detroit, MI

Joseph M. Hoxworth, Phoenix, Arizona

Raymond Y. Huang, Boston, MA

Gábor Janiga, Magdeburg, Germany

Christof Karmonik, Houston, TX

Timothy J. Kaufmann, Rochester, MN

Hillary R. Kelly, Boston, MA

Toshiumi Kinoshita, Akita, Japan

Alexander W. Korutz, Chicago, IL

Stephen F. Kralik, Houston, TX

Alexander Lerner, Los Angeles, CA

Yinsheng Li, Madison, WI

Franklin A. Marden, Chicago, IL

Markus A. Möhlenbruch, Heidelberg, Germany

Kambiz Nael, Los Angeles, CA

Renato Hoffmann Nunes, Sao Paulo, Brazil

Sasan Partovi, Cleveland, OH

Johannes A.R. Pfaff, Salzburg, Austria

Laurent Pierot, Reims, France

Alireza Radmanesh, New York, NY

Prashant Raghavan, Baltimore, MD

Eytan Raz, New York, NY

Paul M. Ruggieri, Cleveland, OH

Sebastian Schafer, Madison, WI

Maksim Shapiro, New York, NY

Timothy Shepherd, New York, NY

James Shin, New York, NY

Mark S. Shiroishi, Los Angeles, CA

Bruno P. Soares, Baltimore, MD

Jason F. Talbot, San Francisco, CA

Ruth Thiex, Everett, Washington

Vincent Thijs, Melbourne, Victoria, Australia

Anderanik Tomasian, Los Angeles, CA

Fabio Triulzi, Milan, Italy

Anja G. van der Kolk, Utrecht, the Netherlands

Arastoo Vossough, Philadelphia, PA

Elysa Widjaja, Toronto, Ontario, Canada

Leonard Yeo, Singapore

Woong Yoon, Gwangju, South Korea

David M. Yousem, Evergreen, CO

Carlos Zamora, Chapel Hill, NC

Chengcheng Zhu, Seattle, WA

EDITORIAL FELLOW

Vivek Yedavalli, Baltimore, MD

SPECIAL CONSULTANTS TO THE EDITOR

AJNR Blog Editor

Neil Lall, Denver, CO

Case of the Month Editor

Nicholas Stence, Aurora, CO

Case of the Week Editors

Matylda Machnowska, Toronto, Ontario, Canada

Anvita Pauranik, Calgary, Alberta, Canada

Vinil Shah, San Francisco, CA

Classic Case Editor

Sandy Cheng-Yu Chen, Taipei, Taiwan

Health Care and Socioeconomics Editor

Pina C. Sanelli, New York, NY

Physics Editor

Greg Zaharchuk, Stanford, CA

Podcast Editor

Courtney Tomblinson, Nashville, TN

Deputy Podcast Editor

Kevin Hiatt, Winston-Salem, NC

Twitter Editor

Jacob Ormsby, Albuquerque, New Mexico

Official Journal:

American Society of Neuroradiology

American Society of Functional Neuroradiology

American Society of Head and Neck Radiology

American Society of Pediatric Neuroradiology

American Society of Spine Radiology

Founding Editor

Juan M. Taveras

Editors Emeriti

Mauricio Castillo, Robert I. Grossman,

Michael S. Huckabee, Robert M. Quencer

Managing Editor

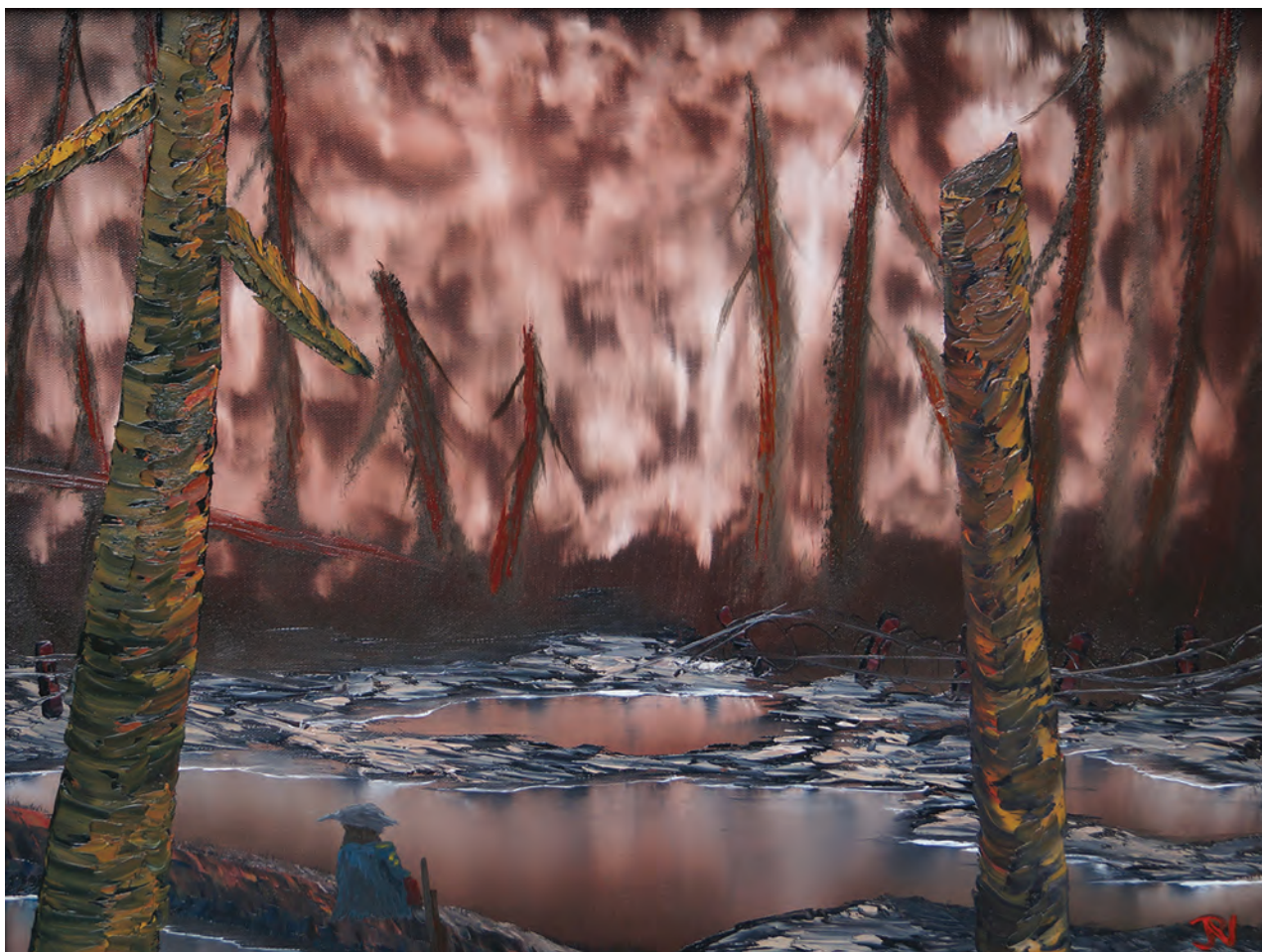
Karen Halm

Assistant Managing Editor

Laura Wilhelm

Executive Director, ASNR

Mary Beth Hepp



Title: Argonne Forest 1918. This oil on canvas painting measures 18" by 24" and depicts a solitary soldier amidst the hellscape of devastation wrought on the battlefields of the First World War. Now 103 years in the past, the Meuse-Argonne offensive was a part of the endgame leading to the November 11th armistice. To this day it remains the deadliest battle in American history with over 350,000 casualties between all participants. The "shell-shock" of World War I would eventually lead to our understanding today of posttraumatic stress disorder. Of note, the newly discovered x-rays were used for the first time on a battlefield to identify bullet fragments in wounded soldiers during the Great War.

Joshua P. Nickerson, MD, Associate Professor of Radiology, Division Chief of Neuroradiology, Oregon Health & Sciences University, Portland, Oregon

Endovascular Management of Intracranial Dural AVFs: Principles

 K.D. Bhatia,  H. Lee,  H. Kortman,  J. Klostranec,  W. Guest,  T. Wälchli,  I. Radovanovic,  T. Krings, and  V.M. Pereira



ABSTRACT

SUMMARY: Intracranial dural AVFs are abnormal communications between arteries that supply the dura mater and draining cortical veins or venous sinuses. They are believed to form as a response to venous insults such as thrombosis, trauma, or infection. Classification and management are dependent on the presence of drainage/reflux into cortical veins because such drainage markedly elevates the risk of hemorrhage or venous congestion, resulting in neurologic deficits. AVFs with tolerable symptoms and benign drainage patterns can be managed conservatively. Intolerable symptoms, presentation with hemorrhage/neurologic deficits, or aggressive drainage patterns are indications for intervention. Treatment options include microsurgical disconnection, endovascular transarterial embolization, transvenous embolization, or a combination. This is the first in a series of 3 articles on endovascular management of intracranial dural AVFs, in which we outline the principles and outcomes of endovascular treatment.

ABBREVIATIONS: dAVF = dural AVF; ECA = external carotid artery; GKRS = gamma knife radiosurgery; TA = transarterial; TV = transvenous

This is the first in a series of 3 articles on the endovascular management of intracranial dural AVFs (dAVFs) based on our experience in treating these lesions during the past 25 years at Toronto Western Hospital. In this introductory article, we outline the epidemiology, classification, diagnosis, and management principles. In the following 2 articles, we detail the principles of transarterial and transvenous embolization, respectively.

Definition

Intracranial dAVFs are abnormal direct vascular communications between arteries that supply the dura mater and draining cortical veins or dural venous sinuses, without a normal intervening capillary network.¹⁻³


Arterial supply may be composed of a single feeder or multiple feeders.^{1,2} The supplying arteries most often originate external to the dura mater (eg, the middle meningeal artery arising from the internal maxillary artery)¹ but can less commonly arise from intradural pial artery branches, which are known to supply dural structures (eg, the artery of Davidoff and Schechter arising from the posterior cerebral artery and supplying the inferior medial tentorium).⁴⁻⁷ Secondary induced pial supply from vessels that do not normally supply the dura is well-described in the literature;⁴ however, if these vessels are the sole arterial supply, the lesion is, by definition, a pial vascular malformation rather than a dAVF.^{1,4}

Venous drainage can be directly into cortical veins, directly into the dural venous sinuses, or into dural venous sinuses with reflux into the cortical veins.^{2,3,8} Possible arterial supply and venous drainage patterns are demonstrated in Fig 1.

Received February 2, 2021; accepted after revision July 7.

From the Divisions of Neuroradiology (K.D.B., H.L., H.K., J.K., W.G., T.K., V.M.P.) and Neurosurgery (T.W., I.R., T.K., V.M.P.), Toronto Western Hospital, Toronto, Ontario, Canada; Department of Medical Imaging (K.D.B.), Sydney Children's Hospital Network, Westmead, New South Wales, Australia; Division of Paediatrics (K.D.B.), Faculty of Medicine, University of Sydney, Camperdown, New South Wales, Australia; Division of Paediatrics (K.D.B.), Faculty of Medicine, University of New South Wales, Kensington, New South Wales, Australia; and Division of Medical Imaging (K.D.B.), Faculty of Medicine, Macquarie University, Macquarie Park, New South Wales, Australia.

Please address correspondence to Kartik Dev Bhatia, MD, Department of Medical Imaging, Sydney Children's Hospital Network, Corner Hawkesbury Rd and Hainsworth St, Westmead, NSW, 2145, Australia; e-mail: kartikdevbhatia@gmail.com

 Indicates open access to non-subscribers at www.ajnr.org

 Indicates article with supplemental on-line appendix.

<http://dx.doi.org/10.3174/ajnr.A7304>

Epidemiology

Intracranial dAVFs are rare lesions with a detection rate of <1 per 100,000 persons in any given year across a variety of populations (0.16–0.51).⁹⁻¹¹ Clinical presentation is most often between 50 and 70 years of age, and there is a mild female predominance (female/male ratio, 11:9).⁹⁻¹² dAVFs represent approximately 10%–15% of all intracranial vascular malformations.^{1,9,13} The most common locations (in descending order) are the transverse-sigmoid sinus, cavernous sinus, and tentorium.^{2,11,12,14}

Intracranial hemorrhage is the initial clinical presentation in 12%–18% of cases.^{2,11,12,14} Risk factors for hemorrhagic presentation (in descending order of risk) include previous hemorrhage, cortical

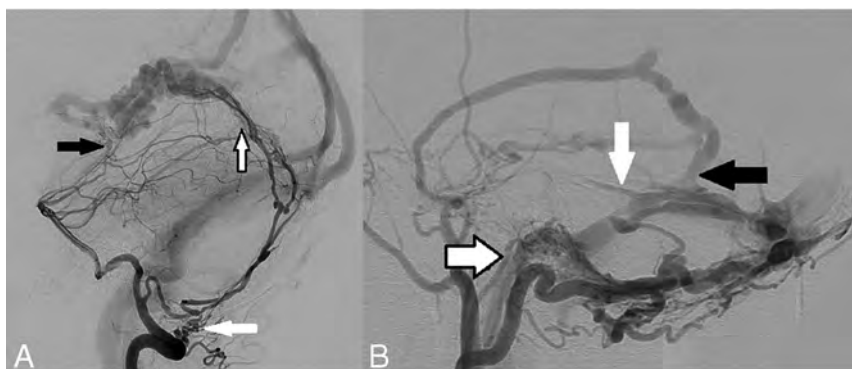


FIG 1. Arterial supply and venous drainage patterns in dAVFs. A, Arterial supply: Left vertebral artery angiogram in a lateral projection shows a falcotentorial dAVF with all 3 different forms of arterial supply: 1) extracranial origin of a dural artery: left posterior meningeal artery arising from the extracranial distal V3 segment of the left vertebral artery (*white arrow*) and providing posterior supply to the fistula via the artery of the falx cerebelli; 2) intradural origin of a dural artery: Artery of Davidoff and Schechter arising from the P1–2 junction of the left posterior cerebral artery, traveling along the free edge of the tentorium cerebelli and supplying the AVF from its undersurface (*black arrow*); 3) secondary-induced pial artery supply: several small, irregular, induced pial branches from the distal aspect of the left superior cerebellar artery supplying the posterior aspect of the fistula (*black border arrow*). Reproduced from Bhatia K et al.⁷ B, Venous drainage: Left external carotid artery angiogram in a lateral projection in a patient with multiple intracranial dAVFs demonstrates different patterns of venous drainage. A large left transverse sinus fistula is present with supply from an enlarged squamous temporal branch of the middle meningeal artery and draining directly into the transverse sinus (*black arrow*). There is sinus reflux of contrast into the torcula (Cognard IIa) and cortical venous reflux into the vein of Labbe (*white arrow*, Cognard IIb). This is a Cognard IIa+b AVF. A left condylar fistula is also present with arterial supply from the jugular branch of the left ascending pharyngeal artery (*black border arrow*) and draining directly into a condylar vein (direct cortical venous drainage). This is a Cognard III AVF.

venous reflux, cortical venous ectasia, location (craniocervical junction, tentorium, transverse-sigmoid sinus, anterior cranial fossa, superior sagittal sinus), and male sex.^{2,8,12} Nonhemorrhagic neurologic deficits (including focal deficits, encephalopathy, and seizures) represent 12%–20% of clinical presentations and are also associated with cortical venous reflux and intracranial venous hypertension.^{8,12,14} Direct cortical venous drainage, cortical venous reflux, and hemorrhagic presentation are more common in men.^{2,8}

The pathogenesis of dural AVFs is debated, but pathology involving the intracranial venous system appears to play a central role.¹³ Such pathology can include prothrombotic disorders and hormonal states predisposing to venous sinus occlusion (including pregnancy), previous cranial surgery, trauma, chronic venous hypertension, and infection such as mastoiditis adjacent to the sigmoid sinus.^{15,16} Venous sinus thrombosis with venous hypertension is thought to promote formation of dural AVFs via ischemia-related angiogenesis.¹⁷

Classification

Both Cognard et al² and Borden et al³ demonstrated that the natural history of dAVFs was related to the pattern of venous drainage, and this was the basis for their respective classification systems. In both classification systems, dAVFs can be broadly divided into benign (Borden I, Cognard I–IIa) and aggressive (Borden II–III, Cognard IIb–V) patterns of venous drainage (Table).^{2,3} Benign venous drainage is characterized by drainage

into the dural venous sinuses without cortical venous reflux. Aggressive venous drainage is characterized by cortical venous reflux (Borden II, Cognard IIb) or direct cortical venous drainage \pm ectasia (Borden III, Cognard III–IV). An aggressive venographic pattern strongly correlates with and predicts the occurrence of intracranial hemorrhage and nonhemorrhagic neurologic deficits.^{2,3,8} These venous drainage patterns are demonstrated in Fig 1B.

In addition to the above classification schemes based on the presence of venous reflux, dAVFs can also be classified on the basis of their anatomic location and the embryologic epidural compartment into which they drain. The Lasjaunias-Geibprasert classification system was proposed in 2008, dividing cranial and spinal dAVFs into 3 embryologically determined epidural drainage compartments (ventral, dorsal, and lateral epidural types).¹⁸ Each of these drainage patterns are associated with differing sex distributions, rates of cortical venous reflux, and clinical presentations (benign versus aggressive).¹⁸ The utility of this classification system is the ability

to understand the anatomic-embryologic basis for the aggressive behavior of a dAVF and to help predict the natural history based on location. Therefore, it does not replace the important Borden or Cognard systems, but rather provides additional information.

Ventral epidural drainage (eg, basiocciput, sigmoid sinus) involves drainage toward the extracranial ventral venous plexuses, is more common in women, and has a more benign presentation. Dorsal epidural drainage (eg, transverse sinus, superior sagittal sinus) typically involves drainage into dural venous sinuses. Lateral epidural drainage (eg, petrous, ethmoid, falcotentorial junction) is the most aggressive group due to drainage directly into cortical veins.¹⁸ These lateral epidural locations are more commonly affected in men.^{12,19,20} Therefore, the higher rate of hemorrhagic presentation in men may be explained by the relatively sex-specific anatomic distribution of dAVFs and aggressive venous drainage patterns seen in the lateral epidural group.^{2,8,18}

Natural History

In benign dAVFs (Borden I, Cognard I–IIa), Gross and Du,⁸ in 2012, demonstrated no intracranial hemorrhages or new neurologic deficits during 409 lesion-years of follow-up. This was consistent with the original findings of Cognard et al,² in 1995, who reported nonaggressive clinical presentations in 83 of 84 patients with type I dAVFs and no intracranial hemorrhages in 111 patients with type I–IIa dAVFs. Asymptomatic or minimally

Venous drainage pattern classification in intracranial dAVFs

	Classification of Borden et al ³		Classification of Cognard et al ²	
Benign venous drainage patterns	I	Drains to dural sinus No CVR	I	Drains to dural sinus No sinus reflux No CVR
			IIa	Drains to dural sinus Sinus reflux present No CVR
Aggressive venous drainage patterns	II	Drains to dural sinus CVR present	IIb	Drains to dural sinus No sinus reflux CVR present
			IIa + b	Drains to dural sinus Sinus reflux present CVR present
	III	Direct drainage to cortical veins Or Drainage to an isolated segment of dural sinus	III	Direct drainage to cortical veins No venous ectasia
			IV	Direct drainage to cortical veins Venous ectasia present
			V	Spinal perimedullary venous drainage

Note:—CVR indicates cortical venous reflux.

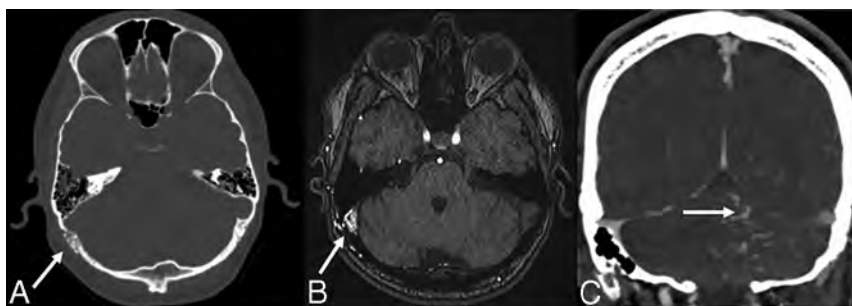


FIG 2. Noninvasive imaging characteristics of dAVFs. A, Axial bone window noncontrast CT image of a patient with a right transverse-sigmoid sinus dAVF demonstrates enlarged right retro-mastoid transosseous vascular channels from occipital artery feeders (*white arrow*). B, Axial TOF-MRA image in the same patient demonstrates abnormal hyperintense signal in the right transverse-sigmoid sinus junction (*white arrow*) due to arterialization of the sinus, with adjacent asymmetrically enlarged occipital artery feeders. C, Coronal contrast-enhanced CT image in a patient with a left transverse sinus dAVF demonstrates enlarged tortuous pial veins over the left cerebellum (*white arrow*), resulting from cortical venous reflux.

symptomatic patients, regardless of classification status, have a low annual hemorrhage risk of 2%.⁸

On the other hand, the odds ratio of intracranial hemorrhage in patients with cortical venous reflux is 17.5.¹² The Toronto Brain Vascular Malformation Study Group previously reported clinical outcomes in untreated or undertreated patients with cortical venous reflux, identifying an annual nonhemorrhagic neurologic deficit rate of 6.9%, an annual hemorrhage rate of 8.1%, an annual mortality rate of 10.4%, and a total annual event rate of 15%.²¹

Studies on the natural history of dAVFs stratified by venous drainage patterns report annual hemorrhage rates of 6% with cortical venous reflux, 10% with direct cortical venous drainage, and 21% with cortical venous ectasia.⁸ A nonhemorrhagic neurologic deficit at initial presentation is associated with a 10% annual hemorrhage rate and an initial hemorrhagic presentation with a 46% future annual hemorrhage rate.⁸ The highest risk period for rebleeding is within the first 2 weeks after the initial hemorrhage (up to 35%),²² suggesting that these patients should be treated more acutely.

Diagnosis

Consideration of a diagnosis of dAVF may be based initially on the clinical presentation and noncontrast imaging findings. Clinical presentations of non-hemorrhagic dAVFs include pulsatile tinnitus (particularly for lesions adjacent to the petrous bone or transverse-sigmoid sinus),²³ chemosis and proptosis (for carotid cavernous fistulas due to congestion of the ophthalmic veins),²⁴ progressive early-onset dementia (due to congestion of the deep venous system of the diencephalon and striatum),²⁵ and seizures (due to congestion of the superficial venous system of the cortex).² A background history of dural venous sinus thrombosis, intracranial infection, cranial surgery, or head trauma may also be suggestive.¹³ Hemorrhagic

presentation is typically with sudden onset of severe headache, seizures, focal neurologic deficits, or loss of consciousness.¹³

Noncontrast Imaging. Noncontrast imaging findings suggestive of a nonhemorrhagic dAVF include serpiginous dilated cortical veins (mildly hyperattenuating on noncontrast CT, hypointense T2/FLAIR flow voids on MR imaging), vasogenic edema secondary to venous congestion, and dilated transosseous vascular channels (particularly in the temporal and occipital bones) best appreciated on the bone window settings of CT imaging (Fig 2A).^{26,27} This latter finding is also useful to distinguish a pial vascular malformation from a dAVF (because only the latter would be supplied by enlarged transosseous arterial vessels).²⁷

Clinical presentation of nonhemorrhagic dAVFs with seizures is typically associated with superficial venous congestion, which, on noninvasive imaging, is characterized by vasogenic edema in the subcortical white matter and enlarged T2 FLAIR serpiginous flow voids over the cerebral convexities.² Clinical presentation

with dementia is typically associated with deep venous congestion, characterized by edema in the thalami/basal ganglia, as well as ventriculomegaly.²⁵ Pulsatile tinnitus as a presenting symptom usually indicates proximity of the fistula to the petrous temporal bone or sigmoid sinus and is seen with fistulas involving the transverse-sigmoid sinuses, petrous ridge, or hypoglossal canal.²³ Proptosis and chemosis, usually associated with carotid cavernous dAVFs, will typically manifest on imaging with enlarged superior ophthalmic veins.²⁴

Noncontrast imaging findings in hemorrhagic dAVFs can include subdural, subarachnoid, intraparenchymal, and/or intraventricular hemorrhage.²⁸ A particularly suggestive finding is the combination of subdural and intraparenchymal hemorrhage; this pattern occurs most commonly with traumatic brain injury; but outside the setting of trauma, it should raise suspicion of a dAVF.²⁸⁻³⁰ Aneurysmal or parenchymal AVMs related to hemorrhage may involve the intraparenchymal and subarachnoid spaces but usually do not rupture the arachnoid mater to enter the subdural space.²⁸ In dAVFs, however, enlarged cortical veins traverse the subarachnoid and subdural spaces; thus, venous rupture can be associated with this otherwise uncommon pattern outside the setting of trauma.^{29,30}

TOF-MRA is a useful initial vascular imaging technique for detection of high-flow dAVFs.³¹ The typical suppression of caudally directed venous flow undertaken to acquire TOF-MRA without venous contamination is useful in detecting abnormal early venous filling as a result of dAVFs.³² High-flow AVFs, as a result of transmission of intravascular protons that have undergone excitation in a caudal section directly into cortical veins or dural venous sinuses, can thus result in abnormal hyperintense signal within intracranial venous structures.³³ Examples of this are demonstrated in Figs 2B and 3D.

Contrast-Enhanced Noninvasive Imaging. CT angiography and gadolinium-enhanced MR angiography are useful in demonstrating early venous filling in dAVFs but require precise timing of image acquisition relative to the administration of the contrast bolus to ensure that venous enhancement is truly a result of arteriovenous shunting rather than venous contamination from late timing.³⁴ A classic imaging finding in carotid cavernous fistulas is asymmetric cavernous sinus enhancement on CT angiography, often in association with enlargement of the superior ophthalmic vein.³⁵ Contrast-enhanced CT and MR imaging are also both useful for demonstrating venous congestion and indirect evidence of cortical venous reflux, characterized by enlarged tortuous pial veins over the cerebral or cerebellar convexities (Fig 2C). The presence of venous congestion and cortical venous reflux would also be supported by ipsilateral white matter vasogenic edema and enlarged serpiginous surface vessels on precontrast CT or T2 FLAIR sequences.

Time-resolved gadolinium-enhanced MR angiography is a particularly useful noninvasive imaging tool for the characterization of dAVFs because it allows assessment of the contrast bolus in multiple phases.³⁶ The use of 4D CTA is also increasing for this diagnostic purpose.³⁷

DSA. Ultimately, DSA is the criterion standard for the diagnosis and assessment of dAVFs.³⁸ In our practice, we use 6-vessel

cerebral angiography, including assessment of the upper neck and facial structures within the FOV as appropriate, to ensure identification of all the important arterial feeders to the AVF and to fully appreciate the venous drainage pattern and impact on the venous drainage of the normal brain parenchyma. In addition, we use a magnified high-frame-rate (typically 6 frames per second) DSA centered on the fistulous point to fully understand the angioanatomy, architecture, and flow dynamics of the fistula. The use of 3D rotational angiography with reconstruction of the volumetric acquisition in multiple planes (essentially creating a cone-beam CTA with intra-arterial injection), timed to demonstrate the arterial feeders and the venous drainage pathway, allows detailed assessment of all arterial feeders and their relationship to the skull base foramina.³⁹ A sample case involving the facial arcade is demonstrated in Fig 3.

These additional techniques allow us to identify external carotid artery (ECA)-ICA anastomoses and cranial nerve arterial supplies that may be at risk during endovascular treatment and thus reduce our treatment-related risk profile. Selective injection of the ascending pharyngeal artery, occipital artery, and/or the internal maxillary artery is often useful (in combination with selective 3D rotational angiography) to demonstrate important arterial feeders that may not be appreciated when there is shunting across multiple other arterial supply points.⁴⁰ An example of the utility of such selective injection is for identification of the facial nerve arterial arcade (in particular the petrous branch of the middle meningeal artery) via internal maxillary or middle meningeal artery injection for assessment of petrous AVFs,⁴¹ in which there are often multiple competing occipital artery feeders obscuring the arcade on more proximal ECA injections. The utility of 3D rotational angiography is demonstrated in Fig 3B, -C.

Management

Our management of dAVFs is guided by 2 main principles:

1. Detailed anatomic assessment (based on DSA findings)
2. Multidisciplinary discussion.

Detailed Anatomic Assessment. We undertake detailed anatomic assessment of the DSA imaging (including 3D rotational angiography with MPRs) to assist in management decision-making via a 4-step process:

1. Benign vs aggressive: We determine whether the AVF is angiographically benign or aggressive on the basis of the absence or presence of cortical venous reflux/drainage.
2. Arterial supply and venous drainage: We determine all visible arterial supplies to the AVF, the location of the fistulous point, and the primary venous drainage points. Cure of the AVF via embolization will be dependent on successful occlusion of the fistulous point and the foot of the draining vein.
3. Risk from a transarterial (TA) embolization approach: Based on the arterial supply, we determine the risk of cranial nerve palsy or potential embolization across ECA-ICA anastomoses that would be associated with a TA embolization approach (eg, an AVF supplied primarily by branches of the neuromeningeal division of the ascending pharyngeal artery would pose a high risk of cranial nerve IX, X, and XII palsy via a transarterial

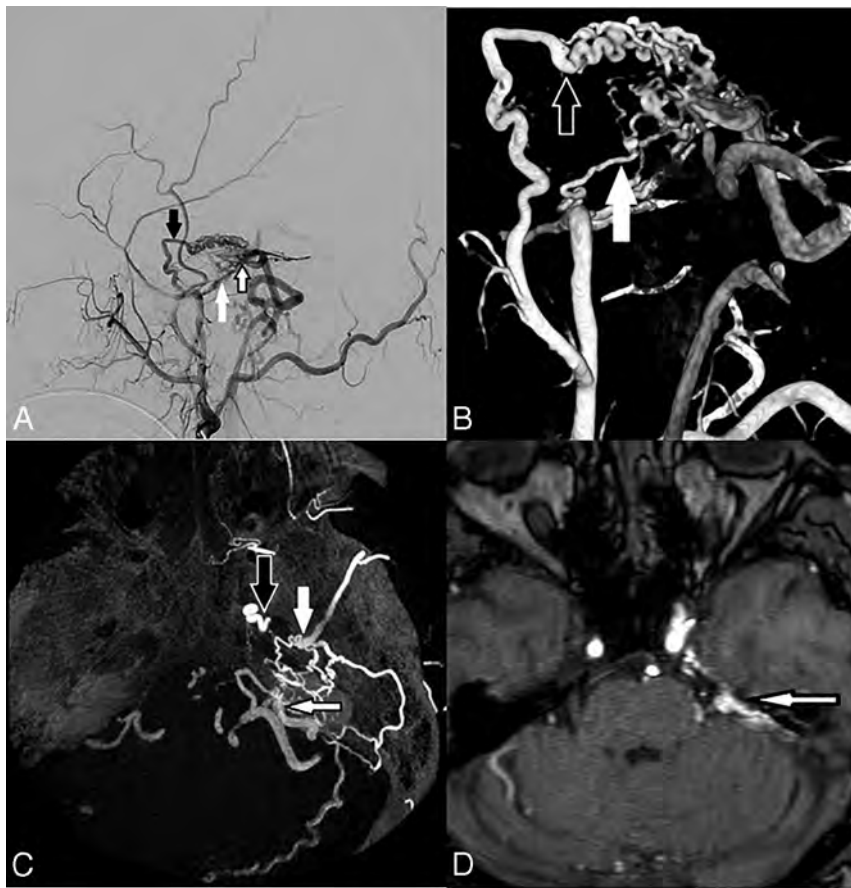


FIG 3. Angiographic assessment of a left petrous dAVF. *A*, Lateral projection DSA of a left ECA injection shows arterial supply to the AVF by the petrous branch of the middle meningeal artery (white arrow), a component of the facial nerve arterial arcade, by the accessory meningeal artery (black arrow) with an intervening nidus before the venous drainage and the fistula draining into the petrosal vein (black-border arrow) over the posterior superior surface of the left petrous temporal bone. *B*, 3D rotational DSA via a left ECA injection in the lateral projection reconstruction again shows the petrous branch of the left middle meningeal artery (white arrow) and the accessory meningeal artery (white border arrow) entering a nidal network before the fistulous point. *C*, Reconstructed axial MPR MIP image of a 3D rotational DSA via a left ECA injection demonstrates, in exquisite anatomic detail, the petrous branch of the left middle meningeal artery extending posteriorly from the foramen spinosum over the petrous temporal bone (white arrow), accessory meningeal artery entering via foramen ovale (black arrow), and the draining petrosal vein (black border arrow). This level of anatomic detail and spatial relationship to the skull base foramina is difficult to appreciate on standard DSA images, and this allows assessment of the potential risks of facial nerve ischemia that may be associated with a transarterial approach. *D*, Axial TOF-MRA image demonstrates pathologic hyperintense signal in the left petrosal vein (black border arrow) due to pre-excited protons entering via the high-flow left petrosal dAVF. *A–C*, Reproduced from the supplemental material of Bhatia et al.⁴¹

approach). These risks are discussed in detail in the second article of this series focused on TA embolization.

4. Risk from a transvenous (TV) embolization approach: Based on the venous drainage pattern, we determine the risk of intracranial hemorrhage, venous infarction, or long-term intracranial venous hypertension that would be associated with a TV embolization approach (eg, in a patient with a single/dominant transverse sinus, coil occlusion of that sinus for treatment of an AVF may pose a long-term risk of venous hypertension). These risks are discussed in detail in the third article of this series focused on TV embolization.

Multidisciplinary Discussion. We discuss all new AVF cases at our monthly multidisciplinary neurovascular meeting, attended by interventional neuro-radiologists, cerebrovascular surgeons, vascular neurologists, and gamma knife radiosurgeons. In emergent cases requiring more rapid decision-making (eg, clinical presentation with intracranial hemorrhage or progressive nonhemorrhagic neurologic deficits), the management discussion is undertaken acutely among the admitting cerebrovascular surgeon, the on-call interventional neuroradiologist, and, when appropriate (eg, presentation with seizures), the treating vascular neurologist. The advantages of multidisciplinary discussion include the potential range of management options that can be considered as well as engagement of all relevant specialties early in the treatment course.

Decision to Offer Interventional Treatment. The first and most important decision made during the multidisciplinary discussion is whether the patient requires interventional treatment of the AVF or conservative management with clinical and imaging follow-up. This decision is based primarily on the venous drainage pattern and the associated natural history, ie, whether the AVF has a benign or aggressive venous drainage pattern. All patients with aggressive venous drainage patterns should be offered treatment because of the poor natural history.

In patients with benign drainage patterns, interventional treatment may still be offered if the symptoms cause significant functional disability and the patient is willing to accept the risks of intervention to reduce that disability

(eg, severe pulsatile tinnitus can interfere with sleep and quality of life, in some cases contributing to mood disorders and even suicide). For patients with benign drainage patterns and tolerable symptoms, we recommend conservative management with annual clinical and imaging follow-up (because benign drainage patterns can transform into aggressive patterns with time in approximately 2%–4% of patients).^{2,8,13,20}

The major risk factor for conversion from benign to aggressive drainage is spontaneous thrombosis of the ipsilateral draining vein, which may be heralded by a change (increase or decrease) in the patient's symptoms.^{2,13,20} Such change in symptoms warrants

earlier follow-up and imaging.² In our practice, we use contrast-enhanced time-resolved MR angiography for follow-up of conservatively managed patients because it allows noninvasive assessment of the intracranial circulation in multiple phases and has a high sensitivity for detecting aggressive venous drainage patterns.^{36,42} In patients with contraindications for MR imaging, 4D CTA is also an option to avoid repeat invasive DSAs.³⁷

Treatment Options. For patients in whom interventional treatment is indicated, 4 major treatment options are available:

1. TA embolization
2. TV embolization
3. Microsurgical disconnection
4. Gamma knife radiosurgery (GKRS).

Endovascular Approaches. At our institution, we have adopted an endovascular-first approach to treating intracranial AVFs when possible, based on improving angiographic and clinical cure rates because technology and strategies have evolved in the past 2 decades.⁴³ A major technologic advancement was the development of modern liquid embolic agents (in particular, ethylene-vinyl alcohol copolymer) that allow embolization in a more controlled fashion than ethanol or glue, resulting in higher angiographic cure rates.^{43,44} The use of these agents has resulted in modified endovascular treatment strategies, in which plug formation, dual microcatheter techniques (pressure cooker), or flow arrest via a dual-lumen balloon are used to allow antegrade (for TA approaches) or retrograde (for TV approaches) controlled advancement of the embolic agent to occlude the fistulous point.⁴⁴⁻⁴⁷

Detailed descriptions of the techniques used during TA and TV embolization are provided in the second and third articles of this series.

Microsurgical Disconnection. In cases in which the estimated risks associated with TA and/or TV embolization are elevated, microsurgical disconnection is an effective treatment option. In this setting, multidisciplinary discussion is particularly useful to weigh the risks and benefits of endovascular-versus-surgical approaches. We have frequently encountered cases in which the endovascular approach is difficult and associated with a high risk of cranial nerve palsy or stroke, while being a relatively simple case for microsurgical disconnection (eg, petrous AVFs involving the facial nerve arterial arcade or anterior cranial fossa AVFs supplied by ethmoidal branches of the ophthalmic artery). The surgical goal is to disconnect the draining vein of the AVF using aneurysm clips or ligation.⁴⁸ Even if achieving this surgical goal does not result in angiographic cure, it will usually result in disconnection of the dangerous aspect of the AVF, the cortical venous reflux, thus converting an aggressive AVF into a benign one.^{19,48}

However, the invasive nature of open surgical approaches is associated with potential complications that are often avoided by endovascular approaches, such as CSF leak, pseudomeningocele formation, hydrocephalus, infection, and wound pain.^{14,19} In addition, the tissue disruption associated with an operation is a potential trigger for further dAVF development. A strong

working relationship between interventional neuroradiologists and cerebrovascular surgeons is useful in selecting the most appropriate treatment approach for any given AVF, to minimize the risk of complications from either an endovascular or open surgical approach.

GKRS. GKRS, while being an effective treatment option for parenchymal AVMs, has a more limited role in the treatment of dAVFs. In our experience, the long-term outcomes after GKRS for dAVFs are suboptimal (50% angiographic cure rate), and some patients require further treatment via 1 of the 3 main modalities above.⁴⁹ GKRS is a useful alternative for symptom palliation in patients who have failed other treatments or are averse to endovascular/surgical intervention.^{43,49} An example of the utility of GKRS is reducing the severity of pulsatile tinnitus in patients with incurable or recurrent transverse sinus AVFs.⁴⁹

CONCLUSIONS

Intracranial dAVFs are stratified by the absence or presence of cortical venous reflux. These lesions are best managed using the principles of detailed angiographic anatomic assessment and multidisciplinary discussion. We detail TA and TV embolization techniques in our next 2 articles.

Disclosures: Timo Krings—UNRELATED: Consultancy: Stryker, Penumbra, Medtronic, Cerenovus Royalties: Thieme; Stock/Stock Options: Marblehead.

REFERENCES

1. Newton TH, Cronqvist S. **Involvement of dural arteries in intracranial arteriovenous malformations.** *Radiology* 1969;93:1071–78 CrossRef Medline
2. Cognard C, Gobin YP, Pierot L, et al. **Cerebral dural arteriovenous fistulas: clinical and angiographic correlation with a revised classification of venous drainage.** *Radiology* 1995;194:671–80 CrossRef Medline
3. Borden JA, Wu JK, Shucart WA. **A proposed classification for spinal and cranial dural arteriovenous fistulous malformations and implications for treatment.** *J Neurosurg* 1995;82:166–79 CrossRef Medline
4. Osada T, Krings T. **Intracranial dural arteriovenous fistulas with pial arterial supply.** *Neurosurgery* 2019;84:104–15 CrossRef Medline
5. Weinstein M, Stein R, Pollock J, et al. **Meningeal branch of the posterior cerebral artery.** *Neuroradiology* 1974;7:129–31 CrossRef Medline
6. Wollschlaeger PB, Wollschlaeger G. **An infratentorial meningeal artery** [in German]. *Radiologe* 1965;5:451–52 Medline
7. Bhatia KD, Kortman H, Walchli T, et al. **Artery of Davidoff and Schechter supply in dural arteriovenous fistulas.** *AJNR Am J Neuroradiol* 2020;41:300–04 CrossRef Medline
8. Gross BA, Du R. **The natural history of cerebral dural arteriovenous fistulae.** *Neurosurgery* 2012;71:594–602; discussion 602–03 CrossRef Medline
9. Al-Shahi R, Bhattacharya JJ, Currie DG, et al; Scottish Intracranial Vascular Malformation Study Collaborators. **Prospective, population-based detection of intracranial vascular malformations in adults: the Scottish Intracranial Vascular Malformation Study (SIVMS).** *Stroke* 2003;34:1163–69 CrossRef Medline
10. Kuwayama N. **Epidemiologic survey of dural arteriovenous fistulas in Japan: clinical frequency and present status of treatment.** *Acta Neurochir Suppl* 2016;123:185–88 CrossRef Medline
11. Piippo A, Niemela M, van Popta J, et al. **Characteristics and long-term outcome of 251 patients with dural arteriovenous fistulas in a defined population.** *J Neurosurg* 2013;118:923–34 CrossRef Medline

12. Hiramatsu M, Sugiu K, Hishikawa T, et al. **Epidemiology of dural arteriovenous fistula in Japan: analysis of Japanese Registry of Neuroendovascular Therapy (JR-NET2).** *Neurol Med Chir (Tokyo)* 2014;54:63–71 CrossRef Medline
13. Elhammady MS, Ambekar S, Heros RC. **Epidemiology, clinical presentation, diagnostic evaluation, and prognosis of cerebral dural arteriovenous fistulas.** *Handb Clin Neurol* 2017;143:99–105 CrossRef Medline
14. Hiramatsu M, Sugiu K, Hishikawa T, et al. **Results of 1940 embolizations for dural arteriovenous fistulas: Japanese Registry of Neuroendovascular Therapy (JR-NET3).** *J Neurosurg* 2019 June 28. [Epub ahead of print] CrossRef Medline
15. Lasjaunias P, Berenstein A, terBrugge K. *Surgical Neuroangiography: Vol.2: Clinical and Endovascular Treatment Aspects in Adults.* 2nd ed. Springer-Verlag; 2004
16. Houser OW, Campbell JK, Campbell RJ, et al. **Arteriovenous malformation affecting the transverse dural venous sinus—an acquired lesion.** *Mayo Clin Proc* 1979;54:651–61 Medline
17. Lawton MT, Jacobowitz R, Spetzler RF. **Redefined role of angiogenesis in the pathogenesis of dural arteriovenous malformations.** *J Neurosurg* 1997;87:267–74 CrossRef Medline
18. Geibprasert S, Pereira V, Krings T, et al. **Dural arteriovenous shunts: a new classification of craniospinal epidural venous anatomical bases and clinical correlations.** *Stroke* 2008;39:2783–94 CrossRef Medline
19. Lawton MT, Sanchez-Mejia RO, Pham D, et al. **Tentorial dural arteriovenous fistulae: operative strategies and microsurgical results for six types.** *Neurosurgery* 2008;62:110–24; discussion 124–25 CrossRef Medline
20. Gross BA, Albuquerque FC, Moon K, et al. **Evolution of treatment and a detailed analysis of occlusion, recurrence, and clinical outcomes in an endovascular library of 260 dural arteriovenous fistulas.** *J Neurosurg* 2017;126:1884–93 CrossRef Medline
21. van Dijk JM, terBrugge KG, Willinsky RA, et al. **Clinical course of cranial dural arteriovenous fistulas with long-term persistent cortical venous reflux.** *Stroke* 2002;33:1233–36 CrossRef Medline
22. Duffau H, Lopes M, Janosevic V, et al. **Early rebleeding from intracranial dural arteriovenous fistulas: report of 20 cases and review of the literature.** *J Neurosurg* 1999;90:78–84 CrossRef Medline
23. Miller TR, Serulle Y, Gandhi D. **Arterial abnormalities leading to tinnitus.** *Neuroimaging Clin N Am* 2016;26:227–36 CrossRef Medline
24. Miller NR. **Diagnosis and management of dural carotid-cavernous sinus fistulas.** *Neurosurg Focus* 2007;23:E13 CrossRef Medline
25. Brito A, Tsang AC, Hilditch C, et al. **Intracranial dural arteriovenous fistula as a reversible cause of dementia: case series and literature review.** *World Neurosurg* 2019;121:e543–53 CrossRef Medline
26. Letourneau-Guillon L, Cruz JP, Krings T. **CT and MR imaging of non-cavernous cranial dural arteriovenous fistulas: findings associated with cortical venous reflux.** *Eur J Radiol* 2015;84:1555–63 CrossRef Medline
27. Alatakis S, Koulouris G, Stuckey S. **CT-demonstrated transcalvarial channels diagnostic of dural arteriovenous fistula.** *AJNR Am J Neuroradiol* 2005;26:2393–96 Medline
28. Heit JJ, Iv M, Wintermark M. **Imaging of intracranial hemorrhage.** *J Stroke* 2017;19:11–27 CrossRef Medline
29. Snyder VS, Chen JY, Hansen LA. **Ruptured dural arteriovenous fistula/malformation.** *Acad Forensic Pathol* 2017;7:299–311 CrossRef Medline
30. Hernandez-Diaz ZM, Llibre-Guerra JC, Artech-Prior M, et al. **Spontaneous subdural hematoma and behavioral changes due to a dural arteriovenous fistula. A case report and literature review.** *Behav Sci (Basel)* 2019;9:63 CrossRef Medline
31. Azuma M, Hirai T, Shigematsu Y, et al. **Evaluation of intracranial dural arteriovenous fistulas: comparison of unenhanced 3T 3D time-of-flight MR angiography with digital subtraction angiography.** *Mag Reson Med Sci* 2015;14:285–93 CrossRef Medline
32. Kwon BJ, Han MH, Kang HS, et al. **MR imaging findings of intracranial dural arteriovenous fistulas: relations with venous drainage patterns.** *AJNR Am J Neuroradiol* 2005;26:2500–07 Medline
33. Wilcock DJ, Jaspan T, Worthington BS. **Problems and pitfalls of 3-D TOF magnetic resonance angiography of the intracranial circulation.** *Clin Radiol* 1995;50:526–32 CrossRef Medline
34. Grossberg JA, Howard BM, Saindane AM. **The use of contrast-enhanced, time-resolved magnetic resonance angiography in cerebrovascular pathology.** *Neurosurg Focus* 2019;47:E3 CrossRef Medline
35. Chen CC, Chang PC, Shy CG, et al. **CT angiography and MR angiography in the evaluation of carotid cavernous sinus fistula prior to embolization: a comparison of techniques.** *AJNR Am J Neuroradiol* 2005;26:2349–56 Medline
36. Farb RI, Agid R, Willinsky RA, et al. **Cranial dural arteriovenous fistula: diagnosis and classification with time-resolved MR angiography at 3T.** *AJNR Am J Neuroradiol* 2009;30:1546–51 CrossRef Medline
37. In 't Veld M, Fronczek R, Dos Santos MP, et al. **High sensitivity and specificity of 4D-CTA in the detection of cranial arteriovenous shunts.** *Eur Radiol* 2019;29:5961–70 CrossRef Medline
38. Serulle Y, Miller TR, Gandhi D. **Dural arteriovenous fistulae: imaging and management.** *Neuroimaging Clin N Am* 2016;26:247–58 CrossRef Medline
39. Botsford A, Shankar JJS. **Digital subtraction angiography-Dynavision in pretreatment planning for embolization of dural arterio-venous fistulas.** *J Neuroimaging* 2018;28:112–17 CrossRef Medline
40. Eesa M, Sharma P, Mitha AP, et al. **Angiographic computed tomography with selective microcatheterization in delineating surgical anatomy in the case of a dural arteriovenous fistula: technical note.** *J Neurosurg* 2009;111:916–18 CrossRef Medline
41. Bhatia KD, Kortman H, Lee H, et al. **Facial nerve arterial arcade supply in dural arteriovenous fistulas: anatomy and treatment strategies.** *AJNR Am J Neuroradiol* 2020;41:687–92 CrossRef Medline
42. Reinacher PC, Stracke P, Reinges MH, et al. **Contrast-enhanced time-resolved 3-D MRA: applications in neurosurgery and interventional neuroradiology.** *Neuroradiology* 2007;49(Suppl 1):S3–13 CrossRef Medline
43. Signorelli F, Gory B, Maduri R, et al. **Intracranial dural arteriovenous fistulas: a review of their current management based on emerging knowledge.** *J Neurosurg Sci* 2017;61:193–206 CrossRef Medline
44. Mantilla D, Le Corre M, Cagnazzo F, et al. **Outcome of transarterial treatment of dural arteriovenous fistulas with direct or indirect cortical venous drainage.** *J Neurointerv Surg* 2018;10:958–63 CrossRef Medline
45. Chapot R, Stracke P, Velasco A, et al. **The pressure cooker technique for the treatment of brain AVMs.** *J Neuroradiol* 2014;41:87–91 CrossRef Medline
46. Zhang G, Zhu S, Wu P, et al. **The transvenous pressure cooker technique: a treatment for brain arteriovenous malformations.** *Interv Neuroradiol* 2017;23:194–99 CrossRef Medline
47. Dabus G, Linfante I, Martínez-Galdámez M. **Endovascular treatment of dural arteriovenous fistulas using dual lumen balloon microcatheter: technical aspects and results.** *Clin Neurol Neurosurg* 2014;117:22–27 CrossRef Medline
48. Radovanovic I, Wallace M. **Cranial dural arteriovenous fistula disconnection.** In: Jandial R, McCormick P, Black P, eds. *Core Techniques in Operative Neurosurgery.* Elsevier; 2019
49. Dmytriw AA, Schwartz ML, Cusimano MD, et al. **Gamma knife radiosurgery for the treatment of intracranial dural arteriovenous fistulas.** *Interv Neuroradiol* 2017;23:211–20 CrossRef Medline

Arachnoid Membranes: Crawling Back into Radiologic Consciousness

 S. Lu,  A. Brusic, and  F. Gaillard



ABSTRACT

SUMMARY: The arachnoid membranes are projections of connective tissue in the subarachnoid space that connect the arachnoid mater to the pia mater. These are underappreciated and largely unrecognized by most neuroradiologists despite being found to be increasingly important in the pathogenesis, imaging, and treatment of communicating hydrocephalus. This review aims to provide neuroradiologists with an overview of the history, embryology, histology, anatomy, and normal imaging appearance of these membranes, as well as some examples of their clinical importance.

ABBREVIATIONS: ETV = endoscopic third ventriculostomy; LM = Lilliequist membrane

The subarachnoid space is traversed by projections of connective tissue covered in leptomeningeal cells that connect the arachnoid mater to the pia mater. These have a variety of morphologies ranging from thin cylinders (referred to as “pillars,” “rods,” or “trabeculae”) to more elongated flattened structures (referred to as “septa”).¹ In some areas, these septa are particularly extensive, forming semicontinuous sheets referred to as “arachnoid membranes” (also known as “subarachnoid trabecular membranes” or “inner arachnoid membranes”). The subarachnoid cisterns, typically named according to the brain structures they abut, are often separated from each other by these membranes, which, in turn, determine the flow of CSF from one cistern to the next.

The importance of arachnoid membranes is well-known within the neurosurgery community because these membranes, together with the subarachnoid cisterns, provide natural avenues for dissection during surgery.² In contrast, current neuroradiologists and modern radiology literature are less familiar with their existence and anatomy despite their impact on everyday clinical imaging and their potential importance in understanding a variety of conditions characterized by abnormal CSF flow.

This review seeks to provide neuroradiologists with an overview of the histology, embryology, anatomy, and normal imaging appearance of these membranes, as well as some examples of their clinical importance.

History

While the dura and pia mater were described by Galen in the second century AD,³ the intervening arachnoid mater was not described until the 17th century. Gerardus Blasius (1626–1692) was the first to describe and name the arachnoid layer of the meninges in 1664, naming it in recognition of its cobweb-like traversing membranes and trabeculations, and Frederick Ruysch (1638–1731) confirmed that the arachnoid mater comprised a complete layer surrounding the brain.^{4,5} In the 1690s, Humphrey Ridley (1653–1708) wrote about the concept of the subarachnoid cistern, describing the cerebellomedullary, quadrigeminal, and olfactory cisterns.⁵

It was not until the 19th century that the role of the arachnoid membranes in influencing the flow of CSF was recognized. In 1842, Francois Magendie (of foramen of Magendie fame; 1783–1855) demonstrated that CSF in the ventricles freely communicates with the subarachnoid space, and in 1869, Axel Key (1832–1901) and Magnus Retzius (1842–1919) published detailed drawings of the subarachnoid cisterns and the arachnoid trabeculations and, with a series of experiments using injected dye, demonstrated the free communication of CSF through the fenestrations in the arachnoid.⁶

The importance of the arachnoid membranes in neurosurgery was recognized by Gazi Yasargil (1925), one of the pioneers of microneurosurgery, who introduced the technique of moving from 1 cistern to another during neurosurgical procedures by

Received May 2, 2021; accepted after revision July 29.

From the Department of Radiology (S.L., A.B., F.G.), Royal Melbourne Hospital, Parkville, Victoria, Australia; and Faculty of Medicine, Dentistry, and Health Sciences (F.G.), University of Melbourne, Parkville, Victoria, Australia.

Please address correspondence to Shisheng Lu, MBBS, Department of Radiology, Royal Melbourne Hospital, 300 Grattan St, Parkville VIC 3050, Australia; e-mail: lushisheng@gmail.com

 Indicates open access to non-subscribers at www.ajnr.org

 Indicates article with online supplemental data.

<http://dx.doi.org/10.3174/ajnr.A7309>

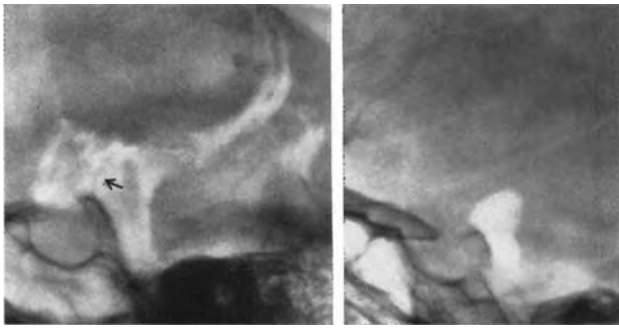


FIG 1. Lateral pneumoencephalogram demonstrating the LM (left) and the air column arrested in the interpeduncular cistern against the LM (right). Arrow in the left image points to the LM (left). Reproduced with permission from Liliequist.⁸ Copyright (1956) SAGE Publications.

dividing the arachnoid membranes that separate the cisterns.² Yasargil also noted that the arachnoid membranes were often porous with various-sized openings and that the openings could become plugged and obliterated after subarachnoid hemorrhage.

The radiologic importance of the anatomy of the subarachnoid space dates back to the very earliest days of imaging. In 1919, a mere 24 years after Wilhelm Röntgen took the first-ever x-ray image (of the hand of his wife on December 22, 1895), Walter Dandy developed pneumoencephalography. At the time a novel technique, this aided the diagnosis and localization of intracranial tumors and was widely used until the 1970s. Pneumoencephalography was an invasive and unpleasant procedure, involving injecting air either directly into the ventricles or into the lumbar subarachnoid space and maneuvering the patient to allow the air to float into the intracranial subarachnoid space and ventricles.⁷ This procedure caused the CSF to be displaced, creating greater contrast between the brain parenchyma and the ventricles, sulci, cisterns, and recesses on cranial radiography. Thus, distortion in the shape or alteration in the location of normal structures could be identified, and the presence of a tumor, inferred. Incidentally, it was recognized that air tended to accumulate within predictable areas of the subarachnoid space, indirectly allowing imaging of the arachnoid membranes.

It was only in 1956 that a Swedish neuroradiologist, Bengt Liliequist⁸ (1923–2008), having noted that during pneumoencephalography air often paused in the interpeduncular cistern before gradually filling the chiasmatic cistern, first described the imaging appearance of the membrane bearing his name.⁹ The Liliequist membrane (LM) could often be seen on a lateral pneumoencephalogram as a fine line with a convexity forward, extending from the tip of the dorsum of the sella to the anterior edge of the mammillary bodies (Fig 1).

As pneumoencephalography fell out of favor in preference to the newly developed and noninvasive cross-sectional modalities of CT and MR imaging, so too did routine radiologic visualization of the arachnoid membranes, and, with time, their anatomy largely receded from our collective radiologic memory.

Fortunately, with the advent of higher-field-strength and higher-resolution MR imaging, we are now in a position to once more image these important structures.

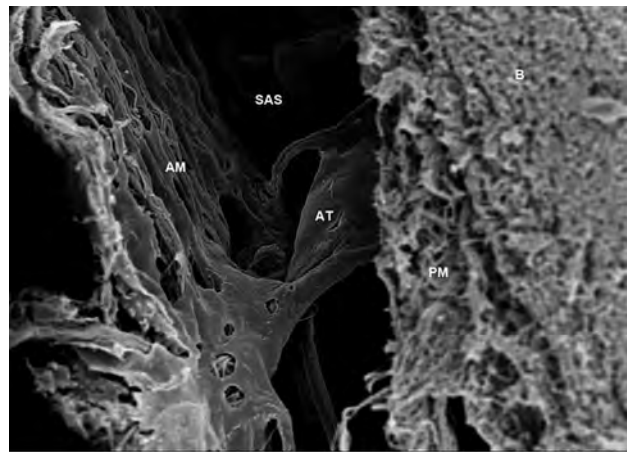


FIG 2. Scanning electron microscope image obtained in the brain of a Sprague-Dawley rat, showing the arachnoid trabeculae (AT) located in the subarachnoid space (SAS) and connected to the arachnoid mater (AM) and pia mater (PM) just next to the brain (B). The parameters are the following: magnification = 2.50 K X; high current = off; electron high tension = 5.00 kV; signal A = InLens; scan speed = 7; focus = 4.6 mm; stage at Z = 45.724 mm; system vacuum = 2.51e-006 mbar; tilt angle = 0.0°; working distance = 4.6 mm. Used with permission from Saboori. Copyright (2020) Wiley.⁴⁸

Embryology

The embryologic development of the subarachnoid space and its membranes occurs in 2 phases. The first is the development of a primitive space-holding mesenchymal layer known as the meninx primitiva, or primitive subarachnoid space, and the second is the development and expansion of lacunae, causing compaction of the mesenchyme.¹⁰

In the first phase, shortly after the closure of the neural tube at approximately days 10–13 postconception (fourth week of pregnancy), mesenchymal cells move from the developing cervical spine into the space formed between the embryonic epithelium and neuroepithelium of the telencephalon.^{10,11} At this stage, the meninx primitiva consists of a gel-like layer of glycosaminoglycans (chains of repeating disaccharides) with widely spaced pluripotent stellate mesenchymal cells and a vascular plexus.¹²

In the second phase, random fluid-filled cavities or lacunae begin to form in this gel-like meninx primitiva, gradually enlarging and pushing the mesenchymal cells apart. Where the walls of the cavities meet, the cells become compacted, forming membranes. At this stage, primary or congenital arachnoid cysts may form as a result of duplication of the arachnoid membranes or failure of meningeal fusion.^{13,14} On the inner and outer aspects of the meninx primitiva, the mesenchymal cells begin to specialize, forming the arachnoid and pia mater; this process is usually complete by day 17.^{10,15} The arachnoid membranes are, therefore, the remaining trabeculated structures joining the 2 inner layers of the meninges.

Histology

Arachnoid septa, trabeculae, and membranes are projections that extend from the arachnoid mater to the pia mater (Fig 2). Arachnoid trabeculae are composed of collagen bundles coated by leptomeningeal cells, which are joined by desmosomes and

gap junctions.¹⁶ Small vessels within the subarachnoid space are enclosed within the trabeculae, and larger vessels are coated by leptomeningeal cells, which are continuous with cells in the trabeculae. Where the trabeculae join the pia mater, the cellular layers of the trabeculae become continuous with the outer layer of the pia mater.

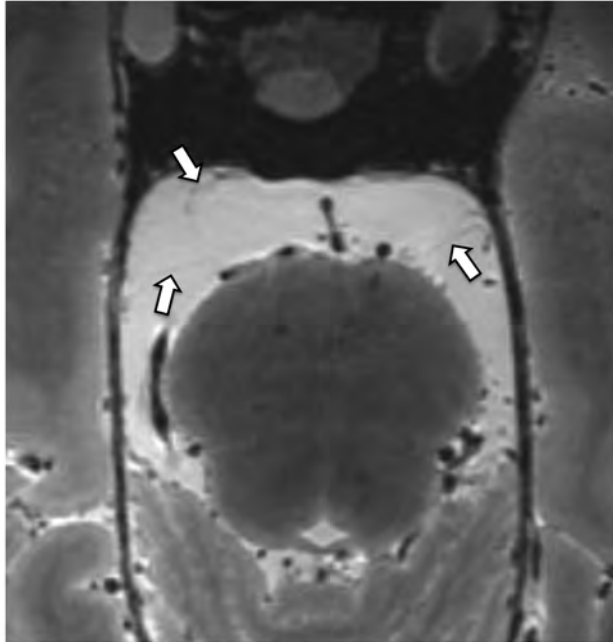


FIG 3. Axial reformat of a high-resolution T2-weighted sequence of a cadaveric head on a 7T MR imaging scanner.⁴⁹ The arachnoid membranes (arrows) in the prepontine cistern are very thin and barely perceptible. Acknowledgment: The authors acknowledge the facilities and scientific and technical assistance of the National Imaging Facility, a National Collaborative Research Infrastructure Strategy capability, at the Melbourne Brain Center Imaging Unit, Department of Radiology, University of Melbourne. Financial support was provided via the “See It, Slice It, Learn It” project funded by a University of Melbourne internal grant.⁴⁹

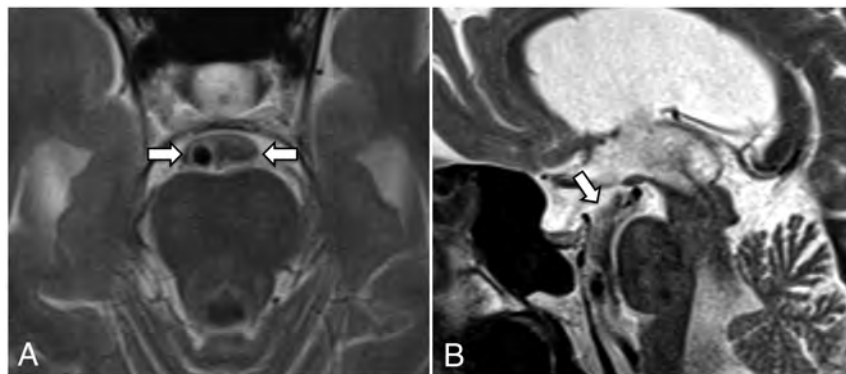


FIG 4. A, T2-weighted axial image (section thickness = 3 mm) shows a prominent CSF flow void around the basilar artery confined to the prepontine cistern. The lateral margins of the flow void (arrows) are likely due to the anterior pontine membranes. B, T2-weighted midline sagittal image (section thickness = 3 mm) demonstrates a CSF flow void tracking along the prepontine and interpeduncular cisterns, with an abrupt change in signal superiorly at the expected location of the diencephalic leaf of the LM (arrow).

In certain areas, very dense networks of semicontinuous trabeculae are present and have the appearance and qualities of true membranes.¹⁷ These membranes divide the subarachnoid space into individual cisterns and provide support for the neurovasculature that passes through them.¹⁷ These arachnoid membranes vary greatly in macroscopic appearance: They can be transparent or semitransparent, membranous or reticulated, porous or intact, and thin or thick, and the same anatomic membrane can appear different in different specimens.⁵

Imaging

The arachnoid membranes were first seen radiologically on pneumoencephalography. As CT and MR imaging became established imaging modalities, however, pneumoencephalography became effectively obsolete in the 1970s.¹⁸ Unfortunately, due to the limitations of spatial resolution of early CT and MR imaging, it was also no longer possible to visualize the arachnoid membranes. It has not been until recently with the development of high-resolution MR imaging techniques, such as the true fast imaging with steady-state precession and CISS (Siemens), FIESTA and FIESTA-C (GE Healthcare), Balanced fast field echo (Philips Healthcare), balanced SARGE and phase-balanced SARGE (Hitachi), and True steady-state free precession (Toshiba), that some of the arachnoid membranes are again sometimes visible on routine imaging.

Normal arachnoid membranes, when visible, appear as thin T2-hypointense lines traversing the CSF in the subarachnoid space. Because the arachnoid membranes are very thin, especially in the absence of disease, most normal membranes remain elusive and difficult to visualize, even with high-resolution high-field-strength scans (Fig 3). Instead, the presence of the arachnoid membranes can often be inferred on most routine scans from the containment and separation of CSF flow voids and artifacts in neighboring subarachnoid cisterns (Fig 4). In contrast, in the presence of subarachnoid hemorrhage, inflammation, or tumor, arachnoid membranes may become thickened, facilitating easier identification, typically on dedicated high-resolution imaging (Fig 5).

Anatomy

Similar to the subarachnoid cisterns, the arachnoid membranes are generally named according to their relationship to the adjacent brain, with the exception of the eponymously named LM. The microsurgical anatomy of multiple arachnoid membranes has been well-described in the neuroanatomy literature,^{17,19-31} and these are summarized in the Online Supplemental Data.⁵ The list is rather extensive, and identification of these membranes is difficult even with high-resolution MR imaging techniques. Furthermore, the exact attachments and boundaries of various membranes are variably described, presumably representing variability not only in description but also in true

anatomy. Nonetheless, it is worthwhile discussing the anatomy of the arachnoid membranes associated with the interpeduncular and prepontine cisterns (Figs 6 and 7) because abnormally thickened

membranes are commonly identified in these cisterns in some patients with communicating hydrocephalus.^{32,33}

The interpeduncular cistern is bounded by the midbrain posteriorly and the 2 leaves of the LM anterior-superiorly and anterior-inferiorly. The LM (Figs 8 and 9) arises from the posterior clinoid processes and dorsum sellae and extends posterior-superiorly, separating into 2 sheets.¹⁹

One sheet, known as the diencephalic leaf, extends posterior-superiorly and attaches to the diencephalon at or anterior to the mammillary bodies. It is fairly complete anteriorly, thus impeding the spread of air on pneumoencephalography, but it is less complete posteriorly near its attachment.²⁶ The diencephalic leaf thus separates the chiasmatic cistern from the interpeduncular cistern. The other sheet, known as the mesencephalic

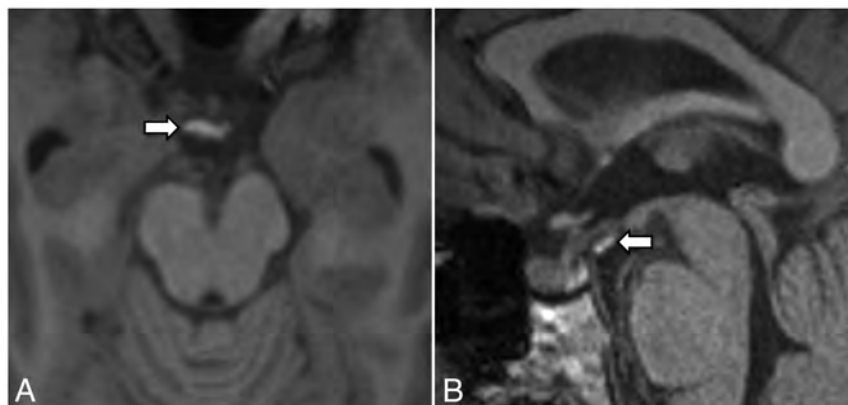


FIG 5. Axial (A) and sagittal (B) T1 MPRAGE images of a patient with subarachnoid hemorrhage show a T1-hyperintense blood product attached to the LM (arrows). The MR imaging examination was performed on day 8 postpresentation.

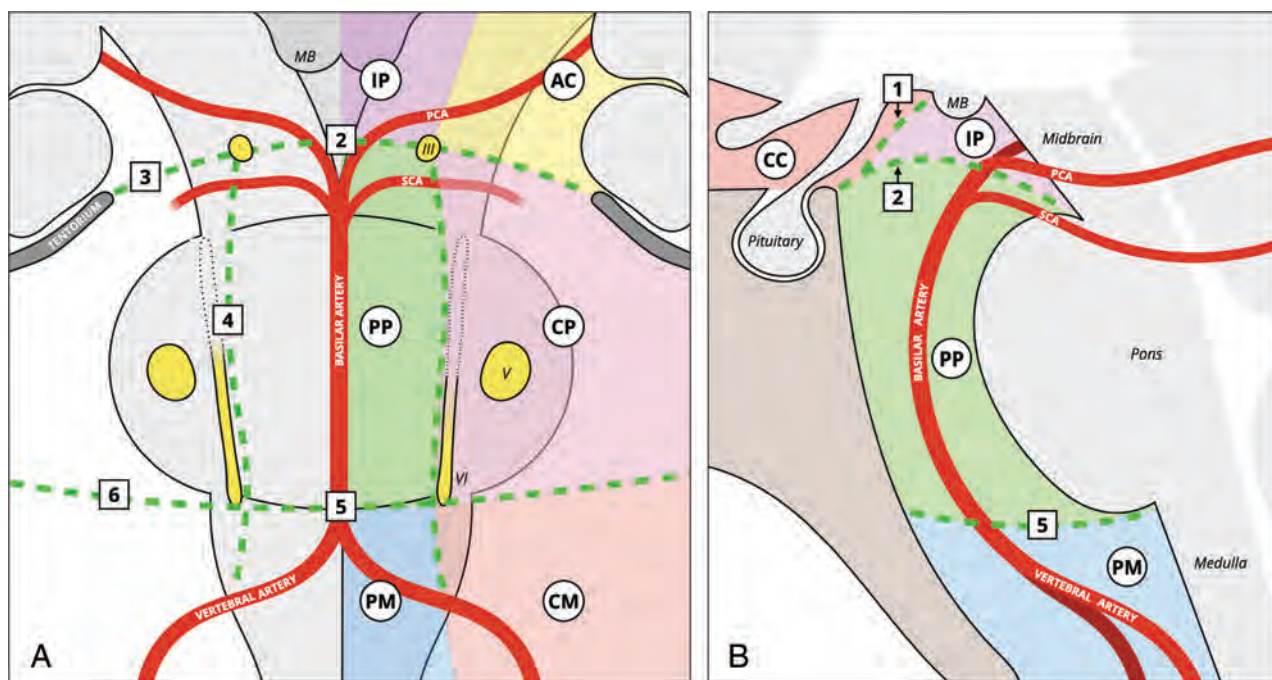


FIG 6. Illustration of arachnoid membranes in relation to the neurovascular structures in the interpeduncular and prepontine cisterns in the coronal (A) and sagittal (B) planes. The LM runs posterior-superiorly from the dorsum sellae and posterior clinoid process. Its diencephalic leaf continues to run posterior-superiorly and attaches to or just anterior to the mammillary bodies, separating the interpeduncular cistern from the chiasmatic cistern. The mesencephalic leaf of the LM extends posteriorly and is divided by the oculomotor nerves into medial and lateral parts. The medial part, attached to the distal basilar artery or the pontomesencephalic junction, separates the interpeduncular cistern from the prepontine cistern. The lateral parts, attached to the tentorium and the mesial temporal lobes, separate the ambient cisterns from the cerebellopontine cisterns. The anterior pontine membranes run on either side of the basilar artery and are medial to the abducens nerves, separating the prepontine cistern from the cerebellopontine cisterns. The medial pontomedullary membrane, located in the midline portion of the pontomedullary sulcus, separates the prepontine cistern from the premedullary cistern. The lateral pontomedullary membranes, located in the lateral portion of the pontomedullary sulcus, separate the cerebellomedullary cisterns from the cerebellopontine cisterns. The numbers represent the following: 1) diencephalic leaf of the LM; 2) medial attachment of the mesencephalic leaf of the LM; 3) lateral attachment of the mesencephalic leaf; 4) anterior pontine membrane; 5) medial pontomedullary membrane; 6) lateral pontomedullary membrane. III indicates the oculomotor nerve; V, trigeminal nerve; VI, abducens nerve; AC, ambient cisterns; CC, chiasmatic cistern; CM, cerebellomedullary cistern; CP, cerebellopontine cistern; IP, interpeduncular cistern; MB, mammillary bodies; PCA, posterior cerebral artery; PM, premedullary cistern; PP, prepontine cistern; SCA, superior cerebellar artery. Reproduced with permission from Frank Gaillard and Radiopaedia.org. Copyright (2021) Radiopaedia.

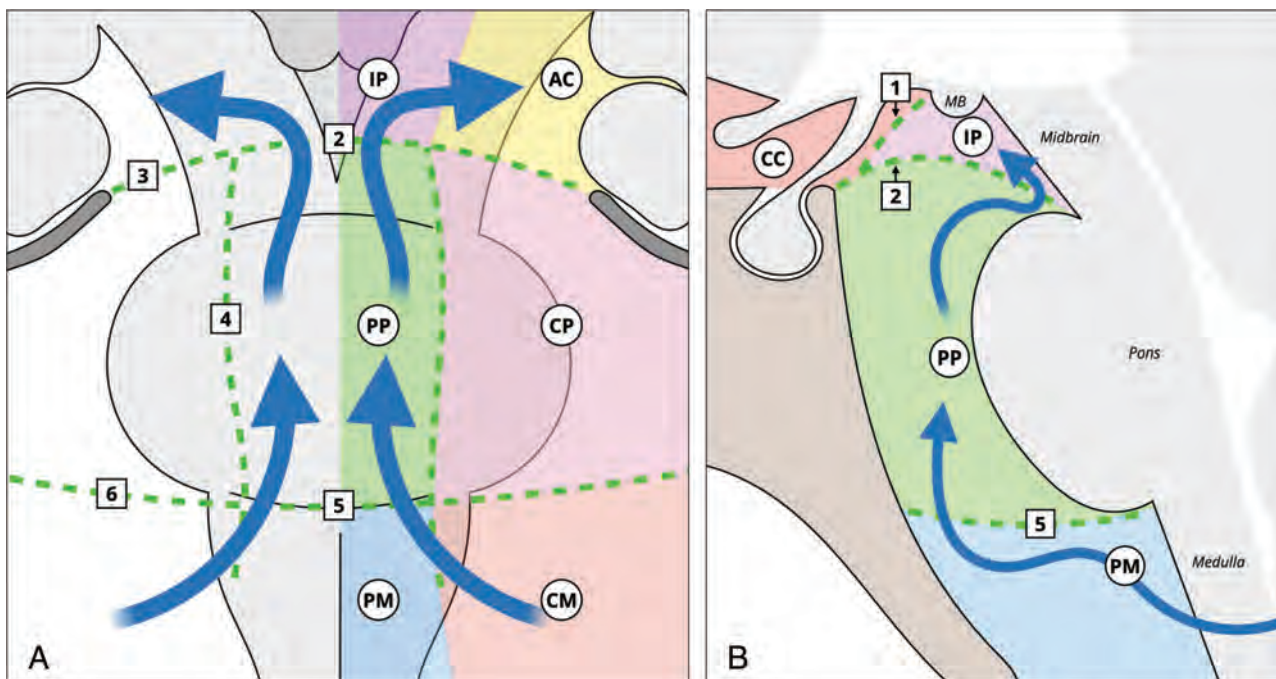


FIG 7. Illustration of arachnoid membranes and the CSF flow at the level of the interpeduncular and prepontine cisterns in the coronal (A) and sagittal (B) planes. The CSF enters the prepontine cistern from the cerebellomedullary and the premedullary cisterns. It runs superiorly within the prepontine cistern and enters the interpeduncular cistern. From there, the CSF can flow laterally and anteriorly into the chiasmatic cistern or posteriorly into the ambient cisterns. The numbers represent the following: 1) diencephalic leaf of the LM; 2) medial attachment of the mesencephalic leaf of the LM; 3) lateral attachment of the mesencephalic leaf; 4) anterior pontine membrane; 5) medial pontomedullary membrane; 6) lateral pontomedullary membrane. AC indicates ambient cisterns; CC, chiasmatic cistern; CM, cerebellomedullary cistern; CP, cerebellopontine cistern; IP, interpeduncular cistern; MB, mammillary bodies; PM, premedullary cistern; PP, prepontine cistern. Reproduced with permission from Frank Gaillard and Radiopaedia.org. Copyright (2021) Radiopaedia.

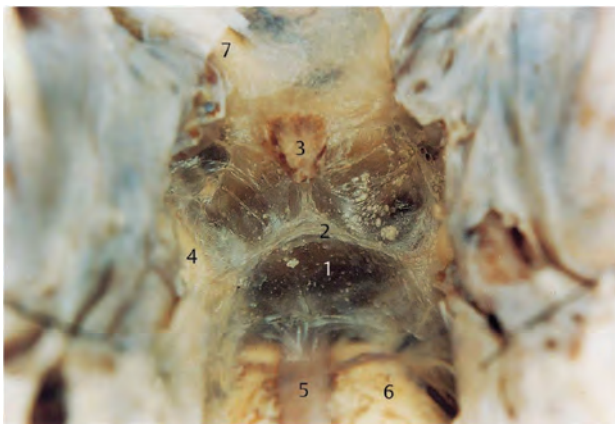


FIG 8. Microsurgical photograph of the LM taken in an adult human cadaveric brain in an oblique coronal view (about 45° to the anterior/posterior commissure line) with the clivus removed, looking up at the attachment between the diencephalic leaf and the mesencephalic leaf of the LM. The numbers represent the following: 1) the mesencephalic leaf of LM; 2) the attachment between the diencephalic leaf and the mesencephalic leaf; 3) the pituitary stalk; 4) the oculomotor nerve; 5) the basilar artery; 6) the pons; and 7) the optic nerve. Reproduced with permission from Lü and Zhu.²³ Copyright (2003) Thieme.

leaf, extends posteriorly and is divided by the oculomotor nerves that course along its upper border into a medial and lateral part. The medial part attaches along the distal basilar artery or the



FIG 9. 3D T2 sampling perfection with application-optimized contrasts by using different flip angle evolution (SPACE sequence; Siemens) left paramedian sagittal image shows the LM with its diencephalic leaf (straight arrow) and the incomplete mesencephalic leaf (curved arrow).

pontomesencephalic junction,^{23,30,31} separating the interpeduncular cistern from the prepontine cistern below. It is seen less frequently on imaging than the diencephalic leaf, in keeping with



FIG 10. 3D T2 SPACE sequence axial image (0.5-mm thickness) at the level of the superior pons reveals the anterior pontine membranes bilaterally (*arrows*). The right anterior pontine membrane appears incomplete posteriorly.

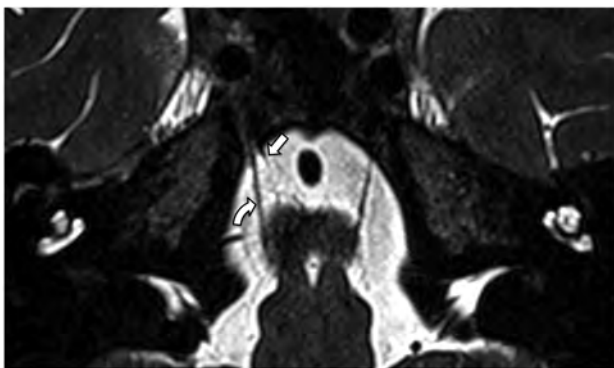


FIG 11. 3D T2 SPACE sequence with an oblique axial reformat (parallel to the abducens nerves) at the level of the lower pons shows an incomplete right anterior pontine membrane (*straight arrow*) medial to the right abducens nerve (*curved arrow*). The left anterior pontine membrane could not be seen at this level.

the microsurgical finding that the mesencephalic leaf is typically thinner, incomplete, or porous.¹⁹ The lateral part fans out to the tentorium and the mesial temporal lobes, usually located between the posterior cerebral arteries and the superior cerebellar arteries, thus separating the ambient cistern from the cerebellopontine cistern.²⁶

The prepontine cistern is separated from the interpeduncular cistern superiorly by the mesencephalic leaf of the LM and is separated from the premedullary cistern inferiorly by the medial pontomedullary membrane, located at the level of the pontomedullary sulcus. Laterally, the prepontine cistern is separated from the cerebellopontine cisterns by the paired paramedian anterior pontine membranes, which run on both sides of the basilar artery

between the pons and the clivus (Fig 10). These membranes ascend in line with the oculomotor nerves superiorly and extend inferiorly along the medial side of the abducens nerves. They become progressively thinner as they extend caudally and may disappear in the lower pons (Fig 11).¹⁹

Clinical Significance

Role in CSF Flow. The subarachnoid space, traversed by the trabeculated arachnoid membranes, is filled with CSF, an ultrafiltrate of plasma, which performs multiple vital functions including nutrient provision, waste removal, buoyancy (reducing the effective weight of the brain from ~1500 g to ~50 g),³⁴ and shock absorption. CSF is primarily produced by the choroid plexus within the ventricles at a rate of ~20 mL/h, with a fairly constant total volume of ~130 mL (in adults) spread between the ventricles (~30 mL) and subarachnoid space surrounding the brain (~25 mL) and cord (~75 mL).^{34,35}

The typical basic explanation of CSF flow is that after production in the choroid plexus, CSF flows through the ventricles (craniocaudal), exiting through the foramina of Luschka and Magendie into the subarachnoid space. Once within the subarachnoid space, it flows through the basal cisterns, over the convexity of the brain, and along the spinal cord where it is absorbed into the blood of the cerebral venous sinuses through arachnoid villi.³⁶ CSF flow is presumed to be driven by a combination of a hydrostatic pressure gradient from the choroid plexus to the arachnoid villi and pulsations of the choroid plexus, with effects of both respiration and cardiac pulsations contributing to pulsatile bidirectional flow.³⁷ Other lesser factors affecting CSF flow are posture, jugular venous pressure, physical exertion, and time of day.³⁶

With much ongoing research in this field, the traditional view of circulatory bulk flow of CSF has increasingly been challenged. Several studies have, instead, identified and described a complex, multidirectional system with continuous fluid exchange at the blood-brain barrier and cell membranes at the CSF/interstitial fluid interface.^{35,38-40} Drainage and absorption of CSF are also more complex than just to the venous sinuses via the arachnoid villi, with drainage to cervical and spinal lymph nodes via the cribriform plate and spinal canal nerve roots also demonstrated.³⁵

Recent studies have also pointed to the presence of a functional cerebral lymphatic or glymphatic system. In this system, CSF enters the Virchow-Robin perivascular spaces around arteries and arterioles in the subarachnoid space; the vessels are lined by the glia limitans, a thin layer of astrocyte foot processes rich in the aquaporin-4 water channels. Movement of CSF across the aquaporin-4 channels into the interstitial space of the brain is the result of convective flow (the transport of a substance by bulk flow, in which bulk flow is often the movement of fluid down a pressure gradient).⁴¹ In the interstitial space, various waste products including amyloid are dissolved in the CSF before the CSF again moves out through aquaporin-4 channels in the Virchow-Robin spaces lining the venules and veins.^{35,40,42}

Nonetheless, a substantial volume of CSF flows from the ventricles, through the basal cisterns, and over the convexity of the brain, and this flow is affected by the anatomy of the arachnoid membranes.⁴³ The semiconstant arachnoid membranes that form the boundaries of the interpeduncular and prepontine

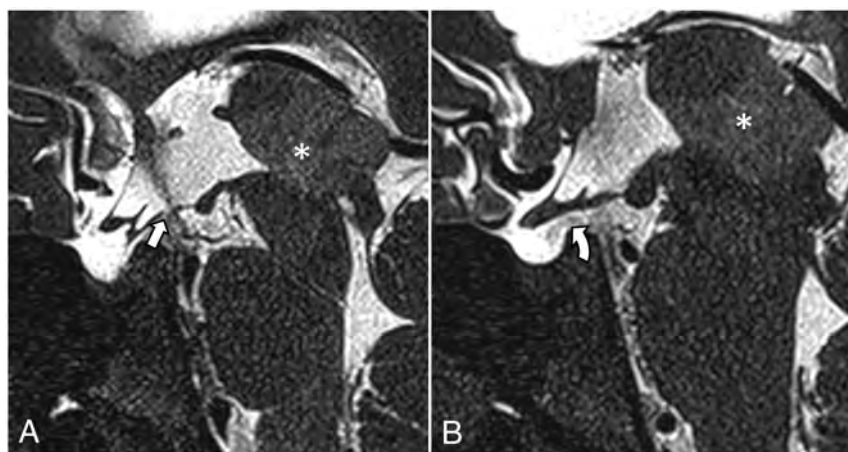


FIG 12. Postendoscopic third ventriculostomy 3D T2 SPACE midsagittal (A) and left paramedian sagittal (B) images in a patient with obstructive hydrocephalus at the level of the third ventricle outlet due to a left thalamic glioma with extension into the pineal gland (*asterisk*). A, The stoma and the CSF flow void from the third ventricle to the interpeduncular cistern are shown (*arrow*). B, The CSF flow void extends into the chiasmatic cistern (*curved arrow*), which suggests that the diencephalic leaf has been fenestrated or is incomplete.

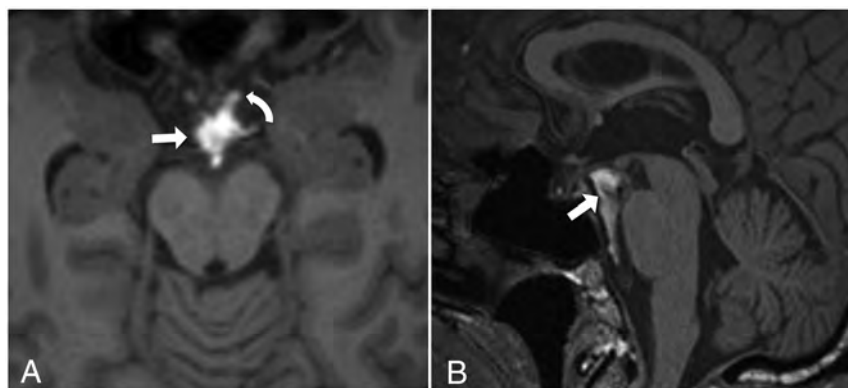


FIG 13. Axial (A) and midline sagittal (B) T1 MPRAGE images in a patient with nonaneurysmal perimesencephalic subarachnoid hemorrhage show that the hyperintense blood is mostly confined to the interpeduncular and prepontine cisterns (*straight arrows*), with only a tiny amount of blood entering the chiasmatic cistern (*curved arrow*).

cisterns may potentially form a major conduit in which the CSF flows in a caudocranial direction in a somewhat predictable fashion. After the CSF exits the fourth ventricle through the foramina of Luschka and enters the cerebellopontine angle, it enters the prepontine cistern via apertures in the anterior pontine membranes. It continues cranially and enters the interpeduncular cistern via the openings in the medial part of the mesencephalic leaf of LM and the medial pontomesencephalic membrane. From the interpeduncular cistern, the CSF may flow either ventrally through the pores in the diencephalic leaf into the chiasmatic cistern or dorsally around the cerebral peduncles into the ambient cisterns (Fig 7). The ventral flow of CSF from the interpeduncular cistern is somewhat limited by the diencephalic leaf, as demonstrated by the arrested air column on the pneumoencephalogram in Fig 1 and the abrupt loss of CSF flow void anterior to the diencephalic leaf in Fig 4B. From here, CSF flows more slowly in the subarachnoid space superiorly over the

cerebral convexities and inferiorly around the spinal cord. Absorption, as mentioned above, is via the arachnoid villi/granulations in the venous sinuses, the cribriform plate in the anterior cranial fossa, and at the spinal nerve roots.

Endoscopic Third Ventriculostomy. Endoscopic third ventriculostomy (ETV) is a surgical procedure used to treat noncommunicating hydrocephalus by creating a bypass for the CSF from the third ventricle to the basal cisterns. It involves introducing an endoscope through the brain parenchyma, usually the right frontal lobe, into the lateral ventricle. From there the endoscope is navigated through the foramen of Monro into the third ventricle. A stoma is created at the floor of the third ventricle allowing CSF to flow out of the third ventricle directly into the interpeduncular cistern.⁴⁴

The importance of perforating the diencephalic leaf of the LM during ETV is well-known in the neurosurgery community. Buxton et al⁴⁵ reported that the diencephalic leaf of the LM may block the flow of CSF from the third ventricle into the interpeduncular and prepontine cisterns and therefore needs to be fenestrated during the operation for a successful ETV. The CSF flow voids from the third ventricle to the interpeduncular cistern can be readily visualized on high-resolution T2-weighted sequences (Fig 12).

Subarachnoid Hemorrhage

The arachnoid membranes separating the cisterns may impede the spread of blood to the adjacent cisterns, much as CSF flow may be obstructed (see section on “Role in CSF Flow” and Fig 7). In cases of aneurysmal subarachnoid hemorrhage, the site of the ruptured aneurysm can often be predicted by assessing the distribution of the blood on the initial unenhanced CT scan. Furthermore, nonaneurysmal perimesencephalic subarachnoid hemorrhage is often localized to the interpeduncular, ambient, and prepontine cisterns without spreading to the chiasmatic cistern (Fig 13). This localization is likely due to the presence of the diencephalic leaf of LM.⁴⁶ However, due to the anatomic variations of the arachnoid membranes and the amount of extravasated blood, the extent of the perimesencephalic subarachnoid hemorrhage can be variable.

Hydrocephalus

Arachnoid membranes may be thickened secondary to inflammation or hemorrhage, and as a result, the apertures in these

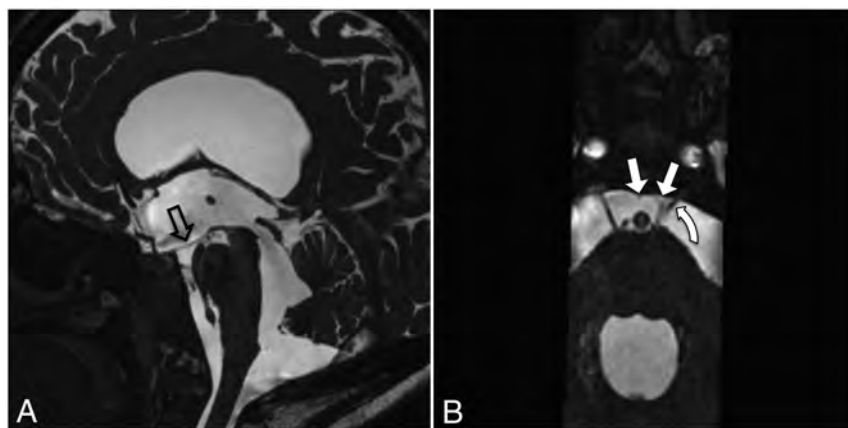


FIG 14. Midline sagittal (A) and reformatted axial (B) CISS sequence images in a patient with chronic extraventricular intracisternal obstructive hydrocephalus. A, Marked hydrocephalus with inferior bowing of the floor of the third ventricle (hollow arrow) and a widely patent cerebral aqueduct. B, The anterior pontine membranes are displaced medially (straight arrows) with the left anterior pontine membrane visibly thickened. The left abducens nerve is displaced medially (curved arrow). The displacement of the anterior pontine membranes may be due to altered CSF flow dynamics and/or tethering from other arachnoid membranes. The displacement and thickening of the membrane are likely the consequence of previous infection, inflammation, or hemorrhage, but they subsequently cause obstruction to CSF flow.

membranes may be occluded. This occlusion impedes the CSF flow within the prepontine and interpeduncular cisterns and can lead to hydrocephalus. In addition, the arachnoid membranes may be displaced due to altered CSF flow dynamics and/or tethering from other arachnoid membranes, further impeding CSF flow. The resultant tetraventricular hydrocephalus is often interpreted as communicating hydrocephalus, but a more accurate term would be extraventricular intracisternal obstructive hydrocephalus.⁴⁷ These obstructive cisternal membranes cannot be visualized on conventional MR images but can be seen on higher-resolution sequences such as the 3D-CISS sequence (Fig 14).^{32,33}

On 3D-CISS imaging, Laith et al³² identified “complex membranes” in the basal cisterns in 18 of 43 patients with hydrocephalus, confirmed surgically in those who underwent ETV. In patients whose ETV failed, absence of flow voids in the basal cisterns (particularly in the prepontine cistern) was usually seen and was attributed to the arrest of CSF flow by these membranes.

In their study of 134 patients with hydrocephalus, Dinçer et al³³ found cisternal membranes causing obstruction in 28 cases. Most of these membranes are located in the prepontine cistern, interpeduncular cistern, or both. Seventeen of 28 cases were proved surgically during ETV, and some of these membranes were fenestrated during the operation.

In patients with tetraventricular hydrocephalus, identifying obstructive arachnoid membranes is crucial because these patients, who would have otherwise been treated with shunt insertion, can be selected for ETV. Furthermore, neurosurgeons can fenestrate these thickened membranes during ETV and, by doing so, potentially increase the success rate of the operation.

CONCLUSIONS



The arachnoid membranes play a role in both normal CSF flow dynamics and conditions characterized by abnormal CSF flow. The abnormally thickened membranes and sometimes the normal membranes can be visualized on high-resolution T2-weighted sequences. Therefore, understanding the presence and anatomy of the arachnoid membranes is becoming increasingly important for neuroradiologists.

REFERENCES

1. Killer HE, Laeng HR, Flammer J, et al. **Architecture of arachnoid trabeculae, pillars, and septa in the subarachnoid space of the human optic nerve: anatomy and clinical considerations.** *Br J Ophthalmol* 2003;87:777–81 CrossRef Medline
2. Yasargil MG, Kasdaglis K, Jain KK, et al. **Anatomical observations of the subarachnoid cisterns of the brain during surgery.** *J Neurosurg* 1976;44:298–302 CrossRef Medline
3. Adeeb N, Deep A, Griessenauer CJ, et al. **The intracranial arachnoid mater: A comprehensive review of its history, anatomy, imaging, and pathology.** *Childs Nerv Syst* 2013;29:17–33 CrossRef Medline
4. Sanan A, van Loveren HR. **The arachnoid and the myth of arachne.** *Neurosurgery* 1999;45:152 CrossRef Medline
5. Lü J. **Arachnoid membrane: the first and probably the last piece of the roadmap.** *Surg Radiology Anat* 2015;37:127–38 CrossRef Medline
6. Connor DE, Nanda A. **Bengt Liliequist: life and accomplishments of a true renaissance man.** *J Neurosurg* 2017;126:645–49 CrossRef Medline
7. Lanska DJ, Moniz, Egaz. In: Aminoff MJ, Daroff RB, ed. *Encyclopedia of the Neurological Sciences*. Elsevier; 2014:92–93 CrossRef
8. Liliequist B. **The anatomy of the subarachnoid cisterns.** *Acta Radiol* 1956;46:61–71 CrossRef Medline
9. Epstein BS. **The role of a transverse arachnoidal membrane within the interpeduncular cistern in the passage of Pantopaque into the cranial cavity.** *Radiology* 1965;85:914–20 CrossRef Medline
10. Mortazavi MM, Quadri SA, Khan MA, et al. **Subarachnoid trabeculae: a comprehensive review of their embryology, histology, morphology, and surgical significance.** *World Neurosurg* 2018;111:279–90 CrossRef Medline
11. O’Rahilly R, Müller F. **The meninges in human development.** *J Neuropathol Exp Neurol* 1986;45:588–608 CrossRef Medline
12. Decimo I, Fumagalli G, Berton V, et al. **Meninges: from protective membrane to stem cell niche.** *Am J Stem Cells* 2012;1:92 Medline
13. Osborn AG, Preece MT. **Intracranial cysts: radiologic-pathologic correlation and imaging approach.** *Radiology* 2006;239:650–64 CrossRef Medline
14. Logan C, Asadi H, Kok H, et al. **Arachnoid cysts: common and uncommon clinical presentations and radiological features.** *J Neuroimaging Psychiatry Neurol* 2016;1:79–84 CrossRef
15. Talbert D. **The embryological development of the form of the trabeculae bridging the subarachnoid space.** *Journal of Trauma & Treatment* 2014;3:198 CrossRef
16. Alcolado R, Weller RO, Parrish EP, et al. **The cranial arachnoid and pia mater in man: anatomical and ultrastructural observations.** *Neuropathol Appl Neurobiol* 1988;14:1–17 CrossRef Medline

17. Vinas FC, Fandino R, Dujovny M, et al. **Microsurgical anatomy of the supratentorial arachnoidal trabecular membranes and cisterns.** *Neurol Res* 1994;16:417–24 CrossRef Medline
18. Hoeffner EG, Mukherji SK, Srinivasan A, et al. **Neuroradiology back to the future: brain imaging.** *AJNR Am J Neuroradiol* 2012;33:5–11 CrossRef Medline
19. Matsuno H, Rhoton AL, Peace D. **Microsurgical anatomy of the posterior fossa cisterns.** *Neurosurgery* 1988;23:58–80 CrossRef Medline
20. Vinas FC, Dujovny M, Fandino R, et al. **Microsurgical anatomy of the arachnoidal trabecular membranes and cisterns at the level of the tentorium.** *Neurol Res* 1996;18:305–12 CrossRef Medline
21. Vinas FC, Dujovny M, Fandino R, et al. **Microsurgical anatomy of the infratentorial trabecular membranes and subarachnoid cisterns.** *Neurol Res* 1996;18:117–25 CrossRef Medline
22. Lü J, Zhu X. **Microsurgical anatomy of the interpeduncular cistern and related arachnoid membranes.** *J Neurosurg* 2005;103:337–41 CrossRef Medline
23. Lü J, Zhu XL. **Microsurgical anatomy of Liliequist's membrane.** *Minim Invasive Neurosurg* 2003;46:149–54 CrossRef Medline
24. Lü J, Zhu XL. **Characteristics of distribution and configuration of intracranial arachnoid membranes.** *Surg Radiol Anat* 2005;27:472–81 CrossRef Medline
25. Lü J, Zhu XL. **Cranial arachnoid membranes: some aspects of microsurgical anatomy.** *Clin Anat* 2007;20:502–11 CrossRef Medline
26. Qi ST, Fan J, Zhang XA, et al. **Reinvestigation of the ambient cistern and its related arachnoid membranes: an anatomical study—laboratory investigation.** *J Neurosurg* 2011;115:171–78 CrossRef Medline
27. Zhang XA, Qi ST, Huang GL, et al. **Anatomical and histological study of Liliequist's membrane: with emphasis on its nature and lateral attachments.** *Childs Nerv Syst* 2012;28:65–72 CrossRef Medline
28. Song-Tao Q, Xi-An Z, Hao L, et al. **The arachnoid sleeve enveloping the pituitary stalk: anatomical and histologic study.** *Neurosurgery* 2010;66:585–89 CrossRef Medline
29. Inoue K, Seker A, Osawa S, et al. **Microsurgical and endoscopic anatomy of the supratentorial arachnoidal membranes and cisterns.** *Neurosurgery* 2009;65:644–64; discussion 665 CrossRef Medline
30. Kurucz P, Baksa G, Patonay L, et al. **Endoscopic anatomical study of the arachnoid architecture on the base of the skull, Part II: level of the tentorium, posterior fossa and the craniovertebral junction.** *Innovative Neurosurg* 2013;1:91–108 CrossRef
31. Volovici V, Varvari I, Dirven CM, et al. **The membrane of Liliequist: a safe haven in the middle of the brain—a narrative review.** *Acta Neurochir (Wien)* 2020;162:2235–44 CrossRef Medline
32. Laitt RD, Mallucci CL, Jaspan T, et al. **Constructive interference in steady-state 3D Fourier-transform MRI in the management of hydrocephalus and third ventriculostomy.** *Neuroradiology* 1999;41:117–23 CrossRef Medline
33. Dinçer A, Kohan S, Özek MM. **Is all “communicating” hydrocephalus really communicating? Prospective study on the value of 3D-constructive interference in steady state sequence at 3T.** *AJNR Am J Neuroradiol* 2009;30:1898–1906 CrossRef Medline
34. McMinn RMH, ed. **Last's Anatomy: Regional and Applied.** 9th ed. Elsevier; 1998
35. Bothwell SW, Janigro D, Patabendige A. **Cerebrospinal fluid dynamics and intracranial pressure elevation in neurological diseases.** *Fluids Barriers CNS* 2019;16:9 CrossRef Medline
36. Sakka L, Coll G, Chazal J. **Anatomy and physiology of cerebrospinal fluid.** *Eur Ann Otorhinolaryngol Head Neck Dis* 2011;128:309–16 CrossRef Medline
37. Dreha-Kulaczewski S, Konopka M, Joseph AA, et al. **Respiration and the watershed of spinal CSF flow in humans.** *Sci Rep* 2018;8:5594 CrossRef Medline
38. Chikly B, Quaghebeur J. **Reassessing cerebrospinal fluid (CSF) hydrodynamics: a literature review presenting a novel hypothesis for CSF physiology.** *J Bodyw Mov Ther* 2013;17:344–54 CrossRef Medline
39. Brinker T, Stopa E, Morrison J, et al. **A new look at cerebrospinal fluid circulation.** *Fluids Barriers CNS* 2014;11:10 CrossRef Medline
40. Iliff JJ, Nedergaard M. **Is there a cerebral lymphatic system?** *Stroke* 2013;44:S93–95 CrossRef Medline
41. Ray L, Iliff JJ, Heys JJ. **Analysis of convective and diffusive transport in the brain interstitium.** *Fluids Barriers CNS* 2019;16:6 CrossRef Medline
42. Bradley WG. **CSF flow in the brain in the context of normal pressure hydrocephalus.** *AJNR Am J Neuroradiol* 2015;36:83138 CrossRef Medline
43. Brodbelt A, Stoodley M. **CSF pathways: a review.** *Br J Neurosurg* 2007;21:510–20 CrossRef Medline
44. Hellwig D, Grotenhuis JA, Tirakotai W, et al. **Endoscopic third ventriculostomy for obstructive hydrocephalus.** *Neurosurg Rev* 2005;28:1 CrossRef Medline
45. Buxton N, Vloeberghs M, Punt J. **Liliequist's membrane in minimally invasive endoscopic neurosurgery.** *Clin Anat* 1998;11:187–90
46. Schwartz TH, Solomon RA. **Perimesencephalic nonaneurysmal subarachnoid hemorrhage: review of the literature.** *Neurosurgery* 1996;39:433–40 CrossRef Medline
47. Kehler U, Gliemroth J. **Extraventricular intracisternal obstructive hydrocephalus: a hypothesis to explain successful 3rd ventriculostomy in communicating hydrocephalus.** *Pediatr Neurosurg* 2003;38:98–101 CrossRef Medline
48. Saboori P. **Subarachnoid space trabeculae architecture.** *Clin Anat* 2021;34:40–50 CrossRef Medline
49. Cleary JO, Yoo PE, Moffat BA, et al. **See it, slice it, learn it: combined ultra-high-field MRI and high-resolution CT for an open source virtual anatomy resource.** In: *Proceedings of the Annual Meeting and Exhibition of the International Society for Magnetic Resonance in Medicine*, April 22–27, 2017; Honolulu, Hawaii

Optimizing Small, Low-Risk, Unruptured Intracranial Aneurysm Treatment Using Game Theory

 A.T. Boltyenkov,  J.J. Wang,  A. Malhotra,  J.M. Katz,  A.R. Dehdashti,  T.G. White,  G. Martinez,  A. Pandya, and  P.C. Sanelli

ABSTRACT

SUMMARY: The incidental diagnosis of unruptured intracranial aneurysms has been increasing in the past several decades. A significant proportion represent small, low-risk, unruptured intracranial aneurysms for which there is equipoise on whether to offer treatment or conservative management. Given this uncertainty, patients may not always be comfortable with their physicians' recommendations. Herein, we use game theory to study the interactions between physicians and patients to determine how conflict and cooperation affect the management of small, low-risk, unruptured intracranial aneurysms. We constructed a game theory model of the interaction between physicians and patients with respect to decision-making for a small, low-risk, unruptured intracranial aneurysm in an asymptomatic patient when there is perceived equipoise between whether to treat or manage conservatively. Assuming that both the physician and patient are rational and eliciting individual patient preferences is not practical, the physician should play the game based on an *ex ante* probability of meeting a patient with a certain type of preference. This recommendation means that the expectations of the physician regarding the patient's preferences should guide the decision to offer treatment or conservative management as a first option for a small, asymptomatic, low-risk, unruptured intracranial aneurysm for which there is clinical equipoise.

ABBREVIATIONS: CM = conservative management; *p* = probability; T = treatment; UIA = unruptured intracranial aneurysm

Roughly 2%–3% of the population has unruptured intracranial aneurysms (UIAs), amounting to approximately 6 million people in the United States.¹ A recent study found a 5-fold increase in annual admissions with diagnoses of UIA during the past 2 decades, whereas the incidence of SAH has remained unchanged despite increases in the diagnosis and treatment of UIAs.² This finding suggests that the substantial growth in the number of UIAs treated has not led to a decrease in the incidence of SAH, leading to the following question: Are most of these UIA treatments necessary and preventive?³

Studies have reported that up to 87.6% of UIAs are tiny, measuring <3–4 mm.⁴ On the basis of large longitudinal series, it is well-established⁵ that small sporadic UIAs have an overall low

risk of rupture; however, in clinical practice, small aneurysms make up the majority of ruptured aneurysms.⁶ Increasingly, physicians may favor preventive treatment for even tiny UIAs to eliminate the risk of SAH.⁷ However, treatment of small UIAs is associated with a relatively high incidence of complications. Conservative management with imaging surveillance is performed to assess changes in the size and morphology that may predict a higher risk of rupture. However, the optimal frequency and duration of imaging are not defined.⁸ The optimal management of small, asymptomatic, low-risk UIAs is unclear,⁹ and uncertainty exists in the current guidelines¹⁰ and available literature, coupled with the lack of a clear understanding of the natural history of small UIAs.⁷ Therefore, the management of small UIAs represents a serious clinical conundrum.¹¹

In our thought experiment, we explored the case of a small, asymptomatic, low-risk UIA for which there is equipoise as to whether to perform interventional/surgical treatment or recommend conservative management.

MATERIALS AND METHODS

We framed the patient-physician interaction in a game theory model. We developed a sequential Bayesian game model between the physician and patient to analyze the decision-making results for small UIAs when patient preferences are considered.

Received May 28, 2021; accepted after revision November 1.

From the Imaging Clinical Effectiveness and Outcomes Research (A.T.B., J.J.W., G.M., P.C.S.), Center for Health Innovations and Outcomes Research, Feinstein Institutes for Medical Research, Manhasset, New York; Siemens Medical Solutions USA (A.T.B., G.M.), Malvern, Pennsylvania; Department of Radiology and Biomedical Imaging (A.M.), Yale School of Medicine, New Haven, Connecticut; Departments of Radiology (J.M.K., P.C.S.) and Neurology (A.R.D., T.G.W.), Donald and Barbara Zucker School of Medicine at Hofstra/Northwell, Manhasset, New York; Department of Neurosurgery (A.R.D., T.G.W.), Hofstra Northwell School of Medicine, Manhasset, New York; and Department of Health Policy and Management (A.P.), Harvard T.H. Chan School of Public Health, Boston, Massachusetts.

Please address correspondence to Artem Boltyenkov, PhD, Center for Health Innovations and Outcomes Research, Feinstein Institutes for Medical Research, Northwell Health, 600 Community Dr, Suite 403, Manhasset, NY 11030; e-mail: artem.boltyenkov@siemens-healthineers.com
http://dx.doi.org/10.3174/ajnr.A7392

Model Design

In the game theory model, we have 2 players: the patient and the physician.

We defined the patients as 2 distinct types: 1) an aggressive patient who prefers to live without the risk of aneurysm rupture and, therefore, prefers the aneurysm treated by an interventional or surgical procedure, even if conservative management is recommended by the physician; and 2) a conservative patient who prefers conservative management and is satisfied with periodic imaging follow-up to assess aneurysm growth or change in morphology.

We define physicians as 2 distinct types: an aggressive and a conservative. These types of physicians differ in their willingness to treat certain small, low-risk aneurysms. On one end of the spectrum, there are more conservative physicians, who prefer to treat only aneurysms that are likely to rupture and who tend to refer many patients to imaging surveillance. On the other end of the spectrum, there are aggressive physicians, willing to treat small UIAs to minimize the possibility of rupture. The size of the UIA considered in equipoise is smaller for an aggressive physician than for a conservative physician.

We designed the game in such a way that the physician makes the first move. We assumed that the physician starts communication with the patient to inform the patient of the UIA diagnosis and discusses the management plan with either interventional/surgical treatment or periodic follow-up as a form of conservative management. Our model does not include a “no care” option for incidentally found UIAs. We assumed that if a physician decides to advocate for aneurysm treatment, this decision is associated with additional time and effort from the physician to explain all of the treatment options, risks, and benefits. Treatment also requires the physician to schedule the patient into a busy clinical workload and entails the physician’s anxiety about treating a smaller, low-risk lesion with more uncertainty of benefit and a higher risk of complication than larger, more clearly indicated aneurysms. This scenario is weighed against the physician’s expertise and experience in successfully treating UIAs to prevent aneurysm rupture with the related morbidity and mortality. The physician has the freedom to decide how to frame the discussion of the aneurysm.

In this model, the physician does not know the exact payoff function for a given individual patient. Instead, the physician has bias about these payoff functions for each patient type (aggressive, conservative). Besides, the physician knows his or her own choice regarding the willingness to treat small, asymptomatic UIAs.

In the model, there is a unique player in the game called “Nature.” Nature can randomly choose the patient and physician type for the game. Because we model the game from the physician’s perspective and the physician knows his or her own type, we modeled the game for each type of physician separately. Let us assume that with the probability p , the patient is an aggressive type, and with the probability $1-p$, the patient is a conservative type. We make the common prior assumption that the probability distribution p is known to all players. In fact, the physician has a belief about the value of p , making this game one with imperfect information. Thus, while the physician is unsure about the type of patient presented for care, the patient has perfect information regarding his or her own risk type.

Next, we will explore the payoff matrices for both physician and patient types to investigate whether there is a pure strategy for the physician. By definition, pure strategy determines all players’ moves throughout the game.

Payoffs for Patient and Physician

The aggressive patient prefers to avoid living with the rupture risk of an UIA and will agree to treatment if offered by the physician. In the case of an aggressive physician, both the patient and the physician prefer treatment, and both get maximum payoff. The conservative physician would like to avoid offering conservative management for the aggressive patient, knowing that the patient would want treatment and be unhappy with an untreated UIA. This scenario could lead to an unsatisfied patient, while at the same time, the physician misses the opportunity to have occupational satisfaction in performing the treatment procedure.

The conservative patient will prefer to continue living with the UIA and undergo periodic imaging follow-up and will not agree to interventional treatment if offered by the physician. In case of a conservative physician, both the patient and physician prefer conservative management, and both get the maximum payoff. The aggressive physician would like to avoid wasting time and effort explaining the risks, benefits, and alternatives of treatment to the conservative patient because the patient would be unlikely to agree to treatment and the patient may lose trust in the physician whom they believe is offering unnecessary care. This scenario could lead to an unsatisfied patient, while at the same time the physician misses the opportunity to use his or her time more efficiently with some other patient.

Therefore, for each player, there are 2 options: treatment (T) or conservative management (CM). For both types of physicians, for an aggressive patient, the dominant strategy is T, while for a conservative patient, the dominant strategy is CM. A physician will follow the patient’s decision to avoid conflict. Thus, we assume the following scoring system for the game: a patient will get 2 points for his or her preference and deduct 2 points for the nonpreferred option. The patient will add 1 point if there is no conflict with the physician and deduct 1 point if there is a conflict with the physician. The physician will add 1 point for no conflict with the patient and deduct 1 point if there is a conflict with the patient. In addition, an aggressive physician will add 2 points if treatment is selected by both the patient and the physician. A conservative physician will add 2 points if conservative management is selected by both parties. Hence, the Bayesian Normal Form representation of the game is shown in Fig 1 (aggressive physician) and Fig 2 (conservative physician).

On the basis of the Bayesian Normal Form representation, we developed the payoff matrices for both types of physicians, as shown in Table 1 (aggressive physician) and Table 2 (conservative physician).

RESULTS

Given the above, the aggressive physician faces the following dilemma: If the aggressive physician chooses T, the payoff will be $p \times (3) + (1-p) \times (-1) = 4p-1$. If the aggressive physician chooses CM, the payoff will be $p \times (-1) + (1-p) \times (1) = 1-2p$. Thus,

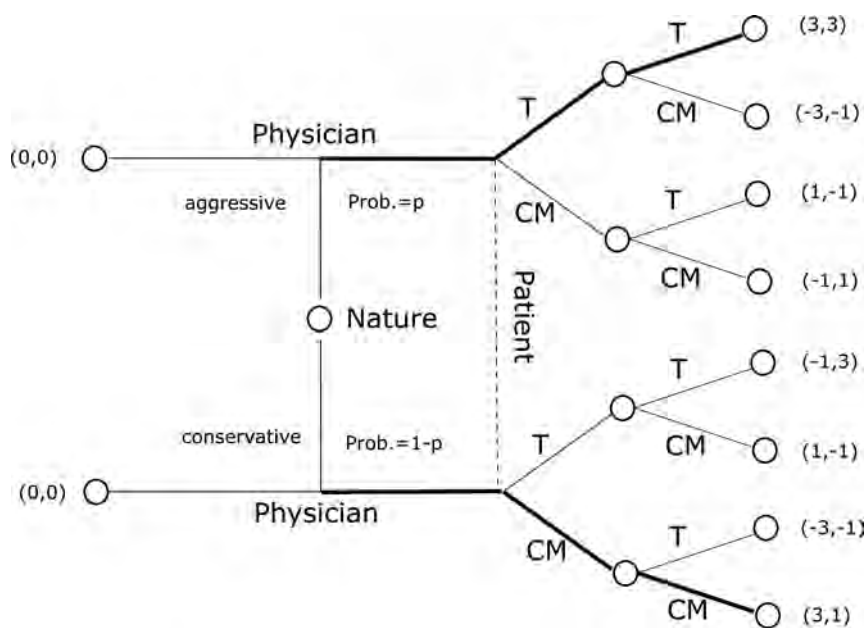


FIG 1. Bayesian Normal Form representation (aggressive physician). Prob. indicates probability.

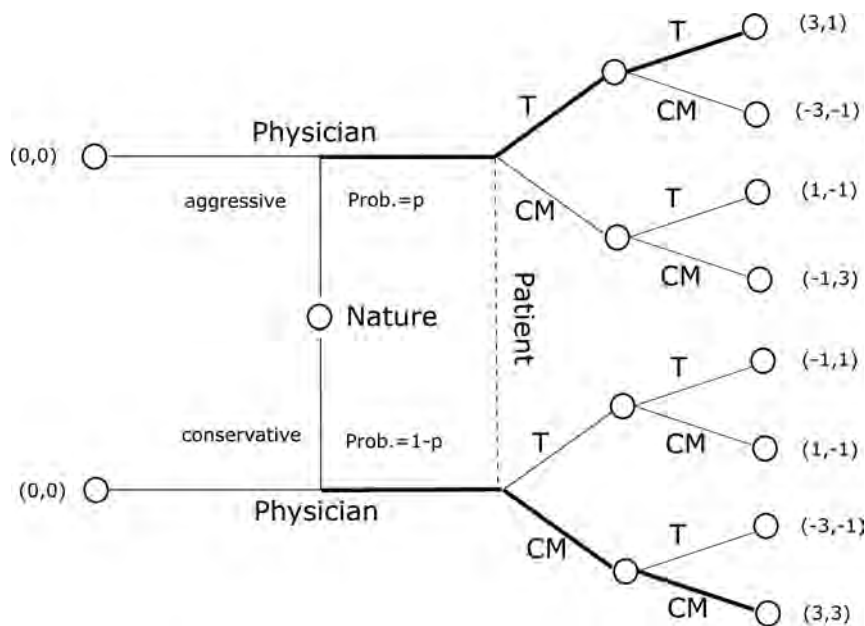


FIG 2. Bayesian Normal Form representation (conservative physician). Prob. indicates probability.

if $4p-1 > 1-2p$, then $p > 1/3$, the aggressive physician will choose T. If $p < 1/3$, the aggressive physician will choose CM. The aggressive physician will flip a coin to decide the choice if $p = 1/3$.

Similarly, the conservative physician faces the following dilemma: If the conservative physician chooses T, the payoff will be $p \times (1) + (1-p) \times (-1) = 2p-1$. If the conservative physician chooses CM, the payoff will be $p \times (-1) + (1-p) \times (3) = 3-4p$. Thus, if $2p-1 > 3-4p$, then $p > 2/3$, the conservative physician will choose T. If $p < 2/3$, the conservative physician will choose

CM. The conservative physician will flip a coin to decide the choice if $p = 2/3$.

Thus, whether the patient is offered first treatment or conservative management depends on both the physician type and the physician's belief of the probability that the patient is an aggressive type.

In our Bayesian game, we have a pure strategy for each type of patient, but the physician does not have a pure strategy because the physician does not know the type of patient presenting for care. Therefore, the physician must play a mixed strategy, using his or her belief about the patient type based on the probability of facing each type of patient.

The optimal mixed strategy in this game is a perfect Bayesian Nash equilibrium, in which each player maximizes the payoffs given his or her belief about the state of Nature and the strategies played by other players. Assuming that both the physician and patient are rational and eliciting individual patient preferences is not practical, it makes sense for the physician to play the game according to the perfect Bayesian Nash equilibrium. The physician will choose the strategy on the basis of the probability of meeting an aggressive patient. The practical implication of this result is that a physician is interested in knowing *ex ante* the proportion of aggressive and conservative patients in the population that he or she is serving. The difference between an aggressive and conservative physician would be in the threshold value of the p that they would use to determine whether to offer treatment or conservative management as a first option.

DISCUSSION

For incidentally detected UIAs, physicians need to consider multiple factors when considering treatment, such as patient preferences, including the anxiety of the patient or the patient's family, the right not to know or patient autonomy, the age of the patient, the complexity of the aneurysm, the risk of aneurysm rupture, and so forth.¹² The diagnosis of a UIA can be a source of stress to the patient. Therefore, the optimal care for patients with a UIA should take patient preferences into account. In clinical practice, it may be time-consuming for a physician to allocate time to elicit individual patient preferences.

Table 1: Combined payoff matrix for both types of patients (aggressive physician)

Physician Type, Aggressive	Physician's Actions	
	T	CM
Patient's actions		
Prefers T (aggressive with p)	(3, 3)	(1, -1)
CM (conservative with probability $1-p$)	(1, -1)	(3, 1)

Table 2: Combined payoff matrix for both types of patients (conservative physician)

Physician Type, Conservative	Physician's Actions	
	T	CM
Patient's actions		
Prefers T (aggressive with p)	(3, 1)	(1, -1)
CM (conservative with probability $1-p$)	(1, -1)	(3, 3)

Our model suggests that a more efficient approach would be to ascertain the patient preferences in the target population the physician is serving to know how many are aggressive-versus-conservative types. Knowing this and knowing his or her own personal preference toward being more aggressive or more conservative with treatment, the physician can choose the more appropriate strategy on which treatment option to offer first every time the physician encounters the situation of equipoise with a small, asymptomatic UIA.

UIAs can be associated with a not-negligible risk of treatment-related complications with associated morbidity and mortality, as well as the risk of recurrence and rupture despite treatment.¹³ Furthermore, it has been reported that for low-risk aneurysms, the benefits of treatment are marginal or even negative, being about 1 life-year for a 20-year-old patient, falling to 0 life-years for a 60-years-old patient, and becoming marginally negative for older patients.¹⁴

Risk-stratification models provide information for physicians on how to use optimal clinical strategies under conditions of uncertainty in the context of a true patient diagnosis.¹⁵ Unfortunately, they do not take into account patient preference. Recently, researchers have been calling for greater patient involvement in decision-making, after receiving precise and detailed information regarding his or her individual aneurysm risk, as well as the potential risks of treatment.¹⁶ Our model demonstrates how patients and physicians could interact to achieve optimal outcomes when approaching small UIAs when clinical equipoise is present.

One limitation of our model is that there may be many more patient types than just aggressive and conservative. For example, a third type of patient might exist who is undecided about whether to be treated or followed up and for whom detailed information about the benefits and risks of both management options would be most valuable. Nevertheless, this patient type does not fundamentally change the model because the main insight from the model is that the physician should start discussions with the patient with the strategy preferred by the most prevalent patient type. If the most prevalent patient type is equally interested in both treatment options, the optimal physician strategy would be to give an overview of the differences between treatment options, instead of starting with one of the

options. There may also be multiple physician types with different incentives regarding treatment of small UIAs. Additionally, the payoff matrices may have different values than we used in our thought experiment. Our aim was to investigate the importance of taking patient preferences into account in the decision-making about the treatment of small UIAs, and we found that patient preference can impact ultimate treatment decisions if one is attempting to achieve optimal outcomes.

Finally, this model assumes equipoise in the physician's drive to treat versus monitor an aneurysm. If the conversation between the patient and the physician regarding the relative risks of treatment versus observation is presented as "a time bomb ticking in your head" versus "most likely this aneurysm will never bleed," the patient will likely be led to very different treatment choices. Thus, patient preference is linked to physician preference in terms of the level at which treatment is offered or physician comfort with risk-taking. In this model, we assume that the physician does not have a preference as to whether to treat or not to treat the aneurysm. Therefore, the physician might consider eliciting patient preferences regarding treatment or observation of UIAs.

Identifying patient preferences would allow the physician to categorize patients into different types and offer them different options in terms of managing their UIA. On the other hand, in practice it may be difficult to elicit an individual patient's preference, and unconscious biases may influence a physician's perceptions. Therefore, it is possible that in clinical practice, an optimal strategy for the physician would be to play the sequential Bayesian game on the basis of the probability of meeting each patient type in their clinical practice, instead of spending time and effort eliciting individual patient preferences. This possibility should not be interpreted as an implicit bias in a clinical scenario because from the clinical perspective, the benefits of treatment are about equal to the risks of treatment. The sequential Bayesian game provides an efficient mechanism to take patient preferences into account quickly in the clinical setting.

In clinical practice, every patient should be offered the opportunity to choose aggressive or conservative management. Our analysis focuses on the first option a physician should prioritize or bring up in discussions with the patient. All other options should also be explained to ensure informed patient decision-making. Nevertheless, if a physician chooses the strategy on the basis of the probability of meeting an aggressive patient, the probability of the patient's acceptance of the first proposed strategy is the highest, saving valuable time for the physician and patient. Besides, with this strategy, there is a higher chance that the patient's preferred small, low-risk UIA management strategy is selected, which increases patient satisfaction.

CONCLUSIONS

Patient preferences need to be taken into account in decision-making to treat or observe low-risk aneurysms when on the basis of other factors like age and medical comorbidities, there is clinical equipoise. On the other hand, eliciting individual patient preferences in clinical care may not be practical. To achieve an optimal outcome, physicians should gauge preferences in their patient population and incorporate this knowledge into their management of small low-risk UIAs. Knowing the proportion of

aggressive patients in their patient population may help physicians determine whether to offer treatment or conservative management first when equipoise exists.

Disclosure forms provided by the authors are available with the full text and PDF of this article at www.ajnr.org.

REFERENCES

1. Vlak MH, Algra A, Brandenburg R, et al. **Prevalence of unruptured intracranial aneurysms, with emphasis on sex, age, comorbidity, country, and time period: a systematic review and meta-analysis.** *Lancet Neurol* 2011;10:626–36 CrossRef Medline
2. Golnari P, Nazari P, Garcia RM, et al. **Volumes, outcomes, and complications after surgical versus endovascular treatment of aneurysms in the United States (1993-2015): continued evolution versus steady-state after more than 2 decades of practice.** *J Neurosurg* 2020;134:848–61 CrossRef Medline
3. Malhotra A, Wu X, Forman HP, et al. **Management of unruptured intracranial aneurysms in older adults: a cost-effectiveness analysis.** *Radiology* 2019;291:411–17 CrossRef Medline
4. Murayama Y, Takao H, Ishibashi T, et al. **Risk analysis of unruptured intracranial aneurysms: prospective 10-year cohort study.** *Stroke* 2016;47:365–71 CrossRef Medline
5. Wiebers DO, Whisnant JP, Huston J 3rd, et al. International Study of Unruptured Intracranial Aneurysms Investigators. **Unruptured intracranial aneurysms: natural history, clinical outcome, and risks of surgical and endovascular treatment.** *Lancet* 2003;362:103–10 CrossRef Medline
6. Malhotra A, Wu X, Forman HP, et al. **Growth and rupture risk of small unruptured intracranial aneurysms: a systematic review.** *Ann Intern Med* 2017;167:26–33 CrossRef Medline
7. Malhotra A, Wu X, Geng B, et al. **Management of small unruptured intracranial aneurysms: a survey of neuroradiologists.** *AJNR Am J Neuroradiol* 2018;39:875–80 CrossRef Medline
8. Wu X, Matouk CC, Mangla R, et al. **Cost-effectiveness of computed tomography angiography in management of tiny unruptured intracranial aneurysms in the United States.** *Stroke* 2019;50:2396–2403 CrossRef Medline
9. Ajiboye N, Chalouhi N, Starke RM, et al. **Unruptured cerebral aneurysms: evaluation and management.** *ScientificWorldJournal* 2015;2015:954954 CrossRef Medline
10. Komotar RJ, Mocco J, Solomon RA. **Guidelines for the surgical treatment of unruptured intracranial aneurysms: the first annual J. Lawrence Pool Memorial Research Symposium—controversies in the management of cerebral aneurysms.** *Neurosurgery* 2008;62:183–93; discussion 193–94 CrossRef Medline
11. Malhotra A, Wu X, Forman HP, et al. **Management of tiny unruptured intracranial aneurysms: a comparative effectiveness analysis.** *JAMA Neurol* 2018;75:27–34 CrossRef Medline
12. Wardlaw JM, White PM. **The detection and management of unruptured intracranial aneurysms.** *Brain* 2000;123:205–21 CrossRef Medline
13. Yamaki VN, Brinjikji W, Murad MH, et al. **Endovascular treatment of very small intracranial aneurysms: meta-analysis.** *AJNR Am J Neuroradiol* 2016;37:862–67 CrossRef Medline
14. Benes V3, Mitchell P, Molyneux AJ, et al. **Endovascular coiling in 131 patients with low complication rate justifies treating most unruptured intracranial aneurysms.** *Cent Eur Neurosurg* 2010;71:1–7 CrossRef Medline
15. Thompson BG, Brown RD Jr, Amin-Hanjani S, et al; American Heart Association Stroke Council, Council on Cardiovascular and Stroke Nursing, and Council on Epidemiology and Prevention; American Heart Association; American Stroke Association. **Guidelines for the Management of Patients with Unruptured Intracranial Aneurysms: a Guideline for Healthcare Professionals from the American Heart Association/American Stroke Association.** *Stroke* 2015;46:2368–400 CrossRef Medline
16. Pierot L, Gawlitza M, Soize S. **Unruptured intracranial aneurysms: management strategy and current endovascular treatment options.** *Expert Rev Neurother* 2017;17:977–86 CrossRef Medline

Sodium MRI at 7T for Early Response Evaluation of Intracranial Tumors following Stereotactic Radiotherapy Using the CyberKnife

L. Huang, J. Bai, R. Zong, J. Zhou, Z. Zuo, X. Chai, Z. Wang, J. An, Y. Zhuo, F. Boada, X. Yu, Z. Ling, B. Qu, L. Pan, and Z. Zhang



ABSTRACT

BACKGROUND AND PURPOSE: Conventionally, early treatment response to stereotactic radiotherapy in intracranial tumors is often determined by structural MR imaging. Tissue sodium concentration is altered by cellular integrity and energy status in cells. In this study, we aimed to investigate the feasibility of sodium MR imaging at 7T for the preliminary evaluation of radiotherapeutic efficacy for intracranial tumors.

MATERIALS AND METHODS: Data were collected from 16 patients (12 men and 4 women, 24–75 years of age) with 22 intracranial tumors who were treated with stereotactic radiation therapy using CyberKnife at our institution between December 1, 2016, and August 15, 2019. Sodium MR imaging was performed at 7T before and 48 hours, 1 week, and 1 month after CyberKnife radiation therapy. Tissue sodium concentration (TSC) was calculated and analyzed based on manually labeled regions of tumors.

RESULTS: Ultra-high-field sodium MR imaging clearly showed the intratumoral signal, which is significantly higher than that of normal tissue ($t = 5.250$, $P < .001$), but the edema zone has some influence. The average TSC ratios of tumor to CSF in the 22 tumors, contralateral normal tissues, edema zones, frontal cortex, and frontal white matter were 0.66 (range, 0.23–1.5), 0.30 (range, 0.15–0.43), 0.58 (range, 0.25–1.21), 0.25 (range, 0.17–0.42), and 0.30 (range, 0.19–0.49), respectively. A total of 12 tumors in 8 patients were scanned at 48 hours, 1 week, and 1 month after treatment. The average TSC at 48 hours after treatment was 0.06 higher than that before treatment and began to decrease at 1 week. The TSC ratios of 10 continued to decline and 2 tumors increased at 1 month, respectively. Tumor volume decreased by 2.4%–99% after 3 months.

CONCLUSIONS: Changes in the TSC can be quantified by sodium MR imaging at 7T and used to detect radiobiologic alterations in intracranial tumors at early time points after CyberKnife radiation therapy.

ABBREVIATIONS: ATPase = adenosine triphosphatase; CK = CyberKnife; SRT = stereotactic radiotherapy; TSC = tissue sodium concentration; VEGF = vascular endothelial growth factor

Stereotactic radiation therapy (SRT) is an established and effective treatment for intracranial tumors. This therapy consists of a single or a few administrations of high-dose radiation therapy to well-defined tumor targets, rather than repeat low-dose irradiation of tumor cells and normal cells. CyberKnife (CK; Accuray) is a compact, image-guided linear accelerator with a robotic manipulator that is designed for stereotactic radiosurgery

and SRT.¹ Several studies have suggested that radiosurgery may induce apoptotic tumor cell death.^{2–4} The specific cellular changes induced by dose fractionation involving a single or a few high-dose treatments remain unclear. An adequate imaging response of brain tumors after CK involves stable or reduced tumor volumes on serial conventional imaging. However, the biologic changes of the internal environment and cytologic levels of the tumor occur earlier than the visible volume changes after

Received May 8, 2021; accepted after revision November 5.

From the Departments of Neurosurgery (L.H., R.Z., J.Z., X.Y., Z.L., L.P.) and Radiation Oncology (J.B., B.Q.), The First Medical Center of PLA General Hospital, Beijing, China; Department of Neurosurgery (L.H.), The Hospital of 81st Group Army PLA, Zhangjiakou, China; State Key Laboratory of Brain and Cognitive Science (Z. Zou, X.C., Z.W., Y. Z., Z. Zhang), Institute of Biophysics, Chinese Academy of Sciences, Beijing, China; University of Chinese Academy of Sciences (Z. Zou, X.C., Z.W., Y. Z., Z. Zhang), Beijing, China; CAS Center for Excellence in Brain Science and Intelligence Technology (Z. Zou, X.C., Z.W., Y. Z., Z. Zhang), Chinese Academy of Sciences, Beijing, China; Siemens Shenzhen Magnetic Resonance Ltd (J.A.), Shenzhen, China; and Department of Radiology (F.B.), Center for Advanced Imaging Innovation and Research, New York University Grossman School of Medicine, New York, New York.

This work was supported by the National Natural Science Foundation of China (82001804, 31730039), the Ministry of Science and Technology of China grant (2019YFA0707103), and the Chinese Academy of Sciences grants (XDB32010300, ZDBS-LY-SM028).

Please address correspondence to Longsheng Pan, MD, Department of Neurosurgery, The First Medical Center of PLA General Hospital, Fuxing Rd Yard 28, Beijing 100853, China; e-mail: panls301@163.com

Indicates open access to non-subscribers at www.ajnr.org

Indicates article with online supplemental data.

<http://dx.doi.org/10.3174/ajnr.A7404>

Signal intensity of ROIs in sodium images

	Untreated	48 Hours	1 Week	1 Month
Tumor (mean)	22.85 (SD, 2.61)	24.19 (SD, 2.45)	22.28 (SD, 0.27)	36.08 (SD, 0.12)
CSF (mean)	23.23 (SD, 7.56)	24.43 (SD, 2.66)	27.53 (SD, 0.33)	25.92 (SD, 0.26)
Ratio	0.98	0.99	0.80	1.39

radiation therapy. Conventional MR imaging can only show volumetric changes, so there is a lag effect. Thus, increasing numbers of studies are trying to find specific biomarkers of brain tumors for early prediction of therapeutic effects.⁵⁻¹⁰

The biologic parameters of tumor cells, such as acid-base and ionic balance, are different from those of normal cells before treatment⁹ and after radiation therapy¹¹ and chemotherapy.¹² Sodium is the second most abundant MR imaging–active nucleus in the human body, and sodium concentration is sensitive to disease because it is an indicator of cellular and metabolic integrity and ion homeostasis.^{13,14} The cellular process of the sodium ion ($^{23}\text{Na}^+$) homeostasis proceeds via coupled exchange with the potassium ions (K^+) between the intra- and extracellular spaces using the Na^+/K^+ -adenosine triphosphatase (ATPase) enzyme.¹⁵ Dysregulation of the Na^+/K^+ -ATPase or impairment of ATPase-dependent processes causes loss of Na^+ homeostasis and, therefore, increased intracellular sodium concentration, ultimately leading to cell death.¹⁶ Therefore, the Na^+ ion concentration is very sensitive to changes of the tissue metabolic state and cell membrane integrity. Since 1983, sodium MR imaging has been used to detect the Na^+ ions present at different concentrations in various tissues.¹⁷ However, because this technique has a low signal-to-noise ratio and spatial resolution and the imaging time is long, the related research is limited. With the continuous development of MR imaging equipment and technology, the imaging quality of Na^+ continues to improve.

Previous studies have found that the tissue sodium concentration (TSC) is higher than that in normal tissue in patients with diseases such as brain tumors,⁸ stroke,¹⁸ multiple sclerosis,¹⁹ and Huntington disease.²⁰ In 2006, Schepkin et al²¹ detected the early cellular changes of cytotoxin therapy using sodium and proton diffusion MR imaging. They observed that the ADC value and the early TSC increase occurred before the volume change and showed a linear relationship.²¹ This finding suggests that these noninvasive imaging patterns can be used as predictive biomarkers of tumor treatment response. There have been few reports on the application of sodium MR imaging to the evaluation of radiation therapy, and there are no relevant reports evaluating the effects of SRT with CK. Huang et al²² published a case report about this method in 2018. Nevertheless, sodium MR imaging may be a useful noninvasive biomarker for evaluating the early tumor response to therapy, allowing timely adjustment of individualized treatment plans. The goal of the present study was to use sodium MR imaging to noninvasively quantify total TSC and to test whether TSC is altered in intracranial tumors.

MATERIALS AND METHODS

Patient and Tumor Characteristics

We enrolled 16 patients with a total of 22 tumors diagnosed as intracranial tumors by imaging diagnosis or pathology who

underwent SRT with CK from December 1, 2016, to August 15, 2019, at our hospital. Twelve patients were men (75%) and 4 were women (25%), and they had a median age of 52.4 years (range, 24–75 years) at the time of initial CK therapy. The tumors were numbered between 1 and 16 (ie, 1–3,

4.1, 4.2, 5, 6.1, 6.2, 7, 8, 9.1, 9.2, 9.3, 10–14, 15.1, 15.2, 15.3, and 16). Written informed consent was obtained from each participant before study inclusion, and the study was approved by the institutional review board of PLA General Hospital (No. S2018-119-01). All the patients' other treatments followed the principles of primary disease treatment. More patient details are described in the Online Supplemental Data. The patients underwent pretreatment sodium and proton MR imaging scans at a human 7T MR research system (Siemens Healthcare, Erlangen, Germany) and were then treated with SRT using CK. In total, 8 patients (who had a total of 12 tumors) completed follow-up scans at 48 hours, 1 week, and 1 month after treatment.

Quantitative Sodium MR Imaging

Sodium and proton imaging was performed on a human 7T MR research system (Siemens Healthcare, Erlangen, Germany). Proton imaging was first conducted with a 32-channel head coil (Nova Medical Head Coil 1TX/32RX). B_0 shimming parameters were recorded for subsequent shimming during the sodium imaging. Structural and diffusion images were acquired according to the protocols in the Table. Sodium MR imaging was acquired with a homemade birdcage coil. Sodium images with TEs of 0.30 and 2.32 ms were acquired using the twisted projection imaging sequence²³ with the following parameters: FOV = $224 \times 224 \times 224 \text{ mm}^3$, resolution = $3.5 \times 3.5 \times 3.5 \text{ mm}^3$, TR = 174 ms, flip angle = 90° , and acquisition time = 12 minutes 53 seconds.

The sodium images with different TEs were postprocessed to correct for B_0 bias.²⁴ The TSC maps were linearly corrected with reference to tube phantoms with known sodium concentrations of 30, 60, 90, and 120 mM.²⁴ The ROIs for analysis were manually defined on the sodium images by a neurosurgeon. The ratios of the TSC signal between different tissues and CSF were calculated and compared.

ROI Analysis

The ROI analysis was performed in MRICron (<https://www.nitrc.org/projects/mricron>). The tumor ROI was manually defined as a sphere with a radius of 2 mm. The maximum, minimum, and average signal intensities of the ROI were obtained, and the average was selected as the final value. The corresponding information about CSF, contralateral normal tissue, gray matter, and white matter of the frontal cortex was measured by the same method. To reduce error, we used the ratio of TSC values between the ROI and CSF to assess the differences among scans.

Statistical Analysis

We used SPSS 22.0 (IBM) for statistical analyses, using paired *t* tests to analyze the differences in TSC before and after treatment and between different tumors and tissues. $P < .05$ was considered significant. Routine contrast-enhanced MR imaging was performed after

3 months of treatment, and the rate of change in tumor volume before and after treatment was calculated. Tumor dimensions were measured using the Coniglobus formula: $V = 1/6\pi \times a$ (diameter length) $\times b$ (diameter width) $\times m$ (section thickness) $\times c$ (section number).²⁵

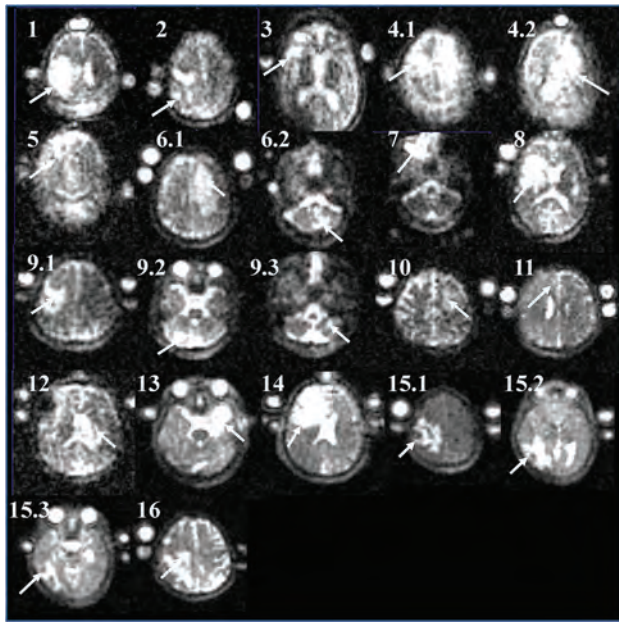


FIG 1. Sodium MR images after B_0 correction of 22 tumors. The arrows pointed to the positions of tumors.

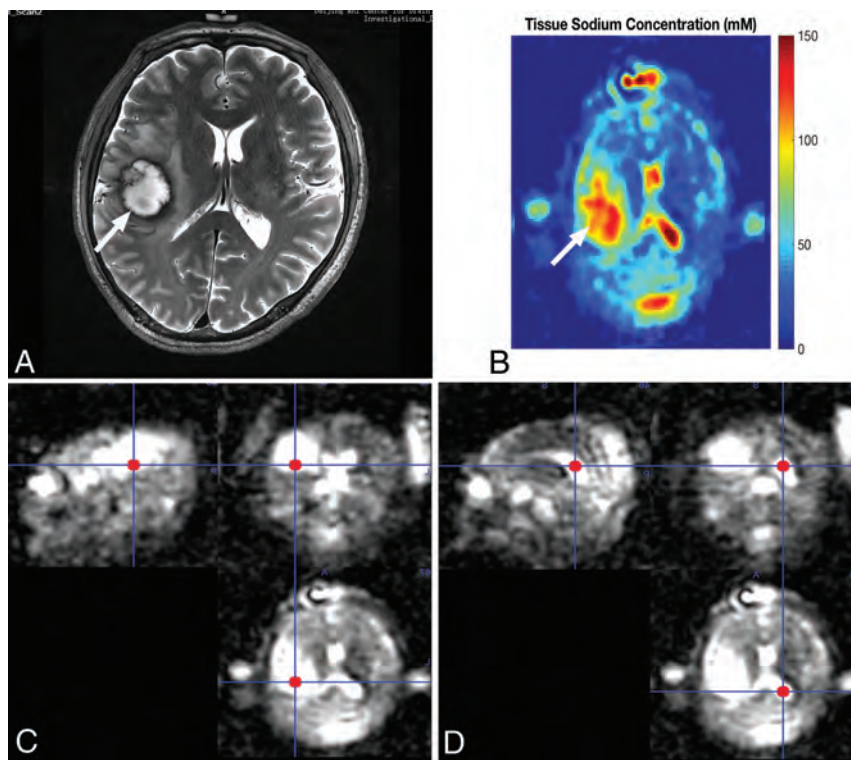


FIG 2. Proton and sodium MR imaging of tumor 1 at 7T. A, Axial T2-weighted image shows brain metastasis of rectal cancer at the right frontal-parietal lobe. B, The reconstructed sodium image. C and D, The ROI of the tumor and CSF in MRIcron software with the quantitative result.

RESULTS

The target irradiation dose to the ROI was 18–22.5 Gy, and the isodose line was 70%–75%, which was completed in 3 fractions. Ultra-high-field sodium MR imaging after B_0 correction clearly showed the intratumoral signal, which is higher than that of normal tissue, but the edema zone has some influence (Fig 1). The uncorrected images can be found in the Online Supplemental Figure. Figure 2 shows the imaging of tumor 1 and the TSC quantitative method. The average TSC ratios between tumor and CSF in the 22 tumors, the contralateral normal tissues, edema zones, frontal cortex, and frontal white matter were 0.66 (range, 0.23–1.5), 0.30 (range, 0.15–0.43), 0.58 (range, 0.25–1.21), 0.25 (range, 0.17–0.40), and 0.30 (range, 0.19–0.49), respectively. The TSC in the tumor before treatment was higher than that in normal tissue ($t = 5.934$, $P < .01$), and the TSC of cortical white matter was higher than that of gray matter ($t = 5.243$, $P = < .01$). Although the average TSC in tumors was higher than that in edema zones, there was no significant difference ($t = 1.694$, $P = .10$).

Figure 3 shows the quantitative results of the 22 tumors. The TSC results in different tumors show that brain metastases of liver cancer were the most frequent tumor type in this study. Tumor volume decreased by 2.4%–99% at 3 months after treatment. The TSC values measured in the 12 tumors at 48 hours after treatment were higher than those before treatment by a mean of 0.06. The TSC values of tumors increased by varying degrees at 48 hours after CK treatment and decreased after 1 week. After 1 month, the TSC values continued to decline in 10 tumors, but increased in 2 tumors.

Tumor volume decreased by 2.4%–99% after 3 months. Two tumors showed a second peak in TSC after 1 month and relapsed at 6 and 12 months after treatment. Figure 4 shows a typical case (tumor 14), for which sodium MR imaging signal intensity is listed in the Table.

DISCUSSION

Currently, SRT is used as the main initial treatment for some intracranial tumors, and it can also be used as an adjuvant treatment for postoperative residue or recurrence. The traditional method of evaluating radiotherapeutic efficacy is to observe changes of tumor size using CT/MR imaging after 3 months. However, that method has the disadvantages of the hysteresis effect and the impossibility of observing changes in the intracellular environment of the tumor. Thus, an increasing number of researchers have been exploring noninvasive and quantifiable methods of detecting changes of the intracellular environment after radiation therapy. Sodium MR imaging has mostly been

investigated in intracranial tumors before tumor treatment. For example, Ouwerkerk et al⁹ used hydrogen and sodium MR imaging to quantify the differences in the sodium concentration between normal brain tissue and tumor tissue in 2003. However, studies of sodium MR imaging scans acquired at multiple time points before and after radiation therapy have not been reported. In this study, a good signal-to-noise ratio was obtained under 7T field intensity, and the image quality was satisfactory.

We now discuss environmental changes in tumors. Malignant tumors are characterized by angiogenesis and cell proliferation. This unregulated cell division, which leads to tumor growth, can result from changes in Na⁺/K⁺-ATPase exchange kinetics and increased intracellular sodium concentration,²⁶ accompanied by tumor deterioration.²⁷ Similarly, the increase of tumor neovascularization and interstitial space increases the extracellular volume fraction, which is also related to the potential of the tumor.²⁸ As a result, TSC levels are increased in malignant tumor tissues. The sodium MR imaging data of 22 tumors in 16 patients before

treatment were analyzed and compared. The TSC of the 22 tumors was 55% higher than that of the contralateral normal brain tissue. This result is similar to those of the quantitative analysis of 20 cases of gliomas by Ouwerkerk et al,⁹ who found that the TSC in the tumor and surrounding tissues was 50%–60% higher than that on the contralateral side. In this study, the TSC values in tumors were generally higher than those in edema zones and contralateral normal tissues, while the TSC values in the white matter were higher than those in the gray matter. The TSC values of tumors and edema zones were significantly different from those of normal tissue. Previous studies have also found increased sodium signal intensity in tumors of mice,²⁹ rats,³⁰ and human brains.³¹

Our results showed increased TSC values in additional tumor types, such as metastases, lymphomas, and meningiomas. There is not very good differentiation between the TSC increases in tumors and edema zones. Although the average TSC of tumor tissue in this study was higher than that in edema zones, there was no significant difference. The edema zones surrounding 7 tumors (27.2%) had

higher signal values than the tumors. The pathologic result of the tumors was lung adenocarcinoma. Brain metastases tend to produce vasogenic edema, which is caused by the accumulation of protein-rich fluids in the extracellular space after the blood-brain barrier is destroyed. The increased volume of extracellular space increases the extracellular volume fraction, which also results in an increased TSC value in the edema zone.

The tumor's mechanism of destruction of the blood-brain barrier has 2

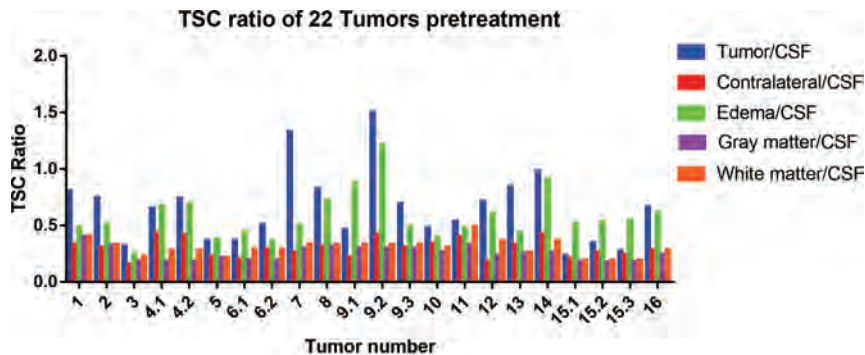


FIG 3. TSC ratio of 22 tumors pretreatment.

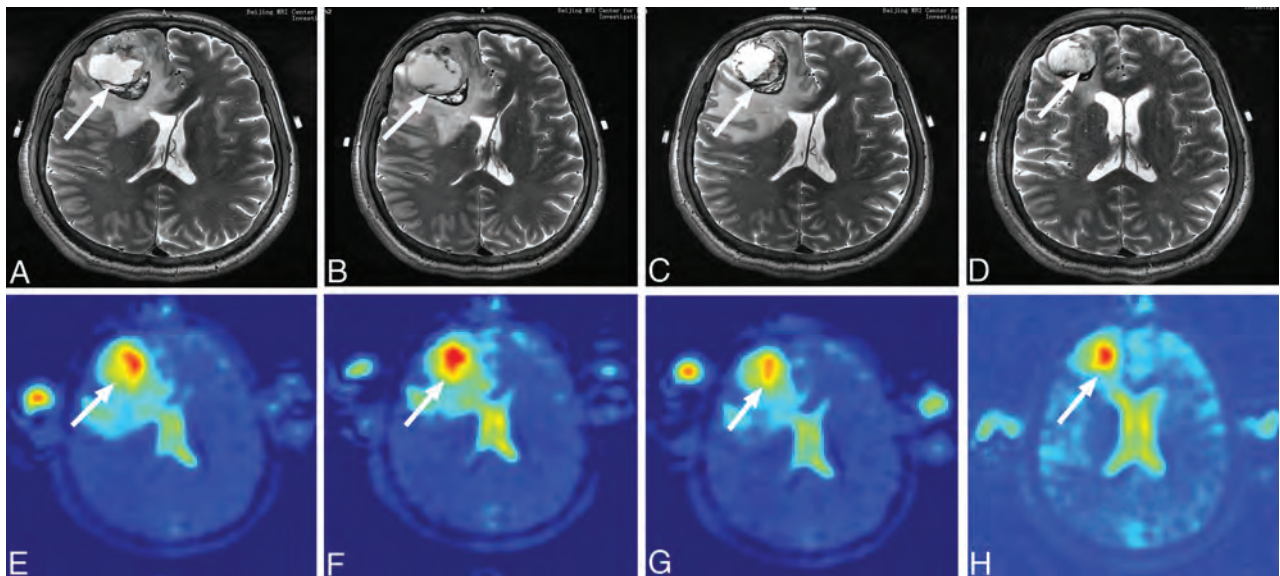


FIG 4. A, Axial T2-weighted image showing brain metastasis of pulmonary neuroendocrine carcinoma complicated with adenocarcinoma (tumor 14). B, T2-weighted image 48 hours after CK. C, T2-weighted image 1 week after CK. D, T2-weighted image 1 month after CK. E, Sodium MR imaging pretreatment. F, Sodium MR imaging 48 hours after CK. G, Sodium MR imaging 1 week after CK. H, Sodium MR imaging 1 month after CK. The arrows pointed to the metastasis.

main components: First, there is local production of factors that increase the tumor's vascular permeability, such as vascular endothelial growth factor (VEGF),³² glutamate,³³ and leukotriene.³⁴ Second, tumor vascular endothelial cells lack tight connections between them. The loss of blood-brain barrier integrity in brain tumors is largely attributable to the VEGF, the expression of which is also upregulated in gliomas, meningiomas, and metastatic tumors.³⁵⁻³⁸ VEGF expression has also been found to be significantly different in different pathologic types: VEGF expression in lung adenocarcinoma was observed to be significantly higher than that in squamous cell carcinoma.³⁹ The increased TSC values that we observed in the brain metastatic edema zones of lung adenocarcinoma also reflect the severity of the edema, which may be related to the actions of VEGF. This point needs to be confirmed by further research.

Our observed TSC values reflect the total amount of Na^+ inside and outside the cell, so the increased TSC values in tumors and edema zones may reflect this change in ion balance. In particular, a 60% increase in the Na^+ concentration in tumors requires a several-fold increase in intracellular Na^+ , a similar increase in the extracellular volume fraction, or a combination of both. The reason for this change is the decrease of Na^+/K^+ -ATPase enzyme activity and the change in Na/H exchange kinetics, which lead to the increase of intracellular Na^+ concentration and participate in malignant transformation of tumors. In this study, we only collected roughly descriptive statistics about the pathologic results of breast cancer brain metastases, lung cancer brain metastases, lymphomas, rectal cancer brain metastases, meningiomas, and liver cancer brain metastases. Among them, the Na^+ concentration in brain metastases of liver cancer was the highest, and that of breast cancer was the lowest. Biller et al⁶ showed that 7T sodium MRI can be used to help with the grading of gliomas in a study of 34 patients with World Health Organization grades I-IV untreated gliomas. Bartha et al⁷ characterized the metabolic profile of low-grade gliomas using short TE ^1H -MR spectroscopy and assessing the correlations between metabolite levels and sodium MR imaging. Although the Glu concentration is reduced and that of myoinositol is elevated in low-grade glioma tissue, the $\text{NAA}/^{23}\text{Na}$ ratio was the most sensitive indicator of pathologic tissue. Biller et al⁶ found that the sodium signal was even superior to the molecular signature of *IDH* mutation status for progression prediction in gliomas. The information provided by sodium MR imaging may help to classify neoplasias at an early stage, reduce invasive tissue characterization procedures such as stereotactic biopsy specimens, and promote improved and individualized patient management in neuro-oncology by using imaging signatures of brain tumors. Future work should examine the potential for these metabolic parameters to distinguish among tumors of different pathologic types.

It is speculative to judge the prognosis of a tumor by the sodium concentration data before treatment. Multi-time quantitative observations could capture the changes of tumor sodium concentration in the early stage of SRT with CK more directly and help analyze the relationships between tumor TSC and internal environmental changes. In previous animal studies, only

sodium MR imaging was used to observe the changes of tumors after chemotherapy.⁴⁰ The imbalance of Na^+/K^+ -ATPase and ATP-dependent processes in cells can lead to ion imbalance, which, in turn, increases intracellular sodium. Because the ionic gradient can no longer be maintained, this issue can lead to cell death.⁴¹ According to Thulborn et al,⁸ these bioscales can monitor the spatial distribution of tissue responses to radiation treatment on at least a weekly basis. Such rapid feedback could be used to guide patient-adaptive radiation treatment and avoid excessive radiation administration when no response can be achieved.

The purpose of this study was to determine the change rule of TSC before any change in tumor volume occurs. Therefore, we assessed the volume and TSC of 12 lesions in 8 patients before treatment and 48 hours, 1 week, and 1 month after treatment and observed the overall change trends. The first TSC peak appeared within 48 hours after radiation therapy. Cell volume reduction and chromatin-condensed cells may have apoptotic characteristics,⁴¹ whereas sodium overload may be strongly related to apoptosis and even cause apoptosis itself. The first Na^+ concentration peak after CK SRT was caused by sodium overload after radiation, which, in turn, caused an increase in apoptosis, as reflected by the resulting destruction of cell membrane integrity. This result is consistent with our previous results of apoptosis imaging.⁴² The number of cells decreased at the later stage of apoptosis, and TSC subsequently decreased. These preliminary results suggest that sodium MR imaging provides reliable evidence in the early evaluation of the efficacy of radiation therapy for intracranial tumors. Tumors 7 and 14 showed a second TSC peak after 1 month, and those patients relapsed at 6 and 12 months after treatment, respectively. We speculate that this relapse was related to the active recurrence and proliferation of these tumors, increased cell division, resistance to radiation therapy, and vascular proliferation. These results illustrate that sodium MR imaging provides important supplementary information about biologic activity. It can be measured quantitatively and is noninvasive. Although sodium MR imaging is only used as a complementary method to proton MR imaging or other imaging methods such as PET, its great clinical value is still worthy of further study.

There are still several limitations of our study. The dual-tuned coil was not available, so B_0 shimming was completed with the proton coil, and the shimming parameters were transferred to sodium imaging. The change of coil resulted in the variation of the B_0 field, though we tried to keep the position of the patient consistent. It downgraded the performance of B_0 shimming and the SNR of sodium imaging. Other limitations of our study included the retrospective design, the small number of patients, and the relatively short follow-up period. More time points of follow-up and a larger sample are required to establish the long-term efficacy of sodium MR imaging. Improved software and technology are necessary to achieve accurate quantification of Na^+ concentrations because the current applications have many problems, and we will continue to study such improvements. Therefore, we must be cautious with our conclusions because the present findings are preliminary. Although a longer follow-up period and a larger sample are necessary to confirm these results, this study of

the evaluation of radiotherapeutic effects using sodium MR imaging for intracranial tumors had very encouraging results.

CONCLUSIONS

Changes in the TSC using sodium MR imaging can be used to detect radiobiologic alterations in brain tumors at early time points after CK radiation therapy. It can provide supplementary information to assist with individualized and accurate tumor treatment.

ACKNOWLEDGMENTS

The authors thank Fernando E. Boada from New York University for providing the twisted projection imaging sequence and tuning the scanning parameters.

Disclosure forms provided by the authors are available with the full text and PDF of this article at www.ajnr.org.

REFERENCES

- Adler JR, Murphy MJ, Chang SD, et al. **Image-guided robotic radiosurgery.** *Neurosurgery* 1999;44:1299–306; discussion 1306–07 Medline
- Witham TF, Okada H, Fellows W, et al. **The characterization of tumor apoptosis after experimental radiosurgery.** *Stereotact Funct Neurosurg* 2005;83:17–24 CrossRef Medline
- Tsuzuki T, Tsunoda S, Sakaki T, et al. **Tumor cell proliferation and apoptosis associated with the Gamma Knife effect.** *Stereotact Funct Neurosurg* 1996;66(Suppl 1):39–48 CrossRef Medline
- Kurita H, Ostertag CB, Baumer B, et al. **Early effects of PRS-irradiation for 9L gliosarcoma: characterization of interphase cell death.** *Minim Invasive Neurosurg* 2000;43:197–200 CrossRef Medline
- Haneder S, Giordano FA, Konstandin S, et al. **²³Na-MRI of recurrent glioblastoma multiforme after intraoperative radiotherapy: technical note.** *Neuroradiology* 2015;57:321–26 CrossRef Medline
- Biller A, Badde S, Nagel A, et al. **Improved brain tumor classification by sodium MR imaging: prediction of IDH mutation status and tumor progression.** *AJNR Am J Neuroradiol* 2016;37:66–73 CrossRef Medline
- Bartha R, Megyesi JF, Watling CJ. **Low-grade glioma: correlation of short echo time 1H-MR spectroscopy with ²³Na MR imaging.** *AJNR Am J Neuroradiol* 2008;29:464–70 CrossRef Medline
- Thulborn KR, Lu A, Atkinson IC, et al. **Quantitative sodium MR imaging and sodium bioscales for the management of brain tumors.** *Neuroimaging Clin N Am* 2009;19:615–24 CrossRef Medline
- Ouwkerk R, Bleich KB, Gillen JS, et al. **Tissue sodium concentration in human brain tumors as measured with ²³Na MR imaging.** *Radiology* 2003;227:529–37 CrossRef Medline
- Laymon CM, Oborski MJ, Lee VK, et al. **Combined imaging biomarkers for therapy evaluation in glioblastoma multiforme: correlating sodium MRI and F-18 FLT PET on a voxel-wise basis.** *Magn Reson Imaging* 2012;30:1268–78 CrossRef Medline
- Baskar R, Lee KA, Yeo R, et al. **Cancer and radiation therapy: current advances and future directions.** *Int J Med Sci* 2012;9:193–99 CrossRef Medline
- Schepkin VD, Bejarano FC, Morgan T, et al. **In vivo magnetic resonance imaging of sodium and diffusion in rat glioma at 21.1 T.** *Magn Reson Med* 2012;67:1159–66 CrossRef Medline
- Nagy I, Lustyk G, Lukács G, et al. **Correlation of malignancy with the intracellular Na⁺:K⁺ ratio in human thyroid tumors.** *Cancer Res* 1983;43:5395–402 Medline
- Ng KH, Bradley DA, Looi LM. **Elevated trace element concentrations in malignant breast tissues.** *Br J Radiol* 1997;70:375–82 CrossRef Medline
- Rose AM, Valdes R. **Understanding the sodium pump and its relevance to disease.** *Clin Chem* 1994;40:1674–85 Medline
- Madelin G, Kline R, Walvick R, et al. **A method for estimating intracellular sodium concentration and extracellular volume fraction in brain in vivo using sodium magnetic resonance imaging.** *Sci Rep* 2014;4:4763 CrossRef Medline
- Hilal SK, Maudsley AA, Simon HE, et al. **In vivo NMR imaging of tissue sodium in the intact cat before and after acute cerebral stroke.** *AJNR Am J Neuroradiol* 1983;4:245–49 Medline
- Jones SC, Kharlamov A, Yanovski B, et al. **Stroke onset time using sodium MRI in rat focal cerebral ischemia.** *Stroke* 2006;37:883–88 CrossRef Medline
- Maarouf A, Audoin B, Konstandin S, et al. **Topography of brain sodium accumulation in progressive multiple sclerosis.** *Magn Reson Mater Phys* 2014;27:53–62 CrossRef Medline
- Reetz K, Romanzetti S, Dogan I, et al. **Increased brain tissue sodium concentration in Huntington's disease: a sodium imaging study at 4 T.** *Neuroimage* 2012;63:517–24 CrossRef Medline
- Schepkin VD, Chenevert TL, Kuszpit K, et al. **Sodium and proton diffusion MRI as biomarkers for early therapeutic response in subcutaneous tumors.** *Magn Reson Imaging* 2006;24:273–78 CrossRef Medline
- Huang L, Zhang Z, Qu B, et al. **Imaging of sodium MRI for therapy evaluation of brain metastases with CyberKnife at 7T: a case report.** *Cureus* 2018;10:e2502 CrossRef Medline
- Lu A, Atkinson IC, Claiborne TC, et al. **Quantitative sodium imaging with a flexible twisted projection pulse sequence.** *Magn Reson Med* 2010;63:1583–93 CrossRef Medline
- O'Donnell M, Edelstein WA. **NMR imaging in the presence of magnetic field inhomogeneities and gradient field nonlinearities.** *Med Phys* 1985;12:20–06 CrossRef Medline
- Kothari RU, Brott T, Broderick JP, et al. **The ABCs of measuring intracerebral hemorrhage volumes.** *Stroke* 1996;27:1304–05 CrossRef Medline
- Spector M, O'Neal S, Racker E. **Phosphorylation of the beta subunit of Na⁺K⁺-ATPase in Ehrlich ascites tumor by a membrane-bound protein kinase.** *J Biol Chem* 1980;255:8370–73 CrossRef Medline
- Cameron IL, Smith NK, Pool TB, et al. **Intracellular concentration of sodium and other elements as related to mitogenesis and oncogenesis in vivo.** *Cancer Res* 1980;40:1493–50 Medline
- Weidner N. **Tumor angiogenesis: review of current applications in tumor prognostication.** *Semin Diagn Pathol* 1993;10:302–13 Medline
- Summers RM, Joseph PM, Kundel HL. **Sodium nuclear magnetic resonance imaging of neuroblastoma in the nude mouse.** *Invest Radiol* 1991;26:233–41 CrossRef Medline
- Thulborn KR, Davis D, Adams H, et al. **Quantitative tissue sodium concentration mapping of the growth of focal cerebral tumors with sodium magnetic resonance imaging.** *Magn Reson Med* 1999;41:351–59 CrossRef Medline
- Hashimoto T, Ikehira H, Fukuda H, et al. **In vivo sodium-23 MRI in brain tumors: evaluation of preliminary clinical experience.** *Am J Physiol Imaging* 1991;6:74–80 Medline
- Senger DR, Brown LF, Claffey KP, et al. **Vascular permeability factor, tumor angiogenesis and stroma generation.** *Invasion Metastasis* 1994;14:385–94 Medline
- Baethmann A, Maier-Hauff K, Schürer L, et al. **Release of glutamate and of free fatty acids in vasogenic brain edema.** *J Neurosurg* 1989;70:578–91 CrossRef Medline
- Black KL, Hoff JT, McGillicuddy JE, et al. **Increased leukotriene C4 and vasogenic edema surrounding brain tumors in humans.** *Ann Neurol* 1986;19:592–95 CrossRef Medline
- Carlson MR, Pope WB, Horvath S, et al. **Relationship between survival and edema in malignant gliomas: role of vascular endothelial growth factor and neuronal pentraxin 2.** *Clin Cancer Res* 2007;13:2592–98 CrossRef Medline

36. Provias J, Claffey K, delAguila L, et al. **Meningiomas: role of vascular endothelial growth factor/vascular permeability factor in angiogenesis and peritumoral edema.** *Neurosurgery* 1997;40:1016–26 CrossRef Medline
37. Strugar JG, Criscuolo GR, Rothbart D, et al. **Vascular endothelial growth/permeability factor expression in human glioma specimens: correlation with vasogenic brain edema and tumor-associated cysts.** *J Neurosurg* 1995;83:682–89 CrossRef Medline
38. Yano S, Shinohara H, Herbst RS, et al. **Expression of vascular endothelial growth factor is necessary but not sufficient for production and growth of brain metastasis.** *Cancer Res* 2000;60:4959–67 Medline
39. Zebrowski BK, Yano S, Liu W, et al. **Vascular endothelial growth factor levels and induction of permeability in malignant pleural effusions.** *Clin Cancer Res* 1999;5:3364–68 Medline
40. Schepkin VD, Ross BD, Chenevert TL, et al. **Sodium magnetic resonance imaging of chemotherapeutic response in a rat glioma.** *Magn Reson Med* 2005;53:85–92 CrossRef Medline
41. Boada FE, LaVerde G, Jungreis C, et al. **Loss of cell ion homeostasis and cell viability in the brain: what sodium MRI can tell us.** *Curr Top Dev Biol* 2005;70:77–101 CrossRef Medline
42. Sun L, Zhou K, Wang W, et al. **[18F]ML-10 imaging for assessment of apoptosis response of intracranial tumor early after radiosurgery by PET/CT.** *Contrast Media Mol Imaging* 2018;2018:1–9 CrossRef Medline

Automated Color-Coding of Lesion Changes in Contrast-Enhanced 3D T1-Weighted Sequences for MRI Follow-up of Brain Metastases

 D. Zopfs,  K. Laukamp,  R. Reimer,  N. Grosse Hokamp,  C. Kabbasch,  J. Borggreffe,  L. Pennig,  A.C. Bunck,  M. Schlamann, and  S. Lennartz



ABSTRACT

BACKGROUND AND PURPOSE: MR imaging is the technique of choice for follow-up of patients with brain metastases, yet the radiologic assessment is often tedious and error-prone, especially in examinations with multiple metastases or subtle changes. This study aimed to determine whether using automated color-coding improves the radiologic assessment of brain metastases compared with conventional reading.

MATERIALS AND METHODS: One hundred twenty-one pairs of follow-up examinations of patients with brain metastases were assessed. Two radiologists determined the presence of progression, regression, mixed changes, or stable disease between the follow-up examinations and indicated subjective diagnostic certainty regarding their decisions in a conventional reading and a second reading using automated color-coding after an interval of 8 weeks.

RESULTS: The rate of correctly classified diagnoses was higher (91.3%, 221/242, versus 74.0%, 179/242, $P < .01$) when using automated color-coding, and the median Likert score for diagnostic certainty improved from 2 (interquartile range, 2–3) to 4 (interquartile range, 3–5) ($P < .05$) compared with the conventional reading. Interrater agreement was excellent ($\kappa = 0.80$; 95% CI, 0.71–0.89) with automated color-coding compared with a moderate agreement ($\kappa = 0.46$; 95% CI, 0.34–0.58) with the conventional reading approach. When considering the time required for image preprocessing, the overall average time for reading an examination was longer in the automated color-coding approach (91.5 [SD, 23.1] seconds versus 79.4 [SD, 34.7] seconds, $P < .001$).

CONCLUSIONS: Compared with the conventional reading, automated color-coding of lesion changes in follow-up examinations of patients with brain metastases significantly increased the rate of correct diagnoses and resulted in higher diagnostic certainty.

ABBREVIATION: ACC = automated color-coding

Metastatic disease to the human brain represents the most common intracranial tumor in adults and has substantial implications for prognosis and therapy planning.^{1,2} Brain metastases occur in up to 30% of all patients in oncology, among which melanoma, breast cancer, lung cancer, and colorectal cancer are the most common underlying diseases.^{3,4} MR imaging was established early

as the technique of choice for screening and follow-up of patients with increased risk of brain metastases.^{5,6} Its excellent soft-tissue contrast and spatial resolution were found to be crucial for improving imaging-based assessment and follow-up of almost any neuro-oncologic disease.^{5,7,8} Because most brain metastases tend to show a strong gadolinium contrast enhancement, contrast media-enhanced T1WI sequences are a cornerstone of imaging brain metastases.^{5,8}

While the capabilities of MR imaging for the depiction of small brain metastases are unquestionable, accurate assessment of multiple sequences and planes can be tedious and error-prone in daily radiologic routine. In particular, the interval appearance of new small lesions or a subtle increase or decrease in lesion size may be easily missed in follow-up examinations, though these findings might have important therapeutic implications.^{9,10} Furthermore, in patients with multiple metastatic lesions that show a mixed response to treatment on follow-up examinations, the radiologist might be prone to a satisfaction-of-search bias, leading to an inaccurate diagnosis.^{11,12}

Received April 11, 2021; accepted after revision October 6.

From the Institute for Diagnostic and Interventional Radiology (D.Z., K.L., R.R., N.G.H., C.K., L.P., A.C.B., M.S., S.L.), Faculty of Medicine and University Hospital Cologne, University of Cologne, Cologne, Germany; and Department of Radiology (J.B.), Neuroradiology and Nuclear Medicine, Johannes Wesling University Hospital, Ruhr University Bochum, Bochum, Germany.

This work was supported by the Koeln Fortune Program/Faculty of Medicine, University of Cologne, grant No. 330/2020.

Please address correspondence to David Zopfs, MD, Institute for Diagnostic and Interventional Radiology, Faculty of Medicine and University Hospital Cologne, University of Cologne, Kerpener Str 62, Cologne, Germany; e-mail: David.zopfs@uk-koeln.de



Indicates open access to non-subscribers at www.ajnr.org

<http://dx.doi.org/10.3174/ajnr.A7380>

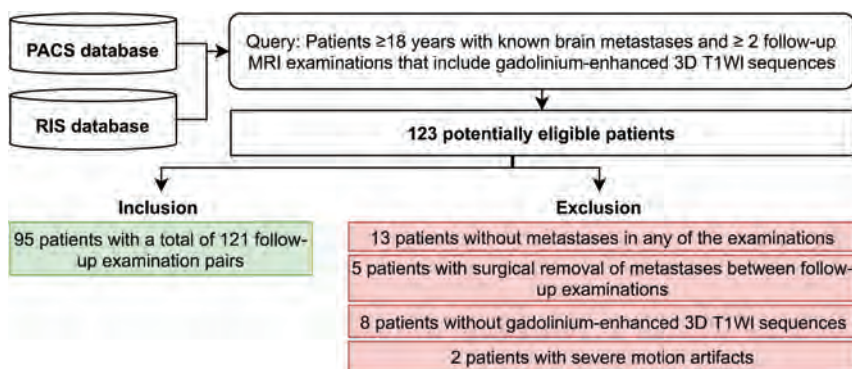


FIG 1. Inclusion and exclusion of study subjects.

Table 1: Detailed scanning parameters of the Ingenia and Achieva scanners^a

Parameter	Ingenia 3T ^b	Ingenia 1.5T ^b	Achieva 3T ^b	Achieva 1.5T ^b
FOV (mm)	512 × 512	384 × 384	480 × 480	288 × 288
Matrix	280 × 278	244 × 246	412 × 414	256 × 256
Section thickness (mm)	0.9	1.6	1.2	1.6
Spacing	0.48	0.8	0.6	0.8
TR (ms)	9.00	25.00	9.35	25.00
TE (ms)	4	7.86	4.68	7.97

^a All parameters refer to gadolinium-enhanced 3D T1-weighted sequences.

^b Philips Healthcare.

Table 2: Detailed scanning parameters of the Intera, Panorama and Avanto scanners^a

Parameter	Intera 1.5T ^b	Panorama 1T ^b	Avanto 1.5T ^c
FOV (mm)	448 × 448	512 × 512	256 × 256
Matrix	224 × 223	292 × 290	256 × 246
Section thickness (mm)	2	1.6	1
Spacing	1	0.8	0.98
TR (ms)	18.01	25.00	19.00
TE (ms)	10.1	9.2	2.91

^a All parameters refer to gadolinium-enhanced 3D T1-weighted sequences.

^b Philips Healthcare.

^c Siemens.

Recently, automated color-coding (ACC) of longitudinal MR imaging follow-up examinations has been reported to be beneficial for the assessment of brain lesions. This finding was reported for ACC of FLAIR sequences on follow-up examinations in multiple sclerosis, using different software approaches.¹³⁻¹⁵ Other studies applied similar techniques to the neuro-oncologic follow-up of patients with astrocytomas and high-grade gliomas.¹⁶⁻¹⁸ On the basis of these previous results, our hypothesis was that application of ACC at the follow-up assessment of brain metastases would yield comparable diagnostic benefits. Therefore, the purpose of this study was to compare the assessment of gadolinium-enhanced, 3D T1-weighted MR imaging follow-up examinations of patients with brain metastases between a conventional reading approach and an approach using ACC.

MATERIALS AND METHODS

Patients

The institutional review board (University Hospital Cologne) reviewed and approved the study plan and waived the need for informed patient consent due to the retrospective character of the

study. The PACS and the radiologic information system (ORBIS; Dedalus HealthCare) were retrospectively screened for patients 18 years of age or older who were diagnosed with metastatic disease in the brain. Inclusion criteria comprised 2 consecutive MR imaging examinations of the brain for follow-up that included contrast-enhanced 3D T1WI sequences between January 2013 and June 2019. The examinations were either performed in our institution or provided from referring institutions. This initial screening yielded 123 patients. After exclusion of 13 patients without metastases in any of the 2 scans, 5 patients with interim surgery of brain metastases between follow-up examinations, 8 patients without contrast-enhanced 3D T1WI acquisitions, and 2 patients with severe motion artifacts, 95 patients with 121 follow-up pairs remained for study inclusion: 82 patients with 1 follow-up pair, 7 patients with 2 follow-up pairs, 4 patients with 3 follow-up pairs, 2 patients with 4 follow-up pairs, and 1 patient with 5 follow-up pairs. Figure 1 depicts inclusion and exclusion of study subjects.

Image Acquisition

Gadolinium-enhanced (0.5 mmol/mL, gadoterate meglumine, Dotarem; Guerbet), T1-weighted sequences with fat suppression and the use of a standard head coil were acquired within the regular brain metastases follow-up in

our institution. Moreover, further 3D T1-weighted sequences with heterogeneous contrast media protocols from different vendors and scanner generations were included from referring institutions. The data set comprised different field strengths of 1T ($n = 3$), 1.5T ($n = 20$), and 3T ($n = 219$). Tables 1 and 2 give an overview of detailed MR imaging acquisition parameters.

Ground Truth Annotation

To establish a reference standard for a follow-up diagnosis, a radiologist with 4 years of experience and a senior neuroradiologist with 11 years of experience double-checked the radiologic reports for all included follow-up pairs in a consensus reading. These radiologists were not involved in the comparative assessment, which is outlined below. We refrained from using fixed size thresholds as proposed in the Response Assessment in Neuro-Oncology criteria for brain metastases (RANO-BM) criteria¹⁹ because our study was directed toward investigating the use of ACC for clinical evaluation outside of the trials. For each of the patients and follow-up pairs, respectively, the reference standard was determined as the following:

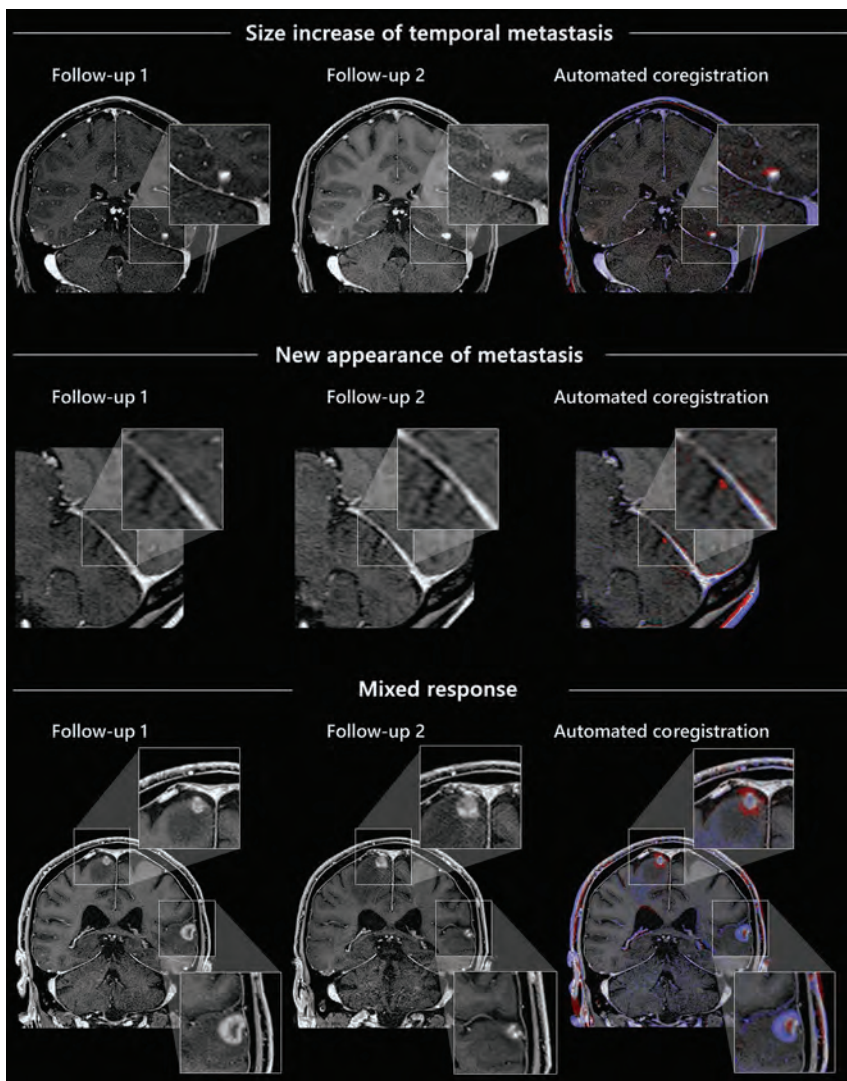


FIG 2. Examples of the automated coregistration of follow-up examinations and color-coding of longitudinal changes in contrast-enhanced, T1-weighted 3D sequences.

1. Stable (no change regarding number or size of metastases)
2. Progressive disease (any number of new interval metastases and/or any unequivocal increase in lesion size)
3. Disease regression (any number of intermittently disappeared metastases and/or any unequivocal decrease in lesion size) or
4. Mixed changes (the presence of components in 2 and 3 above).

To avoid inclusion of pseudoprogressions or erroneous inclusion of lesions, both radiologists had full access to all imaging and correlative clinical data.

Follow-up Assessment of Brain Metastasis

To compare the conventional follow-up assessment with the ACC approach, 2 readers with 3 and 4 years of experience in neuroradiologic imaging independently reviewed all MR imaging follow-up pairs in 2 dedicated reading sessions. Both readers were blinded to the above-mentioned ground truth diagnoses as well

as clinical data that could give an indication of them. Readings were performed at the same workstation under standardized reading conditions with a time interval of 8 weeks between the conventional reading and the reading using ACC, to avoid a recall bias. The patient order was randomized before each reading session.

In the first session, the conventional readout was performed as in clinical routine using a side-by-side setup within the PACS. Manual linking and coregistration of follow-up pairs were allowed.

In the second session, the ACC approach was conducted independently by both readers, each of whom reviewed the same follow-up pairs as in the conventional approach, using a CE-certified and FDA-approved software that facilitates ACC of follow-up examinations of the same patient (MR Longitudinal Brain Imaging [LoBI]; Philips Healthcare). The software is integrated into the vendor's image viewer (Intellispace Portal, Version 11; Philips Healthcare), however is not constrained to MR images generated by Philips Healthcare scanners and generally applicable. The software automatically performs a rigid coregistration. Then, the application performs an intensity normalization and subsequent subtraction of the selected sequences. After coregistration, normalization, and subtraction, both sequences are linked at the same anatomic level, allowing manual correction if necessary. Additionally, the software creates an overlay map,

which highlights a focal increase in signal intensity in red and a focal decrease in signal intensity in blue, respectively (Fig 2). The color intensity of the color-coding can be adjusted seamlessly. Both linked sequences and the overlay map are displayed side by side and can be viewed simultaneously on the same anatomic level.

In both reading sessions, readers were asked to pick one of the following diagnoses determined in the reference standard annotation (stable disease, disease progression, disease regression, or mixed changes). Additionally, they indicated diagnostic certainty regarding their decision on a 5-point Likert scale.

The average time required for loading the images within the PACS was recorded in the conventional reading session. The average time required for loading the application and processing the images was recorded in the second reading when using the ACC software. Furthermore, the time from being presented with the images to making the diagnosis was recorded for each follow-up examination pair in both reading sessions. All time measurements were performed by a radiologist not involved in the readouts.

Table 3: Rate of correctly classified diagnoses for each disease condition comparing the conventional reading and the reading with automated coregistration

	Conventional Reading	Reading with Automated Coregistration	P Value
Follow-up pairs with disease progression	81.7% (49/60)	93.3% (56/60)	.07
Follow-up pairs with disease regression	81.7% (49/60)	100.0% (60/60)	.003
Follow-up pairs with mixed changes	50.0% (31/62)	88.7% (55/62)	<.001
Follow-up pairs with stable disease	83.3% (50/60)	83.3% (50/60)	.77
All disease conditions	74.0% (179/242)	91.3% (221/242)	<.001

Table 4: Information on numbers and average sizes of lesions in included patients

	First Examination	Second Examination
Lesion count (No.)		
0	9	0
1	22	21
2	25	26
3	19	18
4	4	8
5	6	10
6	5	6
7	6	6
8	1	2
9	1	0
10	2	2
Lesion size (mm)		
Smallest lesion	4.3 + 4.2	3.7 + 2.7
Average lesion	8.8 + 7.3	8.3 + 6.7
Largest lesion	14.2 + 9.8	12.8 + 8.8

Statistical Analysis

The rate of correctly classified diagnoses was calculated for each type of diagnosis (ie, disease progression, disease regression, mixed changes, stable disease) and as an overall rate including all follow-up pairs. The rates of correctly classified diagnoses attained by the readers were compared between the 2 reading approaches using the McNemar test. We refrained from calculating the diagnostic accuracy and specificity due to the study focus on patients with known metastatic brain disease and the corresponding lack of healthy study subjects. Likert scales were compared using the Wilcoxon signed-rank test. Interreader agreement was evaluated using the Cohen κ and interpreted as follows: excellent agreement ($\kappa \geq 0.8$), good agreement ($\kappa \geq 0.6$), moderate agreement ($\kappa \geq 0.4$), and poor agreement ($\kappa < 0.4$). A P value $< .05$ was considered statistically significant. Rates of correctly classified diagnoses are indicated by percentages, and Likert scales, as median and interquartile range. Continuous variables are indicated by mean (SD).

RESULTS

Patients

Of the 95 included patients, 55 were women and 40 were men. The mean patient age was 61 (SD, 14) years (range, 27–86 years). The underlying primary tumor was malignant melanoma in 41 patients, lung cancer in 31 patients, breast cancer in 13 patients, rectal cancer in 4 patients, sarcoma in 2 patients, esophageal cancer in 2 patients, and renal cancer as well as pancreatic cancer in 1 patient each. Seventy-two of 121 follow-up pairs had the same scanner type and similar protocols, respectively, whereas 49/121 of the follow-up pairs had differences in scanner type and/or image acquisitions.

Comparison of Follow-up Assessment with and without ACC of Lesion Changes

In the reading with automated coregistration, the rate of correctly classified diagnoses was 91.3% (221/242) compared with 74.0% (179/242) in the reading without coregistration ($P < .05$). Regarding the individual diagnosis, the rate of correctly classified diagnoses for disease progressions was higher in the reading with coregistration and color-coding (93.3%, 56/60) compared with the conventional reading (81.7%, 49/60), yet without attaining statistical significance ($P = .07$). Conversely, all follow-up pairs showing disease regressions were correctly identified in the ACC approach (100.0%, 60/60) compared with a rate of 81.7% (49/60) correctly classified disease regressions in the conventional reading ($P < .05$). The lowest detection rate in the conventional reading approach was found for mixed changes (50.0%, 31/62). However, by using automated coregistration and color-coding, the rate of correctly classified diagnoses for mixed change was significantly increased to 88.7% (55/62; $P < .05$). In contrast, the rate of correctly classified stable disease was the same in both reading approaches (83.3%, 50/60; $P = .77$). There were 2 follow-up pairs for reader 1, and 3 for reader 2, in which a stable disease status was incorrectly diagnosed differently. For one follow-up pair, the incorrect diagnosis made was mixed changes, for the other 4 follow-up pairs, it was disease progression.

For the subgroup of follow-up pairs with divergent image acquisitions or scanner types, respectively, the overall proportion of correctly identified diagnoses was even slightly higher than in the overall collective, both in the conventional reading (75.5%, 37/49, versus 74%, 179/242) and the ACC approach (96.9%, 95/98, versus 91.3%, 221/242). Table 3 gives an overview of the correctly classified diagnoses. Table 4 indicates lesion numbers and lesion sizes.

Subjective diagnostic certainty was rated significantly higher in the ACC approach, 4 (range, 3–5), compared with the conventional reading, 2 (range, 2–3) ($P < .05$, Fig 3).

The mean reading time for both readers was 74.2 (SD, 34.7) seconds in the conventional reading approach and was reduced to 51.8 (SD, 23.1) seconds in the ACC approach ($P < .001$, Fig 4). The mean time required for loading the images within the PACS was 5.2 (SD, 0.6) seconds in the conventional reading, and the mean time required for loading the application and processing the images was 39.7 (SD, 1.4) seconds for the ACC software. Thus, the overall mean assessment time was longer in the ACC approach (91.5 [SD, 23.1] seconds) compared with the conventional reading using the PACS software (79.4 [SD, 34.7] seconds, $P < .001$).

Interrater agreement between both readers increased from a moderate agreement ($\kappa = 0.46$; 95% CI, 0.34–0.58) in the conventional reading approach to an excellent agreement ($\kappa = 0.80$; 95% CI, 0.71–0.89) in the ACC reading approach.

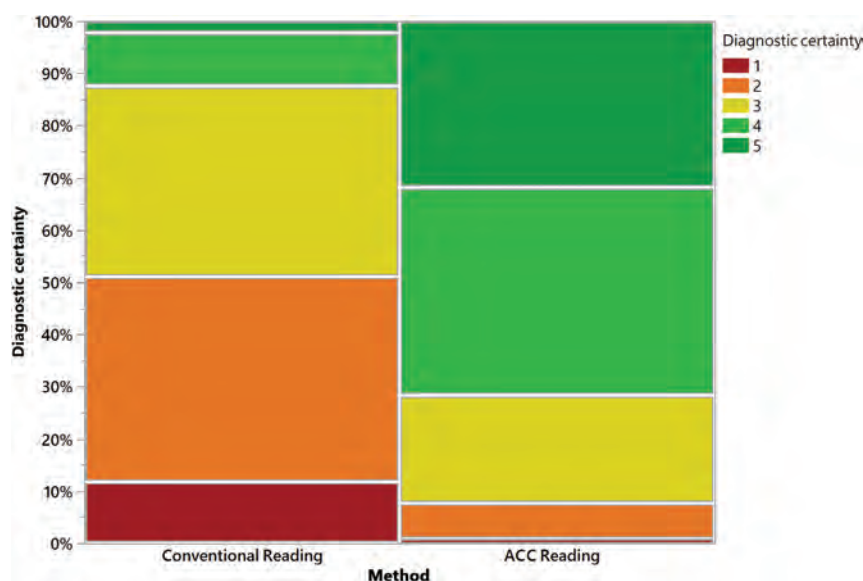


FIG 3. Diagnostic certainty of both readers regarding decision-making in the conventional approach and the automated coregistration and color-coding reading approach. ACC indicates automated color-coding.

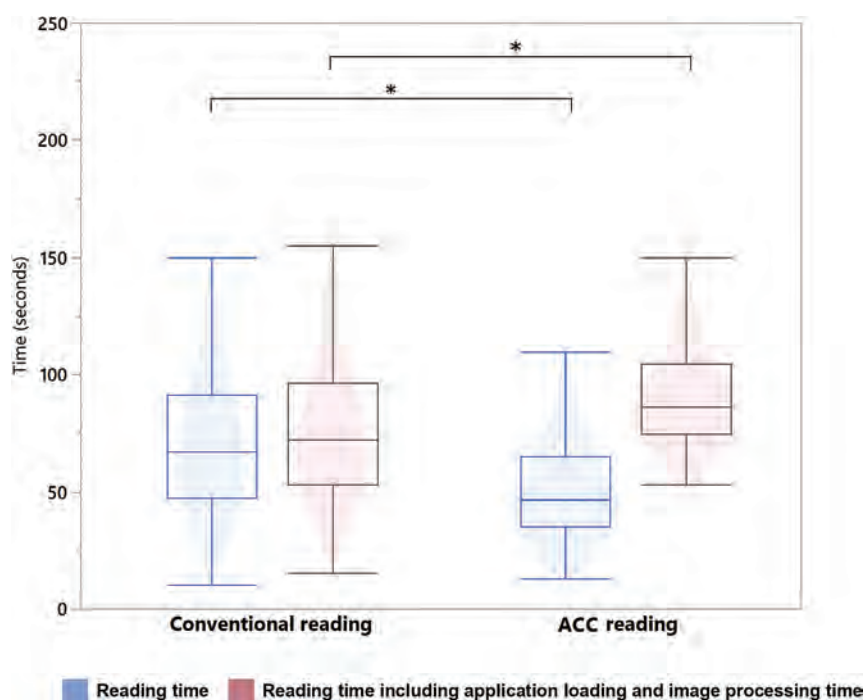


FIG 4. Reading time was significantly reduced in the automated coregistration and color-coding approach in comparison with the conventional approach. However, the longer loading and processing time required for the automated coregistration of 3D sequences led to a longer overall assessment time for this approach. ACC indicates automated color-coding.

DISCUSSION

In this study, we evaluated whether ACC of follow-up MR imaging examinations can improve the assessment of patients with brain metastases compared with a conventional reading approach regularly performed in daily radiologic routine. We found a significant improvement in the rate of correctly classified diagnoses

for disease progression, disease regression, and mixed changes while the determination of stable disease did not benefit from using the ACC software. Concordant to these findings, the inter-reader agreement and the diagnostic certainty were higher in the reading with ACC. While the reading time itself was significantly lower with the ACC software, this advantage was nullified by the higher application loading and image-processing time, leading to a slightly higher overall assessment time in the ACC approach.

To our knowledge, our study is the first to evaluate the ACC for longitudinal metastasis assessment based on gadolinium-enhanced T1-weighted sequences. Our results are in line with previous studies investigating different software using similar concepts of automated coregistration and highlighting of lesion changes as well as studies using the same software for longitudinal evaluation of lesion changes in FLAIR images.^{13,15,16,18} Galletto Pregliasco et al¹⁵ found a higher sensitivity and subjective confidence in the detection of new lesions on MR imaging of patients with multiple sclerosis using automated coregistration and a colored overlay map to depict lesion development. Lennartz et al¹⁶ reported a higher sensitivity and diagnostic accuracy for the longitudinal assessment of astrocytomas in FLAIR sequences, in particular for subtle changes. Compared with astrocytomas, the assessment of brain metastases may be much more challenging and burdensome, particularly when there are a high number of lesions. This challenge is reflected by the relatively low rate of correct diagnoses for mixed changes we found in the conventional reading approach. The overall workload resulting from these follow-up examinations is further enhanced because follow-up of brain metastases is such a frequently requested examination in daily clinical routine and the number of ordered examinations is increasing.²⁰

The high clinical relevance of brain metastasis assessment underlines the need for remedies for reducing the workload, while, at the same time, providing comparable or higher accuracy. Diagnostic assessment of MR imaging follow-up studies with mixed or subtle changes might specifically benefit from ACC of changes in consideration of a satisfaction-of-search bias and fatigue of radiologists.^{11,21-23}

Another important aspect of diagnostic tools is the ease of use and simplicity of implementation. In light of the recently growing use of artificial intelligence and deep learning–based applications, fully automated detection and assessment of brain metastases and cerebral lesions seems to be a promising concept.^{24,25} However, besides ethical concerns, a straightforward integration into the daily routine is often problematic because these approaches usually involve experimental and complex networks, potentially hampering use in daily routine.^{26–28} In contrast, the software evaluated in our study is launched within the PACS and may, therefore, be suitable for a routine workflow implementation. Of note, readers attained an even higher overall proportion of correct diagnoses in the subgroup of patients with divergent scanner types or protocols between the 2 examinations compared with the overall data set, which indicates that the proposed approach can alleviate interscanner and protocol differences in clinical routine.

In our study, we found a higher overall reading time including application loading times when using the ACC software, a finding that contrasts with previous studies reporting comparable or shorter reading times with this software.^{15,16} While the shorter time required for the readout itself is in line with previous studies, the overall higher assessment time we found is most likely because we used 3D image acquisitions, which require higher processing power. The time required for loading and processing the images for ACC is certainly, in part, dependent on the computing power of the workstation and servers used. Therefore, it can be assumed that loading times might be improved with optimized hardware configurations, but they still may represent a potential hurdle for clinical implementation when using 3D data sets as input data.

While the overall rate of correctly diagnosed follow-up pairs with stable diseases remained constant between the 2 reading approaches, taking into account both readers, the assessment with the coregistration software led to a false determination of mixed disease in 1 case and progressive disease in 4 cases, all of which had been correctly diagnosed as stable disease using the conventional reading approach. Whereas our study does not show a tendency of the investigated software to significantly promote false-positive diagnoses, the potential pitfall of overemphasizing lesion changes should be considered when using the software clinically, and a potentially lower specificity should be assessed in a larger-scale clinical investigation.

Most important, we did not assess the response of metastases as per the RANO-BM criteria.¹⁹ The underlying reason for that was that application of these criteria is mostly limited to clinical trials. On the contrary, we aimed to assess the application of the ACC software in the more common scenario of clinical brain metastases assessment outside of such trials. The results that we found might, therefore, not be generalizable to a RANO-BM response assessment. We encourage further investigations to evaluate the applicability and diagnostic value of the ACC software for assessing brain metastasis in clinical trials. Furthermore, the mixed changes category that we included is not included in the RANO-BM criteria. The reason to define this category is that we aimed to evaluate the use of the ACC software for this atypical response pattern because it is considered more prevalent in the

increasingly used immune checkpoint inhibitor therapies and is, therefore, of clinical relevance.

There are further limitations to this study that need to be addressed. The results of this study are based on a retrospective and monocentric study design. It was focused on contrast-enhanced 3D T1-weighted sequences, while the full readout of MR imaging follow-up in patients with cerebral metastases comprises >1 sequence. Another limitation is that most examinations used in this study were performed on 3T systems, which might limit generalizability to systems with lower field strengths. Moreover, we did not include patients with movement artifacts. In clinical routine, the presence of such artifacts can be expected to negatively impact the assessment using the proposed approach or even lead to technical failure of the application in the worst case. Last, a recall bias cannot be excluded, though we chose to set an 8-week latency period between the sessions and to randomize the order of patients before each reading session.

CONCLUSIONS

This study demonstrated an improved assessment of brain metastases when using a reading approach with ACC, particularly in regard to the detection of mixed-lesion changes. Therefore, we suggest considering such tools in clinical environments with a high throughput of follow-up MR imaging for the longitudinal assessment of brain metastasis.

Disclosures: Nils Grosse Hokamp—UNRELATED: Expert Testimony: Philips Healthcare*; Grants/Grants Pending: Philips Healthcare*; Payment for Lectures Including Service on Speakers Bureaus: Philips Healthcare; Other: Bristol-Myers Squibb. Jan Borggrefe—UNRELATED: Payment for Lectures Including Service on Speaker Bureaus: Speaker Bureau Philips, Philips Healthcare 2018/2019. Lenhard Pennig—UNRELATED: Grants/Grants Pending: Philips Healthcare, Comments: research support unrelated to this specific project.* Simon Lennartz—UNRELATED: Grants/Grants Pending: Philips Healthcare, Comments: institutional research support unrelated to this project.* *Money paid to the institution.

REFERENCES

1. Achrol AS, Rennert RC, Anders C, et al. **Brain metastases.** *Nat Rev Dis Primers* 2019;5:5 CrossRef Medline
2. Wen PY, Loeffler JS. **Management of brain metastases.** *Oncology (Williston Park)* 1999;13:941–54; discussion 961–62, 69 Medline
3. Barnholtz-Sloan JS, Sloan AE, Davis FG, et al. **Incidence proportions of brain metastases in patients diagnosed (1973 to 2001) in the Metropolitan Detroit Cancer Surveillance System.** *J Clin Oncol* 2004;22:2865–72 CrossRef Medline
4. Soffietti R, Rudà R, Mutani R. **Management of brain metastases.** *J Neurol* 2002;249:1357–69 CrossRef Medline
5. Pope WB. **Brain metastases: neuroimaging.** *Handb Clin Neurol* 2018;149:89–112 CrossRef Medline
6. Sze G, Milano E, Johnson C, et al. **Detection of brain metastases: comparison of contrast-enhanced MR with unenhanced MR and enhanced CT.** *AJNR Am J Neuroradiol* 1990;11:785–91 Medline
7. Deuschl C, Kirchner J, Poeppel TD, et al. **¹¹C-MET PET/MRI for detection of recurrent glioma.** *Eur J Nucl Med Mol Imaging* 2018;45:593–601 CrossRef Medline
8. Kaufmann TJ, Smits M, Boxerman J, et al. **Consensus recommendations for a standardized brain tumor imaging protocol for clinical trials in brain metastases.** *Neuro Oncol* 2020;22:757–72 CrossRef Medline
9. Patel N, Horsfield MA, Banahan C, et al. **Detection of focal longitudinal changes in the brain by subtraction of MR images.** *AJNR Am J Neuroradiol* 2017;38:923–27 CrossRef Medline

10. Lassman AB, DeAngelis LM. **Brain metastases.** *Neurol Clin* 2003;21:1–23 CrossRef Medline
11. Berbaum KS, Franken EA, Dorfman DD, et al. **Satisfaction of search in diagnostic radiology.** *Invest Radiol* 1990;25:133–40 Medline
12. Ganesan A, Alakhras M, Brennan PC, et al. **A review of factors influencing radiologists' visual search behaviour.** *J Med Imaging Radiat Oncol* 2018;62:747–57 CrossRef Medline
13. Zopfs D, Laukamp KR, Paquet S, et al. **Follow-up MRI in multiple sclerosis patients: automated co-registration and lesion color-coding improves diagnostic accuracy and reduces reading time.** *Eur Radiol* 2019;29:7047–54 CrossRef Medline
14. Dahan A, Pereira R, Malpas CB, et al. **PACS integration of semiautomated imaging software improves day-to-day MS disease activity detection.** *AJNR Am J Neuroradiol* 2019;40:1624–29 CrossRef Medline
15. Galletto Pregliasco A, Collin A, Guéguen A, et al. **Improved detection of new MS lesions during follow-up using an automated MR coregistration-fusion method.** *AJNR Am J Neuroradiol* 2018;39:1226–32 CrossRef Medline
16. Lennartz S, Zopfs D, Nobis A, et al. **MRI follow-up of astrocytoma: automated coregistration and color-coding of FLAIR sequences improves diagnostic accuracy with comparable reading time.** *J Magn Reson Imaging* 2020;52:1197–206 CrossRef Medline
17. van der Hoorn A, Yan J-L, Larkin TJ, et al. **Validation of a semi-automatic co-registration of MRI scans in patients with brain tumors during treatment follow-up.** *NMR Biomed* 2016;29:882–89 CrossRef Medline
18. Chitphakdithai N, Chiang VL, Duncan JS. **Non-rigid registration of longitudinal brain tumor treatment MRI.** *Annu Int Conf IEEE Eng Med Biol Soc* 2011;2011:4893–96 CrossRef Medline
19. Lin NU, Lee EQ, Aoyama H, et al; Response Assessment in Neuro-Oncology (RANO) group. **Response assessment criteria for brain metastases: proposal from the RANO group.** *Lancet Oncol* 2015;16:e270–78 CrossRef Medline
20. Chokshi FH, Hughes DR, Wang JM, et al. **Diagnostic radiology resident and fellow workloads: a 12-year longitudinal trend analysis using national Medicare aggregate claims data.** *J Am Coll Radiol* 2015;12:664–69 CrossRef Medline
21. Taylor-Phillips S, Stinton C. **Fatigue in radiology: a fertile area for future research.** *Br J Radiol* 2019;92:20190043 CrossRef Medline
22. Stec N, Arje D, Moody AR, et al. **A systematic review of fatigue in radiology: is it a problem?** *AJR Am J Roentgenol* 2018;210:799–806 CrossRef Medline
23. Maskell G. **Error in radiology: where are we now?** *Br J Radiol* 2019;92:20180845 CrossRef Medline
24. Grøvik E, Yi D, Iv M, et al. **Deep learning enables automatic detection and segmentation of brain metastases on multisequence MRI.** *J Magn Reson Imaging* 2020;51:175–82 CrossRef Medline
25. Laukamp KR, Thiele F, Shakirin G, et al. **Fully automated detection and segmentation of meningiomas using deep learning on routine multiparametric MRI.** *Eur Radiol* 2019;29:124–32 CrossRef Medline
26. Geis JR, Brady AP, Wu CC, et al. **Ethics of artificial intelligence in radiology: summary of the Joint European and North American Multisociety Statement.** *Radiology* 2019;293:436–40 CrossRef Medline
27. Recht MP, Dewey M, Dreyer K, et al. **Integrating artificial intelligence into the clinical practice of radiology: challenges and recommendations.** *Eur Radiol* 2020;30:3576–84 CrossRef Medline
28. Tang A, Tam R, Cadrin-Chênevert A, et al; Canadian Association of Radiologists (CAR) Artificial Intelligence Working Group. **Canadian Association of Radiologists White Paper on Artificial Intelligence in Radiology.** *Can Assoc Radiol J* 2018;69:120–35 CrossRef Medline

Clinical Feasibility of Ultrafast Contrast-Enhanced T1-Weighted 3D-EPI for Evaluating Intracranial Enhancing Lesions in Oncology Patients: Comparison with Standard 3D MPRAGE Sequence

 K.H. Ryu,  H.J. Baek,  S. Skare,  E. Cho,  I.C. Nam,  T.H. Kim, and  T. Sprenger



ABSTRACT

BACKGROUND AND PURPOSE: Contrast-enhanced 3D T1WI is a preferred sequence for brain tumor imaging despite the long scan time. This study investigated the clinical feasibility of ultrafast contrast-enhanced T1WI by 3D echo-planar imaging compared with a standard contrast-enhanced 3D MPRAGE sequence for evaluating intracranial enhancing lesions in oncology patients.

MATERIALS AND METHODS: Sixty-one patients in oncology underwent brain MR imaging including both contrast-enhanced T1WI, 3D-EPI and 3D MPRAGE, in a single examination session for evaluating intracranial tumors. Two neuroradiologists evaluated image quality, lesion conspicuity, diagnostic confidence, number and size of the lesions, and contrast-to-noise ratio measurements from the 2 different sequences.

RESULTS: Ultrafast 3D-EPI T1WI did not reveal significant differences in diagnostic confidence, contrast-to-noise ratio_{lesion/parenchyma} and the number of enhancing lesions compared with MPRAGE ($P > .05$). However, ultrafast 3D-EPI T1WI revealed inferior image quality, inferior anatomic delineation and greater susceptibility artifacts with fewer motion artifacts than images obtained with MPRAGE. The mean contrast-to-noise ratio_{WM/GM} and visual conspicuity of the lesion on ultrafast 3D-EPI T1WI were lower than those of MPRAGE ($P < .001$).

CONCLUSIONS: Ultrafast 3D-EPI T1WI showed comparable diagnostic performance with sufficient image quality and a 7-fold reduction in scan time for evaluating intracranial enhancing lesions compared with standard MPRAGE, even though it was limited by an inferior image quality and frequent susceptibility artifacts. Therefore, we believe that ultrafast 3D-EPI T1WI may be a viable option in oncology patients prone to movement during imaging studies.

ABBREVIATIONS: CE = contrast-enhanced; CNR = contrast-to-noise ratio; ICC = intraclass correlation coefficient; SPACE = sampling perfection with application-optimized contrasts by using different flip angle evolutions

Precise evaluation of intracranial malignancy is important in oncology patients for accurate staging and proper treatment planning.¹⁻³ Contrast-enhanced (CE) T1WI is an essential sequence in oncology patients used to evaluate malignant intracranial lesions, given its excellent capacity for soft-tissue contrast and contrast-

enhancing effects following gadolinium injection.⁴⁻⁶ In clinical practice, magnetization-prepared 3D gradient recalled-echo pulse sequences including MPRAGE, 3D turbo field echo, and brain volume imaging are widely used for evaluating brain tumors.⁷⁻⁹ These 3D sequences are suitable for detecting small, enhancing lesions due to the high spatial resolution and 3D evaluation of tumor burden.¹⁰ However, high-resolution isotropic T1WI sequences usually require 2–5 minutes of scan time, and T1WI sequences are typically obtained twice, pre- and postgadolinium administration.¹¹ This longer scan duration can be a major drawback for patients in oncology who do not tolerate long scan times due to poor general conditions.

Recently, Norbeck et al¹¹ developed a rapid T1-weighted brain imaging sequence using a fat-suppressed multishot 3D-EPI, and this novel 3D-EPI sequence can be used to rapidly acquire isotropic T1-weighted volumes using a high phase-encoding bandwidth and radiofrequency pulses that reduce magnetization

Received August 21, 2021; accepted after revision October 29.

From the Departments of Radiology (K.H.R., H.J.B., E.C., I.C.N.) and Internal Medicine (T.H.K.), Gyeongsang National University School of Medicine and Gyeongsang National University Changwon Hospital, Changwon, Korea; Department of Radiology (H.J.B.), Institute of Health Sciences, Gyeongsang National University School of Medicine, Jinju, Korea; Departments of Neuroradiology (S.S.) and Clinical Neuroscience (S.S., T.S.), Karolinska Institute, Stockholm, Sweden; and MR Applied Science Laboratory Europe (T.S.), GE Healthcare, Stockholm, Sweden.

Please address correspondence to Hye Jin Baek, MD, PhD, Department of Radiology, Gyeongsang National University School of Medicine and Gyeongsang National University Changwon Hospital, 11 Samjeongja-ro, Seongsan-gu, Changwon 51472, Korea; e-mail: sartre81@gmail.com



Indicates article with online supplemental data.

<http://dx.doi.org/10.3174/ajnr.A7391>

transfer effects. This study suggested the potential clinical application of ultrafast 3D-EPI T1WI to assess brain tumors with <30 seconds of scan time.¹¹ However, the study did not fully evaluate the overall image quality or the diagnostic performance of this ultrafast 3D T1WI sequence, and too few cases were included to assess the clinical utility of the novel sequence. To the best of our knowledge, no previous studies have compared this novel ultrafast 3D-EPI T1WI sequence with the conventional 3D T1WI sequence for detecting intracranial lesions. Therefore, we investigated the clinical feasibility of the ultrafast 3D-EPI T1WI for evaluating intracranial enhancing lesions in oncology patients compared with conventional 3D T1WI, by assessing the overall image quality and diagnostic performance.

MATERIALS AND METHODS

Study Population

We retrospectively reviewed the medical records database of our institution and identified 61 patients who underwent diagnostic brain MR imaging, including CE ultrafast 3D-EPI T1WI and CE MPRAGE in a single session from August 2020 to February 2021. The 2 sets of CE 3D T1WI sequences were obtained to evaluate intracranial lesions in oncology patients with known or suspected intracranial tumors. The identified patients included 38 men and 23 women (age range, 19–81 years; mean age, 61 years). The indications for MR imaging were as follows: work-up or follow-up of brain metastasis (54/61, 88.5%) with known malignancies (lung cancer, 42; breast cancer, 9; prostate cancer, 2; and rectal cancer, 1) and follow-up of known primary brain tumors (7/61, 11.5%) (glioblastoma, 4; anaplastic oligodendroglioma, 1; anaplastic astrocytoma, 1; and brain stem glioma, 1).

Retrospective data collection and analysis were performed according to our institutional review board guidelines. This study was approved by the institutional review board at Gyeongsang National University Changwon Hospital. The institutional review board determined that patient approval and informed consent were not required for reviewing images and records due to the retrospective nature of the study.

Imaging Acquisition

MR imaging was performed using a 3T system (Signa Architect; GE Healthcare) with a 48-channel head coil. In addition to the postgadolinium ultrafast 3D-EPI T1WI and MPRAGE sequences, standard imaging sequences with axial T1WI, axial T2WI, axial FLAIR, and a 3D multiecho gradient-echo sequence (susceptibility-weighted angiography, ie, T2 star-weighted angiography) were acquired. Technical details of the MR imaging sequences are provided in the Online Supplemental Data. A dose of 0.2 mL/kg body weight of gadoteric acid (Dotarem 0.5 mmol/mL; Guerbet) was administered with an MR imaging-compatible power injector (MRXperion; Medrad Inc.), followed by a saline flush of 30 mL. The first postcontrast scan was started 2 minutes after injection of the contrast agent. At our institution, we use the ultrafast 3D-EPI T1WI for clinical purposes in patients restless during the scan, and the decision to acquire the ultrafast protocol images during examination is made by attending neuroradiologists during the day or supervising technologist at night or on holidays. The 2 different 3D T1WIs were obtained by inconsistent order with ultrafast 3D-

EPI T1WI followed by MPRAGE in 29 patients and by reverse order in 32 patients.

Qualitative Radiologic Assessment

All data sets were anonymized and randomized. Two readers reviewed all images using a PACS and were blinded to the clinical diagnosis. However, readers were not blinded to the type of sequences due to the distinctive characteristic of the sequences. Two attending neuroradiologists with 11 and 6 years of experience performed an independent analysis of ultrafast 3D-EPI T1WI and MPRAGE to assess the overall image quality and diagnostic performance of the ultrafast 3D-EPI T1WI from a clinical feasibility perspective. Readers were instructed to report every intracranial contrast-enhancing lesion not assignable to the normal anatomic structure. When the reviewers detected an enhancing brain tumor, it was marked with an arrow on the captured images with the enhancing tumors. In case of disagreement between the 2 readers, a decision was made by consensus. Reconstructive images were provided in the axial, sagittal, and coronal planes with 1-mm section thickness. The score of each item for qualitative assessment was rated using a 5-point Likert scale¹² as shown in the Online Supplemental Data.

Quantitative Radiologic Assessment

The readers drew an ROI in the largest enhancing lesion in each patient that was >0.5 cm in the largest diameter. Entirely necrotic or cystic lesions without a solid component were excluded from the contrast-to-noise (CNR) measurements because a suitable ROI could not be drawn. The CNR of contrast-enhancing brain lesions was estimated for both ultrafast 3D-EPI T1WI and MPRAGE using the following formula:

$$\text{CNR}_{\text{lesion/parenchyma}} = (\text{SI}_{\text{lesion}} - \text{SI}_{\text{parenchyma}}) / \text{SD}_{\text{parenchyma}},$$

where signal intensity (SI) is the average signal intensity of the ROI, and SD is the SD of the ROI. SI and SD for the calculation of $\text{CNR}_{\text{lesion/parenchyma}}$ values were taken from the adjacent normal-appearing white matter and not from the image background. ROIs were carefully placed in the center of the enhancing lesion, avoiding tumor margins. ROIs of each 2 contrast-enhanced sequences were placed visually in a side-to-side comparison on 2 monitors using enlarged imaging data. The area of the ROI was dependent on the enhancing lesion size, varying between 20 and 42 mm². The ROI from adjacent parenchyma measured 20 mm². Furthermore, the CNR for the GM and WM differentiation was estimated using the following formula:

$$\text{CNR}_{\text{WM/GM}} = (\text{SI}_{\text{WM}} - \text{SI}_{\text{GM}}) / \text{SD}_{\text{WM}}.$$

For the assessment of $\text{CNR}_{\text{WM/GM}}$, ROIs were centrally placed in the splenium of the corpus callosum and in the left thalamus. Each ROI measured 20 mm². The longest diameters of the largest enhancing lesion in each patient were measured in both ultrafast 3D-EPI T1WI and MPRAGE.

Statistical Analysis

The Kolmogorov-Smirnov test was used to test the distribution of variables. Normality was rejected for the number of lesions, size of the lesions, $\text{CNR}_{\text{WM/GM}}$, and $\text{CNR}_{\text{lesion/parenchyma}}$; thus, the

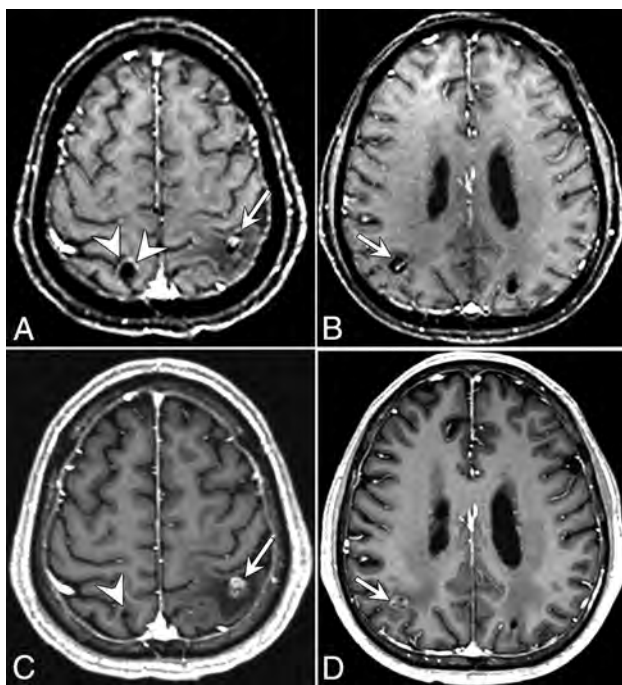


FIG 1. A 63-year-old man who underwent brain MR imaging for metastasis work-up due to lung cancer. Upper row (A and B) displays CE ultrafast 3D-EPI T1WI; the lower row (C and D) displays standard MPRAGE. The enhancing hemorrhagic nodules in both parietal lobes are well-visualized on both ultrafast 3D-EPI T1WI and standard MPRAGE. However, the size of the enhancing portions is underestimated on ultrafast 3D-EPI T1WI due to susceptibility artifacts of the hemorrhagic component (arrows). Whereas eccentric hyperintensity of the hemorrhagic nodule in the right parietal lobe on ultrafast 3D-EPI T1WI was misinterpreted as an enhancing portion (arrowheads, A), there was no enhancing component on standard MPRAGE (arrowhead, C). Therefore, the eccentric hyperintensity (arrowheads, A) was considered as a pseudolesion due to signal pileup artifacts adjacent to the hemorrhagic portion.

Wilcoxon signed rank test was used to evaluate differences. The reader's rating, lesion conspicuity, and diagnostic confidence were ordinal variables; thus, the Wilcoxon signed rank test was used. The intraclass correlation coefficient (ICC) was performed to assess the reliability of the number of lesions and the size of the lesions between the two 3D T1 sequences. We interpreted ICC values as follows: <0.5, poor reliability; 0.5–0.75, moderate reliability; 0.75–0.9, good reliability; and >0.9, excellent reliability.¹³

Interobserver agreement between the 2 readers was calculated by weighted κ statistics; 0–0.20, 0.21–0.40, 0.41–0.60, 0.61–0.80, and 0.81–1.00 were interpreted as slight, fair, moderate, substantial, and almost perfect agreement, respectively, on the basis of the method of Landis and Koch.¹⁴

We performed all statistical analyses with MedCalc, Version 19.8 (MedCalc Software) and SPSS, Version 24.0 (IBM). *P* values < .05 were considered statistically significant.

RESULTS

Study Population

Of the 61 included patients, 36 (59.0%) presented with the following enhancing intracranial lesions: brain metastasis (22/36, 61.1%), glioblastoma multiforme (5/36, 13.9%), meningioma (3/

36, 8.3%), anaplastic oligodendroglioma (1/36, 2.8%), anaplastic astrocytoma (1/36, 2.8%), cavernous sinus hemangioma (1/36, 2.8%), vestibular schwannoma (1/36, 2.8%), trigeminal schwannoma (1/36, 2.8%), and subacute infarction (1/36, 2.8%).

Diagnostic Performance of the Two 3D T1 Sequences

There was no statistically significant difference in terms of mean diagnostic confidence between the ultrafast 3D-EPI T1WI and MPRAGE (4.78 [SD, 0.48] versus 4.86 [SD, 0.35], *P* = .180). However, the mean visual conspicuity scores of contrast-enhancing lesions on ultrafast 3D-EPI T1WI were significantly inferior to those of MPRAGE (4.11 [SD, 0.40] versus 4.94 [SD, 0.23], *P* < .001), though the mean score of lesion conspicuity for the ultrafast 3D-EPI T1WI was >4 points and demonstrated well-depicted lesions with adequately visualized margins.

The number of enhancing lesions detected on the ultrafast 3D-EPI T1WI and MPRAGE did not show any significant differences (152 lesions versus 150 lesions; *P* = .577), and the results of the ICC demonstrated excellent agreement (0.998; 95% CI, 0.997–0.999). When we considered MPRAGE as a reference standard, 3 enhancing lesions on the ultrafast 3D-EPI T1WI were considered pseudolesions due to signal pileup by susceptibility artifacts from hemorrhage (Fig 1). In addition, in 1 patient, ultrafast 3D-EPI T1WI could not detect an enhancing lesion of the temporal lobe base because of susceptibility artifacts in the skull base (Fig 2), whereas there was a case of susceptibility artifacts in the temporal lobe base misinterpreted as a brain metastasis on ultrafast 3D-EPI T1WI (Fig 3).

There was no statistically significant difference with regard to the longest diameters of the largest enhancing lesions in each patient when comparing ultrafast 3D-EPI T1WI and MPRAGE (mean, 1.76 [SD, 1.16] versus 1.73 [SD, 1.12] cm; *P* = .180), and there was excellent agreement between the 2 different 3D T1WI sequences (ICC = 0.996; 95% CI, 0.993–0.998).

Image Quality Assessment

The image quality scores of the 2 readers and the corresponding interobserver reliability are shown in the Online Supplemental Data. Although the assessment of overall image quality and anatomic delineations on the ultrafast 3D-EPI T1WI showed significantly lower scores than those of MPRAGE (*P* < .001), the ultrafast 3D-EPI T1WI showed sufficient image quality, with >3 points on the average rating of the assessment. For the susceptibility artifacts, ultrafast 3D-EPI T1WI showed significantly more severe susceptibility artifacts compared with MPRAGE (*P* < .001); however, motion artifacts were significantly lower in ultrafast 3D-EPI T1WI than in MPRAGE (*P* < .001) (Online Supplemental Data). The interobserver agreement of the 2 readers showed moderate agreement in most items of image quality assessment, except for paradoxically low values due to the imbalanced number of concordant and discordant pairs.^{15,16}

The mean value of CNR_{WM/GM} was significantly lower for the ultrafast 3D-EPI T1WI than for MPRAGE (2.30 [SD, 1.76] versus 5.88 [SD, 2.00], respectively; *P* < .001). In addition, the mean value of CNR_{lesion/parenchyma} of the ultrafast 3D-EPI T1WI was also lower than that of MPRAGE; however, there was no

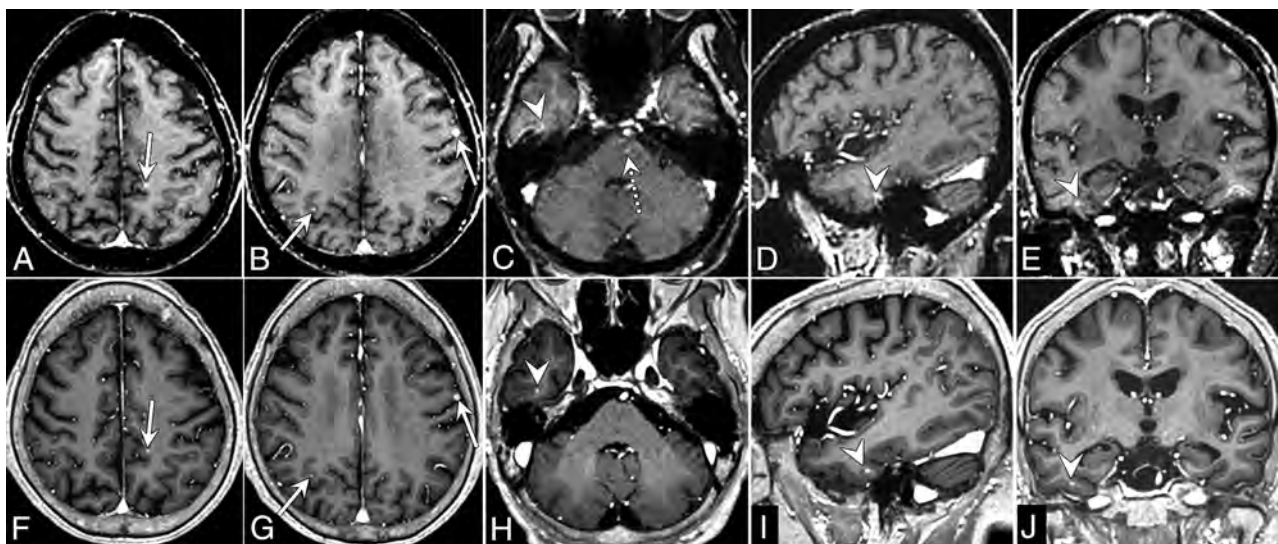


FIG 2. A 73-year-old woman who underwent brain MR imaging for metastasis work-up due to lung cancer. *Upper row (A–E)* displays CE ultrafast 3D-EPI T1WI, and *lower row (F–J)* displays the standard MPRAGE. Multiple enhancing metastatic nodules are well-delineated on both ultrafast 3D-EPI T1WI and standard MPRAGE (arrows, A, B, F, G). An enhancing metastatic nodule in the right temporal lobe base was missed on ultrafast 3D-EPI T1WI by reviewers because it was considered a portion of a susceptibility artifact (arrowheads, C–E). The enhancing metastatic nodule is conspicuously delineated on standard MPRAGE (arrowheads, H–J). Pulsation artifacts of the basilar artery are shown as a hyperintense focus on ultrafast 3D-EPI T1WI (dashed arrow, C); however, the lesion was not interpreted as an enhancing nodule due to its characteristic location.

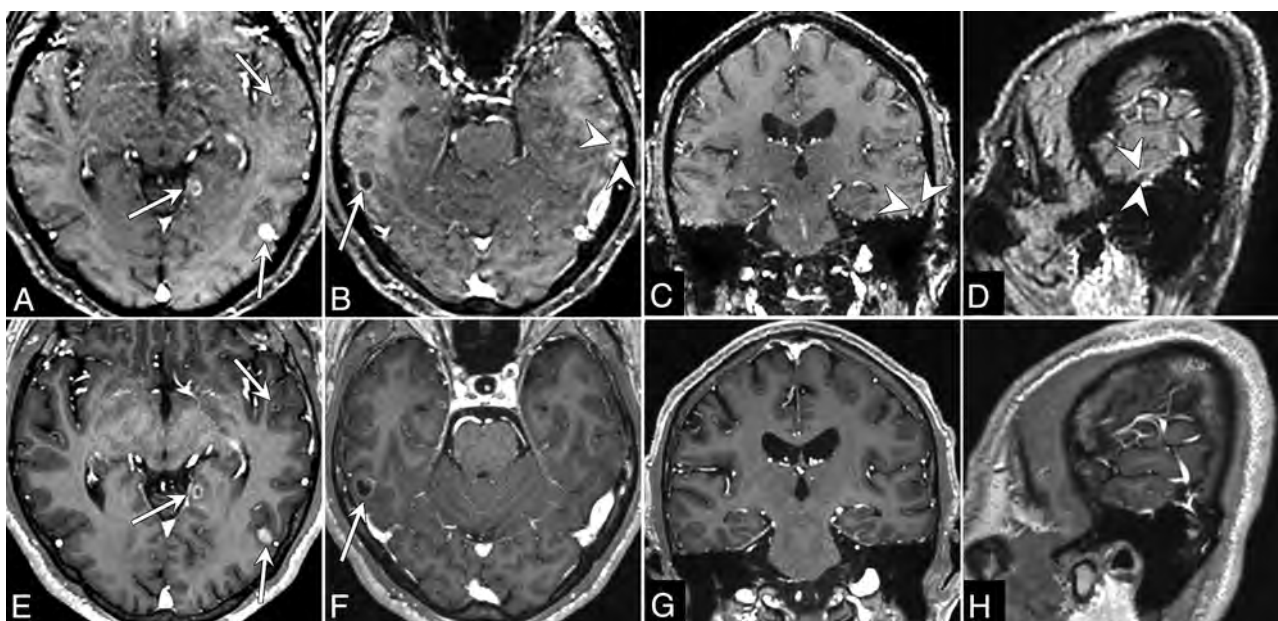


FIG 3. A 68-year-old man who underwent brain MR imaging for metastasis work-up due to lung cancer. *Upper row (A–D)* displays CE ultrafast 3D-EPI T1WI, and *lower row (E–H)* displays standard MPRAGE. Multiple enhancing nodules show that rim enhancement or nodular enhancement in both temporal lobes is well-visualized on both ultrafast 3D-EPI T1WI and standard MPRAGE (arrows, A, B, E, F). On ultrafast 3D-EPI T1WI, a suspicious rim-enhancing nodule was misinterpreted as metastasis by reviewers (arrowheads, B, C, D). However, compared with the standard MPRAGE images, the lesion was confirmed to be a pseudolesion due to susceptibility artifacts in the temporal lobe base.

significant difference between the 2 sequences (16.07 [SD, 12.40] versus 22.45 [SD, 19.90]; $P = .107$).

DISCUSSION

In this study, we determined that the ultrafast 3D-EPI T1WI showed sufficient diagnostic image quality and comparable

diagnostic performance for detecting enhancing intracranial lesions in oncology patients with fewer motion artifacts and a 7-fold reduction in scan time, compared with the standard MPRAGE sequence. Conversely, the ultrafast 3D-EPI T1WI had overall inferior image quality with more susceptibility artifacts and lower $CNR_{GM/WM}$ than the standard MPRAGE sequence.

For the assessment of brain metastasis, a 3D sequence has the advantage in detecting small, enhancing lesions due to the higher spatial resolution, which reduces the partial volume effects compared with 2D sequences.¹⁰ Additionally, a multiplanar reformation is another advantage of 3D sequences for assessing brain tumors within the complex brain anatomy.¹⁷ However, the relatively long scan time required for 3D sequences is a major drawback to applying this sequence in oncology patients presenting with a poor general condition and who cannot tolerate long scan times due to restlessness, which may contribute to increasing motion artifacts and patient anxiety.^{18,19} To date, a few studies have focused on reducing scan times without the loss of important clinical information from CE 3D T1 sequences for brain MR imaging protocols. In a recent study, ultrafast 3D-EPI T1WI was developed using a fat-suppressed multishot 3D-EPI to obtain isotropic T1-weighted volumes, revealing the possibility of clinical application of this novel sequence for brain imaging.¹¹ However, to the best of our knowledge, there have been no studies comparing ultrafast 3D-EPI T1WI and conventional 3D T1 sequences to evaluate intracranial lesions by assessing the diagnostic performance and overall image quality from the perspective of the clinical application.

In this study, ultrafast 3D-EPI T1WI showed diagnostic performance comparable with that of the standard MPRAGE sequence. This result was similar to that of a recent study that showed equivalent diagnostic performance with only marginally higher background noise using a highly accelerated Wave-Controlled Aliasing in Parallel Imaging (Wave-CAIPI; Siemens Healthineers) 3D T1 sampling perfection with application-optimized contrasts by using different flip angle evolutions (SPACE) sequence for detecting brain metastasis at 3T.²⁰ However, the total scan time of the accelerated Wave-CAIPI T1 SPACE sequence was 1 minute 40 seconds, which is >3 times longer than ultrafast 3D-EPI T1WI and is required at the expense of additional calibration and reconstruction effort. In contrast, the ultrafast 3D-EPI T1WI can provide comparable diagnostic confidence and $CNR_{\text{lesion/parenchyma}}$ in 30 seconds using the Cartesian acquisition scheme and the conventional parallel imaging to reduce anxiety and discomfort more efficiently for oncology patients in real-world practice. In particular, our results showed that the $CNR_{\text{lesion/parenchyma}}$ of the ultrafast 3D-EPI T1WI was not significantly different from that of the standard MPRAGE. This finding was consistent with the previous studies that proposed the clinical implication of $CNR_{\text{lesion/parenchyma}}$ to detect enhancing metastatic lesions.²¹⁻²³ We believe that this finding was valuable because $CNR_{\text{lesion/parenchyma}}$ is known as a key factor for contributing the higher detectability of enhancing lesions.^{22,23}

In contrast, the overall image quality of ultrafast 3D-EPI T1WI in our study was considered inferior, compared with representative cases from the previous study,¹¹ even though it is difficult to perform a direct comparison of our image quality with that of the original work at this time. The exact reasons for these differences are unclear, though these may be related to the intrinsic difference in the scanning environment, including the scanner and the number of shots of EPI between the 2 institutions. In general, any newly developed sequence should be validated in various ways to establish its clinical utility. From this perspective, we believe that our results are meaningful in that they can

provide additional information regarding the acquisition of this novel sequence in different scan environments.

With regard to the technical aspects of ultrafast 3D-EPI T1WI, the inherently unavoidable geometric distortion of EPI-derived sequences cannot be completely removed at the air-tissue interface, even though this novel ultrafast 3D-EPI T1WI can further reduce the geometric distortion using the higher number of shots (here equal to 12) with the parallel imaging factor (here equal to 2) in contrast to the 2D-EPI sequence, which typically uses a single shot with parallel imaging.¹¹ While the parallel imaging factor is coil-limited and may not be increased beyond 3 to avoid SNR loss, increasing the number of EPI shots reduces the geometric distortions at the expense of longer scan times. Ultimately, with the number of shots equal to the number of acquired lines, the 3D-EPI sequence will be distortion-free with the same scan time. We found that the current setting of 12 EPI shots gives a reasonable trade-off between scan time and geometric distortions because there was a minimal difference in the overall diagnostic accuracy. However, this sequence still presents the potential limitation relative to overall image quality, which can be degraded by susceptibility artifacts and results in insufficient detection of enhancing lesions near the skull base and brain stem. In addition to the lower SNR, this issue may also contribute to the concerns about the ultrafast 3D-EPI T1WI, such as inferior overall image quality and the lower mean value of the $CNR_{WM/GM}$. Therefore, for the patient in whom the expected lesion is in the vicinity of a tissue-air interface (such as the pituitary gland), where the field inhomogeneity is high, one could increase the number of shots to obtain higher geometric accuracy at the expense of a longer scan time.

Furthermore, we observed hypointense or hyperintense dots in the pons, induced by pulsation artifacts of the basilar artery, which mimicked the small, enhancing lesions at first glance. However, the readers could easily distinguish these characteristic artifacts from pathologic conditions without any remarkable impact on decision-making in this study. It may be helpful to apply a sagittal scan plane with frequency-encoding in the superior-inferior direction to reduce the pulsation artifacts.^{7,11} In addition, the use of inferior saturation bands for the axial image acquisition is another possible option, but this use may significantly decrease the $CNR_{WM/GM}$ due to magnetization transfer effects.¹¹ However, in the current study, we obtained the ultrafast 3D-EPI T1WI with a sagittal scan plane; thus, we did not compare the degree of pulsation artifacts directly between the sagittal and axial scan planes. In the present study, we also observed that accompanying artifacts in and around the hemorrhagic lesion may lead to difficulties in evaluating the enhancing lesion; in particular, susceptibility artifacts of hemorrhagic metastasis may result in the underestimation of the enhancing portion, and signal pileup in the vicinity of hemorrhagic lesions may mimic the enhancing component.¹¹ Therefore, further technical advances are needed to correct the aforementioned issues before expanding the diagnostic use of ultrafast 3D-EPI T1WI in clinical practice.

Despite these shortcomings, ultrafast 3D-EPI T1WI can obtain CE 3D T1WI with a resolution of $1.2 \times 1.2 \times 1.2 \text{ mm}^3$ with a short scan time of 30 seconds, which is approximately 7 times shorter than the standard MPRAGE sequence. In addition,

the diagnostic confidence and $CNR_{\text{lesion/parenchyma}}$ of ultrafast 3D-EPI T1WI were comparable with those of standard MPRAGE. Therefore, ultrafast 3D-EPI T1WI can be used as a feasible alternative in certain clinical situations such as motion-prone patients or for unexpected termination of scans while obtaining conventional 3D T1WI.

This study has several limitations. First, there was an unavoidable selection bias because the data from all patients were evaluated retrospectively, the sample size was small, and the study was conducted in a single center. Second, we could not handle the acquisition order of the 2 different 3D T1WI sequences because of the retrospective study design. Thus, we did not consider the potential differences related to the timing bias between contrast injection and image acquisition, which can increase contrast agent uptake due to the delay. A future prospective study with a large study population is needed to validate the effect of the differences in postcontrast time delay. Third, we did not conduct the study including the patient groups with homogeneous types of brain tumors. In contrast, we took the pragmatic approach to obtain real-time data in daily clinical practice because this study was a feasibility study of the ultrafast 3D-EPI T1WI for identifying lesions in oncology patients. Therefore, it would not be necessary to provide additional analysis according to the specific pathologic diagnosis. Our results showed a clinically acceptable diagnostic image quality and lesion detectability with the benefit of a shorter scan time. Therefore, this broad study population can be helpful to generalize the clinical utility of ultrafast 3D-EPI T1WI to various types of brain tumors. Fourth, pathologic confirmation was not obtained for all brain tumors because patients with multiple brain tumors such as metastases usually do not undergo surgical intervention. Last, we did not apply the recommended time delay for obtaining the enhanced T1WI in brain tumor imaging.^{8,9} Even though previous studies have provided a recommendation for a brain MR imaging protocol in oncology patients,^{8,9} there is often a gap between real-world clinical practice and ideals. For practical reasons, it is believed that many previous studies did not accurately specify the delayed time or apply a delay time of <4 minutes. In this study, it was also difficult to apply the recommended protocol for enhanced T1WI in the study patients because actual clinical situations such as the number of MR imaging systems or the time table of the MR imaging room were inevitably considered.

CONCLUSIONS

We demonstrated that ultrafast 3D-EPI T1WI had a comparable diagnostic performance with sufficient image quality and 7-fold reduction in scan time for evaluating intracranial enhancing lesions in oncology patients compared with the standard MPRAGE sequence, even though it had minor issues due to an inherent geometric distortion. Therefore, we believe that ultrafast 3D-EPI T1WI may be a viable option that can be used clinically in lieu of the conventional 3D T1WI or as a backup sequence in specific clinical situations for oncology patients who cannot tolerate long scan times. Our results should be considered in the technical development of ultrafast 3D-EPI T1WI, and future studies with various clinical scenarios are needed to validate our results and help expand the clinical use of ultrafast 3D-EPI T1WI in daily practice.

ACKNOWLEDGMENTS

We would like to thank our colleagues in the MR imaging section, Seong Jin Kim, Myungwook Lee, and Jae Hyun Lim, for their effort in ensuring that all MR images were obtained optimally, and we also thank Tae Byeong Kim for his help in strengthening our work.

Disclosure forms provided by the authors are available with the full text and PDF of this article at www.ajnr.org.

REFERENCES

1. Kaal EC, Niël CG, Vecht CJ. **Therapeutic management of brain metastasis.** *Lancet Neurol* 2005;4:289–98 CrossRef Medline
2. Ranjan T, Abrey LE. **Current management of metastatic brain disease.** *Neurotherapeutics* 2009;6:598–603 CrossRef Medline
3. Sperduto PW, Kased N, Roberge D, et al. **Summary report on the graded prognostic assessment: an accurate and facile diagnosis specific tool to estimate survival for patients with brain metastases.** *J Clin Oncol* 2012;30:419–25 CrossRef Medline
4. Sze G, Milano E, Johnson C, et al. **Detection of brain metastases: comparison of contrast-enhanced MR with unenhanced MR and enhanced CT.** *AJNR Am J Neuroradiol* 1990;11:785–91 Medline
5. Davis PC, Hudgins PA, Peterman SB, et al. **Diagnosis of cerebral metastases: double-dose delayed CT vs contrast-enhanced MR imaging.** *AJNR Am J Neuroradiol* 1991;12:293–300 Medline
6. Schellinger PD, Meinck HM, Thron A. **Diagnostic accuracy of MRI compared to CCT in patients with brain metastases.** *J Neurooncol* 1999;44:275–81 CrossRef Medline
7. Mugler JP, Brookeman JR. **Three-dimensional magnetization-prepared rapid gradient-echo imaging (3D MPRAGE).** *Magn Reson Med* 1990;15:152–57 CrossRef Medline
8. Ellingson BM, Bendszus M, Boxerman J, et al; Jumpstarting Brain Tumor Drug Development Coalition Imaging Standardization Steering Committee. **Consensus recommendations for a standardized brain tumor imaging protocol in clinical trials.** *Neuro Oncol* 2015;17:1188–98 CrossRef Medline
9. Kaufmann TJ, Smits M, Boxerman J, et al. **Consensus recommendations for a standardized brain tumor imaging protocol for clinical trials in brain metastases.** *Neuro Oncol* 2020;22:757–72 CrossRef Medline
10. Kakeda S, Korogi Y, Hiai Y, et al. **Detection of brain metastasis at 3T: comparison among SE, IR-FSE and 3D-GRE sequences.** *Eur Radiol* 2007;17:2345–51 CrossRef Medline
11. Norbeck O, Sprenger T, Avventi E, et al. **Optimizing 3D EPI for rapid T1-weighted imaging.** *Magn Reson Med* 2020;84:1441–55 CrossRef Medline
12. Likert R. **A technique for the measurement of attitudes.** *Archives of Psychology* 1932;22:1–55
13. Koo TK, Li MY. **A guideline of selecting and reporting intraclass correlation coefficients for reliability research.** *J Chiropr Med* 2016;15:155–63 CrossRef Medline
14. Landis JR, Koch GG. **The measurement of observer agreement for categorical data.** *Biometrics* 1977;33:159–74 CrossRef Medline
15. Viera AJ, Garrett JM. **Understanding interobserver agreement: the kappa statistic.** *Fam Med* 2005;37:360–63 Medline
16. Feinstein AR, Cicchetti DV. **High agreement but low kappa, I: the problems of two paradoxes.** *J Clin Epidemiol* 1990;43:543–49 CrossRef Medline
17. Mugler JP. **Optimized three-dimensional fast-spin-echo MRI.** *J Magn Reson Imaging* 2014;39:745–67 CrossRef Medline
18. Havsteen I, Ohlhues A, Madsen KH, et al. **Are movement artifacts in magnetic resonance imaging a real problem? A narrative review.** *Front Neurol* 2017;8:232 CrossRef Medline

19. Munn Z, Pearson A, Jordan Z, et al. **Patient anxiety and satisfaction in a magnetic resonance imaging department: initial results from an action research study.** *J Med Imaging Radiat Sci* 2015;46:23–29 CrossRef Medline
20. Goncalves Filho AL, Conklin J, Longo MG, et al. **Accelerated post-contrast wave-CAIPI T1 SPACE achieves equivalent diagnostic performance compared with standard T1 SPACE for the detection of brain metastases in clinical 3T MRI.** *Front Neurol* 2020;11:587327 CrossRef Medline
21. Mugler JP 3rd, Brookeman JR. **Theoretical analysis of gadopentetate dimeglumine enhancement in T1-weighted imaging of the brain: comparison of two-dimensional spin-echo and three-dimensional gradient-echo sequences.** *J Magn Reson Imaging* 1993;3:761–69 CrossRef Medline
22. Komada T, Naganawa S, Ogawa H, et al. **Contrast-enhanced MR imaging of metastatic brain tumor at 3 Tesla: utility of T(1)-weighted SPACE compared with 2D spin echo and 3D gradient echo sequence.** *Magn Reson Med Sci* 2008;7:13–21 CrossRef Medline
23. Kammer N, Coppenrath E, Treitl K, et al. **Comparison of contrast-enhanced modified T1-weighted 3D TSE black-blood and 3D MPAGE sequences for the detection of cerebral metastases and brain tumours.** *Eur Radiol* 2016;26:1818–25 CrossRef Medline

Pretreatment ADC Histogram Analysis as a Prognostic Imaging Biomarker for Patients with Recurrent Glioblastoma Treated with Bevacizumab: A Systematic Review and Meta-analysis

R. Kurokawa, A. Baba, M. Kurokawa, A. Capizzano, O. Hassan, T. Johnson, Y. Ota, J. Kim, A. Hagiwara, T. Moritani, and A. Srinivasan

ABSTRACT

BACKGROUND: The mean ADC value of the lower Gaussian curve (ADC_L) derived from the bi-Gaussian curve-fitting histogram analysis has been reported as a predictive/prognostic imaging biomarker in patients with recurrent glioblastoma treated with bevacizumab; however, its systematic summary has been lacking.

PURPOSE: We applied a systematic review and meta-analysis to investigate the predictive/prognostic performance of ADC_L in patients with recurrent glioblastoma treated with bevacizumab.

DATA SOURCES: We performed a literature search using PubMed, Scopus, and EMBASE.

STUDY SELECTION: A total of 1344 abstracts were screened, of which 83 articles were considered potentially relevant. Data were finally extracted from 6 studies including 578 patients.

DATA ANALYSIS: Forest plots were generated to illustrate the hazard ratios of overall survival and progression-free survival. The heterogeneity across the studies was assessed using the Cochrane Q test and I² values.

DATA SYNTHESIS: The pooled hazard ratios for overall survival and progression-free survival in patients with an ADC_L lower than the cutoff values were 1.89 (95% CI, 1.53–2.31) and 1.98 (95% CI, 1.54–2.55) with low heterogeneity among the studies. Subgroup analysis of the bevacizumab-free cohort showed a pooled hazard ratio for overall survival of 1.20 (95% CI, 1.08–1.34) with low heterogeneity.

LIMITATIONS: The conclusions are limited by the difference in the definition of recurrence among the included studies.

CONCLUSIONS: This systematic review with meta-analysis supports the prognostic value of ADC_L in patients with recurrent glioblastoma treated with bevacizumab, with a low ADC_L demonstrating decreased overall survival and progression-free survival. On the other hand, the predictive role of ADC_L for bevacizumab treatment was not confirmed.

ABBREVIATIONS: ADC_L = mean ADC value of the lower Gaussian curve; HR = hazard ratio; OS = overall survival; PFS = progression-free survival; QUADAS-2 = Quality Assessment of Diagnostic Accuracy Studies 2; VEGF = vascular endothelial growth factor

Glioblastoma remains the most common and lethal primary malignant tumor of the CNS, with a median overall survival of 8–14 months despite aggressive surgery, chemotherapy,

and radiation.^{1,2} Histologically, glioblastoma is characterized by tumor cell anaplasia, necrosis, and prominent angiogenesis mediated by the vascular endothelial growth factor (VEGF), constituting a rationale for targeted therapy.³ Bevacizumab is a humanized anti-VEGF monoclonal immunoglobulin 1 antibody, and its use for recurrent glioblastoma was approved by the US Food and Drug Administration in 2009. Although several clinical trials failed to demonstrate its contribution to extending patient survival in newly diagnosed glioblastoma or progressive glioblastoma,^{4–6} prolonged progression-free survival (PFS) and overall survival (OS) have been reported in the recurrence setting with either bevacizumab alone or in combination with other chemotherapy.⁷

Received September 8, 2021; accepted after revision November 15.

From the Division of Neuroradiology (R.K., A.B., M.K., A.C., O.H., Y.O., J.K., T.M., A.S.), Department of Radiology, University of Michigan, Ann Arbor, Michigan; Department of Biostatistics (T.J.), University of Michigan School of Public Health, Ann Arbor, Michigan; and Department of Radiology (A.H.), Juntendo University School of Medicine, Tokyo, Japan.

Please address correspondence Ryo Kurokawa, MD, PhD, Division of Neuroradiology, Department of Radiology, University of Michigan, Ann Arbor, MI, 1500 E Medical Center Dr, UH B2, Ann Arbor, MI 48109; e-mail: kuroro63@gmail.com; @Rdiag2

Indicates article with online supplemental data.
<http://dx.doi.org/10.3174/ajnr.A7406>

MR imaging is an essential imaging technique for diagnosis, treatment planning, and evaluation of therapeutic effects in patients with glioblastoma. A meta-analysis by Choi et al¹⁸ demonstrated the benefit of perfusion MR imaging, including dynamic susceptibility contrast MR imaging and dynamic contrast-enhanced MR imaging, as a predictive and prognostic imaging biomarker in patients with recurrent glioblastoma treated with bevacizumab. There have also been many studies investigating the performance of DWI as a predictive/prognostic imaging biomarker in recurrent glioblastoma.^{9–18} In particular, several studies have reported the usefulness of the mean ADC value of the lower Gaussian curve (ADC_L) derived from the bi-Gaussian curve-fitting histogram analysis,^{9–14} however, a systematic summary of this topic has been lacking.

The purpose of this study was to systematically review the literature and investigate the predictive/prognostic role of pretreatment DWI, especially ADC_L, in patients with recurrent glioblastoma receiving bevacizumab treatment.

MATERIALS AND METHODS

Protocol

This study was performed in accordance with the Preferred Reporting Items for Systematic Reviews and Meta-Analyses 2020 statement.¹⁹

Study Selection

We searched the PubMed, Scopus, and EMBASE data bases using the following search terms on August 24, 2021, without any language or date limits:

- ((glioblastoma)OR(GBM)) AND ((avastin) OR (bevacizumab)) AND ((ADC) OR (apparent diffusion coefficient)) for PubMed
- (glioblastoma OR gbm) AND (avastin OR bevacizumab) AND (adc OR (apparent AND diffusion AND coefficient)) for EMBASE
- ALL ((glioblastoma OR gbm) AND (avastin OR bevacizumab) AND (adc OR (apparent AND diffusion AND coefficient) AND (LIMIT-TO (SUBJAREA, "MEDI")))) for Scopus

Publications that met all of the following criteria were considered eligible:

- Participants: patients were clinically, radiologically, and/or histologically diagnosed with recurrent glioblastoma treated with bevacizumab and underwent pretreatment MRI
- Index test: ADC_L
- Outcome: hazard ratio (HR) for PFS or OS between patients with high and low ADC_L
- Study design: retrospective or prospective observational studies and clinical trials.

Exclusion criteria were as follows:

- The full text was unavailable.
- It was not a peer-reviewed journal publication.
- The relationship between ADC and survival was not analyzed, or the HRs were not calculated or could not be estimated.
- The index was not ADC_L.

- Possible duplication of patients: the study with a smaller number of patients was excluded.
- Review, systematic review, or meta-analysis.

Non-English references were translated into English using Google Translate (translate.google.com) and examined.

Data Analyses

Two board-certified radiologists with 9 and 6 years of experience in neuroradiology reviewed the full text of the eligible studies by consensus. Any disagreements were resolved by another board-certified radiologist with 13 years of experience in neuroradiology. We collected authors names, publication year, the region where patients were included, period of patient inclusion, study methods, trial name, number of patients, mean or median age, sex, the definition of recurrence of glioblastoma, treatment regimen, MR imaging vendor/model/magnetic field strength, b-values, ROI placement method, ADC type, the cutoff value of ADC, how the cutoff value was determined, and outcomes (HRs for OS and PFS). When the original study did not report the 95% confidence intervals of HRs, we estimated them using all the available data from the reported statistics.

Quality and Risk-of-Bias Assessment

We used the Quality Assessment of Diagnostic Accuracy Studies 2 (QUADAS-2).²⁰ QUADAS-2 is based on the 4 domains (patient selection, index test, reference standard, and flow and timing). These domains are assessed regarding the risk of bias, and the first 3 domains are also assessed in terms of applicability.

Statistics

A forest plot was generated to illustrate the HRs for OS and PFS in patients with an ADC_L lower than the cutoff values along with upper and lower 95% CIs. The pooled HR with 95% CIs was calculated using the fixed-effects model. The heterogeneity across the studies was assessed using the Cochrane Q test and I² values. I² values were interpreted as follows: 0%–29%, low; 30%–49%, moderate; and 50%–90%, considerable heterogeneity. *P* values < .05 were considered statistically significant. Statistical analyses were performed using Review Manager (RevMan, Version 5.4; <https://training.cochrane.org/online-learning/core-software-cochrane-reviews/revman>).

RESULTS

Study Selection

A total of 1344 abstracts were screened, of which 113 duplications were excluded. A total of 1148 articles were excluded by title and abstract screening. After excluding 77 articles according to the inclusion/exclusion criteria, finally, 6 studies including a total of 578 patients met the selection criteria for the systematic review.^{9–14} The process of study selection is summarized in Fig 1. Publications in this systematic review ranged from 2012 to 2020.

Study Characteristics

The individual study characteristics are summarized in the Online Supplemental Data. A total of 578 patients with recurrent glioblastoma treated with bevacizumab and 236 patients treated

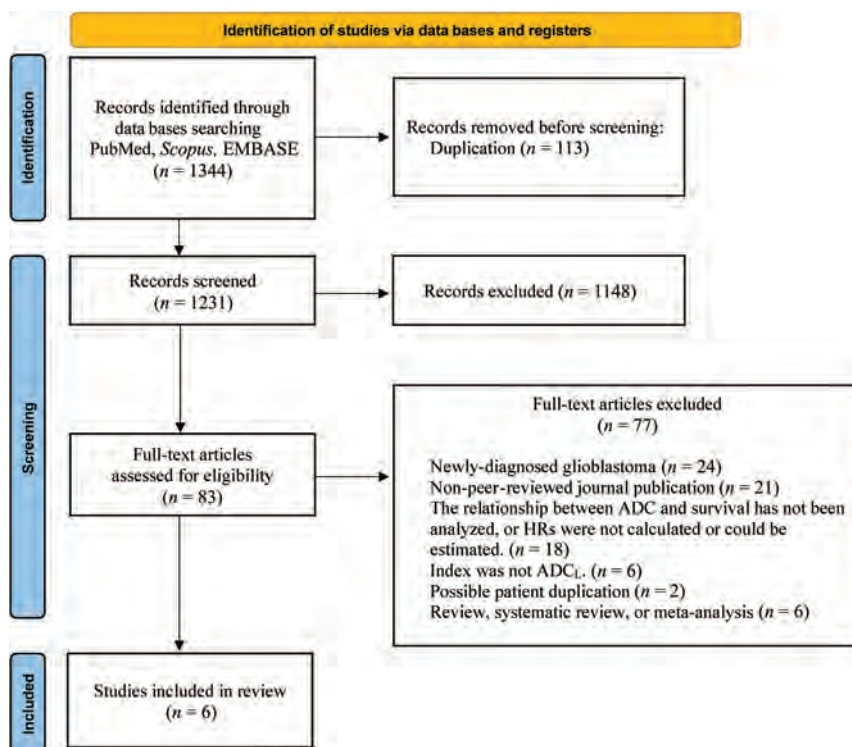


FIG 1. Flow diagram of study selection.

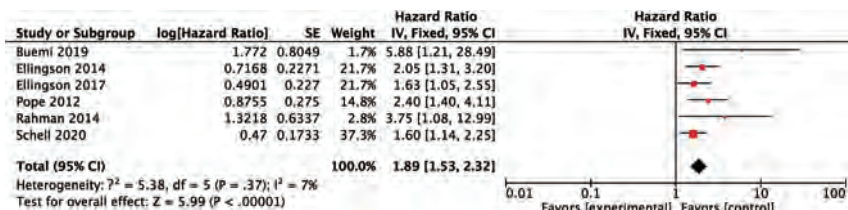


FIG 2. A forest plot summarizing the HR of OS in patients treated with bevacizumab with the ADC_L lower than the cutoff values compared with those with the ADC_L higher than the cutoff values. SE indicates standard error; IV, instrumental variable.

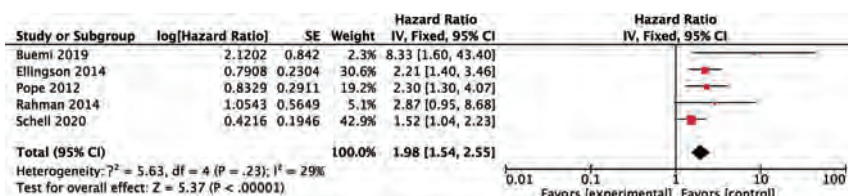


FIG 3. A forest plot summarizing the HR of PFS in patients treated with bevacizumab with the ADC_L lower than the cutoff values compared with those with the ADC_L higher than the cutoff values. SE indicates standard error; IV, instrumental variable.

without bevacizumab (hereafter, the bevacizumab-free cohort) were included. The mean or median patient age was approximately 50 years in each study. The VOI was acquired in the enhancing tumor areas, and ADC histogram analysis was performed with the bi-Gaussian fitting model, though 1 study used the 3 peaks model.¹⁰

The ADC_L was generated on the basis of the fitting curve, and OS and PFS were compared using cutoff values of $1.050\text{--}1.240 \times 10^{-3} \text{ mm}^2/\text{s}$ and $1.050\text{--}1.241 \times 10^{-3} \text{ mm}^2/\text{s}$, respectively. The cutoff value was determined by averaging^{9,13,17} the hierarchical Bayesian method,¹⁴ where the OS difference among patient cohorts was the largest,¹² or based on empiric thresholds identified in previous studies,¹¹ though the method was not described in detail in 1 study.¹⁰ These studies excluded the areas of macroscopic cystic, hemorrhagic, and necrotic changes from the VOIs for ADC histogram analyses. Three studies^{11,12,14} compared the OS of the bevacizumab-free cohort depending on the ADC_L , though only 2 studies compared PFS.^{11,14}

Quality and Risk-of-Bias Assessment

The results of QUADAS-2 are summarized in the Online Supplemental Data. Most studies had a low risk of bias in terms of patient selection, index test, reference standard, and flow and timing. Studies that did not describe whether the participants were consecutive, randomized, or neither were considered to have an uncertain risk of bias regarding the patient selection. A study in which the method of the definition of ADC_L and the cutoff value determination were not described in detail was considered to have an uncertain risk of bias regarding the index test and reference standard.

Meta-analysis

HRs for OS in patients with an ADC_L lower than the cutoff values were available in all of the 6 studies, and the pooled HR of the lower ADC_L was 1.89 (95% CI, 1.53–2.32), indicating worse survival (Fig 2). The lower 95% CI of HRs for OS was >1.00 in all studies. The heterogeneity of HRs for OS was considered low with the Q value in the Cochran Q test of 5.38 ($P = .37$) and an I^2 of 7%. The comparison of HRs for PFS was available in 5 studies, and the pooled HR with an ADC_L lower than the cutoff values was 1.98 (95% CI, 1.54–2.55) (Fig 3). Although the lower 95% CI of HR for PFS was <1.00 in 1 study,¹⁰ the heterogeneity of HRs for PFS was low, with the Q value in the Cochran Q test of 5.63 ($P = .23$) and an I^2

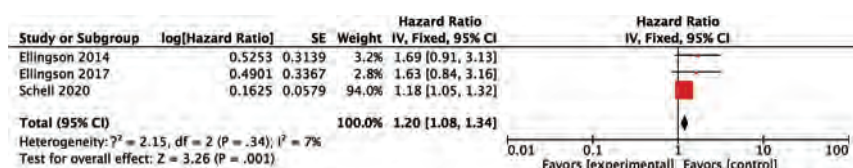


FIG 4. A forest plot summarizing the HR of OS in the bevacizumab-free cohort with the ADC_L lower than the cutoff values compared with those with the ADC_L higher than the cutoff values. SE indicates standard error; IV, instrumental variable.

of 29%. For studies with a bevacizumab-free cohort, no differences in OS or PFS were found, depending on the ADC_L in 2 of 3 studies,^{11,12} whereas the significant differences in OS and PFS were retained in the bevacizumab-free cohort in 1 study.¹⁴ The pooled HR of the lower ADC_L for OS in this subgroup was 1.20 (95% CI, 1.08–1.34) with a low heterogeneity (the Q value in Cochran Q test was 2.15 [$P = .34$] and the I^2 was 7%; Fig 4).

DISCUSSION

DWI is a unique technique that allows noninvasive observation of the microstructure of tumors and surrounding brain tissues and is widely used in daily clinical practice. In this study, the high prognostic performance of the ADC_L for survival was confirmed in patients with recurrent glioblastoma treated with bevacizumab. The meta-analysis demonstrated that a lower ADC_L on pretreatment MR imaging was related to unfavorable survival with pooled HRs of 1.89 (95% CI, 1.53–2.32) for OS and 1.98 (95% CI, 1.54–2.55) for PFS, with low heterogeneity among the studies. However, the subgroup analysis with the patients treated without bevacizumab (the bevacizumab-free cohort) also showed a high pooled HR for OS of 1.20 (95% CI, 1.08–1.34), indicating that although the ADC_L has a prognostic value, uncertainty remains as to whether the ADC_L has a predictive value for bevacizumab treatment.

Noninvasive characterization of glioblastoma using MR imaging has been extensively studied to predict the treatment effect and subsequent patient survival in patients with recurrent glioblastoma treated with bevacizumab. Focused sequences included perfusion MR imaging,^{8,21–24} ³¹P MR spectroscopy,^{25,26} and ADC.^{9–18} Choi et al⁸ demonstrated that the pooled HRs between responders and nonresponders to bevacizumab, as defined by the relative CBV on dynamic susceptibility contrast MR imaging, were 0.47 (95% CI, 0.29–0.76) for OS and 0.46 (95% CI, 0.28–0.76) for PFS, indicating that tumor perfusion was decreased in responders, resulting in longer survival. The results of their meta-analysis showed the utility of perfusion MR imaging in patients with recurrent glioblastoma being treated with bevacizumab, though the timing of perfusion MR imaging differed among the studies (ie, changes of relative CBV values and posttreatment relative CBV were assessed simultaneously). The results in the present study may be more uniformly applicable to individual cases, given that all the timing of ADC_L values was during pretreatment.

The biologic mechanisms of the worse survival in patients with tumors showing a low ADC_L have not been pathologically proved. One hypothesis is that a more hypoxic or hypercellular nature of the tumor is represented by a low ADC_L, making bevacizumab

treatment less effective and the tumor more aggressive, as Ellingson et al¹¹ pointed out. Indeed, the correlation between high tumor cellularity and low ADC values is known. However, ADC values fluctuate depending on the degree of intratumoral vascular edema, cystic change, and necrosis.²⁷ The evaluated studies in this meta-analysis excluded the areas of macroscopic cystic, hemorrhagic, and necrotic changes from the

VOIs for ADC histogram analysis, but intratumoral microscopic changes and vascular edema might have affected the results.

In their study with vestibular schwannomas, Plotkin et al²⁸ reported that the higher the pretreatment ADC value, the greater was the bevacizumab-induced tumor shrinkage, suggesting that the higher ADC was associated with a higher degree of intratumoral vascular edema, which is more likely to respond to anti-VEGF therapy. Similarly, in recurrent glioblastoma, intratumoral vascular edema and microscopic cystic/necrotic changes, as well as tumor cellularity, might have affected the ADC values. To elucidate this, further studies with radiopathologic correlation will be necessary.

Not only for patients with recurrent glioblastoma but also for those with newly diagnosed glioblastoma, the prognostic performance of pretreatment ADC_L has been reported.^{29–31} Notably, these studies showed opposite results from each other as well as from this study; ie, the study by Wirsching et al²⁹ demonstrated that a longer OS was associated with a higher ADC_L, whereas the other 2 studies^{30,31} reported a trend in which longer OS was associated with a lower ADC_L or a lower mean ADC, respectively. It remains to be seen whether the differences in the results among these studies and the present study reflect differences in the nature of newly diagnosed and recurrent glioblastoma and/or the effect of heterogeneity exaggerated by the limited number of studies. Further studies of newly diagnosed glioblastoma treated with bevacizumab and its relationship with pretreatment ADC value are warranted to clarify this issue.

There are some limitations to this study. First, like all meta-analyses, the conclusions of this study are limited by the heterogeneity of the included studies, such as patient age, the regimen, and different factors used in the multivariate analyses, though the results of Cochran Q tests and I^2 values for OS and PFS indicated low heterogeneity, implying that the pooled results were robust. Second, the definition of the recurrence of glioblastoma varied among the included studies. Third, the definition of glioblastoma could be different from that of the 2021 World Health Organization Classification.³² Further investigation is needed to determine the role of ADC_L in glioblastoma in the new definition. Third, unclear risk of bias remained in 1–2 studies in terms of patient selection, index test, and reference standard. Finally, the methodology of the meta-analysis was limited by the inability to obtain 1 potentially relevant reference for a full-text review.

CONCLUSIONS

The systematic review and meta-analysis of this study support the prognostic value of ADC_L in patients with recurrent glioblastoma treated with bevacizumab, with a low ADC_L demonstrating

decreased OS and PFS. On the other hand, the role of ADC_L as a predictive imaging biomarker was not confirmed.

Disclosure forms provided by the authors are available with the full text and PDF of this article at www.ajnr.org.

REFERENCES

- Ostrom QT, Patil N, Cioffi G, et al. **CBTRUS Statistical Report: Primary Brain and Other Central Nervous System Tumors Diagnosed in the United States in 2013–2017.** *Neuro Oncol* 2020;22:iv1–96 CrossRef Medline
- Van Meir EG, Hadjipanayis CG, Norden AD, et al. **Exciting new advances in neuro-oncology: the avenue to a cure for malignant glioma.** *CA Cancer J Clin* 2010;60:166–93 CrossRef Medline
- Lu-Emerson C, Duda DG, Emblem KE, et al. **Lessons from anti-vascular endothelial growth factor and anti-vascular endothelial growth factor receptor trials in patients with glioblastoma.** *J Clin Oncol* 2015;33:1197–213 CrossRef Medline
- Chinot OL, Wick W, Mason W, et al. **Bevacizumab plus radiotherapy-temozolomide for newly diagnosed glioblastoma.** *N Engl J Med* 2014;370:709–22 CrossRef Medline
- Wick W, Gorlia T, Bendszus M, et al. **Lomustine and bevacizumab in progressive glioblastoma.** *N Engl J Med* 2017;377:1954–63 CrossRef Medline
- Gilbert MR, Dignam JJ, Armstrong TS, et al. **A randomized trial of bevacizumab for newly diagnosed glioblastoma.** *N Engl J Med* 2014;370:699–708 CrossRef Medline
- Diaz RJ, Ali S, Qadir MG, et al. **The role of bevacizumab in the treatment of glioblastoma.** *J Neurooncol* 2017;133:455–67 CrossRef Medline
- Choi SH, Jung SC, Kim KW, et al. **Perfusion MRI as the predictive/prognostic and pharmacodynamic biomarkers in recurrent malignant glioma treated with bevacizumab: a systematic review and a time-to-event meta-analysis.** *J Neurooncol* 2016;128:185–94 CrossRef Medline
- Pope WB, Qiao XJ, Kim HJ, et al. **Apparent diffusion coefficient histogram analysis stratifies progression-free and overall survival in patients with recurrent GBM treated with bevacizumab: a multicenter study.** *J Neurooncol* 2012;108:491–98 CrossRef Medline
- Rahman R, Hamdan A, Zweifler R, et al. **Histogram analysis of apparent diffusion coefficient within enhancing and nonenhancing tumor volumes in recurrent glioblastoma patients treated with bevacizumab.** *J Neurooncol* 2014;119:149–58 CrossRef Medline
- Ellingson BM, Sahebjam S, Kim HJ, et al. **Pretreatment ADC histogram analysis is a predictive imaging biomarker for bevacizumab treatment but not chemotherapy in recurrent glioblastoma.** *AJNR Am J Neuroradiol* 2014;35:673–79 CrossRef Medline
- Ellingson BM, Gerstner ER, Smits M, et al. **Diffusion MRI phenotypes predict overall survival benefit from anti-VEGF monotherapy in recurrent glioblastoma: converging evidence from phase II trials.** *Clin Cancer Res* 2017;23:5745–56 CrossRef Medline
- Buemi F, Guzzardi G, Del Sette B, et al. **Apparent diffusion coefficient and tumor volume measurements help stratify progression-free survival of bevacizumab-treated patients with recurrent glioblastoma multiforme.** *Neuroradiol J* 2019;32:241–49 CrossRef Medline
- Schell M, Pflüger I, Brugnara G, et al. **Validation of diffusion MRI phenotypes for predicting response to bevacizumab in recurrent glioblastoma: post-hoc analysis of the EORTC-26101 trial.** *Neuro Oncol* 2020;22:1667–76 CrossRef Medline
- Pope WB, Kim HJ, Huo J, et al. **Recurrent glioblastoma multiforme: ADC histogram analysis predicts response to bevacizumab treatment.** *Radiology* 2009;252:182–89 CrossRef Medline
- Patel KS, Everson RG, Yao J, et al. **Diffusion magnetic resonance imaging phenotypes predict overall survival benefit from bevacizumab or surgery in recurrent glioblastoma with large tumor burden.** *Neurosurg* 2020;87:931–38 CrossRef Medline
- Park JE, Kim HS, Park SY, et al. **Identification of early response to anti-angiogenic therapy in recurrent glioblastoma: amide proton transfer-weighted and perfusion-weighted MRI compared with diffusion-weighted MRI.** *Radiology* 2020;295:397–406 CrossRef Medline
- Zhang M, Gulotta B, Thomas A, et al. **Large-volume low apparent diffusion coefficient lesions predict poor survival in bevacizumab-treated glioblastoma patients.** *Neuro Oncol* 2016;18:735–43 CrossRef Medline
- Page MJ, McKenzie JE, Bossuyt PM, et al. **The PRISMA 2020 statement: an updated guideline for reporting systematic reviews.** *BMJ* 2021;372:n71 CrossRef Medline
- Whiting PF, Rutjes AW, Westwood ME, et al; QUADAS-2 Group. **QUADAS-2: a revised tool for the quality assessment of diagnostic accuracy studies.** *Ann Intern Med* 2011;155:529–36 CrossRef Medline
- Aquino D, Di Stefano AL, Scotti A, et al. **Parametric response maps of perfusion MRI may identify recurrent glioblastomas responsive to bevacizumab and irinotecan.** *PLoS One* 2014;9:e90535 CrossRef Medline
- Harris RJ, Cloughesy TF, Hardy AJ, et al. **MRI perfusion measurements calculated using advanced deconvolution techniques predict survival in recurrent glioblastoma treated with bevacizumab.** *J Neurooncol* 2015;122:497–505 CrossRef Medline
- Kickingereder P, Wiestler B, Burth S, et al. **Relative cerebral blood volume is a potential predictive imaging biomarker of bevacizumab efficacy in recurrent glioblastoma.** *Neuro Oncol* 2015;17:1139–47 CrossRef Medline
- Leu K, Enzmann DR, Woodworth DC, et al. **Hypervascular tumor volume estimated by comparison to a large-scale cerebral blood volume radiographic atlas predicts survival in recurrent glioblastoma treated with bevacizumab.** *Cancer Imaging* 2014;14:31 CrossRef Medline
- Wenger KJ, Hattingen E, Franz K, et al. **Intracellular pH measured by 31 P-MR-spectroscopy might predict site of progression in recurrent glioblastoma under antiangiogenic therapy.** *J Magn Reson Imaging* 2017;46:1200–08 CrossRef Medline
- Hattingen E, Bähr O, Rieger J, et al. **Phospholipid metabolites in recurrent glioblastoma: in vivo markers detect different tumor phenotypes before and under antiangiogenic therapy.** *PLoS One* 2013;8:e56439 CrossRef Medline
- Huang WY, Wen JB, Wu G, et al. **Diffusion-weighted imaging for predicting and monitoring primary central nervous system lymphoma treatment response.** *AJNR Am J Neuroradiol* 2016;37:2010–18 CrossRef Medline
- Plotkin SR, Stemmer-Rachamimov AO, Barker FG, 2nd, et al. **Hearing improvement after bevacizumab in patients with neurofibromatosis type 2.** *N Engl J Med* 2009;361:358–67 CrossRef Medline
- Wirsching HG, Roelcke U, Weller J, et al. **MRI and ¹⁸FET-PET predict survival benefit from bevacizumab plus radiotherapy in patients with isocitrate dehydrogenase wild-type glioblastoma: results from the randomized ARTE trial.** *Clin Cancer Res* 2021;27:179–88 CrossRef Medline
- Omuro A, Beal K, Gutin P, et al. **Phase II study of bevacizumab, temozolomide, and hypofractionated stereotactic radiotherapy for newly diagnosed glioblastoma.** *Clin Cancer Res* 2014;20:5023–31 CrossRef Medline
- Pope WB, Lai A, Mehta R, et al. **Apparent diffusion coefficient histogram analysis stratifies progression-free survival in newly diagnosed bevacizumab-treated glioblastoma.** *AJNR Am J Neuroradiol* 2011;32:882–89 CrossRef Medline
- Louis DN, Perry A, Wesseling P, et al. **The 2021 WHO Classification of Tumors of the Central Nervous System: a summary.** *Neuro Oncol* 2021;23:1231–51 CrossRef Medline

Large Culprit Plaque and More Intracranial Plaques Are Associated with Recurrent Stroke: A Case-Control Study Using Vessel Wall Imaging

 G. Wu,  H. Wang,  C. Zhao,  C. Cao,  C. Chai,  L. Huang,  Y. Guo,  Z. Gong,  D.L. Tirschwell,  C. Zhu, and  S. Xia



ABSTRACT

BACKGROUND AND PURPOSE: Intracranial atherosclerotic plaque features are potential factors associated with recurrent stroke, but previous studies only focused on a single lesion, and few studies investigated them with perfusion impairment. This study aimed to investigate the association among whole-brain plaque features, perfusion deficit, and stroke recurrence.

MATERIALS AND METHODS: Patients with ischemic stroke due to intracranial atherosclerosis were retrospectively collected and categorized into first-time and recurrent-stroke groups. Patients underwent high-resolution vessel wall imaging and DSC-PWI. Intracranial plaque number, culprit plaque features (such as plaque volume/burden, degree of stenosis, enhancement ratio), and perfusion deficit variables were recorded. Logistic regression analyses were performed to determine the independent factors associated with recurrent stroke.

RESULTS: One hundred seventy-five patients (mean age, 59 [SD, 12] years; 115 men) were included. Compared with the first-time stroke group ($n = 100$), the recurrent-stroke group ($n = 75$) had a larger culprit volume ($P = .006$) and showed more intracranial plaques ($P < .001$) and more enhanced plaques ($P = .003$). After we adjusted for other factors, culprit plaque volume (OR, 1.16 per 10-mm³ increase; 95% CI, 1.03–1.30; $P = .015$) and total plaque number (OR, 1.31; 95% CI, 1.13–1.52; $P < .001$) were independently associated with recurrent stroke. Combining these factors increased the area under the curve to 0.71.

CONCLUSIONS: Large culprit plaque and more intracranial plaques were independently associated with recurrent stroke. Performing whole-brain vessel wall imaging may help identify patients with a higher risk of recurrent stroke.

ABBREVIATIONS: HR-VWI = high-resolution vessel wall imaging; IQR = interquartile range

Intracranial atherosclerosis is the primary etiology of stroke in Asia,¹ and the risk of recurrent stroke in these patients is high even under aggressive medication.² Identification of the risk

factors associated with recurrent stroke is essential for secondary stroke prevention.

The degree of stenosis is a well-recognized predictor of recurrent stroke, and patients with >50% stenosis are recommended for more aggressive treatment.^{3,4} However, vulnerable atherosclerotic plaques with <50% stenosis can also lead to stroke events.^{5,6} The development of high-resolution vessel wall imaging (HR-VWI) has enabled the visualization of vulnerable features (intraplaque hemorrhage, outward remodeling, neurovascularity) in vivo and has provided important insight into plaque vulnerability rather than the degree of stenosis alone.^{7,8} The use of whole-brain HR-VWI also allows the evaluation of multiple lesions simultaneously.⁹

Previous HR-VWI studies of intracranial plaques focused on comparing patients with stroke and asymptomatic patients.^{10,11} However, investigations of intracranial plaque features associated with recurrent stroke are still rare. A few studies found that plaque enhancement¹² and plaque burden¹³ were associated with stroke recurrence. However, these studies focused on MCA stenosis rather than whole-brain evaluation. Recent studies found


Received July 14, 2021; accepted after revision November 2.

From The School of Medicine (G.W., H.W.), Nankai University, Tianjin, China; Department of Radiology (C. Zhao), First Central Clinical College, Tianjin Medical University, Tianjin, China; Department of Radiology (C. Cao), Tianjin University Huanhu Hospital, Tianjin, China; Departments of Radiology (C. Chai, L.H., Y.G., S.X.) and Neurology (Z.G.), Tianjin First Central Hospital, School of Medicine, Nankai University, Tianjin, China; and Departments of Neurology (D.L.T.) and Radiology (C. Zhu), University of Washington, Seattle, Washington.

Shuang Xia and Chengcheng Zhu contributed equally to this study as co-senior authors.

This work was supported by the National Natural Science Foundation of China (grant No. 81871342 to S. Xia and grant No. 81901728 to C. Chai), the Natural Science Foundation of Tianjin (grant No. 20JCQNJC01250 to C. Cao), and the National Key R&D Programme of China (grant No. 2019YFC0120903 to S. Xia).

Please address correspondence to Shuang Xia, MD, PhD, Department of Radiology, Tianjin First Central Hospital, School of Medicine, Nankai University, Tianjin 300192, China; e-mail: xiashuang77@163.com

 Indicates open access to non-subscribers at www.ajnr.org

 Indicates article with online supplemental data.

<http://dx.doi.org/10.3174/ajnr.A7402>

that the total plaque number was a novel imaging marker of intracranial atherosclerosis,^{14,15} evaluating the entire cerebral arterial tree may provide additional information. However, the relationship with stroke recurrence was not studied in these research. Perfusion impairment is also related to recurrent stroke¹⁶ but has been rarely studied together with whole-brain HR-VWI features.¹⁶

Our study aimed to evaluate intracranial total plaque number by whole-brain HR-VWI; explore the difference in intracranial culprit plaque features, total plaque number, and perfusion deficit between first-time and recurrent stroke groups using HR-VWI and DSC-PWI; and find the association between these factors with stroke recurrence.

MATERIALS AND METHODS

Study Patients

This retrospective single-center observational study was approved by the Ethics Committee of Tianjin First Central Hospital, and the requirement of patient informed consent was waived. From September 2016 to September 2020, the patients who underwent HR-VWI in our hospital and met the following inclusion criteria were selected, and their clinical and MR imaging data were reviewed. Inclusion criteria were the following: 1) older than 18 years of age; 2) ischemic stroke in the unilateral MCA or posterior circulation territory based on positive findings on DWI; 3) DSC-PWI included in the MR imaging protocol; 4) all MR images acquired at the same scan session within 30 days of symptom onset; 5) intracranial atherosclerosis considered as the etiology of stroke events based on the following: confirmation of intracranial large arterial atherosclerotic plaque upstream of the stroke territory, identification of atherosclerotic plaque on the parent artery for patients with an isolated infarct in the penetrating artery territory, no imaging evidence of aortic arch atherosclerosis, no clinical or imaging evidence of cardioembolism, and exclusion of other etiologies by relevant clinical history and examination; and 6) complete clinical data and satisfactory imaging quality. Exclusion criteria included the following: 1) patients with recurrent events in the territories different from the previous ischemic territories; 2) acute lacunar infarction on DWI; 3) acute ischemic stroke involving other arterial territories (anterior cerebral artery, bilateral circulation, both anterior and posterior circulation); 4) nonatherosclerosis vasculopathy; 5) evidence of cardioembolism (such as recent myocardial infarction within 1 month, atrial fibrillation, mitral stenosis, prosthetic valve thrombosis, and endocarditis); 6) $\geq 50\%$ stenosis or the presence of vulnerable carotid plaques (the presence of intraplaque hemorrhage, large lipid-rich necrotic core, or irregular surface) of the ipsilateral extracranial carotid artery on HR-VWI; 7) complex aortic arch plaque (plaque of ≥ 4 mm or with irregular ulceration) confirmed by CTA; and 8) poor imaging quality and incomplete clinical data. Clinical information, including age, sex, vascular risk factors (the diagnostic criteria are shown in the Online Supplemental Data), preadmission statin use, symptom onset to HR-VWI interval, NIHSS score on admission, and several blood biochemical indexes, was recorded for each patient.

Patient Groupings

Patients were divided into the recurrent-stroke group and the first-time stroke group, and there were no overlapping patients between these 2 groups. The patients with recurrent-stroke events met the following criteria: acute neurologic deficit on admission that fitted the definition of acute ischemic stroke, high-intensity signal on DWI, previous ischemic stroke history confirmed by hospital records, and corresponding encephalomalacia in the same territory on FLAIR.^{17,18} The symptoms and signs of initial strokes had resolved before the symptom onset of recurrent-stroke events.¹⁷ The patients in the first-time stroke group had the same criteria as the recurrent-stroke group, except for the previous stroke history and corresponding encephalomalacia on FLAIR.

Imaging Protocol

All MR images were obtained on a 3T whole-body system (Magnetom Prisma; Siemens) with a 64-channel head-and-neck coil. The imaging protocol included DWI, FLAIR, strategically acquired gradient-echo imaging,¹⁹ precontrast T1-weighted HR-VWI, DSC-PWI, and postcontrast HR-VWI (parameters are detailed in the Online Supplemental Data). DWI helped the localization of the acute cerebral ischemic lesion. FLAIR was used to confirm the remote cerebral infarction. DSC-PWI was used for the evaluation of perfusion deficits. HR-VWI was performed using the inversion recovery prepared sampling perfection with application-optimized contrast by using different flip angle evolutions (SPACE)²⁰ sequence in a sagittal plane optimized for intracranial plaque evaluation and flow signal suppression. The SPACE sequence was nonselective excitation and covered the whole brain. DSC-PWI was performed with contrast agent injection (0.2 mL/kg; 0.9% sodium chloride flush, 15 mL; flush rate, 2 mL/s) using gadobenate dimeglumine. Postcontrast HR-VWI was performed after DSC-PWI.

Imaging Analysis

Quantitative analysis of plaque features (except plaque volume) was performed using the PACS. The plaque volume was measured semiautomatically using commercial volumetric analysis software, ITK-SNAP 3.8.0 (www.itksnap.org).²¹ The perfusion evaluation was performed using commercial software, Fast-Processing of Ischemic Stroke software (F-STROKE; Version 1.0.18; Neuroblom). MR imaging analyses were performed by 2 neuroradiologists (G.W. and C.Z. with 8 and 6 years of experience, respectively). The reviewers had access to the source images and reconstructed images but were blinded to the clinical information.

Plaque Identification. Due to the small size of the intracranial arteries, only the large arteries were analyzed, including intracranial ICAs (cavernous and supraclinoid segments), A1 and A2 segments of the anterior cerebral arteries, M1 and M2 segments of MCAs, P1 and P2 segments of posterior cerebral arteries, basilar arteries, and intracranial segments of the vertebral arteries. An atherosclerotic plaque was identified as focal vessel wall thickening with reference to adjacent proximal, distal, or contralateral vessel segments,²² regardless of whether it caused luminal stenosis. Multiple plaques could be on the same arterial segment, and the determination of multiple plaques was as follows (Online

Supplemental Data): Two plaques were considered as 2 separate plaques if they were discontinuous and had a normal arterial wall between them. The plaques that involved several segments were counted as separate plaques for each segment.

Plaque Classification. A plaque located upstream of the infarct lesion was defined as a culprit plaque when it was the only plaque within the vascular territory of the stroke or the most stenotic plaque when multiple plaques existed within the same vascular territory of the stroke.²² A plaque was considered a probably-culprit plaque if it was within the vascular territory but not the most stenotic plaque.²² A plaque was defined as nonculprit plaque if it was not within the vascular territory of stroke.²² During the identification of plaque, any disagreements between the 2 reviewers were resolved by discussion and consensus under the guidance of a senior neuroradiologist (Y.G. with 17 years of experience in neuroradiology).

Plaque Feature Measurement. By means of the multiplanar reformation function of the PACS, the lumen and vessel boundaries were manually segmented (Online Supplemental Data) at the most stenotic location of the plaque on the reformatted cross-sectional postcontrast HR-VWI. For the evaluation of intraplaque hemorrhage and plaque-enhancement grading, the plaque was observed section by section on the reformatted images of precontrast and postcontrast HR-VWI. The following parameters of culprit plaque and probably-culprit plaque were derived from the measurements:

1. Plaque area = vessel area – lumen area.
2. Plaque burden = $(1 - \text{lumen area}/\text{vessel area}) \times 100\%$.²³
3. Arterial remodeling ratio = vessel area/reference vessel area.
The arterial remodeling pattern at the lesion site was categorized as positive remodeling if the arterial remodeling ratio was >1.05 .²³
4. Eccentric index = $(1 - \text{minimum wall thickness}/\text{maximum wall thickness}) \times 100\%$. The plaque was classified as eccentric if the eccentric index was ≥ 0.5 , and concentric if < 0.5 .²⁴
5. A plaque with intraplaque hemorrhage was defined if the signal intensity of its brightest part on the precontrast HR-VWI was higher than 150% of the signal intensity of the reference vessel wall.²⁵
6. With precontrast and postcontrast HR-VWI, the enhancement ratio¹³ and enhancement grading^{22,26} of plaque were analyzed using previously established methods,^{13,22,26} detailed in the Online Supplemental Data. A plaque was considered enhanced if the enhancement degree was grades 1 and 2.
7. The degree of stenosis = $(1 - \text{lumen diameter}/\text{reference lumen diameter at the normal proximal site}) \times 100\%$.²⁷

The plaque volume was measured semiautomatically using ITK-SNAP 3.8.0 software. On the cross-sectional slices of postcontrast HR-VWI, the plaque boundaries were delineated section by section, and the volume of each plaque was recorded (Online Supplemental Data).

All the above plaque features were evaluated for the culprit and probably-culprit plaques, but only the enhancement grading

was analyzed for nonculprit plaques. In addition, intracranial total plaque number and enhanced plaque number were recorded for each patient.

Perfusion Deficit Evaluation. By means of Fast-Processing of Ischemic Stroke software (F-STROKE; Version 1.0.18), the time-to-maximum volumes with different thresholds were automatically calculated. Three different variables were recorded for each patient as follows:

1. The hypoperfusion volume was defined as the hypoperfusion volume of time-to-maximum with a threshold of >6 seconds.²⁸
2. Hypoperfusion intensity ratio = (the hypoperfusion volume of time-to-maximum with a threshold of >10 seconds)/(the hypoperfusion volume of time-to-maximum with a threshold of >6 seconds).²⁹
3. Hypoperfusion existed if the hypoperfusion volume was >0 mL.

Statistical Analysis

The clinical and imaging features of the 2 groups were analyzed. The frequency and distribution of plaques per arterial segment were also explored. Continuous variables were provided using mean (SD) or median (interquartile range [IQR]). Categorical variables were presented as frequencies. All group differences of culprit plaque features and perfusion deficits were compared using the Student *t* test, Mann-Whitney *U* test, or χ^2 test as appropriate. Because the same patient might have multiple probably-culprit plaques, the generalized estimating equations with a robust covariance matrix estimator were used for the differences in probably-culprit plaque features between the first-time and recurrent-stroke groups. Clinical and imaging variables with a *P* value $< .1$ from the univariable analysis were included in the following analysis: Multivariable logistic regression analysis (forward likelihood ratio method) was used for determining the independent factors associated with patients with recurrent stroke. Reproducibility assessment was evaluated using intraclass correlation coefficients (continuous variables) (Online Supplemental Data). Two-sided *P* $< .05$ indicated statistical significance in all analyses. The receiver operating characteristic curves were analyzed for parameters with independent significance. The Delong test was performed for comparison of the area under the curve values. SPSS 24.0 (IBM) and MedCalc 19.0.4 (MedCalc Software) were used for all analyses.

RESULTS

Patient Characteristics

From September 2016 to September 2020, one hundred seventy-five patients (mean age, 59 [SD, 12] years; 115 men) were included in the final analysis (Fig 1). As Table 1 shows, the median interval between symptom onset and HR-VWI was 10 (IQR, 6–15) days. Among these patients, 75 patients had recurrent stroke and 100 patients had first-time stroke. The median stroke recurrence time was 15.0 (IQR, 11.0–21.0) months in the recurrent-stroke group. Patients with recurrent stroke had a higher proportion of preadmission statin use (22.7% versus 7.0%, *P* = .003) than those with first-time stroke. Age, sex, conventional

risk factors, the interval between symptom onset and HR-VWI, NIHSS score, blood biochemical indexes, and stroke event frequencies in different vascular territories were not statistically different between these 2 groups.

Reproducibility of Imaging Measurements

There was good interreviewer and intrareviewer agreement with all intraclass correlation coefficients being ≥ 0.89 (Online Supplemental Data).

Plaque Distribution and Locations

A total of 786 atherosclerotic plaques were identified in 175 patients. A mean number of 4.5 (SD, 2.3) plaques was identified per patient, with 2.8 (SD, 1.4) plaques in the anterior circulation and 2.6 (SD, 1.4) plaques in the posterior circulation (detailed in Fig 2 and the Online Supplemental Data). In the recurrent-stroke group, 53 patients had anterior circulation stroke events, with 44 (83.0%) culprit plaques in the MCAs; 10 (45.4%) culprit plaques were detected in the basilar arteries in 22 cases of posterior circulation stroke. In the first-time stroke group, 71 patients had anterior circulation stroke events, with 66 (93.0%) culprit plaques in the MCAs; 13 (44.8%) culprit plaques were detected in the basilar arteries in 29 cases of posterior circulation stroke. The distribution of culprit plaques showed no statistical difference between the 2 groups ($P = .36$, Online Supplemental Data). In addition, 54

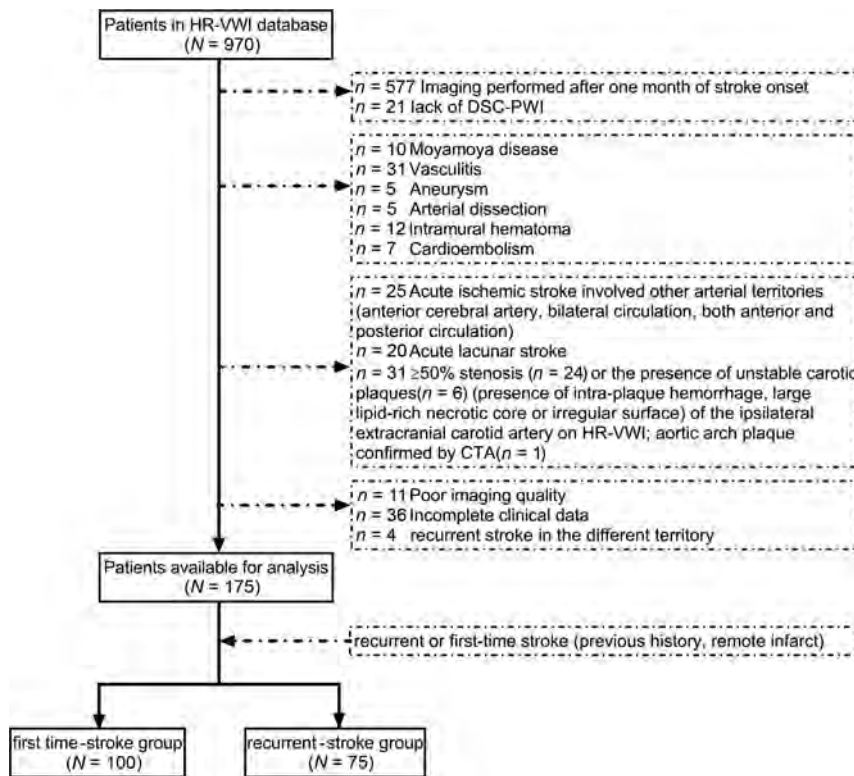


FIG 1. Flow chart of the study population and patient grouping.

Table 1: Clinical characteristics of the study population

Variables	All Patients (n = 175)	First-Time Stroke Group (n = 100)	Recurrent-Stroke Group (n = 75)	P Value ^a
Age (mean) (yr)	59 (SD, 12)	57 (SD, 13)	61 (SD, 10)	.13
Sex (male) (%)	115 (65.7)	68 (68.0)	47 (62.7)	.46
Hypertension (No.) (%)	145 (82.9)	85 (85.0)	60 (80.0)	.39
Diabetes mellitus (No.) (%)	74 (42.3)	38 (38.0)	36 (48.0)	.19
Coronary heart disease (No.) (%)	35 (20.0)	23 (23.0)	12 (16.0)	.25
Hyperlipidemia (No.) (%)	68 (38.9)	37 (37.0)	31 (41.3)	.56
Systolic blood pressure (median) (IQR) (mm Hg)	150 (135–163)	146 (131–162)	153 (140–167)	.13
Diastolic blood pressure (median) (IQR) (mm Hg)	87 (79–95)	87 (78–96)	87 (80–93)	.98
Smoking (No.) (%)	83 (47.4)	49 (49.0)	34 (45.3)	.63
Preadmission statin use (No.) (%) ^b	24 (13.7)	7 (7.0)	17 (22.7)	.003
Onset-to-HR-VWI time (median) (IQR) (days)	10 (6–15)	11 (6–15)	10 (6–15)	.93
Admission NIHSS score (median) (IQR)	2 (1–4)	2 (1–4)	3 (2–4)	.11
White blood cell count (median) (IQR) (10 ⁹ /L)	7.2 (6.2–8.3)	7.4 (6.4–8.5)	7.1 (5.9–8.3)	.19
Fasting blood glucose level (median) (IQR) (mmol/L)	5.8 (4.9–7.9)	5.8 (4.8–7.8)	5.8 (5.1–8.0)	.65
Total cholesterol level (mean) (mmol/L)	4.6 (SD, 1.1)	4.6 (SD, 1.0)	4.7 (SD, 1.2)	.68
High-density lipoprotein level (median) (IQR) (mmol/L)	1.0 (0.9–1.2)	1.0 (0.9–1.2)	1.0 (0.9–1.2)	.99
Low-density lipoprotein level (mean) (mmol/L)	3.1 (SD, 0.9)	3.1 (SD, 0.8)	3.0 (SD, 1.0)	.37
Triglyceride level (median) (IQR) (mmol/L)	1.5 (1.2–2.0)	1.4 (1.1–2.0)	1.5 (1.2–2.0)	.97
Stroke territories				.96
Anterior circulation (No.) (%)	124 (70.9)	71 (71.0)	53 (70.7)	
Posterior circulation (No.) (%)	51 (29.1)	29 (29.0)	22 (29.3)	

^a Comparison between the recurrent-stroke group and first-time stroke group.

^b Preadmission statin use was defined as regular statin medication for more than a month before the index stroke.

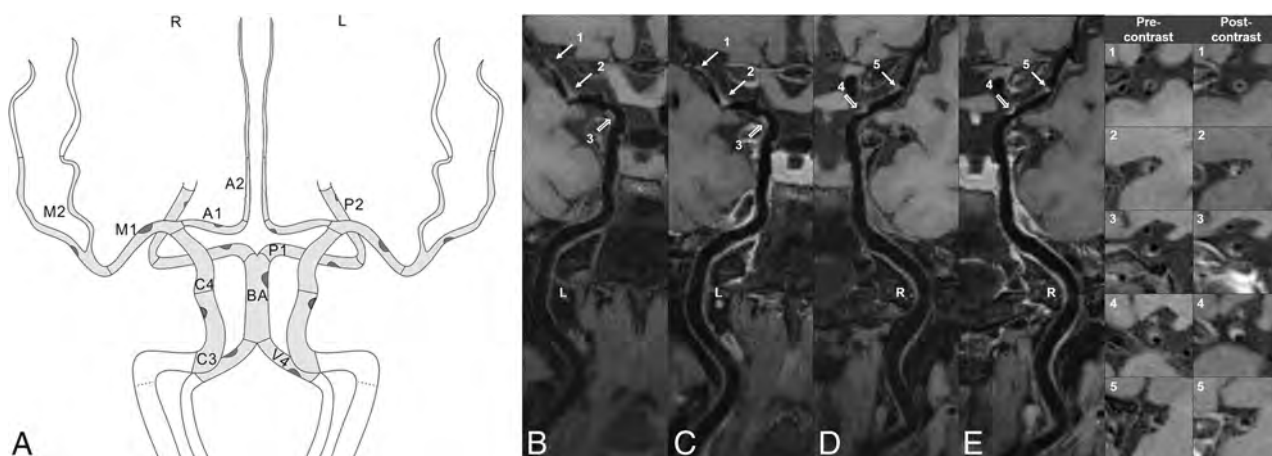


FIG 2. Intracranial plaque distribution and frequency. The schematic figure (A) shows analyzed artery segments with the frequency of intracranial plaques. The segments are shown in light gray: intracranial ICAs (cavernous/C3 and supraclinoid/C4 segments), A1 and A2 segments, M1 and M2 segments, P1 and P2 segments, basilar artery (BA), and intracranial vertebral arteries (V4). The frequency of plaques in the cohort ($n = 175$) is illustrated through plaques. A large dark-gray plaque indicates a higher frequency of plaques within the specific segment. The detailed results are listed in the Online Supplemental Data. The HR-VWI shows a patient with 5 intracranial plaques. Precontrast images indicate 2 left M1 plaques (B, arrows), 1 left ICA plaque (B, hollow arrow), 1 right M1 plaque (D, arrow), and 1 right ICA plaque (D, hollow arrow). Postcontrast HR-VWI (C and E) shows that the plaques are enhanced in different degrees. The last 2 columns show the cross-sectional views of each plaque. L indicates left; R, right.

Table 2: Imaging features of the study population

Variables	All Patients ($n = 175$)	First-Time Stroke Group ($n = 100$)	Recurrent-Stroke Group ($n = 75$)	P Value ^a
Culprit plaque features on high-resolution vessel wall imaging				
Plaque area (median) (IQR) (mm^2)	5.8 (3.7–7.5)	5.8 (3.5–7.4)	5.7 (4.2–7.8)	.40
Plaque burden (median) (IQR) (%)	74.6 (55.9–87.9)	72.9 (54.9–85.6)	75.0 (60.6–89.9)	.26
Plaque volume (median) (IQR) (mm^3)	45.8 (31.3–67.7)	41.3 (27.6–60.2)	50.7 (34.3–74.6)	.006
Arterial remodeling ratio (median) (IQR)	1.2 (1.0–1.5)	1.2 (1.0–1.5)	1.2 (1.0–1.5)	.83
Positive remodeling (No.) (%)	122 (69.7)	70 (70.0)	52 (69.3)	.92
Eccentric index (median) (IQR)	0.6 (0.4–0.7)	0.6 (0.4–0.7)	0.6 (0.4–0.7)	.54
Eccentricity (No.) (%)	110 (62.9)	61 (61.0)	49 (65.3)	.56
Intraplaque hemorrhage (No.) (%)	59 (33.7)	35 (35.0)	24 (32.0)	.68
Degree of stenosis (median) (IQR) (%)	44.7 (31.3–63.6)	44.1 (30.7–59.8)	46.8 (32.6–71.8)	.23
Enhancement ratio (median) (IQR)	1.6 (1.3–2.0)	1.6 (1.2–2.0)	1.6 (1.3–1.9)	.89
Plaque No. of each patient				
Total plaque No. (median) (IQR)	4 (3–6)	4 (2–5)	5 (4–7)	<.001
Enhanced plaque No. (median) (IQR)	2 (1–4)	2 (1–3)	3 (2–4)	.003
Hypoperfusion volume (median) (IQR) (mL)	0 (0–17.4)	0 (0–24.5)	0 (0–15.4)	.67
Hypoperfusion intensity ratio (median) (IQR)	0 (0–0)	0 (0–0)	0 (0–0)	.94
Hypoperfusion (No.) (%)	55 (31.4)	29 (29.0)	26 (34.7)	.42

^a Comparison between recurrent-stroke group and first-time stroke groups.

and 43 probably-culprit plaques were identified in the recurrent- and first-time stroke groups, respectively.

Imaging Features between Patients with First-Time and Recurrent Stroke

All the imaging features of 175 patients and comparisons between the 2 groups are shown in Table 2. The recurrent-stroke group had culprit plaques with larger volumes ($P = .006$) compared with the first-time stroke group. No significant difference in other culprit plaque features was detected between the 2 groups (plaque area, $P = .40$; plaque burden, $P = .26$; arterial remodeling ratio, $P = .83$; positive remodeling, $P = .92$; eccentric index, $P = .54$; eccentricity, $P = .56$; intraplaque hemorrhage, $P = .68$; degree of stenosis, $P = .23$; enhancement ratio, $P = .89$). Compared with the first-time

stroke group, the recurrent-stroke group showed significantly more intracranial plaques per patient (median, 5 lesions; IQR, 4–7 lesions versus median, 4 lesions, IQR, 2–5 lesions; $P < .001$) and more enhanced intracranial plaques per patient (median, 3 lesions; IQR, 2–4 lesions versus median, 2 lesions; IQR, 1–3 lesions; $P = .003$). No significant difference in perfusion deficit variables and HR-VWI features of probably-culprit plaques was detected between the 2 groups (Table 2 and Online Supplemental Data, all $P > .05$).

Association between Imaging Features with Patients with Recurrent Stroke

As Table 3 shows, culprit plaque volume, total plaque number, and enhanced plaque number were included in the multivariable analysis. After multicollinearity diagnosis (Online Supplemental Data),

Table 3: Univariable and multivariable analysis to identify parameters associated with patients with recurrent stroke compared with patients with the first-time stroke

Variables	Univariable Regression Analysis			Multivariable Regression Analysis		
	OR	95% CI	P Value	OR	95% CI	P Value
Culprit plaque volume ^a	1.17	1.04–1.31	.008	1.16	1.03–1.30	.015
Total plaque No.	1.32	1.14–1.53	<.001	1.31	1.13–1.52	<.001
Enhanced plaque No.	1.32	1.09–1.60	.005	NA	NA	.89

Note:—NA indicates not available.

^aOR based on every cubic millimeter increase.

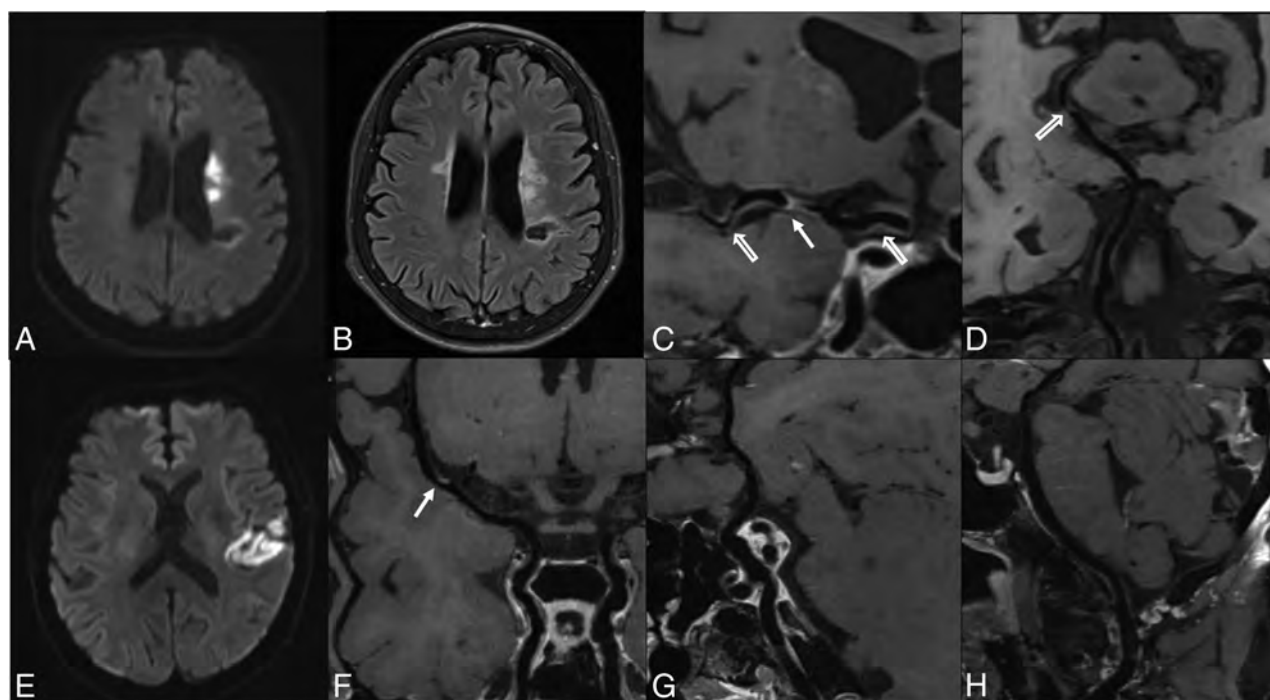


FIG 3. Representative patients of recurrent- and first-time stroke groups. *Upper row*, A 64-year-old female patient with right-limb weakness and inarticulateness for 5 days. MR imaging was performed 9 days after symptom onset. DWI (A) shows a left basal ganglia infarction, FLAIR (B) shows a remote infarction on the left centrum semiovale, and HR-VWI (C and D) indicates M1 culprit plaque (arrow) (39.4 mm³), and other plaques detected in the left MCA, internal carotid artery, and left posterior cerebral artery (hollow arrows). The total plaque number is 5. *Lower row*, A 63-year-old male patient who presented with sudden abasia and inarticulateness for 2 hours. MR imaging was performed 5 days after the symptom onset. DWI (E) shows left insular and temporal lobe infarction, HR-VWI (F) shows a culprit plaque in the left M1 segment (arrow) (18.6 mm³), and no other plaques (G and H) are detected in other intracranial arteries. The total plaque number is 1.

culprit plaque volume (OR, 1.16 per 10-mm³ increase; 95% CI, 1.03–1.30; $P = .015$) and total plaque number (OR, 1.31; 95% CI, 1.13–1.52; $P < .001$) were the imaging features independently associated with patients with recurrent strokes. The area under the curve value was 0.62 (95% CI, 0.54–0.70) for culprit plaque volume, 0.66 (95% CI, 0.59–0.74) for total plaque number, and 0.71 (95% CI, 0.61–0.79) for combining 2 factors with a sensitivity of 84.0% and specificity of 53.0%. The combined model increased the area under the curve to 0.71, higher than any variable alone (all, $P < .05$). The representative cases are shown in Fig 3.

DISCUSSION

There were 3 important findings in the current study. First, HR-VWI was used to investigate the whole-brain plaque in patients with first-time and recurrent stroke; and it had additional values compared with investigating a single lesion. Second, patients with

recurrent stroke presented with larger culprit plaque, more intracranial plaques, and more enhanced intracranial plaques compared with patients with first-time stroke. Third, culprit plaque volume and intracranial total plaque number were 2 independent features associated with patients with stroke recurrence by HR-VWI measurement. Combining culprit plaque volume and total plaque number might improve the differentiation between patients with recurrent and first-time stroke. Our study highlights the importance of performing whole-brain vessel wall imaging and evaluating the atherosclerotic plaques in the entire large cerebral arterial tree.

Atherosclerosis is a systemic disease that involves multiple vascular beds. The average number of intracranial plaques in our cohort was 4.5 per patient. Previous studies using 7T MR imaging found 4.9 or 4.5 plaques per patient in the symptomatic patients of the same age.^{15,30} Although 7T scanners performed better in detecting lesions, we believe that the discrepancy was probably

due to the susceptibility of Chinese patients to intracranial artery stenosis, with earlier onset age and higher prevalence.³¹

In our study, patients with recurrent-stroke events had larger culprit plaques (measured by plaque volume) than those with first-time stroke events. No significant difference in other culprit plaque features such as the degree of stenosis,⁴ plaque enhancement,^{12,32} and plaque burden¹³ was detected between the 2 groups, which was also reported by a recent similar study.¹⁶ Plaque burden¹³ and its progression with time³³ were reported to be associated with stroke recurrence. Although plaque burden might cover both luminal stenosis and outward remodeling changes, the information based on measurement from 1 section might be very limited. Instead, plaque volume would be more representative of the actual plaque burden; the result would also indicate the value of HR-VWI in evaluating arterial wall changes. A longitudinal MR imaging study showed that the progression of carotid plaque volume was independently associated with recurrent cerebral ischemic events.³⁴ In contrast, another follow-up HR-VWI study found that the progression of intracranial culprit plaque burden rather than the progression of plaque volume was associated with recurrence.³³ Our results differed from the latter, possibly because they included patients with both stroke and transient ischemic attack, but we only focused on patients with stroke; their analysis was based on 2D imaging data, making the measurement not accurate enough, while our study adopted 3D whole-brain scanning. Longitudinal studies using 3D HR-VWI are still needed to explore the association between plaque volume and stroke recurrence. The Warfarin versus Aspirin for Symptomatic Intracranial Disease trial showed that >70% stenosis predicted recurrent stroke.⁴ Our study did not show the degree of stenosis independently associated with the recurrent-stroke group, possibly because most of our study population had moderate stenosis (median, 44.7%; IQR, 31.3%–63.6%). These plaques without severe stenosis could also lead to stroke, a finding that agreed with those in a recent meta-analysis.⁵

Several recent studies also demonstrated that culprit plaque enhancement or enhancement ratio was related to recurrent stroke.^{12,13,32} Our study quantitatively analyzed the culprit enhancement ratio but did not get a similar result. Instead of culprit plaque enhancement, our study indicated that the patients with recurrent-stroke events had more enhanced plaques, which might indicate more vulnerable plaques. The underlying reasons might be poorly controlled systemic risk factors, hemodynamic abnormality, inflammatory reaction, and corresponding physiologic and biochemical reactions, which would aggravate and facilitate the progression of atherosclerosis.^{35,36} Also, the median stroke-recurrence time was 15.0 (IQR, 11.0–21.0) months in the recurrent-stroke group, and that might be long enough to ignore the effect of the previous strokes on the plaque enhancement.³⁷

Although no significant difference was detected in these features (except plaque volume) in our study, the evaluation of vulnerable plaque features was still necessary. For example, the plaque with large volumes might easily block penetrating arteries leading to infarct. Also, the vulnerable plaques were inclined to rupture, resulting in artery-to-artery embolism, and the stenotic plaques could cause hypoperfusion downstream. The retrospective nature might be a reason for the insignificance of our study; future larger-

scale prospective studies are needed to identify the plaque vulnerability and its association with stroke recurrence.

The intracranial total plaque number was independently associated with the recurrent-stroke group in our study. Investigators in the Clopidogrel in High-Risk Patients with Acute Non-disabling Cerebrovascular Events (CHANCE) study³ found higher stroke recurrence at 90 days among patients with multiple intracranial artery stenoses (>50%) identified on MRA than those without. The Chinese IntraCranial AtheroSclerosis (CICAS) study³⁸ found that the patients in the group with medium intracranial atherosclerosis burden showed more stroke recurrence at 12 months (adjusted hazard ratio, 1.96; $P = .027$) with more patients with mild stenosis in this group. These previous studies using TOF-MRA indicated the necessity of analyzing the entire large cerebral artery tree and of the plaques with mild stenosis needing to be fully accessed. TOF-MRA as a conventional luminal imaging method could have flow artifacts, overestimate the luminal stenosis, or miss mild stenotic plaques; even DSA would miss up to 26.1% of nonstenotic plaques.⁸ Compared with angiographic imaging, HR-VWI performed better because it could quantify luminal stenosis accurately and reproducibly,⁸ detect more nonstenotic plaques,⁸ and evaluate several vulnerable features. Moreover, our study adopting the whole-brain HR-VWI scan was capable of the simultaneous evaluation of large cerebral arteries. Our results, more intracranial plaques in patients with recurrent stroke, may indicate a heavy atherosclerosis burden and poor systemic disease control in our patients.^{14,15}

Our study also evaluated several perfusion deficit variables, but no difference was detected between groups. The perfusion deficit in patients with intracranial atherosclerosis could lead to stroke events and was related to recurrent stroke. The cerebral hypoperfusion downstream due to stenotic plaques or artery-to-artery embolism caused by ruptured vulnerable plaques might result in cerebral infarct.³⁹ A recent study on a similar topic using arterial spin-labeling found that the hypoperfusion volume ratio, which correlated with collateral grades, was associated with stroke recurrence.¹⁶ Their findings were different from ours, possibly due to the cross-sectional retrospective nature of our study and the arterial spin-labeling perfusion imaging with multiple postlabelling delays they used possibly providing information about both hypoperfusion and collateral flow.

There were several limitations to this study. First, although culprit plaque volume and plaque number were independent imaging factors associated with patients with recurrent stroke in our cohort, these findings may be coincidental. Ischemic stroke due to intracranial atherosclerosis is a multifactorial disease; the imaging markers we explored may result from multiple clinical factors. The future evaluation of stroke risk should be more comprehensive. Second, our study was retrospective. The measurement of plaque features probably happened after the plaque rupture, so the associations between plaque features and recurrence needed further evaluation in the prospective study. Third, our study was cross-sectional. The factors associated with patients with recurrent stroke might not present in the first-time stroke as baseline features. Longitudinal studies are needed to confirm our findings. Last, due to the long scan time of the MR imaging protocols, only patients without severe symptoms were enrolled,

probably leading to more patients with low NIHSS scores in our cohort. In addition, this study did not include extracranial carotid plaques; future studies applying large-coverage head-and-neck HR-VWI on concomitant intracranial and extracranial atherosclerosis would provide additional insights.⁴⁰

CONCLUSIONS

Large culprit plaque and more intracranial atherosclerotic plaques were independently associated with recurrent stroke. Performing whole-brain vessel wall imaging may help better identify patients with a higher risk of recurrent stroke.

Disclosure forms provided by the authors are available with the full text and PDF of this article at www.ajnr.org.

REFERENCES

- Banerjee C, Chimowitz MI. Stroke caused by atherosclerosis of the major intracranial arteries. *Circ Res* 2017;120:502–13 CrossRef Medline
- Chimowitz MI, Lynn MJ, Derdeyn CP, et al; SAMMPRIS Trial Investigators. Stenting versus aggressive medical therapy for intracranial arterial stenosis. *N Engl J Med* 2011;365:993–1003 CrossRef Medline
- Zhu B, Liu H, Pan Y, et al; CHANCE Investigators. Elevated neutrophil and presence of intracranial artery stenosis increase the risk of recurrent stroke. *Stroke* 2018;49:2294–2300 CrossRef Medline
- Kasner SE, Chimowitz MI, Lynn MJ, et al. Predictors of ischemic stroke in the territory of a symptomatic intracranial arterial stenosis. *Circulation* 2006;113:555–63 CrossRef Medline
- Wang Y, Liu X, Wu X, et al. Culprit intracranial plaque without substantial stenosis in acute ischemic stroke on vessel wall MRI: a systematic review. *Atherosclerosis* 2019;287:112–21 CrossRef Medline
- Mazighi M, Labreuche J, Gongora-Rivera F, et al. Autopsy prevalence of intracranial atherosclerosis in patients with fatal stroke. *Stroke* 2008;39:1142–47 CrossRef Medline
- Zhu C, Tian X, Degnan AJ, et al. Clinical significance of intraplaque hemorrhage in low- and high-grade basilar artery stenosis on high-resolution MRI. *AJNR Am J Neuroradiol* 2018;39:1286–92 CrossRef Medline
- Tian X, Tian B, Shi Z, et al. Assessment of intracranial atherosclerotic plaques using 3D black-blood MRI: comparison with 3D time-of-flight MRA and DSA. *J Magn Reson Imaging* 2021;53:469–78 CrossRef Medline
- Zhu C, Haraldsson H, Tian B, et al. High resolution imaging of the intracranial vessel wall at 3 and 7 T using 3D fast spin echo MRI. *MAGMA* 2016;29:559–70 CrossRef Medline
- Xu WH, Li ML, Gao S, et al. In vivo high-resolution MR imaging of symptomatic and asymptomatic middle cerebral artery atherosclerotic stenosis. *Atherosclerosis* 2010;212:507–11 CrossRef Medline
- Zhang DF, Chen YC, Chen H, et al. A high-resolution MRI study of relationship between remodeling patterns and ischemic stroke in patients with atherosclerotic middle cerebral artery stenosis. *Front Aging Neurosci* 2017;9:140 CrossRef Medline
- Song X, Zhao X, Liebeskind DS, et al. Incremental value of plaque enhancement in predicting stroke recurrence in symptomatic intracranial atherosclerosis. *Neuroradiology* 2020;62:1123–31 CrossRef Medline
- Ran Y, Wang Y, Zhu M, et al. Higher plaque burden of middle cerebral artery is associated with recurrent ischemic stroke: a quantitative magnetic resonance imaging study. *Stroke* 2020;51:659–62 CrossRef Medline
- Zwartbol MHT, van der Kolk AG, Ghaznawi R, et al; SMART Study Group. Intracranial vessel wall lesions on 7T MRI (magnetic resonance imaging). *Stroke* 2019;50:88–94 CrossRef Medline
- Lindenholz A, van der Kolk AG, van der Schaaf IC, et al. Intracranial atherosclerosis assessed with 7-T MRI: evaluation of patients with ischemic stroke or transient ischemic attack. *Radiology* 2020;295:162–70 CrossRef Medline
- Lyu J, Ma N, Tian C, et al. Perfusion and plaque evaluation to predict recurrent stroke in symptomatic middle cerebral artery stenosis. *Stroke Vasc Neurol* 2019;4:129–34 CrossRef Medline
- Coull AJ, Rothwell PM. Underestimation of the early risk of recurrent stroke: evidence of the need for a standard definition. *Stroke* 2004;35:1925–29 CrossRef Medline
- Kolominsky-Rabas PL, Weber M, Gefeller O, et al. Epidemiology of ischemic stroke subtypes according to TOAST criteria: incidence, recurrence, and long-term survival in ischemic stroke subtypes: a population-based study. *Stroke* 2001;32:2735–40 CrossRef Medline
- Chen Y, Liu S, Wang Y, et al. STRategically Acquired Gradient Echo (STAGE) imaging, Part I: creating enhanced T1 contrast and standardized susceptibility weighted imaging and quantitative susceptibility mapping. *Magn Reson Imaging* 2018;46:130–39 CrossRef Medline
- Fan Z, Yang Q, Deng Z, et al. Whole-brain intracranial vessel wall imaging at 3 Tesla using cerebrospinal fluid-attenuated T1-weighted 3D turbo spin echo. *Magn Reson Med* 2017;77:1142–50 CrossRef Medline
- Yushkevich PA, Piven J, Hazlett HC, et al. User-guided 3D active contour segmentation of anatomical structures: significantly improved efficiency and reliability. *Neuroimage* 2006;31:1116–28 CrossRef Medline
- Qiao Y, Zeiler SR, Mirbagheri S, et al. Intracranial plaque enhancement in patients with cerebrovascular events on high-spatial-resolution MR images. *Radiology* 2014;271:534–42 CrossRef Medline
- Qiao Y, Anwar Z, Intrapromkul J, et al. Patterns and implications of intracranial arterial remodeling in stroke patients. *Stroke* 2016;47:434–40 CrossRef Medline
- Yamagishi M, Terashima M, Awano K, et al. Morphology of vulnerable coronary plaque: insights from follow-up of patients examined by intravascular ultrasound before an acute coronary syndrome. *J Am Coll Cardiol* 2000;35:106–11 CrossRef Medline
- Wu F, Song H, Ma Q, et al; WISP Investigators. Hyperintense plaque on intracranial vessel wall magnetic resonance imaging as a predictor of artery-to-artery embolic infarction. *Stroke* 2018;49:905–11 CrossRef Medline
- van der Kolk AG, Zwanenburg JJ, Brundel M, et al. Intracranial vessel wall imaging at 7.0-T MRI. *Stroke* 2011;42:2478–84 CrossRef Medline
- Samuels OB, Joseph GJ, Lynn MJ, et al. A standardized method for measuring intracranial arterial stenosis. *AJNR Am J Neuroradiol* 2000;21:643–46 Medline
- Liu S, Luo Y, Wang C, et al. Combination of plaque characteristics, pial collaterals, and hypertension contributes to misery perfusion in patients with symptomatic middle cerebral artery stenosis. *J Magn Reson Imaging* 2020;51:195–204 CrossRef Medline
- Olivot JM, Mlynash M, Inoue M, et al. Hypoperfusion intensity ratio predicts infarct progression and functional outcome in the DEFUSE 2 Cohort. *Stroke* 2014;45:1018–23 CrossRef Medline
- Fakih R, Roa JA, Bathla G, et al. Detection and quantification of symptomatic atherosclerotic plaques with high-resolution imaging in cryptogenic stroke. *Stroke* 2020;51:3623–31 CrossRef Medline
- Leng X, Hurford R, Feng X, et al. Intracranial arterial stenosis in Caucasian versus Chinese patients with TIA and minor stroke: two contemporaneous cohorts and a systematic review. *J Neurol Neurosurg Psychiatry* 2021;92:590–97 CrossRef Medline
- Kim JM, Jung KH, Sohn CH, et al. Intracranial plaque enhancement from high resolution vessel wall magnetic resonance imaging predicts stroke recurrence. *Int J Stroke* 2016;11:171–79 CrossRef Medline
- Shi Z, Li J, Zhao M, et al. Progression of plaque burden of intracranial atherosclerotic plaque predicts recurrent stroke/transient ischemic attack: a pilot follow-up study using higher-resolution MRI. *J Magn Reson Imaging* 2021;54:560–70 CrossRef Medline
- Lu M, Peng P, Cui Y, et al. Association of progression of carotid artery wall volume and recurrent transient ischemic attack or stroke: a

- magnetic resonance imaging study. *Stroke* 2018;49:614–20 CrossRef Medline
35. Libby P. **The changing landscape of atherosclerosis.** *Nature* 2021;592:524–33 CrossRef Medline
 36. Souilhol C, Harmsen MC, Evans PC, et al. **Endothelial-mesenchymal transition in atherosclerosis.** *Cardiovasc Res* 2018;114:565–77 CrossRef Medline
 37. Kwee RM, Qiao Y, Liu L, et al. **Temporal course and implications of intracranial atherosclerotic plaque enhancement on high-resolution vessel wall MRI.** *Neuroradiology* 2019;61:651–57 CrossRef Medline
 38. Sun P, Liu L, Pan Y, et al. **Intracranial atherosclerosis burden and stroke recurrence for symptomatic intracranial artery stenosis (sICAS).** *Aging Dis* 2018;9:1096–1102 CrossRef Medline
 39. Gao S, Wang YJ, Xu AD, et al. **Chinese ischemic stroke subclassification.** *Front Neurol* 2011;2:6 CrossRef Medline
 40. Xu Y, Yuan C, Zhou Z, et al. **Co-existing intracranial and extracranial carotid artery atherosclerotic plaques and recurrent stroke risk: a three-dimensional multicontrast cardiovascular magnetic resonance study.** *J Cardiovasc Magn Reson* 2016;18:90 CrossRef Medline

Stroke Mimics in the Acute Setting: Role of Multimodal CT Protocol

 E. Prodi,  L. Danieli,  C. Manno,  A. Pagnamenta,  E. Pravata,  L. Roccatagliata,  C. Städler,  C.W. Cereda, and  A. Cianfoni



ABSTRACT

BACKGROUND AND PURPOSE: Ischemic stroke can be mimicked by nonischemic conditions. Due to emphasis on the rapid treatment of acute ischemic stroke, it is crucial to identify these conditions to avoid unnecessary therapies and potential complications. We investigated the performance of the multimodal CT protocol (unenhanced brain CT, CTA, and CTP) to discriminate stroke mimics from acute ischemic stroke.

MATERIALS AND METHODS: We retrospectively selected multimodal CT studies performed for clinical suspicion of acute ischemic stroke in our center in a 24-month period, including patients with at least 1 follow-up imaging study (brain CT or MR imaging). Hemorrhagic strokes were excluded. We measured the performance of multimodal CT, comparing the original diagnostic results with the final clinical diagnosis at discharge.

RESULTS: Among 401 patients, a stroke mimic condition was diagnosed in 89 (22%), including seizures (34.8%), migraine with aura attack (12.4%), conversion disorder (12.4%), infection (7.9%), brain tumor (7.9%), acute metabolic condition (6.7%), peripheral vertigo (5.6%), syncope (5.6%), transient global amnesia (3.4%), subdural hematoma (1.1%), cervical epidural hematoma (1.1%), and dural AVF (1.1%). Multimodal CT sensitivity, specificity, and accuracy were 24.7%, 99.7%, and 83%. Multimodal CT revealed peri-ictal changes in 13/31 seizures and diagnosed 7/7 brain tumors, 1/1 dural AVF, and 1/1 subdural hematoma. CT perfusion played a pivotal diagnostic role.

CONCLUSIONS: Multimodal CT demonstrated low sensitivity but high specificity in the diagnosis of stroke mimics in the acute setting. The high specificity of multimodal CT allows ruling out stroke and thereby avoiding unnecessary revascularization treatment in patients with diagnosis of a stroke mimic.

ABBREVIATIONS: CECT = contrast-enhanced CT; EEG = electroencephalogram; iCVE = ischemic cerebrovascular event; SM = stroke mimics; Tmax = time-to-maximum

The clinical management of ischemic stroke requires a fast diagnostic workflow to refer patients to early revascularization.¹ One of the challenges in the diagnosis of ischemic stroke is


related to the presence of stroke mimic conditions, which are nonischemic disorders with clinical presentations similar to those of stroke. These disorders include seizures, systemic infections, brain tumors, toxic-metabolic conditions, positional vertigo, syncope, migraine, transient global amnesia, dementia, demyelinating disease, conversion disorder, and others.^{2,3} The prevalence of stroke mimics (SM) has been reported in up to 31% of patients with suspected acute stroke referred to the emergency department.⁴ Although complications of IV rtPA treatment in SM are rare,^{5,6} an accurate diagnosis is desirable to avoid unnecessary treatment and possible complications. Timely brain imaging is critical in the management of patients in this setting. MR imaging with diffusion-weighted imaging is the most sensitive technique to diagnose ischemic stroke. However, MR imaging is not routinely available in the emergency setting in many facilities; therefore, CT remains the first imaging method of choice in most centers. NCCT reliably rules out brain hemorrhage, but its

Received June 22, 2021; accepted after revision October 6.

From the Departments of Neuroradiology (E.Prodi, L.D., E.Pravata, A.C.) and Neurology (C.M., C.S., C.W.C.), Neurocenter of Southern Switzerland, EOC, Lugano, Switzerland; Unit of Clinical Epidemiology (A.P.), Ente Ospedaliero Cantonale, Bellinzona, Switzerland; Department of Intensive Care Medicine (A.P.), Ente Ospedaliero Cantonale, Mendrisio, Switzerland; Division of Pneumology (A.P.), University Hospital of Geneva, Geneva, Switzerland; Department of Health Science (DISSAL) (L.R.), University of Genova, Genova, Italy; Department of Neuroradiology (A.C.), Inselspital Bern, University of Bern, Bern, Switzerland; and Faculty of Biomedical Sciences (E. Pravata), Università della Svizzera Italiana, Lugano, Switzerland.

Carlo W. Cereda and Alessandro Cianfoni contributed equally to this work.

Please address correspondence to Elena Prodi, MD, Neurocenter of Southern Switzerland, Department of Neuroradiology, Via Tesserete 46, Lugano, 6900, Switzerland; e-mail: elena.prodi@eoc.ch

 Indicates open access to non-subscribers at www.ajnr.org

 Indicates article with online supplemental data.

<http://dx.doi.org/10.3174/ajnr.A7379>

sensitivity to identify early signs of brain ischemia is low in the first 6 hours from the onset of symptoms.^{7,8} Complementary CT techniques add further information on the presence, extent, and pathogenesis of ischemic stroke. CTA allows evaluating the status of neck and brain vessels and identifying a proximal arterial occlusion. CTP readily identifies areas of hypoperfused brain and allows estimating the presence of an ischemic core and an ischemic penumbra.⁹

A multimodal CT approach, including NCCT, CTA, and CTP, is used in many centers for the diagnosis of acute stroke,⁸ though the use of perfusion is not required by actual guidelines in the first 6 hours from stroke onset.¹ Although multimodal CT has been reported to be able to distinguish some SM such as seizures, migraine, space-occupying lesions, infections, toxic-metabolic conditions, and others,¹⁰ there are scarce systematic studies on the diagnostic performance of multimodal CT in the diagnosis of SM, with most studies focusing on the diagnostic performance of CTP in seizures as a subgroup of SM.¹¹⁻¹³

In this study, we aimed to evaluate the overall diagnostic performance of multimodal CT for the diagnosis of SM not limited to seizures in the setting of acute stroke care.

MATERIALS AND METHODS

This is a retrospective study based on a single medical center with a comprehensive stroke unit that offers 24/7 admission of patients with acute stroke, clinical and imaging diagnoses, and systemic and endovascular treatment.

The study was approved by the local institutional Ethics Committee, Comitato Etico Cantonale. The study cohort included all consecutive patients who underwent a multimodal CT examination in the acute setting for suspected acute stroke in a 24-month period. Exclusion criteria were as follows: hemorrhagic stroke; incomplete multimodal CT (ie, lack of ≥ 1 imaging protocol component); examinations judged to be of nondiagnostic quality by the original interpreting neuroradiologist due to artifacts, poor patient cooperation, or other technical issues; and lack of at least 1 imaging follow-up (CT or MR imaging) necessary to confirm or rule out an acute brain ischemic lesion.

Triage of Clinical Patients

At our center, patients with clinical suspicion of acute ischemic stroke are promptly referred to a multimodal CT stroke imaging protocol after clinical evaluation by a neurologist, including an NIHSS evaluation.

Multimodal CT at Admission

Multimodal CT stroke imaging was performed using a dual-source 128-section CT scanner (Somatom Definition Flash; Siemens) as follows: NCCT of the head was followed by CTP acquired with a toggling-table technique, encompassing a brain coverage of 100 mm along the z-axis for 45 seconds with a temporal resolution of 1.5 seconds. We then performed CTA in a dual-energy mode from the aortic arch to the vertex with a bolus-tracking technique, placing the density-monitoring ROI in the ascending aorta with a trigger threshold of 100 HU. Contrast-enhanced CT (CECT) was acquired 4 minutes after the first

injection of contrast medium when required. The details of CT technical parameters are reported in the Online Supplemental Data.

Postprocessing was performed by a CT technologist. Parametric qualitative maps of CBF, CBV, MTT, time-to-drain, and time-to-maximum (Tmax) were obtained from CTP data using a commercial perfusion package (VPCT-Neuro; Siemens). Arterial input and venous output time-attenuation curves were generated with ROIs automatically drawn on the anterior cerebral artery and the superior sagittal sinus, respectively. The CT technologist checked the correct positioning of the ROIs, the quality of the curves, and the presence of movement artifacts. Postprocessing of CTA source images was performed with multiplanar overlapping MIP reformatting. Images were sent, saved, and visualized in the PACS.

Follow-up CT and MR Imaging Examinations

Follow-up CT and MR imaging examinations were performed at a mean of 1.7 (SD, 2.6) days from admission before patient discharge, with MR imaging in 64% and CT in 36% of cases. NCCT was performed as described above. MR imaging was performed on a 3T scanner (Magnetom Skyra; Siemens) with a protocol consisting of at least the following sequences: axial DWI, axial FSE T2WI, axial FLAIR T2WI, and axial gradient recalled-echo T2*WI. The details of technical MR imaging parameters are shown in the Online Supplementary Data. Additional sequences, MRA, or postcontrast administration imaging were performed in selected cases as necessary.

Imaging Diagnosis at Admission and Retrospective Imaging Diagnosis

Images were rapidly interpreted and reported by a staff neuroradiologist who had access to the patient's clinical information. The group of 7 reporting neuroradiologists included physicians with a subspecialty in neuroradiology and experience ranging from 1 to 15 years. Radiology reports were archived in the radiology information system, integrated into the hospital informatics system.

For this study, 2 neuroradiologists (E.P. and L.D.) retrospectively reviewed, in consensus, the original reports of the multimodal CT study performed at admission and assigned the imaging diagnosis to 1 of 3 different categories: 1) evidence of acute ischemic vascular event (iCVE) on imaging; 2) evidence of an acute condition other than iCVE on imaging, likely the cause of the clinical presentation (SM); and 3) no evidence of acute iCVE or SM on imaging. The imaging diagnosis based on the report of the multimodal CT at admission was considered the index text to be evaluated for performance.

Discharge Diagnosis and Retrospective Discharge Diagnosis

The discharge diagnosis documented and archived in the hospital informatics system was considered the final diagnosis. The discharge report with the final diagnosis was signed in consensus by 2 staff stroke neurologists and 1 neurology fellow on the basis of relevant clinical, imaging, electroencephalogram (EEG), and laboratory data. For this study, the diagnosis at discharge was retrospectively reviewed in consensus by 1 neurology fellow (C.M.) and 1 neuroradiologist (E.P.) and dichotomized into 2 final

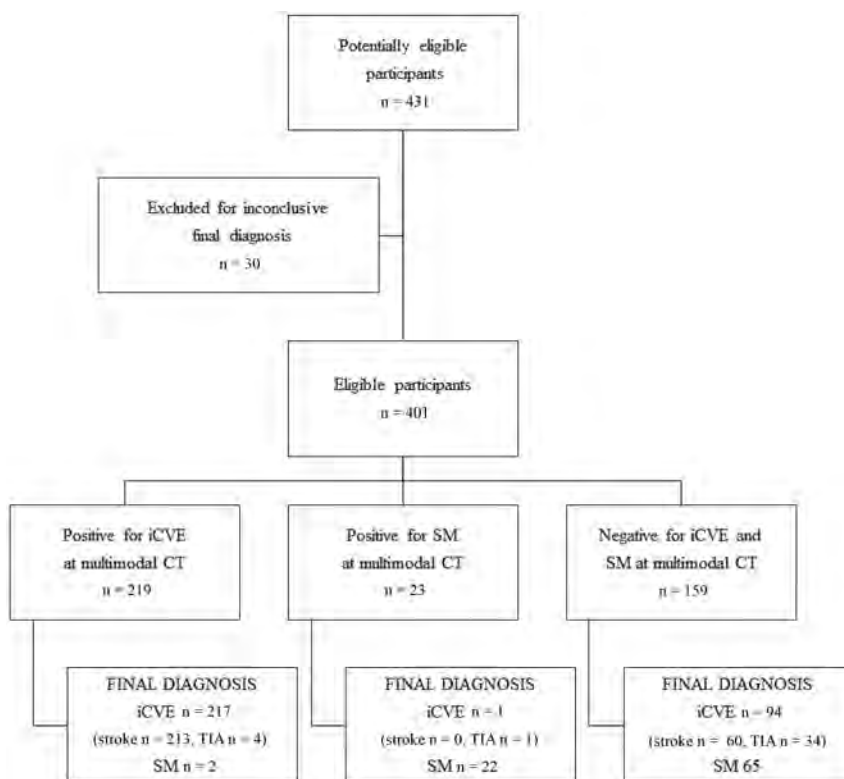


FIG 1. Study design diagram.

diagnoses: iCVE and SM. iCVE included stroke and TIA.^{14,15} For TIA, the likelihood of an ischemic event was rated with a version of the Precise Diagnostic Score scale.¹⁶ SM were cases in which the clinical details did not suggest an ischemic vascular etiology and another convincing explanation for the symptoms was found throughout supportive investigations. A few cases remained without a conclusive final diagnosis, even after evaluation of all available follow-up data. These included cases with less convincing clinical features, in which an alternative explanation for the clinical syndrome may have been present, but there was no definite proof of a nonstroke. These cases were excluded from the analysis. The final diagnosis at discharge for each patient was considered the reference diagnostic standard to establish true-positive, true-negative, false-positive, and false-negative and, therefore, to determine the accuracy of multimodal CT at admission.

Data Analysis

Descriptive statistics were presented as arithmetic mean with an SD or as median with interquartile range for quantitative data. Qualitative data were presented as absolute numbers with percentages. Comparisons of quantitative data among the 3 multimodal CT groups were performed with the Kruskal-Wallis test. With a statistically significant *P* value, we performed post hoc tests (Mann-Whitney), taking into account the multiple comparisons. Qualitative data among groups of patients were compared using the χ^2 test. With statistically significant results, we made post hoc comparisons with the appropriate critical level adjustment.

Comparisons between the diagnostic test and the reference standard permitted calculating sensitivity, specificity, positive and negative predictive values, positive and negative likelihood ratios, and accuracy with the corresponding 95% confidence intervals. Contemplating an option of uncertainty in the multimodal CT results, we built 3×2 contingency tables. In 3×2 tables, we considered nonevaluable results as negative results, assuming a higher prevalence of a final diagnosis of iCVE.¹⁷

All tests were conducted 2-sided, and *P* values < .05 were considered statistically significant. STATA, Version 15 (StatCorp) and MedCalc (MedCalc Software) were used for all statistical analyses.

RESULTS

Four hundred thirty-one patients fulfilled the inclusion criteria; 30 patients were excluded from the analysis due to an uncertain final diagnosis. Therefore 401 patients were included in our study population: 219 men and 182 women (mean age, 71 [SD 14] years; range, 25–97 years).

The results of multimodal CT at admission (index test) were categorized as diagnostic of iCVE (*n* = 219), diagnostic of SM (*n* = 23), and negative for both iCVE and SM (*n* = 159).

The clinical final diagnosis (reference standard) was dichotomized into diagnoses of iCVE (*n* = 312) and SM (*n* = 89). The iCVEs were further subdivided into diagnoses of stroke (*n* = 273) and TIA (*n* = 39) (Fig 1).

The sex distribution was similar among different categories of multimodal CT diagnoses (male/female ratios, respectively, 122:97, 15:8, 82:77 for the categories of multimodal CT diagnoses of iCVE and SM, and negative for both iCVE and SM, *P* = .298) and final diagnoses (male/female ratios, respectively, 180:132 and 39:50 for the final diagnoses of iCVE and SM, *P* = .087).

Age distribution significantly differed between the categories of final diagnosis, respectively, 73 (SD, 13) years in the final diagnosis of iCVE and 66 (SD, 11) years in the final diagnosis of SM (*P* = .002).

The prevalence of SM in our population was 22%, including seizures (*n* = 31, 34.8%), migraine with aura attack (*n* = 11, 12.4%), conversion disorder (*n* = 11, 12.4%), infection (*n* = 7, 7.9%), brain tumor (*n* = 7, 7.9%), acute metabolic condition (*n* = 6, 6.7%), peripheral vertigo (*n* = 5, 5.6%), syncope (*n* = 5, 5.6%), transient global amnesia (*n* = 3, 3.4%), subdural hematoma (*n* = 1, 1.1%), cervical epidural hematoma (*n* = 1, 1.1%) and dural AVF (*n* = 1, 1.1%) (Table 1). More specifically, infections included 1 viral undetermined encephalitis and 6 systemic infections; brain tumors were all primitive glial tumors; and metabolic causes included 2 cases of hepatic encephalopathy, 2 cases of drug-related encephalopathy, 1 case of hyponatremia, and 1 case of hypoglycemia.

Statistical analysis results are shown in Table 2. Multimodal CT sensitivity, specificity, and accuracy for the diagnosis of SM were 24.7% (95% CI, 16.2%–35%), 99.7% (95% CI, 98.2%–100%), and 83% (95% CI, 79%–86.6%), respectively. Multimodal CT revealed peri-ictal changes in 13/31 seizures, 7/7 brain tumors, 1/1 dural AVF, and 1/1 subdural hematoma, while it revealed no relevant abnormal findings in 18/31 seizures, 11/11 migraines with aura attack, 11/11 conversion disorders, 7/7 infections, 5/5 cases of peripheral vertigo, 6/6 metabolic conditions, 5/5 cases of syncope, 3/3 cases of transient global amnesia, and 1/1 cervical epidural hematoma. When we excluded a priori undetectable SM conditions on multimodal CT (conversion disorders, peripheral vertigo, syncope, transient global amnesia), multimodal CT sensitivity, specificity, and accuracy were 33.9% (95% CI, 22.6%–46.7%), 99.7% (95% CI, 98.4%–100%), and 89% (95% CI, 85.6%–91.9%), respectively.

Table 1: SM and stroke mimics with diagnostic findings at multimodal CT

SM (n = 89)	SM with Diagnostic Findings at Multimodal CT
Seizures (n = 31) (34.8%)	13/31 (42%)
Migraine with aura attack (n = 11) (12.4%)	None
Conversion disorders (n = 11) (12.4%)	None
Infections (n = 7) (7.9%)	None
Brain tumors (n = 7) (7.9%)	7/7 (100%)
Metabolic causes (n = 6) (6.7%)	None
Peripheral vertigo (n = 5) (5.6%)	None
Syncope (n = 5) (5.6%)	None
Transient global amnesia (n = 3) (3.4%)	None
Subdural (n = 1) (1.1%)	1/1 (100%)
Dural arteriovenous fistula (n = 1) (1.1%)	1/1 (100%)
Cervical epidural hematoma (n = 1) (1.1%)	None

The specificity of multimodal CT for the diagnosis of SM in our study was high: Only 2/85 SM were diagnosed as stroke, and only 1/327 iCVEs was misdiagnosed as a stroke mimic on multimodal CT. More specifically, in 1 case, a subtle cortico-subcortical density was interpreted as a stroke, despite normal findings on perfusion maps, and the final diagnosis was aseptic meningoencephalitis, while 1 other false-positive diagnosis of stroke was derived from an erroneous interpretation of hypoperfusion, non-matching vascular territories such as a watershed hemodynamic hypoperfusion, which was, instead, a postseizure abnormality. The false-positive stroke mimic occurred, instead, in a patient with a vague perfusion asymmetry, which was interpreted as a possible postseizure abnormality, but the final diagnosis was a TIA. No imaging diagnosis of the cervical epidural hematoma was obtained on admission multimodal CT due to subtle and overlooked findings at CTA of the neck.

The role of each of the multimodal CT techniques in the diagnosis of a stroke mimic is shown in Table 3.

A hyperperfusion pattern (increased CBV and CBF ± reduced MTT/Tmax) was observed in 7/13 seizures and 6/7 tumors (Fig 2 and Online Supplemental Data), while 6/13 seizures and 1/7 tumors showed a hypoperfusion pattern (increased MTT/Tmax ± reduced CBV and CBF) (Online Supplemental Data). While CT + CTA showed positive findings in 41% of detected SM, perfusion CT alone showed positive findings in 95.5% of them.

We also evaluated the sensitivity, specificity, and accuracy of multimodal

Table 2: Statistical analysis results

	Multimodal CT in the Diagnosis of SM	Multimodal CT in the Diagnosis of SM (Excluding A Priori CT, Undetectable SM)	Multimodal CT in the Diagnosis of Definite Stroke (TIA Excluded)	Multimodal CT in the Diagnosis of iCVE (TIA Included)
SE (%) (95% CI) (%)	24.7 (16.2–35)	33.9 (22.6–46.7)	78 (72.6–82.8)	69.6 (64.1–74.6)
SP (%) (95% CI) (%)	99.7 (98.2–100)	99.7 (98.4–100)	97.8 (92.1–99.7)	97.8 (92.1–99.7)
PLR (%) (95% CI) (%)	77.1 (10.5–564.3)	113.7 (15.6–828.9)	34.7 (8.8–136.9)	31 (7.9–122.1)
NLR (%) (95% CI) (%)	0.8 (0.7–0.9)	0.7 (0.6–0.8)	0.2 (0.2–0.3)	0.3 (0.3–0.4)
PPV (%) (95% CI) (%)	95.7 (75–99.4)	95.7 (75.1–99.4)	99.1 (96.4–99.8)	99.1 (96.5–99.8)
NPV (%) (95% CI) (%)	82.3 (80.5–84)	88.6 (86.8–90.3)	59.2 (53.6–64.5)	47.8 (43.6–52.1)
ACC (%) (95% CI) (%)	83 (79–86.6)	89 (85.6–91.9)	82.9 (78.6–86.6)	75.8 (71.3–79.9)

Note:—SE indicates sensitivity; SP, specificity; PLR, positive likelihood ratio; NLR, negative likelihood ratio; PPV, positive predictive value; NPV, negative predictive value; ACC, accuracy.

Table 3: Role of each multimodal CT technique (NCCT, CTA, CTP, CE) in the diagnosis of SM

SM Detected on Multimodal CT	NCCT/CECT	CTA	CTP
Seizure, 7/13 (54%)	Neg ^a /no CE	Neg	↑CBV ↑CBF ↓MTT/Tmax
Seizure, 6/13 (46%)	Neg/no CE	Neg	↓CBV ↓CBF ↓MTT/Tmax
Brain tumor, 6/7 (86%)	Hypodensity, mass effect/CE in 3/6	Neg	↑CBV ↑CBF ↓MTT/Tmax
Brain tumor, 1/7 (14%)	Hypodensity, mass effect/no CE	Neg	↓CBV ↓CBF ↓MTT/Tmax
Subdural hematoma, 1/1	Subdural collection/no CE	Vessel displacement	Neg
AVF, 1/1	Neg/redundant vessels on CECT	Redundant vessels	↑CBV ↑CBF ↓MTT/Tmax

Note:—Neg indicates negative for acute findings; CE, contrast enhancement; ↑, increased; ↓, decreased.

^a Although negative for acute finding, NCCT showed the following in 4 different patients: 2 subdural collections and 1 cavernoma, which were already known from previous examinations, and 1 chronic left parietal middle cerebral infarct.

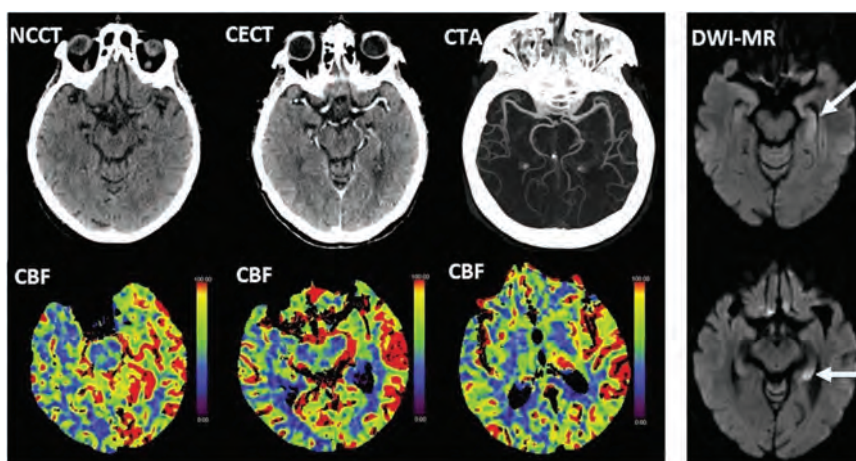


FIG 2. Left panel: elevated CBF consistent with hyperperfusion involving the left temporo-occipito-parietal cortex and left pulvinar in a 77-year-old woman with acute right-sided motor impairment, right hemineglect, aphasia, and conjugate eye deviation to the right. Note normal findings on NCCT, CECT, and CTA. Right panel: Diffusion MR imaging excludes ischemia and demonstrates seizure changes (arrows) in the left hippocampus.

CT for the diagnosis of stroke, which were, respectively, 78% (95% CI, 72.6%–82.8%), 97.8% (95% CI, 92.1%–99.7%), and 82.9% (95% CI, 78.6%–86.6%), in line with previous reports.^{18–20} The sensitivity, specificity, and accuracy of multimodal CT in the diagnosis of total iCVE (stroke and TIA) were, respectively, 69.6% (95% CI, 64.1%–74.6%), 97.8% (95% CI, 92.1%–99.7%), and 75.8% (95% CI, 71.3%–79.9%) (Table 2).

Among 89 patients with SM in our cohort, 82% underwent MR imaging at follow-up. MR imaging determined the diagnosis of SM in only 5 patients, with no relevant findings on multimodal CT (7% of patients with SM examined by MR imaging). Among these, there were patients with transient global amnesia ($n = 3$) and postictal hippocampal ($n = 1$) and cortical ($n = 1$) diffusion restriction. The remainder of the diagnoses of SM were established on the basis of other anamnestic, serologic, CSF, or EEG findings.

DISCUSSION

In this study, we aimed to examine the overall performance of multimodal CT for the diagnosis of SM in the context of clinical suspicion of acute ischemic stroke, demonstrating low sensitivity but high specificity with high positive predictive values and fairly high negative predictive values (respectively, 25.6%, 99.7%, 95.6%, and 83.8%). So far in the literature, the performance of CTP has been assessed mostly with regard to seizure-related SM, with a recent case-control study on a large seizure-related stroke mimic population demonstrating sensitivity, specificity, and positive and negative predictive values, respectively, of 38%, 86%, 42%, and 83% for CTP hyperperfusion in patients with ongoing seizure (ictal state).¹¹

In our population, as in previous studies,^{6,21} seizure was the most common stroke mimic. We were able to recognize 13/31 (42%) seizures on the basis of perfusion abnormalities on multimodal CT, with a hyperperfusion pattern in 7/13 (54%) and a hypoperfusion pattern in 6/13 (46%). Because in many of our

patients, EEG was not obtained at the time of multimodal CT acquisition, it is not possible to correlate these perfusion abnormality patterns with an ictal or postictal state.

Van Cauwenberge et al¹¹ reported that CTP can reliably differentiate acute ischemic stroke from ictal seizure, respectively, characterized by cortico-subcortical hypoperfusion and cortical hyperperfusion. Conversely, they showed that CTP findings may overlap in acute ischemic stroke and postictal seizure, both characterized by cortico-subcortical hypoperfusion, though seizure-related hypoperfusion typically follows a nonvascular distribution. In our study, the specificity of multimodal CT for the diagnosis of SM was high: Only 2/85 SM were diagnosed as stroke, and only 1/327 iCVEs was misdiagnosed as a stroke mimic; 2 of 3 of

these misdiagnoses were related to a misinterpretation of hypoperfusion findings, with a postictal seizure erroneously interpreted as a stroke and vice versa. Therefore, our results confirm the potential overlap of CTP findings between postictal hypoperfusion and acute ischemic stroke.

We detected all brain tumors present in our cohort by multimodal CT. Abnormal findings were visible on NCCT and CECT due to the presence of mass effect, vasogenic edema, and/or contrast enhancement. CTP showed hyperperfusion in 6/7 (86%) and hypoperfusion in 1/7 (14%) brain tumors. Perfusion abnormalities in brain tumors may be related to the nature of the lesion, with typical hyperperfusion in high-grade gliomas, or to induced seizure.²²

In our cohort, none of the patients with an attack of migraine with aura had recognizable multimodal CT findings, though perfusion abnormalities have been described in migraine, mostly on MR imaging studies demonstrating abnormalities ranging from hypoperfusion to hyperperfusion, with a typical nonvascular distribution,^{23–25} which can be associated to an increase of distal cortical vessel representation.²⁶

None of the toxic-metabolic conditions or infections in our cohort were detected by multimodal CT, though in these cases, NCCT may variably show areas of hypoattenuation or swelling, with possible contrast enhancement. Perfusion findings have also been anecdotally described in case reports such as in Wernicke encephalopathy,²⁷ Hashimoto encephalopathy,²⁸ and viral infections.^{29,30}

In addition, we did not encounter, in our cohort, luxury perfusion conditions, which may pose a challenge in a differential diagnosis between a postreperfusion iCVE and a stroke mimic. Luxury perfusion represents, in fact, the recovery of CBF to normal or increased levels in regions of infarcted brain when re-vascularization is established after a stroke, sometimes spontaneously. Luxury perfusion commonly occurs in subacute strokes but has also been reported in <24-hour strokes.³¹

In our study, the sensitivity of multimodal CT for the diagnosis of SM was low (25.6%) and remained low (34.4%; 95% CI, 22.9–47.3), even excluding SM, which are a priori considered to be undetectable by multimodal CT (such as conversion disorder, positional vertigo, syncope, and transient global amnesia). Due to its low sensitivity, multimodal CT cannot, therefore, be considered an efficient diagnostic tool for SM. In our cohort, 82% of SM underwent MR imaging at follow-up, and MR imaging has determined the diagnosis of SM in only 5 patients, with no relevant findings on multimodal CT (7% of SM examined by MR imaging). Although MR imaging allows ruling out stroke and may give a further hint of the diagnosis of SM, the diagnosis of these conditions relies on other complementary tests, such as serum and CSF analysis or EEG findings.

Conversely, our study outlines the high specificity of multimodal CT for the diagnosis of SM. This may support the clinician in the choice of avoiding revascularization treatment in SM with positive findings on multimodal CT. Among the different multimodal CT techniques, CTP was the most useful in the detection of SM, demonstrating abnormal findings in 95.5% of the overall diagnoses of SM performed by multimodal CT. Despite the current debate about the usefulness of CTP in patients with stroke in the first 6 hours from symptom onset,¹ CTP has the potential to detect perfusion abnormalities related to stroke mimic conditions and in cases in which brain CT is typically silent, such as in seizures.

Limitations in this study are related to the retrospective type of the analysis and to the relatively small number of subjects, which might have precluded some uncommon SM from being part of our population. There are, indeed, other vascular dysregulation conditions that might have a clinical presentation similar to that of stroke and may show CTP abnormalities, that we did not encounter in this study, such as posterior reversible encephalopathy syndrome³² and reversible cerebral vasoconstriction syndrome.³³

Another limitation is related to a selection bias in our study population, because we included only patients who underwent a full multimodal CT protocol at admission. We, therefore, excluded either patients with iCVE or those with SM without a multimodal CT protocol (ie, patients transferred from neighboring hospitals where CTP was not performed in the acute setting). Also, patients with a very high clinical suspicion of SM (such as those with hypoglycemia, positional vertigo, and migraine) might not have been referred to the multimodal CT protocol. Nonetheless, the prevalence of SM in our cohort was 21%, within the range of previous reports.^{4,34} Subjects with a final diagnosis of SM were younger than those with a final diagnosis of iCVE, and this difference was statistically significant. This finding is in line with the expected epidemiology of patients with SM. Indeed, clinical indicators of a mimic condition, though nonspecific, include young age and lack of a history of hypertension, hyperlipidemia, atrial fibrillation, diabetes, and coronary artery disease.²¹ Moreover, some patients with minor stroke who presented at admission as having a TIA, with complete symptom regression, did not undergo a full multimodal CT protocol and were, therefore, excluded from the study.

Finally, this was a monocentric study, and it may limit the generalizability of our findings. In particular, our series benefitted

from consultant neurology review before imaging and a subspecialist neuroradiology review at time of imaging.

CONCLUSIONS

Multimodal CT has a low sensitivity for the diagnosis of SM. MR imaging and further investigation (serum and CSF analysis and EEG) are required to obtain a definite diagnosis of these conditions. On the contrary, the high specificity of multimodal CT for the diagnosis of stroke mimic can support the clinician in the choice of avoiding revascularization treatment in patients diagnosed with SM on multimodal CT.

ACKNOWLEDGMENTS

We thank Matteo Merli, Istituto Imaging della Svizzera Italiana, Ente Ospedaliero Cantonale, Lugano, Switzerland, for CT technical support; and the Clinical Trial Unit, Ente Ospedaliero Cantonale, Bellinzona, Switzerland, for assistance in research project development.

Disclosure forms provided by the authors are available with the full text and PDF of this article at www.ajnr.org.

REFERENCES

1. Powers WJ, Rabinstein AA, Ackerson T, et al. **Guidelines for the Early Management of Patients with Acute Ischemic Stroke: 2019 Update to the 2018 Guidelines for the Early Management of Acute Ischemic Stroke—a Guideline for Healthcare Professionals from the American Heart Association/American Stroke Association.** *Stroke* 2019;50:e344–418 CrossRef Medline
2. Norris JW, Hachinski VC. **Misdiagnosis of stroke.** *The Lancet* 1982;319:328–31 CrossRef
3. Libman RB, Wirkowski E, Alvir J, et al. **Conditions that mimic stroke in the emergency department implications for acute stroke trials.** *Arch Neurol* 1995;52:1119–22 CrossRef Medline
4. Merino JG, Luby M, Benson RT, et al. **Predictors of acute stroke mimics in 8187 patients referred to a stroke service.** *J Stroke Cerebrovasc Dis* 2013;22:e397–403 CrossRef Medline
5. Tsigvoulis G, Zand R, Katsanos AH, et al. **Safety of intravenous thrombolysis in stroke mimics.** *Stroke* 2015;46:1281–87 CrossRef Medline
6. Winkler DT, Fluri F, Fuhr P, et al. **Thrombolysis in stroke mimics frequency, clinical characteristics, and outcome.** *Stroke* 2009;40:1522–25 CrossRef Medline
7. Lev MH, Farkas J, Rodriguez VR, et al. **CT angiography in the rapid triage of patients with hyperacute stroke to intraarterial thrombolysis: accuracy in the detection of large vessel thrombus.** *J Comput Assist Tomogr* 2001;25:520–28 Medline
8. Wintermark M, Sanelli PC, Albers GW, et al; Society of Neurointerventional Surgery. **Imaging recommendations for acute stroke and transient ischemic attack patients: a joint statement by the American Society of Neuroradiology, the American College of Radiology and the Society of Neurointerventional Surgery.** *J Am Coll Radiol* 2013;10:828–32 CrossRef Medline
9. Demeestere J, Wouters A, Christensen S, et al. **Review of perfusion imaging in acute ischemic stroke.** *Stroke* 2020;51:1017–24 CrossRef Medline
10. Vilela P. **Acute stroke differential diagnosis: stroke mimics.** *Eur J Radiol* 2017;96:133–44 CrossRef Medline
11. Van Cauwenberge MG, Dekeyser S, Nikoubashman O, et al. **Can perfusion CT unmask postictal stroke mimics? A case-control study of 133 patients.** *Neurology* 2018;91:E1918–27 CrossRef Medline

12. Lucas L, Gariel F, Menegon P, et al. **Acute ischemic stroke or epileptic seizure? Yield of CT perfusion in a code stroke situation.** *AJNR Am J Neuroradiol* 2021;42:49–56 CrossRef Medline
13. Gonzalez-Martinez A, Trillo S, de Quirós C, et al. **Predictors of perfusion computed tomography alterations in stroke mimics attended as stroke code.** *Eur J Neurol* 2021;28:1939–48 CrossRef Medline
14. Sacco RL, Kasner SE, Broderick JP, et al; Council on Nutrition, Physical Activity and Metabolism. **An updated definition of stroke for the 21st century: a statement for healthcare professionals from the American Heart Association/American Stroke Association.** *Stroke* 2013;44:2064–89 CrossRef Medline
15. Easton JD, Saver JL, Albers GW, et al; Interdisciplinary Council on Peripheral Vascular Disease. **Definition and evaluation of transient ischemic attack: a scientific statement for healthcare professionals from the American Heart association/American Stroke Association Stroke Council; Council on Cardiovascular Surgery and Anesthesia; Council on Cardiovascular Radiology and Intervention; Council on Cardiovascular Nursing—and the Interdisciplinary Council on Peripheral Vascular Disease.** *Stroke* 2009;40:2276–93 CrossRef Medline
16. Cereda CW, George PM, Inoue M, et al. **Inter-rater agreement analysis of the Precise Diagnostic Score for suspected transient ischemic attack.** *Int J Stroke* 2016;11:85–92 CrossRef Medline
17. Schuetz GM, Schlattmann P, Dewey M. **Use of 3×2 tables with an intention to diagnose approach to assess clinical performance of diagnostic tests: meta-analytical evaluation of coronary CT angiography studies.** *BMJ* 2012;345:e6717 CrossRef Medline
18. Kloska SP, Nabavi DG, Gaus C, et al. **Acute stroke assessment with CT: do we need multimodal evaluation?** *Radiology* 2004;233:79–86 CrossRef Medline
19. Biesbroek JM, Niesten JM, Dankbaar JW, et al. **Diagnostic accuracy of CT perfusion imaging for detecting acute ischemic stroke: a systematic review and meta-analysis.** *Cerebrovasc Dis* 2013;35:493–501 CrossRef Medline
20. Shen J, Li X, Li Y, et al. **Comparative accuracy of CT perfusion in diagnosing acute ischemic stroke: a systematic review of 27 trials.** *PLoS One* 2017;12:e0176622 CrossRef Medline
21. Hand PJ, Kwan J, Lindley RJ, et al. **Distinguishing between stroke and mimic at the bedside: the Brain Attack Study.** *Stroke* 2006;37:769–75 CrossRef Medline
22. Jain R. **Perfusion CT imaging of brain tumors: an overview.** *AJNR Am J Neuroradiol* 2011;32:1570–77 CrossRef Medline
23. Floery D, Vosko MR, Fellner FA, et al. **Acute-onset migrainous aura mimicking acute stroke: MR perfusion imaging features.** *AJNR Am J Neuroradiol* 2012;33:1546–52 CrossRef Medline
24. Förster A, Wenz H, Kerl HU, et al. **Perfusion patterns in migraine with aura.** *Cephalalgia* 2014;34:870–76 CrossRef Medline
25. Jadhav V. **Computed tomography perfusion abnormalities in migraine mimicking acute stroke presentation (P06.157.).** *Neurology* 2013;80(7):P06.157
26. Masuzaki M, Utsunomiya H, Yasumoto S, et al. **A case of hemiplegic migraine in childhood: transient unilateral hyperperfusion revealed by perfusion MR imaging and MR angiography.** *AJNR Am J Neuroradiol* 2001;22:1795–97 Medline
27. Bhan A, Advani R, Kurz KD, et al. **Wernicke's encephalopathy mimicking acute onset stroke diagnosed by CT perfusion.** *Case Rep Neurol Med* 2014;2014:673230 CrossRef Medline
28. Cho BH, Cheon K, Lee KY. **Hashimoto encephalopathy mimicking acute ischemic stroke: perfusion-weighted magnetic resonance imaging.** *J Clin Neurol* 2018;14:586–87 CrossRef Medline
29. de Lucas EM, Mandly GA, Gutiérrez A, et al. **Computed tomography perfusion usefulness in early imaging diagnosis of herpes simplex virus encephalitis.** *Acta Radiol* 2006;47:878–81 CrossRef Medline
30. Vallabhaneni D, Naveed MA, Mangla R, et al. **Perfusion imaging in autoimmune encephalitis.** *Case Rep Radiol* 2018;2018:3538645 CrossRef Medline
31. Nagar VA, McKinney AM, Karagulle AT, et al. **Reperfusion phenomenon masking acute and subacute infarcts at dynamic perfusion CT: confirmation by fusion of CT and diffusion-weighted MR images.** *AJR Am J Roentgenol* 2009;193:1629–38 CrossRef Medline
32. Hedna VS, Stead LG, Bidari S, et al. **Posterior reversible encephalopathy syndrome (PRES) and CT perfusion changes.** *Int J Emerg Med* 2012;5:12 CrossRef Medline
33. Miller TR, Shivashankar R, Mossa-Basha M, et al. **Reversible cerebral vasoconstriction syndrome, Part 2: diagnostic work-up, imaging evaluation, and differential diagnosis.** *AJNR Am J Neuroradiol* 2015;36:1580–88 CrossRef Medline
34. Hemmen TM, Meyer BC, McClean TL, et al. **Identification of non-ischemic stroke mimics among 411 code strokes at the University of California, San Diego, Stroke Center.** *J Stroke Cerebrovasc Dis* 2008;17:23–25 CrossRef Medline

Can Shunt Response in Patients with Idiopathic Normal Pressure Hydrocephalus Be Predicted from Preoperative Brain Imaging? A Retrospective Study of the Diagnostic Use of the Normal Pressure Hydrocephalus Radscale in 119 Patients

J.F. Carlsen, A.D.L. Backlund, C.A. Mardal, S. Taudorf, A.V. Holst, T.N. Munch, A.E. Hansen, and S.G. Hasselbalch



ABSTRACT

BACKGROUND AND PURPOSE: The Normal Pressure Hydrocephalus Radscale is a combined scoring of 7 different structural imaging markers on preoperative brain CT or MR imaging in patients with idiopathic normal pressure hydrocephalus: callosal angle, Evans Index, Sylvian fissure dilation, apical sulcal narrowing, mean temporal horn diameter, periventricular WM lesions, and focal sulcal dilation. The purpose of this retrospective study was to assess the performance of the Normal Pressure Hydrocephalus Radscale in distinguishing idiopathic normal pressure hydrocephalus shunt responders from nonresponders.

MATERIALS AND METHODS: The preoperative MR imaging and CT scans of 119 patients with idiopathic normal pressure hydrocephalus were scored using the Normal Pressure Hydrocephalus Radscale. A summary shunt-response score assessed within 6 months from ventriculoperitoneal shunt surgery, combining the effect on cognition, gait, and urinary incontinence, was used as a reference. The difference between the mean Normal Pressure Hydrocephalus Radscale for responders and nonresponders was tested using the Student *t* test. The area under the curve was calculated for the Normal Pressure Hydrocephalus Radscale to assess shunt response. To ascertain reproducibility, we assessed the interobserver agreement between the 2 independent observers as intraclass correlation coefficients for the Normal Pressure Hydrocephalus Radscale for 74 MR imaging scans and 19 CT scans.

RESULTS: Ninety-four (79%) of 119 patients were shunt responders. The mean Normal Pressure Hydrocephalus Radscale score for shunt responders was 8.35 (SD, 1.53), and for nonresponders, 7.48 (SD, 1.53) ($P = .02$). The area under the curve for the Normal Pressure Hydrocephalus Radscale was 0.66 (range, 0.54–0.78). The intraclass correlation coefficient for the Normal Pressure Hydrocephalus Radscale was 0.86 for MR imaging and 0.82 for CT.

CONCLUSIONS: The Normal Pressure Hydrocephalus Radscale showed moderate discrimination for shunt response but cannot, on its own, be used for selecting patients with idiopathic normal pressure hydrocephalus for shunt surgery.

ABBREVIATIONS: AUC = area under the curve; CA = callosal angle; DESH = disproportionately enlarged subarachnoid space hydrocephalus; EI = Evans index; iNPH = idiopathic normal pressure hydrocephalus; MMSE = Mini-Mental State Examination; NPH = normal pressure hydrocephalus; PVWML = periventricular WM lesions

The pathophysiology of idiopathic normal pressure hydrocephalus (iNPH) remains largely enigmatic.^{1,2} Equally enigmatic are the mechanisms of the only known effective treatment, shunting of the CSF.³ In light of these shortcomings in our understanding, the

diagnosis of iNPH, as suggested by international guidelines, is based on the combined evaluation of iNPH symptoms, brain imaging, and CSF pressure dynamics.⁴ Nevertheless, even after a thorough clinical work-up, a substantial number of patients with iNPH do not benefit from shunt surgery.^{5,6} Although generally considered a minor and safe neurosurgical procedure, complications following shunt surgery are not uncommon, including postoperative hematoma, shunt infection, and subdural hematomas arising from over-drainage.^{6,7} Weighing the chance of shunt response against the risk of complications is a prime challenge for attending neurologists and neurosurgeons.

Preoperative brain imaging has long been used to establish dilation of the brain ventricles in patients with iNPH.^{8,9} In addition, preoperative imaging is used to rule out other types of degenerative

Received June 13, 2021; accepted after revision October 7.

From the Department of Radiology (J.F.C., C.A.M., A.E.H.), Department of Neurology (S.T., S.G.H.), Danish Dementia Research Centre, and Department of Neurosurgery (A.V.H., T.N.M.), Rigshospitalet, Copenhagen University Hospital, Copenhagen, Denmark; Department of Radiology (A.D.L.B.), Hospital of North Zealand, Hillerød, Denmark; Department of Clinical Medicine (T.N.M., A.E.H.), University of Copenhagen, Copenhagen, Denmark; and Department of Epidemiology Research (T.N.M.), Statens Serum Institut, Copenhagen, Denmark.

Please address correspondence to Jonathan Frederik Carlsen, MD, Department of Radiology, Rigshospitalet, Copenhagen University Hospital, Blegdamsvej 9, 2100 Copenhagen OE, Denmark; e-mail: Jonathan.frederik.carlsen@regionh.dk

<http://dx.doi.org/10.3174/ajnr.A7378>

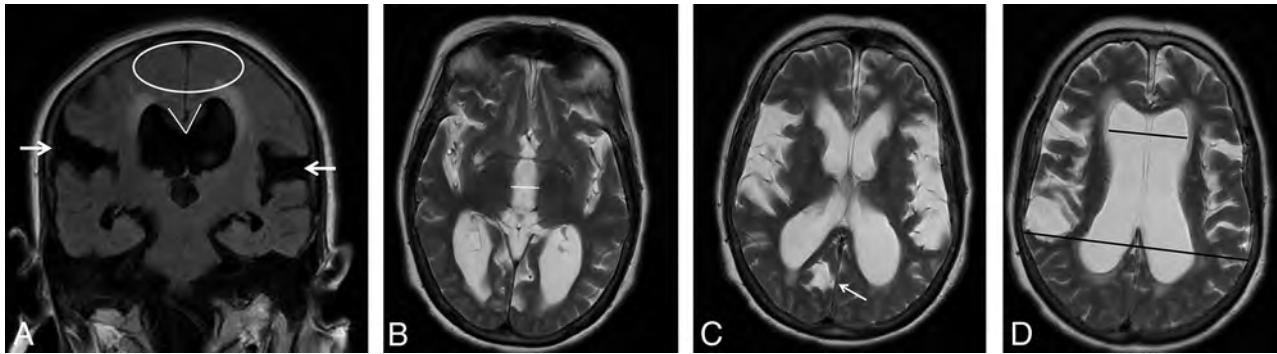


FIG 1. MR imaging of a 79-year-old female shunt-responder with an NPH Radscale score of 11. A, Coronal FLAIR image shows marked bilateral Sylvian fissure dilation (*white arrows*), apical narrowing of sulci (*white ellipse*), a narrow CA (65°), and marked periventricular hyperintensities. B–D, Axial T2 images at different levels show measurement of third ventricle diameter (*white line*), sulcal dilation (*white arrow*), and measurements used for the Evans ratio calculation (*black lines*).

brain disease, vascular disease, and other types of hydrocephalus before shunt surgery.⁹ Several studies have tried to use anatomic imaging markers for predicting shunt response, with varying results.^{10–12} These imaging markers include measurements of the callosal angle (CA), Evans index (EI), and temporal horn diameter and evaluation of the presence of disproportionately enlarged subarachnoid space hydrocephalus (DESH), focal sulcal dilation, and focal ventricle bulging. Recently, the Normal Pressure Hydrocephalus (NPH) Radscale, a composite score based on evaluations of 7 different anatomic imaging markers, has been proposed as a predictor of shunt response.¹³ The NPH Radscale has been shown to have a good correlation with the severity of iNPH symptoms in a randomly selected group of 168 volunteers older than 65 years of age.¹⁴ Furthermore, the NPH Radscale had a high area under the curve (AUC) for discerning healthy, age-matched adults from iNPH shunt responders.¹³ No studies using the NPH Radscale to discern iNPH shunt responders from nonresponders have been published.

In this retrospective study, we aimed to evaluate the usefulness of the NPH Radscale performed on preoperative brain imaging to predict shunt response assessed 6 months after the operation.

MATERIALS AND METHODS

Inclusion of Patients and Preoperative Evaluation

The patients included in this retrospective study underwent shunt surgery for NPH at the Department of Neurosurgery, Copenhagen University Hospital, from 2013 to 2020. Approval of retrospective recording of patient data was given by the hospital direction board. All data were recorded from the electronic patient journal and the hospital radiology information system/PACS.

In the study inclusion period, 133 patients were consecutively diagnosed with probable or possible NPH according to clinical guidelines and, consequently, received a ventriculoperitoneal shunt.¹⁵ All patients were evaluated at an interdisciplinary conference between clinicians from the Memory Clinic at the Danish Dementia Research Center and the Department of Neurosurgery, Rigshospitalet, Copenhagen University Hospital, before referral to surgery. The evaluation was based on the presence of iNPH symptoms, including gait disturbance, radiologic characteristics, and results of CSF dynamic measurements obtained whenever possible. These included a lumbar infusion test with measurement of

resistance to outflow and, in some, supplemented by a lumbar tap test with removal of 40 mL of CSF with prior and postobjective evaluation of gait (CELDA System; Likvor). The infusion test and the lumbar tap test were regarded as supportive, not imperative, for decisions about shunting, especially in patients with possible iNPH.¹⁶ Major urogenital, musculoskeletal, or neurologic comorbidities were recorded before the operation.

Excluded Patients

Brain imaging had been performed in different hospitals with differing protocols. Eleven patients without either an available brain CT or MR imaging performed within 1 year before surgery were excluded. The remaining 122 brain scans were assessed for eligibility, and 3 MR imaging scans with no T2 or FLAIR sequences were deemed insufficient and were excluded. Finally, 119 patients, 20 with CT scans and 99 with MR imaging scans were included. Of these 119 patients, 114 patients had undergone a preoperative lumbar infusion test and 55 had undergone a lumbar tap test as part of the clinical work-up.

Brain Image Assessment

All scans were assessed by 1 neuroradiologist with 10 years' experience (J.F.C.). To ascertain reproducibility, 2 independent readers (A.D.L.B. and C.A.M., respectively), also assessed 74 random MR imaging scans and 19 CT scans. The 2 additional readers were radiology residents in their last year of residency. All readings were performed blinded to the other readers' evaluations and shunt-response evaluations.

The 7 imaging parameters that compose the NPH Radscale were assessed in accordance with Kockum et al¹⁴ (Fig 1). For CA measurements, a coronal plane perpendicular to the intercommissural plane was reconstructed for both MR imaging and CT when not available.¹⁷ Periventricular white matter lesions (PVWML) were assessed on T2 and/or FLAIR images for MR imaging. All other assessments were performed on available sequences and reconstructions.

The CA and the mean temporal horn diameter were measured in degrees and millimeters, respectively. The presence of focally enlarged sulci was noted as either present or not. Narrowing of the apical sulci was assessed as 0 = normal or wider than normal, 1 = slight compression/parafalcine compression,

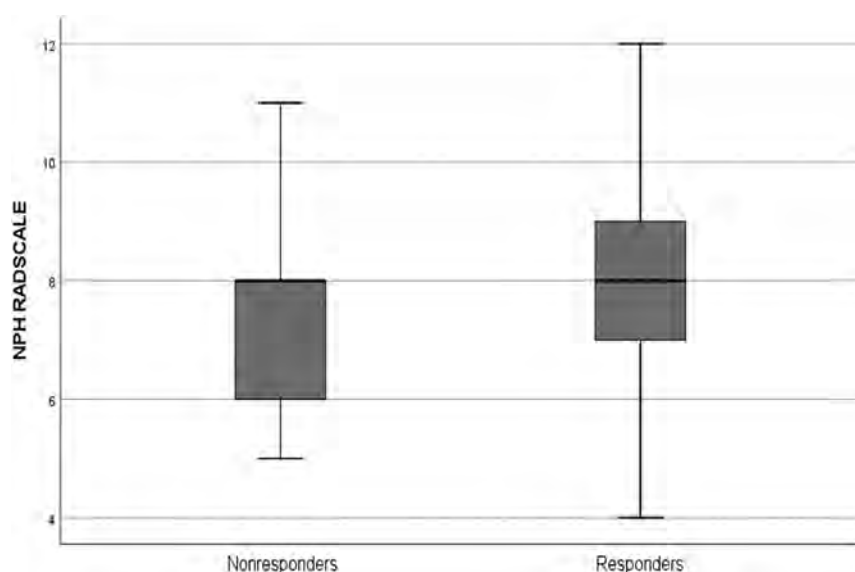


FIG 2. A boxplot of NPH Radscale values (y-axis) for responders and nonresponders, respectively. The *thick black line* is the median; and box upper and lower margins are 75th and 25th percentiles, respectively. *Whiskers* represent upper and lower ranges.

and 2 = definite compression. Sylvian fissure dilation was rated as present or not. PVWML were evaluated as either 0 = normal, including capping and pencil-thin lining, 1 = increased PVWML, and 2 = confluent areas of PVWML.

In addition to the imaging parameters used for NPH Radscale scoring, readers measured third ventricle diameter in millimeters and assessed ventricular focal bulging.¹⁸ Furthermore, readers assessed the presence of DESH if apical sulci were disproportionately narrow compared with Sylvian fissure dilation.

Shunt-Response Evaluation

Shunt-response evaluation was performed at outpatient follow-up visits at the Memory Clinic at the Danish Dementia Research Center approximately 6 months after shunt surgery. Gait and cognition were evaluated by using a 10-m gait test and the Mini-Mental State Examination (MMSE).¹⁹ Urinary continence was evaluated by interviewing patients and/or caregivers. Gait and continence were scored by 8- and 6-point scales, respectively.²⁰ Changes in gait and continence were evaluated as the following: 1) worsening = increase of the score by 1 or more, 2) no effect = no change in scores, 3) moderate effect = a decrease in score by 1, and 4) substantial effect = a decrease in the score by ≥ 2 . Changes in cognition were evaluated as the following: 1) worsening = a decrease in the MMSE score by 2 or more, 2) no effect = change by -1 to $+1$, 3) moderate effect = an increase in the score by 2, and 4) substantial effect = an increase in the score by ≥ 3 . The evaluations for gait, continence, and MMSE were then each scored on a scale from -1 to 2: worsening = -1 , no change = 0, moderate effect = 1, and substantial effect = 2. A summary shunt response score from -3 to 6 was accordingly obtained.

Shunt response was defined as a summary shunt response score of ≥ 1 . Due to the retrospective design of the study, postoperative objective measures for gait and cognition were available in

only approximately 80% of the patients. In the remaining patients, scores were obtained by interviewing patients and/or caregivers.

Complications within 1 year from the operation in the form of shunt revision due to shunt malfunction or displacement, shunt revision due to overdrainage, overdrainage without shunt revision, as well as infection, stroke, or death due to shunt surgery were recorded.

Statistics

Statistics were performed using SPSS, Version 25.0 (IBM). Means are presented as mean (SD); medians are presented as median (range). The Student *t* test with nonequal variances assumed was used to test distributions among continuous data. Distributions of binary variables were tested using the χ^2 test. For ranked data, a Wilcoxon rank test was performed. Logistic regression was used to test among patient age, sex,

comorbidities, CA, EI, narrowing of apical sulci, Sylvian fissure dilation, DESH, third ventricle diameter, mean temporal horn diameter, ventricular focal bulging, focally enlarged sulci, and PVWML; shunt response was the outcome. To test the robustness of the logistic regression, we performed the same analyses for the entire patient cohort and then twice more on patients randomly assigned to 2 groups with 60 and 59 patients in each group.

Receiver operating characteristic curves were performed for continuous data, and the AUCs were calculated. For the CA, the AUC was calculated for 180 degrees $-CA$, because the CA is inversely proportional to the likelihood of shunt response shunt response. The Youden index was calculated for the NPH Radscale to find the optimal cutoff.

To assess interrater variability, we calculated intraclass coefficients, κ values, and Spearman rank coefficients for continuous, binary, and ranked data, respectively, and evaluated them according to Landis and Koch.²¹

RESULTS

Of the 119 patients included in the study, 78 (65.5%) were men and 41 (34.5%) were women. The median age was 77 years (range, 55–90 years). The mean MMSE score was 25.25 (SD, 4.17). The mean time from preoperative imaging to the operation was 190 (SD, 89) days.

The mean summary shunt response score was 2.06 (SD, 1.68). Of 119 patients, 94 (79.0%) were shunt responders. Comorbidities were registered for 77 (65%) patients. There was no significant difference in the distribution of comorbidities between responders, 61 of 94 (65%), and nonresponders, 16 of 25 (64%) ($P = .93$).

The median NPH Radscale score for the entire cohort was 8 (range, 4–12). The median score for shunt responders was 8 (range, 4–12), and the median score for nonresponders was also 8 (range, 5–11) (Fig 2). Complications were seen in 39 (33%)

Table 1: Distribution of different imaging parameters for the entire population for responders and nonresponders

	Score	Total	Responders	Nonresponders	P Value
Patients (No.)		119	94	25	
EI ^a		0.39 (0.046)	0.39 (0.046)	0.38 (0.046)	.28 ^c
CA ^a		73.0 (17.4)	71.9 (16.7)	77.2 (19.7)	.23 ^c
Third ventricle diameter ^a		14.2 (3.14)	14.3 (3.00)	14.1 (3.72)	.75 ^c
Mean temporal horn diameter ^a		8.14 (2.40)	8.38 (2.40)	7.26 (2.22)	.03 ^c
NPH Radscale ^a		8.17 (1.56)	8.35 (1.53)	7.48 (1.53)	.02 ^c
DESH ^b	Present	60 (50.4%)	49 (52.1%)	11 (44%)	.47 ^d
	Not present	59 (49.6%)	45 (47.9%)	14 (56%)	
Focal bulging	Present	14 (11.8%)	12 (12.8%)	2 (8.0%)	.73 ^e
	Not present	105 (88.2%)	82 (87.2%)	23 (92.0%)	
Focally enlarged sulci ^b	Present	22 (18.5%)	17 (18.1%)	5 (20.0%)	.78 ^e
	Not present	97 (81.5%)	77 (81.9%)	20 (80.0%)	
Sylvian fissure dilation ^b	Present	101 (84.9%)	83 (88.3%)	18 (72.0%)	.05 ^e
	Not present	18 (15.1%)	11 (11.7%)	7 (28%)	
Narrow sulci ^b	2	47 (39.5%)	29 (30.9%)	4 (16.0%)	.19 ^f
	1	39 (32.8%)	30 (31.9%)	9 (36.0%)	
	0	33 (27.7%)	35 (37.2%)	12 (48.0%)	
PVWML ^b	2	55 (46.2%)	47 (50.0%)	8 (32.0%)	.16 ^f
	1	47 (39.5%)	34 (36.2%)	13 (52.0%)	
	0	17 (14.3%)	13 (13.8%)	4 (16.0%)	

^a Continuous data are presented as means (SD).

^b Categorical and ordinal data are presented as No. (%).

^c Student *t* test.

^d χ^2 test.

^e Fisher exact test.

^f Mann-Whitney *U* test.

Table 2: Interrater correlations for continuous evaluations for MR imaging and CT

	MR Imaging (n = 74)			CT (n = 19)		
	ICC	LB	UB	ICC	LB	UB
EI	0.914	0.863	0.946	0.974	0.932	0.990
CA	0.934	0.895	0.958	0.856	0.626	0.945
Mean temporal horn diameter	0.943	0.909	0.964	0.917	0.784	0.968
Third ventricle diameter	0.918	0.869	0.948	0.966	0.911	0.987
NPH Radscale	0.858	0.774	0.910	0.819	0.531	0.930

Note:—LB indicates lower bound; UB, upper bound; ICC, intraclass correlation coefficient.

patients. More nonresponders, 16 of 25 (64%), than responders, 23 of 94 (24%), experienced complications ($P < .001$).

Preoperative Imaging Findings and Shunt Response

All patients had an EI of ≥ 0.3 . Means and SDs for all imaging parameters are presented in Table 1. The NPH Radscale, mean temporal horn diameter, and Sylvian fissure dilation were significantly different between responders and nonresponders.

In the logistic regression analysis, only Sylvian fissure dilation and mean temporal horn diameter were significantly correlated with shunt response ($P = .017$ and $P = .028$). All other covariates were not significantly correlated with shunt response. For the logistic regression performed in the 2 groups of evenly and randomly distributed patients, Sylvian fissure dilation and the Evans index were significantly correlated with shunt response in the first group ($P = .018$ and $P = .038$), while mean temporal horn diameter was the last remaining variable in the second group, though it was not significantly associated with shunt response ($P = .068$).

The AUC was 0.66 for the NPH Radscale, range 0.54–0.78, ($P = .02$), 0.60 for the CA, range 0.47–0.72, ($P = .06$), 0.59 for the EI, range 0.46–0.73, ($P = .07$), 0.64 for mean temporal horn

diameter, range 0.53–0.76, ($P = .06$), and 0.54 for third ventricle diameter, range 0.40–0.67, ($P = .07$). The Youden index for the NPH Radscale was 0.239, yielding a sensitivity and specificity of 0.48 and 0.76, respectively, at a cutoff for shunt response of ≥ 9 . The AUC for the NPH Radscale for the 80 patients without complications was 0.59, range 0.36–0.83, ($P = .35$).

Interobserver Agreement

Interoperator variability was assessed for both MR imaging and CT (Tables 2–4). For all continuous assessments, agreement was either excellent or good for both MR imaging and CT. For all categorical assessments, agreement was good or fair, except for focal bulging, which showed no agreement, and PVWML, which showed excellent agreement for CT scans.

DISCUSSION

This is the first study to evaluate the ability of the NPH Radscale to discern iNPH shunt responders from nonresponders. Although the average NPH Radscale score for shunt responders was significantly higher than for nonresponders, there was only moderate discrimination between the 2 groups, with an AUC =

Table 3: Kappa statistics for binary categorical evaluations for MR imaging and CT

	MR Imaging (n = 74)			CT (n = 19)		
	κ	UB	LB	κ	UB	LB
DESH	0.569	0.402	0.736	0.607	0.247	0.967
Focal bulging	0.354	0.090	0.617	−0.145	−0.282	−0.006
Focally enlarged sulci	0.617	0.393	0.841	0.650	0.292	1.008
Sylvian fissure dilation	0.617	0.393	0.841	0.477	0.025	0.979

Note:— κ Indicates Kappa statistics; LB, lower bound; UB, upper bound; DESH, disproportionately enlarged subarchmoid space hydrocephalus.

Table 4: Spearman rank statistics for non-binary categorical evaluations for MR imaging and CT

	MR Imaging (n = 74)			CT (n = 19)		
	Spearman Rank	UB	LB	Spearman Rank	UB	LB
Narrow sulci	0.626	0.464	0.747	0.787	0.518	0.914
PVWML	0.691	0.550	0.794	0.826	0.596	0.930

Note:—LB indicates lower bound; UB, upper bound; pvWML, periventricular white matter hyperintensities.

0.66. Interoperator agreement for the NPH Radscale was excellent for MR imaging and good for CT.

The NPH Radscale was proposed by Kockum et al,¹⁴ in 2018. It is a composite score based on quantitative and qualitative structural brain image assessments. Although originally evaluated on brain CT, all the imaging parameters have frequently been assessed separately on brain MR imaging in other studies.^{18,22,23} Indeed, interobserver and intraobserver variability has been reported for MR imaging and CT previously by the same group, showing good agreement for both.²⁴

The NPH Radscale has shown good discrimination between shunt responders and a healthy population of individuals older than 65 years of age.¹³ In this study, brain CT was performed no more than 8 days before the operation, and the median NPH Radscale score for shunt responders was 10, compared with 8 in our study. Because no data on nonresponders are presented, it can only be guessed whether the difference lies in the timing and quality of preoperative imaging and the resulting NPH Radscale assessment, in different quantifications of shunt response, or in a genuine difference among the studied populations. A very recent study of 100 possible or probable patients with iNPH undergoing a lumbar tap test showed that the NPH Radscale could not satisfactorily discriminate between patients responding to the tap test and those who did not.²⁵ Although the lumbar tap test is only a surrogate measure of actual shunt response, this finding is in line with the data presented here.

There is no consensus or guidelines concerning the definition of shunt response or when it should be assessed. We found a shunt response in 80% of patients, which is in line with findings in most larger studies.^{18,26,27}

Our findings suggest that the structural changes traditionally described in patients with iNPH cannot, on their own, account for the reversibility of iNPH symptoms. Both nonresponders with high NPH Radscale scores and responders with low NPH Radscale scores were observed. The moderate AUC was not attributable to a skewed distribution of complications between responders and nonresponders because the AUC for patients without complications was similar to that for the whole group. Previous studies have tried to predict shunt response from preoperative anatomic brain imaging, but the results are heterogeneous.^{10–12} One study investigating

a similar, composite anatomic score in 50 patients with iNPH showed a difference between shunt responders and nonresponders on a group level but did not report on diagnostic accuracy.²⁸ In concordance with our data, this finding may suggest that other pathophysiologic mechanisms not visible on structural brain imaging may underlie the response to shunting observed in some patients with iNPH.²⁹ Furthermore, the response to shunting is associated with compliance to physical training after the operation, which was not accounted for in this study.³⁰

Several studies on advanced MR imaging and iNPH have been published. Some studies have focused on aqueductal flow to predict shunt response. Discouragingly, most studies found no discrimination for shunt response with aqueductal flow, though it was reduced after the operation.^{31,32} Perfusion imaging has been applied to predict shunt response, suggesting either no discrimination or lowered medial frontal cortex or cingulate gyrus blood flow.^{33–35} The studies were, however, too small to warrant any firm conclusions. The findings for both aqueductal flow and brain perfusion imaging emphasize that although some physiologic parameters may be skewed in patients with iNPH, their reversibility following shunt surgery does not correlate with the clinical shunt response.

Another aspect to consider in patients with iNPH is the timing of both symptom onset and the advent of structural changes and how the reversibility of symptoms relates to these time points.

In a small study of brain imaging in patients with iNPH, both the EI of >0.3 and third ventricle diameter were shown to be enlarged and increasingly enlarged in the years before symptom onset.³⁶ In another study, some patients with asymptomatic ventriculomegaly developed symptoms of iNPH during a follow-up period of 3 years, while another study found clinical and structural progression after 1 year in patients with asymptomatic ventriculomegaly.^{37,38} Nonshunted patients with slight iNPH symptoms have, however, shown little progression in an earlier study.³⁹ These findings support the notion that even though structural brain changes are correlated with and may precede iNPH symptomatology, they cannot, on their own, predict the reversibility of iNPH symptoms.

Recently artificial intelligence has been used to measure volumes of different anatomic brain regions in shunt responders versus nonshunted patients, with good results.⁴⁰ Also, a support-

vector machine–based algorithm has been shown to reliably predict an anatomic NPH pattern on brain imaging as defined by a consensus of 4 neuroradiologists, and a deep learning network has been trained to discern patients with NPH from those with Alzheimer disease and healthy controls in a small study population.^{41,42} No studies have examined whether artificial intelligence can be used to separate iNPH shunt responders from nonresponders, but this could be a method to extend the utility of structural brain imaging beyond the interpretative skills of neuroradiologists.

Strengths and Limitations

This study was performed in a single center with a standard setup and long experience in iNPH evaluation. All radiologic evaluations were performed by the same experienced neuroradiologist. The major limitation is the retrospective design of the study, with missing data on objective measurement of outcomes for a subset of patients. However, these data were obtained by interviews of the next of kin and caregivers, ensuring no loss to follow-up. Furthermore, brain imaging was performed in different hospitals, with varying times from shunt surgery and scan protocols. This feature may have hampered the diagnostic potential of the images. However, predefined inclusion criteria for the sequences included in MR images were used, and we found that a consistent image evaluation was feasible. Therefore, the interrater agreement for most parameters, including the NPH Radscale, was good and comparable with that in earlier studies.²⁴ For logistic regression analyses, there is a risk of collinearity when assessing multiple imaging parameters to diagnose the same pathophysiology on the same brain scan. To test the robustness of the analyses, we performed them first on the entire cohort and then on all patients randomized to 2 groups. The variables that came out significant for the whole group, came out as significant in the first of the split groups and as the last, insignificant parameter before exclusion in the second split group, indicating that the findings were robust to some extent. Collinearity should, however, still be considered for these kinds of analyses.

It is well-known that MR imaging is better for assessing WM vascular disease, but because PVWML are part of the NPH Radscale evaluation, we chose to classify them uniformly for this analysis.

Also, the limited follow-up time of 6 months does not allow us to associate imaging findings with long-term outcomes. Possibly, better outcome measures, including cognitive tests and gait or balance measures, could have been obtained with prospective evaluation.

CONCLUSIONS

In this study, the use of the NPH Radscale on preoperative imaging yielded moderate discrimination for shunt response. We conclude that currently, the NPH Radscale cannot, on its own, be used to select patients for shunt surgery. Further prospective evaluations should be performed to ascertain the usefulness of the NPH Radscale.

Disclosure forms provided by the authors are available with the full text and PDF of this article at www.ajnr.org.

REFERENCES

1. Fasano A, Espay AJ, Tang-Wai DF, et al. **Gaps, controversies, and proposed roadmap for research in normal pressure hydrocephalus.** *Mov Disord* 2020;35:1945–54 CrossRef Medline
2. Wang Z, Zhang Y, Hu F, et al. **Pathogenesis and pathophysiology of idiopathic normal pressure hydrocephalus.** *CNS Neurosci Ther* 2020;26:1230–40 CrossRef Medline
3. Bassi MA, Lopez MA, Confalone L, et al. **Normal pressure hydrocephalus: diagnosis and treatment.** *Nature* 2020;388:539–47 CrossRef Medline
4. Andersson J, Rosell M, Kockum K, et al. **Challenges in diagnosing normal pressure hydrocephalus: evaluation of the diagnostic guidelines.** *eNeurologicalSci* 2017;7:27–31 CrossRef Medline
5. Halperin JJ, Kurlan R, Schwalb JM, et al. **Practice guideline: idiopathic normal pressure hydrocephalus: response to shunting and predictors of response.** *Neurology* 2015;85:2063–71 CrossRef Medline
6. Giordan E, Palandri G, Lanzino G, et al. **Outcomes and complications of different surgical treatments for idiopathic normal pressure hydrocephalus: a systematic review and meta-analysis.** *J Neurosurg* 2019;131:1024–36 CrossRef Medline
7. Bergsneider M, Black PML, Klinge P, et al. **INPH guidelines, part IV: surgical management of idiopathic normal-pressure hydrocephalus.** *Neurosurgery* 2005;57:S2–29–39 CrossRef
8. Bradley WG, Kortman KE, Burgoyne B. **Flowing cerebrospinal fluid in normal and hydrocephalic states: appearance on MR images.** *Radiology* 1986;159:611–16 CrossRef Medline
9. Pereira Damasceno B, Damasceno BP. **Normal pressure hydrocephalus: diagnostic and predictive evaluation.** *Dement Neuropsychol* 2015;9:350–55 CrossRef Medline
10. Ishikawa M, Oowaki H, Takezawa M, et al. **Disproportionately enlarged subarachnoid space hydrocephalus in idiopathic normal-pressure hydrocephalus and its implication in pathogenesis.** *Acta Neurochir Suppl* 2016;122:287–90 CrossRef Medline
11. Craven CL, Toma AK, Mostafa T, et al. **The predictive value of DESH for shunt responsiveness in idiopathic normal pressure hydrocephalus.** *J Clin Neurosci* 2016;34:294–98 CrossRef Medline
12. Grahne K, Jusue-Torres I, Szujewski C, et al. **The quest for predicting sustained shunt response in normal-pressure hydrocephalus: an analysis of the callosal angle's utility.** *World Neurosurg* 2018;115:e717–22 CrossRef Medline
13. Kockum K, Virhammar J, Riklund K, et al. **Diagnostic accuracy of the iNPH radscale in idiopathic normal pressure hydrocephalus.** *PLoS One* 2020;15:e0232275 CrossRef Medline
14. Kockum K, Lilja-Lund O, Larsson EM, et al. **The idiopathic normal-pressure hydrocephalus radscale: a radiological scale for structured evaluation.** *Eur J Neurol* 2018;25:569–76 CrossRef Medline
15. Relkin N, Marmarou A, Klinge P, et al. **Diagnosing idiopathic normal-pressure hydrocephalus.** *Neurosurgery* 2005;57(Suppl 3):S4–16 CrossRef Medline
16. Eklund A, Smielewski P, Chambers I, et al. **Assessment of cerebrospinal fluid outflow resistance.** *Med Biol Eng Comput* 2007;45:719–35 CrossRef Medline
17. Virhammar J, Laurell K, Cesarini KG, et al. **The callosal angle measured on MRI as a predictor of outcome in idiopathic normal-pressure hydrocephalus.** *J Neurosurg* 2014;120:178–84 CrossRef Medline
18. Virhammar J, Laurell K, Cesarini KG, et al. **Preoperative prognostic value of MRI findings in 108 patients with idiopathic normal pressure hydrocephalus.** *AJNR Am J Neuroradiol* 2014;35:2311–18 CrossRef Medline
19. Folstein MF, Folstein SE, McHugh PR. **“Mini-mental state”: a practical method for grading the cognitive state of patients for the clinician.** *J Psychiatr Res* 1975;12:189–98 CrossRef Medline
20. Hellström P, Klinge P, Tans J, et al. **A new scale for assessment of severity and outcome in iNPH.** *Acta Neurol Scand* 2012;126:229–37 CrossRef Medline
21. Landis JR, Koch GG. **The measurement of observer agreement for categorical data.** *Biometrics* 1977;33:159–74 CrossRef Medline

22. Kuchcinski G, Jacquiez C, Baroncini M, et al. **Idiopathic normal-pressure hydrocephalus: diagnostic accuracy of automated sulcal morphometry in patients with ventriculomegaly.** *Clin Neurosurg* 2019;85:E747–55 CrossRef Medline
23. Hong YJ, Kim MJ, Jeong E, et al. **Preoperative biomarkers in patients with idiopathic normal pressure hydrocephalus showing a favorable shunt surgery outcome.** *J Neurol Sci* 2018;387:21–26 CrossRef Medline
24. Kockum K, Virhammar J, Riklund K, et al. **Standardized image evaluation in patients with idiopathic normal pressure hydrocephalus: consistency and reproducibility.** *Neuroradiology* 2019;61:1397–406 CrossRef Medline
25. Laticevschi T, Lingenberg A, Armand S, et al. **Can the radiological scale “iNPH radscale” predict tap test response in idiopathic normal pressure hydrocephalus?** *J Neurol Sci* 2021;420:117239 CrossRef Medline
26. Agerskov S, Wallin M, Hellström P, et al. **Absence of disproportionately enlarged subarachnoid space hydrocephalus, a sharp callosal angle, or other morphologic MRI markers should not be used to exclude patients with idiopathic normal pressure hydrocephalus from shunt surgery.** *AJNR Am J Neuroradiol* 2019;40:74–79 CrossRef Medline
27. Kojoukhova M, Koivisto AM, Korhonen R, et al. **Feasibility of radiological markers in idiopathic normal pressure hydrocephalus.** *Acta Neurochir (Wien)* 2015;157:1709–19 CrossRef Medline
28. Shinoda N, Hirai O, Hori S, et al. **Utility of MRI-based disproportionately enlarged subarachnoid space hydrocephalus scoring for predicting prognosis after surgery for idiopathic normal pressure hydrocephalus: Clinical research.** *J Neurosurg* 2017;127:1436–42 CrossRef Medline
29. Yamada S, Ishikawa M, Nozaki K. **Exploring mechanisms of ventricular enlargement in idiopathic normal pressure hydrocephalus: a role of cerebrospinal fluid dynamics and motile cilia.** *Fluids Barriers CNS* 2021;18:20 CrossRef Medline
30. Modesto PC, Pinto FC. **Home physical exercise program: analysis of the impact on the clinical evolution of patients with normal pressure hydrocephalus.** *Arq Neuropsiquiatr* 2019;77:860–70 CrossRef
31. Shanks J, Markenroth Bloch K, Laurell K, et al. **Aqueductal CSF stroke volume is increased in patients with idiopathic normal pressure hydrocephalus and decreases after shunt surgery.** *AJNR Am J Neuroradiol* 2019;40:453–59 CrossRef Medline
32. Hamilton RB, Scalzo F, Baldwin K, et al. **Opposing CSF hydrodynamic trends found in the cerebral aqueduct and prepontine cistern following shunt treatment in patients with normal pressure hydrocephalus.** *Fluids Barriers CNS* 2019;16:2–13 CrossRef Medline
33. Ziegelitz D, Starck G, Kristiansen D, et al. **Cerebral perfusion measured by dynamic susceptibility contrast MRI is reduced in patients with idiopathic normal pressure hydrocephalus.** *J Magn Reson Imaging* 2014;39:1533–42 CrossRef Medline
34. Ziegelitz D, Arvidsson J, Hellström P, et al. **Pre-and postoperative cerebral blood flow changes in patients with idiopathic normal pressure hydrocephalus measured by computed tomography (CT)-perfusion.** *J Cereb Blood Flow Metab* 2016;36:1755–66 CrossRef Medline
35. Ziegelitz D, Arvidsson J, Hellström P, et al. **In patients with idiopathic normal pressure hydrocephalus postoperative cerebral perfusion changes measured by dynamic susceptibility contrast magnetic resonance imaging correlate with clinical improvement.** *J Comput Assist Tomogr* 2015;39:531–40 CrossRef Medline
36. Engel DC, Adib SD, Schuhmann MU, et al. **Paradigm-shift: radiological changes in the asymptomatic iNPH-patient to be: An observational study.** *Fluids Barriers CNS* 2018;15:5 CrossRef Medline
37. Kimihira L, Iseki C, Takahashi Y, et al. **A multi-center, prospective study on the progression rate of asymptomatic ventriculomegaly with features of idiopathic normal pressure hydrocephalus on magnetic resonance imaging to idiopathic normal pressure hydrocephalus.** *J Neurol Sci* 2020;419:117166 CrossRef Medline
38. Suehiro T, Kazui H, Kanemoto H, et al. **Changes in brain morphology in patients in the preclinical stage of idiopathic normal pressure hydrocephalus.** *Psychogeriatrics* 2019;19:557–65 CrossRef Medline
39. Czepko R, Cieslicki K. **Repeated assessment of suspected normal pressure hydrocephalus in non-shunted cases: a prospective study based on the constant rate lumbar infusion test.** *Acta Neurochir (Wien)* 2016;158:855–63 CrossRef Medline
40. Wu D, Moghekar A, Shi W, et al. **Systematic volumetric analysis predicts response to CSF drainage and outcome to shunt surgery in idiopathic normal pressure hydrocephalus.** *Imaging Informatics and Artificial Intelligence.* <https://doi.org/10.1007/s00330-020-07531-z>. Accessed March 18, 2021
41. Rau A, Kim S, Yang S, et al. **SVM-based normal pressure hydrocephalus detection.** *Clin Neuroradiol* 2021 Jan 26. [Epub ahead of print] CrossRef
42. Irie R, Otsuka Y, Hagiwara A, et al. **A novel deep learning approach with a 3D convolutional ladder network for differential diagnosis of idiopathic normal pressure hydrocephalus and Alzheimer's Disease.** *Magn Reson Med Sci* 2020;19:351–58 CrossRef Medline

Decreased Craniocervical CSF Flow in Patients with Normal Pressure Hydrocephalus: A Pilot Study

S.M. Stöcklein, M. Brandlhuber, S.S. Lause, A. Pomschar, K. Jahn, R. Schniepp, N. Alperin, and B. Ertl-Wagner

ABSTRACT

BACKGROUND AND PURPOSE: Normal pressure hydrocephalus is characterized by systolic peaks of raised intracranial pressure, possibly due to a reduced compliance of the spinal CSF spaces. This concept of a reduced spinal CSF buffer function may be reflected by a low cervical CSF outflow from the cranium. The aim of this study was to investigate craniocervical CSF flow rates by phase-contrast MR imaging in patients with normal pressure hydrocephalus.

MATERIALS AND METHODS: A total of 42 participants were included in this prospective study, consisting of 3 study groups: 1) 10 patients with normal pressure hydrocephalus (mean age, 74 [SD, 6] years, with proved normal pressure hydrocephalus according to current scientific criteria); 2) eighteen age-matched healthy controls (mean age, 71 [SD, 5] years); and 3) fourteen young healthy controls (mean age, 21 [SD, 2] years, for investigation of age-related effects). Axial phase-contrast MR imaging was performed, and the maximal systolic CSF and total arterial blood flow rates were measured at the level of the upper second cervical vertebra and compared among all study groups (2-sample unpaired *t* test).

RESULTS: The maximal systolic CSF flow rate was significantly decreased in patients with normal pressure hydrocephalus compared with age-matched and young healthy controls (53 [SD, 40] mL/m; 329 [SD, 175] mL/m; 472 [SD, 194] mL/m; each *P* < .01), whereas there were no significant differences with regard to maximal systolic arterial blood flow (1160 [SD, 404] mL/m; 1470 [SD, 381] mL/m; 1400 [SD, 254] mL/m; each *P* > .05).

CONCLUSIONS: The reduced maximal systolic craniocervical CSF flow rate in patients with normal pressure hydrocephalus may be reflective of a reduced compliance of the spinal CSF spaces and an ineffective spinal CSF buffer function. Systolic craniocervical CSF flow rates are an easily obtainable MR imaging-based measure that may support the diagnosis of normal pressure hydrocephalus.

ABBREVIATIONS: ACB_{max} = maximal arterial blood flow rate to the brain during systole; CSF_{max} = maximal CSF flow rate from the brain to the spinal canal during systole; DESH = disproportionately enlarged subarachnoid space hydrocephalus; HC-M = age-matched healthy controls; HC-Y = healthy young controls; Ø = diameter; NPH = normal pressure hydrocephalus; VENC = velocity-encoding

Normal pressure hydrocephalus (NPH) is the most frequent form of hydrocephalus in elderly patients.¹ It is characterized by the clinical syndrome of progressive gait disturbance, cognitive deficits, and urinary incontinence, the so-called Hakim-Adams triad.¹ NPH has been shown to be responsive to CSF

shunting, with the likelihood of symptom improvement better in the early stages of the disorder,^{2,3} emphasizing the importance of an early diagnosis. However, the diagnosis of NPH remains a major challenge.

Typical imaging findings in NPH include ventricular enlargement with an Evans index of >0.31,⁴ a narrow callosal angle (<90°),⁵ periventricular high-signal changes representing transependymal cerebral fluid egress,^{6,7} tight sulci in the convexities of the cerebral hemispheres,⁸ and an enlarged Sylvian fissure (disproportionately enlarged subarachnoid space hydrocephalus [DESH] criteria).⁴

Phase-contrast MR imaging allows the quantification and characterization of pulsatile flow with high spatial and temporal resolution.⁹ Arterial inflow, venous outflow, and CSF flow to and from the brain can be quantified in relation to the cardiac cycle.⁹ Several studies have described higher CSF oscillations at the level

Received May 31, 2021; accepted after revision October 16.

From the Departments of Radiology (S.M.S., M.B.), Neurology, and Friedrich-Baur-Institute (FBI) of the Department of Neurology (K.J.), and Neurology (R.S.), Ludwig-Maximilians-University Munich, Munich, Germany; Department of Dermatology (S.S.L.), Bethesda Hospital, Freudenberg, Germany; Radiological Office (A.P.), Centre for Radiology, Munich, Germany; Department of Radiology (N.A.), University of Miami, Coral Gables, Florida; and Department of Medical Imaging (B.E.-W.), The Hospital for Sick Children, University of Toronto, Toronto, Ontario, Canada.

S.M. Stöcklein and M. Brandlhuber contributed equally to the study.

Please address correspondence to Martina Brandlhuber, MD, Department of Radiology, Ludwig-Maximilians-University Munich, Marchioninistr 15, 81377 Munich, Germany; e-mail: Martina.Brandlhuber@med.uni-muenchen.de
<http://dx.doi.org/10.3174/ajnr.A7385>

Table 1: Participant demographics

	NPH	HC-M	HC-Y
Study participants (No.)	10	18	14
Sex (female/male)	8/2	11/7	8/6
Age (mean) (min/max) (yr)	74 (SD, 6.2) (60/82)	71 (SD, 5.3) (60/86)	21 (SD, 1.7) (19/24)

Note:—Max indicates maximum; min, minimum.

of the aqueduct^{10–12} as well as lower total cerebral blood flow at the cervical level in patients with NPH.^{11,13,14}

The pathophysiology of NPH has not been fully elucidated. Chronic hypertension may cause periventricular ischemia,^{15,16} resulting in ventricular enlargement^{15,16} and reduced compliance of the CSF spaces.¹⁷ Periventricular ischemia may also locally increase venous resistance, leading to a decrease of CSF absorption, thereby further contributing to ventricular enlargement.¹⁸ New concepts have attributed the pathophysiology of NPH to abnormal dynamics of CSF and blood flow,^{19–23} including hyperdynamic CSF flow in the aqueduct, reduced cerebral blood flow,²² increased CSF pulse pressure, and pathologic conditions of CSF reabsorption.¹⁸ Despite the name, intracranial pressure is not always normal in NPH;²⁴ systolic peaks of raised intracranial pressure are frequently observed.²⁰ In healthy individuals, CSF outflow compensates for systolic intracranial volume peaks to avoid increased pressure.²⁴ In patients with NPH, the systolic intracranial pressure peaks may be due to a reduced compliance of the spinal CSF spaces, which may be reflected by an inefficient craniospinal CSF outflow. To our knowledge, craniospinal CSF flow in the upper cervical spine has not been assessed in patients with NPH.

We, therefore, aimed to investigate spinal craniospinal CSF flow rates in patients with NPH and compare them with those in age-matched and younger healthy controls. We hypothesized that craniospinal CSF outflow is reduced in patients with NPH as a sign of a lowered buffer function of the spinal CSF spaces. Moreover, we intended to provide an MR imaging–based tool that may help diagnose NPH using instrumental instead of clinical metrics.

MATERIALS AND METHODS

Subjects

Institutional review board (Ethics Committee of the Medical Department, LMU Munich) approval was obtained before the study, and all subjects provided written informed consent. A total of 42 study participants were included in this prospective study (for patient demographics see Table 1). We defined 3 study groups: 1) ten patients with proved NPH according to current scientific criteria (see more details below);^{25,26} 2) eighteen age-matched, healthy controls (HC-M); and 3) fourteen young healthy controls (HC-Y) for the investigation of age-related effects.

A detailed history of all participants was obtained with a special focus on neurologic and cardiovascular disorders. Exclusion criteria for all groups were MR imaging–based contraindications such as cardiac pacemakers, cochlear implants or other ferromagnetic implants; claustrophobia; and any severe non-neurologic disorder. Inclusion criteria were defined as group-specific for the NPH, HC-M, and HC-Y groups.

Before inclusion in the NPH group of the study, patients were diagnosed with NPH at the Department of Neurology at Ludwig-Maximilians-University of Munich. Diagnosis was based on clinical neurologic parameters, imaging parameters, and the lumbar tap test.

Neurologic parameters were evaluated by detailed neurologic examinations and tests. To evaluate the symptom complex of dementia, we performed several neurocognitive tests, including the Mini-Mental State Examination, psychomotor velocity during visual tracking, object recognition and naming, Verbal Learning and Recall Performance, Number Connection Test, and general linguistic competence. For assessment of gait instability, a 3D gait analysis was performed; gait pattern was analyzed by functional gait assessment, and both the Timed Up and Go test and the 10 Meter Walk Test were conducted. The symptom of urinary incontinence was identified by clinical anamnesis.

NPH was considered proved when a typical hypokinetic apractic gait disturbance was present, together with at least 1 more of the Hakim triad symptoms (dementia and/or urinary incontinence), along with no other reason for hydrocephalus and gait disturbance.

For evaluation of NPH imaging parameters, an initial CT of the brain was acquired and imaging features of NPH were assessed. NPH was considered proved if the following conditions were present: hydrocephalus with an Evans index of >0.3 , tight sulci in the convexities of the cerebral hemispheres, and an enlarged Sylvian fissure (DESH criteria⁴).

The lumbar tap test (removing 30 mL of CSF through a lumbar puncture) was performed before and after neurologic testing.

To verify NPH, positive findings on a lumbar tap test were necessary, ie, an objective improvement of gait instability after the lumbar tap test. This was defined as at least 20% improvement compared with the initial performance during gait analysis, in detail, $\geq 20\%$ increase of maximum walking speed measured for >10 m (10 Meter Walk Test). An objective improvement of dementia after the lumbar tap test was defined as at least 10% performance enhancement compared with the initial value during neuropsychological testing.

The inclusion criteria for the NPH group were a proved NPH diagnosed earlier at the Department of Neurology at Ludwig-Maximilians-University of Munich, a minimum of 60 years of age, and an insidious onset of symptoms with progression of symptoms during at least 3 months. The exclusion criterion for the NPH group was a secondary hydrocephalus (eg, after craniocerebral trauma or meningitis), whereas the presence of other neurologic diseases without potential influence on the development of hydrocephalus did not constitute an exclusion criterion (eg, tremor or dizziness; Table 2). For characteristics of patients with NPH, see Table 3.

The inclusion criterion for the HC-M group was a mean age (71 [SD, 5 years]) comparable with that of the patients in the NPH group (74 [SD, 6 years]). Exclusion criteria for the HC-M group were the simultaneous occurrence of at least 2 of the 3 symptoms of the Hakim triad and/or the presence of hydrocephalus. Other

exclusion criteria were diseases known to cause hydrocephalus (Table 2).

Inclusion criterion for the HC-Y group was 18–25 years of age; exclusion criteria were analogous to those of the HC-M group (Table 2).

MR Imaging and MR Imaging Flow Rates

Participants were imaged in the supine position, with legs slightly elevated to improve comfort, on a 3T MR imaging scanner (Magnetom Verio; Siemens). A phased-array head and neck coil with a total of 12 channels was used. A pulse oximeter was fixed onto the forefinger to synchronize the measurements with the cardiac cycle (R wave–triggered). MR imaging included both structural and flow MR imaging sequences.

Structural MR images consisted of an axial FLAIR sequence (TR = 7000 ms, TE = 94 ms, FOV = 250 × 175 mm², voxel size = 0.9 × 0.9 × 3.0 mm³) and a sagittal 3D MPRAGE sequence (TR = 11 ms, TE = 4.76 ms, FOV = 210 × 210 mm², voxel size = 1.0 × 1.0 × 0.7 mm³, integrated parallel acquisition techniques with acceleration factor = 2).

Flow imaging to measure hemo- and hydrodynamic parameters consisted of 2 retrospectively gated, velocity-encoded (VENC), cine phase-contrast sequences. To locate the correct positioning,

we used a sagittal phase-contrast 2D localizer with the following parameters: TR = 19.2 ms, TE = 5.1 ms, FOV = 200 × 200 mm², voxel size = 1.0 × 0.8 × 35 mm³. First, a high VENC (80 cm/s) axial sequence was acquired to quantify high-velocity blood flow in the internal carotid arteries and vertebral arteries. A second sequence with a low VENC (8–10 cm/s) was performed to quantify CSF flow. As suggested by Tain et al,²⁷ measurements were obtained at the level of C2, with an orientation perpendicular to the main 4 arteries (left and right internal carotid and vertebral arteries) for the high-VENC sequence and perpendicular to the spinal canal for the low-VENC sequence. Sequence parameters were as follows: TR = 40.25 ms, TE = 7.19 ms, FOV = 130 × 110 mm², voxel size = 0.8 × 0.5 × 6.0 mm³. Phase-contrast imaging was performed for 32 heart cycles and took about 3 minutes, with discrete differences due to the individual heart rates of the study participants.

Postprocessing and Data Analysis

Details of the MR imaging–based measurements of arterial inflow and CSF flow to and from the brain have been described previously.²⁸ In brief, time-dependent volumetric flow rates were calculated by integrating the flow velocities within the luminal cross-sectional areas over all 32 phase-contrast images representing 1 cardiac cycle. This calculation was performed using the semiautomated pulsatility-based lumen-segmentation method to decrease variability.²⁹ Absolute flow rates were obtained for the 4 main cervical arteries (left and right internal carotid arteries; left and right vertebral arteries).

The following volumetric flow rates were defined and calculated for all participants: 1) the maximal CSF flow rate from the brain to the spinal canal during systole (CSF_{max}); and 2) the maximal arterial blood flow rate to the brain during systole (ACB_{max}). Figure 1A, -B provides an example of blood and CSF flow VENC images. All analyses were performed with MRICP software, Version 1.4.35 (Alperin Noninvasive Diagnostics).

To determine the relationship between arterial blood inflow (ACB_{max}) and CSF outflow (CSF_{max}), we calculated the ratio between both parameters for all study groups (CSF_{max}/ACB_{max}).

In addition, the minimal diameter (Ø) of the spinal canal was measured in a midsagittal MPRAGE image at the level of the intervertebral space between the second and third upper cervical vertebrae (Ø_{C2/C3}), (Fig 1C). To define the impact of spinal width on the maximal CSF outflow during systole (CSF_{max}), we performed correlation analysis between both parameters (CSF_{max} and Ø_{C2/C3}).

Statistical Analysis

Statistical analyses were performed using SPSS 17.0 for Windows (IBM) and Matlab (MathWorks). The independence of variables was validated by the χ^2 test. Group differences were analyzed using the 2-sample unpaired *t* test. Correlation analysis was performed using the Pearson correlation

Table 2: Comorbidities of participants^a

Study Group	NPH	HC-M	HC-Y
Arterial hypertension	5/10	6/18	0/14
Arteriovenous malformation	0/10	0/18	2/14
Atrial fibrillation	0/10	2/18	0/14
Headaches	0/10	1/18	1/14
Coronary heart disease	2/10	0/18	0/14
Dizziness	1/10	0/18	0/14
Meningioma ^b	0/10	1/18	0/14
Microangiopathy	1/10	1/18	0/14
Multiple sclerosis	0/10	0/18	4/14
Orthostatic tremor	1/10	0/18	0/14
Peripheral arterial disease	1/10	0/18	0/14
Restless leg syndrome	0/10	1/18	0/14
Seizure disorder	1/10	0/18	1/14
Prior stroke	1/10	3/18	0/14
History of syncope	0/10	1/18	0/14
History of transient ischemic attack	0/10	2/18	0/14

^aData are number of patients per study group.

^bThe meningioma measured 1.2 cm at the maximum.

Table 3: Characteristics of patients with NPH

	Characteristics	No. of Patients
Neurologic parameters (Hakim-Adams triad)	Gait disturbance	10/10
	Urinary incontinence	8/10
	Dementia ^a	8/10
Imaging parameters	Evans index >0.3	10/10
	DESH criteria	10/10
	Ventricular enlargement	6/10
	Signs of transependymal CSF diapedesis	6/10
Lumbar tap test ^b	Objective improvement of gait disturbance	10/10
	Objective improvement of cognitive function	7/10

^aSixty percent progressive disease (predominant impairment of short-term memory).

^bForty percent additionally received a tap test via a Yuohy needle lasting several days.

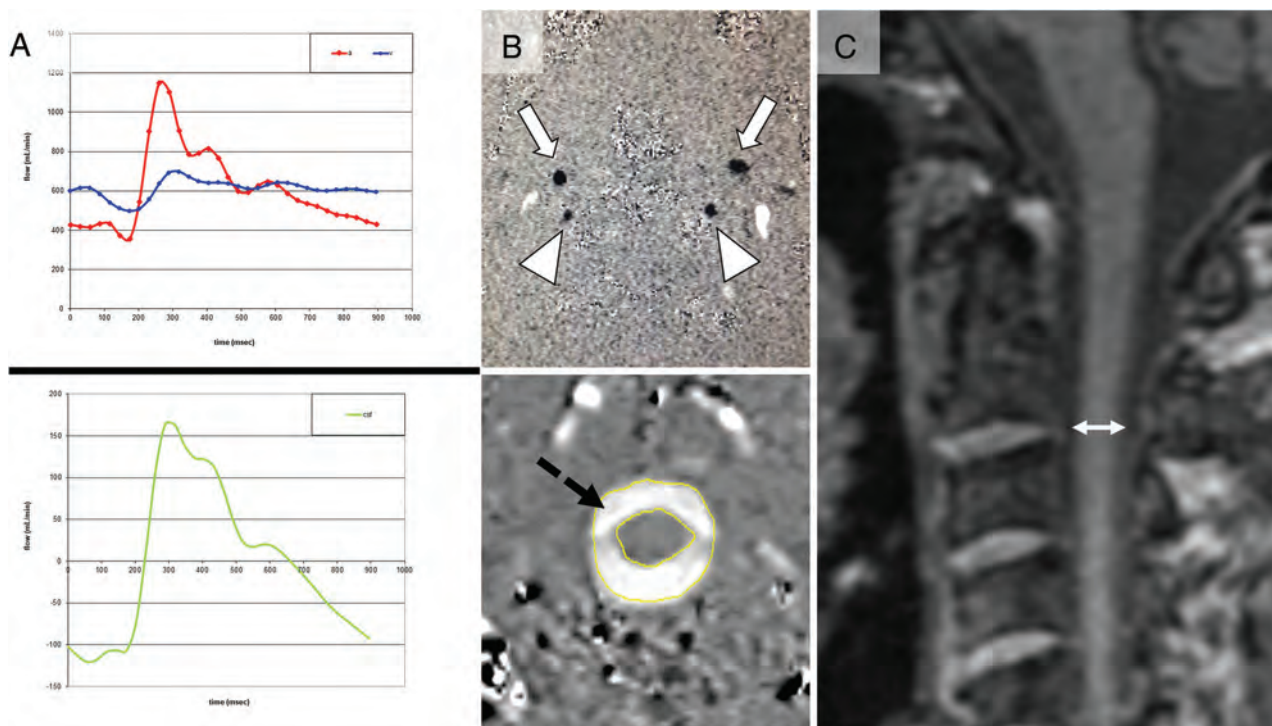


FIG 1. Measurement of CSF/blood flow and spinal canal width. **A**, Craniospinal blood and CSF flow (milliliter/minute) during the cardiac cycle across time (millisecond). The *upper panel* shows the blood flow. During each systole, arterial blood (red) flows into the cranium and venous blood flows in a cardiac direction; outflow is too slow to compensate the resulting increase in intracranial pressure. The *lower panel* shows the resulting fast CSF outflow (green) from the brain to the spinal CSF spaces to buffer pressure peaks. **B**, VENC phase-contrast MR images of blood and CSF. The *upper panel* demonstrates the blood flow through the internal carotid arteries (*arrows*) and vertebral arteries (*arrowheads*), and the internal jugular veins are represented by the *oval white spots* (not marked). The *lower panel* shows the flow of CSF (*black dashed arrow*) from the cranium to the spinal canal. Upward flow is black, while downward flow is white. **C**, Measurement (*double-sided arrow*) of the maximal diameter of the spinal canal in a midsagittal MPRAGE image at the level of the intervertebral space between the second and third upper cervical vertebrae ($\varnothing_{C2/C3}$) is shown.

coefficient. Data are presented as mean (SD). $P < .05$ was considered statistically significant.

RESULTS

Baseline Characteristics

Forty-two participants were included (27 women/15 men). The NPH group consisted of 10 participants (8 women/2 men); the HC-M group, 18 participants (11 women/7 men); and the HC-Y group, 14 participants (8 women/6 men). There was no significant difference between the ages of men compared with female participants for all groups, and there was no significant difference in age between the NPH and HC-M groups. For patient demographics, see Table 1; the comorbidities of the study participants are shown in Table 2. For characteristics of patients with NPH, see Table 3.

CSF_{max} from the Brain

The CSF_{max} was significantly different among the 3 study groups. Compared with the HC-M group, the mean CSF_{max} was significantly decreased in patients with NPH (NPH, 53 [SD, 40] mL/m, versus HC-M, 329 [SD, 175] mL/m; $P < .01$). Moreover, mean CSF_{max} was significantly diminished in the HC-M group compared with the HC-Y group (472 [SD, 194] mL/m, versus HC-M, 329 [SD, 175] mL/m; $P < .05$; Fig 2A).

ACB_{max}

The mean ACB_{max} was not significantly different among the 3 study groups. ACB_{max} was 1160 (SD, 404) mL/m for patients with NPH, 1470 (SD, 381) mL/m for the HC-M group, and 1400 (SD, 254) mL/m for the HC-Y group (each, $P > .05$; Fig 2B).

CSF_{max}/ACB_{max}

To account for a potential impact of ACB_{max} on CSF_{max}, we calculated the ratio between both parameters for all study groups (CSF_{max}/ACB_{max}). CSF_{max}/ACB_{max} was different among the 3 study groups. The CSF_{max}/ACB_{max} was significantly decreased in patients with NPH compared with the age-matched healthy controls (mean NPH, 0.1 [SD, 0.1], versus HC-M, 0.2 [SD, 0.1]; $P < .05$). Moreover, the CSF_{max}/ACB_{max} was significantly diminished in the HC-M group compared with the HC-Y group: 0.3 (SD, 0.1), versus HC-M, 0.2 (SD, 0.1); $P < .05$; Fig 2C).

Minimal Diameter of the Spinal Canal

The minimal midsagittal diameter of the spinal canal ($\varnothing_{C2/C3}$) was different among the 3 study groups. Compared with HC-M, the $\varnothing_{C2/C3}$ was significantly decreased in patients with NPH (NPH, 1.25 [SD, 0.16] cm, versus HC-M, 1.36 [SD, 0.12] cm; $P < .05$). The minimal diameter of the spinal canal ($\varnothing_{C2/C3}$) was significantly larger in HC-Y compared with both HC-M and patients with NPH (HC-Y, 1.48 [SD, 0.08] cm, versus HC-M,

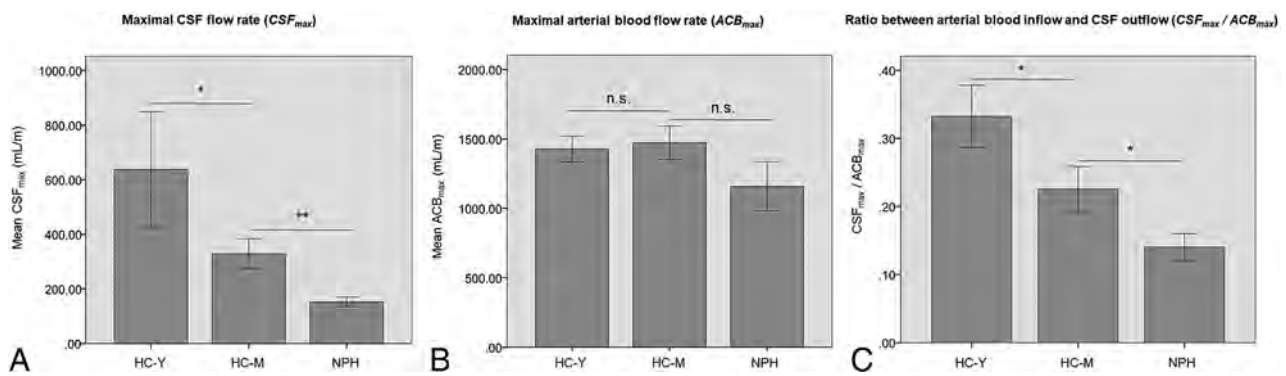


FIG 2. CSF_{max} , ACB_{max} , and the ratio between both parameters (CSF_{max}/ACB_{max}). A, Maximal CSF flow rate (CSF_{max}) in milliliter/minute. B, ACB_{max} in milliliter/minute. C, Ratio between arterial blood inflow and CSF outflow (CSF_{max}/ACB_{max}). The asterisk indicates $P < .05$; double asterisks, $P < .01$; n.s., not significant.

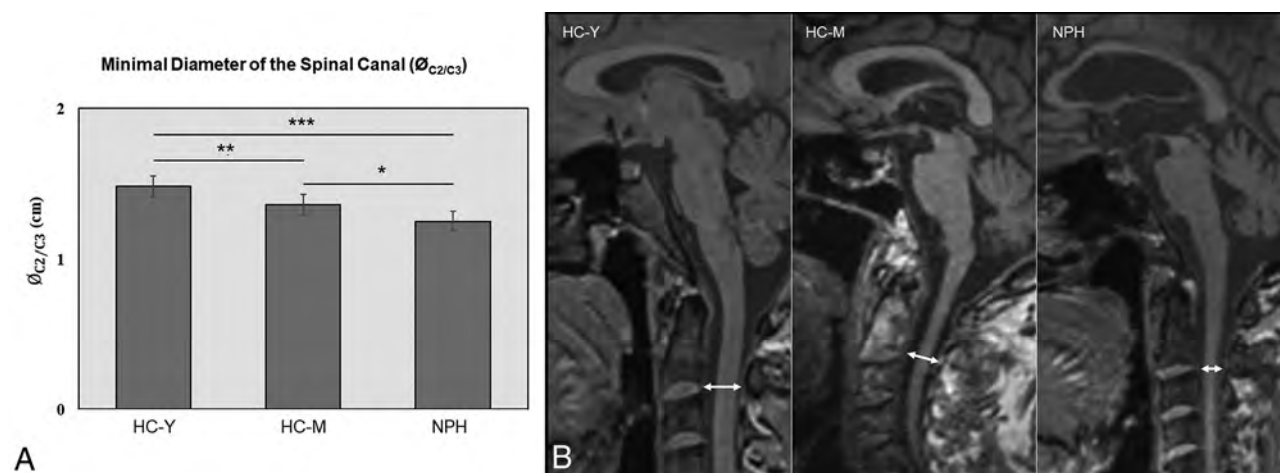


FIG 3. Minimal diameter of the spinal canal ($\phi_{C2/C3}$). A, Minimal diameter of the spinal canal ($\phi_{C2/C3}$) in centimeters. B, Representative MR images (midsagittal T1-weighted image) to measure the minimal diameter of the spinal canal at the level of the intervertebral space between the second and third upper cervical vertebrae (double-sided arrow). The left panel shows an image of an HC-Y, the middle panel shows an HC-M, and the right panel shows an image of a patient with NPH. The asterisk indicates $P < .05$; double asterisks, $P < .01$; triple asterisks, $P < .001$.

1.36 [SD, 0.12] cm; $P < .01$; HC-Y, 1.48 [SD, 0.08] cm, versus NPH, 1.25 [SD, 0.16] cm; $P < .001$) (Fig 3).

Correlation between Spinal Canal Diameter and Maximal CSF Outflow

To define the impact of spinal width on CSF_{max} , we performed a correlation analysis between CSF_{max} and $\phi_{C2/C3}$, and a significantly positive correlation between CSF_{max} and $\phi_{C2/C3}$ was found, showing a lower CSF_{max} with lower spinal diameter ($R = 0.47$; $P < .05$; Fig 4).

DISCUSSION

In this study, we demonstrated a lower CSF_{max} in patients with NPH compared with both age-matched and younger controls, which suggests a lower Windkessel effect and dampening of pulsations of the spinal CSF spaces. Physiologically, craniospinal CSF outflow compensates for systolic intracranial pressure peaks due to pulsatile arterial inflow.²⁴ Our results support new concepts that attribute the pathophysiology of NPH to abnormal dynamics of CSF and blood flow,^{19–23} especially the concept of a

reduced spinal CSF buffer function, represented by a low cervical CSF outflow.

The observed reduction of spinal CSF_{max} in patients with NPH could theoretically be due to a reduced arterial inflow to the brain during systole. However, our results of a reduced CSF_{max} in patients with NPH compared with HC-M and HC-Y remained significant, even when accounting for the potential effect of decreased arterial inflow in patients with NPH. The reduction of CSF_{max} in patients with NPH, therefore, exceeded the expected age-related changes. CSF_{max} could be a direct measure for the reduced compliance of spinal CSF spaces, ie, a reduced spinal buffer function or Windkessel effect, with the systolic peaks of intracranial pressure in patients with NPH not being compensated by CSF outflow. Our results complement the results of earlier studies on compliance of vessels and craniospinal CSF spaces.^{30,31} These prior studies attributed the reduction of cervical CSF pulsations to an arterial loss of pulsatility³¹ and assumed the reduced cervical CSF flow to be a consequence of a decreased arterial expansion due to pathologic changes of arteries and perivascular spaces.³⁰ Recent investigations were able to show that respiration

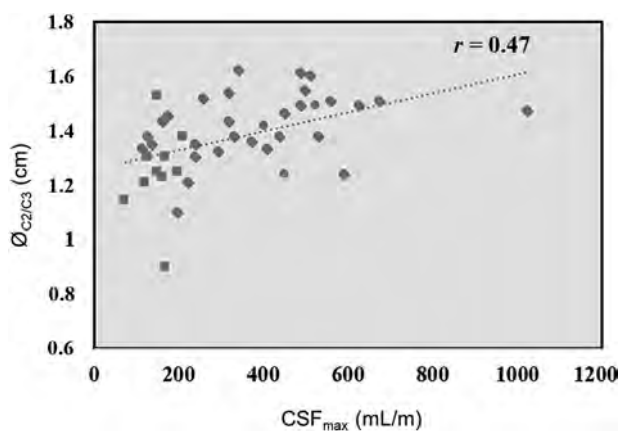


FIG 4. The relationship between spinal canal width and maximal CSF flow. Correlation analysis shows a positive correlation between CSF_{max} and $\varnothing_{C2/C3}$ ($r = 0.47$; $P < .05$).

and the cardiac cycle affect CSF flow at the cervical level.³²⁻³⁴ Besides these influences, a general variation in the direction and magnitude of CSF flow is known to occur in both healthy individuals and patients with NPH,^{35,36} with a redirection³⁵ and mainly retrograde (ie, toward the ventricles) aqueductal flow³⁶ and a cranially directed CSF net flow at the craniocervical junction³⁶ in patients with NPH.

Another new concept that attributes the pathophysiology of NPH to abnormal CSF is that of a hyperdynamic CSF flow in the aqueduct.¹⁹⁻²³ Prior studies analyzed the relation between aqueductal CSF flow and the clinical response to the shunting procedure,^{37,38} demonstrating that aqueductal CSF flow was not able to reliably predict clinical improvement after shunt implantation.^{39,40} Aqueductal CSF flow seems to be strongly correlated with ventricular morphology,⁴¹ showing higher aqueductal CSF oscillations in patients with NPH.¹⁰⁻¹² The lower craniospinal CSF_{max} in patients with NPH observed in our study might correspond to a higher CSF volume in the aqueduct, resulting in a higher oscillatory flow.¹⁰⁻¹² The higher CSF volume in the aqueduct¹⁰⁻¹² may be the consequence of a reduced Windkessel effect of the superior spinal CSF spaces, with CSF outflow from the brain being inefficient to buffer systolic intracranial pressure peaks.

Prior studies have investigated the age dependency of CSF flow values,^{14,31,42-45} demonstrating age dependence of CSF flow parameter,^{14,45} with significantly reduced CSF stroke volumes in the elderly.³¹ However, Lokossou et al⁴⁴ suggested that aging mainly changes cerebral blood flow but preserves blood and CSF interactions, with an age-independent positive correlation between blood and CSF stroke volumes. Our results show a significantly lower CSF_{max} from the brain during systole in older participants compared with young healthy controls ($P < .05$), confirming prior results on age dependency of CSF flow. Additionally, our results show a lower CSF_{max} in patients with NPH compared with age-matched healthy controls, suggesting that the reduction of maximal craniospinal CSF flow in patients with NPH exceeds age-related changes. Our results complement the findings of Abdalla et al,⁴² who differentiated patients with NPH from control subjects with mere age-related brain atrophy based on diverse CSF flow dynamics at the level of the aqueduct.

In our study, the diameter of the spinal canal at the level C2/C3 ($\varnothing_{C2/C3}$) was decreased in patients with NPH compared with both HC-M and HC-Y, and there was a positive correlation between the craniospinal CSF_{max} and $\varnothing_{C2/C3}$. The narrowing of the spinal canal may lead to a blocked craniospinal CSF flow with a reduced dampening of pulse pressure waves. This possibility could explain both the higher aqueductal CSF oscillations in patients with NPH¹⁰⁻¹² and the reduced craniospinal CSF_{max} . The spinal canal narrowing in patients with NPH may be secondary to degenerative changes that may involve hypertrophy and calcification of the ligaments, intervertebral discs, and osseous tissue.⁴⁶ Further studies are necessary to corroborate our findings and evaluate degenerative changes and spinal canal narrowing in patients with NPH.

There are several limitations to our study that need to be considered when interpreting the data. First, our sample sizes are limited. This was at least, in part, due to strict inclusion criteria for the NPH group, requiring at least 2 of the 3 symptoms of the Hakim triad and positive findings on a lumbar tap test without any indication for secondary hydrocephalus. We, nevertheless, were able to demonstrate a significantly reduced CSF_{max} in patients with NPH. Further studies with larger sample sizes will be needed to confirm our results. Second, diagnosing NPH remains challenging, and even with positive findings on a lumbar tap test, some risk of erroneously included patients remains. Finally, we assessed only the diameter of the spinal canal at the level of C2/C3. Further studies are needed to investigate additional spinal canal narrowing in lower segments.

CONCLUSIONS

We observed a reduction of maximal craniospinal CSF flow in patients with NPH compared with HC-M. This effect exceeded age-related changes of CSF flow and remained significant, even when accounting for differential arterial blood flow rates. A reduced compliance of spinal CSF spaces may play an important role in the etiopathogenesis of NPH. Systolic craniospinal CSF flow rates are an easily obtainable MR imaging-based measure that may support the diagnosis of NPH.

Disclosure forms provided by the authors are available with the full text and PDF of this article at www.ajnr.org.

REFERENCES

- Adams RD, Fisher CM, Hakim S, et al. **Symptomatic occult hydrocephalus with "normal" cerebrospinal-fluid pressure: a treatable syndrome.** *N Engl J Med* 1965;273:117-26 CrossRef Medline
- Graff-Radford NR, Godersky JC, Jones MP. **Variables predicting surgical outcome in symptomatic hydrocephalus in the elderly.** *Neurology* 1989;39:1601-04 CrossRef Medline
- Marmarou A, Young HF, Aygok GA, et al. **Diagnosis and management of idiopathic normal-pressure hydrocephalus: a prospective study in 151 patients.** *J Neurosurg* 2005;102:987-97 CrossRef Medline
- Kitagaki H, Mori E, Ishii K, et al. **CSF spaces in idiopathic normal pressure hydrocephalus: morphology and volumetry.** *AJNR Am J Neuroradiol* 1998;19:1277-84 Medline
- Virhammar J, Laurell K, Cesarini KG, et al. **The callosal angle measured on MRI as a predictor of outcome in idiopathic normal-pressure hydrocephalus.** *J Neurosurg* 2014;120:178-84 CrossRef Medline

6. Ghosh S, Lippa C. **Diagnosis and prognosis in idiopathic normal pressure hydrocephalus.** *Am J Alzheimers Dis Other Dement* 2014;29:583–89 CrossRef Medline
7. Iddon JL, Pickard JD, Cross JJ, et al. **Specific patterns of cognitive impairment in patients with idiopathic normal pressure hydrocephalus and Alzheimer's disease: a pilot study.** *J Neurol Neurosurg Psychiatry* 1999;67:723–32 CrossRef Medline
8. Bradley WG, Whittemore AR, Kortman KE Jr, et al. **Marked cerebrospinal fluid void: indicator of successful shunt in patients with suspected normal-pressure hydrocephalus.** *Radiology* 1991;178:459–66 CrossRef Medline
9. Lee VS, Spritzer CE, Carroll BA, et al. **Flow quantification using fast cine phase-contrast MR imaging, conventional cine phase-contrast MR imaging, and Doppler sonography: in vitro and in vivo validation.** *AJR Am J Roentgenol* 1997;169:1125–31 CrossRef Medline
10. El Sankari S, Fichten A, Gondry-Jouet C, et al. **Correlation between tap test and CSF aqueductal stroke volume in idiopathic normal pressure hydrocephalus.** *Acta Neurochir Suppl* 2012;113:43–46 CrossRef Medline
11. El Sankari S, Gondry-Jouet C, Fichten A, et al. **Cerebrospinal fluid and blood flow in mild cognitive impairment and Alzheimer's disease: a differential diagnosis from idiopathic normal pressure hydrocephalus.** *Fluids Barriers CNS* 2011;8:12 CrossRef Medline
12. Shanks J, Markenroth Bloch K, Laurell K, et al. **Aqueductal CSF stroke volume is increased in patients with idiopathic normal pressure hydrocephalus and decreases after shunt surgery.** *AJNR Am J Neuroradiol* 2019;40:453–59 CrossRef Medline
13. Buijs PC, Krabbe-Hartkamp MJ, Bakker CJ, et al. **Effect of age on cerebral blood flow: measurement with ungated two-dimensional phase-contrast MR angiography in 250 adults.** *Radiology* 1998;209:667–74 CrossRef Medline
14. Schmid Daners M, Knobloch V, Soellinger M, et al. **Age-specific characteristics and coupling of cerebral arterial inflow and cerebrospinal fluid dynamics.** *PLoS One* 2012;7:e37502 CrossRef Medline
15. Bradley WG, Whittemore AR, Watanabe AS Jr, et al. **Association of deep white matter infarction with chronic communicating hydrocephalus: implications regarding the possible origin of normal-pressure hydrocephalus.** *AJNR Am J Neuroradiol* 1991;12:31–39 Medline
16. Ritter S, Dinh TT. **Progressive postnatal dilation of brain ventricles in spontaneously hypertensive rats.** *Brain Res* 1986;370:327–32 CrossRef Medline
17. Boon AJ, Tans JT, Delwel EJ, et al. **Dutch Normal-Pressure Hydrocephalus Study: the role of cerebrovascular disease.** *J Neurosurg* 1999;90:221–26 CrossRef Medline
18. Bradley WG. **Normal pressure hydrocephalus: new concepts on etiology and diagnosis.** *AJNR Am J Neuroradiol* 2000;21:1586–90 Medline
19. Kuriyama N, Tokuda T, Miyamoto J, et al. **Retrograde jugular flow associated with idiopathic normal pressure hydrocephalus.** *Ann Neurol* 2008;64:217–21 CrossRef Medline
20. Qvarlander S, Lundkvist B, Koskinen LO, et al. **Pulsatility in CSF dynamics: pathophysiology of idiopathic normal pressure hydrocephalus.** *J Neurol Neurosurg Psychiatry* 2013;84:735–41 CrossRef Medline
21. Bateman GA. **Vascular compliance in normal pressure hydrocephalus.** *AJNR Am J Neuroradiol* 2000;21:1574–85 Medline
- 22.owler BK, Pickard JD. **Normal pressure hydrocephalus and cerebral blood flow: a review.** *Acta Neurol Scand* 2001;104:325–42 CrossRef Medline
23. Silverberg GD. **Normal pressure hydrocephalus (NPH): ischaemia, CSF stagnation or both.** *Brain* 2004;127:947–48 CrossRef Medline
24. Shprecher D, Schwab J, Kurlan R. **Normal pressure hydrocephalus: diagnosis and treatment.** *Curr Neurol Neurosci Rep* 2008;8:371–76 CrossRef Medline
25. Nakajima M, Yamada S, Miyajima M, et al; research committee of idiopathic normal pressure hydrocephalus. **Guidelines for Management of Idiopathic Normal Pressure Hydrocephalus (Third Edition): endorsed by the Japanese Society of Normal Pressure Hydrocephalus.** *Neurol Med Chir (Tokyo)* 2021;61:63–97 CrossRef Medline
26. Williams MA, Relkin NR. **Diagnosis and management of idiopathic normal-pressure hydrocephalus.** *Neurol Clin Pract* 2013;3:375–85 CrossRef Medline
27. Tain RW, Ertl-Wagner B, Alperin N. **Influence of the compliance of the neck arteries and veins on the measurement of intracranial volume change by phase-contrast MRI.** *J Magn Reson Imaging* 2009;30:878–83 CrossRef Medline
28. Alperin N, Mazda M, Lichter T, et al. **From cerebrospinal fluid pulsation to noninvasive intracranial compliance and pressure measured by MRI flow studies.** *Current Medical Imaging Reviews* 2006;2:117–29 CrossRef
29. Alperin N, Lee SH. **PUBS: Pulsatility-based segmentation of lumens conducting non-steady flow.** *Magn Reson Med* 2003;49:934–44 CrossRef Medline
30. Greitz D, Hannerz J, Rahn T, et al. **MR imaging of cerebrospinal fluid dynamics in health and disease: on the vascular pathogenesis of communicating hydrocephalus and benign intracranial hypertension.** *Acta Radiology* 1994;35:204–211 Medline
31. Stoquart-ElSankari S, Balédent O, Gondry-Jouet C, et al. **Aging effects on cerebral blood and cerebrospinal fluid flows.** *J Cereb Blood Flow Metab* 2007;27:1563–72 CrossRef Medline
32. Daouk J, Bouzerar R, Baledent O. **Heart rate and respiration influence on macroscopic blood and CSF flows.** *Acta Radiol* 2017;58:977–82 CrossRef Medline
33. Dreha-Kulaczewski S, Konopka M, Joseph AA, et al. **Respiration and the watershed of spinal CSF flow in humans.** *Sci Rep* 2018;8:5594 CrossRef Medline
34. Vinje V, Ringstad G, Lindström EK, et al. **Respiratory influence on cerebrospinal fluid flow - a computational study based on long-term intracranial pressure measurements.** *Sci Rep* 2019;9:9732 CrossRef Medline
35. Eide PK, Valnes LM, Lindström EK, et al. **Direction and magnitude of cerebrospinal fluid flow vary substantially across central nervous system diseases.** *Fluids Barriers CNS* 2021;18:16 CrossRef Medline
36. Lindström EK, Ringstad G, Mardal KA, et al. **Cerebrospinal fluid volumetric net flow rate and direction in idiopathic normal pressure hydrocephalus.** *Neuroimage Clin* 2018;20:731–41 CrossRef Medline
37. Bradley WG, Scalzo D, Queralt J Jr, et al. **Normal-pressure hydrocephalus: evaluation with cerebrospinal fluid flow measurements at MR imaging.** *Radiology* 1996;198:523–29 CrossRef Medline
38. Sharma AK, Gaikwad S, Gupta V, et al. **Measurement of peak CSF flow velocity at cerebral aqueduct, before and after lumbar CSF drainage, by use of phase-contrast MRI: utility in the management of idiopathic normal pressure hydrocephalus.** *Clin Neurol Neurosurg* 2008;110:363–68 CrossRef Medline
39. Dixon GR, Friedman JA, Luetmer PH, et al. **Use of cerebrospinal fluid flow rates measured by phase-contrast MR to predict outcome of ventriculoperitoneal shunting for idiopathic normal-pressure hydrocephalus.** *Mayo Clin Proc* 2002;77:509–14 CrossRef Medline
40. Blitz AM, Shin J, Balédent O, et al. **Does phase-contrast imaging through the cerebral aqueduct predict the outcome of lumbar CSF drainage or shunt surgery in patients with suspected adult hydrocephalus?** *AJNR Am J Neuroradiol* 2018;39:2224–30 CrossRef Medline
41. Chiang WW, Takoudis CG, Lee SH, et al. **Relationship between ventricular morphology and aqueductal cerebrospinal fluid flow in healthy and communicating hydrocephalus.** *Invest Radiol* 2009;44:192–99 CrossRef Medline
42. Abdalla RN, Ghani Zghair MA. **The role of magnetic resonance imaging cerebrospinal fluid flowmetry in differentiation between normal flow hydrocephalus and involutional brain atrophy.** *J Pak Med Assoc* 2019;69:S78–82 Medline

43. Di Palma C, Goulay R, Chagnot S, et al. **Cerebrospinal fluid flow increases from newborn to adult stages.** *Dev Neurobiol* 2018;78:851–58 CrossRef Medline
44. Lokossou A, Metanbou S, Gondry-Jouet C, et al. **Extracranial versus intracranial hydro-hemodynamics during aging: a PC-MRI pilot cross-sectional study.** *Fluids Barriers CNS* 2020;17:1 CrossRef Medline
45. Sartoretti T, Wyss M, Sartoretti E, et al. **Sex and age dependencies of aqueductal cerebrospinal fluid dynamics parameters in healthy subjects.** *Front Aging Neurosci* 2019;11:19 CrossRef Medline
46. Moghaddamjou A, Badhiwala JH, Fehlings MG. **Degenerative cervical myelopathy: changing frontiers.** *World Neurosurg* 2020;135:377–78 CrossRef Medline

Lesion Volume in Relapsing Multiple Sclerosis is Associated with Perivascular Space Enlargement at the Level of the Basal Ganglia

S.C. Kolbe, L.M. Garcia, N. Yu, F.M. Boonstra, M. Clough, B. Sinclair, O. White, A. van der Walt, H. Butzkueven, J. Fielding, and M. Law

ABSTRACT

BACKGROUND AND PURPOSE: Perivascular spaces surround the blood vessels of the brain and are involved in neuroimmune functions and clearance of metabolites via the glymphatic system of the brain. Enlarged perivascular spaces could be a marker of dysfunction in these processes and, therefore, are highly relevant to monitoring disease activity in MS. This study aimed to compare the number of enlarged perivascular spaces in people with relapsing MS with MR imaging markers of inflammation and brain atrophy.

MATERIALS AND METHODS: Fifty-nine patients (18 with clinically isolated syndrome, 22 with early and 19 with late relapsing-remitting MS) were scanned longitudinally (mean follow-up duration = 19.6 [SD, 0.5] months) using T2-weighted, T1-weighted, and FLAIR MR imaging. Two expert raters identified and counted enlarged perivascular spaces on T2-weighted MR images from 3 ROIs (the centrum semiovale, basal ganglia, and midbrain). Baseline and change with time in the number of enlarged perivascular spaces were correlated with demographics and lesion and brain volumes.

RESULTS: Late relapsing-remitting MS had a greater average number of enlarged perivascular spaces at baseline at the level of the basal ganglia (72.3) compared with early relapsing-remitting MS (60.5) and clinically isolated syndrome (54.7) ($F = 3.4$, $P = .042$), and this finding correlated with lesion volume ($R = 0.44$, $P = .0004$) but not brain atrophy ($R = -0.16$). Enlarged perivascular spaces increased in number with time in all regions, and the rate of increase did not differ among clinical groups.

CONCLUSIONS: Enlarged perivascular spaces at the level of the basal ganglia are associated with greater neuroinflammatory burden, and the rate of enlargement appears constant in patients with relapsing-remitting disease phenotypes.

ABBREVIATIONS: BPF = brain parenchymal fraction; CIS = clinically isolated syndromes; EDSS = Expanded Disability Status Scale; ePVS = enlarged perivascular spaces; PVS = perivascular spaces; RRMS = relapsing-remitting MS

MS is a chronic autoimmune-mediated neuroinflammatory condition associated with neurodegeneration and progressive neurologic disability. The disease course is highly heterogeneous, likely relating to genetic, lifestyle, and treatment variations. There is currently a search for biologic markers for pathophysiologic changes in the brain that are associated with poorer relapse recovery and more rapid disease progression. Such

markers will be useful as outcome measures in treatment trials and for patient monitoring and prognostication.

Perivascular spaces (PVS), also known as Virchow-Robin spaces, are pial-lined, fluid-filled structures that ensheath vessels entering (penetrating arteries) or leaving (draining veins) brain tissue.^{1,2} Due to the extensive vascularity of the brain, PVS occupy a significant proportion of the cerebral volume. Normally, they are visible on MR imaging in 3 characteristic locations: 1) the centrum semiovale penetrating the subcortical white matter, 2) surrounding lenticulostriate arteries entering the basal ganglia, and 3) the midbrain.³ Because PVS are small and usually difficult to identify on clinical MR imaging due to limitations in spatial resolution, increased numbers of PVS are commonly considered to reflect enlargement of the PVS. Previously, enlarged PVS (ePVS) were radiologically classed as incidental findings without pathologic significance⁴ or merely related to aging⁵⁻⁷ but, more recently, have been posited as pathologic markers in the context of cerebral vascular disease

Received April 13, 2021; accepted after revision October 19.

From the Department of Neuroscience (S.C.K., L.M.G., N.Y., F.M.B., M.C., B.S., O.W., A.v.d.W., H.B., J.F., M.L.) Monash University, Melbourne, Victoria, Australia; Departments of Radiology (S.C.K., M.L.) and Neurology (O.W., A.v.d.W., H.B.), Alfred Hospital, Melbourne, Victoria, Australia; and Department of Neurology (N.Y.), The Nanjing Brain Hospital Affiliated with Nanjing Medical University, Nanjing, Jiangsu, China.

Please address correspondence to Scott Kolbe, MD, Department of Neuroscience, Central Clinical School, Monash University, Level 6, 99 Commercial Rd, Prahran, 3181, Victoria, Australia; e-mail: scott.kolbe@monash.edu; @scott_kolbe

Indicates article with online supplemental data.

<http://dx.doi.org/10.3174/ajnr.A7398>

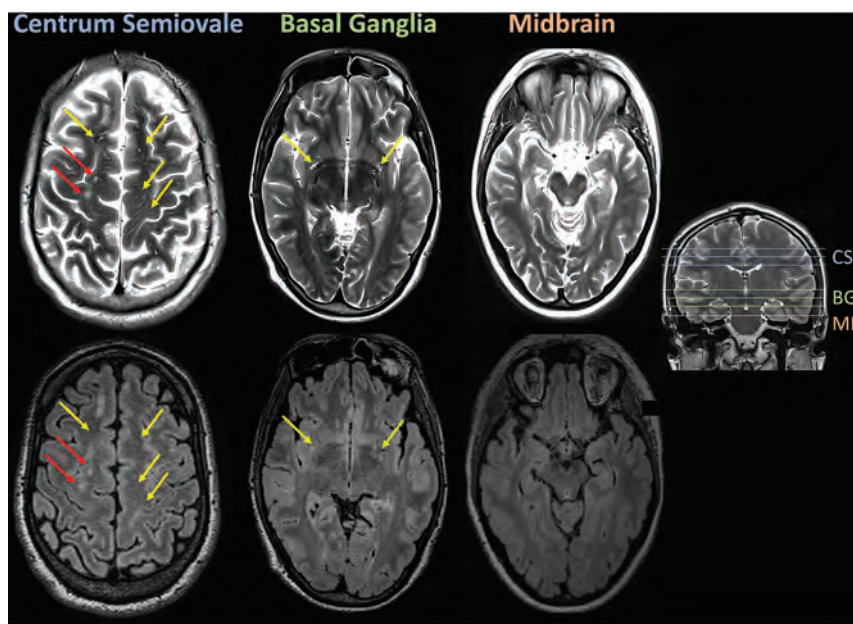


FIG 1. Scans from a sample patient data set illustrating the 3 regions of the brain that were selected for counting ePVS: the centrum semiovale (CS), basal ganglia (BG), and midbrain (MB). PVS were counted if they were evident on T2 (*upper row*) but absent on FLAIR (*lower row*) (*yellow arrows*). Lesions (*red arrows*) were identified as hyperintensities on both T2 and FLAIR.

and dementia.^{4,8-10} More specifically, dilation of the PVS could indicate perivascular inflammation¹¹ or impaired waste clearance to the glial-lymphatic system.^{12,13}

There has been significant interest in exploring ePVS in people with MS, as well as correlations between ePVS and other disease features to better understand what drives ePVS in MS. Previous studies in MS have demonstrated that increased numbers of MR imaging-visible PVS indicative of ePVS are associated with the onset of disease,¹⁴ new lesions,^{11,15} clinical disability,^{16,17} and atrophy.¹⁸ While the relationship between ePVS and lesion load suggests that ePVS are associated with neuroinflammatory burden, the relationship between ePVS and atrophy could merely reflect contraction of the brain parenchyma associated with cerebral atrophy, similar to sulcal and ventricular enlargement. Therefore, this study aimed to evaluate the following: 1) the radiologic disease features (neuroinflammation and/or brain atrophy) that best correlate with the number of ePVS, 2) the rate at which ePVS appear with time, and 3) potential differences in the number of ePVS in different relapsing-remitting disease phenotypes (clinically isolated syndromes [CIS] and early/late relapsing-remitting MS [RRMS]). On the basis of the hypothesis that ePVS are associated with inflammatory burden rather than parenchymal retraction, we expected that the number of ePVS would be positively associated with lesion load (commensurate with increased inflammatory activity) but not atrophy (commensurate with parenchymal retraction). We also expected that ePVS would increase in number with time, and that the number of ePVS gained across time would be associated with the increase in lesion volume. Finally, we expected that ePVS would be more prevalent in subjects at more advanced disease stages.

MATERIALS AND METHODS

Subjects and Clinical Assessments

Fifty-nine patients were recruited to the study and underwent clinical MR imaging sessions as part of their routine clinical care from December 2010 to October 2014. Patients were categorized into 3 groups based on clinical diagnostic criteria¹⁹ and disease duration at baseline: 1) CIS ($n = 18$; mean age = 34.1 [SD, 7.5] years; 14 women/4 men); 2) early RRMS (disease duration <5 years; $n = 22$; mean age = 38.6 [SD, 9.6] years; 19 women/3 men); and 3) late RRMS (disease duration >5 years; $n = 19$; mean age = 49.2 [SD, 9.8] years; 18 women/1 man). Four patients with CIS converted to RRMS during follow-up. In Australia, people with MS are entitled to an annual monitoring MR imaging scan that is government funded. Many patients, thus, underwent serial scanning during the study, with 14 patients (5 with CIS and 5 with early and 4 with late RRMS) having 3 scanning sessions; 26 patients (7 with CIS and 10 with

early and 9 with late RRMS) having 2 scanning sessions; and the remaining 19 patients (6 with CIS and 7 with early and 6 with late RRMS) having 1 scanning session available for analysis. The mean follow-up time for all patients with serial scans was 19.6 (SD, 0.5) months, irrespective of the number of scans. In addition to MR imaging, patients underwent a standard neurologic examination by a consultant neurologist (O.W.) for calculation of the Expanded Disability Status Scale (EDSS). All subjects provided voluntary written consent, and the study was approved by the Human Research Ethics Committee of the Royal Melbourne Hospital, Australia.

MR Imaging Acquisition

Subjects were scanned using a 3T MR imaging scanner (Tim Trio; Siemens), with a body transmit coil and a 12-channel head-receive coil providing full brain coverage. Scans included the following: axial 2D fast spin-echo T2-weighted imaging (TR/TE = 4700/157 ms; flip angle = 120°; in-plane voxel dimensions = $0.7 \times 0.7 \text{ mm}^2$; section thickness = 5 mm); 2D axial FLASH T1-weighted imaging (TR/TE = 250/2.46 ms; flip angle = 70°; in-plane voxel dimensions = $0.43 \times 0.43 \text{ mm}^2$; section thickness = 5 mm) after a single-dose intravenous gadolinium injection; and sagittal acquired 3D FLAIR imaging (TR/TE/TI = 5000/350/1800 ms; flip angle = 120°; voxel dimensions = $0.5 \times 0.5 \times 1 \text{ mm}^3$).

Perivascular Space Quantification

All available T2 scans were anonymized (both within and across subjects), and the number of PVS was quantified manually by a neuroradiologist (L.M.G.) from 3 brain regions proposed by Potter et al:³ the centrum semiovale (3 slices), basal ganglia (3 slices), and midbrain (1 section) (see Fig 1 for examples of identification of

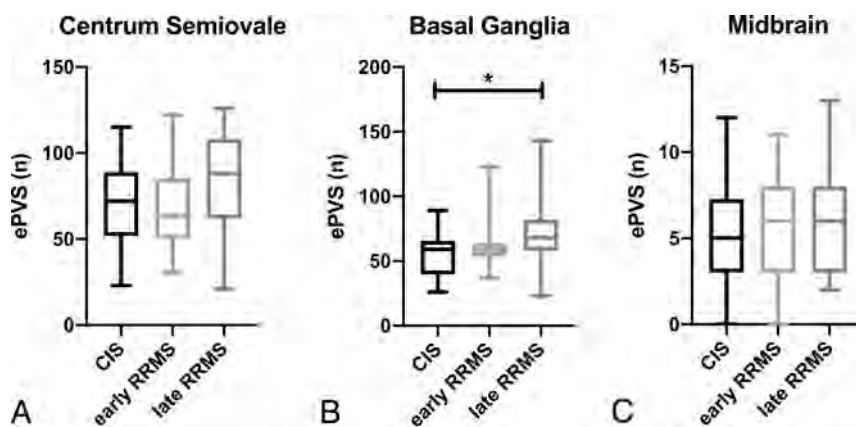


FIG 2. Baseline number of ePVS for CIS and early and late RRMS at the level of centrum semiovale (A), basal ganglia (B), and midbrain (C). The number of ePVS at the level of the basal ganglia were greater in patients in late RRMS than in those with CIS. The asterisk indicates $P < 0.05$.

ePVS). The number of ePVS reported included all ePVS summed across slices because we were not able to determine which ePVS were unique across slices. T2 scans were presented alongside corresponding slices on the FLAIR image (reformatted to the same resolution as T2), and putative perivascular spaces were checked against FLAIR to ensure that there was no FLAIR hyperintensity indicating a lesion rather than ePVS.

Thirty random subjects were also assessed by a second rater (N.Y.) for calculation of interrater reliability. The intraclass correlation between the total number of ePVS detected for the 2 raters from the 30 subjects was 0.83.

Lesion and Brain Volume Quantification

Brain and lesion volumes were calculated from 3D FLAIR scans using a fully automated analysis pipeline. For each subject, a brain mask was calculated using the SPM12 segmentation algorithm (<http://www.fil.ion.ucl.ac.uk/spm/software/spm12>). GM and WM are output as 2 segmentation classes by the algorithm but were added together to calculate total brain volume because gray and white matter were not reliably segmented on FLAIR. The CSF class was added to the brain mask to make an intracranial mask with which to calculate the brain parenchymal fraction (BPF). Lesions were automatically segmented using the Lesion Prediction Algorithm contained within the Lesion Segmentation Tool for SPM12. Lesion masks were generated from the Lesion Prediction Algorithm output and then were used for inpainting the brain masks. From these masks, we calculated the following: intracranial volume, lesion volume, and brain volume. For further statistical analyses, lesion and brain volumes were normalized to intracranial volume by division and expressed as BPF and lesion fraction.

Statistical Analyses

The number of ePVS or rate of change in the number of ePVS was compared between CIS and early and late RRMS groups using 1-way ANOVA (for normally distributed data) with Tukey post hoc tests or Kruskal-Wallis nonparametric tests (for non-normally distributed data). The correlation between the number of ePVS and FLAIR lesion load, single digit modalities test (SDMT), age, and

BPF was calculated using Pearson parametric correlation analysis, and the correlation between the number of ePVS and the EDSS was calculated using the Spearman rank correlation. For lesion volume, the distribution was transformed using a \log_{10} operation (Matlab; MathWorks), which resulted in a normal distribution (tested against the standard normal distribution using the Kolmogorov-Smirnov test, $P = .98$). When significant correlations were identified, multiple linear regression was used to determine whether the relationships with the number of ePVS were independent. To determine whether longitudinal changes in the number of ePVS were statistically significant, we first used linear regression to calculate

the annualized change (regression slope for number versus time) in ePVS for each patient with longitudinal scans. Annualized change was then analyzed using single-sample t tests with the null hypothesis of zero change.

RESULTS

Patient Cohort Description

Summary demographic and disease information for the patients can be found in the Online Supplemental Data. Additionally, only 7/59 patients (CIS, $n = 3$; early RRMS, $n = 3$; late RRMS, $n = 1$) showed any contrast-enhancing lesions on gadolinium+ FLASH scans (a marker of acute rather than historical inflammatory burden). All except 1 of these patients had only 1 gadolinium+ lesion, with a single patient with CIS having 4 gadolinium+ lesions that were not evident in follow-up scans.

Regional Differences in ePVS among Groups at Baseline

The number of ePVS was significantly different among MS clinical phenotypes only at the level of the basal ganglia (CIS, mean = 54.7 [SD, 17.9]; early RRMS, mean = 60.5 [SD, 17.1]; late RRMS, mean = 72.3 [SD, 27.2]; $F_{[2, 56]} = 3.4$, $P = .042$) (Online Supplemental Data and Fig 2). Post hoc pair-wise tests revealed a significant difference between the CIS and late RRMS groups (mean difference = +17.5; 95% CI, 0.9–34.2; $P_{(\text{Tukey adjusted})} = 0.037$). The average number of ePVS for all patients differed strongly across the 3 regions studied, with the greatest number of ePVS in the centrum semiovale (74.0 [SD, 26.7]) followed by the basal ganglia (62.5 [SD, 21.9]), with the midbrain containing, on average, <4% of the total ePVS counted (5.6 [SD, 2.9]).

Correlations between the Number of ePVS and Markers of Inflammation and Neurodegeneration

Given that number of ePVS showed a significant group effect for the basal ganglia only, we chose to focus on this region specifically for correlation analyses. The number of ePVS in the basal ganglia correlated significantly with age ($R = 0.44$, $P < .001$) and logarithmically transformed FLAIR lesion volume ($R = 0.34$, $P = .008$) (Fig 3). Multiple linear regression showed that age and

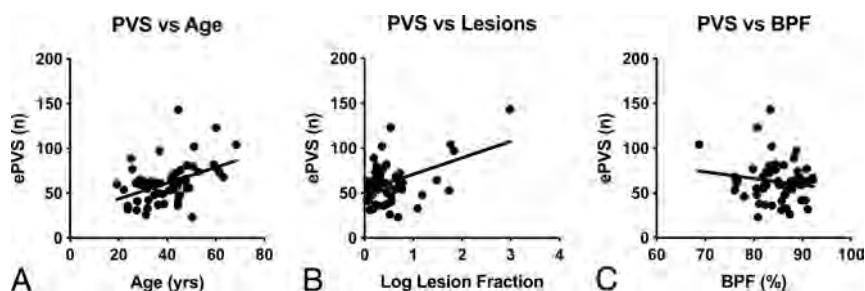


FIG 3. Scatterplots showing significant correlations between the number of ePVS at the level of the basal ganglia and age (A) and lesion volume (B) as a fraction of intracranial volume. C, BPF did not significantly correlate with the number of ePVS at the level of the basal ganglia.

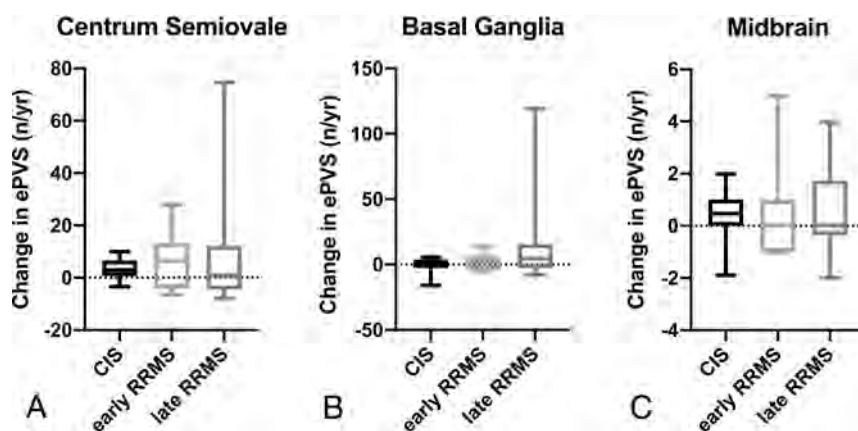


FIG 4. There were no significant differences between MS phenotypes in the annualized rate of change in the number of ePVS at the level of centrum semiovale (A), basal ganglia (B), and midbrain (C).

lesion volume were independently associated with the number of ePVS in the basal ganglia (total model $R^2 = 0.57$, $P < .001$): Each additional year of life was associated with an additional 0.73 enlarged perivascular space (95% CI, 0.27–1.18; $P = .002$), and each additional percentage of brain being classified as lesion was associated with an additional 15.35 ePVS (95% CI, 6.13–24.58; $P = .002$).

The number of ePVS in the basal ganglia did not correlate with disease duration ($R = 0.24$), BPF ($R = -0.16$), or EDSS ($\rho = 0.17$), so these variables were not included in multivariate modeling.

Longitudinal Change in ePVS

Across all patients, the number of ePVS detected significantly increased in the centrum semiovale (mean change = +4.1 [SD, 8.8] ePVS/year, $t_{(\text{single sample})} = 2.8$, $P = .008$), with a near-significant trend toward an increase in the basal ganglia (mean change = +2.3 [SD, 6.8] ePVS/year, $t_{(\text{single sample})} = 2.0$, $P = .054$), but no change in the midbrain (mean change = +0.3 [SD, 1.4] ePVS/year, $t_{(\text{single sample})} = 1.47$, $P = .15$). Among MS phenotypes, there were no significant differences in the rate of change in the number of ePVS (Online Supplemental Data and Fig 4).

The rate of change in ePVS in the midbrain was associated with change in whole-brain lesion volume ($R = 0.44$, $P = .008$). However,

across the patient group as a whole, new FLAIR lesions most commonly appeared in the periventricular WM and centrum semiovale (Fig 5). We did not detect any other correlations between ePVS change and the appearance of contrast-enhancing lesions or change in the BPF or EDSS.

DISCUSSION

Enlarged PVS have been observed in the context of inflammatory neurodegenerative disorders like MS. Enlarged PVS are believed to be associated with blood-brain barrier leakage and associated infiltration of monocytes, lymphocytes, and macrophages in the PVS, in addition to trafficking of toxic metabolites, myelin debris, and other byproducts of neurodegeneration.²⁰ Thus, there is significant interest in the development of neuroimaging markers that can detect and track the formation of ePVS for monitoring these nefarious secondary consequences of neuroinflammation. Here, we investigated the number of ePVS in people with MS (pwMS) and compared their incidence across relapsing-remitting disease phenotypes and across time. We found that the number of visible PVS in the basal ganglia was larger in later disease

stages and was associated with older age and a larger volume of FLAIR lesions. With time, the number of PVS in the centrum semiovale increased, yet there was no significant difference in rates among clinical phenotypes.

A recent meta-analysis²¹ evaluated 9 studies^{11,14,16–18,22–25} of ePVS in MS. The results of our study are partially in agreement with previous findings. First, the meta-analysis reported that people with MS exhibited greater prevalence, counts, and volume of ePVS compared with healthy individuals. However, in contrast to our findings, previous studies have identified correlations between ePVS and clinical disease severity^{11,16,18,23} and cognitive function.¹⁶ The lack of correlation with clinical disease severity could reflect a bias in our sample toward patients at the lower end of the disability spectrum (median EDSS = 0; range, 0–4.5), despite some patients having long-standing disease (maximum disease duration = 31 years). Similar to findings in 1 previous study, our study identified a significant correlation between ePVS and age.¹⁸ We interpret this result to indicate that aging rather than time living with MS contributes more to enlargement of the PVS.

We observed a significant correlation between ePVS counts and FLAIR but not contrast-enhancing lesion load. This result suggests that ePVS might be more associated with historical rather than acute inflammatory burden. However, patients in this study were all receiving ongoing disease-modifying therapies, and we detected only a small number of enhancing lesions in

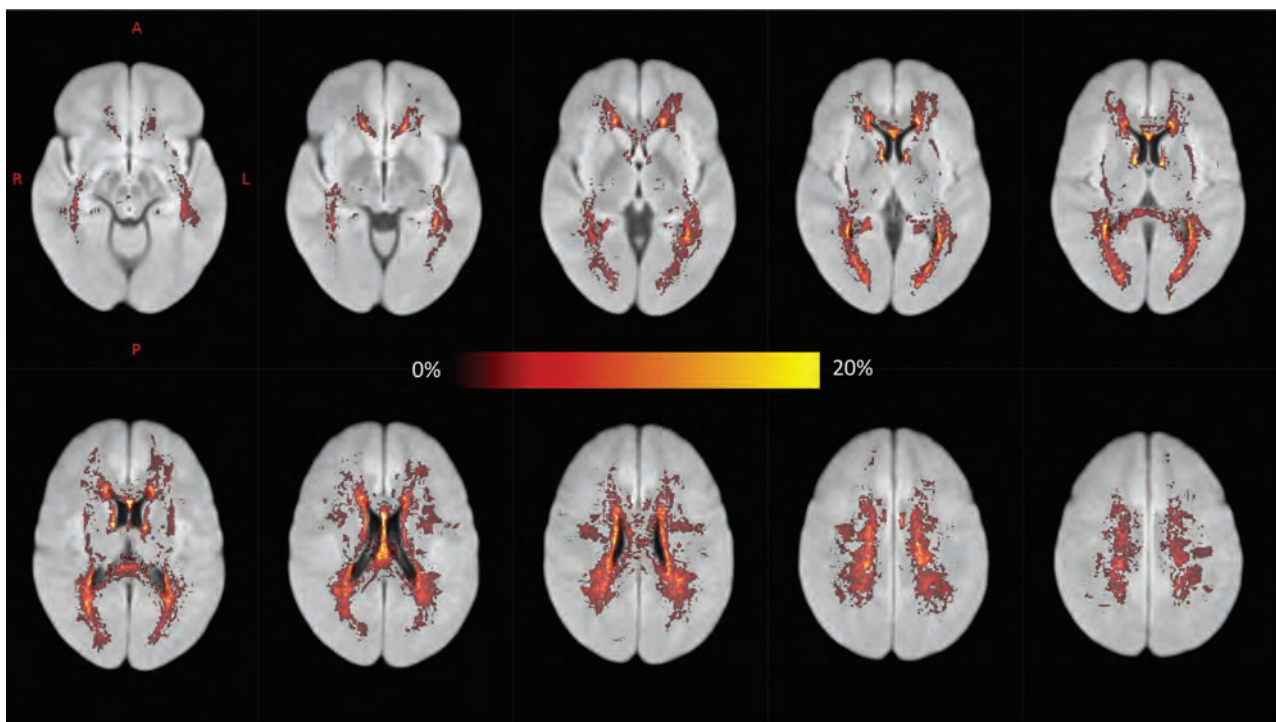


FIG 5. A voxelwise map showing the proportion of patients exhibiting new FLAIR hyperintensities (new lesions or lesion enlargement) during MR imaging follow-up after registration to Montreal Neurological Institute standard space (ie, a value of 20% indicates that 20% of patients developed new hyperintensities in that voxel). New lesions most commonly appeared in the periventricular WM and centrum semiovale.

patients during the study, with most at baseline, so the cohort was not well-suited to studying active inflammation.

Wuerfel et al¹¹ performed monthly imaging follow-up of 18 patients and showed that PVS volumes and counts increased in time points at which contrast-enhancing lesions were detected. Our longitudinal analysis involved less frequent imaging (roughly annual scanning in line with routine clinical monitoring) and did detect significant increases in the number of ePVS in the centrum semiovale. We did not detect many concomitant contrast-enhancing lesions, possibly explained by 2 factors: efficacious treatment (people diagnosed with MS in Australia are entitled to receive high-efficacy monoclonal antibody therapies after diagnosis) and the transiency of contrast enhancement. Therefore, we calculated the change in FLAIR lesion volume during the time period concurrent with PVS quantification as a marker of new inflammatory activity. We detected a significant correlation between the number of new ePVS in the midbrain and lesion-volume change. It is unclear why this region specifically might be affected. However, it is conceivable that inflammatory infiltrates and other metabolic and proteinaceous waste products might build up in more distal PVS channels. Indeed, significant differences in ePVS among disease phenotypes were observed only at the level of the basal ganglia, with patients with later-stage RRMS having significantly more ePVS than those with CIS or early RRMS. The PVS at the level of the basal ganglia are most likely fed by smaller PVS channels originating in deep GM structures such as the striatum and thalamus, which, by virtue of their widespread and long-range axonal connectivity, are confluent affected by multifocal WM lesions in MS.²⁶

We did not detect any correlation between ePVS number and BPF. This finding is consistent with the results of most studies

comparing ePVS and brain volume in MS.^{11,16,17,23,24} Taken together with the results of the present article, we would contend that ePVS in MS are not merely a product of brain parenchymal retraction associated with cerebral atrophy. However, 1 previous study using 7T MR imaging did find a significant correlation between ePVS and brain volume, but, in conflict with our results, not lesion load.¹⁸ This finding could reflect differences in the patient group studied: Patients studied here were relatively free of disability (mean EDSS = 0.53), whereas patients in the previous study had a higher median EDSS of 4, and 12/34 patients had progressive phenotypes. Another possibility is that the increased resolution afforded by 7T imaging (0.8 mm isotropic) in that study could have improved quantification of PVS.

Limitations and Future Directions

Several features of this study limit our interpretations. First, PVS were manually counted from slices on 2D MR imaging. Interrater reliability for this study was reasonable (intraclass correlation = 0.83); however, future studies should ideally use 3D acquisitions and take advantage of recently developed algorithms based on image processing^{27,28} or machine learning²⁹ that allow the automated quantification of the number of PVS and volume from 3D MR imaging. Also, the use of 3D scans of sufficient resolution could allow the tracking of individual ePVS across time to identify which channels of PVS are enlarging and the rate of enlargement. Second, it was not possible using our method to comprehend the connectivity of regional channels of PVS to focal inflammatory lesions due to the limitations of scan resolution. Future studies using high-resolution 3D MR imaging should focus on developing an atlas of the PVS network to act as a template for comparison with focal

pathology. Thus, it might be possible to better understand the causative relationships between inflammation and ePVS. Third, chronic MS lesions may appear as ovoid CSF-filled lesions in the periventricular and juxtacortical WM. As with the other vascular and inflammatory insults, MS plaques are generally distinguished from PVS by surrounding hyperintense T2/FLAIR signal and clinical history; however, it is possible that in severely degenerative lesions, fluid within the lesion core could lead to FLAIR signal attenuation that mimics an enlarged perivascular space. Finally, here we did not investigate the number of ePVS in progressive disease phenotypes, limiting the generalizability of our results. However, our hypothesis was that ePVS are associated with inflammatory aspects of MS; given that inflammatory relapses and the appearance of new lesions occur at a lower rate in progressive disease phenotypes, we expect that the relevance of ePVS in progressive disease phenotypes is limited.

CONCLUSIONS

Here, we showed that the number of ePVS in people with MS is associated with the degree of historical inflammatory burden rather than brain atrophy, indicating that ePVS are likely to be associated with neuroimmune dysfunction. The rate of ePVS accumulation showed a trend toward increasing in later disease stages, which could indicate chronic neuroinflammatory processes. This issue requires further study in a larger cohort including patients in a later stage.

ACKNOWLEDGMENTS

We thank the participants in the research for their time. We would also like to thank Bayer Australia for providing the financial support for this study. We acknowledge the traditional owners of the land on which this research took place, the Wurundjeri people of the Kulin nation, and pay our respects to elders past, present, and emerging.

Disclosures: Scott C. Kolbe—UNRELATED: Grants/Grants Pending: Biogen Australia, Comments: I have been awarded research funding from Biogen Australia*; Payment for Lectures Including Service on Speakers Bureaus: Biogen, Merck, Comments: I have received speaker honoraria from Biogen and Merck. Meaghan Clough—UNRELATED: Employment: Sanofi Genzyme*; Anneke van der Walt—UNRELATED: Consultancy: Roche, Novartis, Merck, Comments: I served on scientific advisory boards; Grants/Grants Pending: Roche, Novartis, Biogen, Merck, Comments: Unrestricted research grants*; Payment for Lectures Including Service on Speakers Bureaus: Roche, Novartis, Biogen, Merck. Helmut Butzkueven—RELATED: Grant: Monash University, Comments: Academic start-up funding*; UNRELATED: Board Membership: Biogen, Merck, Novartis, Comments: Steering Committee fees*; Consultancy: Biogen, Roche, Novartis, Merck, Comments: Advisory Board fees*; Grants/Grants Pending: Biogen, Roche, Novartis, Merck, Comments: research grants to the institution*; Payment for Lectures Including Service on Speakers Bureaus: Biogen, Roche, Novartis, Merck. *Money paid to the institution.

REFERENCES

1. Kwee RM, Kwee TC. **Virchow-Robin spaces at MR imaging.** *Radiographics* 2007;27:1071–86 CrossRef Medline
2. Zhang ET, Inman CB, Weller RO. **Interrelationships of the pia mater and the perivascular (Virchow-Robin) spaces in the human cerebrum.** *J Anat* 1990;170:111–23 Medline
3. Potter GM, Chappell FM, Morris Z, et al. **Cerebral perivascular spaces visible on magnetic resonance imaging: development of a qualitative rating scale and its observer reliability.** *Cerebrovasc Dis* 2015;39:224–31 CrossRef Medline
4. Adams HH, Hilal S, Schwingsenschuh P, et al. **A priori collaboration in population imaging: the Uniform Neuro-Imaging of Virchow-Robin Spaces Enlargement Consortium.** *Alzheimers Dement (Amst)* 2015;1:513–20 CrossRef Medline
5. Barkhof F. **Enlarged Virchow-Robin spaces: do they matter?** *J Neurol Neurosurg Psychiatry* 2004;75:1516–17 CrossRef Medline
6. MacLullich AM, Wardlaw JM, Ferguson KJ, et al. **Enlarged perivascular spaces are associated with cognitive function in healthy elderly men.** *J Neurol Neurosurg Psychiatry* 2004;75:1519–23 CrossRef Medline
7. Zhu YC, Tzourio C, Soumare A, et al. **Severity of dilated Virchow-Robin spaces is associated with age, blood pressure, and MRI markers of small vessel disease: a population-based study.** *Stroke* 2010;41:2483–90 CrossRef Medline
8. Patankar TF, Mitra D, Varma A, et al. **Dilatation of the Virchow-Robin space is a sensitive indicator of cerebral microvascular disease: study in elderly patients with dementia.** *AJNR Am J Neuroradiol* 2005;26:1512–20 Medline
9. Chen W, Song X, Zhang Y; the Alzheimer's Disease Neuroimaging Initiative. **Assessment of the Virchow-Robin spaces in Alzheimer disease, mild cognitive impairment, and normal aging, using high-field MR imaging.** *AJNR Am J Neuroradiol* 2011;32:1490–95 CrossRef Medline
10. Niazi M, Karaman M, Das S, et al. **Quantitative MRI of perivascular spaces at 3T for early diagnosis of mild cognitive impairment.** *AJNR Am J Neuroradiol* 2018;39:1622–28 CrossRef Medline
11. Wuerfel J, Haertle M, Waiczies H, et al. **Perivascular spaces: MRI marker of inflammatory activity in the brain?** *Brain* 2008;131:2332–40 CrossRef Medline
12. Bacynski A, Xu M, Wang W, et al. **The paravascular pathway for brain waste clearance: current understanding, significance and controversy.** *Front Neuroanat* 2017;11:101 CrossRef Medline
13. Rasmussen MK, Mestre H, Nedergaard M. **The glymphatic pathway in neurological disorders.** *Lancet Neurol* 2018;17:1016–24 CrossRef Medline
14. Achiron A, Faibel M. **Sandlike appearance of Virchow-Robin spaces in early multiple sclerosis: a novel neuroradiologic marker.** *AJNR Am J Neuroradiol* 2002;23:376–80 Medline
15. Ge Y, Law M, Herbert J, et al. **Prominent perivenular spaces in multiple sclerosis as a sign of perivascular inflammation in primary demyelination.** *AJNR Am J Neuroradiol* 2005;26:2316–19 Medline
16. Favaretto A, Lazzarotto A, Riccardi A, et al. **Enlarged Virchow Robin spaces associate with cognitive decline in multiple sclerosis.** *PLoS One* 2017;12:e0185626 CrossRef Medline
17. Cavallari M, Egorova S, Healy BC, et al. **Evaluating the association between enlarged perivascular spaces and disease worsening in multiple sclerosis.** *J Neuroimaging* 2018;28:273–77 CrossRef Medline
18. Kilsdonk ID, Steenwijk MD, Pouwels PJ, et al. **Perivascular spaces in MS patients at 7 Tesla MRI: a marker of neurodegeneration?** *Mult Scler* 2015;21:155–62 CrossRef Medline
19. Polman CH, Reingold SC, Banwell B, et al. **Diagnostic criteria for multiple sclerosis: 2010 revisions to the McDonald criteria.** *Ann Neurol* 2011;69:292–302 CrossRef Medline
20. Wardlaw JM, Benveniste H, Nedergaard M, et al; Fondation Leducq Transatlantic Network of Excellence on the Role of the Perivascular Space in Cerebral Small Vessel Disease. **Perivascular spaces in the brain: anatomy, physiology and pathology.** *Nat Rev Neurol* 2020;16:137–53 CrossRef Medline
21. Granberg T, Moridi T, Brand JS, et al. **Enlarged perivascular spaces in multiple sclerosis on magnetic resonance imaging: a systematic review and meta-analysis.** *J Neurol* 2020;267:3199–3212 CrossRef Medline
22. Al-Saeed O, Athyal R, Ismail M, et al. **Significance of Virchow-Robin spaces in patients newly diagnosed with multiple sclerosis: a case-**

- control study in an Arab population. *Med Princ Pract* 2012;21:447–51 CrossRef Medline
23. Conforti R, Cirillo M, Sardaro A, et al. **Dilated perivascular spaces and fatigue: is there a link? Magnetic resonance retrospective 3Tesla study.** *Neuroradiology* 2016;58:859–66 CrossRef Medline
 24. Conforti R, Cirillo M, Saturnino PP, et al. **Dilated Virchow-Robin spaces and multiple sclerosis: 3 T magnetic resonance study.** *Radiology Med* 2014;119:408–14 CrossRef Medline
 25. Etemadifar M, Hekmatnia A, Tayari N, et al. **Features of Virchow-Robin spaces in newly diagnosed multiple sclerosis patients.** *Eur J Radiol* 2011;80:e104–08 CrossRef Medline
 26. Pontillo G, Cocozza S, Lanzillo R, et al. **Determinants of deep gray matter atrophy in multiple sclerosis: a multimodal MRI study.** *AJNR Am J Neuroradiol* 2019;40:99–106 CrossRef Medline
 27. Sepehrband F, Barisano G, Sheikh-Bahaei N, et al. **Image processing approaches to enhance perivascular space visibility and quantification using MRI.** *Sci Rep* 2019;9:12351 CrossRef Medline
 28. Schwartz DL, Boespflug EL, Lahna DL, et al. **Autoidentification of perivascular spaces in white matter using clinical field strength T1 and FLAIR MR imaging.** *Neuroimage* 2019;202:116126 CrossRef Medline
 29. Dubost F, Yilmaz P, Adams H, et al. **Enlarged perivascular spaces in brain MRI: automated quantification in four regions.** *Neuroimage* 2019;185:534–44 CrossRef Medline

A Comparison of Global Brain Volumetrics Obtained from CT versus MRI Using 2 Publicly Available Software Packages

S.W. Fielden, D. Beiler, K.A. Cauley, and V. Troiani



ABSTRACT

BACKGROUND AND PURPOSE: Brain volumetrics have historically been obtained from MR imaging data. However, advances in CT, along with refined publicly available software packages, may support tissue-level segmentations of clinical CT images. Here, brain volumetrics obtained by applying two publicly available software packages to paired CT-MR data are compared.

MATERIALS AND METHODS: In a group of patients ($n = 69$; 35 men) who underwent both MR imaging and CT brain scans within 12 months of one another, brain tissue was segmented into WM, GM, and CSF compartments using 2 publicly available software packages: Statistical Parametric Mapping and FMRIB Software Library. A subset of patients with repeat imaging sessions was used to assess the repeatability of each segmentation. Regression analysis and Bland-Altman limits of agreement were used to determine the level of agreement between segmented volumes.

RESULTS: Regression analysis showed good agreement between volumes derived from MR images versus those from CT. The correlation coefficients between the 2 methods were 0.93 and 0.98 for Statistical Parametric Mapping and FMRIB Software Library, respectively. Differences between global volumes were significant ($P < .05$) for all volumes compared within a given segmentation pipeline. WM bias was 36% (SD, 38%) and 18% (SD, 18%) for Statistical Parametric Mapping and FMRIB Software Library, respectively, and 10% (SD, 30%) and 6% (SD, 20%) for GM (bias \pm limits of agreement), with CT overestimating WM and underestimating GM compared with MR imaging. Repeatability was good for all segmentations, with coefficients of variation of $<10\%$ for all volumes.

CONCLUSIONS: The repeatability of CT segmentations using publicly available software is good, with good correlation with MR imaging. With careful study design and acknowledgment of measurement biases, CT may be a viable alternative to MR imaging in certain settings.

ABBREVIATIONS: BV = brain volume; CNR = contrast-to-noise ratio; DARTEL = Diffeomorphic Anatomical Registration Through Exponentiated Lie Algebra; ICV = intracranial volume; LoA = limits of agreement; SPM = Statistical Parametric Mapping

Detailed analysis of brain volumetric data has been a topic of major interest during the past several decades. Abnormalities of global brain volume (BV) have been identified in multiple sclerosis,¹ amyotrophic lateral sclerosis,² and age-related dementia,³ being just a few examples. Beyond these examples of clinical populations with known brain atrophy, more subtle differences in cortical anatomy as they relate to typical and atypical developmental processes⁴ and individual differences in personality traits⁵ have been studied.

The exquisite soft-tissue contrast of MR imaging has given rise to a number of publicly available software platforms that enable tissue segmentation and statistical analysis of imaging data, with MR imaging thus firmly establishing itself as the criterion standard imaging technique for brain volumetric analysis.⁶⁻⁸ However, MR imaging does have several important limitations: Obtaining high-quality images in the presence of increasingly common implants remains challenging, MR imaging has high cost, and long scan times lead to higher rates of artifact-corrupted images unsuitable for analysis due to poor subject compliance. Compared with MR imaging, CT is much more affordable and available for both patients and imaging departments. It is also less subject to motion artifacts due to its acquisition speed. Historically, prospective neuroimaging research studies using CT have been difficult to justify due to the unavoidable use of ionizing radiation and the limited data obtainable. However, given the nature of CT as a first-line diagnostic tool, the number of CT images available for analysis from existing clinical data—on both

Received August 2, 2021; accepted after revision November 5.

From the Departments of Translational Data Science and Informatics (S.W.F., V.T.) and Medical and Health Physics (S.W.F.) and Geisinger-Bucknell Autism & Developmental Medicine Institute (D.B., V.T.), Geisinger, Lewisburg, Pennsylvania; and Virtual Radiologic Professionals (K.A.C.), Eden Prairie, Minnesota.

Please address correspondence to Samuel W. Fielden, PhD, Geisinger, 100 North Academy Ave, Danville, PA 17822; e-mail: sfielden@geisinger.edu

 Indicates article with online supplemental data.

<http://dx.doi.org/10.3174/ajnr.A7403>

a patient and population level—greatly outnumbers the number of MR images. Therefore, CT appears highly suitable for in vivo study of the brain, and retrospective analysis of CT images that already exist within electronic health records may serve as a useful platform for discovery.

Group-level analysis of brain imaging data for research purposes involves several preprocessing steps, including segmentation of different tissue types (GM, WM, CSF). Any successful tissue segmentation relies on a sufficient contrast-to-noise ratio (CNR) between ≥ 2 tissues to discriminate tissue boundaries. Supported by the relatively strong contrast between parenchyma and CSF and between parenchyma and bone, segmentation of total brain volumes from CT images has been accomplished.^{9,10} However, brain tissue segmentation into GM and WM was considered nonviable for many years due to the low CNR between those tissues. The steady improvement in CT technology and image quality has recently led to several groups taking a second look at segmenting CT images using such diverse approaches as intensity-thresholding,^{11,12} atlas-based,^{13–15} and learning-based methods.¹⁶

Despite this growing interest in CT image analysis and segmentation, validation remains challenging and rare; the administration of ionizing radiation to a volunteer cohort is difficult to justify on ethical grounds, and, to our knowledge, there has been only 1 report of a paired, within-subject comparison of volumes segmented from CT against those segmented from MR imaging. In that study, SPM12 (<http://www.fil.ion.ucl.ac.uk/spm/software/spm12>) was adapted for CT segmentation, and the results were compared with MR imaging segmentations obtained from FreeSurfer (<http://surfer.nmr.mgh.harvard.edu>). The brain volumes derived from the 2 modalities were found to be in good agreement, though the total number of patients with paired data was small (10 and 25 patients in 2 study arms).¹³ Like Statistical Parametric Mapping (SPM), FMRIB Software Library (FSL)¹⁷ is a commonly used, open-source software library that includes an image-processing toolbox designed for analysis of MR images of the brain (<http://fsl.fmrib.ox.ac.uk/fsl/fslwiki/FSL>). Despite being developed for MR imaging, FSL has been used to obtain volumes from brain-extracted head CT images.^{18,19} The goal of the current study was to compare volumes obtained from paired CT and MR imaging data in a broad patient cohort using these 2 publicly available software packages.

MATERIALS AND METHODS

Subjects

This study was reviewed and approved by Geisinger institution's review board. Data were identified for subjects who had undergone CT and high-resolution MR imaging within 12 months of one another. High-resolution MR imaging sequences included MPRAGE, echo-spoiled gradient echo, and fast-spoiled gradient recalled. Patients were referred for stroke, hemorrhage, aneurysm, and tumor. Subjects were excluded if they were scanned with a nonroutine protocol (ie, a pediatric protocol).

Data Acquisition

All noncontrast head CTs were acquired in an axial or helical mode, 120–140 kV(peak), and modulated milliampere, minimum, 50, and maximum, 290 mA, acquired from the foramen

magnum through the vertex with a standard 512×512 matrix, 24-cm FOV at a 5.0-mm section thickness (Online Supplemental Data). MR images varied more considerably across scanners, but generally, scans were acquired as inversion-prepared 3D fast gradient recalled-echo sequences, with in-plane resolutions of 0.8–1.0 mm and sufficient 0.8- to 1.2-mm axial slices to cover the entire brain (Online Supplemental Data).

Image Processing and Analysis

Preprocessing an MR Image File. MR images were converted from DICOM to NIfTI format. Files were then visually inspected to identify any artifacts or gross abnormalities that would prevent accurate processing. These images ($n = 7$) were removed from the pipeline and excluded from further processing. We then completed standard preprocessing steps using Diffeomorphic Anatomical Registration Through Exponentiated Lie Algebra (DARTEL in SPM) or FAST (<http://fsl.fmrib.ox.ac.uk/fsl/fslwiki/fast>)²⁰, described below.

Preprocessing CT Image Files. A series of steps were completed on CT images to adjust image parameters to facilitate image segmentation. Upper and lower threshold limits were first applied to the image using `fslmaths` (<https://open.win.ox.ac.uk/pages/fslcourse/practicals/intro3/index.html>) functions in the FSL software package (upper limit, 100; lower limit, -15). These thresholds were chosen after some preliminary experiments and were generally found to sufficiently retain tissue distinctions and boundaries, while eliminating much of the skull and extraneous noise. The origin point for each scan was adjusted to the anterior commissure using SPM. If the image quality was poor, too “grainy,” or there was a sizable morphologic obstruction that made it difficult to identify the anterior commissure, the image file was excluded from further analysis ($n = 35$). Images were then run through the FSL Brain Extraction Tool (<http://fsl.fmrib.ox.ac.uk/fsl/fslwiki/BET>; BET) with a fractional intensity threshold of 0.01 to remove any skull and nonbrain tissue that remained after the threshold adjustment.²¹ After BET, all files were visually inspected to identify any artifacts or gross abnormalities that would prevent accurate voxel-based morphometry processing. These images were also removed ($n = 49$) from the pipeline and excluded from further processing. The remaining 260 images were run through the voxel-based morphometry or FAST pipelines, outlined below.

Voxel-Based Morphometry Pipeline

Global GM, WM, CSF, BV ($BV = GM + WM$), and total intracranial volumes ($ICVs = GM + WM + CSF$) were estimated for CT and MR images using the DARTEL toolbox in SPM 12.²² First, GM, WM, and CSF segmented images were generated in NIfTI format in native space for both MR imaging and CT image files. In each segmented image, the numeric value of each voxel was an estimation of the fraction of the volume of the voxel representing the corresponding tissue type, ranging between 0 and 1. To compute a specific tissue volume, we discarded voxels with values of < 0.2 (ie, noisy voxels) from the segmented image; the remaining voxels were summed and multiplied by the volume of a voxel in milliliters to represent whole-brain tissue volume.²³ Normalization was then accomplished using DARTEL. The procedure first rigidly transforms each subject's GM and WM

segmented images to Montreal Neurological Institute space and then uses the files for all subjects to create a mean GM template in Montreal Neurological Institute space using an iterative procedure.³ This procedure also yields subject-specific flow-field files that encode the deformation that occurs during the template creation. Then, the native space GM file, the flow-field file, and the mean GM template are processed together to generate a subject-specific normalized-modulated GM image in Montreal Neurological Institute space. The modulation procedure ensures that the whole-brain and regional GM volumes are preserved (relative to the native GM image) postnormalization.

To determine the optimal threshold for the normalized-modulated image, we used a custom procedure. This procedure systematically alters the threshold of the normalized modulated image and, at each threshold value, computes voxel values by following the same steps used for estimating the native space GM volume. The threshold value at which the absolute difference between the native space and normalized modulated image is minimized is then chosen as the optimal threshold. In the normalized modulated file, all voxels with a value below this optimal threshold are zero.

FAST Pipeline

The use of FAST for CT segmentation has been described elsewhere.¹⁸ Briefly, the T1-weighted image-type setting was used, and the number of segmentation classes was set to 3. The Markov random field, iterations, and bias field smoothing values were set to 0.1, 4, and 20.0, respectively, with partial volume segmentation output. Volumes were extracted using the `fslstats` function (<https://open.win.ox.ac.uk/pages/fslcourse/practicals/intro3/index.html>).

Data Pruning

We additionally ran a cluster analysis using R statistical and computing software (<http://www.r-project.org>) to identify any outliers, which were then excluded from the final data set. The analysis identified 16 images with GM, WM, and/or CSF volumes that fell outside the expected range. The initial data pull included images from 8 CT and 7 MR imaging scanners. To reduce possible variation due to scanner make/manufacture, data were included only from resources that had scanned at least 10 patients, reducing analysis to 3 CT and 3 MR imaging scanners. After we removed the inappropriate protocols, failed analysis, outliers, and low resource counts, the final data set included 69 distinct individuals with successfully segmented paired CT/MR imaging data from both FSL and SPM.

Statistics

Data are presented as median (interquartile range) or mean (SD) as appropriate. To determine whether scanner-specific parameters globally affect segmentation results, we compared ICV, BV, and GM and WM volumes across each MR imaging–CT scanner combination using 1-way ANOVA with Tukey post hoc testing between groups. To ensure that no bias was introduced from MR image contrast, we compared segmentation results between contrast-enhanced MR images and those without contrast. Several patients in the final cohort had repeat scans (8 for MR imaging, 165 for CT). Using these, we compared the repeatability of

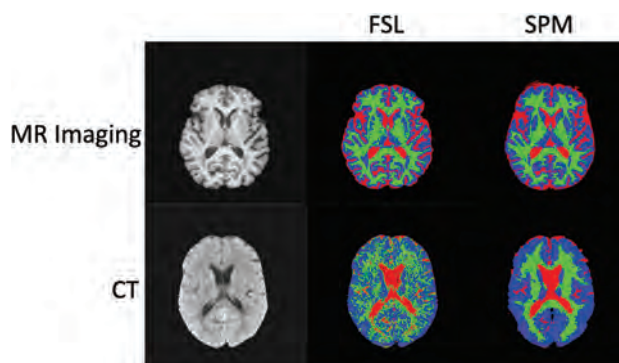


FIG 1. Brain segmentation results. Brain-extracted MR imaging and CT (left) from a 41-year-old male patient at approximately the same section locations, with corresponding segmentation results from FSL and SPM on the right. Visually, both FSL and SPM perform well on MR imaging data, with SPM exhibiting a smoother appearance for segmentation results compared with FSL. Colors in segmentations represent GM (blue), WM (green), and CSF (red).

segmentation results using the coefficient of variation. Regression analysis and Bland-Altman limits of agreement were used to determine the level of agreement between segmentation measures derived from the 2 imaging modalities. When >1 image was available for a subject (CT or MR imaging), 1 image was chosen at random for comparison. *T* tests were used to compare average volumes within each pipeline. For all tests, $P < .05$ was considered significant.

RESULTS

A typical segmentation result from paired MR imaging–CT imaging from a 41-year-old patient is shown in Fig 1. As expected, the segmentation of the MR image is of high quality, with good gray, white, and CSF differentiation. In comparison, while tissue differentiation is readily apparent in the segmentation arising from the CT image, it is of lower visual quality, given the lower SNR and CNR of the base CT image.

Assessment of Interscanner Variability and Repeatability

By 1-way ANOVA, no differences in average ICV, BV, and GM or WM volume were found between any set of scanners (Online Supplemental Data). Repeat measurements from the same subject had low variability (coefficient of variation of <10%) across all volumes and pipelines (Table 1). All further analysis used pooled data from all scanners.

Volume Comparisons between MR Imaging and CT

Regression analysis showed good agreement between volumes derived from MR images versus those derived from CT. The correlation coefficient between the 2 methods was 0.93 for the SPM

Table 1: CoV of global volumes derived from MR and CT

	ICV	BV	GM	WM
MR imaging	3.9%	2.1%	4.0%	3.0%
CT	4.5%	4.4%	5.4%	9.4%

Note:—CoV indicates coefficient of variation.

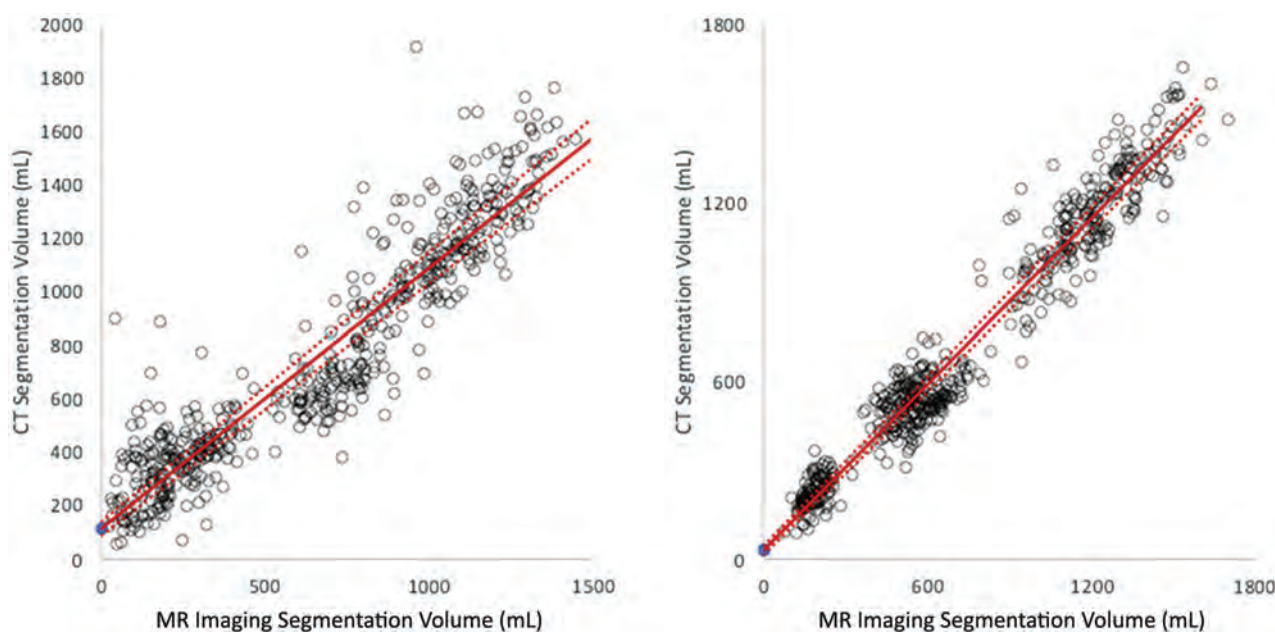


FIG 2. The regression lines between all segmentation volumes (ICV, BV, GM volume, WM volume, CSF) extracted from MR imaging and CT using the SPM pipeline (left) and FSL (right). The SPM regression line has a slope of 0.97 (95% CI, 0.93–1.00, significantly different from identity, $P < .05$) and an intercept of 115 (95% CI, 90–141; $r = 0.93$). The FSL regression line has a slope of 0.93 (95% CI, 0.91–0.95, significantly different from identity, $P < .05$) and an intercept of 31 (95% CI, 15–46; $r = 0.98$).

Table 2: Mean global volumes (mL) extracted from paired MRI/CT images

	SPM			FSL		
	MRI	CT	P Value	MRI	CT	P Value
ICV	1393 (SD, 187)	1178 (SD, 155)	<.001	1295 (SD, 168)	1336 (SD, 155)	<.001
BV	1099 (SD, 151)	1028 (SD, 151)	<.001	1076 (SD, 146)	1147 (SD, 142)	<.001
GM	675 (SD, 115)	735 (SD, 113)	<.001	553 (SD, 80)	523 (SD, 65)	<.001
WM	424 (SD, 95)	295 (SD, 83)	<.001	522 (SD, 75)	625 (SD, 80)	<.001

pipeline and 0.98 for the FSL pipeline (Fig 2). However, differences in global volumes were significant for all volumes compared within a given segmentation pipeline (Table 2).

Bland-Altman analysis of the results from SPM (Fig 3) showed that statistically significant biases were present for ICV (16% bias, limits of agreement [LoA] $\pm 24\%$), BV (6% bias, LoA $\pm 20\%$), GM (10% bias, LoA $\pm 30\%$), and WM (36% bias, LoA $\pm 38\%$), with CT underestimating ICV, BV, and WM, and overestimating GM compared with MR imaging. Bland-Altman analysis of the results from FSL (Fig 4) showed generally more favorable agreement among modalities. Statistically significant biases were present for ICV (3% bias, LoA $\pm 14\%$), BV (6% bias, LoA $\pm 16\%$), GM (6% bias, LoA $\pm 20\%$), and WM (18% bias, LoA $\pm 18\%$), with CT overestimating ICV, BV, and WM, and underestimating GM compared with MR imaging.

DISCUSSION

In this study, the MR imaging–CT segmentations produced by FSL were in closer agreement than those produced by SPM. In the 1 other study reporting paired MR imaging–CT data (which used SPM), volumes were found to agree to within 5%.¹³ In our hands, FSL volumes agreed to within 3%–18% and SPM volumes

agreed to within 16%–36%, with WM being the outlier in both cases. Three important differences between their work and ours should be noted. First, while the CTs in that study were segmented with a modified SPM pipeline, MR images were segmented using another program, FreeSurfer. Second, that study was prospective in nature

and had tight control over cohort inclusion and imaging parameters. By including multiple scanners from each technique with a broad range of clinical protocols in this current study, more relevant metrics for population-level retrospective studies can be obtained. Finally, the CT data included in that study were closer to isotropic resolution than images included here, affecting deformation and registration quality. Investigating the limits of agreement with regard to spatial resolution is a topic for future work.

Repeatability of CT segmentations using these methods is good (coefficient of variation of $<10\%$ for all volumes). Reproducibility studies of brain segmentations generated from MR images have produced coefficients of variation in the range of 0.2%–5.2%, depending on the tissue compartment and software package used.^{24,25} The repeatability metrics reported here compare favorably with these values, especially considering the similar results using MR imaging data within the same pipeline.

BVs are known to decrease with age, with an increasing fraction of ICV taken up by CSF across the decades. Because images were acquired within 1 year of one another and because all comparisons were pair-wise in the main analysis, no age-related correction factors were used in this study.

The population cohort used for this study was not healthy, having been referred for multiple head scans using different

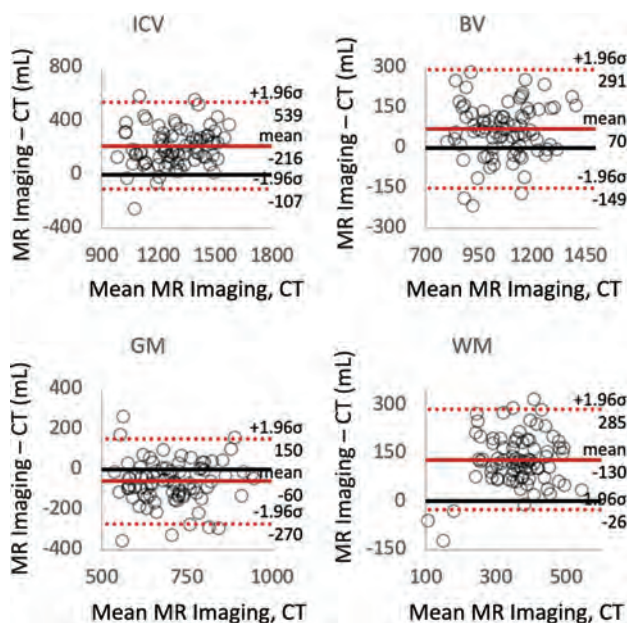


FIG 3. Bland-Altman plots for global volumes derived from MR imaging and CT using the SPM pipeline. Low biases were observed for BV (70 mL; 6%) and GM (60 mL; 10%), with all biases observed being significant ($P < .05$).

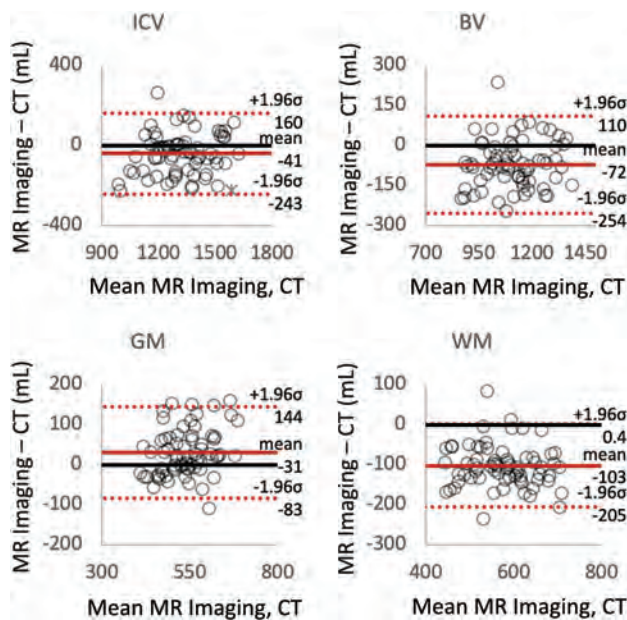


FIG 4. Bland-Altman plots for global volumes derived from MR imaging and CT using the FSL pipeline. Low biases were observed for ICV (41 mL; 3%), BV (72 mL; 6%), and GM (31 mL; 6%), with all biases observed being significant ($P < .05$).

modalities for indications ranging from cancer to trauma. Therefore, close alignment with published values for the various volume and volume fractions reported here should not be anticipated. For reference, a recent review of the literature found BV ranges from 700–1300 HU, GM ranges of 400–700 HU, and WM ranges of 300–625 HU.²⁶

One important limitation discovered in the implementation of these segmentation tools developed for MR imaging–CT data is the high failure rate of the various steps of the processing pipelines. Of 181 patients initially identified, 128 and 125 were successfully analyzed by SPM and FSL, respectively. Of those, 105 were successfully analyzed by both, with the final cohort number of 69 included in this study achieved after further pruning of outliers and of data obtained from resources with low scan counts. This high failure rate (~30%) was largely driven by the brain-extraction step, which often failed by removing large portions of the frontal lobe from CT images or by removing small, somewhat spherical regions of the temporal or parietal lobes. Future developments of CT-specific algorithms for brain extraction are likely to improve this failure rate.

Several factors may explain the differences observed between volumes obtained from CT versus MR imaging in the present study. First is the drastically reduced CNR of a CT brain image compared with its MR imaging counterpart. WM and GM are typically separated by only 5–10 HU on a CT image, with typical noise levels; this feature translates to CNRs in the range of 1–2. An MR image, by comparison, may have a CNR on the order of 10–15, when comparing white and gray matter. The other major factor differentiating MR imaging data from CT is the drastically different resolutions of the 2 modalities. High-resolution MR imaging data, as is typically used for segmentations such as these, are acquired around 1 mm isotropic. Routine brain CT has a high in-plane resolution; however, the through-plane section thickness is typically much larger (the routine CT brain protocol used at our institution has a 5-mm section thickness), causing partial volume averaging of tissue radiodensities in the CT image, further blurring the differences between tissue types.

CONCLUSIONS

MR imaging will undoubtedly remain the criterion standard for brain tissue segmentation and volumetric analysis. Quantitative assessment of volumes is dependent on many variables including imaging technique and segmentation software. However, our study shows that general trends do emerge and that certain volumetric classes can be estimated with a reasonable level of certainty. With careful study design, the convenience, affordability, and availability of CT data should be considered for large, population-based studies of brain volumetrics. Given that CT images are captured much more frequently than MRIs in clinical care, continued improvement of algorithms for estimating brain tissue volumes from CT could have a profound impact for population studies that use existing electronic health records.

Disclosure forms provided by the authors are available with the full text and PDF of this article at www.ajnr.org.

REFERENCES

1. Rudick RA, Fisher E, Lee JC, et al. Use of the brain parenchymal fraction to measure whole brain atrophy in relapsing-remitting MS. *Neurology* 1999;53:1698–98 CrossRef Medline
2. Rajagopalan V, Pioro EP. Brain parenchymal fraction: a relatively simple MRI measure to clinically distinguish ALS phenotypes. *Biomed Res Int* 2015;2015:693206 CrossRef Medline

3. Fjell AM, McEvoy L, Holland D, et al; Alzheimer's Disease Neuroimaging Initiative. **Brain changes in older adults at very low risk for Alzheimer's disease.** *J Neurosci* 2013;33:8237–42 CrossRef Medline
4. Dennis EL, Thompson PM. **Typical and atypical brain development: a review of neuroimaging studies.** *Dialogues Clin Neurosci* 2013;15:359–84 CrossRef Medline
5. Kanai R, Rees G. **The structural basis of inter-individual differences in human behaviour and cognition.** *Nat Rev Neurosci* 2011;12:231–42 CrossRef Medline
6. Ashburner J, Friston KJ. **Unified segmentation.** *Neuroimage* 2005;26:839–51 CrossRef Medline
7. Shattuck DW, Leahy RM. **BrainSuite: an automated cortical surface identification tool.** *Med Image Anal* 2002;6:129–42 CrossRef Medline
8. Smith SM, Jenkinson M, Woolrich MW, et al. **Advances in functional and structural MR image analysis and implementation as FSL.** *Neuroimage* 2004;23:S208–19 CrossRef Medline
9. Adduru V, Baum SA, Zhang C, et al. **A method to estimate brain volume from head CT images and application to detect brain atrophy in Alzheimer disease.** *AJNR Am J Neuroradiol* 2020;41:224–30 CrossRef Medline
10. Liu J, Huang S, Ihar V, et al. **Automatic model-guided segmentation of the human brain ventricular system from CT images.** *Aca. Radiol* 2010;17:718–26 CrossRef Medline
11. DeLeo JM, Schwartz M, Creasey H, et al. **Computer-assisted categorization of brain computerized tomography pixels into cerebrospinal fluid, white matter, and gray matter.** *Comput Biomed Res* 1985;18:79–88 CrossRef Medline
12. Gupta V, Ambrosius W, Qian G, et al. **Automatic segmentation of cerebrospinal fluid, white and gray matter in unenhanced computed tomography images.** *Acad Radiol* 2010;17:1350–58 CrossRef Medline
13. Irimia A, Maher AS, Rostowsky KA, et al. **Brain segmentation from computed tomography of healthy aging and geriatric concussion at variable spatial resolutions.** *Front Neuroinform* 2019;13:9–12 CrossRef Medline
14. Manniesing R, Oei MT, Oostveen LJ, et al. **White matter and gray matter segmentation in 4D computed tomography.** *Sci Rep* 2017;7:119 CrossRef Medline
15. Kemmling A, Wersching H, Berger K, et al. **Decomposing the Hounsfield unit.** *Clin Neuroradiol* 2012;22:79–79 CrossRef Medline
16. Lee TH, Fauzi MF, Komiya R. **Segmentation of CT brain images using unsupervised clusterings.** *J Vis* 2009;12:131–38 CrossRef
17. Jenkinson M, Beckmann CF, Behrens TE, et al. **FSL.** *Neuroimage* 2012;62:782–90 CrossRef Medline
18. Cauley KA, Och J, Yorks PJ, et al. **Automated segmentation of head computed tomography images using FSL.** *J Comput Assist Tomogr* 2017;42:1 Medline
19. Cauley KA, Hu Y, Fielden SW. **Aging and the brain: a quantitative study of clinical CT images.** *AJNR Am J Neuroradiol* 2020;41:809–14 CrossRef Medline
20. Zhang Y, Brady M, Smith M. **Segmentation of brain MR images through a hidden Markov random field model and the expectation-maximization algorithm.** *IEEE Trans Med Imaging* 2001;20:45–57 CrossRef Medline
21. Smith SM. **Fast robust automated brain extraction.** *Hum Brain Mapp* 2002;17:143–55 CrossRef Medline
22. Ashburner J. **A fast diffeomorphic image registration algorithm.** *Neuroimage* 2007;38:95–113 CrossRef Medline
23. Callaert DV, Ribbens A, Maes F, et al. **Assessing age-related gray matter decline with voxel-based morphometry depends significantly on segmentation and normalization procedures.** *Front Aging Neurosci* 2014;6:124 CrossRef Medline
24. Chard DT, Parker GJ, Griffin CM, et al. **The reproducibility and sensitivity of brain tissue volume measurements derived from an SPM-based segmentation methodology.** *J Magn Reson Imaging* 2002;15:259–67 CrossRef Medline
25. Guo C, Ferreira D, Fink K, et al. **Repeatability and reproducibility of FreeSurfer, FSL-SIENAX and SPM brain volumetric measurements and the effect of lesion filling in multiple sclerosis.** *Eur Radiol* 2019;29:1355–64 CrossRef Medline
26. Irimia A. **Cross-sectional volumes and trajectories of the human brain, gray matter, white matter and cerebrospinal fluid in 9473 typically aging adults.** *Neuroinform* 2021;19:347–66 CrossRef Medline

Arterial Collapse during Thrombectomy for Stroke: Clinical Evidence and Experimental Findings in Human Brains and In Vivo Models

Y. Liu, D. Gebrezgabhier, Y. Zheng, A.J. Shih, N. Chaudhary, A.S. Pandey, J.L.A. Larco, S.I. Madhani, M. Abbasi, A.H. Shahid, R.A. Quinton, R. Kadirvel, W. Brinjikji, D.F. Kallmes, and L.E. Savastano



ABSTRACT

BACKGROUND AND PURPOSE: Aspiration thrombectomy has become a preferred approach to recanalize large-vessel occlusion in stroke with a growing trend toward using larger-bore catheters and stronger vacuum pumps. However, the mechanical response of the delicate cerebral arteries to aspiration force has not been evaluated. Here, we provide preclinical and clinical evidence of intracranial arterial collapse in aspiration thrombectomy.

MATERIALS AND METHODS: We presented a clinical case of arterial collapse with previously implanted flow diverters. We then evaluated the effect of vacuum with conventional aspiration catheters (with and without stent retrievers) in a rabbit model ($n=3$) using fluoroscopy and intravascular optical coherence tomography. Then, in a validated human cadaveric brain model, we conducted 168 tests of direct aspiration thrombectomy following an experimental design modifying the catheter inner diameter (0.064 inch, 0.068 inch, and 0.070 inch), cerebral perfusion pressures (mean around 60 and 90 mm Hg), and anterior-versus-posterior circulation. Arterial wall response was recorded and graded via direct transluminal observation.

RESULTS: Arterial collapse was observed in both the patient and preclinical experimental models. In the human brain model, arterial collapse was observed in 98% of cases in the M2 and in all the cases with complete proximal flow arrest. A larger bore size of the aspiration catheter, a lower cerebral perfusion pressure, and the posterior circulation in comparison with the anterior circulation were associated with a higher probability of arterial collapse.

CONCLUSIONS: Arterial collapse does occur during aspiration thrombectomy and is more likely to happen with larger catheters, lower perfusion pressure, and smaller arteries.

ABBREVIATIONS: ACS = arterial collapse score; BA = basilar artery; MAP = mean arterial pressure; OCT = optical coherence tomography

Using aspiration thrombectomy as the first-line approach to recanalize large-vessel occlusion in stroke has attracted increasing attention because direct aspiration is associated with a shorter recanalization time and lower cost,¹ and several

randomized trials have shown noninferiority of direct aspiration compared with stent retrievers.^{2,3} Because higher rates of successful recanalization were seen with larger-catheter bores,⁴ current trends in catheter development support the use of the largest suction catheter that the vessel can accommodate to maximize clot extraction and minimize catheter clogging. In response to this paradigm, newer catheters under development and in the pipeline for commercialization have a larger inner diameter and stronger vacuum power. Although larger-bore catheters were reported to better ingest clots and achieve higher first-pass recanalization,¹ their potential complications related to the increased aspiration flow remain unclear and future research is warranted. In this study, first, we reported a clinical case of arterial collapse detected in an artery previously treated with multiple telescoping flow diverters. Second, we provided further in vivo evidence of arterial collapse in a rabbit model using fluoroscopic visualization of stent retriever collapse and optical coherence tomography (OCT). Third, we conducted a comprehensive

Received May 12, 2021; accepted after revision October 4.

From the Departments of Radiology (Y.L., M.A., R.K., W.B., D.F.K.) and Neurosurgery (J.L.A.L., S.I.M., A.H.S., L.E.S.) and Division of Anatomic Pathology (R.A.Q.), Mayo Clinic, Rochester, Minnesota; Departments of Mechanical Engineering (Y.L., Y.Z., A.J.S.), Neurosurgery (D.G., A.S.P., L.E.S.), and Radiology (N.C.), University of Michigan, Ann Arbor, Michigan; UCSF Graduate Program in Bioengineering (D.G.), University of California Berkeley, San Francisco, California; and Department of Mechanical Engineering (Y.Z.), Worcester Polytechnic Institute, Worcester, Massachusetts.

This work was supported by the National Institutes of Health National Institute of Neurological Disorders and Stroke grant No. NS105853.

Please address correspondence to Luis E. Savastano, MD, PhD, Department of Neurosurgery, Mayo Clinic, 200 First St SW, Rochester, MN 55905; e-mail: Savastano.Luis@mayo.edu; @SavastanoLuisMD

Indicates open access to non-subscribers at www.ajnr.org

Indicates article with supplemental online videos.
<http://dx.doi.org/10.3174/ajnr.A7389>

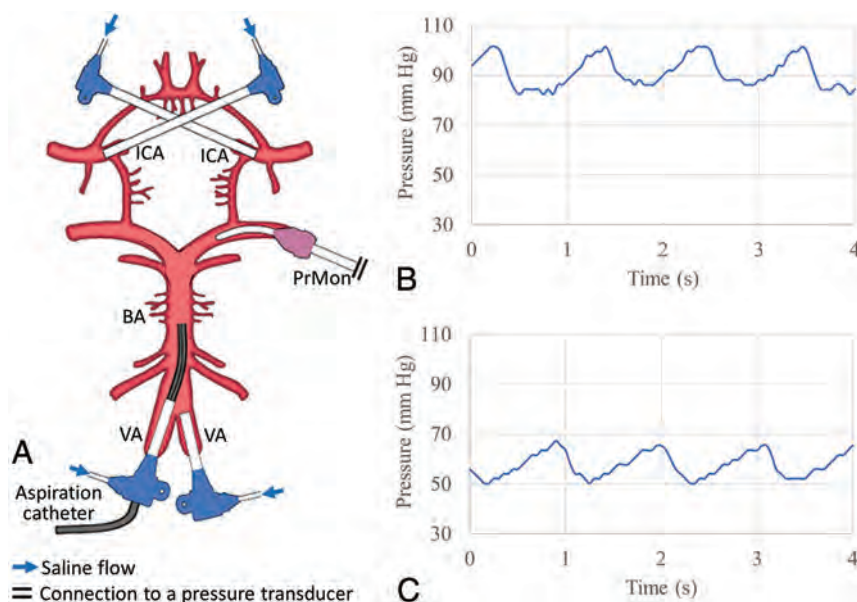


FIG 1. Whole human brain model setup. A, Both the ICA and the vertebral arteries (VA) were cannulated with 8F sheaths, which were connected to a pump system to deliver saline flow at physiologically accurate rates. An aspiration catheter was inserted in the BA. Continuous intra-arterial pressure monitoring (PrMon) informed on high MAP (B) and low MAP (C) conditions.

experimental study in a validated human brain model to analyze the mechanical response of cerebral arteries to different catheter sizes, perfusion pressures, and arteries.

MATERIALS AND METHODS

Rabbit Model

The rabbit model used in this study was previously described and was approved by the Institutional Animal Care and Use Committee (Mayo Clinic).⁵ Briefly, arterial access at the right carotid artery was obtained in adult New Zealand white rabbits ($n = 3$), and a 6F Glidesheath Slender Sheath (Terumo) was advanced under fluoroscopy into the upper third of the thoracic aorta. Then, a 5F Sofia aspiration catheter (MicroVention) was navigated over an 014 Synchro micro-wire (Stryker) and a Marksman microcatheter (Medtronic) to the abdominal aorta. Then, a 6×40 mm Solitaire stent retriever (Medtronic) was deployed with 4 radiopaque markers disposed in the arterial lumen, and the microcatheter was completely removed. The 5F catheter was then connected to a 405 Gomco suction pump (Allied Healthcare) with -650 mm Hg vacuum pressure, and the fluoroscopic changes in the radiopaque marker configuration were recorded. Five cycles of vacuum on/off were repeated in each animal. Then, the stent was removed from the animal, and a 2.7F OCT imaging catheter (Dragonfly OPTIS and OPTIS Integrated System; St. Jude Medical) was introduced into the aorta through the sheath and advanced distal to the 5F aspiration catheter. Under OCT observation, the aspiration catheter was connected to the same vacuum pump, and the changes in the vessel wall were recorded. Five cycles of vacuum on/off were repeated in each animal.

Whole Human Brain Model

The whole human brain model used in this study has been previously described.^{6,7} After institutional approval, fresh adult brains were harvested during research-consented postmortem examinations within 24 hours of death. Extra effort was made to preserve the circle of Willis and minimize damage to perforating arteries. Both ICAs and vertebral arteries were cannulated by 8F sheaths and connected to a pump system to infuse 0.9% saline solution (Fig 1A). The pump system was adjusted to deliver physiologic flow rates of ~ 310 mL/min for each ICA and ~ 160 mL/min for each basilar artery (BA). Before each aspiration test, mean arterial pressure (MAP), defined as the mean of the systolic and diastolic pressure in the target arteries, was adjusted by modifying the resistance of the system by selectively clamping the small branching arteries with aneurysm clips

as needed. To ensure patent leptomeningeal collateralization, we created a focal occlusion of the proximal MCA by strangulating the vessel with a vascular suture and measured the pressure distally and proximally. Pressure was measured by a transducer (15PDAA5 ASDX series; Honeywell). Aspiration catheters were then advanced into the target arteries and connected to an aspiration pump (405 Gomco). The arterial responses to the vacuum were recorded, and videos were analyzed by a team of engineers and neurointerventionalists.

We analyzed the effect of the following variables in relation to arterial wall response: 1) type of cerebral artery exposed to the vacuum: M1 and M2 segments of the MCA and BA; 2) bore size of suction catheters: 0.064 inch (ACE64; Penumbra), 0.068 inch (ACE68; Penumbra), and 0.070 inch (6F Sofia PLUS; MicroVention); 3) MAP within a physiologically relevant spectrum with a “high” mean MAP of 90 [SD, 5] mm Hg (Fig 1B), a “low” mean MAP of 60 [SD, 5] mm Hg (Fig 1C), and flow arrest in the target artery by interrupting flow in the corresponding sheath to mimic the clinical practice of inflating a balloon proximal to the occlusion to reduce distal embolization.

Six M1s, 6 M2s, and 7 BAs from 7 brains were tested, and a total of 171 aspiration tests were performed. For each brain, the ipsilateral M1 and M2 were tested to eliminate any effects of potential damage to the tested side.

Statistical Analysis

To predict the possibility of arterial collapse for different aspiration catheters, flow conditions, and aspiration locations, we performed binomial logistic regression. To decide which variable should be included in the regression model, χ^2 tests were conducted, and variables with $P < .2$ were included in the regression model.

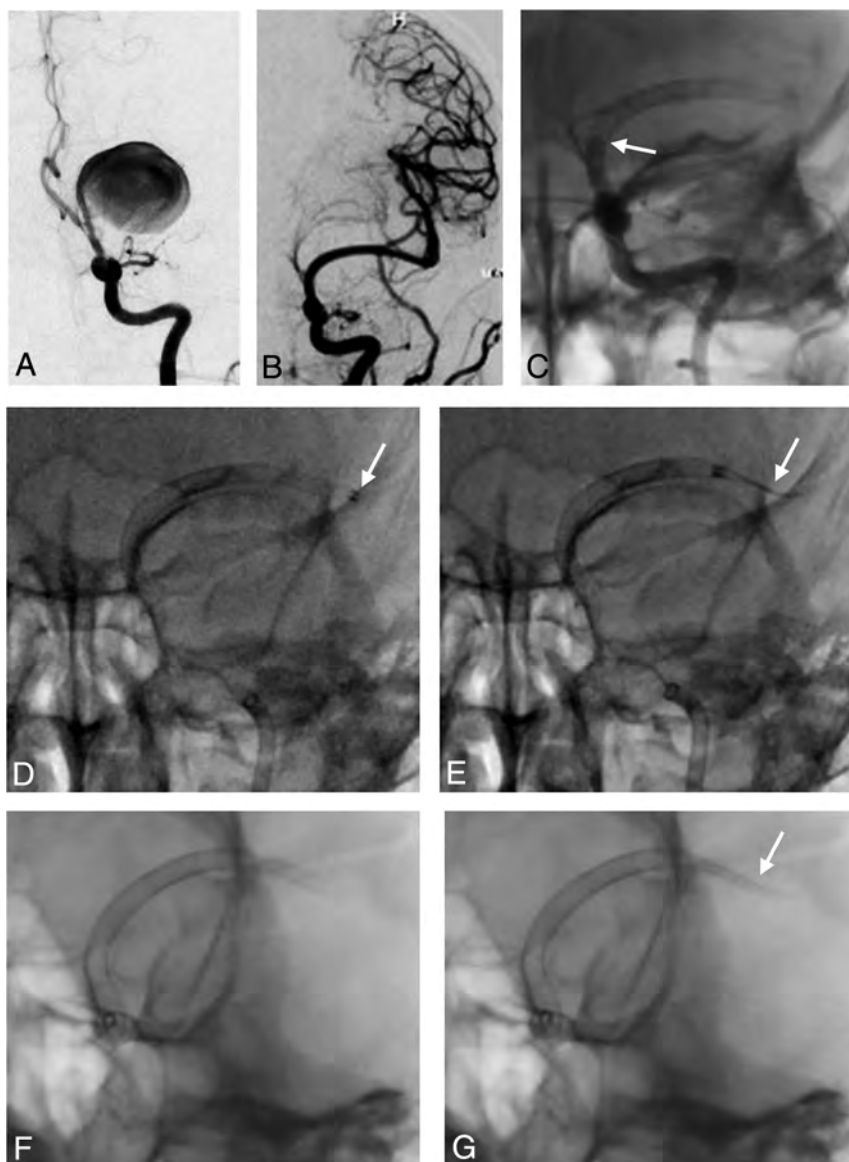


FIG 2. Clinical evidence of arterial collapse. *A*, Left ICA angiography in an anterior-posterior projection demonstrates a giant fusiform aneurysm in the left MCA. *B*, Left ICA angiogram after deployment of multiple telescoping flow diverters with acute occlusion of the aneurysm. *C*, Unsubtracted angiography of the left ICA obtained 5 days postprocedure shows in-stent thrombosis (arrow). *D*, Direct aspiration with a 068 catheter navigated distal to flow diverters (arrow). *E*, Severe collapse of the distal flow diverters on vacuum and device pull back (arrow). *F* and *G*, Partial collapse of the distal telescoping flow diverters with a suction catheter connected to vacuum at the proximal cavernous ICA.

Statistical significance for the independent variables of the regression model was indicated by $P < .05$. The overall calibration error of the regression model was tested using the Hosmer-Lemeshow goodness of fit test. All statistical analyses were performed using SPSS, Version 25 (IBM).

RESULTS

Clinical Case

A 25-year-old woman with seizures and headaches was found to have a giant fusiform aneurysm in the left MCA (Fig 2A). Five

flow diverters (Pipeline Embolization Device; Medtronic) were coaxially implanted from the cavernous ICA to the distal M1 segment of the MCA. Four devices were telescoped to reconstruct the parent artery at the level of the aneurysm, and an extra device was deployed distally to ensure good coverage across the distal fusiform aneurysm into the normal segment of the M1 (Fig 2B). The intervention was uncomplicated, and final angiographic runs demonstrated acute occlusion of the aneurysm neck without in-stent thrombosis and no further filling of the left A1 from a left ICA injection (persistent filling from a contralateral injection). The subject was maintained on dual antiplatelet therapy and had an uneventful course until postoperative day 5 when she developed a left MCA syndrome. Angiography revealed in-stent thrombosis (Fig 2C), and mechanical thrombectomy was performed using a direct aspiration technique with an aspiration catheter (ACE68) and a vacuum pump (ENGINE; Penumbra). In this intervention, the device was advanced over a microwire and microcatheter into an M2 branch using conventional endovascular techniques and then was directly connected to the vacuum pump. This maneuver resulted in a small amount of aspirated blood followed by absent blood flow into the canister. At that point, device pullback was performed under fluoroscopy, revealing severe collapse of the distal flow diverter, which resolved a few seconds after disconnecting the vacuum source (Fig 2D, -E and Online Supplemental Data). This phenomenon was reproducible, even with the aspiration catheter

located at the proximal cavernous segment of the ICA (Fig 2F, -G and Online Supplemental Data). A final run after thrombectomy revealed complete recanalization.

Arterial Collapse in the Rabbit Model

All devices could be navigated into the aorta, and angiography demonstrated arterial patency without dissection or vasospasm (Fig 3A, -B). A vacuum applied to the aspiration catheter resulted in stent-retriever collapse in 100% of cases (Fig 3C, -D and Online Supplemental Data), followed by re-expansion after disconnecting the vacuum source. Collapse was confined to approximately 2 cm

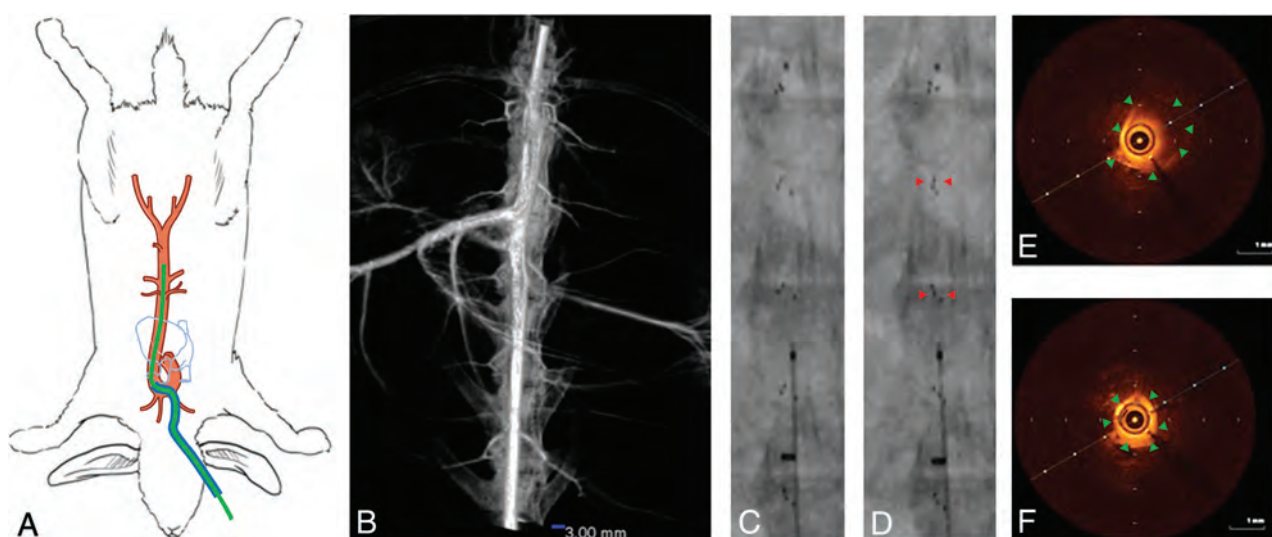


FIG 3. Aortoiliac rabbit model. *A*, Overview of the rabbit model with transcarotid aortic access. A 7F sheath (blue line) was advanced to the upper third of aorta, and a 5F aspiration catheter (green line) was coaxially advanced to the abdomen. *B*, 3D rotational angiography of a rabbit aorta. *C*, A stent retriever was delivered through a microcatheter and unsheathed to expand distal to a 5F aspiration catheter. *D*, On activation of vacuum, the radiopaque markers of the stent came in close proximity, suggesting arterial collapse (arrowheads). The most distal fluoromarker did not collapse. *E*, Intravascular OCT imaging of the aorta depicted the arterial wall (with boundaries indicated by arrowheads) close to the probe, which becomes blurry on the opposite side of the circumference due to the scattering effect of blood. *F*, Vacuum applied to the catheter resulted in arterial collapse visualized by the whole circumference of the arterial wall (with boundaries indicated by arrowheads) in contact with the OCT probe.

of the arterial segment distal to the catheter front end. Arterial collapse was redemonstrated by removing the stent from the vasculature and introducing an OCT imaging probe distal to the aspiration catheter. The vacuum resulted in arterial collapse around the OCT probe (Fig 3E, -F and Online Supplemental Data).

Arterial Collapse in the Whole Human Brain Model

The target pressure and flow within the cerebral vasculature were consistently achieved at baseline. The intra-arterial pressure in the M2 branches after temporary M1 ligation was >60 mm Hg at the high MAP condition, indicating patent leptomeningeal collateralization. Three data points were excluded due to a leak in the vacuum connection, and a total of 168 tests were available for analysis. We consistently observed a 20- to 30-mm Hg pressure drop with the introduction of the suction catheter into the system. Connection of the catheter to the vacuum resulted in macroscopic deformation in 88% (147/168) and arterial collapse in 75% (126/168) of the cases.

In cases with macroscopic deformation, we identified 4 visibly discrepant stages: 1) indentation: focal inward movement of 1 side of the arterial wall closest to the catheter tip, sometimes resulting in low-amplitude reciprocal expansion and contraction of the lumen (Fig 4A and Online Supplemental Data); 2) flutter: reciprocal cycles of focal collapse and re-expansion of the complete arterial lumen circumference distal to the catheter tip (Online Supplemental Data); 3) focal collapse: sustained collapse of a short segment of the whole arterial lumen into the catheter tip (Fig 4B and Online Supplemental Data); and 4) full/extended collapse: complete collapse of a long segment of the artery extending beyond the catheter tip (Fig 4C, -D and Online Supplemental Data). These 4 stages could be observed in the same vessel, and the deformation could transit from full collapse to indentation by gradually reducing the vacuum power. To compare the severity of arterial deformation

with different catheters, locations, and flow conditions, we developed an arterial collapse score (ACS): ACS 1 for indentation, ACS 2 for flutter, ACS 3 for focal collapse, and ACS 4 for full collapse. Cases in which arteries remained unchanged had an ACS of 0.

The incidence rates of different arterial deformation stages and arterial collapse (focal or full) under aspiration thrombectomy for each combination of catheter-location-flow condition are presented in Fig 5 and the Table, respectively. Arterial collapse was consistently observed in 98% of the cases in the M2 ($n = 52$), regardless of catheter sizes and perfusion pressures. Arterial collapse was observed in all the cases with complete proximal flow arrest ($n = 57$). For the rest of the cases ($n = 77$), the probabilities of arterial collapse were 31%, 52%, and 58% for the ACE64, ACE68, and Sofia PLUS catheters; 33% and 59% for the M1 and BA; and 34% and 59% for high and low MAPs, respectively.

The binomial logistic regression model included the catheter inner diameter (0.064 inch, 0.068 inch, and 0.070 inch), cerebral perfusion pressures (60 and 90 mm Hg), and location (M1 and BA) without data from cases with proximal flow arrest or tested in the M2. The Hosmer-Lemeshow test resulted in a χ^2 value of 2.65 and a P value of .96 and did not reject the null hypothesis of the model fitting the data. The binomial logistic regression model showed that a larger inner diameter of the catheter ($P = .034$, OR = 1.246; 95% CI, 1.017–1.528), a lower MAP ($P = .025$, OR = 0.31; 95% CI, 0.116–0.867), and BA compared to M1 ($P = .022$, OR = 0.309; 95% CI, 0.112–0.847) were independent predictors of arterial collapse.

DISCUSSION

In this study, we report the second clinical case of arterial collapse during aspiration thrombectomy published to date, and

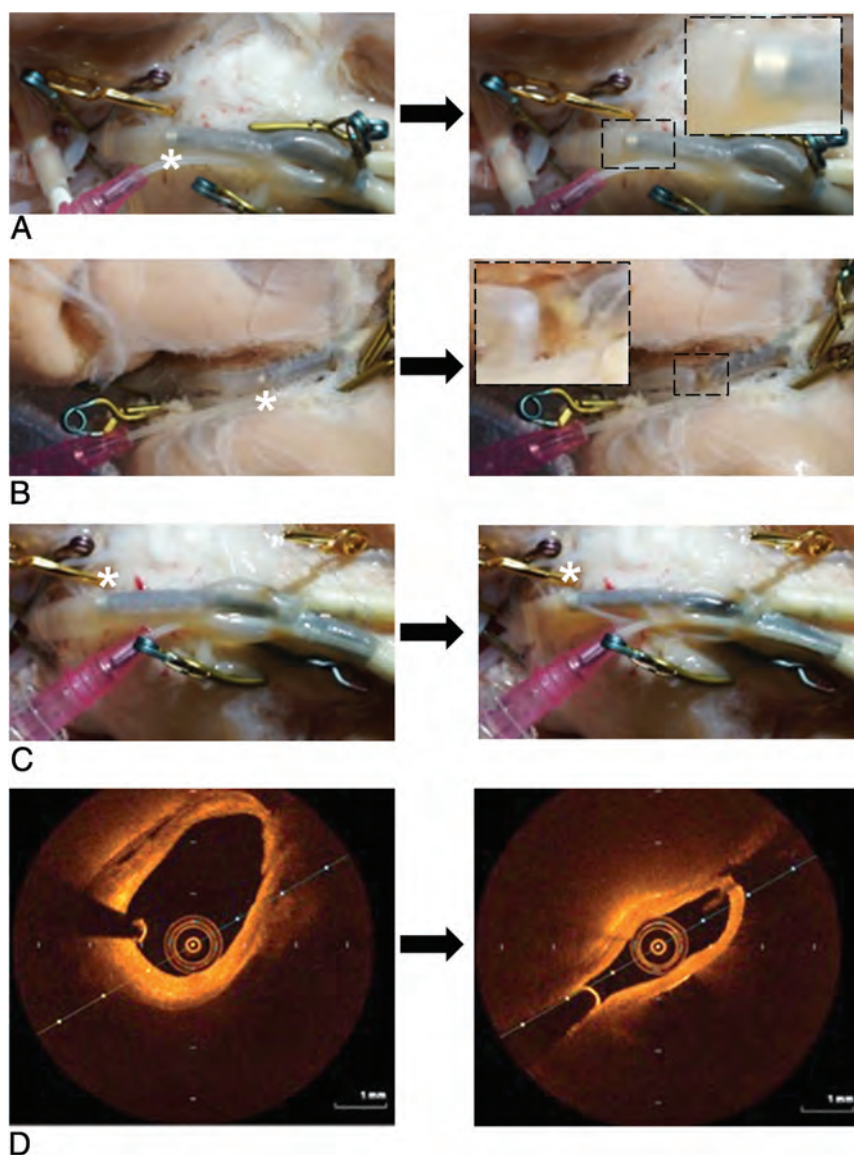


FIG 4. Different modes of arterial collapse in the brain model. A, Indentation at the aspiration catheter tip (*asterisk*) in the BA. B, Focal collapse at the aspiration catheter tip (*asterisk*) in the MCA. C, Full/extended collapse of the BA spanning the catheter tip (*asterisk*). D, OCT shows a full collapse of the BA.

we experimentally demonstrate the occurrence of arterial collapse in 2 different preclinical models. Dossani et al⁸ reported that aspiration using an 072 aspiration catheter in the right ICA causes collapse of a previously deployed radiopaque Neuroform Atlas Stent System (Stryker). Similar to this case, we were able to infer that arterial collapse had occurred, given the radio-opacity of the flow diverters previously implanted. Most interesting, collapse was observed in the most distal flow diverter in the MCA, even when the suction catheter was remotely positioned in the cavernous ICA. This finding suggests that the intraluminal negative pressure was transmitted throughout the “rigid” telescoping system (with 4 overlapping stents) for a long distance within the artery. Furthermore, it suggests that if the negative force was strong enough to collapse an artery buttressed with a high metal count stent (with 30% metal coverage), it will likely be strong enough to collapse a compliant vessel without a stent.

To visualize the effect of vacuum in vivo under experimental conditions, we used a rabbit model previously developed and validated in our lab. The abdominal aorta of rabbits accurately represents the human large cerebral arteries with regard to the lumen diameter (approximately 3.5 mm), mechanical properties, and flow speed.⁵ In our study, arterial collapse was inferred by the approximation of the stent retriever radiopaque markers and was directly visualized with intravascular OCT. Arterial collapse was consistently

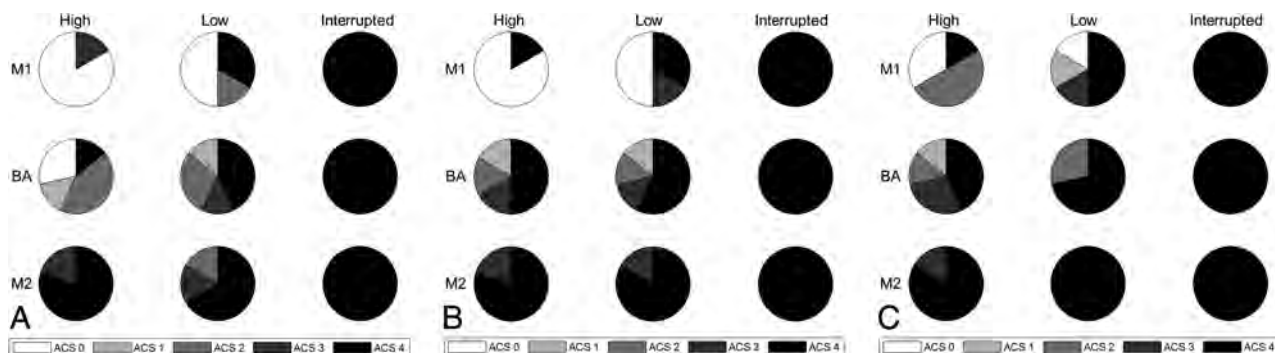


FIG 5. ACS result in the whole human brain model using 3 types of aspiration catheters: ACE64 (A), ACE68 (B), and Sofia PLUS (C). High indicates high mean arterial pressure; Low, low mean arterial pressure; Interrupted, proximal flow arrest.

Incidence rate of focal or full arterial collapse in the human brain model using 3 aspiration catheters and under 3 flow conditions^a

	High	Low	Interrupted
ACE64			
M1	17%	33%	100%
M2	100%	83%	100%
BA	14%	57%	100%
ACE68			
M1	17%	50%	100%
M2	100%	100%	100%
BA	67%	71%	100%
Sofia PLUS			
M1	17%	67%	100%
M2	100%	100%	100%
BA	71%	71%	100%

^aHigh indicates high mean arterial pressure; Low, low mean arterial pressure; Interrupted, proximal flow arrest.

observed and generally confined to the arterial segment immediately distal to the suction catheter tip with luminal reconstitution more distally, likely from collateral flow.

To mechanistically validate the *in vivo* observations and to better understand the impact of different variables in the likelihood of arterial collapse by an experimental design, we used a validated human brain model.^{6,7} Unlike the other models using rigid or semirigid arterial phantoms,⁹⁻¹¹ this validated model uses fresh human cerebral vessels (ie, flexible and collapsible arteries) and can reproduce different physiologic hemodynamic conditions. On connection of the catheter to the vacuum, we frequently observed collapse. This situation is likely due to a decreased antegrade flow, given the introduced catheter concurrent with brisk outflow of blood into the catheter due to the vacuum, reducing the intra-arterial blood pressure to negative levels between the catheter tip and the clot, resulting in arterial wall collapse. Although this situation could theoretically result in flow reversal and “noncontact” thrombectomy with migration of clots toward the suction catheter, we demonstrated that the pressure within the artery rapidly drops to negative values, resulting in arterial collapse. As expected, this phenomenon is more likely to occur at the tip of the suction catheter where the negative pressure is the highest.

Further supporting our hypothesis, we found that a larger catheter bore size is strongly correlated with higher collapsibility. Aspirational flow is proportional to the fourth power of the diameter of the catheter; therefore, small changes in catheter size (or target artery) would result in major increases in the aspiration flow along with a pronounced reduction in the blood inflow through the remaining arterial lumen. The larger the catheter is, the more violent the reduction in intraluminal pressure would be, resulting in more frequent and severe collapse.

On the basis of our findings, arterial collapse may occur within the range of hemodynamic conditions, even with the catheter sizes and vacuum levels generated by commercially available suction catheters; it could become a more serious event with the introduction of the newer generation of larger suction catheters such as the 088 catheter, which almost matches the size of the target artery.

We also found that lower perfusion pressure is correlated with higher collapsibility. This finding can also partially explain the higher collapsibility of the BA compared with the MCA. Although the BA is larger than the MCA, the inflow rate in the

posterior circulation is lower than in the anterior circulation, thus potentially limiting the ability to overcome the aspiration flow generated by catheters. The results also showed that flow arrest using a balloon-guide catheter can cause full arterial collapse during aspiration thrombectomy.

Unfortunately, arterial collapse could be easily overlooked in clinical practice because the arteries are not visualized with fluoroscopy. The common teaching to recognize clot engagement in aspiration thrombectomy (with or without stent) is to turn on the vacuum and wait until there is no flow into the canister. On the basis of our findings, artery collapse would also result in a no-flow situation, which could be misinterpreted as integration with clots. As the artery collapses and hugs the catheter, the friction between the catheter and arterial wall can track the arteries. Such massive forces can denude the endothelial lining, create dissection flaps, and result in vasospasm. Moreover, arterial traction may result in avulsions, which could be an underlying reason for the higher rates of symptomatic intracranial hemorrhage reported in patients with more thrombectomy passes.¹² Such forces can be further intensified when pulling an expanded stent retriever inside a collapsed artery. In older patients with cerebral atrophy, arterial collapse may occur more violently, given less perivascular tissue, thus leading to the adjacent branching vessels being damaged or even torn. Such a failure mechanism has been reported in *ex vivo* human brains.⁶ It has also been reported that the incidence rate of symptomatic intracranial hemorrhage was >3 times higher for M2 occlusions than for M1 occlusions.¹³ Our findings reveal that thrombectomy in the M2 branches results in more frequent and severe collapse and could, therefore, lead to microvascular avulsions during arterial traction.

Our experiments support the importance of advancing the suction catheter into or immediately proximal to the clot before connecting to the vacuum source to mitigate the risk of arterial collapse and possible no-flow situations, and they suggest that for the case of suction catheters, larger is not always better. The selection of the catheter size should be a thoughtful process considering multiple variables including parent vessel size, the configuration of the circle of Willis and collaterals, and the MAPs. Future suction-based technology should be developed to enable more efficient clot removal at equal or lower vacuums and smaller catheter size and/or to inform the interventionalist about the clot/device/artery interaction.

There are a few limitations we would like to acknowledge. First, in this study, clot analogs were not used for either the animal or the *ex vivo* human brain tests. Because clots are generally corks at the catheter tip reducing (or completely stopping) the amount of blood outflow, the intraluminal pressure is unlikely to drop to negative levels resulting in collapse. The testing here conducted without clots can mimic the cases in which aspiration continues after the clot is ingested or when the catheter is not in direct contact with the face of the clot. The failure modes of mechanical thrombectomy including arterial collapse in a human brain model with intraluminal clots have been recently published.⁶ Second, the collateral circulation of the rabbit's aorta is not well-characterized, and extrapolation to human cerebral arteries needs to be done with care because arterial collapse might be overestimated. Third, although pressure and flow are closely measured and controlled during the experiments in *ex vivo* human brains, the reduced vascular tone and mechanical constraints from perivascular tissue could make the arterial wall

more prone to collapse under a vacuum. Additionally, in the human brain model, flow interruption is truly complete in comparison with the clinical use of balloon-guide catheters. These are usually placed in the cervical or petrous ICA and, therefore, do not compromise the inflow from the ophthalmic artery and other collateral pathways. Fourth, the ACS scale was developed on the basis of testing in ex vivo human brains and may not translate to patients. Validation in patients using different sensing technologies or techniques that can monitor the mechanical response of arteries in real time is needed. Finally, the use of saline solution instead of blood (which has a higher viscosity) could result in higher aspiration flows leading to more easily reduced intraluminal pressure. Therefore, translation to clinical care needs to be interpreted with caution.

CONCLUSIONS

Aspiration thrombectomy can result in arterial collapse both clinically and in preclinical experimental models and is directly associated with larger-bore catheters, lower blood pressure, and a smaller target artery.

ACKNOWLEDGMENTS

We thank D. French, C. Prescott, D. Griffiths, and J. Jentzen for their expertise and technical assistance in obtaining human cadaveric specimens. We would also like to thank the Department of Laboratory Medicine and Pathology and the Tissue Request Acquisition Group at the Mayo Clinic, Rochester, for their valuable assistance in obtaining human brains.

Disclosure forms provided by the authors are available with the full text and PDF of this article at www.ajnr.org.

REFERENCES

- Guo X, Miao Z. **Advances in mechanical thrombectomy for acute ischaemic stroke from large vessel occlusions.** *Stroke Vasc Neurol* 2021 Jul 20 [Epub ahead of print] CrossRef Medline
- Lapergue B, Blanc R, Gory B, et al; ASTER Trial Investigators. **Effect of endovascular contact aspiration vs stent retriever on revascularization in patients with acute ischemic stroke and large vessel occlusion: the ASTER randomized clinical trial.** *JAMA* 2017;318:443–52 CrossRef Medline
- Turk AS, Siddiqui A, Fifi JT, et al. **Aspiration thrombectomy versus stent retriever thrombectomy as first-line approach for large vessel occlusion (COMPASS): a multicentre, randomised, open label, blinded outcome, non-inferiority trial.** *Lancet* 2019;393:998–1008 CrossRef Medline
- Almandoz JE, Kayan Y, Wallace AN, et al. **Larger ACE 68 aspiration catheter increases first-pass efficacy of ADAPT technique.** *J Neurointerv Surg* 2019;11:137–40 CrossRef Medline
- Ding Y, Fitzgerald S, Liu Y, et al. **A novel rabbit thromboembolic occlusion model.** *J Neurointerv Surg* 2021;13:1040–43 CrossRef Medline
- Liu Y, Gebrezgiabhier D, Reddy AS, et al. **Failure modes and effects analysis of mechanical thrombectomy for stroke discovered in human brains.** *J Neurosurg* 2021 Jun 4 [Epub ahead of print] CrossRef Medline
- Gebrezgiabhier D, Liu Y, Reddy AS, et al. **A human brain test bed for research in large vessel occlusion stroke.** *J Neurosurg* 2021 Jan 22 [Epub ahead of print] CrossRef Medline
- Dossani RH, Tso MK, Waqas M, et al. **Mechanical thrombectomy of right internal carotid artery terminus occlusion using the ADAPT technique: impact of aspiration on parent vessel.** *J Neurointerv Surg* 2020;12:1148 CrossRef Medline
- Liu Y, Zheng Y, Reddy AS, et al. **Analysis of human emboli and thrombectomy forces in large vessel occlusion stroke.** *J Neurosurg* 2020;134:893–901 CrossRef Medline
- Reddy AS, Liu Y, Cockrum J, et al. **Construction of a comprehensive endovascular test bed for research and device development in mechanical thrombectomy in stroke.** *J Neurosurg* 2020;134:1190–97 CrossRef Medline
- Liu Y, Abbasi M, Arturo Larco JL, et al. **Preclinical testing platforms for mechanical thrombectomy in stroke: a review on phantoms, in vivo animal, and cadaveric models.** *J Neurointerv Surg* 2021;13:816–22 CrossRef Medline
- Maros ME, Brekenfeld C, Broocks G, et al. **Number of retrieval attempts rather than procedure time is associated with risk of symptomatic intracranial hemorrhage thrombolysis in cerebral infarction.** *Stroke* 2021;52:1580–89 CrossRef Medline
- Saber H, Narayanan S, Palla M, et al. **Mechanical thrombectomy for acute ischemic stroke with occlusion of the M2 segment of the middle cerebral artery: a meta-analysis.** *J Neurointerv Surg* 2018;10:620–24 CrossRef Medline

Postprocedural Thrombosis following Endovascular Treatment of Intracranial Aneurysm with Flow Diverters or Coiling: A Histologic Study

J.A. Larco, M. Abbasi, Y. Liu, D. Dai, G. Lanzino, L.E. Savastano, H. Cloft, D.F. Kallmes, R. Kadirvel, and W. Brinjikji



ABSTRACT

Endovascular treatment of aneurysms with flow diverters or coiling is sometimes complicated by intraprocedural or postprocedural thrombosis along or within the devices. Thrombus composition and structure associated with such complications may provide insights into mechanisms of thrombus formation and clinical strategies to remove the thrombus. We present a retrospective histopathologic study of 4 patients who underwent mechanical thrombectomy due to acute occlusion of either implanted flow diverter devices or along coils during the treatment of intracranial aneurysm.

ABBREVIATIONS: CitH3 = anti-citrullinated H3; FD = flow diverter; Gp = glycoprotein; RBC = red blood cell; vWF = von Willebrand factor; WBC = white blood cell

Endovascular treatment of intracranial aneurysms is becoming more commonplace but is sometimes complicated by in situ thrombus formation along coils in the parent artery or within stents and flow diverters (FDs) due to the thrombogenic nature of these devices.¹⁻³ The mechanism of thrombosis is thought to be due to platelet activation because multiple prior studies have shown that complications can be prevented with dual antiplatelet therapy and managed with intra-arterial or intravenous infusion of glycoprotein (Gp) IIb/IIIa inhibitors. When the thrombus is refractory to medical treatment or the distal territory is at risk of infarction, mechanical thrombus removal by endovascular means is performed. Currently, to our knowledge, there are no studies providing insight into the structure of early postprocedural or intraprocedural thrombus related to FDs or coiling procedures. In this study, we sought to evaluate the histopathologic composition and structure of postprocedural or intraprocedural thrombus developing in 4 patients following flow diversion or coiling treatment of aneurysms, with emphasis on the surface characteristics

or shell (defined as the outer 10% of a given thrombus on histologic staining) of these thrombi and implications for therapy.

Case Series

This was a retrospective histopathologic study of 4 patients who underwent mechanical thrombectomy due to acute occlusion of either implanted FD devices or along coils during the treatment of an intracranial aneurysm. This study was approved by the Mayo Clinic institutional review board; the need for informed consent was waived. All embolizations were performed with the patient under full anticoagulation with an activated clotting time of 250–300 seconds. FD treatments were performed after loading patients with aspirin and clopidogrel for elective cases or infusion of tirofiban for acute cases. Mechanical thrombectomy was performed by members of our neurointerventional team using 5F and 6F catheters (Sofia; MicroVention) using the direct aspiration technique.

Patient 1

A 37-year-old woman with a medical history of migraines, tobacco use, and a family history of intracranial aneurysms underwent elective FD placement for a 12-mm left, supraclinoid ICA aneurysm diagnosed during screening, given her family history of intracranial aneurysms. She was placed on 325 mg of aspirin and 75 mg of clopidogrel for 5 days preoperatively, and no platelet aggregation testing was performed. The FD deployment was complicated by stent migration that was found to be partially covering the left anterior cerebral artery (Fig 1), and a second stent was deployed. Five days later, she presented to the emergency department after suddenly developing right-sided hemiparesis and aphasia with an NIHSS score of 9. Noncontrast CT demonstrated no evidence of acute

Received August 16, 2021; accepted after revision October 5.

From the Departments of Radiology (J.A.L., M.A., Y.L., D.D., L.E.S., H.C., D.F.K., R.K., W.B.) and Neurosurgery (J.A.L., M.A., Y.L., G.L., L.E.S., D.F.K., W.B.), Mayo Clinic, Rochester, Minnesota.

J.A. Larco and M. Abbasi contributed equally to this work.

This study is supported by National Institutes of Health grant (No. R01 NS105853) to Waleed Brinjikji and National Institutes of Health grant (No. R01 NS076491) to Ramanathan Kadirvel.

Please address correspondence to Waleed Brinjikji, MD, Departments of Radiology and Neurosurgery, Mayo Clinic, 200 First St SW, Rochester, MN 55905; e-mail: Brinjikji.waleed@mayo.edu; @Wbrinjikji

Indicates open access to non-subscribers at www.ajnr.org

Indicates article with online supplemental data.

<http://dx.doi.org/10.3174/ajnr.A7369>

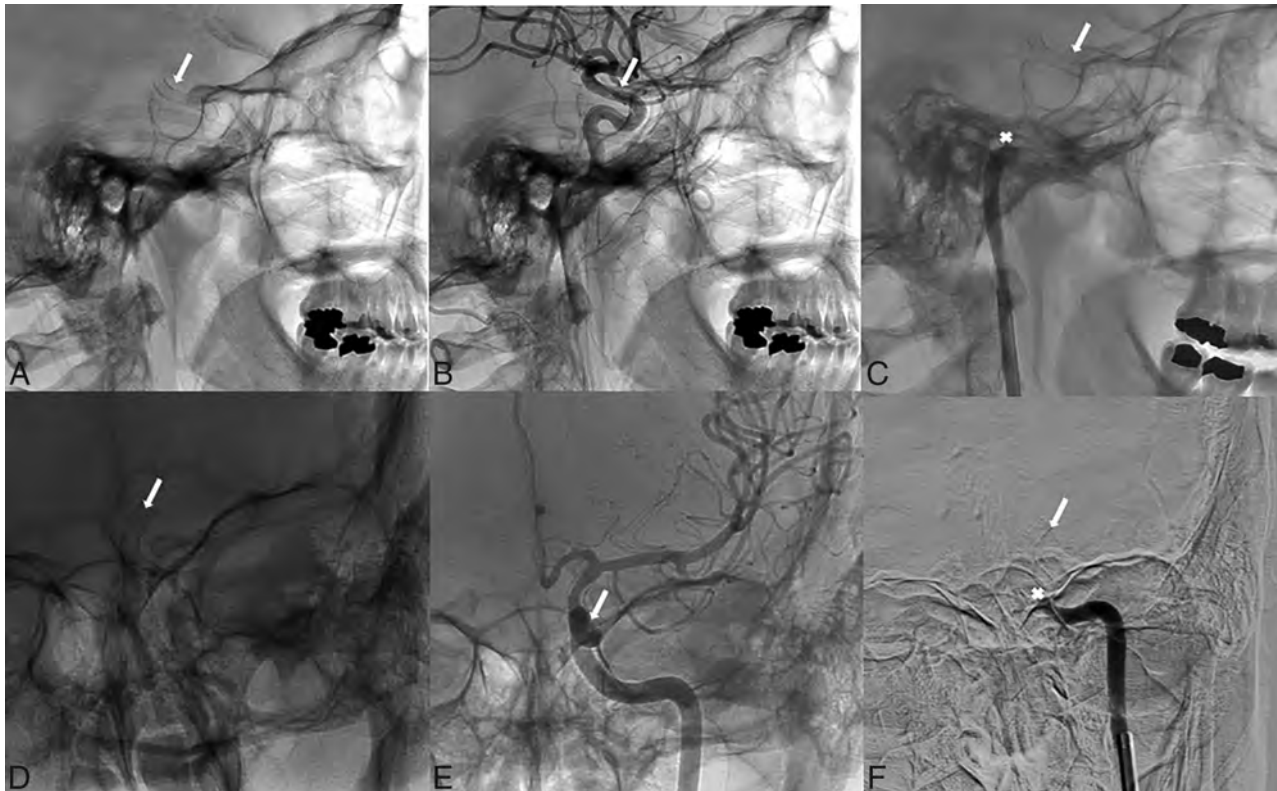


FIG 1. Lateral view showing the final positioning of the FD (white arrow) (A), with a post-procedural contrast-enhanced angiogram (B) and the occlusion site that involves the carotid artery (white asterisk) (C). Anterior-posterior view shows the final position of the FD (D), with a postprocedural contrast-enhanced angiogram (E) and the occlusion site that involves the carotid artery (F).

ischemic stroke or intracranial bleeding. She underwent cerebral angiography, which confirmed the presence of acute stent thrombosis, which was treated with mechanical thrombectomy using a 6F catheter (Sofia Plus; MicroVention), resulting in successful recanalization (modified TIC1 2b) with 1 pass using thromboaspiration. A continuous tirofiban infusion was started for the patient, and follow-up angiography was performed to confirm the patency of the stent. The retrieved thrombus was sent for histologic evaluation. The patient was discharged with no functional disability, and we prescribed dual antiplatelet therapy, switching her from clopidogrel to ticagrelor.

As depicted in Fig 2, the retrieved thrombus was predominantly composed of red blood cells (RBCs) (78.9%) followed by fibrin (13.2%), platelets (4.4%), and white blood cells (WBCs) (3.4%). On immunohistochemistry, the average percentages of platelets (CD42b), von Willebrand factor (vWF), and anti-citrullinated H3 (CitH3, a marker of neutrophil extracellular traps) were 26.1%, 23.7%, and 5.6%, respectively. Additionally, thrombus showed high expression of platelets (CD42b) (67.07%), vWF (34.3%), and CitH3 (28.6%) in the shell of the thrombus (Online Supplementary Data). Inside the thrombus, there were multiple platelet islands surrounded by thick fibrin strains. Within the thrombus, there were RBC-rich portions, which were associated with thin fibrin strains and low expression of CitH3 and vWF (Fig 2).

Patient 2

A 90-year-old woman with a medical history of atrial fibrillation, non-ST-elevation myocardial infarction hypertension, peripheral

artery disease, gastrointestinal bleeding, and subdural hemorrhage presented to our institution with acute headache, right-sided ptosis, myosis, and intractable vomiting. CT and CTA on admission demonstrated a large subarachnoid hemorrhage secondary to bleeding from a posterior communicating artery aneurysm along with intraventricular extension. Cerebral angiography demonstrated a 6.5×8 mm wide-neck right posterior communicating artery aneurysm with an adjacent daughter sac along with fusiform dilation of the supraclinoid ICA just distal to the ruptured aneurysm. The patient was treated with a FD (Pipeline Embolization Device, 4.5×18 mm, PED; Medtronic) and coil embolization (8×20 Axium 3D coil and a 4×12 Axium helical coil; Covidien) after attempted balloon-assisted coiling. A control angiogram demonstrated patency of the stent and intra-aneurysmal thrombosis (Fig 3). The patient was immediately started on a tirofiban infusion. However, immediately after the procedure, she developed left-sided hemiparesis. A new CT scan revealed an early right-hemispheric cerebral infarction secondary to in-stent thrombosis for which she underwent mechanical thrombectomy using a 6F catheter (Sofia Plus) with successful recanalization.

The retrieved thrombus was sent for histologic evaluation. Unfortunately, she had a large, right-hemispheric stroke and died 3 days later because the family opted for comfort measures only. Histomorphology of the thrombus retrieved from this patient is depicted in Fig 4. The thrombus was mainly made of RBCs (52.6%) followed by fibrin (26.9%), platelets (17.1%), and WBCs (3.2%). The average percentages of platelets (CD42b), vWF, and

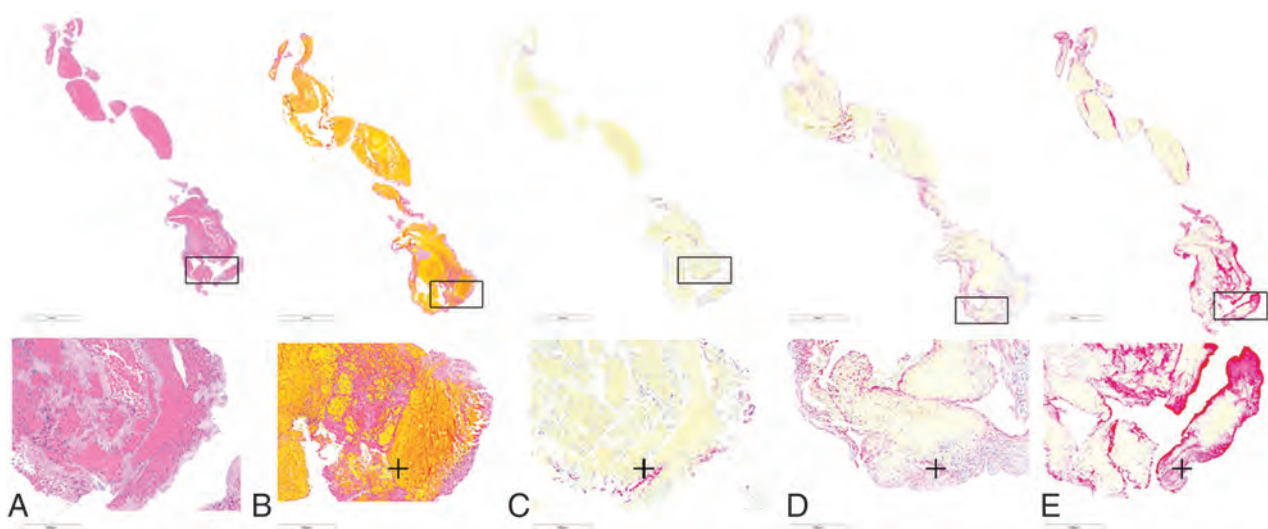


FIG 2. Staining of the thrombus retrieved from patient 1 showing the structure of the thrombus on H&E staining (A), with a high percentage of RBCs in the thrombus (B, Martius Scarlet Blue, stained yellow, identified with the *plus sign*). Peripheral expression of neutrophil extracellular traps (CitH3) (C, stained red, identified with the *plus sign*), vWF (D, stained pink and red, identified with the *plus sign*), and platelets (CD42b) (E, stained red, identified with the *plus sign*) in the thrombus.

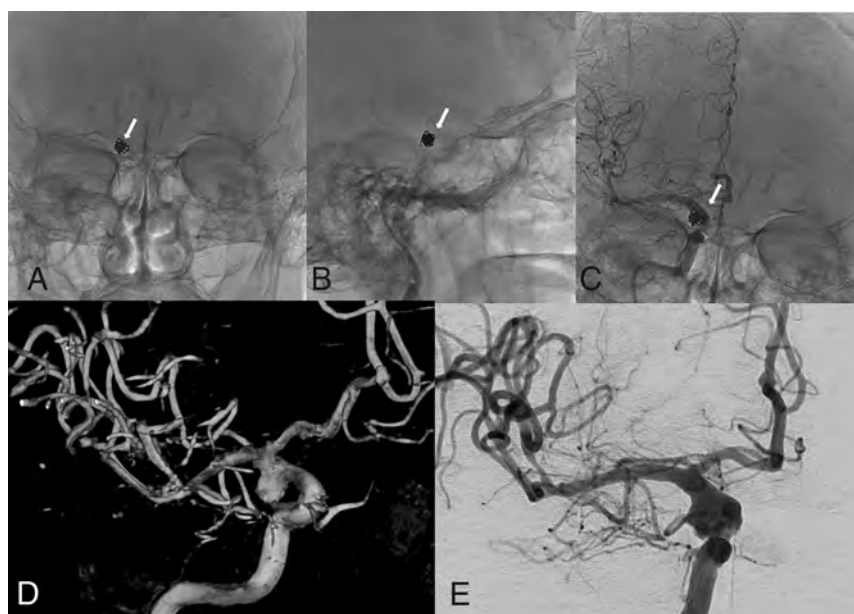


FIG 3. FD implantation with coiling (A–E). Anterior-posterior (A) and lateral (B) views of the post-procedural positioning of the coiled aneurysm (white arrows). Anterior-posterior contrast-enhanced angiogram shows postprocedural patency of the vasculature (C). 3D reconstruction and a contrast-enhanced angiogram show the vasculature architecture and a wide-neck right posterior communicating artery aneurysm with an adjacent daughter sac (D and E).

CitH3 were 31.2%, 29.1%, and 6.4%, respectively (Fig 4). Similar to the first case, this thrombus also had high expression of platelets (CD42b) (78.1%), vWF (73.4%), and CitH3 (28.3%) in the shell of the thrombus (Online Supplementary Data).

Patient 3

A 75-year-old man with a history of gastroesophageal reflux disease and hyperlipidemia, in treatment for colon cancer, presented to our institution with headache, aphasia, dizziness, and confusion. Head

CT on admission demonstrated a large subarachnoid hemorrhage with ventricular extension complicated by obstructive hydrocephalus. The patient became comatose acutely, requiring intubation and the placement of an external intraventricular drain. Cerebral angiography demonstrated an $8.4 \times 6.8 \times 6.6$ mm lobulated anterior communicating artery aneurysm, which was treated with coil embolization (6×15 mm complex Axiom, 5×10 mm helical Axiom, 4×8 mm helical Axiom, 3×6 mm helical Axiom coils). The final control angiogram demonstrated occlusion of the right MCA, which was recanalized in 1 pass of the thrombectomy device (5F catheter, Sofia, Fig 5).

The retrieved thrombus was sent for histologic evaluation. During the ensuing 2 days, the patient's neurologic condition did not improve, and he died 7 days after the initial procedure. Similar to the first 2 cases of flow diversion, the thrombus was mainly composed of RBCs (65.3%) followed by

fibrin (17.6%), platelets (13.1%), and WBCs (4%). The average percentages of platelets (CD42b), vWF, and CitH3 were 37.8%, 11.2%, and 16.4%, respectively (Fig 6). This thrombus also showed high expression of platelets (CD42b) (61.5%), vWF (18.3%), and CitH3 (20.2%) in the shell of the thrombus (Online Supplemental Data).

Patient 4

A 29-year-old woman with unremarkable medical history or previous hospitalizations presented to our institution with a

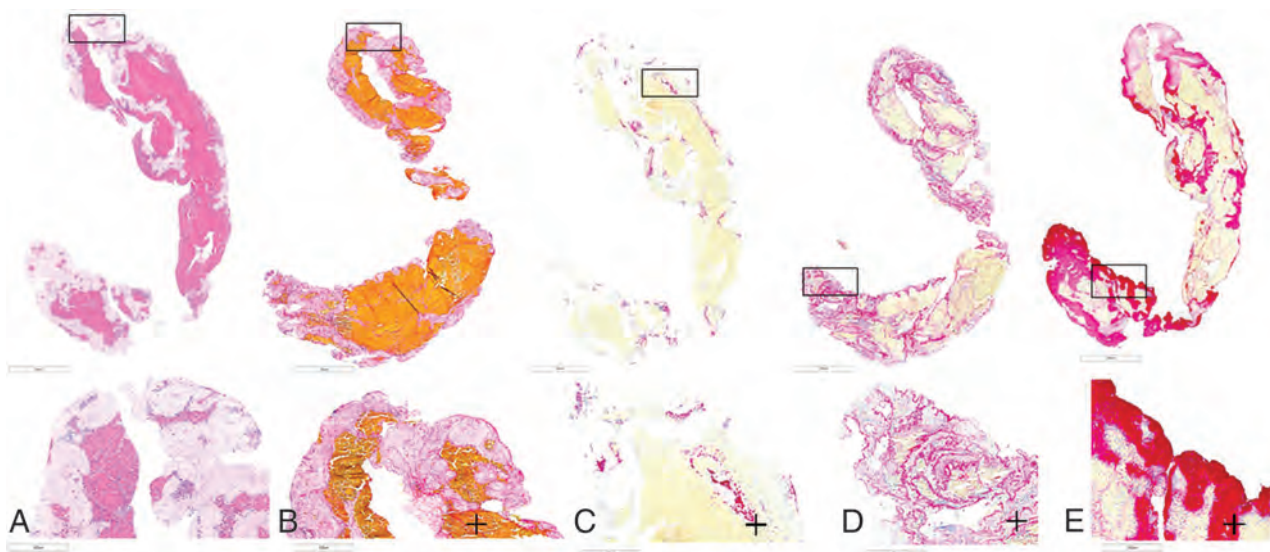


FIG 4. Staining of the thrombus retrieved from patient 2 showing the structure of the thrombus on H&E staining (A) with a high percentage of RBCs in the thrombus (B, Martius Scarlet Blue, stained yellow, identified with the *plus sign*). Peripheral expression of neutrophil extracellular traps (CitH3) (C, stained red, identified with the *plus sign*), vWF (D, stained pink and red, identified with the *plus sign*), and platelets (CD42b) (E, stained red, identified with the *plus sign*) in the thrombus.

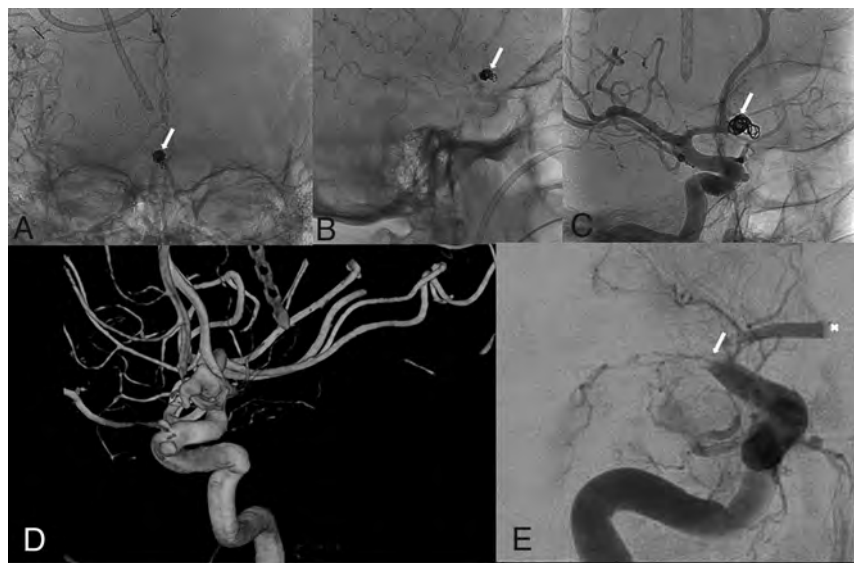


FIG 5. Anterior-posterior (A) and lateral (B) views of the postprocedural positioning of the coiled aneurysm (white arrows). Lateral projection of a contrast-enhanced angiogram and the external intraventricular drain shows in the background (C). 3D reconstruction shows the vascular architecture neighboring the lobulated anterior communicating artery aneurysm (D). Anteroposterior DSA projection demonstrates acute large vessel occlusion (E) (white asterisk).

thunderclap headache radiating to the neck and associated with nausea and vomiting. Noncontrast head CT demonstrated a diffuse subarachnoid hemorrhage in an aneurysmal pattern with a mild intraventricular hemorrhage. A left ICA cerebral angiogram demonstrated a $4 \times 4.5 \times 4.2$ mm lobulated aneurysm at the origin of the posterior communicating artery, which was treated with coil embolization (2.5-mm 3D, 1.5-mm helical coils, Axiom, Fig 7). The procedure was complicated by an embolus to the left M2 trunk that was treated with aspiration thrombectomy. Two passes

of a 5F catheter (Sofia) were required to recanalize the artery. The retrieved thrombus was sent for histologic evaluation. The patient made a full recovery. As depicted in Fig 8, thrombus retrieved from this patient was composed of RBCs (36.8%) followed by fibrin (36.3%), platelets (24.8%), and WBCs (2.1%). On immunohistochemistry, the average percentages of platelets (CD42b), vWF, and CitH3 were 46.1%, 12.3%, and 17.2%, respectively (Fig 8). Additionally, thrombus showed high expression of platelets (CD42b) (71.6%), vWF (36.7%), and CitH3 (35.1%) in the shell of the thrombus. Thrombus had multiple platelet islands surrounded by thick fibrin strains. RBC-rich portions were correlated with thin fibrin strains and low expression of CitH3 and vWF (Online Supplemental Data).

All retrieved thrombi were predominantly composed of RBCs, with an average of 58.2%. The average percentages of platelets (CD42b), vWF, and CitH3 were 35.3%, 19.1%, and 11.4%, respectively. Additionally, all thrombi showed high expression of platelets (CD42b) (69.6%), vWF (40.7%), and CitH3 (29.6%) in the shell.

DISCUSSION

Postprocedural thrombosis is a common complication following intracranial aneurysm treatment with FDs or coiling. In the present study, we performed histologic evaluation of thrombi retrieved from 4 patients with this complication and were able to provide

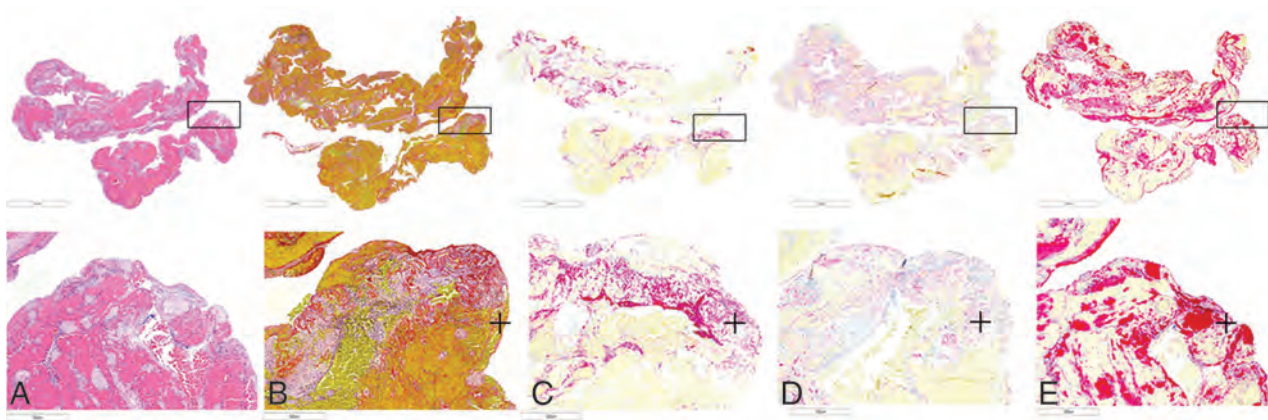


FIG 6. Staining of the thrombus retrieved from patient 3 showing the structure of thrombus on H&E staining (A) with a high percentage of RBCs in the thrombus (B, Martius Scarlet Blue, stained yellow, identified with the *plus sign*). Peripheral expression of neutrophil extracellular traps (CitH3) (C, stained red, identified with the *plus sign*), vWF (D, stained pink and red, identified with the *plus sign*), and platelets (CD42b) (E, stained red, identified with the *plus sign*) in the thrombus.



FIG 7. Anterior-posterior (A) and lateral (B) views of the postprocedural positioning of the coiled aneurysm (white arrows) and the lateral projection of contrast-enhanced DSA (C) showing patency of the artery. 3D reconstruction (D) of the lobulated aneurysm located in the posterior communicating artery. Anterior-posterior DSA (E) projection shows occlusion of M2 (white asterisk).

some unique insights into the mechanisms of thrombosis and clot characteristics in these situations. We found that these thrombi are mostly rich in RBCs but express high levels of platelets, vWF, and Cit-H3 on the periphery and surface, resulting in formation of shell or shell-like encapsulation around the thrombus. This unique structure of these thrombi explains the resistance to IV thrombolytics as demonstrated by Staessens et al.⁴ The distinct pattern of in situ thrombus in patients treated with FDs may be due to a combination of factors, including endothelial injury during embolization and the dense mesh metal in the FDs and the platinum of embolization coils being thrombogenic in nature.

The formation of thrombus in FDs could be due to FD-related factors or patient-related factors.

A number of variables have been reported as contributory to in situ thrombus formation within FDs. These include the thrombogenic character of materials used to construct FDs, malapposition or movement of FDs, and resistance to antiplatelet agents.³ Even third-generation FDs with surface modifications with synthetic biocompatible phosphorylcholine seem to have similar outcomes compared with previous generations of FDs.⁵⁻⁷

Noncompliance with dual antiplatelet therapy and resistance to clopidogrel therapy are also known causes of in-stent thrombosis; however, there is controversy regarding the use of platelet function testing prior to FD implantation and converting known nonresponders to other antiplatelet medications such as ticagrelor or prasugrel.⁸ Although certainly attention to patient compliance and identifying clopidogrel nonresponders before FD treatment should reduce the incidence

of thrombosis formation, we would still have some patients who may have this complication regardless of clopidogrel responsiveness and compliance with medications. One explanation could be related to diurnal fluctuations in platelet reactivity. One study has suggested that clopidogrel activity could vary during the day with peak platelet reactivity in the early morning.⁹

A number of techniques have been reported for revascularization of thromboembolic events during coil embolization or FD treatment.¹⁰ In a prior era, intravascular fibrinolysis with intra-arterial or even IV tPA was used. However, due to decreased efficacy and increased knowledge from the cardiology literature, many interventionalists began administering Gp IIb/IIIa inhibitors such as abciximab and tirofiban with improved results.¹¹ In a

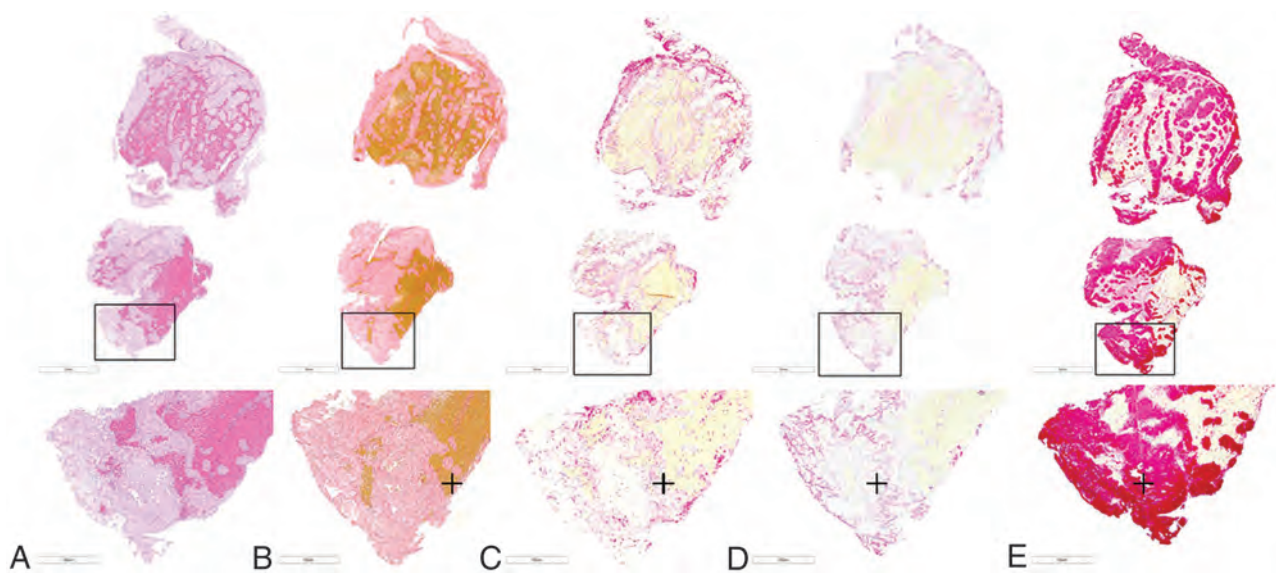


FIG 8. Staining of the thrombus retrieved from patient 4 showing the structure of thrombus on H&E staining (A), with a high percentage of RBCs in the thrombus (B, Martius Scarlet Blue, stained yellow, identified with the *plus sign*). Peripheral expression of neutrophil extracellular traps (CitH3) (C, stained red, identified with the *plus sign*), vWF (D, stained pink and red, identified with the *plus sign*), and platelets (CD42b) (E, stained red, identified with the *plus sign*) in the thrombus.

study of 254 patients with cerebral aneurysms undergoing rescue therapy during aneurysm embolization, it was found that patients who received Gp IIb/IIIa inhibitors had significantly lower rates of mortality and morbidity compared with those receiving tPA.¹² Study by Delvoye et al¹³ accentuated the essential role that GP IIb/IIIa inhibitors play during acute thromboembolic events following endovascular treatment for intracranial aneurysms. The authors compared the in vitro/in vivo effects on thrombus formation of abciximab versus alteplase. Abciximab resulted in a higher rate of final recanalization without increasing the risk of hemorrhage. In a meta-analysis of 23 studies and 516 patients, it was reported that the rate of morbidity was significantly lower in patients treated with Gp IIb/IIIa inhibitors (11% versus 29%) and recanalization rates were significantly higher (72% versus 50%). Notably, there was no difference in intra-arterial-versus-IV administration of Gp IIb/IIIa inhibitor efficacy or safety.¹⁴

Empirically, it seems that the neurointerventional community has realized that platelets are the key to the formation of these in situ thrombi. However, to date, little is known regarding the composition of these thrombi in actual patients. Our study confirmed the importance of platelets as the mediator of thrombosis because our cases had a shell of platelets, vWF, and neutrophil extracellular traps in the periphery of the clot.⁴ As described for each case, we have observed the difference in fibrin structure between platelet-rich areas and RBC-rich areas. Within platelet-rich areas, we observed a thick fibrin strain, whereas RBC-rich areas were associated with thin fibrin strains (Online Supplemental Data). This finding explains the efficacy of Gp IIb/IIIa inhibitors in these patients and why IV tPA fails. In fact, recently published a study examining characteristics of thrombolysis-refractory clots have reported that a high proportion of these have a fibrinolytic-resistant shell consisting of platelets and vWF, similar to findings in our study.¹⁵ The high expression of vWF in the shell of these retrieved thrombi may suggest that some degree of endothelial

damage must have precipitated the periprocedural thrombosis as well as that this primarily comes from the subendothelial connective tissues.

There are limitations to this study. First, only 4 patients were included. Second, we were not able to compare the different dual antiplatelet therapies for preventing thrombosis formation and their effect on clot structure. Third, we were also not able to compare bare or coated FDs or coils in terms of thrombus composition or structure because only PEDs or bare platinum coils were used in our cases. Another limitation of the study is that it was a retrospective single-center study and it may not be generalizable to other centers.

CONCLUSIONS

Postprocedural thrombosis following endovascular treatment of aneurysms is associated with high expression of neutrophil extracellular traps, platelets, and vWF on the thrombus periphery, explaining why these thrombi can be resolved far better with Gp IIb/IIIa inhibitors than with fibrinolytics. More histologic studies are needed to better understand the structure and composition of these types of thrombosis and their association with the timing of thrombosis formation and prevention strategies.


















Disclosure forms provided by the authors are available with the full text and PDF of this article at www.ajnr.org.

REFERENCES

1. Guglielmi G, Vinuela F, Sepetka I, et al. **Electrothrombosis of saccular aneurysms via endovascular approach, Part 1: electrochemical basis, technique, and experimental results.** *J Neurosurg* 1991;75:1-7 CrossRef Medline
2. Cognard C, Pierot L, Anxionnat R, et al; Clarity Study Group. **Results of embolization used as the first treatment choice in a consecutive nonselected population of ruptured aneurysms: clinical results of the Clarity GDC study.** *Neurosurgery* 2011;69:837-41 CrossRef Medline

3. Townsend RK, Wolfe SQ, Anadani M, et al. **Endovascular management of acute postprocedural flow diverting stent thrombosis.** *J Neurointerv Surg* 2020;12:67–71 CrossRef Medline
4. Staessens S, Denorme F, François O, et al. **Structural analysis of ischemic stroke thrombi: Histological indications for therapy resistance.** *Haematologica* 2020;105:498–507 CrossRef Medline
5. Atasoy D, Kandasamy N, Hart J, et al. **Outcome study of the Pipeline embolization device with shield technology in unruptured aneurysms (PEDSU).** *AJNR Am J Neuroradiol* 2019;40:2094–2101 CrossRef Medline
6. Martinez-Galdamez M, Lamin SM, Lagios KG, et al. **Treatment of intracranial aneurysms using the Pipeline Flex embolization device with shield technology: angiographic and safety outcomes at 1-year follow-up.** *J Neurointerv Surg* 2019;11:396–99 CrossRef Medline
7. Rice H, Galdámez MM, Holtmannspötter M, et al. **Periprocedural to 1-year safety and efficacy outcomes with the Pipeline Embolization Device with Shield technology for intracranial aneurysms: a prospective, post-market, multi-center study.** *J Neurointerv Surg* 2020;12:1107–12 CrossRef Medline
8. Gupta R, Moore JM, Griessenauer CJ, et al. **Assessment of dual-anti-platelet regimen for Pipeline embolization device placement: a survey of major academic neurovascular centers in the United States.** *World Neurosurg* 2016;96:285–92 CrossRef Medline
9. Freynhofer MK, Hein-Rothweiler R, Haller PM, et al. **Diurnal variability of on-treatment platelet reactivity in clopidogrel versus prasugrel treated acute coronary syndrome patients: a pre-specified TROPICAL-ACS Sub-Study.** *Thromb Haemost* 2019;119:660–67 CrossRef Medline
10. Park KY, Yeon JY, Kim BM, et al. **Efficacy and safety of flow-diverter therapy for recurrent aneurysms after stent-assisted coiling.** *AJNR Am J Neuroradiol* 2020;41:663–68 CrossRef Medline
11. Jeong HW, Jin SC. **Intra-arterial infusion of a glycoprotein IIb/IIIa antagonist for the treatment of thromboembolism during coil embolization of intracranial aneurysm: a comparison of abciximab and tirofiban.** *AJNR Am J Neuroradiol* 2013;34:1621–25 CrossRef Medline
12. Brinjikji W, McDonald JS, Kallmes DF, et al. **Rescue treatment of thromboembolic complications during endovascular treatment of cerebral aneurysms.** *Stroke* 2013;44:1343–47 CrossRef Medline
13. Delvoye F, Loyau S, Labreuche J, et al. **Intravenous abciximab as a rescue therapy for immediate reocclusion after successful mechanical thrombectomy in acute ischemic stroke patients.** *Platelets* 2021 April 11. [Epub ahead of print] CrossRef Medline
14. Brinjikji W, Morales-Valero SF, Murad MH, et al. **Rescue treatment of thromboembolic complications during endovascular treatment of cerebral aneurysms: a meta-analysis.** *AJNR Am J Neuroradiol* 2015;36:121–25 CrossRef Medline
15. Di Meglio L, Desilles JP, Ollivier V, et al. **Acute ischemic stroke thrombi have an outer shell that impairs fibrinolysis.** *Neurology* 2019;93:E1686–98 CrossRef Medline

Proximal Region of Carotid Atherosclerotic Plaque Shows More Intraplaque Hemorrhage: The Plaque at Risk Study

 G.A.J.C. Crombag,  M. Aizaz,  F.H.B.M. Schreuder,  F. Benali,  D.H.K. van Dam-Nolen,  M.I. Liem,  C. Lucci,  A.F. van der Steen,  M.J.A.P. Daemen,  W.H. Mess,  A. van der Lugt,  P.J. Nederkoorn,  J. Hendrikse,  P.A.M. Hofman,  R.J. van Oostenbrugge,  J.E. Wildberger, and  M.E. Kooi



ABSTRACT

BACKGROUND AND PURPOSE: Intraplaque hemorrhage contributes to lipid core enlargement and plaque progression, leading to plaque destabilization and stroke. The mechanisms that contribute to the development of intraplaque hemorrhage are not completely understood. A higher incidence of intraplaque hemorrhage and thin/ruptured fibrous cap (upstream of the maximum stenosis in patients with severe [$\geq 70\%$] carotid stenosis) has been reported. We aimed to noninvasively study the distribution of intraplaque hemorrhage and a thin/ruptured fibrous cap in patients with mild-to-moderate carotid stenosis.

MATERIALS AND METHODS: Eighty-eight symptomatic patients with stroke ($<70\%$ carotid stenosis included in the Plaque at Risk study) demonstrated intraplaque hemorrhage on MR imaging in the carotid artery plaque ipsilateral to the side of TIA/stroke. The intraplaque hemorrhage area percentage was calculated. A thin/ruptured fibrous cap was scored by comparing pre- and postcontrast black-blood TSE images. Differences in mean intraplaque hemorrhage percentages between the proximal and distal regions were compared using a paired-samples *t* test. The McNemar test was used to reveal differences in proportions of a thin/ruptured fibrous cap.

RESULTS: We found significantly larger areas of intraplaque hemorrhage in the proximal part of the plaque at 2, 4, and 6 mm from the maximal luminal narrowing, respectively: 14.4% versus 9.6% ($P = .04$), 14.7% versus 5.4% ($P < .001$), and 11.1% versus 2.2% ($P = .001$). Additionally, we found an increased proximal prevalence of a thin/ruptured fibrous cap on MR imaging at 2, 4, 6, and 8 mm from the MR imaging section with the maximal luminal narrowing, respectively: 33.7% versus 18.1%, $P = .007$; 36.1% versus 7.2%, $P < .001$; 33.7% versus 2.4%, $P = .001$; and 30.1% versus 3.6%, $P = .022$.

CONCLUSIONS: We demonstrated that intraplaque hemorrhage and a thin/ruptured fibrous cap are more prevalent on the proximal side of the plaque compared with the distal side in patients with mild-to-moderate carotid stenosis.


ABBREVIATIONS: FC = fibrous cap; IPH = intraplaque hemorrhage; QIR TSE = quadruple inversion recovery turbo spin-echo; TRFC = thin/ruptured fibrous cap

Rupture of a vulnerable atherosclerotic plaque is an important underlying cause of myocardial infarction and stroke.¹ Noninvasive visualization of plaque vulnerability has demonstrated that intraplaque hemorrhage (IPH) contributes to enlargement of the lipid core and plaque progression, leading to plaque destabilization.^{2,3} Indeed, we and others have

demonstrated that IPH on MR imaging is a strong predictor of future cerebrovascular events.^{4–6} This finding has led to the recognition of IPH as a key marker and pathologic factor contributing to plaque vulnerability.

This work was supported by the Center for Translational Molecular Medicine (www.ctmm.nl), project PARISK (grant 01C-202), and the Netherlands Heart Foundation. This project has received funding from the European Union Horizon 2020 research and innovation program under the Marie Skłodowska-Curie grant agreement No 722609. M.E. Kooi is supported by an Aspasia Grant 2018/SGw/00460457 from Nederlandse Organisatie voor Wetenschappelijk Onderzoek. J. Hendrikse received funding from the European Research Council under the European Union's Horizon 2020 program (H2020)/European Research Council grant agreement No. 637024. F.H.B.M. Schreuder is supported by the Netherlands Heart Foundation (2019T060).

Please address correspondence to M. Eline Kooi, MD, Department of Radiology and Nuclear Medicine, Maastricht University Medical Centre, PO Box 5800, 6202 AZ Maastricht, the Netherlands; e-mail: eline.kooi@mumc.nl

 Indicates open access to non-subscribers at www.ajnr.org

 Indicates article with online supplemental data.

<http://dx.doi.org/10.3174/ajnr.A7384>

Received July 20, 2021; accepted after revision October 14.

From the Departments of Radiology and Nuclear Medicine (G.A.J.C.C., M.A., F.B., P.A.M.H., J.E.W., M.E.K.), Clinical Neurophysiology (W.H.M.), and Neurology (R.J.v.O.), Maastricht University Medical Center, Maastricht, the Netherlands; CARIM School for Cardiovascular Diseases (G.A.J.C.C., M.A., R.J.v.O., J.E.W., M.E.K.), Maastricht University, Maastricht, the Netherlands; Department of Neurology & Donders Institute for Brain Cognition & Behaviour (F.H.B.M.S.), Radboud University Medical Center, Nijmegen, the Netherlands; Departments of Radiology and Nuclear Medicine (D.H.K.v.D.-N., A.v.d.L.) and Biomedical Engineering (A.F.v.d.S.), Erasmus University Medical Center, University Medical Center Rotterdam, Rotterdam, the Netherlands; and Departments of Neurology (M.I.L., P.J.N.) and Pathology (M.J.A.P.D.), Amsterdam University Medical Centres, University of Amsterdam, Amsterdam, the Netherlands; and Department of Radiology (C.L., J.H.), University Medical Center Utrecht, Utrecht, the Netherlands.

However, the underlying mechanisms of IPH development are not completely understood. Most often, leakage of erythrocytes from intraplaque microvessels is proposed as a cause for IPH.^{7,8} In contrast, we recently observed fewer microvessels in plaques with IPH,⁹ suggesting that damage to the plaque luminal surface such as fissures and rupture of the fibrous cap (FC) could contribute to IPH.^{8,10} It was demonstrated in histologic specimens that IPH occurs more frequently in the proximal part of the plaque,^{11,12} where the biomechanical wall stress is usually higher,^{13–16} due to arterial pressure wave reflection. In a histopathologic study, we demonstrated that IPH occurred in regions with FC fissures and juxtaluminal calcifications. Juxtaluminal calcifications may lead to increased biomechanical wall stress.¹⁷ Fissures were found in 58% of plaques with grossly intact luminal surfaces. Most of the fissures (88%) occurred in the proximal region of the plaque. The fissures were connected to IPH (92%) and calcifications (43%), while they were connected to microvessels in only 25% of cases.¹⁷

Previous histologic studies were dependent on patient populations that underwent carotid endarterectomy, usually patients with severe carotid stenosis. MR imaging allows investigation of carotid plaques, even in patients with a lower grade of stenosis in which the arterial pressure wave reflection will be less severe.^{18–20}

This study aimed to investigate, noninvasively, whether there is a difference in volume of IPH and the status of the FC in the proximal-versus-distal regions in a relatively large group of patients with stroke with mild-to-moderate carotid stenosis and IPH.

MATERIALS AND METHODS

Study Design

Baseline MR imaging data were analyzed from patients included in the Plaque at Risk (PARISK) study that demonstrated IPH. PARISK is a large, prospective, multicenter cohort study investigating whether plaque imaging enables us to better identify patients with carotid stenosis who have an increased stroke risk.²¹ Patients with a recent (<3 months) TIA or ischemic stroke in the anterior circulation and carotid artery plaque of >2 mm but <70% stenosis ipsilateral to the side of TIA/stroke were prospectively included. The degree of stenosis was determined with Doppler sonography or with CTA. An upper cutoff value of 70% was used on the basis of the NASCET criteria.²² Institutional medical ethical committee approval was obtained, and all patients provided written informed consent.

MRI

The MR imaging protocol has been described in detail previously.²¹

In brief, multisequence carotid MR imaging was performed on a 3T whole-body scanner (Achieva or Ingenia, Philips Healthcare, or Discovery MR 750, GE Healthcare). A dedicated 8-channel phased-array coil (Shanghai Chenguang Medical Technologies) or a 4-channel carotid coil (PACC-ST30, Machnet B.V. Roden, the Netherlands) was used. Dedicated vessel wall image-analysis software (VesselMass; Leiden University Medical Center, the Netherlands) was used to analyze the MR images of the ipsilateral carotid plaque. After an extensive training period and demonstrating good interobserver agreement with a validation set that was previously delineated in consensus by experts (with >7 and >10 years of experience, respectively), the trained observers

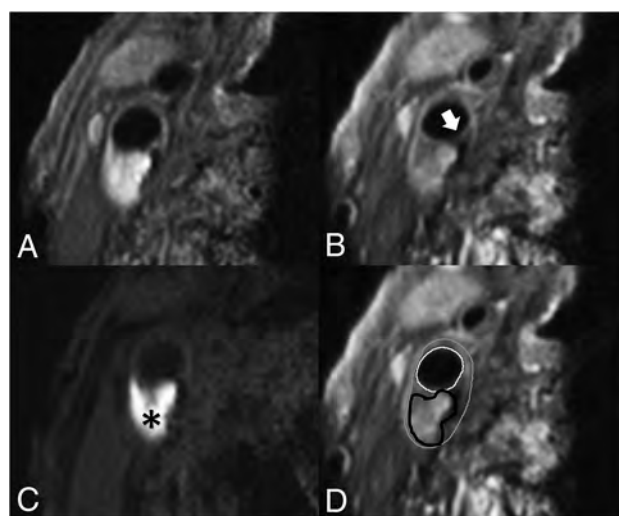


FIG 1. Transversal MR images of carotid plaque in the right carotid artery. We acquired the following MR images: precontrast T1-weighted QIR TSE (A), postcontrast T1-weighted QIR TSE (B), T1-weighted inversion recovery turbo field echo (C). D, The same image as in B, including the contours delineating intraplaque hemorrhage and the inner and outer vessel wall: white = lumen, gray = outer vessel wall, black = intraplaque hemorrhage. C, A hyperintense signal in the bulk of the plaque can be clearly observed, indicating the presence of intraplaque hemorrhage (black asterisk). B, An interruption of the signal enhancement adjoining the lumen can be observed, indicating a TRFC (white arrow).

manually delineated the outer vessel wall, luminal area, and plaque components as previously described.²³ Image quality was rated on a 5-point scale.²⁴ Patients were excluded if the mean image quality score was <2.

The vessel wall and luminal area were delineated on the pre-contrast T1-weighted double inversion recovery FSE images (center 2) or the quadruple inversion recovery turbo spin-echo (QIR TSE) (center 1, 3, and 4) images. IPH delineation was performed on T1-weighted inversion recovery turbo field echo images (center 1, 3, and 4) or 3D T1-weighted fat-suppressed spoiled gradient-echo images (center 2).

IPH was delineated by visual observation and was defined as hyperintense signal within the bulk of the plaque compared with the adjacent sternocleidomastoid muscle and was manually delineated per section by the trained observers. FC status was dichotomized as thick versus thin or ruptured.²⁵ When a continuous signal enhancement on the postcontrast images between the lipid rich necrotic core and the lumen was identified, the FC status was classified as “intact and thick.” When no or an interrupted area of enhancement was identified, the FC status was classified as “thin and/or ruptured.” In slices without a lipid rich necrotic core, there is no interrupted area of signal enhancement; therefore, the status of the FC is scored by definition as “intact and thick” (Fig 1).

Previously, we have shown that our method of scoring IPH demonstrated good agreement between MR imaging and histology.²⁶ Interobserver reproducibility for the detection of IPH was very good ($\kappa = 0.86$). We also demonstrated an overall very good interobserver reproducibility of MR image analysis (for carotid

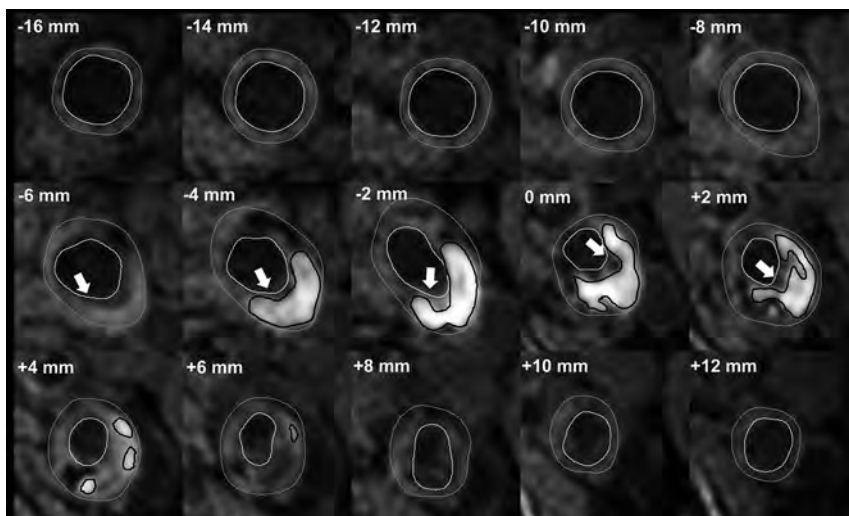


FIG 2. A patient's dataset acquired with an inversion recovery turbo field echo sequence. Delineation of the inner and outer vessel walls and IPH in every 2-mm-thick MR imaging section proximal and distal to the section with the narrowest lumen (0 mm). Gray outline = outer vessel wall, white outline = inner vessel wall, black outline = IPH, white arrow (−6 mm to +2 mm) = MR imaging slices in which the FC status is scored as thin or ruptured. The status of the FC was determined by using the postcontrast T1-weighted QIR TSE sequence. There is a larger volume of IPH at the proximal side of the section with the narrowest lumen (0 mm), and most of the slices with a TRFC cap are also located at the proximal side.

lumen volume, wall volume, and total vessel volume: intraclass correlation coefficient/coefficient of variation = 0.96/7.7%, 0.95/8.8%, and 0.92/12.8%, respectively).²⁷ Interobserver reproducibility of FC status assessment was good ($\kappa = 0.60$ – 0.71).²⁸ Also, we have previously shown a very good overall interscan/intraobserver reproducibility in a study in which patients were scanned twice within a mean of 4 (SD, 2.9) days (for carotid lumen volume and wall volume: intraclass coefficient/coefficient of variation = 0.99/7.2% and 0.99/7.1%, respectively).²⁷ The interscan/intraobserver reproducibility for the detection of IPH and FC status were very good ($\kappa = 1.00$).²⁷ On the basis of these delineations, the dedicated vessel wall imaging software package automatically calculates the luminal and vessel wall area and the areas of each plaque component per section. Using the vessel wall and IPH areas, we calculated the percentage of IPH of the total vessel wall area per section. Starting at the section with the narrowest lumen, the IPH area and the presence of a thin/ruptured fibrous cap (TRFC) were determined for the neighboring proximal and distal slices at an interval of 2 mm (ie, the MR imaging section thickness) (Fig 2).

Plaque Composition in Proximal-versus-Distal Regions

The proximal region of the plaque is defined as the region proximal to the imaging section with the narrowest lumen (lumen with the absolute lowest area based on luminal contour). The vessel wall area was calculated for each MR imaging section. We generated a histogram of the distribution of the mean IPH area percentage. In addition, we also calculated differences in absolute areas of IPH between the proximal and distal parts of the plaque. The distribution of MR imaging slices with a TRFC at each MR imaging section position proximal and distal to the MR imaging section with the narrowest lumen was also assessed. Section

positions with data from <25 patients are excluded in these histograms because of the small statistical power.

Statistical Analyses

Statistical analyses were performed using SPSS 24.0 (IBM). A P value < .05 was considered statistically significant. To analyze the differences between proximal and distal areas of IPH, we used a paired t test to compare the slices proximal (− n) and distal (+ n) to the section with the narrowest lumen (ie, Section 0). The paired t test was also used to test the overall difference in absolute IPH area between the proximal and distal regions. A McNemar test was used to analyze differences in proportions of the FC status between the proximal and distal slices, per section and overall per patient.

RESULTS

Of 244 included patients, 6 patients withdrew from the study. Of the remaining 238 patients, another 14

patients were excluded due to bad quality scores of the MR imaging ($n = 4$), incomplete MR imaging protocol ($n = 2$), or absence of MR imaging data due to claustrophobia ($n = 6$) or obesity ($n = 2$). Of the remaining 224 patients, 88 patients (39%) demonstrated IPH on the ipsilateral side. Baseline patient characteristics are shown in the Online Supplemental Data. For the analysis of the FC status, another 5 patients were excluded because no post-contrast MR imaging was available (Online Supplemental Data).

The mean IPH area percentage was significantly larger in the proximal part of the plaque (Fig 3A). The largest mean IPH area percentage is observed 4 mm proximal to the narrowest lumen. The proximal-versus-distal area percentages of IPH are at 2, 4, and 6 mm from the narrowest lumen, respectively: 14.4% versus 9.6% ($P = .04$), 14.7% versus 5.4% ($P < .001$), and 11.1% versus 2.2% ($P = .001$). The MR images at 8 and 10 mm from the narrowest lumen also show a higher mean area percentage of IPH proximal compared with distal; however, this difference was not significant (7.5% versus 2.2%, $P = .056$; 5% versus 1.1%, $P = .077$) (Table 1). Also, the absolute IPH area in the proximal region was significantly higher compared with the distal region at 2, 4, 6, 8, and 10 mm from the narrowest lumen, respectively (0.11 versus 0.07 cm², $P = .019$; 0.12 versus 0.04 cm², $P < .001$; 0.10 versus 0.01 cm², $P < .001$; 0.06 versus 0.01 cm², $P = .005$; and 0.03 versus 0.0003 cm², $P = .004$).

In these patients with IPH, 76% demonstrated a TRFC. The proximal region of the plaque in patients with IPH showed a higher prevalence of a TRFC compared with the distal region at 2, 4, 6, and 8 mm from the MR imaging section with the narrowest lumen, respectively: 33.7% versus 18.1%, $P = .007$; 36.1% versus 7.2%, $P < .001$; 33.7% versus 2.4%, $P = .001$; and 30.1% versus 3.6%, $P = .022$. At 10 mm from the narrowest lumen, the

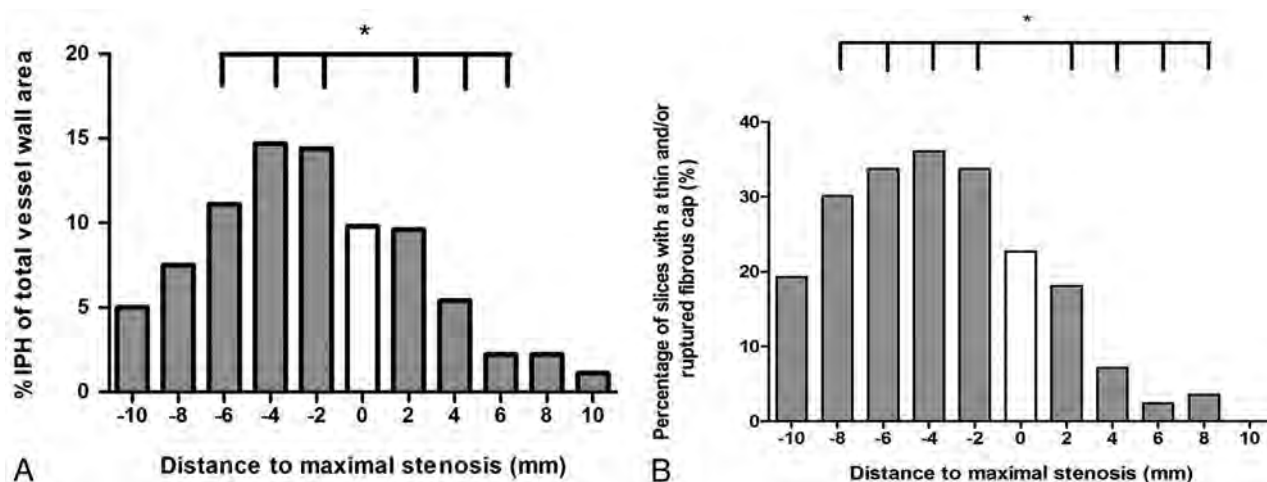


FIG 3. A, Histogram showing significantly larger mean IPH areas in the proximal region of the plaque compared with the distal region. Mean IPH area percentages are shown for each section in relation to the smallest lumen. The *white bar* indicates the section with the narrowest lumen (distance = 0 mm), the bars on the left with the negative numbers are slices proximal (proximally), and the bars on the right with the positive numbers indicate the slices distal to the smallest lumen. Each section has a thickness of 2 mm. An *asterisk* indicates a statistically significant difference ($P < .05$) between the proximal and distal slices using a paired *t* test. B, Prevalence of a TRFC plotted for each section position with respect to the section with the smallest lumen (0). The bars on the left with the negative numbers are slices proximal, and the bars on the right with the positive numbers indicate the slices distal to the smallest lumen. An *asterisk* indicates a statistically significant difference ($P < .05$) between the proximal and distal slices using a McNemar test.

Table 1: Differences in mean IPH area (% of total vessel wall) between proximal and distal regions

Longitudinal Distance from Section with Smallest Lumen (mm)	No. of Slices Where Proximal and Distal Sections Are Available	Mean % IPH with Respect to Total Vessel Wall Area in the Proximal Region	Mean % IPH with Respect to Total Vessel Wall Area in the Distal Region	P Value
2	66	14.4 (SD, 1.9)	9.6 (SD, 2.1)	.040
4	59	14.7 (SD, 1.7)	5.4 (SD, 1.8)	<.001
6	45	11.1 (SD, 1.6)	2.2 (SD, 1.3)	.001
8	39	7.5 (SD, 1.5)	2.2 (SD, 1.5)	.056
10	34	5.0 (SD, 1.4)	1.1 (SD, 1)	.077

Table 2: Differences in prevalence of a TRFC between proximal and distal regions

Longitudinal Distance from Section with Narrowest Lumen (mm)	No. of Slices Where Proximal and Distal Sections Are Available	TRFC (No.) (%) Proximal Region	TRFC (No.) (%) Distal Region	P Value
2	63	28 (33.7)	15 (18.1)	.007
4	56	30 (36.1)	6 (7.2)	<.001
6	43	28 (33.7)	2 (2.4)	.001
8	38	25 (30.1)	3 (3.6)	.022
10	33	16 (19.3)	0 (0)	1.0

prevalence of a TRFC was also higher in the proximal region; however, it was not significant (19.3% versus 0%; $P = 1.0$) (Table 2). Overall, 66 (75%) patients demonstrated a TRFC on the proximal side, while this number was 19 (22%) on the distal side ($P < .001$) (Fig 3B).

To investigate whether the position of the stenosis relative to the carotid bifurcation affects the distribution of intraplaque hemorrhage, we divided the patients into 2 groups, ie, 50% of the patients with the most distal position of the stenosis and 50% of the patients with the most proximal position. The median difference in the position of the narrowest lumen with respect to the bifurcation was 10 mm

between these 2 groups. Both groups showed more IPH at the proximal side of the carotid plaque (data not shown).

DISCUSSION

The present study demonstrates larger mean IPH areas on the proximal region compared with the distal region of carotid plaques assessed with MR imaging in patients with TIA and stroke with mild-to-moderate carotid artery stenosis. Additionally, we found that TRFCs are more frequently located in the proximal region.

The higher prevalence of a TRFC on the proximal side of the plaques was also reported in a previous study with symptomatic and asymptomatic individuals.²⁹ This could be caused by differences in

the wall stress and wall shear stress between the upstream and downstream parts of the plaque. Similarly, increased prevalence of ulcerations in the proximal region of the carotid atherosclerotic plaque has been reported.^{30,31} The increased prevalence of a TRFC on the proximal side could be related to the increased amount of intraplaque hemorrhage in this region because IPH might also develop from the luminal side via fissures or rupture of the FC.¹⁷ A previous PARISK substudy has shown an association between the disrupted plaque surface and intraplaque hemorrhage on MR imaging.¹⁰

Previously, Fagerberg et al¹¹ also described a higher incidence of severe carotid atherosclerotic lesions (containing IPH, macrophages, TRFC) proximal compared with distal in histopathologic specimens. Their population consisted of 40 patients scheduled for carotid endarterectomy with severe stenosis, while patients included in our analysis had a mild-to-moderate stenosis. Yilmaz et al²⁹ and Dirksen et al³² also demonstrated significantly more macrophages and rupture sites at the proximal side in patients with carotid stenosis who underwent carotid endarterectomy. Yilmaz et al found an equal prevalence of intraplaque hemorrhage between the proximal and distal regions (22% versus 23%) in their study of symptomatic and asymptomatic patients with carotid endarterectomy with >70% carotid stenosis.²⁹ However, they did not investigate differences in the area of IPH. Our results also demonstrate that in a group of patients with a mild-to-moderate degree of stenosis in which the arterial pressure wave reflection is less severe, the proximal region still shows significantly more IPH. Thus, also in this population, biomechanical or hemodynamic factors may relate to IPH.

The larger areas of IPH on the proximal part of the plaque may be related to differences in wall stress, which is often increased in the proximal part of the plaque¹³⁻¹⁶ due to arterial pressure wave reflection at the stenosis. The local blood pressure is typically 3 orders of magnitude larger than wall shear stress³³ and, therefore, is the dominant factor for plaque deformation and plaque rupture.³⁴ A large population study, eg, the Rotterdam Study, demonstrated that pulse pressure, the driving force for plaque deformation, is the strongest determinant of IPH, independent of cardiovascular disease risk factors and other blood pressure components.³⁵ Plaque deformation could lead to local tissue damage such as fissures in the FC or rupture of microvessels, causing development or progression of IPH. Most interesting, population studies also showed that pulse pressure is an independent predictor of coronary heart disease,³⁵ cardiovascular mortality in men,³⁶ multiple adverse cardiovascular outcomes,³⁷ and stroke.³⁸ The latter meta-analysis demonstrated that a relatively small increase in pulse pressure (10 mm Hg) was associated with the occurrence of stroke.³⁸ Therefore, studies have recently been advocated to assess therapies targeted at a reduction of pulse pressure.³⁸

Previous studies have assessed plaque biomechanics using computational models with inherent assumptions. Most of these studies focused on plaque rupture rather than IPH development.^{39,40} Huang et al⁴¹ showed that by using an image-based computational model in 5 patients, the IPH is associated with higher structural wall stress. Teng et al⁴² demonstrated that by using a numeric model based on 4 surgery specimens, local tissue deformations were larger around microvasculature surrounded by red blood cells, indicative of IPH.

Wall stress is not to be confused with wall shear stress, caused by frictional (eg, hemodynamic) forces due to blood flow. Wall shear stress is usually also higher in the upstream region with laminar flow, while the turbulent flow downstream of the maximal stenosis is associated with low shear stress levels.^{11,12,14,33,43-47} High wall shear stress promotes apoptosis of vascular smooth-muscle cells.⁴⁸ It also leads to an increased expression of endothelial adhesion molecules, resulting in an accumulation of macrophages,³² which will result in an increased amount of metalloproteinases, which can break down the matrix of the overlying FC and, therefore, contribute to destabilization of the plaque.^{12,30,32} This will tip the scale toward matrix breakdown instead of cap-reinforcing matrix synthesis by smooth-muscle cells.¹⁴ Thus, increased wall shear stress in the upstream region may lead to degradation of the FC, which can also contribute to the development of IPH.

A limitation of the present study is the lack of hemodynamic and biomechanical data (ie, the distribution of wall stress and wall shear stress). Computational fluid dynamics and 4D flow MR imaging can be used to determine wall stress and wall shear stress.^{46,47} Future studies are warranted that include computational fluid dynamics or 4D flow MR imaging to directly relate the local distribution of IPH and TRFC to wall stress and wall shear stress. If a causal relation is proved, it may lead to evaluation of new treatment options, such as pulse-pressure reduction.

Another limitation in the PARISK study is that different scanners and coils were used at different centers. Consequently, there were differences in the image quality of datasets coming from different centers.

CONCLUSIONS

We demonstrated that IPH is more prevalent on the proximal side of the plaque compared with the distal side in patients with mild-to-moderate stenosis. This prevalence may indicate that biomechanical and hemodynamic factors play an important role in the development of IPH. The results of our study suggest that radiologists could pay attention to whether they observe abnormal soft tissue in the proximal region of the plaque when reviewing carotid MRA and CTA examinations.

ACKNOWLEDGMENTS

Participating centers: Academic Medical Center, Amsterdam (P.J. Nederkoorn); Erasmus Medical Center, Rotterdam (A. van der Lugt, P.J. Koudstaal); Almere (M. Limburg); Kennemer Gasthuis, Haarlem (M. Weisfelt); Laurentius Ziekenhuis, Roermond (A.G. Korten); Maasstad Ziekenhuis, Rotterdam (R. Saxena); Maastricht University Medical Center (M.E. Kooi, R.J. van Oostenbrugge, W.H. Mess); Sint Antonius Ziekenhuis, Nieuwegein (S.C. Tromp); Sint Franciscus Gasthuis, Rotterdam (S.L.M. Bakker); Slotervaartziekenhuis, Amsterdam (N.D. Kruyt); Tergooi Ziekenhuizen, Hilversum/Blaricum (J.R. de Kruijk); University Medical Center Utrecht (J. Hendrikse, G.J. de Borst); Viecuri Medisch Centrum, Venlo (B.J. Meems); Vlietland Ziekenhuis, Schiedam (J.C.B. Verhey); IJsseland Ziekenhuis, Capelle a/day IJssel (A.D. Wijnhoud); Zuyderland, Sittard (N.P. van Orshoven)/Heerlen (A.H.C.M.L. Schreuder).

REFERENCES

- Bentzon JF, Otsuka F, Virmani R, et al. **Mechanisms of plaque formation and rupture.** *Circ Res* 2014;114:1852–66 CrossRef Medline
- Daemen MJ, Kooi ME. **Intraplaque hemorrhage as a stimulator of episodic growth of advanced, but nonsymptomatic atherosclerotic lesions bridging the gap.** *JACC Cardiovasc Imaging* 2009;2:1390–92 CrossRef Medline
- Underhill HR, Yuan C, Yarnykh VL, et al. **Arterial remodeling in [corrected] subclinical carotid artery disease.** *JACC Cardiovasc Imaging* 2009;2:1381–89 CrossRef Medline
- Gupta A, Baradaran H, Schweitzer AD, et al. **Carotid plaque MRI and stroke risk: a systematic review and meta-analysis.** *Stroke* 2013;44:3071–77 CrossRef Medline
- Kwee RM, van Oostenbrugge RJ, Mess WH, et al. **MRI of carotid atherosclerosis to identify TIA and stroke patients who are at risk of a recurrence.** *J Magn Reson Imaging* 2013;37:1189–94 CrossRef Medline
- Schindler A, Schinner R, Altaf N, et al. **Prediction of stroke risk by detection of hemorrhage in carotid plaques: meta-analysis of individual patient data.** *JACC Cardiovasc Imaging* 2019;13(2 Pt 2):395–406 CrossRef Medline
- Virmani R, Kolodgie FD, Burke AP, et al. **Atherosclerotic plaque progression and vulnerability to rupture: angiogenesis as a source of intraplaque hemorrhage.** *Arterioscler Thromb Vasc Biol* 2005;25:2054–61 CrossRef Medline
- Falk E, Nakano M, Bentzon JF, et al. **Update on acute coronary syndromes: the pathologist's view.** *Eur Heart J* 2013;34:719–728 CrossRef Medline
- Crombag G, Schreuder F, van Hoof RH, et al. **Microvasculature and intraplaque hemorrhage in atherosclerotic carotid lesions: a cardiovascular magnetic resonance imaging study.** *J Cardiovasc Magn Reson* 2019;21:15 CrossRef Medline
- van Dijk AC, Truijman MT, Hussain B, et al. **Intraplaque hemorrhage and the plaque surface in carotid atherosclerosis: the Plaque at Risk study (PARISK).** *AJNR Am J Neuroradiol* 2015;36:2127–33 CrossRef Medline
- Fagerberg B, Ryndel M, Kjell Dahl J, et al. **Differences in lesion severity and cellular composition between in vivo assessed upstream and downstream sides of human symptomatic carotid atherosclerotic plaques.** *J Vasc Res* 2010;47:221–30 CrossRef Medline
- Cicha I, Worner A, Urschel K, et al. **Carotid plaque vulnerability: a positive feedback between hemodynamic and biochemical mechanisms.** *Stroke* 2011;42:3502–10 CrossRef Medline
- Gao H, Long Q, Kumar Das S, et al. **Study of carotid arterial plaque stress for symptomatic and asymptomatic patients.** *J Biomech* 2011;44:2551–57 CrossRef Medline
- Slager CJ, Wentzel JJ, Gijzen FJ, et al. **The role of shear stress in the destabilization of vulnerable plaques and related therapeutic implications.** *Nat Clin Pract Cardiovasc Med* 2005;2:456–64 CrossRef Medline
- Wenk JF. **Numerical modeling of stress in stenotic arteries with microcalcifications: a parameter sensitivity study.** *J Biomech Eng* 2011;133:014503 CrossRef Medline
- Thrysoe SA, Oikawa M, Yuan C, et al. **Longitudinal distribution of mechanical stresses in carotid plaques of symptomatic patients.** *Stroke* 2010;41:1041–43 CrossRef Medline
- Daemen MJ, Ferguson MS, Gijzen FJ, et al. **Carotid plaque fissure: an underestimated source of intraplaque hemorrhage.** *Atherosclerosis* 2016;254:102–08 CrossRef Medline
- Saba L, Yuan C, Hatsukami TS, et al; Vessel Wall Imaging Study Group of the American Society of Neuroradiology. **Carotid Artery Wall Imaging: Perspective and Guidelines from the ASNR Vessel Wall Imaging Study Group and Expert Consensus Recommendations of the American Society of Neuroradiology.** *AJNR Am J Neuroradiol* 2018;39:E9–31 CrossRef Medline
- Truijman MT, Kwee RM, van Hoof RH, et al. **Combined 18F-FDG PET-CT and DCE-MRI to assess inflammation and microvascularization in atherosclerotic plaques.** *Stroke* 2013;44:3568–70 CrossRef Medline
- Ota H, Yarnykh VL, Ferguson MS, et al. **Carotid intraplaque hemorrhage imaging at 3.0-T MR imaging: comparison of the diagnostic performance of three T1-weighted sequences.** *Radiology* 2010;254:551–63 CrossRef Medline
- Truijman MT, Kooi ME, van Dijk AC, et al. **Plaque at Risk (PARISK): prospective multicenter study to improve diagnosis of high-risk carotid plaques.** *Int J Stroke* 2014;9:747–54 CrossRef Medline
- Kim S, Kwak HS, Hwang SB, et al. **Dynamic change of carotid intraplaque hemorrhage volume in subjects with mild carotid stenosis.** *Eur J Radiol* 2018;105:15–19 CrossRef Medline
- Crombag G, Spronk HM, Nelemans P, et al. **No association between thrombin generation and intra-plaque haemorrhage in symptomatic carotid atherosclerotic plaques: the Plaque at RISK (PARISK) study.** *Thromb Haemost* 2018;118:1461–69 CrossRef Medline
- Yuan C, Mitsumori LM, Ferguson MS, et al. **In vivo accuracy of multispectral magnetic resonance imaging for identifying lipid-rich necrotic cores and intraplaque hemorrhage in advanced human carotid plaques.** *Circulation* 2001;104:2051–56 CrossRef Medline
- Takaya N, Yuan C, Chu B, et al. **Association between carotid plaque characteristics and subsequent ischemic cerebrovascular events: a prospective assessment with MRI: initial results.** *Stroke* 2006;37:818–23 CrossRef Medline
- Cappendijk VC, Cleutjens KB, Heeneman S, et al. **In vivo detection of hemorrhage in human atherosclerotic plaques with magnetic resonance imaging.** *J Magn Reson Imaging* 2004;20:105–10 CrossRef Medline
- Kwee RM, van Oostenbrugge RJ, Mess WH, et al. **Carotid plaques in transient ischemic attack and stroke patients: one-year follow-up study by magnetic resonance imaging.** *Invest Radiol* 2010;45:803–09 CrossRef Medline
- Kwee RM, van Engelshoven JM, Mess WH, et al. **Reproducibility of fibrous cap status assessment of carotid artery plaques by contrast-enhanced MRI.** *Stroke* 2009;40:3017–21 CrossRef Medline
- Yilmaz A, Lipfert B, Cicha I, et al. **Accumulation of immune cells and high expression of chemokines/chemokine receptors in the upstream shoulder of atherosclerotic carotid plaques.** *Exp Mol Pathol* 2007;82:245–55 CrossRef Medline
- Lovett JK, Rothwell PM. **Site of carotid plaque ulceration in relation to direction of blood flow: an angiographic and pathological study.** *Cerebrovasc Dis* 2003;16:369–75 CrossRef Medline
- de Weert TT, Cretier S, Groen HC, et al. **Atherosclerotic plaque surface morphology in the carotid bifurcation assessed with multidetector computed tomography angiography.** *Stroke* 2009;40:1334–40 CrossRef Medline
- Dirksen MT, van der Wal AC, van den Berg FM, et al. **Distribution of inflammatory cells in atherosclerotic plaques relates to the direction of flow.** *Circulation* 1998;98:2000–03 CrossRef Medline
- Gijzen FJ, Wentzel JJ, Thury A, et al. **Strain distribution over plaques in human coronary arteries relates to shear stress.** *Am J Physiol Heart Circ Physiol* 2008;295:H1608–14 CrossRef Medline
- Hoeks AP, Reesink KD, Hermeling E, et al. **Local blood pressure rather than shear stress should be blamed for plaque rupture.** *J Am Coll Cardiol* 2008;52:1107–08; author reply 1108–09 CrossRef Medline
- Selwaness M, van den Bouwhuysen QJ, Verwoert GC, et al. **Blood pressure parameters and carotid intraplaque hemorrhage as measured by magnetic resonance imaging: the Rotterdam Study.** *Hypertension* 2013;61:76–81 CrossRef Medline
- Benetos A, Rudnicki A, Safar M, et al. **Pulse pressure and cardiovascular mortality in normotensive and hypertensive subjects.** *Hypertension* 1998;32:560–64 CrossRef Medline
- Selvaraj S, Steg PG, Elbez Y, et al. **Pulse pressure and risk for cardiovascular events in patients with atherothrombosis: from the REACH Registry.** *J Am Coll Cardiol* 2016;67:392–403 CrossRef Medline

38. Liu FD, Shen XL, Zhao R, et al. **Pulse pressure as an independent predictor of stroke: a systematic review and a meta-analysis.** *Clin Res Cardiol* 2016;105:677–86 CrossRef Medline
39. Holzapfel GA, Mulvihill JJ, Cunnane EM, et al. **Computational approaches for analyzing the mechanics of atherosclerotic plaques: a review.** *J Biomech* 2014;47:859–69 CrossRef Medline
40. Cardoso L, Weinbaum S. **Changing views of the biomechanics of vulnerable plaque rupture: a review.** *Ann Biomed Eng* 2014;42:415–31 CrossRef Medline
41. Huang X, Teng Z, Canton G, et al. **Intraplaque hemorrhage is associated with higher structural stresses in human atherosclerotic plaques: an in vivo MRI-based 3D fluid-structure interaction study.** *Biomed Eng Online* 2010;9:86 CrossRef Medline
42. Teng Z, He J, Degnan AJ, et al. **Critical mechanical conditions around neovessels in carotid atherosclerotic plaque may promote intraplaque hemorrhage.** *Atherosclerosis* 2012;223:321–26 CrossRef Medline
43. Siegel JM, Markou CP, Ku DN, et al. **A scaling law for wall shear rate through an arterial stenosis.** *J Biomech Eng* 1994;116:446–51 CrossRef Medline
44. Stroud JS, Berger SA, Saloner D. **Numerical analysis of flow through a severely stenotic carotid artery bifurcation.** *J Biomech Eng* 2002;124:9–20 CrossRef Medline
45. Fukumoto Y, Hiro T, Fujii T, et al. **Localized elevation of shear stress is related to coronary plaque rupture: a 3-dimensional intravascular ultrasound study with in-vivo color mapping of shear stress distribution.** *J Am Coll Cardiol* 2008;51:645–50 CrossRef Medline
46. Tuentner A, Selwaness M, Arias Lorza A, et al. **High shear stress relates to intraplaque haemorrhage in asymptomatic carotid plaques.** *Atherosclerosis* 2016;251:348–54 CrossRef Medline
47. Zhang G, Zhang S, Qin Y, et al. **Differences in wall shear stress between high-risk and low-risk plaques in patients with moderate carotid artery stenosis: a 4D flow MRI study.** *Front Neurosci* 2021;15:678358 CrossRef Medline
48. Wang Y, Qiu J, Luo S, et al. **High shear stress induces atherosclerotic vulnerable plaque formation through angiogenesis.** *Regen Biomater* 2016;3:257–67 CrossRef Medline

Impact Analysis of Different CT Configurations of Carotid Artery Plaque Calcifications on Cerebrovascular Events

L. Saba, H. Chen, R. Cau, G.D. Rubeis, G. Zhu, F. Pisu, B. Jang, G. Lanzino, J.S. Suri, Y. Qi, and M. Wintermark



ABSTRACT

BACKGROUND AND PURPOSE: CT is considered the standard reference both for quantification and characterization of carotid artery calcifications. Our aim was to investigate the relationship among different types of calcium configurations detected with CT within the plaque with a novel classification and to investigate the prevalence of cerebrovascular events.

MATERIALS AND METHODS: Seven hundred ninety patients (men = 332; mean age, 69.7 [SD, 13] years; 508 symptomatic for cerebrovascular symptoms and 282 asymptomatic) who underwent computed tomography of the carotid arteries were retrospectively included in this institutional review board–approved study. The plaque was classified into 6 types according to the different types of calcium configurations as the following: type 1, complete absence of calcification within the plaque; type 2, intimal or superficial calcifications; type 3, deep or bulky calcifications; type 4, adventitial calcifications with internal soft plaque of <2 mm thickness; type 5, mixed patterns with intimal and bulky calcifications; and type 6, positive rim sign.

RESULTS: The highest prevalence of cerebrovascular events was observed for type 6, for which 89 of the 99 cases were symptomatic. Type 6 plaque had the highest degree of correlation with TIA, stroke, symptoms, and ipsilateral infarct for both sides with a higher prevalence in younger patients. The frequency of symptoms observed by configuration type significantly differed between right and left plaques, with symptoms observed more frequently in type 6 calcification on the right side (50/53; 94%) than on the left side (39/46; 85%, $P < .001$).

CONCLUSIONS: We propose a novel carotid artery plaque configuration classification that is associated with the prevalence of cerebrovascular events. If confirmed in longitudinal analysis, this classification could be used to stratify the risk of occurrence of ischemic events.

ABBREVIATION: IPH = intraplaque hemorrhage

Ischemic stroke is one of the leading causes of mortality and disability worldwide.¹ Several studies have demonstrated that atherosclerosis involving the carotid arteries is responsible for a significant portion of acute ischemic strokes (up to 25%).^{2,3} In the past 20 years, the role of carotid plaque imaging in risk stratification of ischemic stroke has evolved considerably. Several recently published articles suggest that the mere degree of stenosis,

considered the only criterion for risk stratification at a time when advanced imaging was not available, is not the best parameter to predict the stability and vulnerability of the plaque and its potential for causing cerebrovascular events.^{2,4,5} Therefore, there has been great emphasis on identifying additional imaging features that can be used to select the best therapeutic approach.

A number of parameters have been identified that are associated with an increased risk of plaque rupture, including intraplaque haemorrhage,^{6,7} lipid-rich necrotic core,⁸ rupture of the fibrous cap, and contrast plaque enhancement.⁹ Other features such as a thick fibrous cap have been linked to a reduced risk of stroke. The role of calcium, present in 50%–60% of carotid plaques, is controversial,¹⁰ and the relationship between the amount and topographic distribution of vascular wall calcifications and plaque vulnerability have not been evaluated. Some studies have found that carotid plaque calcification is associated with plaque stability and may be considered a protective plaque feature,^{11–14} while others have found that it could represent an independent marker of ischemic symptoms.¹⁵ The significance of calcifications

Received July 14, 2021; accepted after revision November 15.

From the Department of Radiology (L.S., R.C., F.P.), Azienda Ospedaliero Universitaria di Cagliari, Cagliari, Italy; Department of Radiology (H.C., G.Z., B.J., M.W.), Division of Neuroradiology, Stanford University Hospital, Stanford, California; Department of Radiology, UOC of Diagnostic and Interventional Neuroradiology (G.D.R.), San Camillo-Forlanini Hospital, Rome, Italy; Department of Neurologic Surgery (G.L.), Mayo Clinic, Rochester, Minnesota; Stroke Monitoring and Diagnostic Division (J.S.S.), AtheroPoint, Roseville, California; and Department of Xuanwu Hospital (Y.Q.), Capital Medical University, Beijing, China.

Please address correspondence to Luca Saba, MD, Azienda Ospedaliero Universitaria (A.O.U.) of Cagliari-Polo di Monserrato, Department of Medical Imaging, Via Tola 7, Cagliari, 09128, Italy; e-mail: lucasaba@tiscali.it; @lucasaba1TA

Indicates article with online supplemental data.

<http://dx.doi.org/10.3174/ajnr.A7401>

and their distribution in carotid artery plaques are controversial,¹⁵⁻¹⁷ and it is unclear whether the level of carotid calcification should be considered an element of plaque stability or instability. Eisenmenger et al¹⁸ proposed a model that includes the positive rim sign, maximum soft-plaque thickness, the NASCET stenosis, and ulceration to predict intraplaque hemorrhages (IPHs) on computed tomography (CT). A positive rim sign was defined as adventitial calcification (<2 mm thick) with internal soft plaque (>2 mm thickness). This model had excellent IPH prediction with an area under the curve of 0.94.¹⁸

Calcium in a carotid artery plaque can be identified with different imaging techniques. Among these, CT is considered the standard reference both for quantification and characterization of carotid artery calcifications.¹⁹⁻²¹ Our hypothesis is that it is possible to classify the CTA patterns of calcifications in the carotid plaque by identifying subgroups that can be more frequently associated with the presence of symptomatic cerebrovascular events. We have, therefore, developed a novel classification based on the different calcium configurations.

In this study, we identified various carotid artery plaque subgroups on the basis of their morphology as visualized on CTA and assessed their clinical significance in a large cohort of symptomatic and asymptomatic patients.

MATERIALS AND METHODS

Study Design and Patient Population

Institutional review board approval was obtained, and informed consent was waived because of the retrospective nature of the study. This 2-center retrospective study was performed in 2 tertiary centers (Azienda Ospedaliera Universitaria di Cagliari [site A] and Stanford University Hospital [site B] between March 2013 and May 2020. All examinations were performed according to established standard-of-care CTA protocols. Patient characteristics including age, sex, clinical symptoms, medical history, and clinical outcomes were recorded.

Patients 18 years of age or older with bilateral carotid artery plaques (thickness of ≥ 1.5 mm, according to the Mannheim intima-media thickness consensus) were included.²² Excluded were subjects younger than 18 years of age and those in whom the CTA was performed for reasons other than suspected atherosclerotic disease (ie, dissection) or other etiologies for ischemic stroke such as a cardiac embolic source, embolism from the thoracic aorta, and vertebrobasilar artery disease. The degree of stenosis was measured according to the NASCET criteria.²³ We also excluded patients with other neurologic conditions such as brain neoplasms, demyelinating disease, and so forth.

According to a standardized protocol, CTA of the carotid artery was obtained in asymptomatic patients when carotid sonography showed significant stenosis (>50% measured according to the NASCET criteria) or features of plaque vulnerability (ulcerations, irregular surface) and when carotid sonography could not adequately assess the degree of stenosis and plaque characteristics because of anatomic conditions. Moreover, all subjects presenting with acute cerebrovascular events underwent CTA of the carotid arteries at the time of their acute CT of the head.

Definition of Symptomatic

Patients were classified by the treating neurologist using the Trial of Org 10172 in Acute Stroke Treatment (TOAST) criteria.²⁴ Consequently, a patient was considered symptomatic after experiencing a TIA or ischemic stroke in either cerebral hemisphere. TIA was considered a brief (<24 hours) episode of neurologic dysfunction such as hemiparesis, hemisensory loss, dysarthria, dysphasia, or monocular blindness. If the episode of neurologic dysfunction exceeded 24 hours, it was classified as a stroke. A lacunar stroke was defined as a stroke causing one of the traditional clinical lacunar syndromes without evidence of cerebral cortical dysfunction. Such patients also had normal CT/MR imaging findings or a relevant brain stem or subcortical hemispheric lesion with a diameter of <0.5 cm.²⁵ A patient was considered symptomatic within a time window of up to 3 months after symptom onset. For our model of analysis, we considered both carotid arteries in each patient: The symptomatic carotid was the one ipsilateral to the symptoms and the asymptomatic carotid was the contralateral one.

CT Technique

Due to the range of time for data collection and the bicenter approach, CTA of the carotid arteries was performed with multiple scanner technologies according to a standardized protocol. As a general approach, patients were placed in the supine position with the head tilted back to prevent dental artifacts. The coverage was from the aortic arch to the carotid siphon in a caudocranial direction.

Plaque Calcification Configuration

Carotid plaques were classified into 6 subgroups based on calcium configurations (Fig 1):

- Type 1: complete absence of calcification within the plaque
- Type 2: intimal or superficial calcifications
- Type 3: deep or bulky calcifications
- Type 4: adventitial calcifications with internal soft plaque of <2-mm-thickness; negative rim sign
- Type 5: mixed patterns with intimal and bulky calcifications
- Type 6: positive rim sign.

A superficial calcification was defined as a calcified nodule located at the intimal-lumen interface or close to the lumen, whereas a deep calcification was defined as a calcified nodule located at the media/adventitia border or close to the adventitia. The presence of both deep and superficial calcifications was regarded as a mixed category.²⁶ Bulky calcification was defined as calcification measuring >2 mm thick without associated thin adventitial calcification.¹⁸

The classification was performed by 2 radiologists; in the case of conflicts between the readers, the decision was made by a third senior reader expert in vascular imaging. Interobserver and intraobserver (within a 2-month timeframe) agreement was recorded. Interactive window/level settings were usually set at W850: L300.²⁷ This approach was adopted because calcifications may show variable edge and halo blurring depending on the window level, which could change the size (expressed in millimeters) of the calcification; therefore, we opted for this static approach.

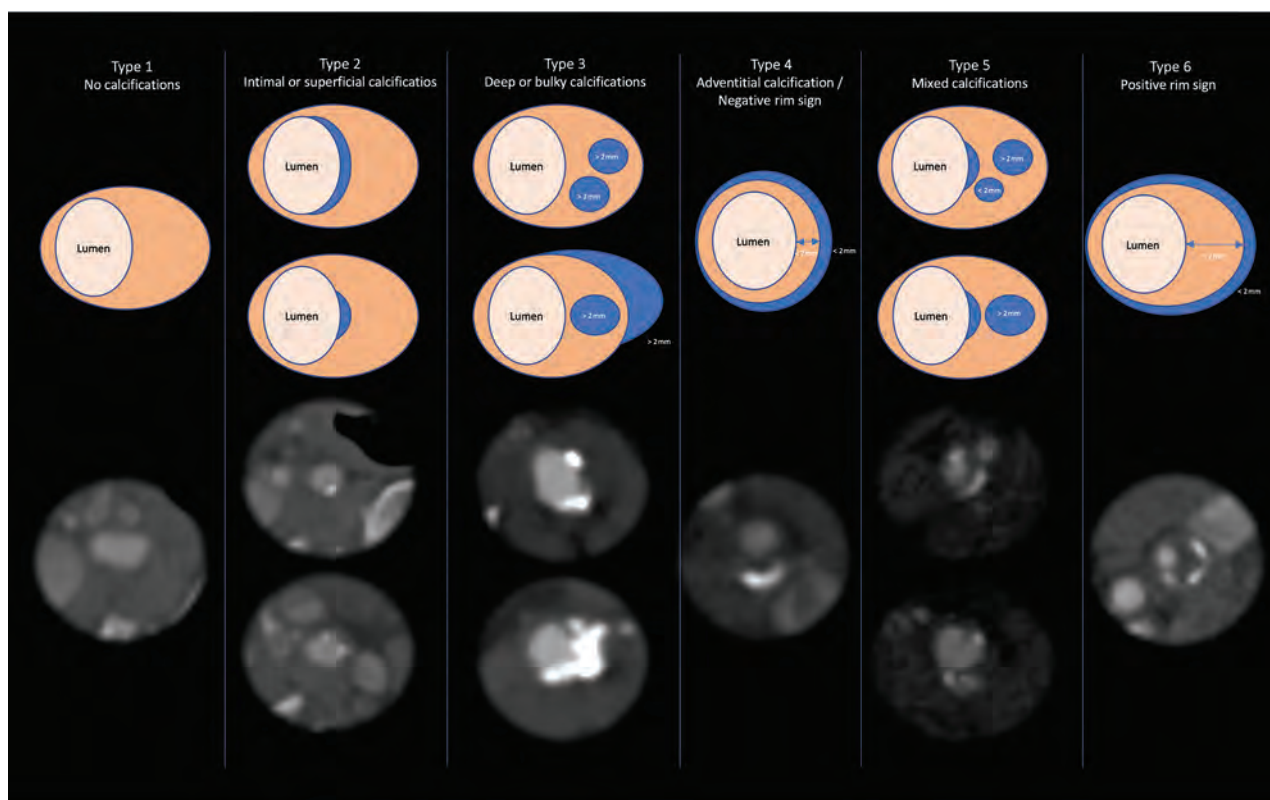


FIG 1. Scheme showing the different types of configurations with the corresponding CTA findings.

Table 1: Demographic and risk factors

	Symptoms		P Value
	No	Yes	
Sex			
Female	159	299	.5
Male	123	209	
Age (mean value in years)	69.1 (SD, 12)	70.1 (SD, 13)	.68
Hypertension			
No	110	177	.25
Yes	172	331	
Smoking status			
<2 years	66	143	.26
>2 years	56	105	
No	160	260	
CAD			
No	231	407	.54
Yes	51	101	
Diabetes			
No	207	383	.54
Yes	75	125	
Hyperlipidemia			
No	101	116	<.001 ^a
Yes	181	392	

Note:—CAD indicates coronary artery disease.

^aSignificant.

Statistical Analysis

Continuous variables were presented as mean (SD) or median (with interquartile range) values. Categorical variables were described as frequency rates and percentages. Comparisons of continuous data were performed using the independent samples *t* test or

Mann-Whitney *U* test. Shapiro-Wilk tests were used to check continuous variables for normal distribution. Categorical variables were compared using a χ^2 test or Fisher exact test as appropriate. Comparisons between groups were performed using a 1-way ANOVA for continuous variables with normal distributions; the Kruskal-Wallis test was used for continuous variables with non-normal distributions. A Tukey multiple comparison test was performed to determine statistically significant changes between each group. Inter-/intraobserver agreement was measured using a weighted Cohen κ analysis. A *P* value < .05 was considered statistically significant. The Pearson ρ was used to correlate types of plaque with traditional risk factors, infarct, stroke, symptoms, and degree of stenosis. All statistical analyses were performed using SPSS Statistics, Version 25 (IBM).

RESULTS

Baseline Characteristics

The study included 790 patients (men = 42%, women = 58%; mean age, 69.7 [SD, 13] years; age range, 23–102 years) with bilateral plaques, 508 symptomatic and 282 asymptomatic. Clinical and demographic characteristics are summarized in Table 1. The mean degree of stenosis was 61% in the symptomatic patients and 30% in the asymptomatic ones. Plaque on the right side was 39%; and on the left side, 41%.

Plaque Calcification Type and Symptoms

The crosstabulation among the types of calcifications is given in Table 2. The frequency of symptoms observed by configuration type significantly differed between right and left plaques, with

symptoms observed more frequently in type 6 calcification on the right side (50/53; 94%) than on the left side (39/46, 85%; $P < .001$).

We found that the absence of calcification on one side is frequently associated with absence of calcification on the contralateral side. However, the weighted overall Cohen κ value was poor, with a value of 0.297. We also tested the inter- and intraobserver concordance; the values are summarized in the Online Supplemental Data.

In the analysis of the correlations among the types of calcifications and symptomatic status (by considering 1580 sides), the highest prevalence of symptomatic plaques was observed for type 6, in which 89 of the 99 plaques were symptomatic. A complete summary of the findings is shown in Fig 2.

We also checked the impact of side by analyzing the association between the right/left carotid artery plaque configurations and the presence of symptoms (right stroke, left stroke/absence of stroke for asymptomatic patients); the results are summarized in Fig 2. The Pearson χ^2 test showed a statistically significant difference for different types of configurations for both right and left plaques ($P < .001$). Figure 3 shows the relationship among different plaque configurations on the right/left side versus the measured risk factors.

There was an increasing correlation from type 1 to type 6 plaque configurations with symptoms, stroke, ipsilateral infarct, TIA, and NASCET degree of stenosis for both sides. In particular, the highest degree of correlation was found for ipsilateral infarct, ranging from -0.067 for type 1 to 0.21 for type 6 on right side and from -0.11 for type 1 to 0.21 for type 6 on left side (see Fig 4 for

further details). No other traditional risk factors for cerebrovascular diseases reached the same degree of correlation (Fig 4). Moreover, as observed in the Online Supplemental Data, by plotting the types of calcifications with age and degree of stenosis, type 6 plaque configuration was more common in younger patients, with a bimodal distribution for stenosis degree (mild and severe) on both sides.

DISCUSSION

In the present study, we grouped the different types of calcium configurations we encountered in our daily clinical practice by proposing a novel classification system to verify whether some configurations are more likely to be associated with cerebrovascular events.

The analysis of the association between the types of calcifications and the presence of symptoms (by considering 1580 sides) showed that the highest risk of cerebrovascular events is seen for type 6, in which 89 of the 99 patients were symptomatic. These results were also confirmed by the correlation analysis, in which type 6 had the highest degree of correlation with symptoms, stroke, TIA, and ipsilateral infarct. Our results also confirm that the presence of a positive rim sign is significantly associated with cerebrovascular events, but from the analysis of the other ORs, it is quite obvious that the different types of calcium configurations play a different role, with an increasing OR according to the analyzed class. Moreover, after analyzing the relative frequency of plaque configurations among different ages and degrees of stenosis,^{28,29} type 6 was more frequent in younger patients, with a bimodal distribution with regard to the NASCET degree of stenosis (mild and severe).

The type 1 class identifies those carotid artery plaques without calcification within the plaque, and somewhat surprisingly, we found that plaques without any calcium have an OR of 0.5, which suggests that such plaques are not associated with an increased frequency of cerebrovascular events.

When one introduces a new classification, it is important to test the inter-/intraobserver agreement, and we found

Table 2: Crosstabulation between calcified plaque on the right and left sides

Calcification Type on the Right Side	Calcification Type on the Left Side						Total
	Type 1	Type 2	Type 3	Type 4	Type 5	Type 6	
Type 1	213	15	19	3	8	3	261
Type 2	20	15	39	6	5	2	87
Type 3	39	40	107	19	21	15	241
Type 4	6	6	32	11	7	10	72
Type 5	5	7	26	10	19	9	76
Type 6	6	3	25	8	4	7	53
Total	289	86	248	57	64	46	790

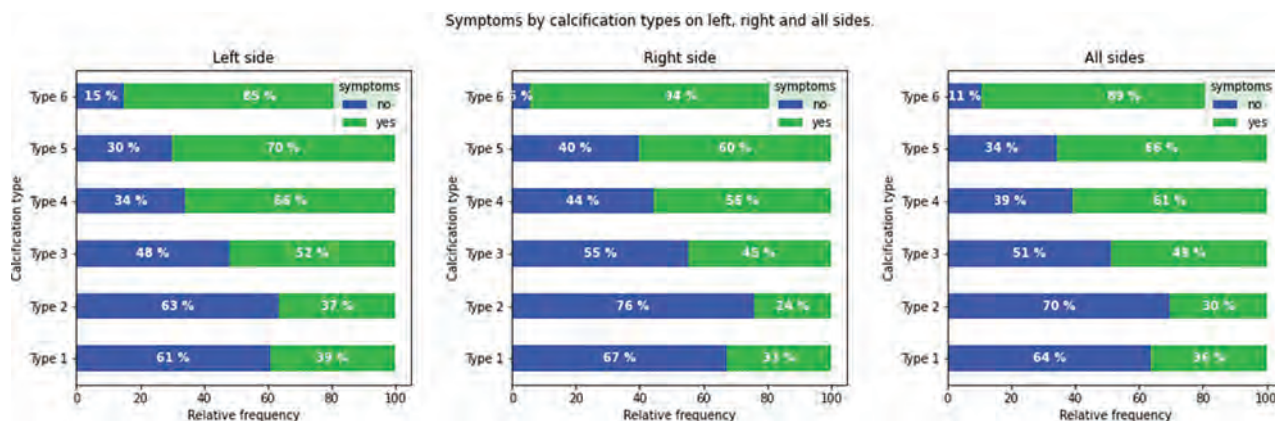


FIG 2. Bar plots in symptomatic and asymptomatic subjects according to the plaque configuration for the total plaque count (A), the right side (B), and left side (C).

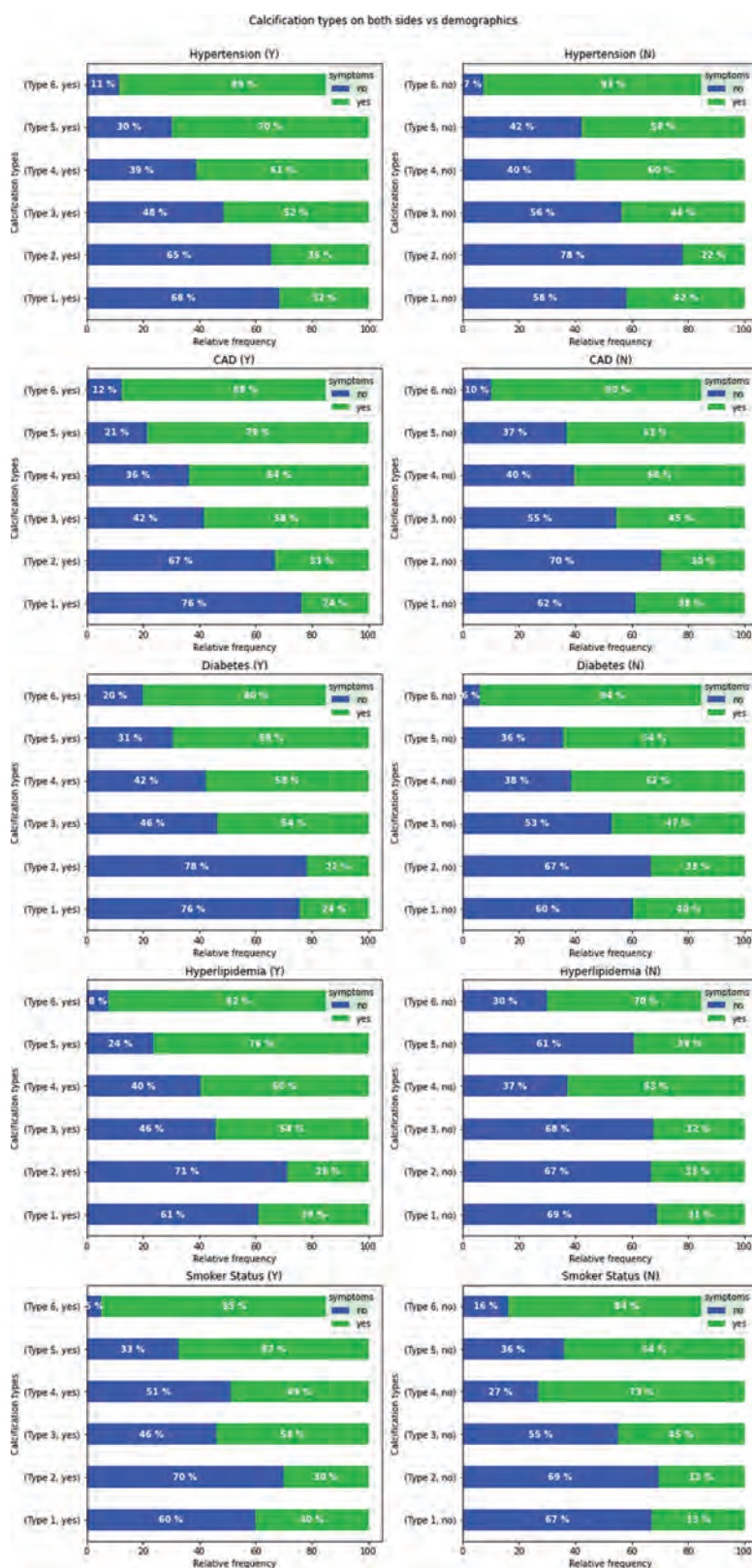


FIG 3. Bar plots in symptomatic and asymptomatic subjects according to the plaque configuration for the total on the right (*upper row*) and left (*lower row*) sides for cardiovascular risk factors. CAD indicates coronary artery disease; Y, yes; N, no.

that the configurations are quite good and reproducible. The overall concordance is good, with a better intraobserver agreement than interobserver agreement. In particular, the type 1 category has excellent values of reproducibility; also, types 4 and 6 have optimal values. Types 2 and 3 have suboptimal values. However, a further evolution to improve the reproducibility could be to apply machine learning algorithms,³⁰ to move from a subjective assessment to a more objective and reproducible type classification.

As expected, we found that the mean degree of stenosis was 64% in symptomatic patients and 35% in asymptomatic ones by confirming that the degree of stenosis is an important parameter, even if this could be considered an indirect parameter influenced by the volume of plaque and the different remodeling pathways.

We have also checked the impact by side, by analyzing the association between the right/left carotid artery plaque configurations and the presence of symptoms (right stroke/left stroke/absence of stroke for asymptomatic patients), and a statistically significant difference for different types of configurations for both right and left plaques was found. Figure 3 shows the relationship between the different plaque configurations on the right/left sides versus the measured risk factors. Moreover, we found that the absence of calcification on one side is not associated with the absence of calcification on the contralateral side: The Cohen κ value was poor (0.297).

To date, there are no grading systems describing carotid artery calcium configurations and distributions. However, there are studies that have demonstrated how some types of configurations can influence the risk of ipsilateral cerebrovascular events. Eisenmenger et al¹⁸ showed that the positive rim sign is predictive of an increased stroke risk because it is associated with the presence of IPH within the plaque.

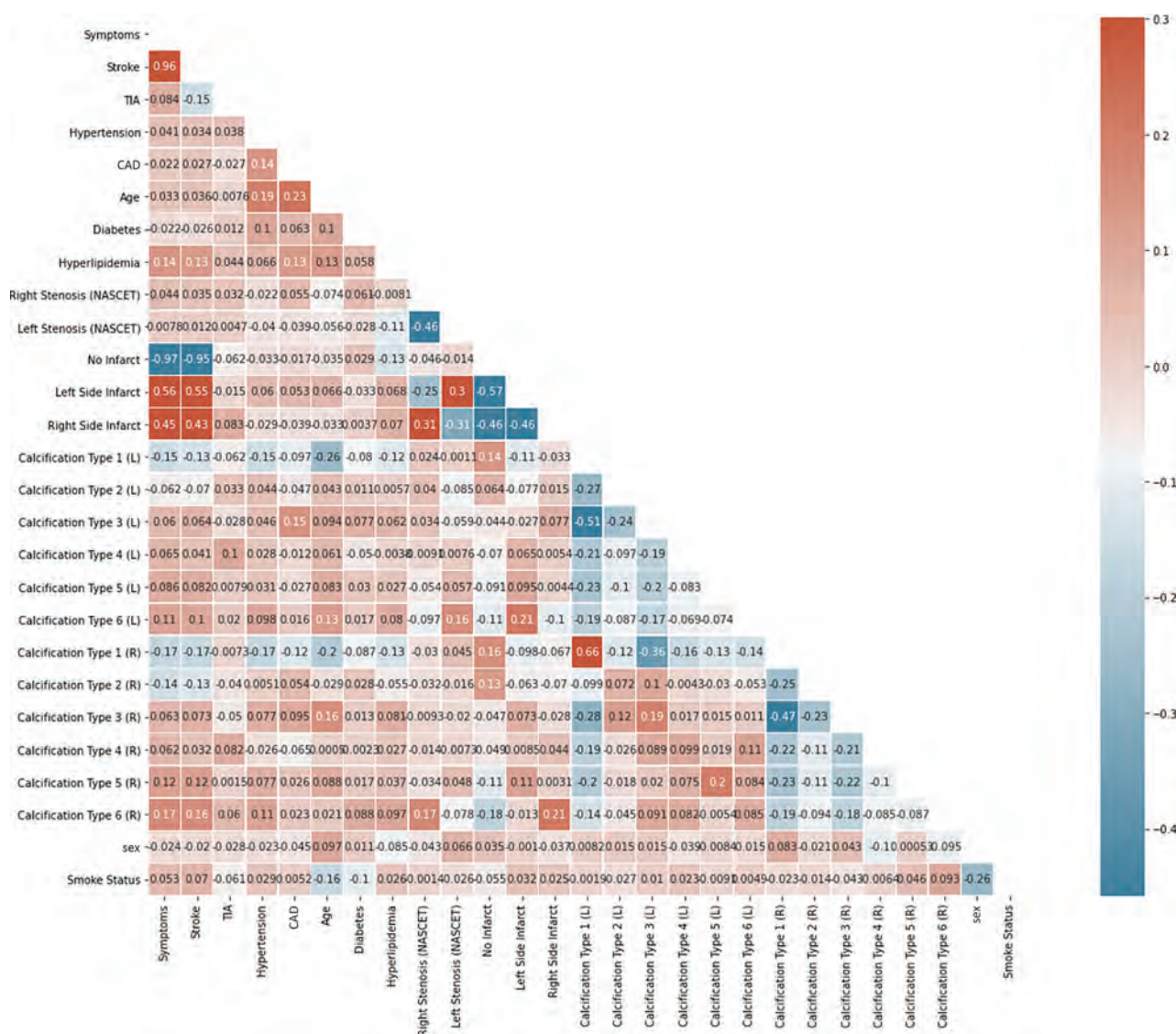


FIG 4. The Pearson ρ correlogram shows the correlation test among the different demographic variables and the calcification types. Each box represents a correlation test, the blue values represent negative correlations, and the red values represent positive associations. CAD indicates coronary artery disease; L, left; R, right.

Recently, Yang et al²⁶ demonstrated that superficial calcifications were associated with an increased risk of IPH and subsequent risk of cerebrovascular events. Xu et al³¹ reported a similar association in 2010 using MR imaging. This could be explained by exploring the pathophysiology of the IPH, in which the leakage from the vasa vasorum could produce a blood collection with subsequent space occupation and shift and compression of the adjacent structures with superimposition of the calcification. However, the problem could be also more complex: Van den Bouwhuisen et al,³² in 2015, found that a larger carotid calcification volume at the level of the bifurcation was related to the presence of IPH. This is an interesting finding because this association did not seem to be driven simply by plaque size or atherosclerotic burden because it did not alter after an adjustment was made for wall thickness. The association was even more pronounced in persons with a low degree of carotid stenosis. They also found that larger calcification volumes were associated with a lower prevalence of lipid core, which was more pronounced at a higher degree of stenosis (>30%).

The findings of this study do not suggest that some types of calcifications are vulnerable but that these are associated with other parameters related to the vulnerability. This concept is clear by comparing types 4 and 6 in which the calcium morphology is exactly the same, but the difference is due to the thickness of the soft-tissue component (<2 and >2 mm for types 4 and 6, respectively). Our results confirm that the role of calcium is complex. It is implicated in different metabolic processes, which are sometimes conflicting and overlapping.¹⁷ One important point is that with CT, we can explore a partial element of this complexity, the geometric configuration, and we have found that this could potentially represent a biomarker.

The potential utility of this novel classification relies on the opportunity to classify carotid artery plaque according to the calcium configuration and characteristics, and CT is an optimal technique for this task because it provides excellent visualization of calcification due to the marked x-ray attenuation properties of calcium.³³ Further prospective studies would be necessary to test

the potential impact of these configurations on the occurrence of cerebrovascular events.³⁴

Our study has limitations. The first one is that due to the retrospective nature of our analysis, the 2 cohorts we have analyzed were not similar due to the statistically significant difference in the hyperlipidemia prevalence. This could have introduced a bias because hyperlipidemia could play a role in the atherogenic process by stimulating some specific pathways. In particular, medial calcification is not associated with atherosclerosis, and it is not typically linked to dyslipidemia, whereas this association is more robust for intimal calcifications³⁵ because hyperlipidemia leads to accumulation of lipoproteins in the subendothelial space of cardiovascular tissues, which leads to formation of mildly oxidized phospholipids, which are known bioactive factors in vascular cell calcification.^{36,37} Second, this is a retrospective cross-sectional study in which we have not explored the relationship between the types of carotid plaque configurations and the occurrence of cerebrovascular events but we have assessed the relationship between the calcium configuration and the presence of events.

Our data need confirmation in a prospective, longitudinal cohort to confirm our hypothesis and validate our classification; thus, our results should be considered preliminary. Therefore, although suggesting that some types of calcium configurations within the plaque can be markers of instability, we cannot distinguish whether there is a causative relationship between the 2 or if the calcification is a mere epiphenomenon of the concomitant atherosclerotic process. Nevertheless, our results suggest that imaging can explore the complexity of calcium configurations and offer an option of stratification and that calcium configurations may be of value as an indirect marker of plaque instability.

CONCLUSIONS

We suggest a carotid artery plaque configuration classification that is associated with the presence of cerebrovascular events. If confirmed in longitudinal analysis, this classification could be used to stratify the risk of occurrence of ischemic events.

Disclosure forms provided by the authors are available with the full text and PDF of this article at www.ajnr.org.

REFERENCES

- Gorelick PB. **The global burden of stroke: persistent and disabling.** *Lancet Neurol* 2019;18:417–18 CrossRef Medline
- Saba L, Saam T, Jäger HR, et al. **Imaging biomarkers of vulnerable carotid plaques for stroke risk prediction and their potential clinical implications.** *Lancet Neurol* 2019;18:559–72 CrossRef Medline
- Kamel H, Merkler AE, Iadecola C, et al. **Tailoring the approach to embolic stroke of undetermined source.** *JAMA Neurol* 2019;76:855–57 CrossRef Medline
- Wasserman BA, Wityk RJ, Trout HH, et al. **Low-grade carotid stenosis: looking beyond the lumen with MRI.** *Stroke* 2005;36:2504–13 CrossRef Medline
- Naghavi M, Libby P, Falk E, et al. **From vulnerable plaque to vulnerable patient: a call for new definitions and risk assessment strategies, Part II.** *Circulation* 2003;108:1772–78 CrossRef Medline
- Schindler A, Schinner R, Altaf N, et al. **Prediction of stroke risk by detection of hemorrhage in carotid plaques: meta-analysis of individual patient data.** *JACC Cardiovasc Imaging* 2020;13:395–406 CrossRef Medline
- Saba L, Micheletti G, Brinjikji W, et al. **Carotid intraplaque-hemorrhage volume and its association with cerebrovascular events.** *AJNR Am J Neuroradiol* 2019;40:1731–37 CrossRef Medline
- Underhill HR, Hatsukami TS, Fayad ZA, et al. **MRI of carotid atherosclerosis: clinical implications and future directions.** *Nat Rev Cardiol* 2010;7:165–73 CrossRef Medline
- Saba L, Lai ML, Montisci R, et al. **Association between carotid plaque enhancement shown by multidetector CT angiography and histologically validated microvessel density.** *Eur Radiol* 2012;22:2237–45 CrossRef Medline
- Baradaran H, Al-Dasuqi K, Knight-Greenfield A, et al. **Association between carotid plaque features on CTA and cerebrovascular ischemia: a systematic review and meta-analysis.** *AJNR Am J Neuroradiol* 2017;38:2321–26 CrossRef Medline
- Kwee RM. **Systematic review on the association between calcification in carotid plaques and clinical ischemic symptoms.** *J Vasc Surg* 2010;51:1015–25 CrossRef Medline
- Nandalur KR, Hardie AD, Raghavan P, et al. **Composition of the stable carotid plaque: Insights from a multidetector computed tomography study of plaque volume.** *Stroke* 2007;38:935–40 CrossRef Medline
- Saba L, Montisci R, Sanfilippo R, et al. **Multidetector row CT of the brain and carotid artery: a correlative analysis.** *Clin Radiol* 2009;64:767–78 CrossRef Medline
- Barrett HE, Van der Heiden K, Farrell E, et al. **Calcifications in atherosclerotic plaques and impact on plaque biomechanics.** *J Biomech* 2019;87:1–12 CrossRef Medline
- Nandalur KR, Baskurt E, Hagspiel KD, et al. **Carotid artery calcification on CT may independently predict stroke risk.** *AJR Am J Roentgenol* 2006;186:547–52 CrossRef Medline
- Moradi M, Mehdi M, Mahdavi B, et al. **The relation of calcium volume score and stenosis of carotid artery.** *J Stroke Cerebrovasc Dis* 2020;29:104493 CrossRef Medline
- Saba L, Nardi V, Cau R, et al. **Carotid artery plaque calcifications: lessons from histopathology to diagnostic imaging.** *Stroke* 2022;53:290–97 CrossRef Medline
- Eisenmenger LB, Aldred BW, Kim SE, et al. **Prediction of carotid intraplaque hemorrhage using adventitial calcification and plaque thickness on CTA.** *AJNR Am J Neuroradiol* 2016;37:1496–503 CrossRef Medline
- Saba L, Lanzino G, Lucatelli P, et al. **Carotid plaque CTA analysis in symptomatic subjects with bilateral intraplaque hemorrhage: a preliminary analysis.** *AJNR Am J Neuroradiol* 2019;40:1538–45 CrossRef Medline
- Saba L, Yuan C, Hatsukami TS, et al. **Carotid Artery Wall Imaging: Perspective and Guidelines from the ASNR Vessel Wall Imaging Study Group and Expert Consensus Recommendations of the American Society of Neuroradiology.** *AJNR Am J Neuroradiol* 2018;39:E9–31 CrossRef Medline
- Baradaran H, Ng CR, Gupta A, et al. **Extracranial internal carotid artery calcium volume measurement using computer tomography.** *Int Angiol* 2017;36:445–61 CrossRef Medline
- Touboul PJ, Hennerici MG, Meairs S, et al. **Mannheim Carotid Intima-Media Thickness and Plaque Consensus (2004–2006–2011).** *Cerebrovasc Dis* 2012;34:290–96 CrossRef Medline
- Saba L, Mallarini G. **Comparison between quantification methods of carotid artery stenosis and computed tomographic angiography.** *J Comput Assist Tomogr* 2010;34:421–30 CrossRef Medline
- McArdle PF, Kittner SJ, Ay H, et al; NINDS SiGN Study. **Agreement between TOAST and CCS ischemic stroke classification: the NINDS SiGN Study.** *Neurology* 2014;83:1653–60 CrossRef Medline
- Benson JC, Payabvash S, Mortazavi S, et al. **CT perfusion in acute lacunar stroke: detection capabilities based on infarct location.** *AJNR Am J Neuroradiol* 2016;37:2239–44 CrossRef Medline
- Yang J, Pan X, Zhang B, et al. **Superficial and multiple calcifications and ulceration associate with intraplaque hemorrhage in the carotid atherosclerotic plaque.** *Eur Radiol* 2018;28:4968–77 CrossRef Medline

27. Saba L, Mallarin G. **Window settings for the study of calcified carotid plaques with multidetector CT angiography.** *AJNR Am J Neuroradiol* 2009;30:1445–50 CrossRef Medline
28. Howard DPJ, Gaziano L, Rothwell PM. **Risk of stroke in relation to degree of asymptomatic carotid stenosis: a population-based cohort study, systematic review, and meta-analysis.** *Lancet Neurol* 2021;20:193–202 CrossRef Medline
29. Kelly-Hayes M. **Influence of age and health behaviors on stroke risk: lessons from longitudinal studies.** *J Am Geriatr Soc* 2010;58: (Suppl 2):S325–28 CrossRef Medline
30. Saba L, Biswas M, Kuppili V, et al. **The present and future of deep learning in radiology.** *Eur J Radiol* 2019;114:14–24 CrossRef Medline
31. Xu X, Ju H, Cai J, et al. **High-resolution MR study of the relationship between superficial calcification and the stability of carotid atherosclerotic plaque.** *Int J Cardiovasc Imaging* 2010;26:143–50 CrossRef Medline
32. van den Bouwhuisen QJ, Bos D, Ikram MA, et al. **Coexistence of calcification, intraplaque hemorrhage and lipid core within the asymptomatic atherosclerotic carotid plaque: the Rotterdam Study.** *Cerebrovasc Dis* 2015;39:319–24 CrossRef Medline
33. Mccollough CH, Boedeker K, Cody D, et al. **Principles and applications of multienergy CT: report of AAPM Task Group 291.** *Med Phys* 2020;47:e881–912 CrossRef Medline
34. Saba L, Brinjikji W, Spence JD, et al. **Roadmap consensus on carotid artery plaque imaging and impact on therapy strategies and guidelines: an international, multispecialty, expert review and position statement.** *AJNR Am J Neuroradiol* 2021;42:1566–75 CrossRef Medline
35. Akers EJ, Nicholls SJ, Bartolo BD. **Plaque calcification.** *Arterioscler Thromb Vasc Biol* 2019;39:1902–10 CrossRef Medline
36. Tintut Y, Hsu JJ, Demer LL. **Lipoproteins in cardiovascular calcification: potential targets and challenges.** *Front Cardiovasc Med* 2018;5:172 CrossRef Medline
37. Demer LL, Tintut Y. **Vascular calcification: pathobiology of a multifaceted disease.** *Circulation* 2008;117:2938–48 CrossRef Medline

Thin-Slice Pituitary MRI with Deep Learning–Based Reconstruction for Preoperative Prediction of Cavernous Sinus Invasion by Pituitary Adenoma: A Prospective Study

M. Kim, H.S. Kim, J.E. Park, S.Y. Park, Y.-H. Kim, S.J. Kim, J. Lee, and M.R. Lebel



ABSTRACT

BACKGROUND AND PURPOSE: Accurate radiologic prediction of cavernous sinus invasion by pituitary adenoma remains challenging. We aimed to assess whether 1-mm-slice-thickness MRI with deep learning–based reconstruction can better predict cavernous sinus invasion by pituitary adenoma preoperatively and to estimate the depth of invasion and degree of contact in relation to the carotid artery, compared with 3-mm-slice-thickness MRI.

MATERIALS AND METHODS: This single-institution, prospective study included 67 consecutive patients (mean age, 53 [SD, 12] years; 28 women), between January and August 2020, who underwent a combined contrast-enhanced T1-weighted imaging protocol of 1-mm-slice-thickness MRI + deep learning–based reconstruction and 3-mm-slice-thickness MRI. An expert neuroradiologist who was blinded to the imaging protocol determined cavernous sinus invasion using the modified Knosp classification on 1-mm-slice-thickness MRI + deep learning–based reconstruction and 3-mm-slice-thickness MRI, respectively. Reference standards were established by the consensus of radiologic, intraoperative, pathologic, and laboratory findings. The primary end point was the diagnostic performance of each imaging protocol, and the secondary end points included depth of invasion and degree of contact in relation to the carotid artery.

RESULTS: The diagnostic performance of 1-mm-slice-thickness MRI + deep learning–based reconstruction (area under the curve, 0.79; 95% CI, 0.69–0.89) in predicting cavernous sinus invasion by pituitary adenoma was higher than that of 3-mm-slice-thickness MRI (area under the curve, 0.61; 95% CI, 0.52–0.70; $P < .001$). One-millimeter-slice-thickness MRI + deep learning–based reconstruction demonstrated greater depth of invasion by pituitary adenomas from the medial intercarotid line than 3-mm-slice-thickness MRI (4.07 versus 3.12 mm, $P < .001$). A higher proportion of cases were in a greater degree of contact with the intracavernous ICA with 1-mm-slice-thickness MRI + deep learning–based reconstruction than with 3-mm-slice-thickness MRI (total encasement, 37.3% versus 13.4%, $P < .001$; $>270^\circ$, 38.8% versus 16.4%, $P < .001$).

CONCLUSIONS: Compared with 3-mm-slice-thickness MRI, 1-mm-slice-thickness MRI + deep learning–based reconstruction showed a higher diagnostic performance in preoperatively predicting cavernous sinus invasion by pituitary adenomas and demonstrated a greater depth and degree of contact in relation to the carotid artery.

ABBREVIATIONS: AUC = area under the receiver operating characteristic curve; CNN = convolutional neural network; DLR = deep learning–based reconstruction; 1-mmMRI = 1-mm-slice-thickness MRI without deep learning–based reconstruction; 3-mmMRI = 3-mm-slice-thickness MRI; 1-mmMRI + DLR = 1-mm-slice-thickness MRI with deep learning–based reconstruction; TSA = transsphenoidal approach

Preoperative evaluation of cavernous sinus invasion by a pituitary adenoma is important for establishing the safest and most effective treatment strategy for patients. Surgical resection by a transsphenoidal approach (TSA) is the first-line treatment for most macroadenomas,^{1,2} and accurate evaluation of cavernous sinus invasion is crucial to avoid injury to the ICA and

cranial nerves.^{3–5} Complete resection of pituitary adenomas is recommended to achieve endocrinologic remission for a functioning pituitary adenoma and to lower the rate of recurrence, while incomplete resection followed by radiation therapy may be recommended for pituitary adenomas with cavernous sinus invasion.^{4,6,7}

Received March 17, 2021; accepted after revision October 9.

From the Department of Radiology and Research Institute of Radiology (M.K., H.S.K., J.E.P., S.J.K.), Departments of Clinical Epidemiology and Biostatistics (S.Y.P.), and Neurosurgery (Y.-H.K.), University of Ulsan College of Medicine, Asan Medical Center, Seoul, Korea; GE Healthcare (J.L.), Seoul, Korea; GE Healthcare (M.R.L.), Calgary, Alberta, Canada; and Department of Radiology (M.R.L.), University of Calgary, Calgary, Alberta, Canada.

Please address correspondence to Ho Sung Kim, MD, PhD, Department of Radiology and Research Institute of Radiology, University of Ulsan College of Medicine, Asan Medical Center 88 Olympic-ro 43-gil, Songpa-Gu, Seoul 05505, South Korea; e-mail: radhskim@gmail.com

Indicates article with online supplemental data.
<http://dx.doi.org/10.3174/ajnr.A7387>

Radiologic evaluation of cavernous sinus invasion relies on delineating the morphologic relationship between the pituitary adenoma and the cavernous sinus.⁸ In particular, parasellar extension of the pituitary adenoma in relation to the lines drawn between the intracavernous and supracavernous ICAs underlies the modified Knosp classification, which is the most commonly used criteria for evaluating cavernous sinus invasion radiologically.^{8,9} While MR imaging with 2- to 3-mm slice thickness is commonly used for pituitary imaging,¹⁰ evaluation of parasellar extension by a pituitary adenoma remains challenging due to the inherently small size of the sellar fossa and delicate anatomy of the cavernous sinus.

A previous study by our group showed that high-spatial-resolution pituitary imaging may be achieved by applying deep learning-based reconstruction (DLR) to thin-slice MR imaging and demonstrated its diagnostic value in a postoperative setting.¹¹ Reducing the slice thickness is inevitably accompanied by an increased noise level, decreasing the signal-to-noise ratio and degrading the image quality. A novel deep learning-based MR image reconstruction pipeline based on a deep convolutional neural network (CNN) was used to provide denoising, reduce truncation artifacts, and improve edge sharpness.¹² It was trained with a supervised learning approach using pairs of images representing near-perfect and conventional MR images, and its technical performance has been previously reported.^{11,12} DLR can be easily applied to the 2D spin-echo sequence commonly used in pituitary imaging, and we hypothesized that DLR may be applied to 1-mm-slice-thickness MR imaging (1-mmMRI) to enable better delineation of the morphologic relationship between a pituitary adenoma and the cavernous sinus.

The aim of this study was to assess whether 1-mm-slice-thickness MR imaging with deep learning-based reconstruction (1-mmMRI+DLR) can better predict cavernous sinus invasion by a pituitary adenoma preoperatively and estimate the depth of invasion and degree of contact in relation to the carotid artery, compared with 3-mm-slice-thickness MR imaging (3-mmMRI).

MATERIALS AND METHODS

Participants

This prospective study (clinicaltrials.gov, NCT04268251) was approved by the institutional review board of Asan Medical Center before patient enrollment, and written informed consent was obtained from all patients. Seventy-six consecutive patients undergoing brain MR imaging for preoperative evaluation of pituitary adenomas between January 2020 and August 2020 were enrolled in this study and underwent a combined imaging protocol of 1-mmMRI+DLR and 3-mmMRI within 24 hours before TSA. The primary end point was the diagnostic performance of 1-mmMRI+DLR and 3-mmMRI in preoperatively predicting cavernous sinus invasion. Secondary end points included the depth of invasion and degree of contact by a pituitary adenoma in relation to the carotid artery.

Patients whose pathologic diagnosis was not pituitary adenoma ($n = 4$), patients who failed to undergo the combined MR imaging protocol ($n = 3$), and patients whose operation was cancelled ($n = 2$) were excluded from the study, leaving 67 patients for final inclusion.

MR Imaging Acquisition Protocol

MR imaging was performed with a 3T system (Signa Architect; GE Healthcare) using a 48-channel head coil. All patients underwent the MR imaging protocol dedicated to the pituitary gland within 1 month before TSA, which included the following: sagittal T1-weighted imaging: TR/TE, 611/13 ms; flip angle, 90°; FOV, 200 × 200 mm; matrix, 260 × 260; slice thickness, 3 mm with no gap; scan time, 3 minutes 40 seconds; coronal T2-weighted imaging: TR/TE, 4197/90 ms; flip angle, 90°; FOV, 180 × 180 mm; matrix, 360 × 360; slice thickness, 3 mm with no gap; scan time, 2 minutes 52 seconds; coronal T1-weighted imaging: TR/TE, 500/13 ms; flip angle, 90°; FOV, 180 × 180 mm; matrix, 260 × 260; slice thickness, 3 mm with no gap; scan time, 3 minutes; sagittal contrast-enhanced T1-weighted imaging: TR/TE, 611/13 ms; flip angle, 90°; FOV, 200 × 200 mm; matrix, 260 × 260; slice thickness, 3 mm with no gap; scan time, 3 minutes 40 seconds; axial contrast-enhanced T1-weighted imaging: TR/TE, 467/17 ms; flip angle, 90°; FOV, 230 × 185 mm; matrix, 300 × 224; slice thickness, 4 mm with 2-mm gap; scan time, 2 minutes 33 seconds; and coronal contrast-enhanced T1-weighted imaging: TR/TE, 500/13 ms; flip angle, 90°; FOV, 180 × 180 mm; matrix, 260 × 260; slice thickness, 3 mm with no gap; scan time, 3 minutes.

All patients underwent an additional MR imaging protocol for preoperative evaluation of pituitary adenoma within 24 hours before TSA, which included the following: sagittal contrast-enhanced T1-weighted imaging: TR/TE, 611/13 ms; flip angle, 90°; FOV, 200 × 200 mm; matrix, 260 × 260; slice thickness, 3 mm with no gap; scan time, 3 minutes 40 seconds; coronal contrast-enhanced T1-weighted imaging: TR/TE, 500/13 ms; flip angle, 90°; FOV, 180 × 180 mm; matrix, 260 × 260; slice thickness, 3 mm with no gap; scan time, 3 minutes; and coronal contrast-enhanced T1-weighted imaging: TR/TE, 698/16 ms; flip angle, 90°; FOV, 180 × 180 mm; matrix, 320 × 260; slice thickness, 1 mm with no gap; scan time, 4 minutes 8 seconds.

DLR

A vendor-supplied prototype version of DLR (AIR Recon DL; GE Healthcare) was used to reconstruct the 1-mm-slice-thickness images. Development of the image reconstruction pipeline and performance of the phantom and in vivo studies have been previously reported.^{11,12} In brief, the pipeline took raw k -space data of 1-mm-slice thickness imaging as its input and generated high-fidelity images as its output.¹² It was designed to offer a user-tunable reduction in image noise, truncation artifacts, and edge blurring. By means of a supervised learning approach, the CNN was trained with pairs of images representing near-perfect and conventional MR images. The near-perfect training data were high-resolution images with minimal ringing artifacts and extremely low noise levels, while the conventional training data were synthesized from near-perfect images to create lower-resolution versions with increased ringing artifacts and higher noise levels. A training data base of 4 million unique image/augmentation combinations was available to ensure the generalizability and robustness of the CNN across all anatomies; image augmentation including rotations and flips, intensity gradients, phase manipulations, and additional Gaussian noise were applied. The network was trained with gradient back-propagation via the Adam optimizer.

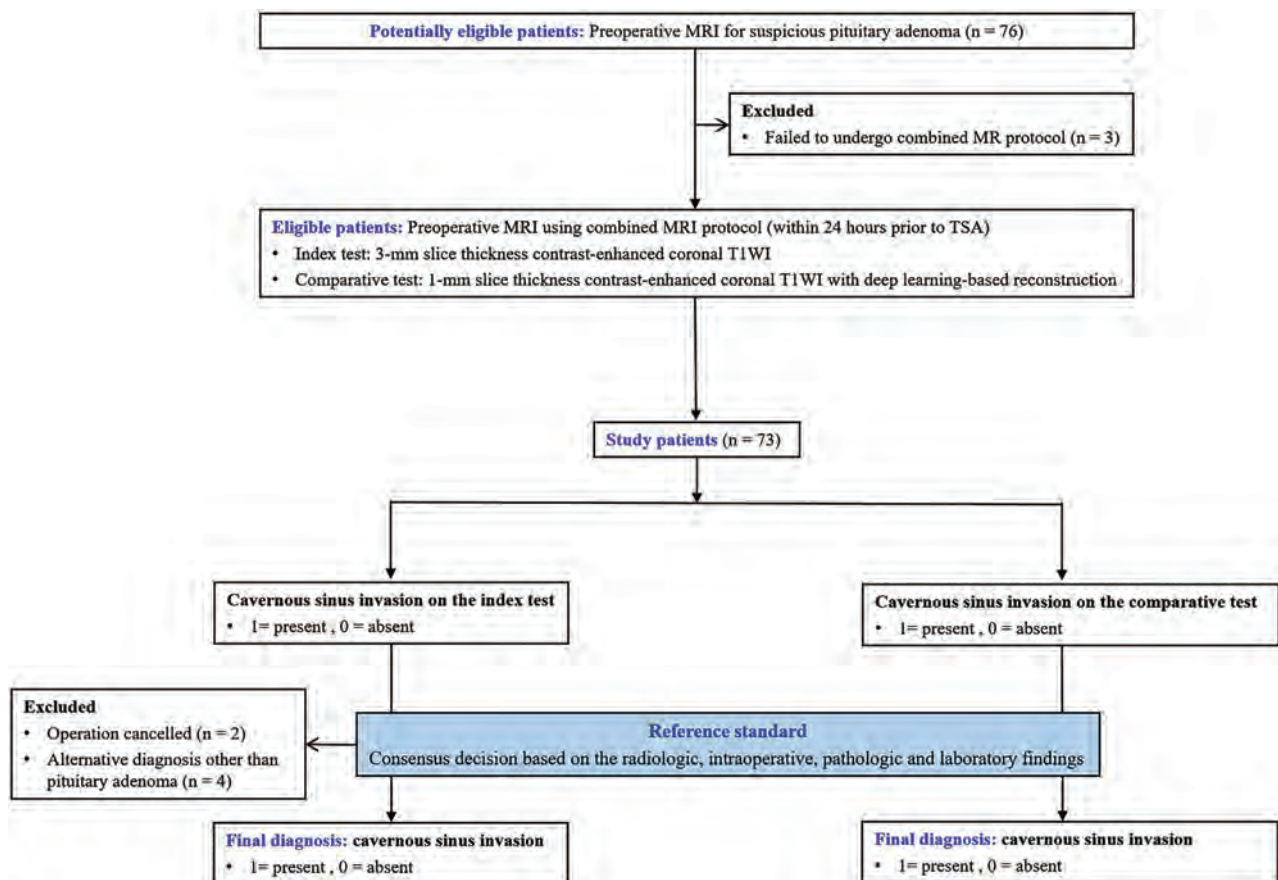


FIG 1. Patient inclusion process and image analysis.

Image Analysis

Image analysis for preoperatively predicting cavernous sinus invasion was performed when preoperative MR imaging with a combined imaging protocol of 1-mmMRI+DLR and 3-mmMRI was performed within 24 hours before TSA. Image analysis was performed by an expert neuroradiologist (M.K., with 6 years of experience in neuroradiology), who was blinded to clinical information and the imaging protocol (1-mm MRI+DLR versus 3-mmMRI) in accordance with the method described in the previous study, which demonstrated good interobserver agreement in diagnosing cavernous sinus invasion.¹¹ MR imaging set 1 consisted of 3-mm-slice-thickness contrast-enhanced sagittal T1WI and 3-mm-slice-thickness contrast-enhanced coronal T1WI, and MR imaging set 2 consisted of 3-mm-slice-thickness contrast-enhanced sagittal T1WI and 1-mm-slice-thickness contrast-enhanced coronal T1WI with DLR for each patient. The reader was asked to determine cavernous sinus invasion (0 = absent, 1 = present) on MR imaging sets 1 and 2 presented in a random order according to the modified Knosp classification (0, 1, 2, 3A, 3B, and 4).⁹ The modified Knosp classification relies on the extent of parasellar extension in relation to the lines connecting the medial, central, and lateral aspects of the cross-section of the intracavernous and supracavernous ICAs, with further subclassification depending on the involvement of the superior and inferior ICA compartments into grades 3A and 3B.⁹ While different outcomes in terms of invasiveness, rate of gross total resection, and endocrinologic remission have been

demonstrated between grades 3A and 3B, no consensus currently exists as to the optimal cutoff for determining cavernous sinus invasion, and grades 3A and 3B were both applied.⁹

The reader was also asked to estimate the depth of invasion by measuring the maximal parasellar extension of the pituitary adenoma in millimeters in relation to the medial intercarotid line and to assess the degree of contact of the pituitary adenoma with the intracavernous ICA (0 = no contact, 1 = $<90^\circ$, 2 = $<180^\circ$, 3 = $<270^\circ$, 4 = $<360^\circ$, 5 = total encasement). When bilateral cavernous sinus invasion was suspected, the cavernous sinus with a higher suspicion of invasion was evaluated. Before patient enrollment, the reader underwent a training session with an experienced neuroradiologist (H.S.K., with 22 years of experience in neuroradiology) for the modified Knosp classification and determination of cavernous sinus invasion. During training, typical and difficult examples of cavernous sinus invasion and each modified Knosp classification were shown, and methods for assessing the depth of invasion in relation to the medial intercarotid line and degree of contact with the intracavernous ICA were demonstrated. Figure 1 summarizes the patient inclusion process and image analysis.

Reference Standards

Reference standards for cavernous sinus invasion were established by the consensus of the neuroradiologist, neurosurgeons, pathologists, and endocrinologists based on radiologic, intraoperative, pathologic, and laboratory findings. An experienced neuroradiologist

Table 1: Clinical characteristics of the patients^a

Characteristics	
Total	67
Age (yr)	53 (SD, 12)
No. of female patients	28 (42)
Functioning adenoma	14 (21)
Prolactin	5 (7.5)
Growth hormone	7 (10)
Adrenocorticotrophic hormone	1 (1.5)
Thyroid stimulating hormone	1 (1.5)
CS invasion by reference standard	29 (43)
Residual tumor following operation determined by follow-up MR imaging	11 (16)
Postoperative stereotactic radiation therapy	7 (10)

Note:—CS indicates cavernous sinus.

^a Data are expressed as the mean (SD) or numbers with percentages in parenthesis.

(H.S.K.), who was blinded to the image analysis by the reader of the study, independently evaluated preoperative MR images as well as immediate postoperative and subsequent follow-up MR images for radiologic evaluation of cavernous sinus invasion. Two neurosurgeons explicitly documented or verbally communicated the intraoperative evaluation of cavernous sinus invasion in each patient as present, absent, or indeterminate. The cases in which the radiologic and intraoperative findings were discrepant were discussed at interdepartmental meetings. The pathologic report was reviewed for documentation of sinus or dural invasion, and endocrinologic remission was evaluated for the cases of functioning pituitary adenoma. The patients with residual pituitary adenoma on follow-up MR images or without endocrinologic remission requiring subsequent treatment were noted. The final decision on the presence or absence of cavernous sinus invasion was made by incorporating radiologic, intraoperative, pathologic, and laboratory findings in a multidisciplinary approach.

Statistical Analysis

Previous studies reported the diagnostic performance of radiologically predicting cavernous sinus invasion with the area under the receiver operating characteristic curve (AUC) of up to 0.83.^{8,9,13} Sample size calculation showed that 76 individuals are needed with a significance level of 5% ($\alpha = .05$) and a power of 80% ($\beta = 0.2$) to improve the diagnostic performance of predicting cavernous sinus invasion from an AUC of 0.83 to 0.93. To evaluate the diagnostic performance of the 1-mmMRI+DLR and 3-mmMRI in diagnosing cavernous sinus invasion, we calculated the AUC, sensitivity, specificity, positive predictive value, and negative predictive value. The comparison of the AUCs was performed by the DeLong test. Because a previous study demonstrated a difference in invasiveness between pituitary adenomas with extension into the superior and inferior compartments of the cavernous sinus,⁹ diagnostic performances with the modified Knosp classification $\geq 3B$ and $\geq 3A$ as cavernous sinus invasion were calculated separately. The depth of invasion assessed on the 1-mmMRI+DLR and 3-mmMRI was compared using a paired *t* test. Evaluation of the degree of contact of pituitary adenomas with the intracavernous ICA was compared using the McNemar test. $P < .05$ was considered indicative of a statistically significant difference. Statistical analyses were performed using R statistical and computing software (Version 3.6.1; <http://www.r-project.org>).

RESULTS

Patient Characteristics

Clinical characteristics of the patients are shown in Table 1. A total of 67 patients (mean age, 53 [SD, 12] years; 28 women, 42%) were enrolled, and all patients underwent resection of the pituitary adenoma by a transsphenoidal approach within 24 hours. There were 14 patients (21%) with functioning pituitary adenomas, which included 5 prolactinomas (7.5%), 7 growth hormone–releasing pituitary adenomas (10%), 1 adrenocorticotrophic hormone–releasing pituitary adenoma (1.5%), and 1 thyroid stimulating hormone–releasing pituitary adenoma (1.5%). There were 29 pituitary adenomas (43%) with cavernous sinus invasion by the reference standard. All patients underwent ≥ 1 immediate postoperative or follow-up MR imaging, and 11 patients (16%) were shown to have residual tumor. Seven patients (10%) underwent postoperative stereotactic radiation therapy for presumed residual tumor.

Diagnosis of Cavernous Sinus Invasion on 3-mmMRI and 1-mmMRI+DLR

The diagnostic performance of 3-mmMRI, 1-mmMRI, and 1-mmMRI+DLR in preoperatively diagnosing cavernous sinus invasion is presented in the Online Supplemental Data. The diagnostic performance of 1-mmMRI+DLR (AUC = 0.79; 95% CI, 0.69–0.89) was higher than that of 3-mmMRI (AUC = 0.61; 95% CI, 0.52–0.70; $P < .001$) and 1-mmMRI (AUC = 0.62; 95% CI, 0.49–0.74; $P < .001$) according to the modified Knosp classification when grades 3B and 4 were considered as cavernous sinus invasion. When grade 3A, 3B, and 4 were considered as cavernous sinus invasion, the diagnostic performance of 1-mmMRI+DLR (AUC = 0.80; 95% CI, 0.70–0.90) showed a trend toward higher diagnostic performance than 3-mmMRI (AUC = 0.74; 95% CI, 0.64–0.85; $P = .24$) and 1-mmMRI (AUC = 0.77; 95% CI, 0.65–0.86; $P = .15$), without statistical significance. The modified Knosp classifications of 3-mmMRI, 1-mmMRI, and 1-mmMRI+DLR are shown in the Online Supplemental Data. The images of cavernous sinus invasion demonstrated on 1-mmMRI+DLR but not on 3-mmMRI are shown in Fig 2.

Evaluation of the Depth of Invasion and Degree of Contact with the Intracavernous ICA by Pituitary Adenoma on 3-mmMRI and 1-mmMRI+DLR

The depth of invasion and degree of contact by pituitary adenomas with the intracavernous ICA evaluated on 3-mmMRI and 1-mmMRI+DLR are presented in Table 2. The depth of invasion of pituitary adenomas measured from the medial intercarotid line was higher on 1-mmMRI+DLR (4.07 mm; 95% CI, 3.35–4.80 mm) than on 3-mmMRI (3.12 mm; 95% CI, 2.44–3.81 mm; $P < .001$) and 1-mmMRI (3.82 mm; 95% CI, 3.10–4.55 mm; $P = .004$). The proportion of cases identified as the intracavernous ICA totally encased by the pituitary adenoma was higher on 1-mmMRI+DLR (25/67, 37.3%) than on 3-mmMRI (9/67, 13.4%; $P < .001$) and 1-mmMRI (13/67, 19.4%; $P = .02$). The proportion of cases identified as the intracavernous ICA of $> 270^\circ$ in contact with the pituitary adenoma was higher on 1-mmMRI+DLR (26/67, 38.8%) than on 3-mmMRI (11/67, 16.4%; $P < .001$) and 1-mmMRI (15/67, 22.4%; $P = .04$), and the proportion of cases identified as the intracavernous ICA of $> 180^\circ$ in contact with pituitary adenomas was higher on 1-

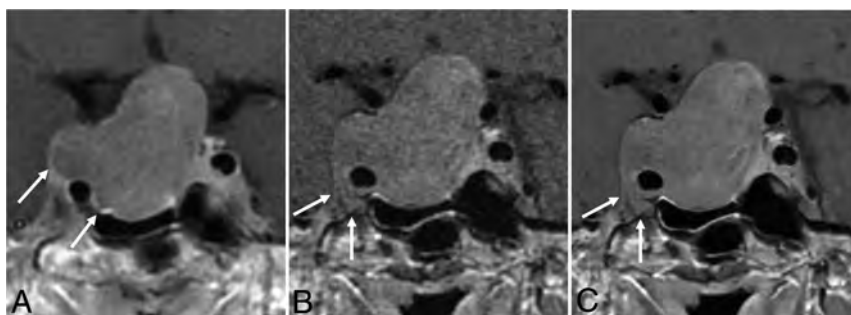


FIG 2. A 55-year-old man who underwent a combined MR imaging protocol for preoperative evaluation of pituitary adenoma. On a 3-mmMRI, coronal, contrast-enhanced T1-weighted image (A), the tumor is present beyond the lateral intercarotid line (modified Knosp classification 3A) and is about 180° in contact with the intracavernous ICA. One-mmMRI, coronal, contrast-enhanced T1-weighted image (B) was reconstructed using DLR (C), and the tumor is shown to encase the intracavernous ICA (arrows, modified Knosp classification 4).

Table 2: Depth of invasion and degree of contact with the intracavernous ICA by pituitary adenoma on 3-mmMRI, 1-mmMRI and 1-mmMRI with DLR^a

	3-mmMRI	P Value	1-mmMRI	P Value	1-mmMRI+DLR
Depth of invasion (mm)	3.12 (2.44–3.81)	<.001	3.82 (3.10–4.55)	.004	4.07 (3.35–4.80)
Degree of contact with intracavernous ICA					
Total encasement	9 (13.4%)	<.001	13 (19.4%)	.02	25 (37.3%)
>270°	11 (16.4%)	<.001	15 (22.4%)	.04	26 (38.8%)
>180°	17 (25.4%)	.001	21 (31.3%)	.11	30 (44.8%)

^a P value was calculated by using paired *t* test for depth of invasion and McNemar test for degree of contact with the intracavernous ICA. Data are mean or number of patients, and data in parentheses are 95% confidence intervals unless otherwise specified.



FIG 3. A 60-year-old woman who underwent a combined MR imaging protocol for preoperative evaluation of pituitary adenoma. On a 3-mmMRI, coronal, contrast-enhanced T1-weighted image (A), the tumor is present beyond the median intercarotid line but not beyond the median intercarotid line (modified Knosp classification 1) and is <180° in contact with the intracavernous ICA. One-mmMRI, coronal, contrast-enhanced T1-weighted image (B) was reconstructed with DLR (C), and the tumor is shown to extend beyond the median intercarotid line (modified Knosp classification 2) and is <270° in contact with the intracavernous ICA (arrows).

mmMRI+DLR (30/67, 44.8%) than on 3-mmMRI (17/67, 25.4%; *P* = .001). Figure 3 demonstrates greater depth of invasion and degree of contact in relation to the ICA on 1 mm-MRI+DLR compared with 3-mmMRI and 1-mmMRI.

DISCUSSION

In this prospective study, 1-mmMRI+DLR showed higher diagnostic performance in preoperatively predicting cavernous sinus

invasion by pituitary adenomas than 3-mmMRI. In addition, pituitary adenomas showed greater depth of invasion and a higher degree of contact in relation to the carotid artery on 1-mmMRI+DLR than on 3-mmMRI. This finding illustrates that thin-slice pituitary MR imaging with DLR allows better delineation of the morphologic relationship in the sellar fossa and achieves high spatial resolution with the relatively high signal-to-noise ratio that is required to accurately diagnose cavernous sinus invasion preoperatively.

Attempts to improve the radiologic accuracy of diagnosing cavernous sinus invasion by pituitary adenoma included the use of proton density-weighted imaging for identifying defects in the medial wall of the cavernous sinus¹⁴ as well as a 3D spin-echo sequence,¹⁵ volumetric interpolated brain examination,¹⁶ and contrast-enhanced sampling perfection with application-optimized contrasts by using different flip angle evolutions.¹⁷ Moreover, a radiomics approach using contrast-enhanced T1- and T2-weighted imaging showed better diagnostic performance than the clinico-radiologic models, and the diagnostic performance with an AUC of up to 0.83 on the test set was reported.¹³ However, these approaches require additional image sequences with no established protocols and parameters or heavy post-imaging processing and analysis. On the other hand, DLR can be easily applied to the commonly used 2D spin-echo sequence, with rapid processing time enabling high spatial resolution without compromising image quality by image denoising with sharp edges and reduced artifacts. Our study showed that 43% of patients had pituitary adenomas with cavernous sinus invasion by the reference standard, which was higher than that previously reported of up to 21%,^{8,18,19} and this result may be due to

the tertiary nature of the study center with a high prevalence of large, invasive pituitary adenomas. This was detected with 69% sensitivity using 1-mmMRI+DLR, and the diagnostic performance of 1-mmMRI+DLR was higher than that of 3-mmMRI in preoperatively predicting cavernous sinus invasion. While patients in this study underwent a combined imaging protocol of 1-mmMRI+DLR and 3-mmMRI, 1-mmMRI+DLR offers a better diagnostic value than 3-mmMRI without compromising image quality and may be considered to potentially replace 3-mmMRI.

The most widely used grading system for evaluating the parasellar extension of pituitary adenomas proposed by Knosp et al⁸ and later modified by Micko et al⁹ relies on the circular cuts of ICAs on the coronal section and uses the medial, median, and lateral lines drawn between the intracavernous and supracavernous ICAs. By increasing the number of slices that allows simultaneous visualization of the intracavernous and supracavernous ICAs, 1-mmMRI+DLR might allow more detailed evaluation of parasellar extension of the tumor in relation to the intercarotid lines and intracavernous ICA. In addition, 1-mmMRI+DLR may enable delineation of the presence of tumor at the lateral aspect of the intracavernous ICA. This accounted for the greater depth of invasion and higher proportion of pituitary adenomas with a greater degree of contact with the intracavernous ICA and grade IV tumors using 1-mmMRI+DLR, though it also resulted in false-positive cases. In addition, there was 1 case of pituitary adenoma with the tumor present lateral to the lateral intercarotid line at the superior cavernous compartment, which was made less conspicuous on 1-mmMRI+DLR by negating the partial volume average effect. In our study, 1-mmMRI+DLR showed higher diagnostic performance than 3-mmMRI in grade 3B and 4 pituitary adenomas according to the modified Knosp classification, whereas no significant difference was seen between 1-mmMRI+DLR and 3-mmMRI in pituitary adenomas with grades 3A, 3B, and 4. This finding supports 1-mmMRI+DLR as possibly being useful in using the modified Knosp classification with differentiation of involvement into the superior and inferior compartments of the cavernous sinus.

There are several limitations in this study. First, this was a single-center study with a relatively small sample size, so a multicenter validation with a larger cohort is required. Second, image analysis was performed by a single reader, which was practically inevitable in this prospective study design. We ensured that the blinded image analysis was performed before surgical resection and the image analysis was in accordance with the previous study that demonstrated good interobserver agreement in diagnosing cavernous sinus invasion.¹¹ Third, there is no established reference standard for determining cavernous sinus invasion by pituitary adenoma, so the reference standard was established by incorporating radiologic, intraoperative, pathologic, and laboratory findings.

CONCLUSIONS

For preoperative prediction of cavernous sinus invasion by pituitary adenoma, 1-mmMRI+DLR showed higher diagnostic performance and demonstrated greater depth of invasion and degree of contact in relation to the carotid artery compared with 3-mmMRI. This finding supports the diagnostic value of thin-slice pituitary imaging with DLR, though further validation in a multicenter study with a larger cohort is required.

Disclosures: Joonsung Lee—UNRELATED: Employment: employee of GE Healthcare. Marc R. Lebel—UNRELATED: Employment: employee of GE Healthcare; Stock/Stock Options: GE Healthcare.

REFERENCES

1. Chuang CC, Lin SY, Pai PC, et al. **Different volumetric measurement methods for pituitary adenomas and their crucial clinical significance.** *Sci Rep* 2017;7:40792 CrossRef Medline
2. Roelfsema F, Biermasz NR, Pereira AM. **Clinical factors involved in the recurrence of pituitary adenomas after surgical remission: a structured review and meta-analysis.** *Pituitary* 2012;15:71–83 CrossRef Medline
3. Nishioka H, Fukuhara N, Horiguchi K, et al. **Aggressive transsphenoidal resection of tumors invading the cavernous sinus in patients with acromegaly: predictive factors, strategies, and outcomes.** *J Neurosurg* 2014;121:505–10 CrossRef Medline
4. Vieira JO Jr, Cukiert A, Liberman B. **Evaluation of magnetic resonance imaging criteria for cavernous sinus invasion in patients with pituitary adenomas: logistic regression analysis and correlation with surgical findings.** *Surg Neurol* 2006;65:130–35; discussion 135 CrossRef Medline
5. Kitano M, Taneda M, Shimono T, et al. **Extended transsphenoidal approach for surgical management of pituitary adenomas invading the cavernous sinus.** *J Neurosurg* 2008;108:26–36 CrossRef Medline
6. Chang EF, Zada G, Kim S, et al. **Long-term recurrence and mortality after surgery and adjuvant radiotherapy for nonfunctional pituitary adenomas.** *J Neurosurg* 2008;108:736–45 CrossRef Medline
7. Greenman Y, Ouaknine G, Veshchev I, et al. **Postoperative surveillance of clinically nonfunctioning pituitary macroadenomas: markers of tumour quiescence and regrowth.** *Clin Endocrinol (Oxf)* 2003;58:763–69 CrossRef Medline
8. Knosp E, Steiner E, Kitz K, et al. **Pituitary adenomas with invasion of the cavernous sinus space: a magnetic resonance imaging classification compared with surgical findings.** *Neurosurgery* 1993;33:610–17; discussion 617–18 CrossRef
9. Micko AS, Wöhrer A, Wolfsberger S, et al. **Invasion of the cavernous sinus space in pituitary adenomas: endoscopic verification and its correlation with an MRI-based classification.** *J Neurosurg* 2015;122:803–11 CrossRef Medline
10. Varrassi M, Cobianchi Bellisari F, Bruno F, et al. **High-resolution magnetic resonance imaging at 3T of pituitary gland: advantages and pitfalls.** *Gland Surg* 2019;8:S208–15 CrossRef Medline
11. Kim M, Kim HS, Kim HJ, et al. **Thin-slice pituitary MRI with deep learning-based reconstruction: diagnostic performance in a post-operative setting.** *Radiology* 2021;298:114–22 CrossRef Medline
12. Lebel RM. **Performance characterization of a novel deep learning-based MR image reconstruction pipeline.** *arXiv.org* 2020 <https://arxiv.org/abs/2008.06559>. Accessed March 18, 2021
13. Niu J, Zhang S, Ma S, et al. **Preoperative prediction of cavernous sinus invasion by pituitary adenomas using a radiomics method based on magnetic resonance images.** *Eur Radiol* 2019;29:1625–34 CrossRef Medline
14. Cao L, Chen H, Hong J, et al. **Magnetic resonance imaging appearance of the medial wall of the cavernous sinus for the assessment of cavernous sinus invasion by pituitary adenomas.** *J Neuroradiol* 2013;40:245–51 CrossRef Medline
15. Lien RJ, Corcuera-Solano I, Pawha PS, et al. **Three-Tesla imaging of the pituitary and parasellar region: T1-weighted 3-dimensional fast spin echo Cube outperforms conventional 2-dimensional magnetic resonance imaging.** *J Comput Assist Tomogr* 2015;39:329–33 CrossRef Medline
16. Davis MA, Castillo M. **Evaluation of the pituitary gland using magnetic resonance imaging: T1-weighted vs. VIBE imaging.** *Neuroradiol J* 2013;26:297–300 CrossRef Medline
17. Wu Y, Wang J, Yao Z, et al. **Effective performance of contrast enhanced SPACE imaging in clearly depicting the margin of pituitary adenoma.** *Pituitary* 2015;18:480–86 CrossRef Medline
18. Hofstetter CP, Nanaszko MJ, Mubita LL, et al. **Volumetric classification of pituitary macroadenomas predicts outcome and morbidity following endoscopic endonasal transsphenoidal surgery.** *Pituitary* 2012;15:450–63 CrossRef Medline
19. Cottier JP, Destrieux C, Brunereau L, et al. **Cavernous sinus invasion by pituitary adenoma: MR imaging.** *Radiology* 2000;215:463–69 CrossRef Medline

MRI Findings in Acute Tonsillar Infections

J. Heikkinen, J. Nurminen, J. Velhonoja, H. Irjala, T. Soukka, T. Happonen, M. Nyman, K. Mattila, and J. Hirvonen



ABSTRACT

BACKGROUND AND PURPOSE: Previous literature is vague on the prevalence and exact nature of abscesses in tonsillar infections, ranging from intratonsillar and peritonsillar collections to deep extension involving the parapharyngeal and retropharyngeal spaces. MR imaging has excellent diagnostic accuracy in detecting neck infections and can potentially clarify this issue. We sought to characterize the spectrum of MR imaging findings regarding tonsillar infections.

MATERIALS AND METHODS: We conducted a retrospective cohort study of emergency neck MR imaging scans of patients with tonsillar infections. Imaging data were assessed in terms of signs of infection and the location of abscesses and were compared with clinical findings, final diagnoses, and surgical findings as reference standards.

RESULTS: The study included 132 patients with tonsillar infection. Of these, 110 patients (83%) had ≥ 1 abscess (99 unilateral, 11 bilateral; average volume, 3.2 mL). Most abscesses were peritonsillar, and we found no evidence of intratonsillar abscess. Imaging showed evidence of parapharyngeal and retropharyngeal extension in 36% and 10% of patients, respectively. MR imaging had a high positive predictive value for both abscesses (0.98) and deep extension (0.86). Patients with large abscesses and widespread edema patterns had a more severe course of illness.

CONCLUSIONS: Emergency neck MR imaging can accurately describe the extent and nature of abscess formation in tonsillar infections.

ABBREVIATIONS: CRP = C-reactive protein; Gd = gadolinium; ITA = intratonsillar abscess; LOS = length of the hospital stay; PPV = positive predictive value; PTA = peritonsillar abscess; SLS = sublingual space; SMS = submandibular space; T2SI = T2-signal intensity; VS = visceral space

Tonsillar infections are common, many are resolved conservatively, but complicated infections with abscesses still cause a substantial amount of morbidity and surgery.¹ While common tonsillar infections can usually be treated on clinical grounds, emergency imaging may be required to identify abscess formation and rule out other diagnoses.² The purpose of imaging is to differentiate abscesses from cellulitis and to describe the true extent of an abscess to select the appropriate treatment. Peritonsillar abscesses (PTAs) are collections of pus in the pharyngeal mucosal space between the tonsillar capsule and the pharyngeal constrictor muscle. While PTAs are not typically considered deep neck infections, they can

become deeply extended abscesses if they rupture through the constrictor muscle to the deep neck spaces such as the parapharyngeal and retropharyngeal spaces.

Emergency neck imaging has traditionally been performed using contrast-enhanced CT. Previous literature on the diagnostic accuracy of CT has focused on deep neck infections, for which the positive predictive value (PPV) for abscesses is about 80%,³⁻⁵ most likely due to the limited soft-tissue contrast of CT. In addition, previous literature on CT has suggested that some abscesses may be located within the tonsillar parenchyma and may not reach the peritonsillar space; these are called “intratonsillar abscesses” (ITAs).⁶ The diagnostic accuracy of the detection of ITA, PTA, and deep extension among patients undergoing emergency neck imaging is not well known, and the relative prevalence of these conditions also remains undetermined.

MR imaging provides superior soft-tissue contrast compared with CT,^{7,8} and emergency neck MR imaging is feasible even in acutely ill patients.⁹ MR imaging can distinguish between reactive nonsuppurative edema and true abscesses in the deep neck spaces and has a high diagnostic accuracy in the detection of neck infections and abscesses.⁹ Therefore, MR imaging might be useful for illustrating the spectrum of tonsillar infections. To our knowledge,

Received July 9, 2021; accepted after revision October 1.

From the Departments of Radiology (J. Heikkinen, J.N., T.H., M.N., K.M., J. Hirvonen), Otorhinolaryngology-Head and Neck Surgery (J.V., H.I.), and Oral and Maxillofacial Surgery (T.S.), University of Turku and Turku University Hospital, Turku, Finland.

Funding was provided by the University of Turku and the Sigrid Juselius Foundation.

Please address correspondence to Jussi Hirvonen, MD, PhD, Department of Radiology, Turku University Hospital, Kiinamylynkatu 4-8, 20521 Turku, Finland; e-mail: jueshi@utu.fi; @jussihirvonen

Indicates open access to non-subscribers at www.ajnr.org

Indicates article with online supplemental data.

<http://dx.doi.org/10.3174/ajnr.A7368>

there are no systematic analyses of radiologic MR imaging findings in tonsillar infections and types of changes associated with a more severe course of illness.

This article aims to describe MR imaging findings regarding tonsillar infections and to investigate the significance of imaging findings related to clinical treatment and outcomes. To elucidate the full spectrum of tonsillar infections, we included patients with uncomplicated tonsillitis, PTA, and deeply extending abscesses.

MATERIALS AND METHODS

We obtained permission from the hospital district board for this retrospective cohort study in a single academic tertiary care referral center. Institutional review board review (approval or waiver) was not sought because it is not required by the national legislature for retrospective studies of existing data. The inclusion criteria were the following: 1) emergency MR imaging between April 1, 2013, and December 31, 2018, for suspected neck infection; 2) MR imaging evidence of infection: high signal of fat-suppressed T2-weighted Dixon images suggesting edema or high signal of fat-suppressed post-gadolinium (post-Gd) T1-weighted Dixon images suggesting abnormal tissue enhancement; 3) a final clinical diagnosis of a tonsillar infection; and 4) diagnostic image quality as determined by the radiologist reading the study. Cases were identified from the PACS and Radiology Information Systems using standard neck MR imaging codes, and data were cross-referenced with patients' medical files.

MR imaging was performed on an Ingenia 3T system using a dS HeadNeckSpine coil configuration (Philips Healthcare) and a Gd-based contrast agent (gadoterate meglumine, Dotarem; Guerbet). Details of the MR imaging protocol can be found in the Online Supplemental Data. The emergency radiology department of our institution has a dedicated emergency MR imaging service. At our institution, MR imaging has become the first-line imaging technique for most patients with suspected neck infections. For almost all patients, MR imaging was the only imaging method.

All imaging data were retrospectively reviewed by 2 fellowship-trained neuroradiologists (J. Heikkinen and J. Hirvonen). To assess the diagnostic accuracy of the MR imaging findings, we used the following clinical reference standards: For infection, we used the final clinical diagnosis from the medical record, and for abscesses, we used the presence or absence of purulence or an abscess cavity during an operation if performed within 48 hours of MR imaging. The methods of surgical proof included open surgery, drainage, or puncture of pus. Because patients without abscesses are much less likely to undergo an operation than patients with abscesses (partial verification bias), we considered patients with no abscesses who recovered uneventfully following conservative treatment (including intravenous antibiotics) as representing true-negatives. The following data were extracted from medical records: age (years), sex (male/female), body mass index (kilogram/square meter), duration of symptoms before imaging (days), C-reactive protein (CRP, milligrams/liter), white blood cell count ($\times 10^9$ /liter), body temperature (degree Celsius), operation (yes/no), treatment in an intensive care unit (yes/no), and length of the hospital stay (LOS, days).

An abscess was defined as an abnormal nonenhancing T2-hyperintense collection with a low ADC surrounded by abnormal tissue enhancement. We classified PTAs as being predominantly

Table 1: Patient characteristics^a

Characteristic	
No. of patients	132
Age (mean) (yr)	42 (SD, 19)
Male (No.) (%)	83 (63%)
Female (No.) (%)	49 (37%)
BMI (kg/m ²)	27.4
CRP (mg/L)	132 ^a (SD, 83)
WBC ($\times 10^9$ /L)	16 ^b (SD, 18)
Body temperature (°C)	37.6 ^c (SD, 0.8)
Duration of symptoms (days)	5.6 ^d (SD, 5)
ICU (No.) (%)	17 (13%)
LOS (mean) (days)	3.9 (SD, 5.8)
Operation (No.) (%)	104 (79%)

Note:—BMI indicates body mass index; ICU, intensive care unit; WBC, white blood cell.

^a Data available for a) 131, b) 131, c) 66, and d) 129 patients. Data are means or No. (%).

superior, inferior, or widespread (both superior and inferior) relative to the craniocaudal midpoint of the palatine tonsil. Deep extension of an abscess was recorded as involvement of the parapharyngeal or retropharyngeal spaces. Uncomplicated PTA and deeply extending abscesses are collectively referred to as pharyngotonsillar abscesses. We also recorded whether abscesses had a multilocular morphology and whether the inflamed palatine tonsil had a striated appearance. We estimated the volume of the non-enhancing area of all the abscesses and measured the ADC and T2-signal intensity (T2SI) ratios between the abscess and the adjacent palatine tonsil. From fat-suppressed T2-weighted Dixon images, we evaluated edema as a high signal in the submandibular space (SMS, inferior to the mylohyoid muscle), sublingual space (SLS, superior to the mylohyoid muscle), and visceral space (VS, infrahyoid soft-tissue space including the larynx, surrounding strap muscles, and thyroid, also including edema in the anterior cervical space between the sternocleidomastoid muscle and the carotid space). To ensure the reliability of these consensus assessments, a third fellowship-trained neuroradiologist (M.N.) independently read a random sample of 60 patients for deep extension and edema patterns (SMS, SLS, VS). All radiologic assessments were conducted blinded to other medical and surgical information.

The results are expressed as percentages, means, and SDs. We used independent samples *t*-tests for comparing continuous variables and χ^2 tests for comparing ordinal data. For assessing the diagnostic accuracy of detecting abscesses and deep extension, we formulated 2×2 tables (MR imaging versus surgical findings) and calculated the sensitivity, specificity, PPV, negative predictive value, and accuracy as previously described.⁹ We evaluated the interrater reliability of the assessments of the edema patterns using the Cohen κ . For the multivariate prediction model for deeply extending abscesses, we used a binary logistic regression model in which all statistically significant univariate predictors entered the model. All data were analyzed using SPSS Statistics for Mac (Version 26; IBM, 2019). *P* values < .05 were considered statistically significant.

RESULTS

Patient Population and Prior Procedures

The study consisted of 132 patients (83 males, 49 females) with a clinically confirmed acute tonsillar infection (Table 1). One additional patient underwent MR imaging due to a suspected PTA but had to be excluded because of motion artifacts. The patients had a

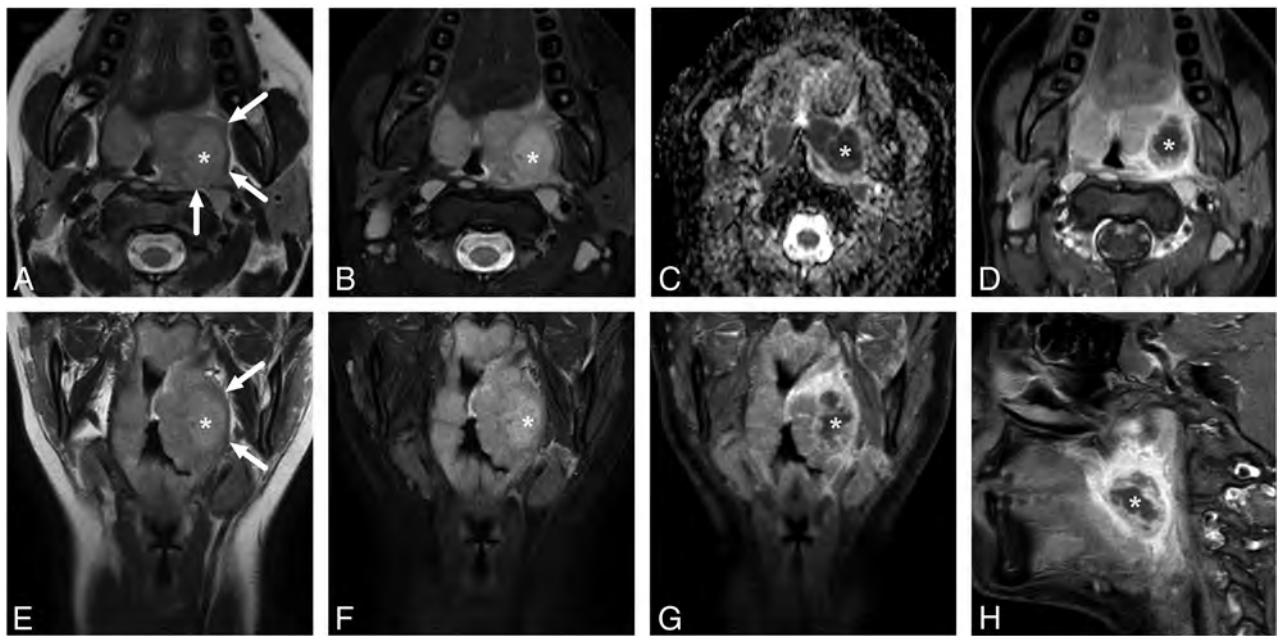


FIG 1. Uncomplicated PTA in an 18-year-old male patient with a sore throat. In-phase axial (A) and coronal (E) as well as fat-suppressed axial (B) and coronal (F) T2-weighted Dixon images reveal a slightly T2-hyperintense abscess (asterisk) lateral to the left palatine tonsil. The edematous pharyngeal constrictor muscle can be seen around the palatine tonsil (arrows in in-phase images A and E). The abscess shows restricted diffusion on the ADC map (C) and a nonenhancing core surrounded by an enhancing rim in axial (D), coronal (G), and sagittal (H) post-Gd fat-suppressed T1-weighted Dixon images.

Table 2: Diagnostic accuracy of MR imaging in the detection of abscesses and deep extension (parapharyngeal, retropharyngeal involvement) in the abscesses^a

MRI	Operation	
	Yes	No
Abscess		
Yes	96	2
No	2	19 ^b
Deep extension		
Yes	36	5
No	6	57

^a Sensitivity, 0.98; specificity, 0.90; PPV, 0.98; negative predictive value, 0.90; accuracy, 0.97. In the complications, sensitivity, 0.88; specificity, 0.90; PPV, 0.86; negative predictive value, 0.92; accuracy 0.89.

^b Conditions of 4 patients were surgically confirmed, and the diagnoses of 15 patients were based on clinical assessment.

mean age of 42 years (range, 9–82 years). The mean duration of symptoms before imaging was about 5 days. One hundred four (79%) patients underwent an operation, and 17 (13%) patients required treatment in the intensive care unit. The mean LOS was 4 days (range, 0–55 days). Imaging showed evidence of ≥ 1 abscess (101 unilateral, 11 bilateral) in 112 patients (85%) (Fig 1) and of parapharyngeal and retropharyngeal extension in 40 (36%) and 11 (10%) patients, respectively.

Among the patients who required imaging, 88 (68%) had not undergone any prior procedure and were imaged swiftly because of suspected deep abscess, whereas 42 (32%) patients had undergone a previous procedure (needle aspiration and/or incision and drainage). Most of these prior procedures (84%) had not yielded pus. Nevertheless, these patients were still suspected of having an abscess on clinical grounds, and imaging showed an abscess in 86% of them.

Diagnostic Accuracy for Abscesses and Deep Extension

All patients had a final clinical diagnosis of tonsillar or pharyngeal infection. Of those with an abscess, 98 (89%) underwent an operation and an abscess was surgically confirmed in 96 patients, suggesting a PPV of 0.98. We had 2 patients with false-positive findings in whom no purulence was found. Six patients underwent an operation without MR imaging evidence of abscess; among these, 4 had true-negative findings and 2 had false-negative findings. Assuming 15 more patients with true-negative findings (ie, patients with a tonsillar infection but no abscess who recovered uneventfully following conservative treatment), we found a sensitivity, specificity, and accuracy of 0.98, 0.90, and 0.97, respectively, for an MR imaging diagnosis of an abscess (Table 2). In our experience, craniocaudal or lateral extension of an abscess far from the tonsil is the most reliable imaging sign of parapharyngeal or retropharyngeal extension (Fig 2). This morphologic assessment of deep extension had an overall sensitivity, specificity, and accuracy of 0.88, 0.90, and 0.89, respectively, as well as substantial agreement in the interobserver analysis (92% agreement, $\kappa = 0.75$).

Imaging Characteristics of Abscesses (Only True-Positives)

In total, we found 110 abscesses by MR imaging (2 false-positive findings were excluded) (Table 3). The mean maximal abscess diameter was 33 mm, and volume was 3.2 mL. Most (ie, 69, 63%) of the abscesses were multilocular, and 78 (71%) had a striated tonsillar appearance in post-Gd T1-weighted images. The mean ADC value was 0.52 (compared with 0.75 in tonsillar tissue; ADC ratio, 0.72). The average T2SI ratio between the abscess and the tonsil was 1.3 (Fig 3). Among the patients with an abscess, only

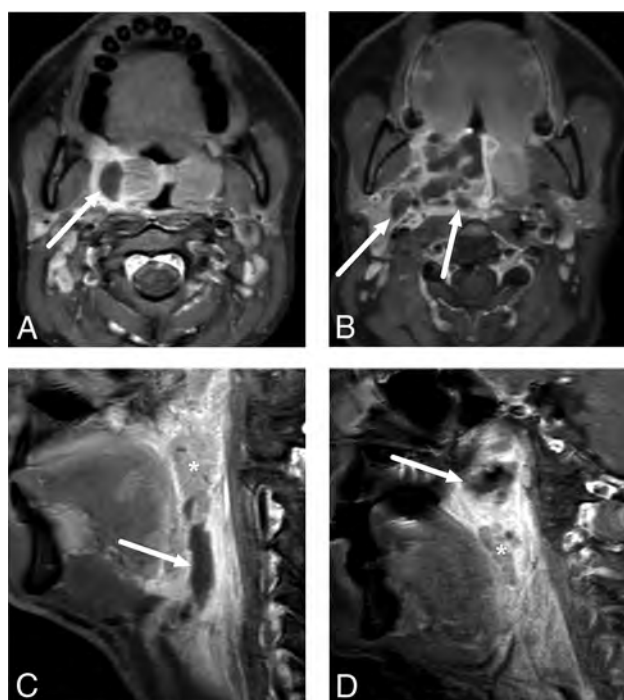


FIG 2. Examples of uncomplicated PTA (A) and abscesses with deep extension (B–D) in different patients. In uncomplicated PTA, the abscess is retained within the pharyngeal constrictor muscle (A). In axial images, a deeply extending PTA is often lobulated and reaches laterally toward the parapharyngeal space, beyond the pharyngeal constrictor muscle (B). In sagittal images, a deeply extending PTA can reach far inferiorly (C) or superiorly (D) from the palatine tonsil (asterisk). The arrows denote abscesses.

Table 3: Imaging characteristics^a

Outcome	
Abscess characteristics	110 (83%) ^b
Maximal abscess diameter (mm)	33 (SD, 22)
Volume (mL)	3.2 (SD, 4.4)
Multilocular	69 (63%)
Striated	78 (71%)
T2SI ratio	1.3 (SD, 0.3)
ADC	0.52 (SD, 0.15)
Abscess location	
Superior	47 (43%)
Inferior	37 (34%)
Widespread	26 (24%)
Edema patterns	
SMS	121 (92%)
SLS	31 (24%)
VS	95 (72%)
Deep extension	41 (37%)
Parapharyngeal	40 (36%)
Retropharyngeal	11 (10%)
Both	10 (9%)

^a Values are No. (%) or means.

^b True-positives.

8% had a higher ADC and 11% had a lower T2SI in the abscess than in the tonsil.

Of the abscesses, 43% were considered superior; 34%, inferior; and 24%, widespread (with superior and inferior extensions) relative to the palatine tonsil. Superior-type abscesses were more

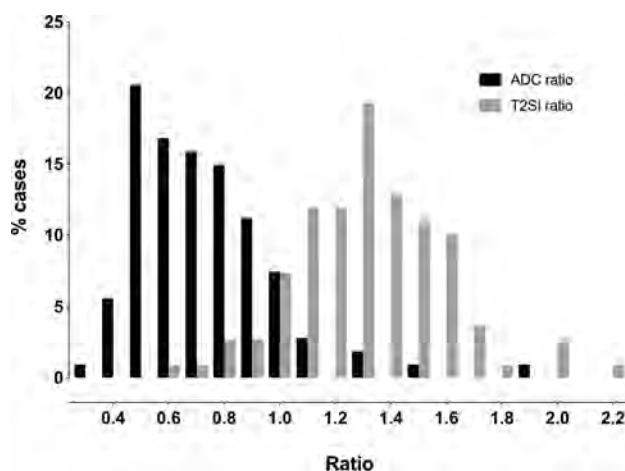


FIG 3. Frequency distributions of ADC and T2SI ratios between the abscesses and the adjacent palatine tonsils. In most patients, the abscesses had a lower ADC and higher T2SI than the palatine tonsils.

common among the younger patients (mean age, 37 years versus 44 and 47 years for inferior and widespread types, $P = .046$) and among women (53% of all 3 abscess types compared with 35% among men, $P = .001$). The superior abscesses were also smaller (20 versus 30 mL and 55 mL, $P = .004$), had fewer deep extensions (22% versus 49% and 29%, $P = .003$), and the associated LOS was shorter (2.8 days versus 3.1 and 5.6 days, $P = .006$) compared with inferior and widespread types, respectively. Larger widespread abscesses had the most admissions to the intensive care unit (50% of all intensive care unit admissions, $P = .045$) and the longest mean LOS (5.6 days versus 2.8 and 3.1 days, $P = .006$).

Edema Patterns

SMS edema was the most common (92%), followed by VS (72%) and SLS (24%) edema (Fig 4). The SMS and SLS edema patterns were not significantly differently distributed among the abscess locations, whereas VS edemas were most common in inferiorly located abscesses (42% versus 33% and 25% in superior and widespread types, $P = .001$). The patients with VS edemas had larger abscesses (3.8 versus 1.5 mL, $P < .001$) and higher CRP (142 versus 90, $P = .005$) than those without. Similarly, the patients with SLS edemas had larger abscesses (4.6 versus 2.7 mL, $P = .047$). In the interobserver analysis, these edema patterns had moderate-to-substantial agreement (93%, 85%, and 78% agreement, and $\kappa = 0.47$, 0.64, and 0.52 for SMS, VS, and SLS, respectively).

Prediction of Parapharyngeal and Retropharyngeal Deep Extension Using Imaging Findings

The patients with deeply extended diseases who underwent an operation were older (47 versus 39 years, $P = .024$) and had higher CRP values (173 versus 116, $P < .001$), larger abscesses (5.4 versus 1.9 mL, $P < .001$), a higher prevalence of VS (95% versus 62%, $P < .001$), SLS (42% versus 15%, $P < .001$), and inferior locations of abscesses (49% versus 22% and 29% in the superior and widespread types, $P = .003$) than the patients with uncomplicated PTAs (Table 4).

In the multivariate analysis, an extended disease was predicted by abscess volume ($P = .012$), CRP ($P = .017$), and SLS edema

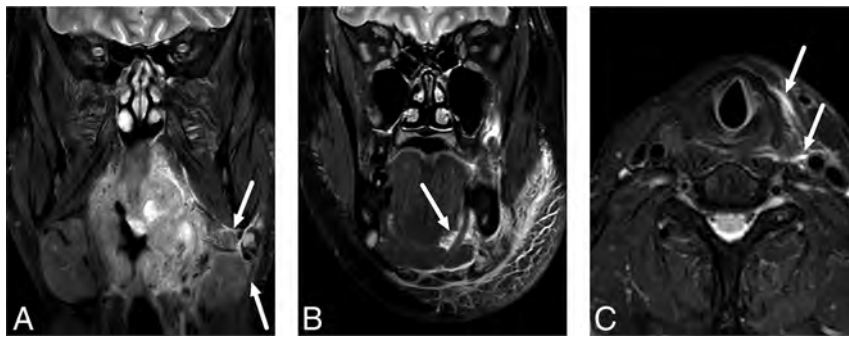


FIG 4. Examples of SMS (A), SLS (B), and VS (C) edema patterns on fat-suppressed T2-weighted Dixon images. Arrows indicate edema.

Table 4: Univariate and multivariate modeling of deep extension of abscesses

	Univariate		Multivariate	
	Statistic ^a	P Value	Odds Ratio	P Value
Age	−2.28	.024	1.03	.054
CRP	−3.81	<.001	1.01	.017
WBC	−0.284	.777		
Location	11.9	.003	1.31	.414
Abscess volume	−4.50	<.001	1.00	.012
SMS	0.993	.501		
SLS	11.4	.001	3.43	.032
VS	15.8	<.001	3.09	.173

Note:—WBC indicates white blood cell count.

^a T-value for continuous variables, χ^2 for nominal variables.

($P = .032$) in patients with a surgically confirmed pharyngotonsillar abscess. This model correctly classified 77% of the patients and explained 47% of the variance (Nagelkerke R^2) (Table 4).

DISCUSSION

This study advances our knowledge of the spectrum of tonsillar infections in several ways. First, MR imaging has a high diagnostic accuracy in detecting abscesses and parapharyngeal and retropharyngeal deep extension. Second, the T2SI of peritonsillar abscesses can be visually close to that of tonsillar tissue and not easily distinguishable from the latter. In addition, the ADC between the abscess and tonsil is often visually similar. These observations support the routine use of Gd-based contrast agents. Third, we found no evidence of intratonsillar abscesses because, by definition, none of the cases had tonsillar tissue surrounding the abscess on all sides; that is, all the abscesses reached the superior constrictor muscle and were, thus, at least peritonsillar in nature. Finally, the patients with large abscesses and widespread edema patterns seemed to have more severe courses of illness.

The primary objective of emergency imaging is to provide a correct diagnosis and an anatomic basis for managing deep neck infections. Although PTAs do not typically require imaging, the patients in the current study underwent emergency MR imaging because either prior procedures had not yielded pus or a deep extension of the disease was primarily suspected. In our study of 98 patients with a radiologically diagnosed abscess who were later treated surgically, 96 had an abscess verified by the criterion standard. Of the false-positives, 1 patient had a hematoma after many

puncture attempts. The second case was a very small abscess identified on MR imaging, and no purulence was identified during the operation. We found a sensitivity, specificity, and accuracy of 0.98, 0.90, and 0.97, respectively, for an MR imaging diagnosis of a pharyngotonsillar abscess. These results compare well with those of previous CT studies with the sensitivity, specificity, and accuracy of <0.90.^{4,10,11}

Among the patients needing imaging for tonsillar infection, 37% had a deep extension to the parapharyngeal or retropharyngeal spaces. For the detection

of parapharyngeal or retropharyngeal extension, the sensitivity, specificity, and accuracy were 0.88, 0.90, and 0.89, respectively, and interobserver agreement was substantial. In our experience, parapharyngeal or retropharyngeal extension should be suspected if the abscess reaches outside the palatine tonsil borders either laterally, superiorly, or inferiorly (Fig 2). Surgical literature shows that most cases of parapharyngeal abscesses are associated with concomitant PTA, suggesting that they are often direct extensions of PTA.¹² Our current results indicate that deep extension can be detected or ruled out accurately by MR imaging.

An ITA is thought to be a purulent collection completely within the tonsillar parenchyma, often considered trapped pus inside a tonsillar crypt. It is suggested to carry a more favorable prognosis and could be treated with less invasive methods than PTA.¹³⁻¹⁷ We rigorously scrutinized all the abscesses for ITAs but could not find a single case in which the abscess was completely surrounded by the tonsillar parenchyma. ITA versus PTA is likely a nomenclature issue, and these 2 types of abscesses may reflect different stages on a spectrum of the same disease, with a variable amount of pus inside the tonsillar parenchyma. It is unknown to what extent CT can differentiate a swollen pharyngeal constrictor muscle and tonsillar parenchyma, therefore between ITAs and PTAs, whereas MR imaging can differentiate them by virtue of ADC maps.

Regarding the location of abscesses, superior types were slightly more common than inferior and widespread types and tended to be smaller and less severe cases overall, with the shortest LOS. Bilateral abscesses were diagnosed in 10% of all patients with abscesses. On average, concomitant contralateral PTAs are discovered intraoperatively in 5.5% of patients.¹⁸ The rate of bilateral PTAs found using CT is not known but may be lower than that found using MR imaging.

Most abscesses have lower ADC values and higher T2SI than the tonsillar tissue itself. In some cases, abscess fluid can be so purulent that the T2SI is not very high (Fig 1). On the other hand, normal tonsillar tissue has a low ADC by virtue of high cellularity, so differentiating the abscess from the tonsil may be challenging. Although only 8% of the patients had higher ADCs and 11% of the patients had lower T2SI in the abscess than in the tonsil, in our experience, post-Gd T1-weighted images are required to delineate pharyngotonsillar abscesses accurately. Future studies should measure the diagnostic accuracy and interobserver agreement when

using only DWI and T2-weighted imaging without a Gd-based contrast agent in cases of pharyngotonsillar abscesses.

Almost all patients with a tonsillar infection had SMS edema, reflecting the anatomic free communication with these spaces. Whether the edema spreads directly or via lymphatic spread is unclear. Tonsillar infections that produce widespread edema patterns are likely to be more severe because the edema crosses the boundaries between the soft-tissue compartments. This finding was demonstrated in our study because the patients with VS and SLS edemas had larger abscesses, and the patients with VS edemas also had significantly higher CRP and longer LOS. In the multivariate analysis, an extended abscess (parapharyngeal or retropharyngeal) was also predicted by SLS edema with a surgically confirmed pharyngotonsillar abscess, even when controlling for CRP. Conversely, an operation rarely revealed an extended abscess in patients without VS and SLS edemas. This finding was especially prominent among patients without VS edemas because only 2 patients had an extended abscess without it.

The strengths of the current study include a large sample size, high-quality 3T MR imaging with a Gd-based contrast agent and DWI, systematic neuroradiologic evaluation of MR imaging findings, thorough clinical characterization, and surgical confirmation of abscesses. However, limitations need to be addressed. A major limitation of our study is that we did not directly compare MR imaging findings in the same patients with those from CT, an established imaging method in current clinical practice. Therefore, we cannot make claims about the overall superiority of MR imaging over CT in patients with tonsillar infections. MR imaging may not always be suitable or available for all patients, and these results may not apply to all facilities. Very few direct comparisons between MR imaging and CT have been made, and future prospective comparative trials should be conducted. This question could also be explored with the increased soft-tissue characterization of dual-energy CT.¹⁹ A recent study showed that a lower tube voltage of 80 kV(peak) improved the delineation of PTA in comparison with the typical 120-kVp tube voltage.²⁰

Furthermore, our study was retrospective in nature; therefore, medical and surgical records may have been incomplete or imprecise. Indications for imaging may have varied; thus, the current results may be biased. Because of partial verification bias (patients without abscesses are much less likely to undergo an operation than patients with abscesses), the proportions of true- and false-negatives are not reliable. Unverified false-negatives (small undetected abscesses that do not require an operation) may overestimate the sensitivity and underestimate the specificity.

Our study may have selection bias toward more severely ill patients, which could have limited our ability to detect ITAs. The surgical results were also sometimes unclear, though in very few cases. The interpretation of some of the MR imaging findings may be subjective: We found moderate-to-substantial interobserver agreement for the edema patterns. Finally, this study is limited by the lack of a control group, and the findings only pertain to patients undergoing emergency MR imaging.

CONCLUSIONS

Emergency neck MR imaging can accurately describe the extent and nature of abscess formation in tonsillar infections.

Disclosure forms provided by the authors are available with the full text and PDF of this article at www.ajnr.org.

REFERENCES

1. Bochner RE, Gangar M, Belamarich PF. A clinical approach to tonsillitis, tonsillar hypertrophy, and peritonsillar and retropharyngeal abscesses. *Pediatr Rev* 2017;38:81–92 CrossRef Medline
2. Steyer TE. Peritonsillar abscess: diagnosis and treatment. *Am Fam Physician* 2002;65:93–96 Medline
3. Elden LM, Grundfast KM, Vezina G. Accuracy and usefulness of radiographic assessment of cervical neck infections in children. *J Otolaryngol* 2001;30:82–89 CrossRef Medline
4. Vural C, Gungor A, Comerici S. Accuracy of computerized tomography in deep neck infections in the pediatric population. *Am J Otolaryngol* 2003;24:143–48 CrossRef Medline
5. Freling N, Roelle E, Schaefer-Prokop C, et al. Prediction of deep neck abscesses by contrast-enhanced computerized tomography in 76 clinically suspect consecutive patients: deep neck abscesses predicted by CECT. *Laryngoscope* 2009;119:1745–52 CrossRef Medline
6. Blair AB, Booth R, Baugh R. A unifying theory of tonsillitis, intratonsillar abscess and peritonsillar abscess. *Am J Otolaryngol* 2015;36:517–20 CrossRef Medline
7. Wang B, Gao BL, Xu GP, et al. Images of deep neck space infection and the clinical significance. *Acta Radiol* 2014;55:945–51 CrossRef Medline
8. Muñoz A, Castillo M, Melchor MA, et al. Acute neck infections: prospective comparison between CT and MRI in 47 patients. *J Comput Assist Tomogr* 2001;25:733–41 CrossRef Medline
9. Nurminen J, Velhonoja J, Heikkinen J, et al. Emergency neck MRI: feasibility and diagnostic accuracy in cases of neck infection. *Acta Radiol* 2021;62:735–42 CrossRef Medline
10. Stone ME, Walner DL, Koch BL, et al. Correlation between computed tomography and surgical findings in retropharyngeal inflammatory processes in children. *Int J Pediatr Otorhinolaryngol* 1999;49:121–25 CrossRef Medline
11. Page NC, Bauer EM, Lieu JE. Clinical features and treatment of retropharyngeal abscess in children. *Otolaryngol Head Neck Surg* 2008;138:300–06 CrossRef Medline
12. Klug TE, Fischer AS, Antonsen C, et al. Parapharyngeal abscess is frequently associated with concomitant peritonsillar abscess. *Eur Arch Otorhinolaryngol* 2014;271:1701–07 CrossRef Medline
13. Wang AS, Stater BJ, Kacker A. Intratonsillar abscess: 3 case reports and a review of the literature. *Int J Pediatr Otorhinolaryngol* 2013;77:605–07 CrossRef Medline
14. Singh GB, Kumar D, Arora R, et al. A rare case of intratonsillar abscess in an adult. *Clin Pract* 2015;5:804 CrossRef Medline
15. Ahmed Ali S, Kovatch KJ, Smith J, et al. Predictors of intratonsillar abscess versus peritonsillar abscess in the pediatric patient. *Int J Pediatr Otorhinolaryngol* 2018;114:143–46 CrossRef Medline
16. Ahmed Ali S, Kovatch KJ, Smith J, et al. Predictors of intratonsillar versus peritonsillar abscess: a case-control series. *Laryngoscope* 2019;129:1354–59 CrossRef Medline
17. Giurintano JP, Kortebein S, Sebelik M, et al. Intratonsillar abscess: a not-so-rare clinical entity. *Int J Pediatr Otorhinolaryngol* 2019;119:38–40 CrossRef Medline
18. Klug TE, Rusan M, Fuursted K, et al. Peritonsillar abscess: complication of acute tonsillitis or Weber's glands infection? *Otolaryngol Head Neck Surg* 2016;155:199–207 CrossRef Medline
19. May MS, Wiesmueller M, Heiss R, et al. Comparison of dual- and single-source dual-energy CT in head and neck imaging. *Eur Radiol* 2019;29:4207–14 CrossRef Medline
20. Scholtz JE, Hüser K, Kaup M, et al. Evaluation of image quality and dose reduction of 80 kVp neck computed tomography in patients with suspected peritonsillar abscess. *Clinical Radiol* 2015;70:e67–73 CrossRef Medline

Morphologic Variants of the Hand Motor Cortex in Developing Brains from Neonates through Childhood Assessed by MR Imaging

F. Wu, H. Zhao, Y. Zhang, M. Wang, C. Liu, X. Wang, Y. Cheng, C. Jin, J. Yang, and X. Li



ABSTRACT

BACKGROUND AND PURPOSE: Knowledge of anatomic markers of the hand motor cortex is essential in the evaluation and treatment of motor neurologic diseases for both adults and developing populations. However, hand motor cortex variants in developing brains remain to be investigated. Our objective was to observe morphologic variants of the hand motor cortex in developing brains from neonates through childhood.

MATERIALS AND METHODS: In this study, 542 participants (0~15 years of age) were retrospectively enrolled and divided into different age groups. The hand motor cortex morphology was evaluated on the basis of 3D TIWI. Variations in hand motor cortex variants were compared among different age groups. Inter-gender and interhemispheric differences of hand motor cortex variants were also evaluated.

RESULTS: Various hand motor cortex variants could be observed in developing brains, even in the neonatal period. One new morphologic shape, “immature Ω ,” was found in neonates and infants. The proportion of this new shape decreased dramatically during the first year after birth, then disappeared after 1 year of age. It persisted for a longer time in the right hemisphere and in males. However, sex or hemispheric effects on the distribution of the proportion of variants were not statistically significant. Furthermore, the proportion of concordance of the bilateral hand motor cortex showed an increasing trend with age ($P = .006$), higher in females than males.

CONCLUSIONS: Various hand motor cortex variants already existed at birth. The distribution of proportions of different variants developmentally varied during the first year after birth and became stable after 1 year of age. The concordance of the bilateral hand motor cortex could be influenced by age and sex.

ABBREVIATIONS: ACPC = anterior/posterior commissure; GA = gestational age; HMC = hand motor cortex; PMA = postmenstrual age

The hand motor cortex (HMC) has been identified as a knob on the precentral gyrus.¹ It is always the recognition and stimulation/treatment target in the evaluation and treatment of neurologic motor diseases (eg, stroke,^{2–6} focal hand dystonia,⁷ and amyotrophic lateral sclerosis⁸) or glioma.⁹ Furthermore, it is

an identifiable neuroanatomic structure for delineating the corticospinal tract.¹⁰ Therefore, the identification of the HMC is essentially important for the exploration of the mechanism of handedness,¹¹ hand motor skills,¹² and eye-hand coordination.¹³

MR imaging provides a nonradiative tool for investigating the morphology of the HMC in vivo. The previous known shape of the HMC is a typical hook^{14,15} on the MR imaging sagittal plane, and a V-shaped anatomic signature¹⁶ and an Ω on the axial plane.¹ The Ω sign was gradually recognized as a reliable landmark for the localization of the HMC.¹⁶ Furthermore, 5 morphologic variants (Ω , medially asymmetric ε , ε , laterally asymmetric ε , and null) of the HMC have been recognized on MR imaging in adults.¹⁵ Knowledge of anatomic markers of the HMC on MR imaging is essential in research and clinical practice, not only for adults but also for the developing population. Specifically, the treatment target of transcranial magnetic stimulation was always placed on the primary motor cortex in children with spastic cerebral palsy with hand dysfunction.^{17,18} For patients with brain tumors, the width and height of the HMC and the distance from the tumor to the HMC on MR imaging are related to neurologic motor deficits.⁹ Although HMC variants have been

Received July 6, 2021; accepted after revision October 20.

From the Department of Radiology (F.W., H.Z., Y.Z., M.W., C.L., X.W., Y.C., C.J., J.Y., X.L.), the First Affiliated Hospital of Xi'an Jiaotong University, Xi'an, China; and Department of Radiology (F.W.), Guangzhou Women and Children's Medical Center, Guangzhou Medical University, Guangzhou, China.

Fan Wu and Huifang Zhao contributed equally to this work.

Jian Yang and Xianjun Li served as senior authors.

This work was supported by the National Natural Science Foundation of China (81971581, 81901823, 81771810, and 81901516) and the Innovation Team Project of Natural Science Fund of Shaanxi Province (2019TD-018).

Please address correspondence to Xianjun Li, PhD, Department of Radiology, the First Affiliated Hospital of Xi'an Jiaotong University, No. 277 West Yanta Road, Xi'an 710061, Shaanxi, China; e-mail: xianj.li@mail.xjtu.edu.cn

Indicates open access to non-subscribers at www.ajnr.org

Indicates article with online supplemental data.

<http://dx.doi.org/10.3174/ajnr.A7386>

recognized in adults,¹⁵ the morphology of the HMC in children may be different from that in adults because the brain develops dramatically during early childhood.^{19,20} However, little information has been reported about the characteristics of the HMC on the developing population, and the effects of age and sex on HMC morphology remain to be assessed. Therefore, it is necessary to investigate the morphology of the HMC in developing brains.

On the basis of the above considerations, this study tried to use MR imaging to investigate the morphologic variants of the HMC in developing brains from neonates through childhood. HMC variants were compared among different age groups. Sex and hemisphere effects on HMC variants were also evaluated. Furthermore, the concordance of the bilateral HMC was analyzed.

MATERIALS AND METHODS

This retrospective study was approved by the institutional review board of the First Affiliated Hospital of Xi'an Jiaotong University. Written informed consent was obtained from parents or guardians of participants.

Subjects

Subjects were enrolled consecutively from August 2012 to December 2019. According to the postnatal age at MR imaging, the enrolled subjects were divided into neonates (age, ≤ 28 days), infants (>28 days to <1 year), toddlers (1 to <3 years), preschool children (3 to <6 years), school-age children (6 to <10 years), and adolescents (10 to <15 years). To reveal more detailed alterations during the neonatal period, we divided neonates into preterm (gestational age [GA], <37 weeks) and term (GA, ≥ 37 weeks) groups. All infants, toddlers, preschool children, school-age children, and adolescents were term birth. Because of the difference in the disease spectrum between the neonate group and other age groups, we performed the inclusion and exclusion using different criteria.

The detailed inclusion and exclusion criteria were as follows:

Inclusion criteria: neonate group: age at MR imaging, ≤ 28 days. Other age groups: 1) GA ≥ 37 weeks; 2) age at MR imaging, 29 days~15 years of age.

Exclusion criteria: 1) abnormal findings on MR imaging or diseases influencing the brain maturation: neonatal group: punctate white matter lesions, metabolic disorders, intracranial hemorrhage, periventricular leukomalacia, congenital malformations of nervous system, hydrocephalus, small for GA, hypoxic-ischemic encephalopathy, and intracranial infection. Other age groups: focal white matter hyperintensity on T2 FLAIR, enlargement of subarachnoid spaces, dilated Virchow-Robin spaces, encephalomalacia, periventricular leukomalacia, congenital malformations of the nervous system, hydrocephalus, malformation of cerebral vessels, metabolic disorders, and others including cerebral trauma and intracranial tumor, epilepsy, febrile convulsion, tic disorder, visual abnormalities, intracranial infection, hypoxic-ischemic encephalopathy, and mental, behavioral, or neurodevelopmental disorders; 2) incomplete MR images or clinical information (including perinatal characteristics and clinical conditions).

Data Acquisition

MR images were acquired using a 3T scanner (Signa HDxt; GE Healthcare) with an 8-channel head coil. 3D fast spoiled gradient

recalled-echo T1WI was performed using the following parameters: TR/TE, 10.42/4.74 ms; isotropic resolution, $1 \times 1 \times 1$ mm³; matrix, 240×240 ; thickness, 1 mm; FOV, 240×240 mm².

Image Processing

The 3D T1WIs of the cerebrum were translated and rotated into the anterior/posterior commissure (ACPC) plane. In adults, the HMC was located at Talairach coordinates of $x = \pm 34$, $y = -29$, $z = 50$.^{15,21} Due to the developmental changes of brain morphology, the optimal level for evaluating the HMC was different across individuals. Here, the ACPC plane was defined as the zero point of the z-axis. Then, the evaluation plane above the ACPC line was located at different coordinates in different age groups: neonates, 32 (SD, 3) mm; infants, 39 (SD, 4) mm; toddlers, 46 (SD, 4) mm; preschool children, 49 (SD, 4) mm; school-age children, 50 (SD, 3) mm; and adolescents 50 (SD, 3) mm.

Morphologic Variant Classification of the HMC

Five different morphologic variants have been found for the adult HMC: Ω , medially asymmetric ε , ε , laterally asymmetric ε , and null.¹⁵ Besides these variants, this work revealed 1 new shape like but different from the Ω type. Because this shape could be found in neonates and infants and disappeared from the toddler period on, this work termed it "immature Ω " (Fig 1). The identification of the immature Ω was performed according to the following appearances: The shape was sloped; the outside angle between any side of the HMC and the base side was $>90^\circ$; the ratio between the height of the HMC and thickness of gray matter was ≥ 4 ; and the ratio between the height and width of the HMC was ≤ 1 . For comparison, the HMC with an outside angle of $\leq 90^\circ$, the ratio between the height of the HMC and thickness of gray matter was ≥ 4 , or the Ω type was classified as the "mature Ω ." Two radiologists (with >5 years' experience in the interpretation of the pediatric brain MR imaging), blinded to the demographic information of participants, independently evaluated the HMC type, and one of them preformed the evaluation twice. Moreover, disagreements across different evaluations were resolved by discussion with a senior radiologist (>15 years' experience).

Statistical Analysis

Statistical analyses were performed using SPSS (Version 18; IBM). Two neuroradiologists independently evaluated the HMC. Intra- and interobserver reliability was evaluated using the κ test. Categorical variables (the distribution of the HMC variant in different age groups) are shown as percentages and percentages in stacked bar charts. Categorical variables were compared using the Monte Carlo method test. $P < .05$ was considered statistically significant. In multiple comparisons, $P < .0024$ (.05/21) was considered statistically significant after the Bonferroni correction. The χ^2 test for trend was performed for the proportion of concordance of the bilateral HMC variants in each age group.

RESULTS

Participants

According to the inclusion and exclusion criteria, this work enrolled 542 participants, including 78 preterm neonates (40 males), 159 term neonates (103 males), 46 infants (32 males), 49 toddlers (33

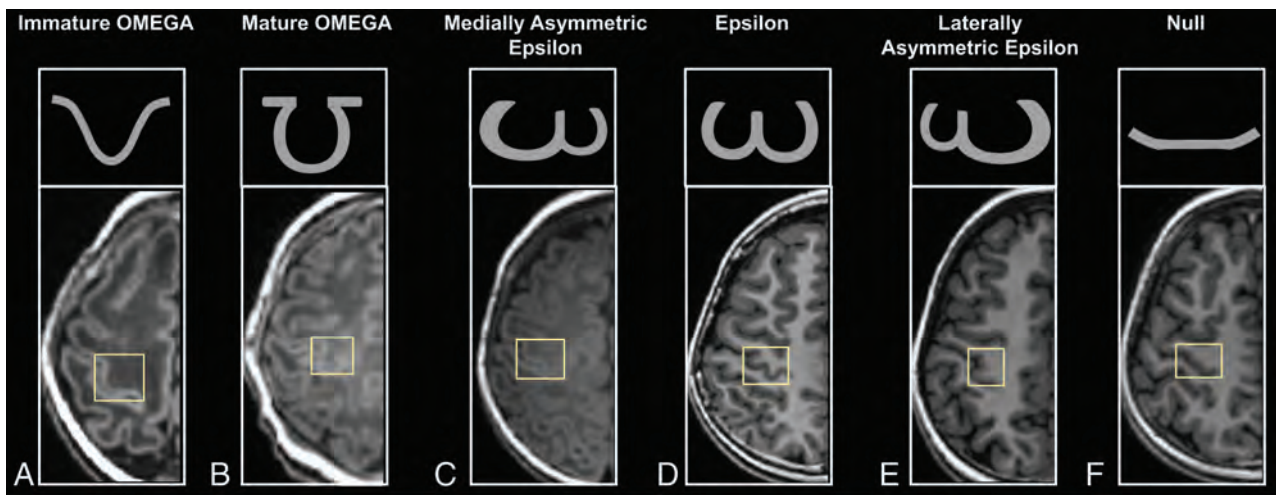


FIG 1. Appearances of HMC variances. Immature Ω (A): preterm neonate (female, GA = 32^{+1} weeks, PMA = 32^{+5} weeks). Mature Ω (B): term neonate (female, GA = 38^{+2} weeks, PMA = 38^{+6} weeks). Medially asymmetric ε (C): infant (female, GA = 39^{+1} weeks, age = 1.18 months). ε (D): adolescent (female, GA = 42 weeks, age = 10.36 years). Laterally asymmetric ε (E): school-age children (female, GA = 39^{+6} weeks, age = 8.37 years). Null (F): preschool children (male, GA = 40 weeks, age = 5.96 years).

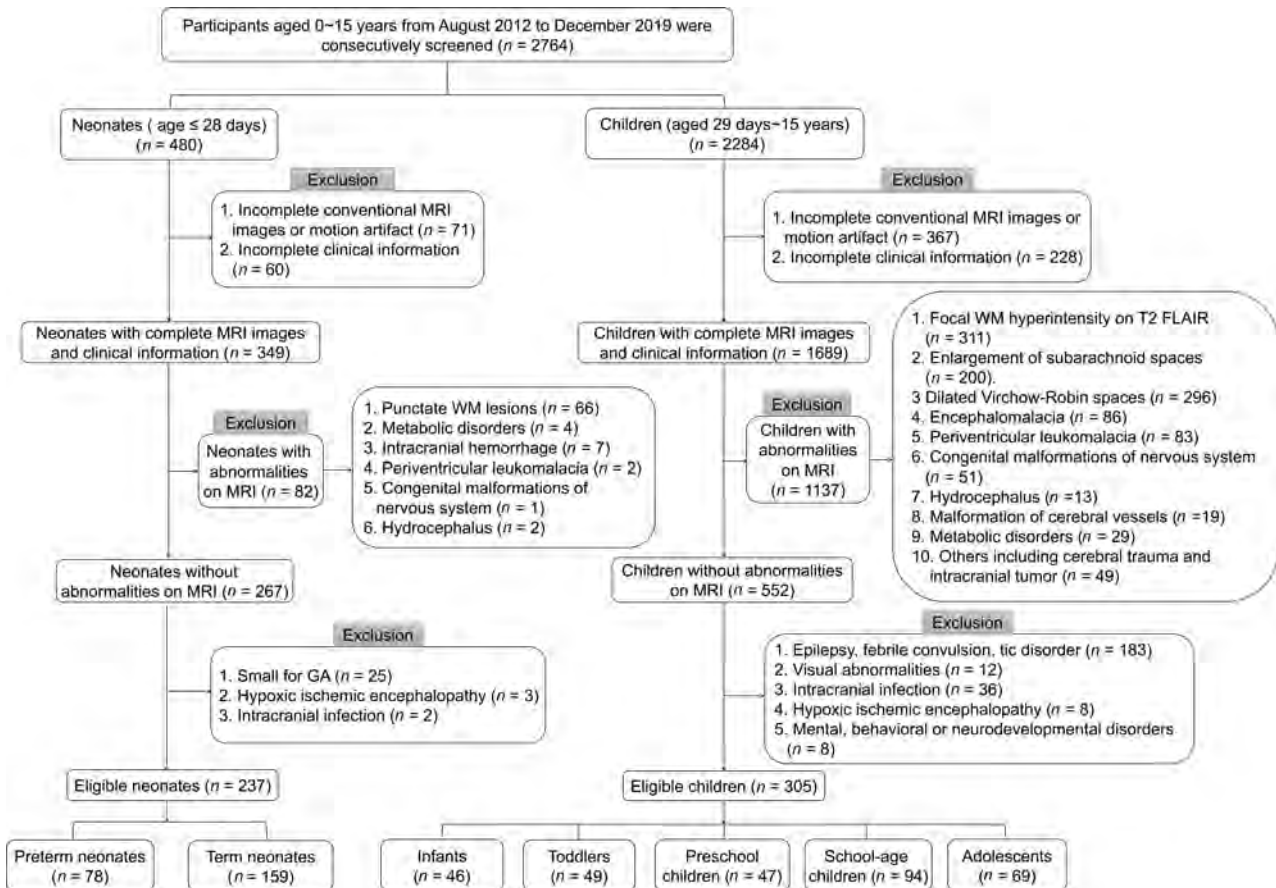


FIG 2. Flow chart of the inclusion and exclusion criteria.

males), 47 preschool children (34 males), 94 school-age children (53 males), and 69 adolescents (41 males) (Fig 2). No significant differences in GA, postnatal age, or postmenstrual age (PMA) at MR imaging were found between males and females in each age group ($P > .05$).

Intra- and Interobserver Reliability

The intraobserver and interobserver agreement for the HMC-type classification was 93.91% (κ value = 0.89; standard error = 0.02) and 90.59% (κ value = 0.84; standard error = 0.02), respectively.

Percentage of Morphologic Variants in Different Age Groups

In total, 6 variants (including 5 conventional variants and the immature Ω) could be found in participants. The sequence of the percentage of 542 participants (1084 HMCs) in descending order was the following: mature Ω (75.65%), ε (14.49%), immature Ω (6.46%), null (2.21%), laterally asymmetric ε (1.11%), and medially asymmetric ε (0.09%). The proportions of HMC variants in different age groups are shown in Fig 3.

The percentage distribution of HMC variants was statistically different across age groups. In the pair-wise comparison across 7 age groups (Online Supplemental Data), there were significant differences in the distribution of the HMC variant between the preterm neonates and other age groups ($P < .0024$). The mature Ω showed the trend of “increasing, relatively stable.” Except for neonates, there was no significant difference in the distribution of the HMC variants among other age groups ($P > .0024$). Specifically, the proportion of the immature Ω HMC decreased from 25.64% in preterm neonates to 8.81% in term neonates, 2.17% in infants, and 0% in toddlers. The proportion of the mature Ω HMC increased from 57.69% in preterm neonates to 73.58% in term neonates and 76.09% in infants and was stable from toddler age on at 76.81%~88.78% (median, 83.25%). The proportion of the ε (9.18%~

20.29%; median, 14.78%), the laterally asymmetric ε (0%~3.26%; median, 1.02%), the medially asymmetric ε (0%~1.09%; median, 0%), and the null HMC (0%~6.41%; median, 1.26%) did not differ significantly among age groups.

Morphologic Variants of the HMC in Different Sexes and Hemispheres

As shown in Fig 4, there was no significant difference in the distribution proportion between males and females or between left and right hemispheres in each age group ($P > .05$). Figure 4 also shows that the immature Ω sign seems to persist for a longer time in infants in the right hemisphere and in males.

Furthermore, the interhemispheric concordance of the HMC variants was also evaluated at the individual level. As for the same variant between the left and right hemispheres, the Ω type accounted for 97.50% (immature Ω accounted for 25%) in preterm neonates, and the null accounted for 2.50%. The Ω type accounted for 95.05% (the immature Ω accounted for 5.94%) in term neonates, the ε accounted for 3.96%, and the lateral ε accounted for 0.99%. The mature Ω was also the HMC variant with the maximum proportion in other age groups (accounting for >90%): infants (90.32%), toddlers (100%), preschool children (94.74%), school-age children (94.12%), and adolescents (91.30%). The proportion of the interhemispheric concordance showed an increasing trend with age ($\chi^2 = 7.540$, $P = .006$).

As for different sexes, the ratios of participants with the same bilateral HMC variant were $\geq 50\%$ in both males and females (Table). The consistency ratio of females was higher than in males in most age groups.

DISCUSSION

This study demonstrated morphologic variants of the HMC in developing brains from neonates through childhood. Besides the previously proposed 5 variants of the HMC in adults,^{1,15} we classified the Ω into 2 subtypes: mature Ω and immature Ω . Results

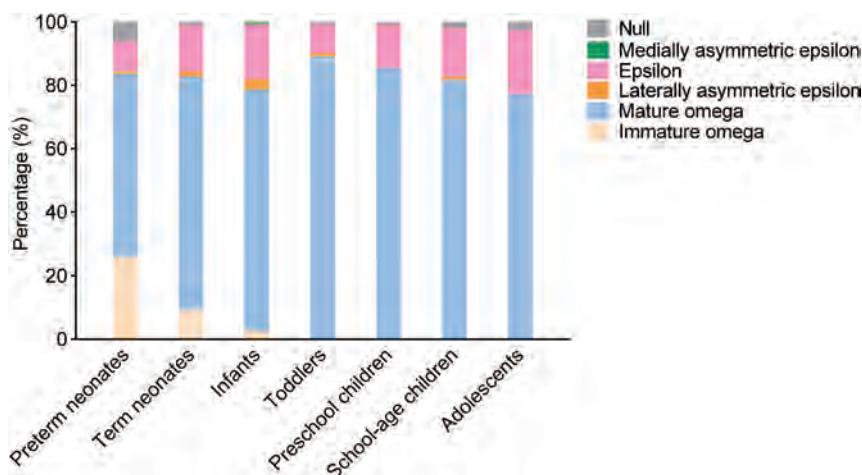


FIG 3. The proportional distribution of HMC variants in different age groups.

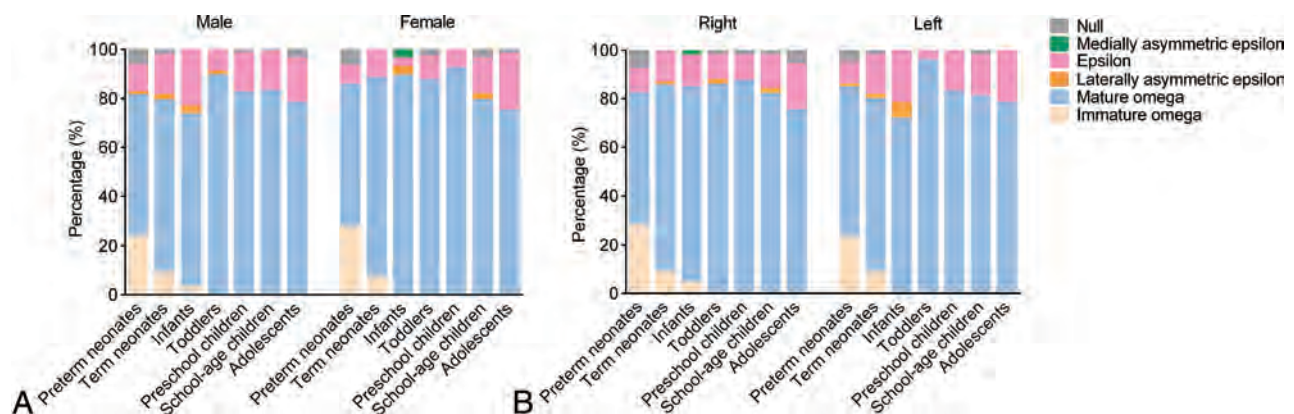


FIG 4. The proportional distribution of HMC variants in different sexes (A) and different hemispheres (B).

The proportion of concordance of the HMC variant in bilateral hemispheres in males and females of different age groups

Age Stage	Male (%)	Female (%)	Total (%)
Preterm neonates	52.50	50.00	51.28
Term neonates	60.19	69.64	63.52
Infants	62.50	78.57	67.39
Toddlers	78.79	75.00	77.55
Preschool children	79.41	84.62	80.85
School-age children	69.81	75.61	72.34
Adolescents	65.85	67.86	66.67
Average	67.01	71.61	68.51

demonstrated that various HMC variants already existed at birth and the proportional distribution of variants changed dramatically during the first year after birth. The concordance of the bilateral HMC showed an increasing trend with age. It could also be influenced by sex. Results here may provide a reference for the future investigations of the influence of pediatric diseases on the HMC.

HMC Morphologic Variants and Brain Development

Results here revealed that various HMC variants already existed in neonates. The immature Ω type accounted for a noticeable proportion. Typically, the central sulcus forms at a GA of 20–23 weeks, while the precentral gyrus forms at a GA of 24–27 weeks, and the secondary cerebral gyrus, at a GA of 32–35 weeks.^{22,23} In this study, the PMA at MR imaging of all neonates was >32 weeks. Therefore, the HMC in the immature state could be observed in neonates here. This study also found that the distribution of proportions in different variants of the HMC dramatically changed with age, especially before 1 year of age. The proportion of the immature HMC decreased, while the mature HMC increased. This observation may be because the cortex is still in a continuous folding process. During the third trimester of gestation, cortical folding changes dramatically in the brain.²⁴ A previous study observed that the synapse formation and the synapse pruning begin around a GA of 20 weeks and the myelin formation begins around a GA from 30 to 32 weeks.²⁵ These observations suggest that changes of the HMC morphology may also be associated with the ongoing myelin sheath and synaptic remodeling processes.^{20,26} It has been proposed that the tension-mediated folding increases as the axons strongly pull the interconnected regions together.²⁷ Development of axons underlying the central sulcus may cause the morphology of the HMC to change toward the mature type.

In addition, the cortical surface area of the precentral gyrus continues to increase after 1 year of age,^{20,28} while the sulci depth remains stable.²⁹ Therefore, the change of the precentral gyrus after 1 year of age here mainly reflects the increase of the gyrus width. Meanwhile, spatial distributions of the sulcal pits (the locally deepest points in sulci) show high consistency between infants and adults.³⁰ In agreement with these cortical maturation characteristics, the proportional distribution in the HMC variants reaches a relatively stable state after 1 year of age.

Potential Influencing Factors on HMC Morphologic Variants

HMC variants in adults have demonstrated that the proportions of sequences from high to low are as follows: Ω , ε , laterally

asymmetric ε , medially asymmetric ε , and null.¹⁵ In this study, the distribution of the mature Ω type in adolescents was similar to that of adults. Meanwhile, there were also differences: The ratio of ε in the current work was higher than that of adults, and the ratios of laterally asymmetric ε and medially asymmetric ε were lower. This finding may be due to a combination of factors of ethnic, genetic, customary, and environmental differences during crucial developmental stages of the brain. Previous studies have shown that the primary motor cortex in higher primates has internal subdivisions in the rostrocaudal direction and in 2 sectors connected to the spinal cord.^{31,32}

Additionally, in a direct electrophysiologic study of humans, the anatomo-functional subdivisions of the HMC include 2 sectors: the caudal one and the rostral one, playing different roles in motor control.³³ The caudal HMC is the most excitable sector. The rostral HMC is a crucial area for shaping functional synergies for hand-object interaction. These findings suggest that the human hand knob is an anatomo-functional heterogeneous region organized along a motor-cognitive gradient.³⁴ Thus, we speculated that the position of the middle fissure of ε in morphology may be related to these 2 sectors in the anatomo-functional subdivision. In families of the enrolled participants, early fine-motor skills of manipulating chopsticks and writing implements are expected.³⁵ Exuberant connectivity of the brain in the early life is pruned by competition, influenced by the early experience.¹⁹ Thus, plasticity and adaptation of the early brain development could lead to differences in the HMC morphology, especially in ε , laterally asymmetric ε , and medially asymmetric ε .¹⁹

The proportion of the same HMC variant in the bilateral hemispheres was higher than that of the inconsistent HMC variants in the bilateral hemispheres. According to comparisons across preterm neonates, term neonates, infants, and toddlers, age was a potential factor influencing the concordance of the HMC variant in the bilateral hemispheres. This finding may be related to the maturation of HMC morphology. With the process of brain development and cortex folding, some of the HMC changed from the immature Ω type into the mature Ω type. This feature may be the main factor leading to the increase of the concordance of the HMC variant in the bilateral hemispheres, especially during the first year after birth. Moreover, the immature Ω sign seems to persist for a longer time on the right side. This interhemispheric difference may be associated with the lateralization of motor function during development. A previous study indicated that early brain lateralization in humans could be influenced or reinforced by the asymmetric posture of the developing fetus.³⁶ From 14 weeks after conception, fetuses preferentially turn their heads to the right and suck on their right thumbs; this preference appears to be maintained throughout pregnancy.³⁷ In addition, most fetuses are in a head-down orientation on the mother's left side, a preferred position during the final trimester, favoring movement of the right arm by providing more space on the right side, thus contributing to the hand motor lateralization.^{36,38} Thus, early increased movement of the right hand may promote the folding and maturation of the left hemisphere HMC. Meanwhile, the neonatal left precentral gyrus

has more efficient communications than the right homolog.³⁹ After delivery and when in a supine position, most neonates prefer to lie with their heads turned to the right, resulting in greater perceptual experience related to the right hand.⁴⁰ Therefore, a shorter persisting time of the immature Ω type in the left hemisphere may be partly a result of the adaption to lateralized functional needs at birth.

Furthermore, the proportion of consistent HMC variants in the bilateral hemispheres was higher in females than that in males. According to a previous study, an interhemispheric concordance for HMC variants was observed only in females.¹⁵ Several studies on brain asymmetry suggested that the male brain may be more lateralized or asymmetric than the female brain.^{41–43} In an animal study, it was also observed that preventing the flow of androgens from the testis to the brain blocks the formation of the normal rightward brain asymmetry in male rats. Similarly, the female pattern can be reversed to the male pattern by neonatal ovariectomy.⁴⁴

These findings suggest that levels of androgenic and ovarian steroids play a part in regulating brain asymmetry. The growth of children is accompanied by changes in the levels of endocrine hormones, including sex hormones in females and males.⁴⁵ Therefore, sex may be another potential influencing factor on the concordance of the HMC variant in the bilateral hemispheres. Moreover, it has been found that males have smaller fractional anisotropy and larger axial diffusivity than females from birth to 2 years of age.⁴⁶ This finding suggests that the motor tract development in males is slightly behind that in females.⁴⁶ Meanwhile, the tension-mediated folding increases as axons strongly pull the interconnected regions together.²⁷ Therefore, a longer persisting time of the immature Ω type in males may be partly a result of the inter-gender difference in the motor-related white matter maturation.

Limitations

There are several limitations. First, although we included a large sample of subjects 0–15 years of age, samples were from 1 single center. Moreover, not all participants were recruited from healthy families. Participants were enrolled partly from the those with healthy findings on examinations and subjects with clinical symptoms (details are listed in Online Supplemental Data). There may be selection bias, though no subjects had abnormalities on MR imaging. Multisite research is necessary in the future to further verify our results. Second, changes in the morphology of individuals were not followed up. Therefore, this was a cross-sectional study. Changes in the variance were solely statistical associations rather than longitudinal observations. Third, this study did not assess the HMC morphology quantitatively. The relationship between morphologic parameters of the HMC and hand function outcomes remains to be investigated in further work.

CONCLUSIONS

This study demonstrated that various HMC variants already existed at birth. The distribution of proportions of different variants developmentally varied during the first year after birth and

became stable after 1 year of age. The concordance of the bilateral HMC could be influenced by age and sex.

Disclosure forms provided by the authors are available with the full text and PDF of this article at www.ajnr.org.

REFERENCES

1. Yousry TA, Schmid UD, Alkadhi H, et al. **Localization of the motor hand area to a knob on the precentral gyrus: a new landmark.** *Brain* 1997;120:141–57 CrossRef Medline
2. Butefisch CM, Kleiser R, Korber B, et al. **Recruitment of contralateral motor cortex in stroke patients with recovery of hand function.** *Neurology* 2005;64:1067–69 CrossRef Medline
3. Dong Y, Dobkin BH, Cen SY, et al. **Motor cortex activation during treatment may predict therapeutic gains in paretic hand function after stroke.** *Stroke* 2006;37:1552–55 CrossRef Medline
4. Zimmerman M, Heise KF, Hoppe J, et al. **Modulation of training by single-session transcranial direct current stimulation to the intact motor cortex enhances motor skill acquisition of the paretic hand.** *Stroke* 2012;43:2185–91 CrossRef Medline
5. Laible M, Grieshammer S, Seidel G, et al. **Association of activity changes in the primary sensory cortex with successful motor rehabilitation of the hand following stroke.** *Neurorehabil Neural Repair* 2012;26:881–88 CrossRef Medline
6. Revill KP, Haut MW, Belagaje SR, et al. **Hebbian-type primary motor cortex stimulation: a potential treatment of impaired hand function in chronic stroke patients.** *Neurorehabil Neural Repair* 2020;34:159–71 CrossRef Medline
7. Kimberley TJ, Pickett KA. **Differential activation in the primary motor cortex during individual digit movement in focal hand dystonia vs. healthy.** *Restor Neurol Neurosci* 2012;30:247–54 CrossRef Medline
8. Wang Y, Li X, Chen W, et al. **Detecting neuronal dysfunction of hand motor cortex in ALS: a MRSI study.** *Somatosens Mot Res* 2017;34:15–20 CrossRef Medline
9. Jingshan L, Shengyu F, Xing F, et al. **Morphometry of the hand knob region and motor function change in eloquent area glioma patients.** *Clin Neuroradiol* 2019;29:243–51 CrossRef Medline
10. Dalamagkas K, Tsintou M, Rathi Y, et al. **Individual variations of the human corticospinal tract and its hand-related motor fibers using diffusion MRI tractography.** *Brain Imaging Behav* 2020;14:696–714 CrossRef Medline
11. van den Berg FE, Swinnen SP, Wenderoth N. **Involvement of the primary motor cortex in controlling movements executed with the ipsilateral hand differs between left- and right-handers.** *J Cogn Neurosci* 2011;23:3456–69 CrossRef Medline
12. Amunts K, Schlaug G, Jäncke L, et al. **Motor cortex and hand motor skills: structural compliance in the human brain.** *Hum Brain Mapp* 1997;5:206–15 CrossRef Medline
13. Mathew J, Eusebio A, Danion F. **Limited contribution of primary motor cortex in eye-hand coordination: a TMS study.** *J Neurosci* 2017;37:9730–40 CrossRef Medline
14. Salamon G, Martini P, Ternier F, et al. **Topographical study of supratentorial brain tumors.** *J Neuroradiol* 1991;18:123–40 Medline
15. Caulo M, Briganti C, Mattei PA, et al. **New morphologic variants of the hand motor cortex as seen with MR imaging in a large study population.** *AJNR Am J Neuroradiol* 2007;28:1480–85 CrossRef Medline
16. Puce A, Constable RT, Luby ML, et al. **Functional magnetic resonance imaging of sensory and motor cortex: comparison with electrophysiological localization.** *J Neurosurg* 1995;83:262–70 CrossRef Medline
17. Gupta M, Lal Rajak B, Bhatia D, et al. **Effect of r-TMS over standard therapy in decreasing muscle tone of spastic cerebral palsy patients.** *J Med Eng Technol* 2016;40:210–16 CrossRef Medline
18. Rajak B, Gupta M, Bhatia D, et al. **Effect of repetitive transcranial magnetic stimulation on hand function of spastic cerebral palsy children.** *Journal of Neurological Disorders* 2017;5:1000329 CrossRef

19. Stiles J, Jernigan TL. **The basics of brain development.** *Neuropsychol Rev* 2010;20:327–48 CrossRef Medline
20. Gilmore JH, Knickmeyer RC, Gao W. **Imaging structural and functional brain development in early childhood.** *Nat Rev Neurosci* 2018;19:123–37 CrossRef Medline
21. Kido DK, LeMay M, Levinson AW, et al. **Computed tomographic localization of the precentral gyrus.** *Radiology* 1980;135:373–77 CrossRef Medline
22. Zilles K, Schleicher A, Langemann C, et al. **Quantitative analysis of sulci in the human cerebral cortex: development, regional heterogeneity, gender difference, asymmetry, intersubject variability and cortical architecture.** *Hum Brain Mapp* 1997;5:218–21 CrossRef Medline
23. White T, Su S, Schmidt M, et al. **The development of gyrification in childhood and adolescence.** *Brain Cogn* 2010;72:36–45 CrossRef Medline
24. Kim H, Lepage C, Maheshwary R, et al. **NEOCIVET: towards accurate morphometry of neonatal gyrification and clinical applications in preterm newborns.** *Neuroimage* 2016;138:28–42 CrossRef Medline
25. Khundrakpam BS, Lewis JD, Zhao L, et al. **Brain connectivity in normally developing children and adolescents.** *Neuroimage* 2016;134:192–203 CrossRef Medline
26. Blanton RE, Levitt JG, Thompson PM, et al. **Mapping cortical asymmetry and complexity patterns in normal children.** *Psychiatry Res* 2001;107:29–43 CrossRef Medline
27. Van Essen DC. **A tension-based theory of morphogenesis and compact wiring in the central nervous system.** *Nature* 1997;385:313–18 CrossRef Medline
28. Remer J, Croteau-Chonka E, Dean DC, et al. **Quantifying cortical development in typically developing toddlers and young children, 1–6 years of age.** *Neuroimage* 2017;153:246–61 CrossRef Medline
29. Li G, Wang L, Shi F, et al. **Construction of 4D high-definition cortical surface atlases of infants: methods and applications.** *Med Image Anal* 2015;25:22–36 CrossRef Medline
30. Meng Y, Li G, Lin W, et al. **Spatial distribution and longitudinal development of deep cortical sulcal landmarks in infants.** *Neuroimage* 2014;100:206–18 CrossRef Medline
31. Rathelot JA, Strick PL. **Subdivisions of primary motor cortex based on cortico-motoneuronal cells.** *Proc Natl Acad Sci U S A* 2009;106:918–23 CrossRef Medline
32. Witham CL, Fisher KM, Edgley SA, et al. **Corticospinal inputs to primate motoneurons innervating the forelimb from two divisions of primary motor cortex and area 3a.** *J Neurosci* 2016;36:2605–16 CrossRef Medline
33. Vigano L, Forna L, Rossi M, et al. **Anatomo-functional characterisation of the human “hand-knob”: a direct electrophysiological study.** *Cortex* 2019;113:239–54 CrossRef Medline
34. Simone L, Viganò L, Forna L, et al. **Distinct functional and structural connectivity of the human hand-knob supported by intraoperative findings.** *J Neurosci* 2021;41:42–43 CrossRef Medline
35. Chow SM, Henderson SE, Barnett AL. **The Movement Assessment Battery for Children: a comparison of 4-year-old to 6-year-old children from Hong Kong and the United States.** *Am J Occup Ther* 2001;55:55–61 CrossRef Medline
36. Duboc V, Dufourcq P, Blader P, et al. **Asymmetry of the brain: development and implications.** *Annu Rev Genet* 2015;49:647–72 CrossRef Medline
37. Hepper PG, Shahidullah S, White R. **Origins of fetal handedness.** *Nature* 1990;347:431 CrossRef Medline
38. Previc FH. **A general theory concerning the prenatal origins of cerebral lateralization in humans.** *Psychol Rev* 1991;98:299–334 CrossRef Medline
39. Ratnarajah N, Rifkin-Graboi A, Fortier MV, et al. **Structural connectivity asymmetry in the neonatal brain.** *Neuroimage* 2013;75:187–94 CrossRef Medline
40. Michel GF. **Right-handedness: a consequence of infant supine head-orientation preference?** *Science* 1981;212:685–87 CrossRef Medline
41. Shaywitz BA, Shaywitz SE, Pugh KR, et al. **Sex differences in the functional organization of the brain for language.** *Nature* 1995;373:607–09 CrossRef Medline
42. Ruigrok AN, Salimi-Khorshidi G, Lai MC, et al. **A meta-analysis of sex differences in human brain structure.** *Neurosci Biobehav Rev* 2014;39:34–50 CrossRef Medline
43. Sowell ER, Peterson BS, Kan E, et al. **Sex differences in cortical thickness mapped in 176 healthy individuals between 7 and 87 years of age.** *Cereb Cortex* 2007;17:1550–60 CrossRef Medline
44. Toga AW, Thompson PM. **Mapping brain asymmetry.** *Nat Rev Neurosci* 2003;4:37–48 CrossRef Medline
45. Herting MM, Maxwell EC, Irvine C, et al. **The impact of sex, puberty, and hormones on white matter microstructure in adolescents.** *Cereb Cortex* 2012;22:1979–92 CrossRef Medline
46. Geng X, Gouttard S, Sharma A, et al. **Quantitative tract-based white matter development from birth to age 2 years.** *Neuroimage* 2012;61:542–57 CrossRef Medline

Pretreatment Normal WM Magnetization Transfer Ratio Predicts Risk of Radiation Necrosis in Patients with Medulloblastoma

J.H. Harreld, P. Zou, N.D. Sabin, A. Edwards, Y. Han, Y. Li, O. Bieri, R.B. Khan, A. Gajjar, G. Robinson, and T.E. Merchant



ABSTRACT

BACKGROUND AND PURPOSE: Radiation necrosis, for which abnormal WM enhancement is a hallmark, is an uncommon complication of craniospinal irradiation in children with medulloblastoma. The magnetization transfer ratio measures macromolecular content, dominated by myelin in the WM. We investigated whether the pretreatment supratentorial (nonsurgical) WM magnetization transfer ratio could predict patients at risk for radiation necrosis after radiation therapy for medulloblastoma.

MATERIALS AND METHODS: Ninety-five eligible patients with medulloblastoma (41% female; mean age, 11.0 [SD, 5.4] years) had baseline balanced steady-state free precession MR imaging before proton or photon radiation therapy. Associations among baseline supratentorial magnetization transfer ratio, radiation necrosis (spontaneously resolving/improving parenchymal enhancement within the radiation field)³, age, and the presence of visible brain metastases were explored by logistic regression and parametric/nonparametric techniques as appropriate.

RESULTS: Twenty-three of 95 (24.2%) children (44% female; mean age, 10.7 [SD, 6.7] years) developed radiation necrosis after radiation therapy (19 infratentorial, 1 supratentorial, 3 both). The mean pretreatment supratentorial WM magnetization transfer ratio was significantly lower in these children (43.18 versus 43.50, $P = .03$). There was no association between the supratentorial WM magnetization transfer ratio and age, sex, risk/treatment stratum, or the presence of visible brain metastases.

CONCLUSIONS: A lower baseline supratentorial WM magnetization transfer ratio may indicate underlying structural WM susceptibility to radiation necrosis and may identify children at risk for developing radiation necrosis after craniospinal irradiation for medulloblastoma.

ABBREVIATIONS: bSSFP = balanced steady-state free precession; CTCAE = Common Terminology Criteria for Adverse Events; M_0 = non-MT-sensitized; M_{MT} = MT-sensitized; MT = magnetization transfer; MTR = magnetization transfer ratio; PFS = posterior fossa syndrome; RN = radiation necrosis; RT = radiation therapy; ST = supratentorial

Radiation necrosis (RN) is a relatively uncommon complication of radiation therapy in children with medulloblastoma,

with a reported incidence ranging from 19% to >30%.¹⁻³ Current pathologic studies of RN suggest that damage to vascular endothelial cells and myelin-producing oligodendrocytes leads to increased vascular permeability, gliosis, and ultimately demyelination.^{4,5} Accordingly, abnormal posttreatment enhancement of nontumoral brain within the radiation field is the imaging hallmark of early radiation necrosis.^{1,2,6}

For most patients with posterior fossa tumors, RN occurs in the posterior fossa within 1 year of radiation therapy (RT) (the “subacute” period), and symptoms are absent.^{1,2,4,7,8} Nevertheless, patients with medulloblastoma have shown significantly greater long-term decline in intelligence quotient and mathematic reasoning scores than identically treated patients without RN.⁶ The ability to predict which patients are likely to develop RN could be useful for implementing mitigation or heightened monitoring strategies. Unfortunately, there are no reliable clinical predictors of RN in this population, including age

Received August 2, 2021; accepted after revision October 20.

From the Department of Radiology (J.H.H.), Dartmouth-Hitchcock Medical Center, Lebanon, New Hampshire; Geisel School of Medicine (J.H.H.), Dartmouth College, Hanover, New Hampshire; Departments of Diagnostic Imaging (P.Z., N.D.S., A.E.), Biostatistics (Y.H., Y.L.), Division of Neurology (R.B.K.), Department of Pediatrics, and Departments of Neuro-Oncology (A.G., G.R.) and Radiation Oncology (T.E.M.), St. Jude Children's Research Hospital, Memphis, Tennessee; Department of Radiology (O.B.), Division of Radiological Physics, University Hospital Basel, Basel, Switzerland; and Department of Biomedical Engineering (O.B.), University of Basel, Allschwil, Switzerland. Drs Giles Robinson and Thomas Merchant are co-senior authors.

This work was supported, in part, by grant No. CA21765 from the National Cancer Institute and by the American Lebanese and Syrian Associated Charities.

Please address correspondence to Julie H. Harreld, MD, Department of Radiology, Dartmouth-Hitchcock Medical Center, Lebanon, NH 03766; e-mail: Julie.H.Harreld@Hitchcock.org

Indicates open access to non-subscribers at www.ajnr.org

Indicates article with online supplemental data.

<http://dx.doi.org/10.3174/ajnr.A7393>

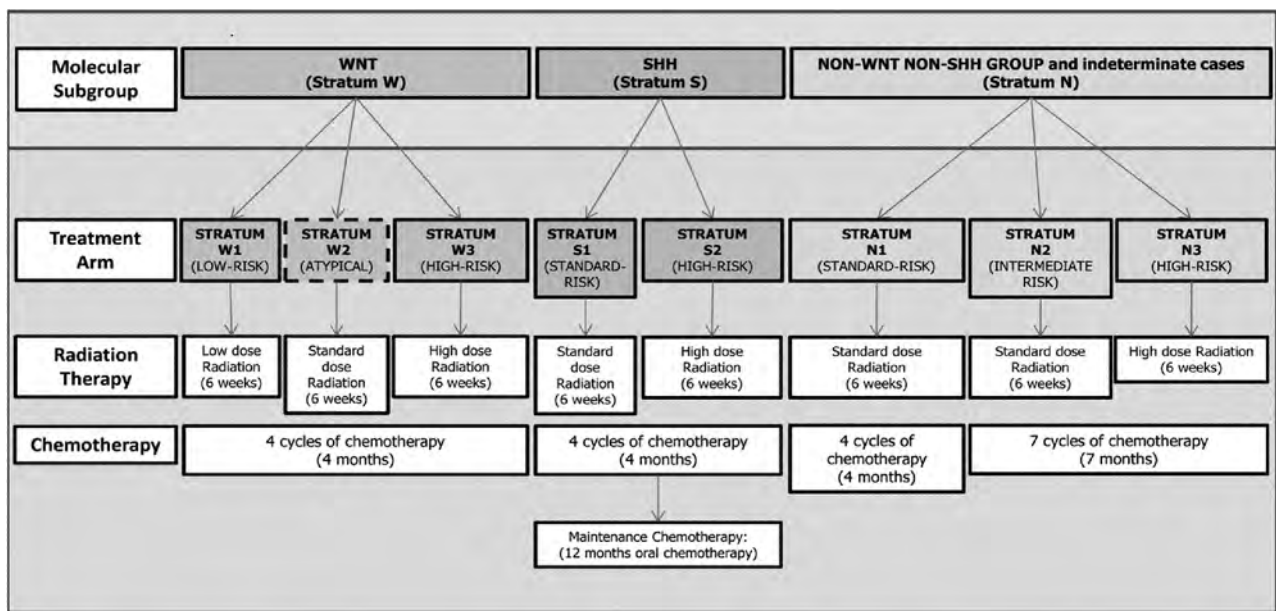


FIG 1. Risk-based treatment stratification schema. SHH indicates *sonic hedgehog*; WNT, *wingless*.

(in patients older than 3 years of age),^{1-3,7,9,10} chemotherapeutic regimen,^{1,10} metastatic status,¹ or photon radiation dose/volume.^{1,9}

Magnetization transfer (MT) imaging quantifies the proportion of myelin (“myelin density”) within a given volume of brain by calculating the ratio of images acquired with and without saturation of myelin/macromolecular protons, the magnetization transfer ratio (MTR).¹¹⁻¹³ An advantage of the MTR over DTI for the study of WM in children is the insensitivity of the MTR to potentially confounding age-related structural changes detectable by DTI.¹³

We hypothesized that patients with lower WM myelin density before treatment would be more susceptible to radiation necrosis. We, therefore, investigated whether the pretreatment MTR of unperturbed supratentorial (ST) WM could predict development of radiation necrosis after RT in patients with medulloblastoma.

MATERIALS AND METHODS

This prospective study was performed with the approval of the St. Jude Children's Research Hospital IRB and informed parental or patient consent and/or assent. Between June 2013 and February 2019, one hundred sixty-four patients with previously untreated medulloblastoma were enrolled in a prospective clinical trial (www.clinicaltrials.gov, NCT01878617) at a single institution. Enrollment criteria included 3 years of age or older and younger than 22 years (younger than 40 years for *sonic hedgehog* medulloblastoma) at diagnosis.

All patients underwent attempted maximal tumor resection. Patients were stratified into low-, standard-, and high-risk treatment groups on the basis of the molecular subgroup, postsurgical tumor volume, histology, *MYC/MYCN*, and metastatic status (M0 to M4) (Fig 1).^{14,15} Treatment guidelines for risk-adapted photon or proton craniospinal and conformal primary (posterior fossa) site irradiation ranged from 15 to 51 Gy (craniospinal

irradiation/primary site) for low-risk patients to 36 to 54 Gy for those at high risk, with additional boost of 45–50.4 Gy to metastatic sites when appropriate. Chemotherapy commenced 6 weeks post-RT (Fig 1).

One hundred twenty-five patients had baseline balanced steady-state free precession (bSSFP) MT imaging after surgery and before RT and chemotherapy. The subacute (“early delayed”) period was defined as up to 1 year after completion of RT.^{1,4,8} Patients without RN and <1 year of follow-up imaging were, therefore, excluded. Patients who developed late effects (>1 year after completing RT) were also excluded because late effects tend to be more clinically relevant and persistent and may differ in underlying pathologic mechanism.^{1,4,8} Follow-up diagnostic imaging was performed at 3-month intervals for the first 3 years, then at 6-month intervals for 3 years. Until March 16, 2015, MT imaging was performed in conjunction with fMRI before or within 2 weeks after beginning RT. After March 16, 2015, MT imaging was performed at the time of baseline, pretreatment diagnostic MR imaging.

3D bSSFP images were acquired on a 3T Magnetom Prisma or Magnetom Skyra scanner (Siemens) with a 64- or 20-channel head and neck coil. Parameters were $\alpha = 30^\circ$, bandwidth = 789 Hz/pixel, FOV = 256 × 256 mm, matrix = 192 × 192, and section thickness = 1.33 mm, yielding 1.33-mm isotropic voxels. TR/TE/radiofrequency pulse duration were 3.09/1.55/200 ms and 4.39/2.2/1500 ms for MT-sensitized (M_{MT}) and non-MT-sensitized (M_0) bSSFP sequences, respectively. Four examinations with legacy equipment Magnetom Tim Trio (Siemens) and head matrix coil (Siemens) were excluded from analysis.

Images were processed using in-house scripts in Matlab (MathWorks). MT images were coregistered with 3D T1-weighted MPRAGE images (TR/TE/TI = 1980/2.26/1000 ms, FOV = 256 × 256 mm, matrix = 256/256, section thickness = 1 mm) for segmentation. ST WM and GM were segmented using related functions from SPM software (<http://www.fil.ion.ucl.ac>).

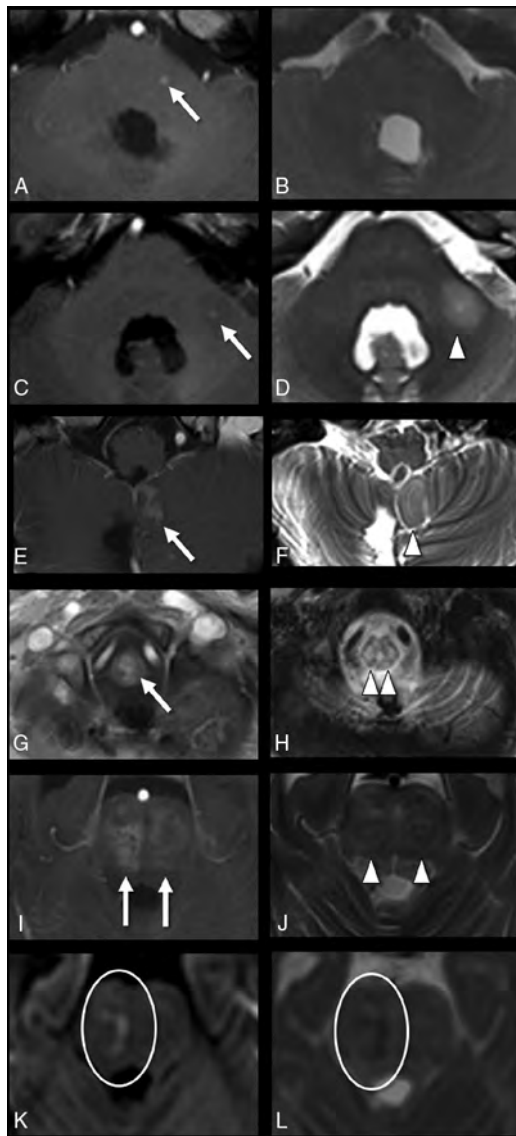


FIG 2. Image grading of radiation necrosis. Arrows show enhancement on postcontrast TIWI (A, C, E, G, I), and arrowheads show edema on T2WI (B, D, F, H, J). Grade 1: Punctate enhancement of the left pons (A) with no edema on T2WI (B). Grade 2: Punctate enhancement of the left middle cerebellar peduncle (C) with edema (D). Grade 3: Confluent enhancement of the left cerebellar tonsil (E) with ipsilateral edema (F). Grade 4: Confluent enhancement involving the cervicomedullary junction bilaterally (G), with bilateral edema (H). Grade 5: Confluent enhancement (I) and edema (J) in the pons bilaterally (J), with restricted diffusion evidenced by increased signal on DWI (K) and low signal on the ADC map (L).

uk/spm/software/spm12) in Matlab (Mathworks, Inc.). MTR was calculated for ST WM in percentage units (*pu*) as

$$MTR = \frac{(M_0 - M_{MT})}{M_0} \times 100pu.$$

A board-certified neuroradiologist with a Certificate of Added Qualification and 10 years' experience interpreting pediatric oncologic neuroimaging prospectively reviewed all baseline MRIs for early delayed RN, defined as new brain parenchymal enhancement within the radiation field that improved or resolved without

additional cancer-directed therapy.^{2,8} Because bulky leptomeningeal metastases could theoretically involve the WM and thereby alter the MTR, ST brain metastases were noted if present. Medical records for suspected cases of RN were reviewed by a pediatric oncologist (G.R.), and symptoms were graded according to the Common Terminology Criteria for Adverse Events (CTCAE), Version 4.03.¹⁶ All suspected cases of RN were reviewed for confirmation by a second board-certified neuroradiologist with a Certificate of Added Qualification and 15 years' experience in interpreting pediatric oncologic neuroimaging. Each confirmed case was then graded in consensus according to the following scale (Fig 2):

- 1) Punctate or stippled enhancement without edema
- 2) Punctate or stippled enhancement with edema (even if bilateral)
- 3) Nodular or confluent enhancement, some edema, does not cross the midline, *Or*, nodular/confluent enhancement, no appreciable edema, crosses the midline
- 4) Confluent enhancement and edema, bilateral or crosses the midline for midline structures
- 5) Confluent enhancement and edema, restricted diffusion.

Times from completion of radiation therapy to the appearance of RN and from the appearance to resolution or improvement of RN were recorded.

Statistical Analysis

The associations between the development of RN and baseline ST WM MTR, patient age, risk group (low, standard, or high), tumor subtype, technique (proton versus photon), and the presence of visible brain metastases were tested using the Wilcoxon rank sum test (continuous variables) or the Fisher exact test (categorical variables). Associations between baseline ST WM MTR and age, sex, risk/treatment stratum, and the presence of visible brain metastases were further assessed with linear/logistic regression and adjusted for magnet and/or coil if appropriate. Maximum imaging and clinical grades were compared among modalities with the Fisher exact test. All statistical evaluations were performed with SAS, Version 9.4. (SAS Institute). A 2-sided significance level of $P < .05$ was considered statistically significant.

RESULTS

Of 125 eligible patients, 30 were excluded for technically inadequate imaging ($n = 11$), legacy equipment ($n = 4$), follow-up < 1 year ($n = 14$), or RN > 1 year after RT ($n = 1$). Of 95 patients included in the final analysis, 23 (24.2%) developed RN (Online Supplemental Data). RN was initially noted on imaging a mean of 146.4 (SD, 58.2) days (range, 34–258 days) after treatment and resolved a mean of 152 (SD, 88.9) days (range, 49–364 days) after onset in 20 patients. Improvement without documented resolution was noted in 3 others: 2 who died of progressive disease (43 and 295 days' imaging follow-up) and another with persistent, though improved, imaging findings (937 days' follow-up).

Baseline MT imaging was acquired an average of 18.4 [SD, 10] days after surgery. ST WM MTR was significantly lower in children who later developed RN than those who did not ($P = .03$, Online Supplemental Data). Demographic and clinical characteristics, including risk/treatment stratum, did not differ (Online Supplemental Data).

On logistic regression, there was no significant association of baseline ST WM MTR with the magnet ($P = .28$). An association between baseline ST WM MTR and the coil approached significance ($P = .07$). When we controlled for the coil, each unit decrease in ST WM MTR at baseline increased the odds of developing RN by 56% (estimate = -0.8153 , OR = 0.44 , $P = .04$). Also when we controlled for the coil, there was no association between ST MTR and age ($P = .41$), sex ($P = .15$), risk/treatment stratum ($P = .60$), tumor subtype ($P = .67$), or the presence of visible brain metastases ($P = .69$).

RN was mild (grades 1–2) on imaging in 18/23 (78.3%) patients and asymptomatic (CTCAE grade 1) in 20/23 (87.0%). Three patients required intervention (CTCAE ≥ 2). Patients with RN (12/23, 52.2%) were more likely than those without RN (20/72, 27.8%) to have posterior fossa syndrome (PFS, $P = .02$), potentially confounding symptom assessment. There was no association between baseline ST WM MTR and PFS ($P = .93$).

Most imaging changes were mild (grades 1 or 2, Fig 2). Cerebellar involvement was most frequent (12/23 patients, 52.2%), and 22/23 (95.7%) had infratentorial RN. Restricted diffusion (grade 5) was observed only in the spinal cord, cervicomedullary junction, pons, and middle cerebellar peduncle (Online Supplemental Data).

There was no significant difference in imaging grade, clinical grade, time to onset, or time to resolution of RN between patients who had photon or proton beam RT or focal (primary site) RT (Online Supplemental Data).

DISCUSSION

RN is an uncommon complication of radiation therapy in patients with medulloblastoma and is associated with long-term cognitive sequelae, despite occurring predominantly in the posterior fossa, remote from ST brain centers responsible for cognition.¹

In this study, we found that decreased pretreatment MTR in normal ST WM predicted posttreatment RN in patients with newly diagnosed medulloblastoma undergoing RT. Baseline MTR was not associated with age, sex, medulloblastoma subtype, risk/treatment stratum, or metastatic status. As in a prior large medulloblastoma cohort,¹ the incidence of subacute RN did not differ significantly by risk/treatment stratum or M stage. Our findings suggest that decreased myelin density, either intrinsic or secondary to tumor and/or surgery, may be a predisposing factor for RN.

Although demyelination is a known consequence of radiation damage,^{4,5} there is currently no known association between myelin density and a predisposition to radiation injury. Our current understanding of genetic variations altering myelin development is driven by analysis in known syndromes.¹⁷ It is possible that other genetic differences in myelination, without clinical manifestations under normal circumstances, could predispose to radiation injury. The field of radiogenomics seeks to identify the genetic basis for differences in susceptibility to radiation injury among individuals.¹⁸ Our findings suggest that genes governing myelin formation could be a high-yield target for investigation.

A second possibility is that the lower pretreatment ST WM MTR we observed in patients with RN resulted from a greater disruption in the posterior fossa from tumor and surgery, sensitizing it to local radiation injury and manifesting as altered myelin density in the ST compartment via diaschisis.

Diaschisis describes a phenomenon in which a focal brain injury manifests as inflammation, degeneration, and demyelination in brain regions connected to, but remote from, the primary injury.^{19–21} Imaging studies showing decreased cortical perfusion²² and disruption of the cerebello-thalamo-cerebral WM tracts on DTI²³ after cerebellar surgery support diaschisis as the mechanism underlying PFS, occurring in 39%–40% of children with medulloblastoma, with a mean latency of 1.7 days.²⁴ Pathologic studies of brain injury in animals show inflammation and hydropic changes in remote diaschisis lesions.^{20,21} Such changes in the ST brain would be expected to reduce myelin density and, therefore, MTR.

The patients with RN in our series had a greater incidence of PFS (52.2%) than those without RN (27.8%), supporting an association between cerebellar injury and RN. The lack of a direct relationship between baseline ST WM MTR and PFS, however, suggests that while surgery-related diaschisis lesions within affected WM tracts may contribute to radiation sensitivity, they are insufficient to explain the lower baseline ST WM MTR we observed in patients who later developed RN.

This study was limited in scope, specifically targeting prediction of subacute (within 1 year post-RT), enhancing radiation injury (RN) in patients with medulloblastoma who consented to and underwent baseline MT imaging. It may not, therefore, represent the overall incidence, frequency, or full spectrum of radiation injury in this population. Furthermore, we did not investigate the association between RN and patient-specific radiation dose or treatment volume, which could vary per the investigator's discretion. We had no reason to suspect a relationship between pretreatment MTR and the subsequent radiation dose; thus, this analysis was not relevant to this possibility. However, it is quite possible for RN to occur despite a normal MTR. While decreased MTR increases the odds of RN, it is not the sole predictor of this complex pathology. RN timing specificity was limited by imaging frequency, which was dictated by the clinical trial protocol except in rare symptomatic presentations requiring additional imaging. Finally, WM MTR values obtained with bSSFP are typically higher than those obtained with 3D MT-prepared spoiled gradient-recalled imaging, with which the values presented here should not be compared.²⁵ bSSFP does, however, offer a markedly shorter imaging time and improved resolution and signal-to-noise ratio, important advantages over spoiled gradient-recalled imaging, particularly in children.²⁵

CONCLUSIONS

Reduced MTR in normal-appearing ST WM at pretreatment baseline predicts the risk for radiation necrosis in patients with medulloblastoma, potentially facilitating heightened monitoring and mitigation strategies. Further validation and study of mechanisms underlying this finding are indicated.

ACKNOWLEDGMENT

The authors would like to acknowledge the invaluable contributions of Elizabeth Sanchez, BS, for keeping us on track even through a global pandemic with her meticulous organization, positive outlook, and unwavering dedication to our patients.

REFERENCES

1. Fouladi M, Chintagumpala M, Laningham FH, et al. **White matter lesions detected by magnetic resonance imaging after radiotherapy and high-dose chemotherapy in children with medulloblastoma or primitive neuroectodermal tumor.** *J Clin Oncol* 2004;22:4551–60 CrossRef Medline
2. Kralik SF, Ho CY, Finke W, et al. **Radiation necrosis in pediatric patients with brain tumors treated with proton radiotherapy.** *AJNR Am J Neuroradiol* 2015;36:1572–78 CrossRef Medline
3. Spreafico F, Gandola L, Marchiano A, et al. **Brain magnetic resonance imaging after high-dose chemotherapy and radiotherapy for childhood brain tumors.** *Int J Radiat Oncol Biol Phys* 2008;70:1011–19 CrossRef Medline
4. Belka C, Budach W, Kortmann RD, et al. **Radiation induced CNS toxicity: molecular and cellular mechanisms.** *Br J Cancer* 2001;85:1233–39 CrossRef Medline
5. Pruzincová L, Steno J, Srbecký M, et al. **MR imaging of late radiation therapy- and chemotherapy-induced injury: a pictorial essay.** *Eur Radiol* 2009;19:2716–27 CrossRef Medline
6. Muscal JA, Jones JY, Paulino AC, et al. **Changes mimicking new leptomeningeal disease after intensity-modulated radiotherapy for medulloblastoma.** *Int J Radiat Oncol Biol Phys* 2009;73:214–21 CrossRef Medline
7. Gunther JR, Sato M, Chintagumpala M, et al. **Imaging changes in pediatric intracranial ependymoma patients treated with proton beam radiation therapy compared to intensity modulated radiation therapy.** *Int J Radiat Oncol Biol Phys* 2015;93:54–63 CrossRef Medline
8. Ball WS Jr, Prenger EC, Ballard ET. **Neurotoxicity of radio/chemotherapy in children: pathologic and MR correlation.** *AJNR Am J Neuroradiol* 1992;13:761–76 Medline
9. Murphy ES, Merchant TE, Wu S, et al. **Necrosis after craniospinal irradiation: results from a prospective series of children with central nervous system embryonal tumors.** *Int J Radiat Oncol Biol Phys* 2012;83:e655–60 CrossRef Medline
10. Plimpton SR, Stence N, Hemenway M, et al. **Cerebral radiation necrosis in pediatric patients.** *Pediatr Hematol Oncol* 2015;32:78–83 CrossRef Medline
11. Bieri O, Scheffler K. **Optimized balanced steady-state free precession magnetization transfer imaging.** *Magn Reson Med* 2007;58:511–18 CrossRef Medline
12. Grossman RI, Gomori JM, Ramer KN, et al. **Magnetization transfer: theory and clinical applications in neuroradiology.** *Radiographics* 1994;14:279–90 CrossRef Medline
13. Moura LM, Kempton M, Barker G, et al. **Age-effects in white matter using associated diffusion tensor imaging and magnetization transfer ratio during late childhood and early adolescence.** *Magn Reson Imaging* 2016;34:529–34 CrossRef Medline
14. Chang CH, Housepian EM, Herbert C Jr. **An operative staging system and a megavoltage radiotherapeutic technic for cerebellar medulloblastomas.** *Radiology* 1969;93:1351–59 CrossRef Medline
15. Gajjar AJ, Robinson GW. **Medulloblastoma-translating discoveries from the bench to the bedside.** *Nat Rev Clin Oncol* 2014;11:714–22 CrossRef Medline
16. Department of Health and Human Services National Institutes of Health, National Cancer Institute. **Common Terminology Criteria for Adverse Events, Version 4.03.** https://evs.nci.nih.gov/ftp1/CTCAE/CTCAE_4.03/CTCAE_4.03_2010-06-14_QuickReference_5x7.pdf. Accessed December 17, 2020
17. Sarret C. **Leukodystrophies and genetic leukoencephalopathies in children.** *Rev Neurol (Paris)* 2020;176:10–19 CrossRef Medline
18. Brothwell MR, West CM, Dunning AM, et al. **Radiogenomics in the era of advanced radiotherapy.** *Clin Oncol (R Coll Radiology)* 2019;31:319–25 CrossRef Medline
19. Taylor DL, Joashi UC, Sarraf C, et al. **Consequential apoptosis in the cerebellum following injury to the developing rat forebrain.** *Brain Pathol* 2006;16:195–201 CrossRef Medline
20. Weishaupt N, Zhang A, Deziel RA, et al. **Prefrontal ischemia in the rat leads to secondary damage and inflammation in remote gray and white matter regions.** *Front Neurosci* 2016;10:81 CrossRef Medline
21. Wiley CA, Bissel SJ, Lesniak A, et al. **Ultrastructure of diaschisis lesions after traumatic brain injury.** *J Neurotrauma* 2016;33:1866–82 CrossRef Medline
22. Miller NG, Reddick WE, Kocak M, et al. **Cerebellocerebral diaschisis is the likely mechanism of postsurgical posterior fossa syndrome in pediatric patients with midline cerebellar tumors.** *AJNR Am J Neuroradiol* 2010;31:288–94 CrossRef Medline
23. Law N, Greenberg M, Bouffet E, et al. **Clinical and neuroanatomical predictors of cerebellar mutism syndrome.** *Neuro Oncol* 2012;14:1294–1303 CrossRef Medline
24. Toescu SM, Hales PW, Aquilina K, et al. **Quantitative MRI in post-operative paediatric cerebellar mutism syndrome.** *Eur J Radiol* 2018;108:43–51 CrossRef Medline
25. Garcia M, Gloor M, Bieri O, et al. **MTR variations in normal adult brain structures using balanced steady-state free precession.** *Neuroradiology* 2011;53:159–67 CrossRef Medline

Features of Visually AcceSable Rembrandt Images: Interrater Reliability in Pediatric Brain Tumors

 A. Biswas,  A. Amirabadi,  M.W. Wagner, and  B.B. Ertl-Wagner



ABSTRACT

BACKGROUND AND PURPOSE: At present, no evidence-based lexicon exists for pediatric intracranial tumors. The Visually AcceSable Rembrandt Images terminology describes reproducible MR imaging features of adult gliomas for prediction of tumor grade, molecular markers, and survival. Our aim was to assess the interrater reliability of the pre-resection features of Visually AcceSable Rembrandt Images in pediatric brain tumors.

MATERIALS AND METHODS: Fifty consecutive pre-resection brain MR imaging examinations of pediatric intracranial neoplasms were independently reviewed by 3 neuroradiologists. The intraclass correlation coefficient for continuous variables and the Krippendorff alpha were used to evaluate the interrater agreement. Subgroup analysis was performed for 30 gliomas.

RESULTS: Parameters with almost perfect agreement ($\alpha > .8$) included tumor location (F1) and proportion of enhancing tumor (F5). Parameters with substantial agreement ($\alpha = .61-.80$) were side of tumor epicenter (F2), involvement of eloquent brain (F3), enhancement quality (F4), proportion of non-contrast-enhancing tumor (F6), and deep white matter invasion (F21). The other parameters showed either moderate ($\alpha = .41-.60$; $n = 11$), fair ($\alpha = .21-.40$; $n = 5$), or slight agreement ($\alpha = 0-.20$; $n = 1$). Subgroup analysis of 30 gliomas showed almost perfect agreement for tumor location (F1), involvement of eloquent brain (F3), and proportion of enhancing tumor (F5); and substantial agreement for side of tumor epicenter (F2), enhancement quality (F4), proportion of noncontrast enhancing tumor (F6), cysts (F8), thickness of enhancing margin (F11), and deep white matter invasion (F21). The intraclass correlation coefficient for measurements in the axial plane was excellent in both the main group (0.984 [F29] and 0.982 [F30]) and the glioma subgroup (0.973 [F29] and 0.973 [F30]).

CONCLUSIONS: Nine features of Visually AcceSable Rembrandt Images have an acceptable interrater agreement in pediatric brain tumors. For the subgroup of pediatric gliomas, 11 features of Visually AcceSable Rembrandt Images have an acceptable interrater agreement. The low degree of reproducibility of the remainder of the features necessitates the use of features tailored to the pediatric age group and is likely related to the more heterogeneous imaging morphology of pediatric brain tumors.

ABBREVIATIONS: VASARI = Visually AccesSable Rembrandt Images; REMBRANDT = REpository for Molecular BRAin Neoplasia DaTA

The terminology for Visually AcceSable Rembrandt Images (VASARI) was created for describing visual and subjective MR imaging features of adult gliomas.¹ It was developed by The Cancer Genome Atlas radiology working group as part of The REpository

for Molecular BRAin Neoplasia DaTA (REMBRANDT) project,² which was, in turn, established to facilitate collaboration among researchers across the globe. The REMBRANDT data set comprises imaging, clinical, and genetic information from 630 patients with gliomas.² VASARI features were developed following review of 88 MR imaging studies from this data set.¹ The goal of the VASARI terminology was to facilitate accurate and reproducible MR imaging interpretations of gliomas across different sites with the help of a controlled terminology incorporating the major subjective features of these tumors. A total of 30 features (F1–F25 [with the exception of F15, which is no longer in use], and F26–F30) form the terminology. Of these, features 1–25 apply to pre-resection subjective MR imaging features, features 26–28 apply to post-resection MR imaging features, whereas features 29 and 30 refer to measurements in 2 planes.¹ These features have been subsequently validated in


Received August 16, 2021; accepted after revision October 20.

From the Department of Diagnostic Imaging, The Hospital for Sick Children, Toronto, Ontario, Canada; and Department of Medical Imaging, University of Toronto, The Hospital for Sick Children, Toronto, Ontario, Canada.

M.W. Wagner and B.B. Ertl-Wagner are joint senior authors.

A. Biswas is partially funded by Ontasian Imaging Laboratory (OIL), Toronto.

Please address correspondence to Birgit Betina Ertl-Wagner, MD, Department of Diagnostic Imaging, The Hospital for Sick Children, 555 University Ave, Toronto, ON, M5G 1X8, Canada; e-mail: birgitbetina.ertl-wagner@sickkids.ca

 Indicates article with online supplemental data.

<http://dx.doi.org/10.3174/ajnr.A7399>

adult gliomas for reproducibility, grading, prediction of molecular markers, and survival.³⁻⁶ Currently, no evidence-based standardized vocabulary exists for imaging features of pediatric brain tumors. We, therefore, aimed to assess the interrater reliability of VASARI features in a sample of consecutive pediatric brain tumors.

MATERIALS AND METHODS

This retrospective study was approved by the institutional research ethics board of the Hospital for Sick Children (REB 1000077073), and informed consent was waived due to the retrospective nature of the study.

Patient Population

A retrospective review of the data base of our institution was performed for patients who had undergone neuro-oncologic brain MR imaging between January 2018 and March 2020. Patients were included according to the following criteria: 1) age younger than 18 years, 2) presence of a de novo diagnosis of an intra-axial tumor on MR imaging, and 3) pretherapeutic status of the intra-cranial tumor. Exclusion criteria were image degradation by artifacts and incomplete image acquisition.

MR Imaging Technique

MR imaging of all except 4 patients was performed at our institution. MR imaging was performed on a 3T magnet (Magnetom Skyra, Siemens, or Achieva, Philips Healthcare) using a 32-channel head coil or on a 1.5T magnet (Achieva) with pediatric 8- or 16-channel head coils. The standardized sequence protocol at our institution included the following sequences: a sagittal 3D T1-weighted sequence with axial and coronal reformats; axial DWI, axial FLAIR, and coronal T2-weighted sequences; an axial SWI or a multiplanar gradient recalled acquisition; a gadolinium-based contrast agent-enhanced axial 3D T1-weighted sequence with coronal and sagittal reformats; and a gadolinium-based contrast agent-enhanced coronal T1-weighted spin-echo sequence. Other sequences performed variably for different patients on the basis of suspected tumor pathology or for preoperative purposes were axial TOF-MRA, contrast-enhanced axial FLAIR, and orbital or spinal imaging. For the 4 patients (glial series neoplasms = 2; embryonal tumor with multilayered rosettes = 1; atypical teratoid/rhabdoid tumor = 1) who were referred to our hospital following MR imaging performed at external sites, the images were uploaded onto our institutional PACS server, with all examinations including T1-weighted, T2-weighted, FLAIR, DWI, and contrast-enhanced T1-weighted sequences.

Analysis of the Study Cohort

Three pediatric neuroradiologists (A.B., M.W.W., B.B.E.-W.), blinded to clinical and neuropathologic data, were provided with the study accession IDs in random reading order (randomized in Excel [Microsoft]). These were read independently by each reader. Assessment of 26 pre-resection VASARI features (F1–F14, F16–F25, and F29–F30) was performed on the PACS workstations. The VASARI features for each study were entered into Google Forms (<https://www.google.com/forms/about/>) created and shared by The Cancer Imaging Archive Team.¹ On completion of all 50 studies by each reader, the data were exported into Excel for further analysis.

Statistical Analysis

All statistical analyses were performed using R (Version 4.0.0; <http://www.r-project.org/>).⁷ The sample size ($n = 50$) was calculated using the kappaSize package in R with the confidence interval approach with binary outcome for a 1-sided 95% confidence interval, 0.2 precision, and an α level of .05. Intraclass correlation coefficients for continuous variables and the Krippendorff alpha⁸ were used to evaluate the interrater agreement. Subgroup analysis was performed for the 30 gliomas of the cohort.

RESULTS

Patient Demographics and Diagnoses

A total of 1097 consecutive neuro-oncologic brain MR imaging studies between January 1, 2018, and March 31, 2020, were reviewed for this study. A total of 1018 studies were acquired after initiation of therapy and were not considered for this study. We further excluded 18 studies with MRIs demonstrating image degradation by artifacts and 11 studies with incompletely acquired MRIs. The first 50 patients (mean age, 8.47 [SD, 5.33] years; range, 1–17 years; 28 males) who fulfilled the inclusion criteria were included for further analysis. The cohort consisted of biopsy-proved glial series neoplasms ($n = 30$), presumed glial series neoplasms ($n = 7$), biopsy-proved medulloblastomas ($n = 6$), a presumed medulloblastoma ($n = 1$), biopsy-proved embryonal tumors with multilayered rosettes ($n = 2$), biopsy-proved atypical teratoid/rhabdoid tumors ($n = 2$), a biopsy-proved ependymoma ($n = 1$), and a brain stem tumor that was presumed to be either a diffuse midline glioma or an embryonal tumor with multilayered rosettes ($n = 1$).

VASARI MR Imaging Analysis of 50 Consecutive Pediatric Brain Tumors

Parameters with almost perfect agreement ($\alpha > .8$) included tumor location (F1) and proportion of enhancing tumor (F5). Those with substantial agreement ($\alpha = .61-.80$) included side of tumor epicenter (F2), involvement of eloquent brain (F3), enhancement quality (F4), proportion of non-contrast-enhancing tumor (F6), and deep white matter invasion (F21). Those with moderate agreement ($\alpha = 0.41-.60$) included proportion of necrosis (F7), cysts (F8), multifocal or multicentric tumor (F9), T1/FLAIR ratio (F10), thickness of enhancing margin (F11), definition of enhancing margin (F12), proportion of edema (F14), presence of hemorrhage (F16), diffusion characteristics (F17), pial invasion (F18), and satellites (F24). Those with fair agreement ($\alpha = 0.21-.40$) included definition of nonenhancing margin (F13), ependymal invasion (F19), cortical involvement (F20), enhancing tumor crossing the midline (F23), and calvarial remodeling (F25), while those with slight agreement ($\alpha = .0-.20$) included non-contrast-enhancing tumor crossing the midline. There was excellent agreement for measurements in the axial plane (F29 and F30), with intraclass correlation coefficients of 0.984 (range, 0.98–0.99) and 0.982 (range, 0.969–0.989), respectively. Results for each parameter are provided in the Online Supplemental Data.

VASARI MR Imaging Analysis of the Subgroup of 30 Consecutive Gliomas

Parameters with almost perfect agreement ($\alpha > .8$) included tumor location (F1), involvement of eloquent brain (F3), and

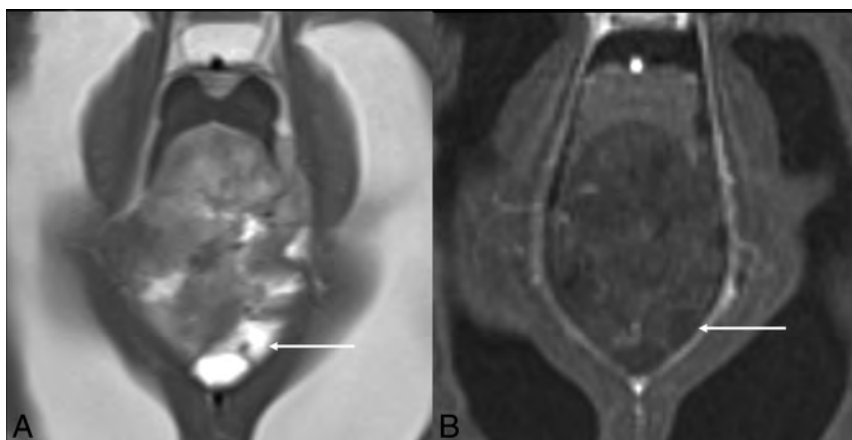


FIG 1. Depiction of cysts versus necrosis. Axial T2-weighted (A) and contrast-enhanced axial T1-weighted (B) images in a 57-week-old child with atypical teratoid/rhabdoid tumor demonstrate peripherally located “fluid-filled” structures (arrow in A) that do not parallel CSF intensity on T1-weighted imaging and do not show irregular rim enhancement (arrow in B), leading to difficulty in characterizing these as cysts or small necrotic pockets as per the VASARI definition.

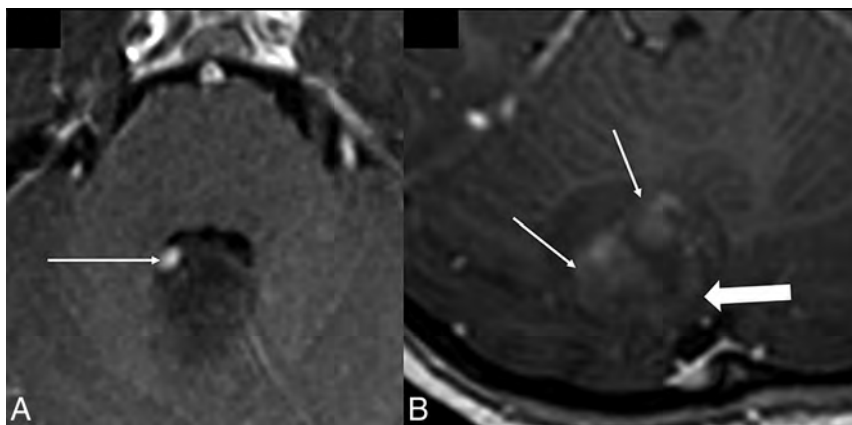


FIG 2. Enhancement characteristics. Axial contrast-enhanced T1-weighted image in a 6-year-old girl with group 4 medulloblastoma (A) shows focal nodular enhancement along the periphery (arrow). Axial contrast-enhanced T1-weighted image in a 13-year-old girl with pilocytic astrocytoma (B) demonstrates spotty central enhancement (arrows) with faint rim enhancement (arrowhead).

proportion of enhancing tumor (F5). Those with substantial agreement ($\alpha = .61-.80$) included side of tumor epicenter (F2), enhancement quality (F4), proportion of non-contrast-enhancing tumor (F6), cysts (F8), thickness of enhancing margin (F11), and deep WM invasion (F21). Those with moderate agreement ($\alpha = .41-.60$) included proportion necrosis (F7), definition of enhancing margin (F12), diffusion characteristics (F17), pial invasion (F18), and enhancing tumor crossing the midline (F23). Those with fair agreement ($\alpha = .21-.40$) included T1/FLAIR ratio (F10), definition of nonenhancing margin (F13), proportion of edema (F14), hemorrhage (F16), ependymal invasion (F19), cortical involvement (F20), satellites (F24), and calvarial remodeling (F25), while those with slight agreement ($\alpha = .0-.20$) included multifocal or multicentric tumor (F9) and non-contrast-enhancing tumor crossing the midline (F22). There was excellent agreement for measurements in the axial plane (F29 and F30), with an intraclass correlation coefficient of 0.973 (range, 0.951–0.986) and 0.973 (range,

0.948–0.987), respectively. Results for each parameter are provided in the Online Supplemental Data.

DISCUSSION

In this study, we analyzed the reliability of the VASARI terminology in pediatric brain tumors. In a group comprising 50 consecutive pediatric brain tumors, we found almost perfect inter-reader agreement for 2 features, substantial agreement for 5 features, and slight-to-moderate agreement for the other features. There was an excellent intraclass correlation coefficient for tumor measurement. In the subgroup comprising 30 consecutive pediatric gliomas, we found almost perfect inter-reader agreement for 3 features, substantial agreement for 6 features, and slight-to-moderate agreement for the other features. Similar to findings in the main group, an excellent intraclass correlation coefficient was found for tumor measurement.

In the adult population, imaging interpretation using VASARI features has been validated for reproducibility,³ prediction of molecular subtype,^{3,9} and prediction of survival¹⁰⁻¹³ in glioblastoma multiforme; and in predicting astrocytoma grade⁵ and molecular markers and survival in diffuse low-grade gliomas.⁴ The development of a controlled, reproducible terminology has allowed collaboration in adult glioma imaging across multiple sites.^{4,14,15}

Our results for tumor location are similar to the results of the VASARI research project,¹ in which there was

high agreement for this parameter. However, there was relatively less agreement for side of tumor epicenter in both the main and subgroups of our study, possibly due to the higher incidence of midline/off-midline tumors such as medulloblastoma and diffuse midline gliomas in our cohort compared with the adult population.

In our study, in both the main group and the glioma subgroup, we showed higher agreement for ordinal parameters such as proportion of enhancing tumor and proportion of nonenhancing tumor but lower agreement for proportion of necrosis, proportion of edema, T1/FLAIR ratio, and thickness of enhancing margin. The lower interrater agreement for proportion of necrosis compared with the adult study was likely due to the difficulty in differentiating tiny cysts from areas of necrosis (Fig 1). There was also difficulty in differentiating peripheral cysts and necrosis from CSF clefts, especially in posterior fossa tumors. Re-definition of these parameters in the context of pediatric tumors, therefore, needs consideration, with perhaps separate terminologies

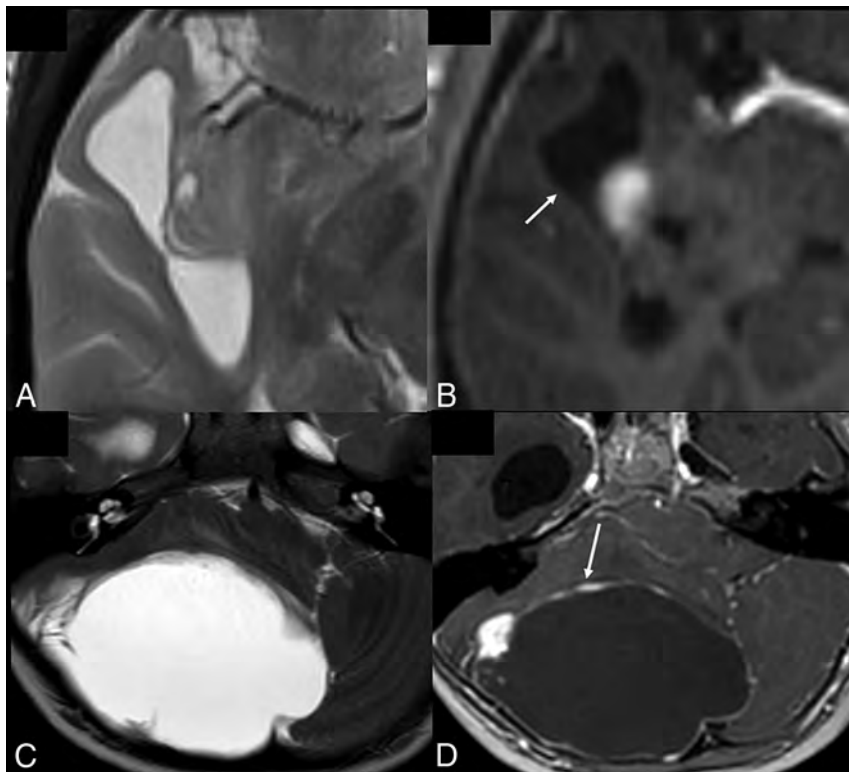


FIG 3. Cysts in pediatric intracranial tumors. A and B, BRAF V600E-positive astrocytoma. Axial T2-weighted and contrast-enhanced axial T1-weighted images show a dominant cyst with an enhancing mural nodule. The cyst wall does not enhance (arrow). C and D, Pilocytic astrocytoma. Axial T2-weighted and contrast-enhanced axial T1-weighted images show a dominant cyst with an enhancing mural nodule. The cyst wall enhances (arrow).

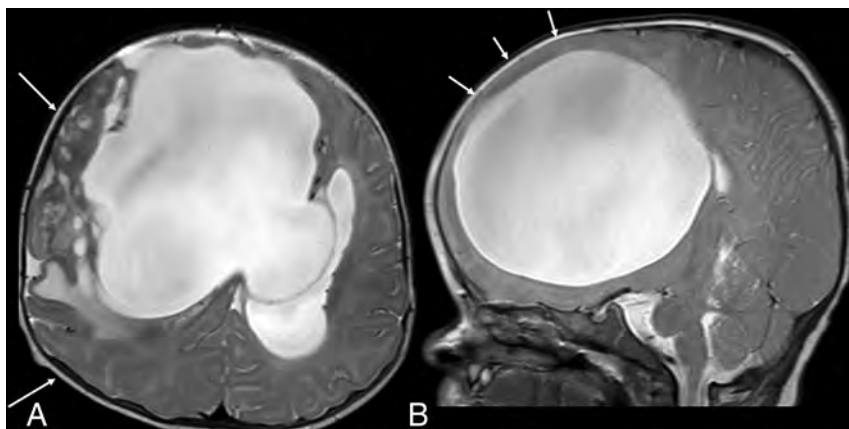


FIG 4. Osseous remodeling. Axial and sagittal T2-weighted images in a 4-month-old infant with a dysembryoplastic infantile ganglioglioma show asymmetric expansion of the calvaria (right > left, arrows in A), which occurs due to open sutures and fontanelles in this age group. Note the bulging anterior fontanelle (arrows in B).

for supratentorial and infratentorial tumors. The concept of the T1/FLAIR ratio was developed to differentiate expansive from infiltrative tumors.¹ It is unclear, however, if this parameter has an important role in pediatric tumors. Moreover, there was uncertainty as to whether the FLAIR hyperintense signal resulted from tumor-related mass effect or infiltration, particularly in the

posterior fossa. The role of this parameter may, therefore, be useful only in the setting of adult gliomas. Certain lesions had a poorly defined rim with scattered pockets of enhancement or focal nodular peripheral enhancement (Fig 2). This issue likely led to poor agreement for parameter F11 (thickness of enhancing margin). Modifying the definition to account for these enhancement patterns in pediatric brain tumors may help to better characterize this feature and may lead to better interreader agreement.

For nominal parameters, there was near-perfect agreement for tumor location, with substantial agreement for side of tumor epicenter, eloquent brain, enhancement quality, and deep white matter invasion and lower agreement for other parameters such as cysts. In the subgroup of gliomas, however, there was substantial agreement for cysts. As we alluded to earlier, there was disparity in differentiating small cysts from necrosis and also peripherally located cysts from CSF clefts. A unifying definition incorporating fluid-filled structures as a single entity, with necrosis, cysts, and CSF clefts as subcategories, may help in better categorizing these components, especially if tumor location (supratentorial versus infratentorial) is also taken into account. Further evaluation of the cystic component (such as number of cysts, dominant cyst, peripheral cyst, cyst wall characteristics) may also prove useful in pediatric tumors, given the higher proportion of tumors with cystic components such as pilocytic astrocytoma, dysembryoplastic neuroepithelial tumors, and ganglioglioma in this population (Fig 3).^{16,17}

Interpretation of diffusivity parameters in heterogeneous tumoral tissue and in the presence of hemorrhage was also challenging in both groups. Additional challenges encountered, particularly in posterior fossa tumors, were differentiation of cortical involvement from cortical distortion

and obscuration from mass effect, and tumors crossing midline. "Crossing the midline," by VASARI definition, included tumors that crossed over to the contralateral side via WM/commissural pathways. No clear definition existed, however, for lesions involving the brain stem. Another challenge we faced was ascertaining pial and/or ependymal invasion in instances in which the tumor

reached the pial and or ependymal surface. Clearer definitions (such as pial enhancement contiguous with the tumor) may help improve interrater agreement in pediatric brain tumors. It would, however, still be challenging to assess nonenhancing components of the tumor that reach the pial and ependymal surfaces.

Slight agreement for calvarial remodeling in both groups may be explained by the absence of a VASARI definition for skull base remodeling and the higher variability of the individual skull base morphology in children, because posterior fossa tumors causing secondary osseous changes were rated inconsistently (Fig 4A). In addition, the ability of the calvaria of very young children to expand in response to raised intracranial pressure (due to open fontanelles and sutures)¹⁸ necessitates the need to update this definition for pediatric tumors (Fig 4B).

There are several limitations to our study. First, the inclusion criteria were all consecutive tumors regardless of tumor pathology. These criteria also included a small number of cases that did not undergo biopsy. Because there is no semantic-based feature set in pediatric brain tumors, and given that in certain situations biopsy is not warranted, we decided to include all consecutive patients with brain tumors diagnosed on imaging. This choice led to a heterogeneous group of tumors with differing tumor biology but also highlighted the need for pediatric-specific and perhaps tumor- or location-specific terminology. We also performed a subgroup analysis only for pediatric gliomas. Second, the sample size was relatively limited but corresponded to our a priori calculations of sample size.

CONCLUSIONS

Although many VASARI features are reproducible in pediatric brain tumors with acceptable interrater agreement, the differing landscape and heterogeneity of pediatric tumors necessitates the use of tailored features, depending on tumor type and location.

Disclosure forms provided by the authors are available with the full text and PDF of this article at www.ajnr.org.

REFERENCES

1. VASARI Research Project. **The Cancer Imaging Archive (TCIA).** <https://wiki.cancerimagingarchive.net/display/Public/VASARI+Research+Project>. Accessed January 13, 2022
2. Gusev Y, Bhuvaneshwar K, Song L, et al. **The REMBRANDT study, a large collection of genomic data from brain cancer patients.** *Sci Data* 2018;5:180158 CrossRef Medline
3. Gutman DA, Cooper LA, Hwang SN, et al. **MR imaging predictors of molecular profile and survival: multi-institutional study of the**

TCGA glioblastoma data set. *Radiology* 2013;267:560–69 CrossRef Medline

4. Zhou H, Vallières M, Bai HX, et al. **MRI features predict survival and molecular markers in diffuse lower-grade gliomas.** *Neuro Oncol* 2017;19:862–70 CrossRef Medline
5. Yu J, Wang M, Song J, et al. **Potential utility of Visually Accessible Rembrandt Images assessment in brain astrocytoma grading.** *J Comput Assist Tomogr* 2016;40:301–06 CrossRef Medline
6. Nicolasjlwan M, Hu Y, Yan C, et al; TCGA Glioma Phenotype Research Group. **Addition of MR imaging features and genetic biomarkers strengthens glioblastoma survival prediction in TCGA patients.** *J Neurosurg* 2015;42:212–21 CrossRef Medline
7. R Core Team. **R: A Language and Environment for Statistical Computing.** http://web.mit.edu/r_v3.4.1/fullrefman.pdf. Accessed January 13, 2022
8. Hayes AF, Krippendorff K. **Answering the call for a standard reliability measure for coding data.** *Communication Methods and Measures* 2007;1:77–89 CrossRef
9. Zhou J, Reddy MV, Wilson BK, et al. **MR imaging characteristics associate with tumor-associated macrophages in glioblastoma and provide an improved signature for survival prognostication.** *AJNR Am J Neuroradiol* 2018;39:252–59 CrossRef Medline
10. Mazurowski MA, Desjardins A, Malof JM. **Imaging descriptors improve the predictive power of survival models for glioblastoma patients.** *Neuro Oncol* 2013;15:1389–94 CrossRef Medline
11. Wangaryattawanich P, Hatami M, Wang J, et al. **Multicenter imaging outcomes study of The Cancer Genome Atlas glioblastoma patient cohort: imaging predictors of overall and progression-free survival.** *Neuro Oncol* 2015;17:1525–37 CrossRef Medline
12. Colen RR, Vangel M, Wang J, et al; TCGA Glioma Phenotype Research Group. **Imaging genomic mapping of an invasive MRI phenotype predicts patient outcome and metabolic dysfunction: a TCGA glioma phenotype research group project.** *BMC Med Genomics* 2014;7:30 CrossRef Medline
13. Jain R, Poisson LM, Gutman D, et al. **Outcome prediction in patients with glioblastoma by using imaging, clinical, and genomic biomarkers: focus on the nonenhancing component of the tumor.** *Radiology* 2014;272:484–93 CrossRef Medline
14. Park CJ, Han K, Shin H, et al. **MR image phenotypes may add prognostic value to clinical features in IDH wild-type lower-grade gliomas.** *Eur Radiol* 2020;30:3035–45 CrossRef Medline
15. Lasocki A, Gaillard F, Gorelik A, et al. **MRI features can predict 1p/19q status in intracranial gliomas.** *AJNR Am J Neuroradiol* 2018;39:687–92 CrossRef Medline
16. Ryall S, Zapotocky M, Fukuoka K, et al. **Integrated molecular and clinical analysis of 1,000 pediatric low-grade gliomas.** *Cancer Cell* 2020;37:569–583.e5 CrossRef Medline
17. Ryall S, Tabori U, Hawkins C. **Pediatric low-grade glioma in the era of molecular diagnostics.** *Acta Neuropathol Commun* 2020;8:30 CrossRef Medline
18. Orrù E, Calloni SF, Tekes A, et al. **The child with macrocephaly: differential diagnosis and neuroimaging findings.** *AJR Am J Roentgenol* 2018;210:848–59 CrossRef Medline

Re-Examining the Cochlea in Branchio-Oto-Renal Syndrome: Genotype-Phenotype Correlation

J. Pao, F. D'Arco, E. Clement, S. Picariello, G. Moonis, C.D. Robson, and A.F. Juliano



ABSTRACT

BACKGROUND AND PURPOSE: Temporal bone imaging plays an important role in the work-up of branchio-oto-renal syndrome. Previous reports have suggested that the unwound or offset cochlea is a highly characteristic marker for branchio-oto-renal syndrome. Our goals were to examine the prevalence of this finding in a branchio-oto-renal syndrome cohort and analyze genetic-phenotypic associations not previously established.

MATERIALS AND METHODS: This multicenter retrospective study included 38 ears in 19 unrelated individuals with clinically diagnosed branchio-oto-renal syndrome and confirmed mutations in the *EYA1* or *SIX1* genes. Two blinded neuroradiologists independently reviewed and documented temporal bone imaging findings in 13 categories for each ear. Imaging phenotypes were correlated with genotypes.

RESULTS: There was excellent interrater agreement for all 13 phenotypic categories ($\kappa \geq 0.80$). Of these, 9 categories showed statistically significant differences between patients with *EYA1*-branchio-oto-renal syndrome and *SIX1*-branchio-oto-renal syndrome. Cochlear offset was present in 100% of patients with *EYA1*-branchio-oto-renal syndrome, but in only 1 ear (12.5%) among patients with *SIX1*-branchio-oto-renal syndrome. A short thorny appearance of the cochlear apical turn was observed in most patients with *SIX1*-branchio-oto-renal syndrome.

CONCLUSIONS: An offset cochlea is associated with the *EYA1*-branchio-oto-renal syndrome genotype. The *SIX1*-branchio-oto-renal syndrome genotype is associated with a different cochlear phenotype that almost always is without offset and has a short thorny tip as the apical turn. Therefore, cochlear offset is not a characteristic marker for all patients with branchio-oto-renal syndrome. The lack of a cochlear offset in a patient with clinically suspected branchio-oto-renal syndrome does not exclude the diagnosis and, in fact, may be predictive of the *SIX1* genotype.

ABBREVIATIONS: BOR = branchio-oto-renal syndrome; ET = Eustachian tube; IAC = internal auditory canal; LSCC = lateral semicircular canal; PSCC = posterior semicircular canal; VA = vestibular aqueduct

Branchio-oto-renal syndrome (BOR) is a common cause of congenital hearing loss, occurring in about 2% of profoundly deaf children,^{1,2} with a prevalence estimated at 1 in 40,000.¹

Melnick et al³ first described autosomally inherited familial branchio-oto-renal dysplasia in a family with hearing loss, cochlear malformation, malformed pinnae, prehelical pits, branchial

cleft fistulas, and renal dysplasia. Subsequent authors found families having similar features but variability in renal abnormalities (branchio-oto or branchio-oto-ureteral syndrome);^{1,2,4} these were attributed to variable gene penetrance.^{2,5} In 1980, Fraser et al¹ observed that not all patients with BOR had hearing loss. Anatomic studies described abnormal ossicles, hypoplastic cochleae, dysplastic semicircular canals, enlarged vestibular aqueducts (VAs), abnormal facial nerves, and bulbous internal auditory canals (IACs).⁶⁻⁸ Current diagnostic criteria are clinically based and dependent on the presence of major and minor criteria

Received August 1, 2021; accepted after revision November 2.

From the Department of Radiology (J.P.), Brigham and Women's Hospital, Harvard Medical School, Boston, Massachusetts; Department of Radiology (F.D.) and Department of Clinical Genetics (E.C.), Great Ormond Street Hospital for Children, London, UK; Department of Women, Child and General and Specialized Surgery (S.P.), University of Campania "Luigi Vanvitelli," Naples, Italy; Department of Paediatric Oncology (S.P.), Neuro-Oncology Unit, Santobono-Pausilipon Children's Hospital, Naples, Italy; Department of Radiology (G.M.), Columbia University Irving Medical Center, New York, New York; Department of Radiology (C.D.R.), Boston Children's Hospital, Harvard Medical School, Boston, Massachusetts; and Department of Radiology (A.F.J.), Massachusetts Eye and Ear, Harvard Medical School, Boston, Massachusetts.

J. Pao and F. D'Arco are co-first authors.

Please address correspondence to Amy F. Juliano, MD, Department of Radiology, Massachusetts Eye and Ear, 243 Charles St, Boston, MA 02114; e-mail: amy_juliano@meei.harvard.edu; @amyjuliano

Indicates article with online supplemental data.
<http://dx.doi.org/10.3174/ajnr.A7396>

Diagnostic criteria for BOR syndrome (Chang et al⁹)^a

Major Criteria	Minor Criteria
Branchial anomalies	External ear anomalies
Deafness	Middle ear anomalies
Preauricular pits	Inner ear anomalies
Renal anomalies	Preauricular tags
	Other: facial asymmetry, palate abnormalities

^aTo meet the criteria for BOR, an individual must meet 3 major criteria, 2 major and at least 2 minor criteria, or 1 major criterion with an affected first-degree relative who meets criteria for BOR.

(Table),⁹ including deafness and anatomic malformations of the ear, neck, and kidney as previously described.

Mutations in *EYA1* were first reported in 1997 as a genetic cause of BOR.¹⁰ Subsequently, mutations in *SIX1* were also identified in individuals with BOR. Approximately 40% of patients with BOR have mutations in the *EYA1* gene⁹ and <4% have mutations in the *SIX1* gene.¹¹ *EYA1* and *SIX1* are critical to mammalian organogenesis, including the otic vesicle. *SIX1* is a transcription factor and is reliant on the binding of EYA-family proteins at the conserved N-terminal (SIX domain) for transcription activation.^{12,13}

Large cohort studies have shown causative genetic mutations identified in only 36%–72% of clinically diagnosed individuals with BOR;^{14–16} therefore, evaluating the phenotype remains essential for diagnosis, even as genetic testing plays an increasingly important role.^{9,14,17–20}

Various temporal bone abnormalities have been described in BOR affecting the ossicles, inner ear, facial nerve course, and IAC. Cochlear malformation is common and is described as anteromedial offset of hypoplastic middle/apical turns away from a tapered basal turn.^{5,21–23} This morphologic appearance has been termed “unwound” or “offset” and has been reported to be a highly specific marker for BOR.^{23,24}

In this study, we focused on BOR genotype-phenotype associations on imaging that have not been previously established. Specifically, we examined the prevalence of the offset cochlea among patients with BOR with a known causative genotype, determined whether there are other temporal bone differences between patients with *EYA1*-BOR and *SIX1*-BOR, and described a new morphologic feature of the *SIX1*-BOR cochlea.

MATERIALS AND METHODS

Patients

This was a multicenter, retrospective review of cases of genetically confirmed BOR syndrome. Patients from 4 institutions were recruited; inclusion criteria were the following: clinical diagnosis of BOR syndrome referred from specialties including Otolaryngology and General/Pediatric Otorhinolaryngology; known causative genetic mutation associated with BOR; and diagnostic temporal bone CT and/or MR imaging available for review. This study was approved by the institutional review board/ethics committee of each institution.

Imaging Methods

All CT scanners across the participating institutions were helical multidetector CT scanners with parameters as follows: 120 kV

(peak), 100–200 mA, section thickness = 0.6–0.625 mm. All MR imaging scanners across the participating institutions were 3T, with the sequence assessed being heavily T2-weighted (driven equilibrium radiofrequency reset pulse [DRIVE; Philips], constructive interference in steady state [CISS; Siemens], or T2 sampling perfection with application-optimized contrasts by using different flip angle evolution [SPACE sequence; Siemens] depending on the vendor). Axial reformats of the temporal bones were created for both CT and MR imaging studies in a plane parallel to the lateral semicircular canal (LSCC) (or estimated as such in cases of anomalous LSCC) and coronal planes perpendicular to the true axial planes before image analyses.

Image Review

Two neuroradiologists with 5 (J.P.) and 15 (A.F.J.) years of experience reviewed all 19 cases. The reviewers were blinded to the original reports, demographics, genetic diagnosis, and the other reviewer's findings. For each case, the following 13 parameters were assessed on the basis of existing definitions and/or descriptions in the literature:^{22,24–33}

- Cochlear offset: yes/no
- Cochlear hypoplasia: yes/no (hypoplasia defined as ≤ 4.3 mm in height in the coronal plane^{26,27})
- Apical hypoplasia: yes/no; morphology if present
- Modiolus: normal/abnormal/absent
- Cochlear fossette stenosis: <1.4 mm/1.4–1.8 mm/>1.8 mm (fossette width measured in the axial plane spanning the inner margins of the bony edges across the base of the modiolus; stenosis was defined as <1.4 mm [in accordance with lower limits in the literature to avoid false-positives]; borderline as 1.4–1.8 mm; and not stenotic as >1.8 mm^{30–33})
- LSCC bone island small: yes/no (normal defined as >3 mm²⁷)
- Posterior semicircular canal (PSCC) anomalous configuration: yes/no
- VA enlargement: yes/no (when equivocal, Pöschl views were generated, and >0.9 mm at midpoint was considered enlarged²⁹)
- Facial nerve canal course medially deviated: yes/no
- Facial nerve canal widened: yes/no (widened defined as >1.42 mm²²)
- IAC widened (bulbous- or funnel-shaped): yes/no
- Eustachian tube (ET) dilated: yes/no
- Ossicular anomalies: yes/no

To accurately assess cochlear morphology, including whether there was apical hypoplasia, we took care to count the turns of the cochlea correctly. Fitch et al⁷ and Chen et al⁵ mentioned “fifths” of a cochlea, with an absent apical turn resulting in four-fifths of the cochlea remaining, designating each half turn as one-fifth of a cochlea, for a total of 2.5 turns. By means of this method, the basal turn spans the length from the round window to the medial bend (the first fifth) and then from the medial bend back laterally (second fifth), completing the basal turn. The middle turn then starts from lateral to medial (the third fifth) and then from medial back to lateral (fourth fifth). Finally, the apical turn extends from lateral to medial (last fifth) (Online Supplemental Data). The portion of the cochlea close to the round window has

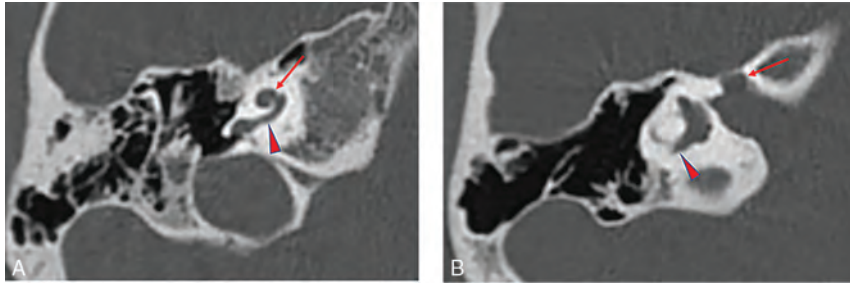


FIG 1. Temporal bone imaging appearance in a patient with *EYA1*-BOR. A, Axial CT image in bone algorithm shows an offset cochlea; the middle turn (arrow) is aligned more anteromedially than usual relative to the basal turn (arrowhead). The cochlea is, overall, small with a hypoplastic apical turn. B, Axial CT image in bone algorithm at a more superior level shows a medialized and widened labyrinthine facial nerve canal (arrow). The PSCC is anomalous, appearing as a blind-ending tubular structure (arrowhead).

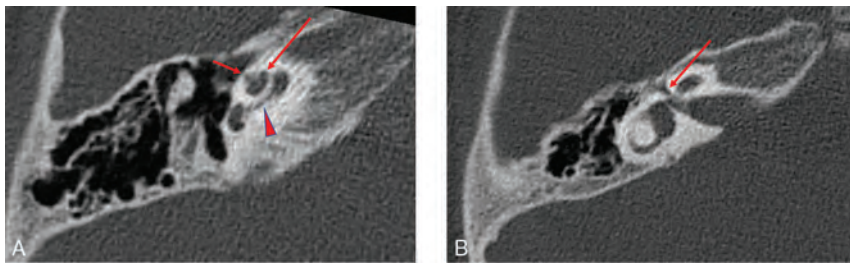


FIG 2. Temporal bone imaging appearance in a patient with *SIX1*-BOR. A, Axial CT image in bone algorithm shows absence of the cochlear offset; the middle turn (long arrow) is normally aligned relative to the basal turn (arrowhead) without anteromedial displacement. The thorny apical turn can also be appreciated (short arrow). B, Axial CT image in bone algorithm at a more superior level shows a normal course of the labyrinthine facial nerve canal (arrow) without medialization or widening.

a bulbous configuration that contributes to the outward convex shape of the cochlear promontory. It contains the most basal part of the cochlear duct and the cul-de-sac of the endolymphatic space where the osseous spiral lamina, spiral ligament, and basilar membrane merge. This portion of the cochlea forms a “three-dimensional (3D) ‘fish-hook’-like shape”^{34–36} and has been referred to as the “hook region” (Online Supplemental Data).^{37,38} The hook region extends from the edge of the vestibule and round window to the point where the cochlea begins to coil. For consistency during image assessment, we considered the hook region of the cochlea as part of the basal turn and thus part of the first fifth.

When there was a disagreement between the 2 reviewers, consensus reading (blinded to genotype) was performed.

Statistical Analysis

Comparison among group demographics was made with the Mann-Whitney *U* test for continuous nonparametric variables. A Cohen weighted κ statistic was calculated to assess interrater reliability for each phenotypic parameter and categorized as poor (<0.2), fair (0.20–0.39), moderate (0.40–0.59), good (0.60–0.79), or excellent (≥ 0.80). Differences between the *EYA1*-BOR and *SIX1*-BOR groups for each parameter were assessed using the Fisher exact test. $P = .05$ was set as the threshold of significance.

Statistical analyses were performed using SAS Studio, Version 3.8 (SAS Institute).

RESULTS

Nineteen unrelated individuals (38 ears) met the inclusion criteria; 15 individuals (30 ears) had mutations in the *EYA1* gene, and 4 individuals (8 ears) had mutations in the *SIX1* gene.

Of the 19 patients, 14 underwent CT and 5 underwent MR imaging. Among the *EYA1* genotype population, there were 11 males and 4 females, with a median age of 4.5 years (range, 2 months to 26 years). Among the *SIX1* genotype population, there were 3 males and 1 female, with a median age of 4 years (range, 3 months to 13 years). There were no statistically significant differences in age and sex among the groups.

Thirteen phenotypic parameters were examined for each ear. Results recorded by the 2 raters showed excellent interrater reliability ($\kappa \geq 0.80$). A few discrepancies were limited to qualitative assessments, including determination of modiolar structure, VA enlargement, facial nerve canal course, IAC width, and ET dilation. Notably, perfect observer agreement was seen for the quantifiable phenotypes, including assessment of the cochlear offset.

Differences in temporal bone features between patients with *EYA1*-BOR and *SIX1*-BOR reached statistical significance ($P < .05$) in 9 of 13 structures evaluated: cochlear offset, cochlear hypoplasia, apical turn hypoplasia, modiolar abnormality, VA enlargement, labyrinthine facial nerve canal medialization, IAC widening, ET dilation, and ossicular abnormalities (Online Supplemental Data). Of these, the structural feature that was most divergent between the 2 patient populations was cochlear offset, which was present in 100% of patients with *EYA1*-BOR and in only 1 ear among the patients with *SIX1*-BOR. This *SIX1*-BOR ear had an offset cochlea that did not resemble the offset cochleae seen among the *EYA1*-BOR population, including absence of basal turn tapering. The *EYA1*-BOR phenotype in our sample population was characterized by having cochlear offset, cochlear hypoplasia, apical turn hypoplasia, abnormal modiolus, VA enlargement, medialization of the facial nerve course, widening of the IAC, ET dilation, and ossicular anomalies (Fig 1). Individuals with *SIX1* mutations were significantly less likely to have these phenotypic anomalies (Fig 2). Cochlear fossa stenosis, a small LSCC bone island, PSCC anomaly, and facial nerve canal widening were less prevalent in the *SIX1*-BOR group but did not reach a statistically significant difference compared with the *EYA1*-BOR group ($P > .05$). The Online Supplemental Data summarize the findings.

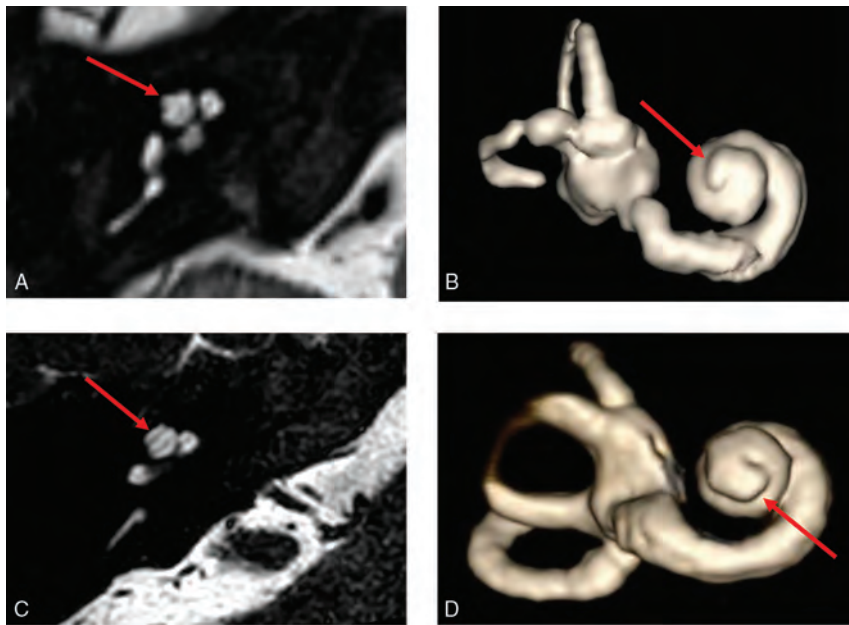


FIG 3. Thorny apical turn of the *SIX1*-BOR cochlea. Axial heavily T2-weighted MR image (A) and 3D reconstruction of the cochlea (B) show a short, thin, protuberant projection forming the apical turn, imparting upon it a thorny morphology (arrows in A and B). Contrast it with the normal apical turn morphology in a patient with normal hearing and no history of BOR or sensorineural hearing loss (C and D), which is longer with a smooth flat appearance and rounded end (arrows in C and D).

Among the *SIX1*-BOR group, the 1 ear with cochlear offset did not have an apical turn, and 2 ears (in 1 patient) did not allow detailed apical turn morphology assessment due to the spatial resolution of MR imaging in that study. In the remaining 5 ears, all had a distinct short protuberant appearance to the cochlear apical turn reminiscent of a poking thorn, which we termed a “thorny” apical turn (Fig 3).

DISCUSSION

In our assessment of 19 patients with BOR, the classic unwound or offset cochlea was seen among all those with the *EYA1* mutation but in only 1 ear among those with the *SIX1* mutation. Notably, however, this cochlea did not have the typical appearance of the *EYA1*-BOR offset cochlea with a tapered basal turn but rather had features more closely resembling a cochlear hypoplasia type 4 (CH4) anomaly.³⁹ In addition, the *SIX1* genotype did not demonstrate most of the other previously described cochlear anomalies nor additional temporal bone findings such as VA enlargement, medially displaced labyrinthine facial nerve, widened IAC, ET dilation, and ossicular anomalies.^{5,21,22,40} Furthermore, most with the *SIX1*-BOR genotype had a characteristic short protuberant thorny apical turn, a feature not seen among the *EYA1*-BOR genotype population. This finding suggests distinct genotype-phenotype differences within BOR syndrome with regard to the temporal bone.

EYA1 was the first gene identified to cause BOR syndrome.^{41–44} It plays a role in the development of the inner ear and surrounding mesenchyme, as well as metanephric cells surrounding ureteric

branches in renal development.⁴⁵ In 2004, Chang et al⁹ analyzed phenotypic data from families with *EYA1* mutations and proposed criteria for clinical diagnosis, ushering in the modern diagnostic criteria for BOR (Table). In 2005, Propst et al²² described temporal bone CT findings in 13 families with BOR syndrome diagnosed on the basis of the criteria of Chang et al. In 2006, the term “offset” was coined by Robson²³ to describe “tapering of the basal turn of the cochlea,” and “small middle and apical turns that are offset anteriorly and appear separated from the basal turn” and deemed “characteristic of BOR syndrome.” Of note, many of these descriptions were made when *EYA1* was the sole known gene for BOR syndrome.

However, in 2003 and 2004, Ruf et al^{17,18} identified a second gene locus that mapped to human chromosome 14q23.1, where the *SIX1*, *SIX4*, and *SIX6* genes reside. Three different *SIX1* mutations were identified in 4 BOR/branchio-oto (BO) kindreds. Thus, *SIX1* became a second known gene that can be associated with BOR syndrome.

Sanggaard et al¹⁹ discovered a low frequency (25%) of branchial arch malformation and the absence of renal pathology among patients with BOR with *SIX1* mutations, and there was one patient with no temporal bone malformation. They suggested that there may be clinical differences in patients with BOR with *EYA1* and *SIX1* mutations. Genotype-phenotype correlation studies are, therefore, of much interest.

We discovered different temporal bone phenotypes: The *SIX1* genotype did not show the classic temporal bone anomalies described in the radiology literature for BOR syndrome. In particular, the unwound or offset cochlea was observed in all individuals in our cohort with the *EYA1* genotype but in almost none with the *SIX1* genotype, showing instead a short, protuberant, thorny apical turn.

Mammalian inner ear development is a complex process dependent on the interaction of many genes. Studies in mouse models showed that during embryologic development, *EYA1* and *SIX1* are both expressed in the ventral part of the otic vesicle from which the cochlear structures are derived.⁴⁶ Most important, expression of *SIX1* in the otic vesicle is dependent on *EYA1*, whereas the expression of *EYA1* is unaffected in *SIX1* murine knockout models.⁴⁷ This finding may explain why the cochlear phenotype in patients with *EYA1*-BOR is more severe than in patients with *SIX1*-BOR. It is of interest that the expression of *SIX1* in the mammalian inner ear is more prominent in the apex of the cochlea than in the base.⁴⁷ This feature may have relevance to the finding of a thorny apical turn in our cohort with the *SIX1* genotype, but further work is needed to understand this issue.

Regarding the 1 case with a unilateral cochlear abnormality with features of CH4, it is unclear whether these features are within the wider spectrum of the *SIX1* phenotype or if there is a secondary explanation. The *SIX1* variant in this case (Cys16Tyr) is notable for its location toward the N-terminal (SIX domain) within an α helix critical for EYA interaction. Although this variant has not been reported before in the literature, a variant at the adjacent amino acid residue (V17E/Val17Glu) has been the subject of functional work. Patrick et al^{12,48} studied the effect of a number of *SIX1* variants on the EYA-SIX1-DNA complex and concluded that *SIX1*-BOR mutations contributed to the disease pathology through at least 2 different mechanisms: In most cases (all C-terminal to this mutation and not in the α helix), the mechanism appeared to be related to diminished ability of *SIX1* to bind DNA; another mechanism was seen in a case of the V17E mutation, in which formation of the *SIX1*-EYA complex was completely abolished and nuclear localization of the complex was not observed. This mechanism was not seen in any of the other *SIX1*-BOR mutations modeled.

Therefore, one theory to account for the unilateral cochlear abnormality in our *SIX1* Cys16Tyr variant is that mutations in the α helical domain are functionally distinct and may lead to a different *SIX1* inner ear phenotype. Of note, an unaffected sibling (*SIX1* genetic analysis normal) of this proband had several ear tags, so it may be that there are secondary genetic modifying factors impacting the clinical presentation; *EYA1* was also fully sequenced, and multiplex ligation-dependent probe amplification was undertaken in the proband with negative findings. Unfortunately, clinical data reported for the V17E case were limited and did not include imaging,¹¹ and the number of reported *SIX1*-BOR cases in the literature overall remains small. It is difficult to draw any firm conclusions from this specific case, but functional studies of the Cys16Tyr *SIX1* variant and further imaging in *SIX1* cases, particularly those involving the α helix, may help resolve this issue.

Some limitations of this study include its retrospective nature, different CT/MR imaging protocols, and its relatively small sample size. In the future, we would benefit from a prospective clinico-radiologic study involving all organ systems involved in BOR syndrome for precise genotype-phenotype correlation.

CONCLUSIONS

We found a significant difference between the BOR *EYA1* and *SIX1* genotype-phenotypes in the temporal bone. The *SIX1* phenotype is associated with a lack of cochlear offset, a thorny apical turn, as well as a relative absence of many other previously reported temporal bone anomalies. This shows that cochlear offset is not a characteristic feature nor a reliable indicator for all BOR cases; specifically, it is seen with the BOR *EYA1* genotype but is not sensitive nor specific for the detection of the BOR *SIX1* genotype. Thus, the lack of cochlear offset on imaging does not exclude the diagnosis of BOR and, in fact, may be predictive of the *SIX1* genotype in an individual with clinically suspected BOR. Careful radiologic delineation of the temporal bone and inner ear structures has the potential to help establish specific and sensitive features to aid in multidisciplinary genomic variant interpretation in suspected cases of BOR.

ACKNOWLEDGMENTS

We would like to thank Julia Wei, MPH, for statistical consultation, and Stephen Kovach, RT, for assistance with 3D modeling and construction.

Disclosure forms provided by the authors are available with the full text and PDF of this article at www.ajnr.org.

REFERENCES

- Fraser FC, Sproule JR, Halal F. Frequency of the branchio-oto-renal (BOR) syndrome in children with profound hearing loss. *Am J Med Genet* 1980;7:341–49 CrossRef Medline
- Heimler A, Lieber E. Branchio-oto-renal syndrome: reduced penetrance and variable expressivity in four generations of a large kindred. *Am J Med Genet* 1986;25:15–27 CrossRef Medline
- Melnick M, Bixler D, Silk K, et al. Autosomal dominant branchio-otorenal dysplasia. *Birth Defects Orig Artic Ser* 1975;115:121–28 Medline
- Melnick M, Bixler D, Nance WE, et al. Familial branchio-oto-renal dysplasia: a new addition to the branchial arch syndromes. *Clin Genet* 1976;9:25–34 CrossRef Medline
- Chen A, Francis M, Ni L, et al. Phenotypic manifestations of branchio-oto-renal syndrome. *Am J Med Genet* 1995;58:365–70 CrossRef Medline
- Fraser FC, Ling D, Clogg D, et al. Genetic aspects of the BOR syndrome—branchial fistulas, ear pits, hearing loss, and renal anomalies. *Am J Med Genet* 1978;2:241–52 CrossRef Medline
- Fitch N, Lindsay JR, Srolovitz H. The temporal bone in the preauricular pit, cervical fistula, hearing loss syndrome. *Ann Otol Rhinol Laryngol* 1976;85(2 Pt1):268–75 CrossRef Medline
- Ng YY, Bellman S, Phelps PD. Computed tomography of earpits-deafness syndrome. *Br J Radiol* 1989;62:947–49 CrossRef Medline
- Chang EH, Menezes M, Meyer NC, et al. Branchio-oto-renal syndrome: the mutation spectrum in *EYA1* and its phenotypic consequences. *Hum Mutat* 2004;23:582–89 CrossRef Medline
- Abdelhak S, Kalatzis V, Heilig R, et al. A human homologue of the *Drosophila* eyes absent gene underlies branchio-oto-renal (BOR) syndrome and identifies a novel gene family. *Nat Genet* 1997;15:157–64 CrossRef Medline
- Kochhar A, Orten DJ, Sorensen JL, et al. *SIX1* mutation screening in 247 branchio-oto-renal syndrome families: a recurrent missense mutation associated with BOR. *Hum Mutat* 2008;29:565 CrossRef Medline
- Patrick AN, Cabrera JH, Smith AL, et al. Structure-function analyses of the human *SIX1*-*EYA2* complex reveal insights into metastasis and BOR syndrome. *Nat Struct Mol Biol* 2013;20:447–53 CrossRef Medline
- Li X, Oghi KA, Zhang J, et al. Eya protein phosphatase activity regulates *Six1*-Dach-Eya transcriptional effects in mammalian organogenesis. *Nature* 2003;426:247–54 CrossRef Medline
- Krug P, Morinière V, Marlin S, et al. Mutation screening of the *EYA1*, *SIX1*, and *SIX5* genes in a large cohort of patients harboring branchio-oto-renal syndrome calls into question the pathogenic role of *SIX5* mutations. *Hum Mutat* 2011;32:183–90 CrossRef Medline
- Morisada N, Nozu K, Iijima K. Branchio-oto-renal syndrome: comprehensive review based on nationwide surveillance in Japan. *Pediatr Int* 2014;56:309–14 CrossRef Medline
- Unzaki A, Morisada N, Nozu K, et al. Clinically diverse phenotypes and genotypes of patients with branchio-oto-renal syndrome. *J Hum Genet* 2018;63:647–56 CrossRef Medline
- Ruf RG, Berkman J, Wolf MT, et al. A gene locus for branchio-otic syndrome maps to chromosome 14q21.3-q24.3. *J Med Genet* 2003;40:515–19 CrossRef Medline

18. Ruf RG, Xu PX, Silvius D, et al. **SIX1 mutations cause branchio-oto-renal syndrome by disruption of EYA1-SIX1-DNA complexes.** *Proc Natl Acad Sci U S A* 2004;101:8090–95 CrossRef Medline
19. Sanggaard KM, Rendtorff ND, Kjaer KW, et al. **Branchio-oto-renal syndrome: detection of EYA1 and SIX1 mutations in five out of six Danish families by combining linkage, MLPA and sequencing analyses.** *Eur J Hum Genet* 2007;15:1121–31 CrossRef Medline
20. Hoskins BE, Cramer CH, Silvius D, et al. **Transcription factor SIX5 is mutated in patients with branchio-oto-renal syndrome.** *Am J Hum Genet* 2007;80:800–04 CrossRef Medline
21. Ceruti S, Stinckens C, Cremers CW, et al. **Temporal bone anomalies in the branchio-oto-renal syndrome: detailed computed tomographic and magnetic resonance imaging findings.** *Otol Neurotol* 2002;23:200–07 CrossRef Medline
22. Propst EJ, Blaser S, Gordon KA, et al. **Temporal bone findings on computed tomography imaging in branchio-oto-renal syndrome.** *Laryngoscope* 2005;115:1855–62 CrossRef Medline
23. Robson CD. **Congenital hearing impairment.** *Pediatr Radiol* 2006;36:309–24 CrossRef Medline
24. Hsu A, Desai N, Paldino MJ. **The unwound cochlea: a specific imaging marker of branchio-oto-renal syndrome.** *AJNR Am J Neuroradiol* 2018;39:2345–49 CrossRef Medline
25. Purcell D, Johnson J, Fischbein N, et al. **Establishment of normative cochlear and vestibular measurements to aid in the diagnosis of inner ear malformations.** *Otolaryngol Head Neck Surg* 2003;128:78–87 CrossRef Medline
26. Shim HJ, Shin JE, Chung JW, et al. **Inner ear anomalies in cochlear implantees: importance of radiologic measurements in the classification.** *Otol Neurotol* 2006;27:831–37 CrossRef Medline
27. D'Arco F, Talenti G, Lakshmanan R, et al. **Do measurements of inner ear structures help in the diagnosis of inner ear malformations? A review of literature.** *Oto Neurotol* 2017;38:e384–92 CrossRef Medline
28. Naganawa S, Koshikawa T, Iwayama E, et al. **MR imaging of the enlarged endolymphatic duct and sac syndrome by use of a 3D fast asymmetric spin-echo sequence: volume and signal-intensity measurement of the endolymphatic duct and sac and area measurement of the cochlear modiolus.** *AJNR Am J Neuroradiol* 2000;219:1664–69 Medline
29. Juliano AF, Ting EY, Mingkwansook V, et al. **Vestibular aqueduct measurements in the 45° oblique (Pöschl) plane.** *AJNR Am J Neuroradiol* 2016;37:1331–37 CrossRef Medline
30. Adunka OF, Jewells V, Buchman CA. **Value of computed tomography in the evaluation of children with cochlear nerve deficiency.** *Otol Neurotol* 2007;28:597–604 CrossRef Medline
31. Wilkins A, Prabhu SP, Huang L, et al. **Frequent association of cochlear nerve canal stenosis with pediatric sensorineural hearing loss.** *Arch Otolaryngol Head Neck Surg* 2012;138:383–88 CrossRef Medline
32. Stjernholm C, Muren C. **Dimensions of the cochlear nerve canal: a radioanatomic investigation.** *Acta Otolaryngol* 2002;122:43–48 CrossRef Medline
33. Henderson E, Wilkins A, Huang L, et al. **Histopathologic investigation of the dimensions of the cochlear nerve canal in normal temporal bones.** *Int J Pediatr Otorhinolaryngol* 2011;75:464–67 CrossRef Medline
34. Stidham KR, Roberson JB Jr. **Cochlear hook anatomy: evaluation of the spatial relationship of the basal cochlear duct to middle ear landmarks.** *Acta Otolaryngol* 1999;119:773–77 CrossRef Medline
35. Li PM, Wang H, Northrop C, et al. **Anatomy of the round window and hook region of the cochlea with implications for cochlear implantation and other endocochlear surgical procedures.** *Otol Neurotol* 2007;28:641–48 CrossRef Medline
36. Schart-Morén N, Agrawal SK, Ladak HM, et al. **Effects of various trajectories on tissue preservation in cochlear implant surgery: a micro-computed tomography and synchrotron radiation phase-contrast imaging study.** *Ear Hear* 2019;40:393–400 CrossRef Medline
37. Kim N, Steele CR, Puria S. **The importance of the hook region of the cochlea for bone-conduction hearing.** *Biophys J* 2014;107:233–41 CrossRef Medline
38. Atturo F, Barbara M, Rask-Andersen H. **On the anatomy of the “hook” region of the human cochlea and how it relates to cochlear implantation.** *Audiol Neurotol* 2014;19:378–85 CrossRef Medline
39. Talenti G, Manara R, Brotto D, et al. **High-resolution 3 T magnetic resonance findings in cochlear hypoplasias and incomplete partition anomalies: a pictorial essay.** *Br J Radiol* 2018;91:20180120 CrossRef Medline
40. Hsu TR, Niu DM. **Fabry disease: review and experience during newborn screening.** *Trends Cardiovasc Med* 2018;28:274–81 CrossRef Medline
41. Smith RJ, Coppage KB, Ankerstjerne JK, et al. **Localization of the gene for branchiootorenal syndrome to chromosome 8q.** *Genomics* 1992;14:841–44 CrossRef Medline
42. König R, Fuchs S, Dukiet C. **Branchio-oto-renal (BOR) syndrome: variable expressivity in a five-generation pedigree.** *Eur J Pediatr* 1994;153:446–50 CrossRef Medline
43. Ni L, Wagner MJ, Kimberling WJ, et al. **Refined localization of the branchiootorenal syndrome gene by linkage and haplotype analysis.** *Am J Med Genet* 1994;51:176–84 CrossRef Medline
44. Wang Y, Treat K, Schroer RJ, et al. **Localization of branchio-oto-renal (BOR) syndrome to a 3 Mb region of chromosome 8q.** *Am J Med Genet* 1994;51:169–75 CrossRef Medline
45. Mackowetzky K, Yoon KH, Mackowetzky EJ, et al. **Development and evolution of the vestibular apparatuses of the inner ear.** *J Anat* 2021;239:801–28 CrossRef Medline
46. Chatterjee S, Kraus P, Lufkin T. **A symphony of inner ear developmental control genes.** *BMC Genet* 2010;11:68 CrossRef Medline
47. Zheng W, Huang L, Wei Z-B, et al. **The role of Six1 in mammalian auditory system development.** *Development* 2003;130:3989–4000 CrossRef Medline
48. Patrick AN, Schiemann BJ, Yang K, et al. **Biochemical and functional characterization of six SIX1 branchio-oto-renal syndrome mutations.** *J Biol Chem* 2009;284:20781–90 CrossRef Medline

Rates of Epidural Blood Patch following Lumbar Puncture Comparing Atraumatic versus Bevel-Tip Needles Stratified for Body Mass Index

J.T. Philip, M.A. Flores, R.D. Beegle, S.C. Dodson, S.A. Messina, and J.V. Murray

ABSTRACT

BACKGROUND AND PURPOSE: Postdural puncture headache, a known complication of lumbar puncture, typically resolves with conservative management. Symptoms persist in a minority of patients, necessitating an epidural blood patch. One method of decreasing rates of postdural puncture headache is using atraumatic, pencil-point needles rather than bevel-tip needles. To the best of our knowledge, this is the first study comparing epidural blood patch rates between pencil- and bevel-tip needles with a subgroup analysis based on body mass index.

MATERIALS AND METHODS: This single-institution retrospective study identified 4435 patients with a recorded body mass index who underwent a lumbar puncture with a 22-ga pencil-tip Whitacre needle, a 20-ga bevel-tip Quincke needle, or a 22-ga Quincke needle. The groups were stratified by body mass index. We compared epidural blood patch rates between 22-ga pencil-tip Whitacre needles versus 22-ga Quincke needles and 22-ga Quincke needles versus 20-ga bevel-tip Quincke needles using the Fischer exact test and χ^2 test.

RESULTS: Postdural puncture headache necessitating an epidural blood patch was statistically more likely using a 22-ga Quincke needle in all patients ($P < .001$) and overweight ($P = .03$) and obese ($P < .001$) populations compared with using a 22-ga pencil-tip Whitacre needle. In the normal body mass index population, there was no statistically significant difference in epidural blood patch rates when using a 22-ga pencil-tip Whitacre needle compared with a 22-ga Quincke needle ($P = .12$). There was no significant difference in epidural blood patch rates when comparing a 22-ga Quincke needle versus a 20-ga bevel-tip Quincke needle in healthy ($P = .70$), overweight ($P = .69$), or obese populations ($P = .44$).

CONCLUSIONS: Using a 22-ga pencil-tip Whitacre needle resulted in lower epidural blood patch rates compared with a 22-ga Quincke needle in all patients. Subgroup analysis demonstrated a statistically significant difference in epidural blood patch rates in overweight and obese populations, but not in patients with a normal body mass index.

ABBREVIATIONS: BMI = body mass index; EBP = epidural blood patch; LP = lumbar puncture; PDPH = postdural puncture headache; 20Q = 20-ga bevel-tip Quincke needle; 22Q = 22-ga bevel-tip Quincke needle; 22W = 22-ga pencil-tip Whitacre needle

The lumbar puncture (LP), first introduced in the late 1800s, is a common and critically important minimally invasive procedure performed across varied medical specialties. Most commonly performed as a diagnostic procedure to obtain CSF for laboratory testing, LPs are also performed for myelography and various therapeutic applications.¹ The risk of severe complications associated with LP is low; however, minor complications

are frequently encountered in clinical practice, the most common being a postdural puncture headache (PDPH).^{2,3} Characteristics of PDPH commonly include positional exacerbation in the upright position. Patients may also experience neck stiffness, nausea, vomiting, hearing loss, tinnitus, vertigo, visual disturbances, and paresthesia. In severe cases, symptoms can include cranial nerve palsies and seizures.¹

The cause of PDPH is believed to be secondary to leakage of CSF from the dural defect created by the needle during the LP.^{1,4,5} There are several accepted noninvasive strategies and treatments to alleviate PDPH; however, the most common invasive treatment is the epidural blood patch (EBP).^{6,7} An EBP requires the patient to undergo another procedure during which a sterile blood draw is performed and subsequently injected into the patient's epidural space to mitigate the leakage of CSF from

Received October 16, 2020; accepted after revision November 10, 2021.

From the AdventHealth Medical Group Radiology at Central Florida (J.T.P., M.A.F., R.D.B., S.C.D.), Orlando, Florida; Department of Neuroradiology (S.A.M.), Mayo Clinic Rochester, Rochester, Minnesota; and Department of Neuroradiology (J.V.M.), Mayo Clinic, Jacksonville, Florida.

Please address correspondence to Justin T. Philip, MD, AdventHealth Medical Group Radiology at Central Florida, 601 E Rollins St, Orlando, FL 32803; e-mail: Justin.philip.md@adventhealth.com
<http://dx.doi.org/10.3174/ajnr.A7397>

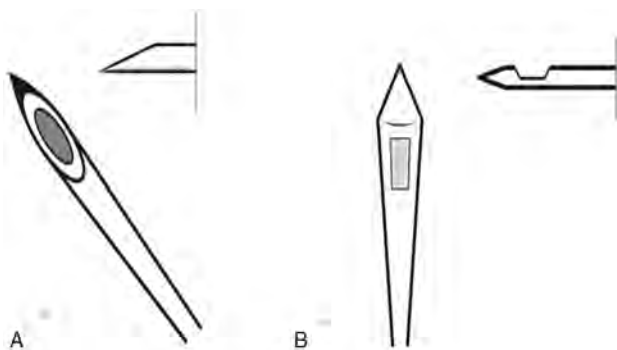


FIGURE. A, A conventional needle with a sharp bevel tip has a cutting tip with the needle orifice incorporated within the tip. B, A pencil-point atraumatic tip has a blunt tip. The orifice is not directly continuous with the tip but rather adjacent to it.

the dural defect. No current consensus exists for the optimal amount of autologous blood to introduce into the epidural space, with the maximum volume dependent on the patient's tolerance. This supplementary procedure for treating PDPH not only carries additional risks of complications, including temporary worsening of headache, infection, low back pain, and radicular pain, but also results in increased cost to the patient and institution.¹

Numerous studies have been conducted to identify the factors related to the increased incidence of PDPH.^{5,8-10} Needles with pencil-point atraumatic tips have been shown to decrease the rates of PDPH compared with conventional needles with a sharp bevel tip (Figure).^{1,5,8-10} Additional identified predisposing factors for PDPH include female sex, prior PDPH, and needle size.^{4,9,11} The impact that body mass index (BMI) has on rates of PDPH is unclear, with prior studies providing evidence that a higher BMI may be protective.^{9,12}

This study highlights our experience with >4400 patients and, to our knowledge, is the first study that compares the incidence of EBP with needle type when stratified for BMI. The objective of this study was to compare EBP rates between pencil- and bevel-tip needles with a subgroup analysis based on BMI.

MATERIALS AND METHODS

Patients and Clinical Data

A single-institution retrospective review was conducted as a quality-improvement project. A Montage (Montage Healthcare Solutions) search for fluoroscopy-guided LP within the radiology department between January 2009 and January 2017 yielded 4854 patients, including inpatient, outpatient, and emergency department referrals. Among these patients, 146 patients were excluded secondary to different needle types or sizes, 110 patients were excluded secondary to unknown needle type or size, and 163 patients were excluded secondary to lack of an available BMI. The total number of patients meeting the inclusion criteria that required EBP within 10 days of the LP was 127.

As per AdventHealth institutional policy, radiologists performed all lumbar punctures under fluoroscopic guidance. No formal criteria existed to determine the use of a Whitacre or

Table 1: Characteristics of study cohort^a

	EBP (n = 127)	No EBP (n = 4308)	P Value
BMI	28.69 (8.09)	29.34 (8.27)	.25
BMI group			.56
<25	47 (3.25)	1399 (96.75)	
25–30	33 (2.65)	1212 (97.35)	
>30	47 (2.69)	1697 (97.31)	
Needle type/size			<.001
22W	30 (1.38)	2147 (98.62)	
20Q	69 (4.6)	1431 (95.4)	
22Q	28 (3.69)	730 (96.31)	

^a The numeric values are reported with percentages in parentheses.

Quincke needle, and the needle use was determined by the radiologist's preference. After the procedure, before discharge, all patients were placed on 1- to 2-hour bed rest with the head of the bed flat. Patients were instructed to drink fluids and refrain from strenuous activity for 24 hours. If patients developed intractable headaches that persisted longer than 48 hours, they were encouraged to call the department for EBP evaluation, at which time the procedure, risks, and benefits would be discussed in detail.

Patients were first stratified on the basis of the needle type used for the procedure, which included the pencil-point tip 22-ga Whitacre (22W) needle (Becton Dickinson Medical) and the sharp bevel-tip 22-ga Quincke (22Q) and 20-ga Quincke (20Q) needles (Becton Dickinson Medical). Further stratification among each group was conducted on the basis of BMI, including normal (BMI ≤ 25), overweight (BMI, 25 to ≤30), and obese (BMI >30). The rates of EBP were determined for each group and compared for 22W versus 22Q, and 22Q versus 20Q.

Statistical Analysis

Numeric variables were summarized as mean (SD). Categorical variables were summarized as frequency (%). A Wilcoxon Mann-Whitney test was used to compare the EBP for numeric variables (BMI) in Table 1. The Kruskal-Wallis test was used to test the BMI among needle type/size groups in Table 2. Multiple logistic regression was used to predict EBP with BMI and needle type/size controlled in Table 3. The χ^2 test was used to compare the EBP for the normal BMI categorical variables in Table 4. The Fisher exact test was used to compare the EBP for the overweight/obese categorical variables in Table 4. All analyses were performed at a significance level of 5% using SAS 9.4 (SAS Institute).

RESULTS

Characteristics of Study Cohort

Table 1 lists the characteristics of patients in our study cohort with regard to EBP use/lack of EBP use. There was no difference in EBP rates when factoring for BMI alone. Needle type impacted the rate of EBP and was lower in the 22W versus 22Q ($P < .001$) and 22W versus 20Q ($P < .001$).

Association of LP Needle Type and Patient's BMI

Table 2 reports an association with the patient's BMI and needle type, with the average BMI of patients in the 22W lower than that in the 22Q/20Q groups ($P < .001$); thus, there was a propensity in this study to use Quincke needles in larger patients.

Table 2: Association of LP needle type and patient's BMI

Variable	22W (n = 2177)	22Q (n = 758)	20Q (n = 1500)	P Value
BMI (mean)	27.75 (SD, 7.11)	33.28 (SD, 10.06)	29.61 (SD, 8.11)	<.001

Table 3: Multiple logistic regression to predict EBP (n = 4435)

	Estimate	P Value	OR (95% CI)
BMI ≤25 vs >30	0.1897	.1334	1.4 (0.922–2.126)
BMI <25 to ≤30 vs >30	−0.0427	.7566	1.11 (0.703–1.753)
BMI >30	Reference	Reference	Reference
22W vs 22Q	−0.777	<.0001	0.343 (0.202–0.582)
20Q vs 22Q	0.4833	<.0001	1.209 (0.769–1.9)
22Q	Reference	Reference	Reference

Table 4: EBP numeric value outcome of each needle type with respect to the BMI subgroup

Variable	EBP	No EBP	P Value
BMI ≤25			
Whitacre–Quincke			.12
22W (%)	17 (2.11)	787 (97.89)	
22Q (%)	7 (4.14)	162 (95.86)	
20Q–22Q			.70
20 ga (%)	23 (4.86)	450 (95.14)	
22 ga (%)	7 (4.14)	162 (95.86)	
BMI >25 to ≤30			
Whitacre–Quincke			.03
22W (%)	8 (1.2)	661 (98.8)	
22Q (%)	6 (3.8)	152 (96.2)	
20Q–22Q			.69
20 ga (%)	19 (4.55)	399 (95.45)	
22 ga (%)	6 (3.8)	152 (96.2)	
BMI >30			
Whitacre–Quincke			<.001
22W (%)	5 (0.71)	699 (99.29)	
22Q (%)	15 (3.48)	416 (96.52)	
20Q–22Q			.44
20 ga (%)	27 (4.43)	582 (95.57)	
22 ga (%)	15 (3.48)	416 (96.52)	

Comparison of Needle Type EBP Rates with BMI Controlled

Table 3 indicates the rates of EBP for each needle type when the BMI was controlled. Results show that there was an association of increased rates of EBP when using the 22Q compared with the 22W. The odds ratio of the EBP rate for the 22W compared with the 22Q was 0.34 (95% CI, 0.20–0.58; $P < .001$), indicating that the use of the Whitacre needle was associated with lower rates of EBP compared with the use of a Quincke needle. The odds ratio of the EBP rate for the 20Q compared with the 22Q was 1.21 ($P < .001$) (95% CI, 0.77–1.9), indicating no association of higher rates of EBP between 20- versus 22-ga Quincke needles.

Comparison of Needle Type EBP Rates Based on BMI Subgroup

The 22W resulted in lower rates of EBP compared with 22Q in the overweight (BMI, 25 to ≤30) and obese (BMI > 30) populations ($P = .03$ and $P < .001$, respectively). There was no statistically significant difference among patients with normal BMIs

($P = .12$). No difference existed in the rates of EBP within each subgroup between the 22Q and 20Q.

DISCUSSION

While multiple studies have shown the superiority of pencil-point needles in reducing the incidence of PDPH,^{1,5,8–10} the rates of EBP between needle type and BMI stratification have not been evaluated. The results of this study show that the use of a pencil-point needle reduces the rates of EBP despite the perceived technical difficulties in the overweight and obese populations. When controlling for BMI, the rates of EBP were lower when using the 22W compared with the 22Q, a finding consistent with that of Hatfield et al.¹³ Although there was a trend toward lower EBP rates among patients with normal BMIs using the 22W compared with the 22Q, there was no statistically significant difference. This could be an area of future study.

At our institution, needle selection was determined on the basis of the radiologist's preference, resulting in increased Quincke use in the obese population. One reason may be due to the physician's preference because the Quincke needle is more maneuverable, making it advantageous in the technically challenging heavier patient populations. However, the most likely explanation is that our institution supplied the Whitacre needle in only the 3.5-inch size, and the longer sizes were not available at the time of this study. This inherent preference resulted in a relatively larger number of Quincke needles used in the overweight/obese population, and a relatively smaller number, in normal-weight patients. Since performing this study, our radiology group has stocked the longer Whitacre needle sizes.

Several studies reported predisposing factors that lead to PDPH, including a history of PDPH and female sex.^{4,9,11} Other potential predisposing factors are a difficult LP, which may result in multiple dural punctures and increased fluoroscopy times. The limitations of this study are that these factors were not analyzed to determine whether a difference occurred between our subgroups and whether possible confounding variables could have occurred.

This study showed no difference in the rates of EBP between the 20Q and 22Q when the BMI was not controlled or within the BMI subgroups. This finding differed from the study performed by Hatfield et al,¹³ which showed that the use of a 20Q resulted in overall increased rates of EBP. The cause of this discrepancy is unclear, but generally, larger needles result in greater rates of PDPH,^{11,14,15} which is believed to be secondary to larger defects in the thecal sac; thus, we recommend the use of smaller-bore needles. The greatest limitation of this study was the retrospective design. Additionally, the lumbar punctures were performed by both board-certified radiologists and radiology residents under direct supervision.

CONCLUSIONS

Our study supports prior evidence that pencil-tip atraumatic needles reduce the rate of PDPH necessitating treatment with an EBP compared with sharp bevel-tip spinal needles. A subgroup analysis suggests that pencil-tip atraumatic needles should be used in overweight and obese populations despite their potentially inherent

technical disadvantages. In patients with normal BMIs, there was an observed trend toward lower EBP rates using pencil-tip atraumatic needles, though this was not statistically significant.

ACKNOWLEDGMENT

We would like to thank the biostatisticians Jiajing Wang and Yuan Du for their help with the statistical analysis.

REFERENCES

1. Turnbull DK, Shepherd DB. **Post-dural puncture headache: pathogenesis, prevention, and treatment.** *Br J Anaesth* 2003;91:718–29 CrossRef Medline
2. Doherty CM, Forbes RB. **Diagnostic lumbar puncture.** *Ulster Med J* 2014;83:93–102 Medline
3. Armon C, Evans RW; Therapeutics and Technology Assessment Subcommittee of the American Academy of Neurology. **Addendum to assessment: prevention of post-lumbar puncture headaches: report of the Therapeutics and Technology Assessment Subcommittee of the American Academy of Neurology.** *Neurology* 2005;65:510–12 CrossRef Medline
4. Headache Classification Committee of the International Headache Society (IHS) **The International Classification of Headache Disorders, 3rd Edition.** *Cephalalgia* 2018;38: 1–211 CrossRef Medline
5. Xu H, Liu Y, Song W, et al. **Comparison of cutting and pencil-point spinal needle in spinal anesthesia regarding postdural puncture headache.** *Medicine (Baltimore)* 2017;96:e6527–29 CrossRef Medline
6. Safa-Tisseront V, Thormann F, Malassiné P, et al. **Effectiveness of epidural blood patch in the management of post-dural puncture headache.** *Anesthesiology* 2001;95:334–39 CrossRef Medline
7. Van Kooten F, Oedit R, Bakker SL, et al. **Epidural blood patch in post dural puncture headache: a randomised, observer-blind, controlled clinical trial.** *J Neurol Neurosurg Psychiatry* 2008;79:553–58 CrossRef Medline
8. Rochwerf B, Almenawer AS, Siemieniuk RAC, et al. **Atraumatic (pencil-point) versus conventional needles for lumbar puncture: a clinical practice guideline.** *BMJ* 2018;361:k1920–26 CrossRef Medline
9. Engedal TS, Ørding H, Vilholm OJ. **Changing the needle for lumbar punctures.** *Clin Neurol Neurosurg* 2015;130:74–79 CrossRef Medline
10. Bertolotto A, Malentacchi M, Capobianco M, et al. **The use of the 25 Sprotte needle markedly reduces post-dural puncture headache in routine neurological practice.** *Cephalalgia* 2016;36:131–38 CrossRef Medline
11. Amorim JA, Gomes de Barros MV, Valença MM. **Post-dural (post-lumbar) puncture headache: risk factors and clinical features.** *Cephalalgia* 2012;32:916–23 CrossRef Medline
12. Franz AM, Jia SY, Bahnson HT, et al. **The effect of second-stage pushing and body mass index on postdural puncture headache.** *J Clin Anesth* 2017;37:77–81 CrossRef Medline
13. Hatfield MK, Handrich SJ, Willis JA, et al. **Blood patch rates after lumbar puncture with Whitacre versus Quincke 22- and 20-ga spinal needles.** *AJR Am J Roentgenol* 2008;190:1686–89 CrossRef Medline
14. Hudgins PA, Fountain AJ, Chapman PR, et al. **Difficult lumbar puncture: pitfalls and tips from the trenches.** *AJNR Am J Neuroradiol* 2017;38:1276–83 CrossRef Medline
15. Lavi R, Rowe JM, Avivi I. **Lumbar puncture: it is time to change the needle.** *Eur Neurol* 2010;64:108–13 CrossRef Medline

MRI Shrimp Sign in Sarcoidosis-Associated Cerebellar Progressive Multifocal Leukoencephalopathy

Adra et al¹ report on the shrimp sign, a highly sensitive and specific neuroimaging finding seen in patients with cerebellar progressive multifocal leukoencephalopathy (PML). We read their article with great interest because PML often poses a diagnostic challenge. This challenge is compounded for HIV-negative patients in whom an etiology of immunocompromise is not readily apparent. In particular, PML may occur in patients with systemic rheumatologic disorders, including those who are not on immunosuppressive or immunomodulatory medications.² In these patients, the shrimp sign described by Adra et al has the potential to avert misdiagnosis and obviate the need for invasive testing, such as brain biopsy.

The association between PML and sarcoidosis was first reported in 1955, when PML was found at postmortem examination in 6 patients with sarcoidosis whose neurologic symptoms that had been mistakenly attributed to neurosarcoidosis. It is hypothesized that general T-lymphocyte dysregulation and anergy, as well as the redistribution of CD4⁺ T-lymphocytes to sites of granuloma formation, may reduce immune surveillance and allow the reactivation of the JC virus in the brain. Misdiagnosis remains common in patients with sarcoidosis who develop PML, which is particularly concerning given the risk of worsened outcomes in patients with PML who are inappropriately treated with immunosuppressive or immunomodulatory therapies for presumed neurosarcoidosis.³ Patients with sarcoidosis and other systemic rheumatologic diseases may also be at higher risk for false-negative CSF JC virus testing results than more severely immunocompromised patients, requiring brain biopsy to facilitate diagnosis.⁴

Here, we report on 2 patients with sarcoidosis who presented with new neurologic symptoms and were successfully diagnosed

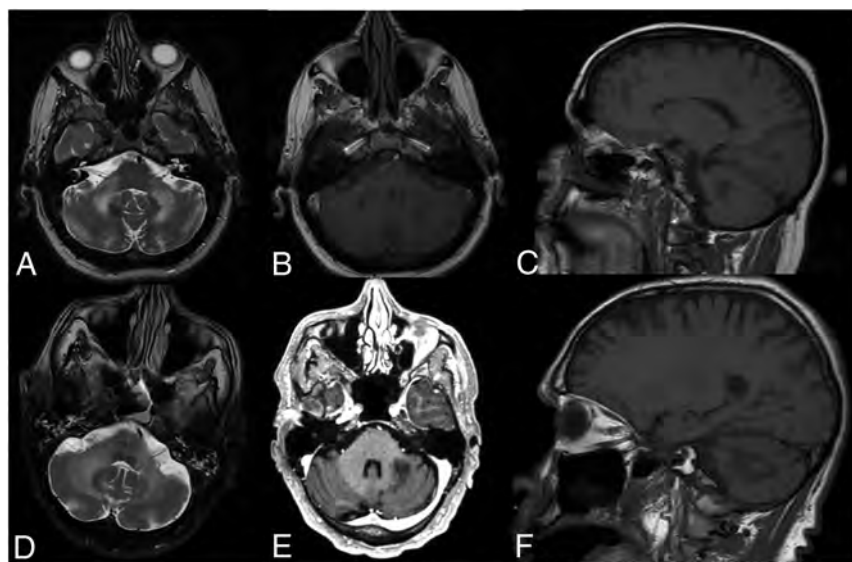


FIGURE. In both cases, brain MR imaging revealed well-defined, T2-hyperintense (patient 1 [A], patient 2 [D]) and T1-hypointense lesions (patient 1 [B and C], patient 2 [E and F]) of the cerebellar white matter abutting and sharply demarcating and outlining the dentate nucleus.

with PML using the MR imaging shrimp sign of Adra et al.¹ Patient 1 is a 49-year-old man with a history of pulmonary sarcoidosis, not on immunosuppression, who presented with imbalance, dysphagia, dysarthria, and incoordination of his right hand. Patient 2 was a 62-year-old man with a history of pulmonary, splenic, and cutaneous sarcoidosis, not on immunosuppression, who presented with incoordination of his left hand, imbalance, and scanning speech. MR imaging of the brain for both patients demonstrated well-defined, T2-hyperintense, T1-hypointense lesions of the cerebellar white matter abutting and sharply demarcating and outlining the dentate nucleus on the axial view (Figure), meeting the inclusion criteria for the shrimp sign of Adra et al. Both patients were misdiagnosed with neurosarcoidosis at an outside hospital, and patient 1 was treated with high-dose steroids. Following review of neuroimaging by physicians familiar with the

shrimp sign, the diagnosis of PML was confirmed by positive CSF JC virus PCR in both cases.

In light of these cases, we encourage physicians involved in the management of patients with sarcoidosis to familiarize themselves with the features of the shrimp sign of Adra et al,¹ which may help avert misdiagnosis and facilitate appropriate care of PML in this unique population.

Disclosure forms provided by the authors are available with the full text and PDF of this article at www.ajnr.org.

P. Anand and K.H. Vincent Lau shared first authorship.

REFERENCES

1. Adra N, Goodheart AE, Rapalino O, et al. **MRI shrimp sign in cerebellar progressive multifocal leukoencephalopathy: description and validation of a novel observation.** *AJNR Am J Neuroradiol* 2021;42:1073–79 CrossRef Medline
2. Anand P, Hotan GC, Vogel A, et al. **Progressive multifocal leukoencephalopathy: a 25-year retrospective cohort study.** *Neurol Neuroimmunol Neuroinflamm* 2019;6:e618 CrossRef Medline
3. Jamilloux Y, Neel A, Lecouffe-Desprets M, et al. **Progressive multifocal leukoencephalopathy in patients with sarcoidosis.** *Neurology* 2014;82:1307–13 CrossRef Medline
4. Ikeda J, Matsushima A, Ishii W, et al. **Brain biopsy is more reliable than the DNA test for JC virus in cerebrospinal fluid for the diagnosis of progressive multifocal leukoencephalopathy.** *Intern Med* 2017;56:1231–34 CrossRef Medline

 P. Anand

 K.H. Vincent Lau

 S. Martinez-Ramirez

Department of Neurology

Boston Medical Center

Boston University School of Medicine

Boston, Massachusetts